Energy, Environment, and Sustainability
Series Editor: Avinash Kumar Agarwal

Achintya Mukhopadhyay
Swarnendu Sen
Dipankar Narayan Basu
Sirshendu Mondal *Editors*

Dynamics and Control of Energy Systems

Springer

Energy, Environment, and Sustainability

Series Editor

Avinash Kumar Agarwal, Department of Mechanical Engineering,
Indian Institute of Technology Kanpur, Kanpur, Uttar Pradesh, India

This books series publishes cutting edge monographs and professional books focused on all aspects of energy and environmental sustainability, especially as it relates to energy concerns. The Series is published in partnership with the International Society for Energy, Environment, and Sustainability. The books in these series are edited or authored by top researchers and professional across the globe. The series aims at publishing state-of-the-art research and development in areas including, but not limited to:

- Renewable Energy
- Alternative Fuels
- Engines and Locomotives
- Combustion and Propulsion
- Fossil Fuels
- Carbon Capture
- Control and automation for Energy
- Environmental Pollution
- Waste Management
- Transportation Sustainability

More information about this series at http://www.springer.com/series/15901

Achintya Mukhopadhyay · Swarnendu Sen ·
Dipankar Narayan Basu · Sirshendu Mondal
Editors

Dynamics and Control of Energy Systems

Springer

Editors
Achintya Mukhopadhyay
Department of Mechanical Engineering
Jadavpur University
Jadavpur, Kolkata, West Bengal, India

Swarnendu Sen
Department of Mechanical Engineering
Jadavpur University
Jadavpur, Kolkata, West Bengal, India

Dipankar Narayan Basu
Department of Mechanical Engineering
Indian Institute of Technology Guwahati
Guwahati, Assam, India

Sirshendu Mondal
Department of Mechanical Engineering
National Institute of Technology Durgapur
Durgapur, West Bengal, India

ISSN 2522-8366 ISSN 2522-8374 (electronic)
Energy, Environment, and Sustainability
ISBN 978-981-15-0535-5 ISBN 978-981-15-0536-2 (eBook)
https://doi.org/10.1007/978-981-15-0536-2

This Springer imprint is published by the registered company Springer Nature Singapore Pte Ltd.
The registered company address is: 152 Beach Road, #21-01/04 Gateway East, Singapore 189721, Singapore

Preface

Energy demand has been rising remarkably due to increasing population and urbanization. Global economy and society are significantly dependent on the energy availability because it touches every facet of human life and activities. Transportation and power generation are two major examples. Without the transportation by millions of personalized and mass transport vehicles and availability of 24×7 power, human civilization would not have reached contemporary living standards.

The International Society for Energy, Environment, and Sustainability (ISEES) was founded at Indian Institute of Technology Kanpur (IIT Kanpur), India in January 2014 with an aim to spread knowledge/awareness and catalyze research activities in the fields of Energy, Environment, Sustainability, and Combustion. The Society's goal is to contribute to the development of clean, affordable, and secure energy resources and a sustainable environment for the society and to spread knowledge in the abovementioned areas and create awareness about the environmental challenges, which the world is facing today. The unique way adopted by the society was to break the conventional silos of specialications (engineering, science, environment, agriculture, biotechnology, materials, fuels, etc.) to tackle the problems related to energy, environment, and sustainability in a holistic manner. This is quite evident by the participation of experts from all fields to resolve these issues. The ISEES is involved in various activities such as conducting workshops, seminars, conferences in the domains of its interests. The society also recognizes the outstanding works done by the young scientists and engineers for their contributions in these fields by conferring them awards under various categories.

Third International Conference on "Sustainable Energy and Environmental Challenges" (III-SEEC) was organized under the auspices of ISEES from December 18 to 21, 2018, 2018 at Indian Institute of Technology Roorkee. This conference provided a platform for discussions between eminent scientists and engineers from various countries including India, USA, Norway, Finland, Sweden, Malaysia, Austria, Hong Kong, Bangaladesh, and Australia. In this conference, eminent speakers from all over the world presented their views related to different aspects of energy, combustion, emissions, and alternative energy resource for sustainable development and cleaner environment. The conference presented five

high-voltage plenary talks from globally renowned experts on topical themes, namely "The Evolution of Laser Ignition Over More than Four Decades" by Prof. Ernst Wintner, Technical University of Vienna, Austria; "Transition to Low Carbon Energy Mix for India", Dr. Bharat Bhargava, ONGC Energy Center; "Energy Future of India", By Dr. Vijay Kumar Saraswat, Hon. Member (S&T) NITI Ayog, Government of India; "Air Quality Monitoring and Assessment in India" by Dr. Gurfan Beig, Safar; and "Managing Large Technical Institutions and Assesmment Criterion for Talent Recruitment and Retention" by Prof. Ajit Chaturvedi, Director, IIT Roorkee.

The conference included 24 technical sessions on topics related to energy and environmental sustainability including 5 plenary talks, 27 keynote talks, and 15 invited talks from prominent scientists, in addition to 84 contributed talks, and 50 poster presentation by students and researchers. The technical sessions in the conference included Advances in IC Engines, Solar Energy, Environmental Biotechnology, Combustion, Environmental Sustainability, Coal and Biomass Combustion/Gasification, Air and Water Pollution, Biomass to Fuels/Chemicals, Combustion/Gas Turbines/Fluid Flow/Sprays, Energy and Environmental Sustainability, Atomization and Sprays, Sustainable Transportation and Environmental Issues, New Concepts in Energy Conservation, Waste to Wealth. One of the highlights of the conference was the Rapid Fire Poster Sessions in (i) Engine/Fuels/Emissions, (ii) Renewable and Sustainable Energy, and (iii) Biotechnology, where 50 students participated with great enthusiasm and won many prizes in a fiercely competitive environment. 200+ participants and speakers attended this 4 days conference, which is also hosted by Dr. Vijay Kumar Saraswat, Hon. Member (S&T) NITI Ayog, Government of India as the chief guest for the book release ceremony, where 14 ISEES books published by Springer, Singapore under a special dedicated series "Energy, environment and sustainability" were released. This was second time in a row that such significant and high-quality outcome has been achieved by any society in India. The conference concluded with a panel discussion on "Challenges, Opportunities and Directions for National Energy Security", where the panelists were Prof. Ernst Wintner, Technical University of Vienna, Prof. Vinod Garg, Central University of Punjab, Bhatinda; Prof. Avinash Kumar Agarwal, IIT Kanpur; and Dr. Michael Sauer, Boku University of Natural resources, Austria. The panel discussion was moderated by Prof. Ashok Pandey, Chairman, ISEES. This conference laid out the roadmap for technology development, opportunities, and challenges in Energy, Environment and Sustainability domain. All these topic are very relevant for the country and the world in present context. We acknowledge the support received from various funding agencies and organizations for the successful conduct of the Third ISEES conference III-SEEC, where these books germinated. We would therefore like to acknowledge NIT Srinagar, Uttarakhand (TEQIP) (special thanks to Prof. S. Soni, Director, NIT, UK), SERB, Government of India (Special thanks to Dr. Rajeev Sharma, Secretary); UP Bioenergy Development Board, Lucknow (special thanks to Sh. P. S. Ojha), CSIR, and our publishing partner Springer (special thanks to Swati Meherishi).

The editors would like to express their sincere gratitude to large number of authors from all over the world for submitting their high-quality work in a timely manner and revising it appropriately at a short notice. We would like express our special thanks to Prof. Asok Ray, Prof. Suman Chakraborty, Prof. Koushik Ghosh, Prof. Saptarshi Basu, Prof. Manmohan Pandey, Prof. Malay K. Das, Prof. Aritra Ganguly, Prof. Balkrishna Mehta, Prof. Dibakar Rakshit, Prof. Lin Chen, Prof. Ujjwal K. Saha, Prof. Arup K. Das, Prof. Suman Ghosh, Prof. Amaresh Dalal, Prof. Vinayak Kulkarni, Prof. Santosh K. Sahu, Prof. Abhishek Saha, Prof. Pallab S. Mahapatra, Prof. Sujit Nath, Prof. E. A. Gopalakrishnan, Prof. J. Venkatramani, Prof. Vineeth Nair, Prof. Lipika Kabiraj, Prof. Aditya Saurabh, Prof. Aparesh Datta, Prof. Sandip Sarkar, Dr. Ayyush Sharma, Dr. Vishnu R. Unni, Dr. Suman Saha, Dr. Meenatchidevi Murugesan, Dr. Samadhan Pawar, and Dr. Abin Krishnan who reviewed various chapters of this monograph and provided their valuable suggestions to improve the manuscripts.

Dynamic behavior of energy systems and their control are becoming important issues in energy conversion and management. New strategies are being developed for these studies, many of which are based on dynamical systems approach. This monograph is a collection of chapters covering research on dynamics and control of energy systems from different areas, namely, aeroelasticity, combustion, multiphase flow, nuclear, chemical, and thermal, and covers systems ranging from large-scale power plants to microscale devices. The chapters are pedagogic in nature, so that they can be accessed by researchers with little prior exposure to dynamical systems and control. In addition, two chapters at the beginning provide a general overview of different aspects of dynamical systems approach and time series analysis. This monograph would be useful for researchers and practicing engineers working in the field of dynamics and control of energy systems. We hope that this book would motivate particularly young researchers to take up new challenges in this area.

Kolkata, India — Achintya Mukhopadhyay
Kolkata, India — Swarnendu Sen
Guwahati, India — Dipankar Narayan Basu
Durgapur, India — Sirshendu Mondal

Contents

Editors and Contributors

About the Editors

Dr. Achintya Mukhopadhyay is a Professor of Mechanical Engineering at Jadavpur University, Kolkata (Calcutta), India. He also served as Professor of Mechanical Engineering at Indian Institute of Technology Madras. Dr.Mukhopadhyay also held visiting positions at Technical University of Munich where he was an Alexander von Humboldt Fellow and University of Illinois at Chicago. Dr.Mukhopadhyay's teaching and research interests include thermodynamics, heat transfer, combustion, multiphase flows and design and analysis of thermal systems. Dr.Mukhopadhyay has over 270 research publications including over 100 international journal publications. Prof. Mukhopadhyay is a Fellow of the West Bengal Academy of Science and Technology and International Society for Energy, Environment and Sustainability, recipient of INSA Teachers Award from Indian National Science Academy and life member of Indian Society of Heat and Mass Transfer and Indian section of the Combustion Institute.

Dr. Swarnendu Sen is a Professor of Mechanical Engineering at Jadavpur University, Kolkata (Calcutta), India. He also held visiting positions in University of Illinois at Chicago and Virginia Tech. He is a recipient of DAAD fellowship, with which he was associated with Technical University of Munich. His teaching and research areas are reacting and Multiphase flow, heat transfer and nanotechnology. Prof. Sen is a Fellow of the West Bengal Academy of Science and Technology and International Society for Energy, Environment and Sustainability. He is a life member of Indian Society of Heat and Mass Transfer and Indian section of the Combustion Institute. He authored about 300 research papers in various international journals and conferences.

Dr. Dipankar Narayan Basu is currently an Associate Professor in the department of Mechanical Engineering at Indian Institute of Technology Guwahati. He received his undergraduate and postgraduate degree from Jadavpur University, Kolkata, and completed his Ph.D. from Indian Institute of Technology Kharagpur in 2011. He served as an Assistant Professor at IIEST Shibpur for four years before joining IIT Guwahati. His principal research interest is in the field of nuclear thermalhydraulics, supercritical heat transfer, microchannel dynamics and fluid-structure interaction. He has co-authored more than 80 referred journal and conference publications. He is a regular reviewer of many reputed international journals and also associated with several sponsored projects.

Dr. Sirshendu Mondal is currently an Assistant Professor of Mechanical Engineering at National Institute of Technology Durgapur, India. He graduated with B.Tech in Mechanical Engineering from Kalyani Govt. Engineering College (KGEC) in 2006. He received M.E. (2008) and Ph.D. (2015) degree from Jadavpur University, Kolkata, India. Dr. Mondal carried out research for his Ph.D. thesis at Jadavpur University, India as a CSIR-SRF (Council of Scientific and Industrial Research- Senior Research Fellow) and partly at Technical University of Munich, Germany as a DAAD (German Academic Exchange Service)

Sandwich Fellow. He then worked as an Institute Post-Doctoral Fellow (IPDF) at IIT Madras for three years (2015-2018). He also served as Assistant Professor of Mechanical Engineering at Amrita Vishwa Vidyapeetham, Kerala. His teaching and research interests include thermodynamics, heat transfer, combustion, I.C. Engine, dynamical systems theory, time series analysis, etc. Dr. Mondal has over 30 research publications including 15 international journal publications and 3 book chapters. He is a recipient of Young Scientist Award of the International Society for Energy, Environment and Sustainability (ISEES) and a life member of ISEES.

Contributors

Manish Kumar Agrawal Discipline of Mechanical Engineering, Mahindra Ecole Centrale, Hyderabad, India

G. Ambika Indian Institute of Science Education and Research, Tirupati, India

M. S. Aswathy Indian Institute of Technology Madras, Chennai, India

Ankan Banerjee Department of Mathematics, National Institute of Technology Durgapur, Durgapur, India

Nikhil A. Baraiya Department of Aerospace Engineering, National Centre for Combustion Research and Development, Indian Institute of Technology Madras, Chennai, India

Dipankar Narayan Basu Department of Mechanical Engineering, Indian Institute of Technology Guwahati, Guwahati, India

Chandrachur Bhattacharya Department of Mechanical Engineering, Pennsylvania State University, State College, USA

S. R. Chakravarthy Department of Aerospace Engineering, National Centre for Combustion Research and Development, Indian Institute of Technology Madras, Chennai, India

Lin Chen Institute of Engineering Thermophysics, Chinese Academy of Sciences, Beijing, China;
School of Aeronautics and Astronautics, University of Chinese Academy of Sciences, Beijing, China

Malay K. Das Energy Conversion and Storage Laboratory, Department of Mechanical Engineering, Indian Institute of Technology Kanpur, Kanpur, UP, India

Tryambak Gangopadhyay Iowa State University, Ames, IA, USA

Suvankar Ganguly TATA Global R&D Division, Jamshedpur, India

Najah F. Ghalyan Department of Mechanical Engineering, Pennsylvania State University, State College, USA

Manojit Ghosh Department of Mathematics, National Institute of Technology Durgapur, Durgapur, India

Paromita Ghosh Department of Mathematics, National Institute of Technology Durgapur, Durgapur, India

Amitava Gupta Department of Power Engineering and School of Nuclear Studies and Applications, Jadavpur University, Kolkata, India

Raghvendra Gupta Indian Institute of Technology Guwahati, Guwahati, Assam, India

Sayan Gupta Department of Applied Mechanics, Indian Institute of Technology Madras, Chennai, India

K. P. Harikrishnan The Cochin College, Cochin, India

Kannan Iyer Department of Mechanical Engineering, Indian Institute of Technology, Bombay, Mumbai, India

M. Jithin Energy Conversion and Storage Laboratory, Department of Mechanical Engineering, Indian Institute of Technology Kanpur, Kanpur, UP, India

Lipika Kabiraj CDC Lab, Department of Mechanical Engineering, IIT Ropar, Rupnagar, PB, India

Prateek Khare Department of Chemical Engineering, Madan Mohan Malaviya University of Technology, Gorakhpur, Uttar Pradesh, India

Amit Kumar Department of Chemical Engineering, Indian Institute of Technology Guwahati, Guwahati, Assam, India

S. Krishna Kumar Indian Institute of Technology Madras, Chennai, India

Anthony Locurto Iowa State University, Ames, IA, USA

James B. Michael Iowa State University, Ames, IA, USA

Deepak Kumar Mishra Indian Institute of Technology Guwahati, Guwahati, Assam, India

Shivangi Mishra Nanomaterial Toxicology Group, CSIR-Indian Institute of Toxicology Research (CSIR-IITR), Lucknow, Uttar Pradesh, India

Mayank Modak Division of Advanced Nuclear Engineering (DANE), Pohang University of Science and Technology (POSTECH), Pohang, South Korea

Sirshendu Mondal Department of Mechanical Engineering, National Institute of Technology Durgapur, Durgapur, India

Sudeepta Mondal Department of Mechanical Engineering, Pennsylvania State University, State College, USA

Achintya Mukhopadhyay Department of Mechanical Engineering, Jadavpur University, Jadavpur, Kolkata, India

Yada Nandukumar Centre for Theoretical Studies, National Institute of Technology Kharagpur, Kharagpur, West Bengal, India

Areai Nuerlan School of Nuclear Science and Technology, Xi'an Jiaotong University, Xian, People's Republic of China

Pinaki Pal Department of Mathematics, National Institute of Technology Durgapur, Durgapur, India

Asok Ray Department of Mechanical Engineering, Pennsylvania State University, State College, USA

Rizwan-uddin Department of Nuclear, Plasma, and Radiological Engineering, University of Illinois at Urbana-Champaign, Urbana, IL, USA

Santosh Kumar Sahu Discipline of Mechanical Engineering, School of Engineering, Indian Institute of Technology, Indore, Madhya Pradesh, India

Sandip Sarkar Department of Mechanical Engineering, Jadavpur University, Kolkata, India

Soumik Sarkar Iowa State University, Ames, IA, USA

Sunetra Sarkar Department of Aerospace Engineering, Indian Institute of Technology Madras, Chennai, India

Aditya Saurabh Department of Mechanical Engineering, IIT Kanpur, Kanpur, UP, India

Swarnendu Sen Department of Mechanical Engineering, Jadavpur University, Jadavpur, Kolkata, India

Avadhesh Kumar Sharma Discipline of Mechanical Engineering, School of Engineering, Indian Institute of Technology, Indore, Madhya Pradesh, India

Lekha Sharma Department of Mathematics, National Institute of Technology Durgapur, Durgapur, India

Richa Sharma Department of Chemical Engineering, Indian Institute of Technology Guwahati, Guwahati, Assam, India

Shiv Singh Nanomaterial Toxicology Group, CSIR-Indian Institute of Toxicology Research (CSIR-IITR), Lucknow, Uttar Pradesh, India;
Light Weight Metallic Materials, Council of Scientific and Industrial Research—Advanced Materials and Processes Research Institute, Bhopal, Madhya Pradesh, India

Tanuj Srivastava Department of Mechanical Engineering, Indian Institute of Technology Guwahati, Guwahati, India

Pranab Sutradhar Department of Mechanical Engineering, Indian Institute of Technology Guwahati, Guwahati, India

Rajesh Kumar Upadhyay Department of Chemical Engineering, Indian Institute of Technology Guwahati, Guwahati, Assam, India

J. Venkatramani Department of Mechanical Engineering, Shiv Nadar University, Greater Noida, India

Neha Vishnoi CDC Lab, Department of Mechanical Engineering, IIT Ropar, Rupnagar, PB, India

Part I
General and Fundamental Aspects

Chapter 1
Dynamic Behaviour, Identification and Control of Energy Systems

Achintya Mukhopadhyay, Dipankar Narayan Basu, Sirshendu Mondal and Swarnendu Sen

Abstract Increasing demands for energy, dwindling reserves of fossil fuel and growing concern for environmental impacts of energy generation call for a multidisciplinary and concerted effort towards energy sustainability. Optimized energy conversion method must consider the dynamic behaviour of the systems, which are mostly complex and nonlinear in nature. Hence a unified framework, based on dynamical systems analysis and time series analysis, needs to be adopted and applied for a wide spectrum of energy systems, ranging from combustion systems, which account for the bulk of energy generation to multiphase systems like natural circulation loops and multicomponent systems like batteries. With increasing contributions from renewable sources like wind and solar energy, nonlinear dynamics associated with aeroelastic and fluid dynamics effects and heat transfer effects also demand serious attention. Energy systems, whose dynamics, need to be studies also span several orders of length scale starting from large thermal and nuclear power plants to microscale devices.

Energy demand of the world is increasing day by day with economic development and improved standard of life. Population growth is also another aiding factor towards the increasing energy demand (Cai et al. 2009). As fallout, the fossil fuel reserve is

A. Mukhopadhyay (✉) · S. Sen
Department of Mechanical Engineering, Jadavpur University, Jadavpur, Kolkata 700032, India
e-mail: achintya.mukho@gmail.com

S. Sen
e-mail: sen.swarnendu@gmail.com

D. N. Basu
Department of Mechanical Engineering, Indian Institute of Technology Guwahati, Guwahati 781039, India
e-mail: dnbasu@iitg.ac.in

S. Mondal
Department of Mechanical Engineering, National Institute of Technology Durgapur, Durgapur 713209, India
e-mail: sirshendumondal13@gmail.com

A. Mukhopadhyay et al. (eds.), *Dynamics and Control of Energy Systems*,
Energy, Environment, and Sustainability,
https://doi.org/10.1007/978-981-15-0536-2_1

also being depleted with time. So, the energy community is at a crucial time juncture. In one side, the community is facing the challenge to supply the regularly increasing demand; on the other hand, there is a need of thought for sustainable energy generation keeping the future generations in mind. Renewable energy sources are being utilised to a great extent to put less pressure on fuel reserve (Turner 1999). Energy generation using fossil fuel is also a dominant contributor towards different pollutants and green house gases (Jacob 1999). It should be mentioned here that United Nations encourages different countries for generating clean and green power (International Energy Outlook 2016). In light of this, modelling, control and experimental works have been extensively conducted in the area of renewable energy (Goel and Sharma 2017).

Except power sector, transportation sector plays a big role in energy consumption. The prime movers required in this sector acts as pivotal energy systems. Oil and gas can be considered as the major players in this sector. However, the locomotives are now utilising electrical power. The demand of battery operated or hybrid cars are also of increasing demand considering the emission from the engines (Fontaras et al. 2008). Continuous endeavour plays a developmental role in this area also.

The complexities of supply and demand dynamics of energy systems are now ever growing. The energy demand to be met should be supplied in an optimised way. This calls for the extensive study of dynamical behaviour of the energy systems and its components. The ultimate aim of the energy professionals is to control the performance of an energy system. But, to carry it out effectively, the dynamic responses of the system as well as its components need to be well known.

Dynamics and control of combustion systems can be considered as a foundation area in control of energy systems. In majority of the energy systems, combustion plays a crucial role of converting chemical energy of fuel to heat, which is utilised in generating useful power. Initially, combustion dynamics and control has been identified as a thrust area of study to encounter instability in jet propulsion related to rockets or aircrafts (Harrje and Reardon 1972). Study of dynamic behaviour possibly has been started with this field in the area of energy systems. Subsequently, it has been taken as an established route of study in other combustion systems (Candel 2002).

Propulsion system combustion chamber dynamics is typically coupled with acoustics. Here, flow of fuel and air is the input to the chamber. Their rates and other properties modulate the dynamic behaviour of combustion in the chamber. The combustion, associated with its heat release also tells upon the dynamics of the system. As the combustion chamber has its own acoustic phenomenon, it feeds its effects back to the system. The control requirement put forward its own feedback loop in the circuit depending on the demand from the system (Candel 2002). Systematic study by the researchers in this area started at the middle of the last century and its requirement has not been reduced in past seventy years. In these systems, a very small perturbation can grow by different ways to modulate the reacting flow.

Present day call is to sustain combustion with a lower emission. Lean combustion can be one of the avenues to lower emission. Again a trouble with lean combustion is to sustain the flame. Normally it is found that at leaner mixture, the instability grows

and finally extinguishes the combustor. So, prediction of this type of flame blowout is necessary for keeping the flame alive (Chaudhari et al. 2013).

Furnace design of the classical steam power plant boilers was less dependent on the combustion dynamics. Those normally hold a huge steam inventory. So, their dynamics is not always synchronised with the demand on turbine side and moves as a slow response device. Present day once through boilers do not carry a large steam inventory as those do not possess the drum. So, the whole system needs to be tuned with the demand. So, the control becomes more critical in these devices. The criticality of their design also needs the input of sub-system level dynamics. These sub-systems encompass the combustion chamber/furnace, thermal hydraulics, heat transfer and many more aspects (Grace and Krejsa 1967).

It is understood, since long, that the flow oscillations in boiler depends on the thermodynamic conditions of the boiler (Jeglic and Grace 1965). Presence of compressible volume in the feed-line has a destabilizing effect on the boiler flow. This oscillation has an effect on the critical heat flux also (Grace and Krejsa 1967). So, thermal hydraulics of the boiler including the heat transfer dynamics has a dominant role on boiler performance.

The above mentioned flow oscillation should also be carefully studied in case of nuclear power plants (Durga Prasad and Pandey 2008). Considering the safety aspects of nuclear plants, the requirement of this studies are becoming more and more critical. Another client for this kind of analysis in the nuclear plant is the reactor itself. To predict the behaviour of the reactor under normal and abnormal operating conditions, these studies are effective and are helping in designing the plants in a more savvy way (March-Leuba et al. 1986).

We can delineate many more such phenomena, associated with energy systems, from which we understand the necessity of study of dynamics and control. However, it is also understood that the systems we are thinking here are mostly non-linear in nature. So, the dynamic behaviour is also shows non-linearity in their behaviour. So, to understand the fundamental aspects of non-linear dynamics is a primary requirement to analyse the dynamic behaviour of any system.

This book is intended to cover a spectrum of areas related to dynamics and control of energy systems. It is formidable to cover all important areas under this subject. We delineate a few areas for discussion in this book to provide an understanding of the subject matter.

Analysis of the time series to characterise a non-linear system is an important aspect. This must be considered as one of the fundamental understanding for dynamic analysis of any system. The measured dynamic data is not always pure. In fact those are always contaminated with different types of noises. The unfolding techniques of the noise embedded real life data obtained from the observations coming from a system also another important area to stress upon.

Natural circulation loop is the most reliable heat transfer mechanism used in phase change systems including boilers, nuclear steam generators etc. Discussion on the nature of flow instabilities occurring in such systems will permit us to fix the design recommendations for such a mechanism. The natural circulation loops operates on the driving force coming from density gradient. In case of supercritical

fluids, nature of the density gradient grossly differs from that of a single phase or two phase systems. An overview of the supercritical natural circulation loop dynamics is also an important area of study. The dynamics and control of a nuclear plant is another important aspect to discuss. This type of plant may act as a base-load plant while the peak demand on the grid is supplied by renewable like wind and solar. Similarly a control strategy of the nuclear reactor is of amply importance.

An energy transfer occurs to the structure from flowing fluid over it above a critical speed. This is resulting in a dynamic instability of self-feeding nature. Investigating the synchronisation of bending and torsional vibration of the structure due to this fluid-structure interaction is needed. A discussion is also necessary about the intermittency in a pitch-plunge aeroelastic system. Vortex induced vibration plays a crucial role in fluid structure interaction. Effect of this is important in designing the aerofoils or any structure submitted to fluid flow past that. Especially this type of interaction occurs for the devices like turbines, compressors etc. A review on stochastic vortex induced vibration for a basic structure can provide an overview of this problem. A review of dynamical effects of flow fluctuation on fluid-structure interaction is also another important area of study.

Syngas combustion is an important area of study. Present scenario of power generation puts a thrust on this area. Syngas combustion has its own uniqueness, which we require to know for combustor design. The combustors act like a thermo-acoustic device, as we previously discussed. The theory of random noise and the theory of oscillators and dynamical systems on noise induced behaviour of a thermo-acoustic device should get a thrust. Discussion about capturing algorithm of combustion instability in a combustion system is also another important aspect. This will provide us the method for instability detection. Real time condition monitoring and prediction of certain phenomenon is of utmost importance for combustion systems.

Micro-devices are experiencing certain phenomenon, which are not so dominant in macro world. So, the nature of instability in micro devices may differ from the same in macro devices. Knowledge is required for dealing with the nature of instabilities and control in micro devices.

Convection is the most critical mode of heat transfer in energy systems. Low dimensional modelling of convection heat transfer is considered as an important aspect in this area. A discussion on the membrane reactor for hydrogen production is felt to be discussed considering the green energy technology development for future. Temperature measurement is a crucial issue in energy systems. A non-intrusive temperature measurement technique, using thermal imaging camera, must get some thrust. Energy storage is a potential area of study, particularly to hook up energy from intermittent sources like renewable. The detailed mathematical modelling and design recommendations for Lithium-Oxygen batteries should be an area of discussion. Lastly, discussion about the dynamics of heat exchangers is required, as it is an important device to cater to various heat transfer needs.

References

Cai YP, Huang GH, Lin QG, Nie XH, Tan Q (2009) An optimization-model-based interactive decision support system for regional energy management systems planning under uncertainty. Expert Syst Appl 36:3470–3482

Candel S (2002) Combustion dynamics and control: progress and challenges. Proc Combust Inst 29:1–28

Chaudhari RR, Sahu RP, Ghosh S, Mukhopadhyay A, Sen S (2013) Flame color as a lean blowout predictor. Int J Spray Combust Dyn 5:49–66

Durga Prasad GV, Pandey M (2008) Stability analysis and nonlinear dynamics of natural circulation boiling water reactors. Nucl Eng Des 238:229–240

Fontaras G, Pistikopoulos P, Samaras Z (2008) Experimental evaluation of hybrid vehicle fuel economy and pollutant emissions over real-world simulation driving cycles. Atmos Environ 42:4023–4035

Goel S, Sharma R (2017) Performance evaluation of stand alone, grid connected and hybridrenewable energy systems for rural application: a comparative review. Renew Sustain Energy Rev 78:1378–1389

Grace TM, Krejsa EA (1967) Analytical and experimental study of boiler instabilities due to feedsystem—subcooled region coupling, Technical note NASA TN D-3961. NASA

Harrje DT, Reardon FH (eds) (1972) Liquid propellant rocket combustion instability, Report NASASP-194. NASA

International Energy Outlook (2016) U.S. Energy Information Administration, Page 1–DOE/EIA-0484; May 2016

Jacob DJ (1999) Introduction to atmospheric chemistry. Princeton University Press, Princeton, NJ

Jeglic FA, Grace TM (1965) Onset of flow oscillations in forced-flow subcooled boiling, Technical note NASA TN D-2821

March-Leuba J, Cacuci DG, Perez RB (1986) Nonlinear dynamics and stability of boiling water reactors: part 1—qualitative analysis. Nucl Sci Eng 93:111–123

Turner JA (1999) A realizable renewable energy future. Science 285:687–689

Chapter 2
Methods of Nonlinear Time Series Analysis and Applications: A Review

G. Ambika and K. P. Harikrishnan

Abstract Many of the real world systems are highly complex with little or no apriori information about the underlying dynamics. We have to depend mostly on measurements or observations of their average responses to study them. These measured or observational data come as a sequence of values at intervals, called time series. A few typical examples are sunspot data, variable star data, x-ray variability of black holes, climate or rainfall data, earth quake data, combustion data, thermoacoustic data, physiological data like EEG, ECG and fMRI, financial market data, output of agricultural crops, gene expression data etc. We present an overview of the techniques used for nonlinear time series analysis, to detect nontrivial structures in such time series data that will indicate the nature of underlying dynamics that produce the data. We start with the method of time delay embedding that can be used to re-construct the dynamics in higher dimension. The geometry and intricate structure of the re-constructed dynamics can then be characterized using two powerful techniques. The first one aims at computing the measures of the fractal geometry of the structure and its scaling properties. The resultant multi-fractal spectrum is uniquely characterized by four parameters that can be computed for each time series or data. The second method involves generating a complex network from the recreated phase space using its recurrence properties. The measures of the recurrence network then helps to identify the dynamical states of the system and their possible transitions. The applications of these techniques to several different types of real data are also included as illustrations.

G. Ambika (✉)
Indian Institute of Science Education and Research, Tirupati 517507, India
e-mail: g.ambika@iisertirupati.ac.in

K. P. Harikrishnan
The Cochin College, Cochin 682002, India
e-mail: kp.hk05@gmail.com

A. Mukhopadhyay et al. (eds.), *Dynamics and Control of Energy Systems*,
Energy, Environment, and Sustainability,
https://doi.org/10.1007/978-981-15-0536-2_2

2.1 Introduction

In the early 1980s, two pioneering papers (Packard et al. 1980; Takens 1981) laid the foundation of what we now call *nonlinear time series analysis*. It is the analysis of data typically in the form of a time series—synthetic or real world—from the viewpoint of dynamical systems, especially those having the special property of *deterministic chaos* (Shuster and Just 2005). The backbone of this analysis is the delay embedding procedure (Sauer et al. 1991; Casdagli et al. 1991) used to re-construct the underlying dynamics in a multi-dimensional space, based on the theoretical understanding that a single variable from a multi-dimensional system contains complete information regarding the dynamics of the system.

The method, in principle, allows us to compute characteristic measures typical of a chaotic system, namely, fractal dimensions (Mandelbrot 1982; Hilborn 1994), Lyapunov exponents (Eckmann et al. 1986), etc., to predict the temporal behavior of the system over a short period and even to develop the model equations in some special cases (Serre et al. 1996). In practice, however, there are a number of issues that restrict the power of this approach, such as: whether the time series has proper sampling and enough data points, whether there are gaps in the data, whether the signal is contaminated by noise, etc. Moreover, the algorithms used for computations have inherent limitations as they involve finite-precision approximations and scalings, among other things. In spite of all these practical difficulties, nonlinear time series analysis (NTSA) has been applied to great effect on thousands of real and synthetic data sets from a wide variety of systems over the last four decades (Raidl 1996; Silva et al. 1999; Sander et al. 2002; Andrzejak et al. 2001; Misra et al. 2004). Even in cases where the signal does not meet the full algorithmic requirements, the results from NTSA can be helpful in getting a first information regarding the nature of dynamics and the noise contamination in the data.

Detecting deterministic nonlinearity in real world data contaminated by different types of noise is still one of the major challenges in NTSA. In most cases, computation of a nonlinear measure alone can not give conclusive evidence regarding nontrivial dynamics in the data. For this, a generally accepted procedure is the method of surrogate analysis (Theiler et al. 1991; Scheiber and Schmitz 1996; Schreiber and Schmitz 2000), which is a statistical hypothesis testing. The method involves generating an ensemble of surrogates from the data. Ideally, surrogate data sets should have the same power spectrum and distribution as the target data. One presumes that the data is linear in nature and has no nonlinear character in its temporal evolution. The data and the surrogates are then analyzed using some nonlinear measure as the test statistic and looks for a statistical rejection of the null hypothesis with a certain confidence level.

In the conventional aproach of NTSA, dimension of the underlying attractor is typically used as the discriminating measure. However, dimension estimates are known to suffer from various algorithmic and computational errors (Eckmann and Ruelle 1992; Grassberger 1988). Moreover, they also require long time series with slow convergence for high embedding dimension in most cases. Over the last one

decade, an alternative approach based on complex networks (Marwan et al. 2009; Donner et al. 2010, 2011) has become more popular. Here the time series is first converted into a complex network and network measures are used to get information regarding inherent dynamics. However, it should be noted that the network approach is a complimentary one to the conventional methods as it is not meant for the accurate determination of dynamical measures, say, dimension, entropy, Lyapunov exponents, etc. Instead, it is more useful in practical applications involving short time series, such as, identifying dynamical transitions as a control parameter is varied, searching for deterministic nonlinearity with a network measure as test statistic, studying the effect of noise on the structure of chaotic attractors, etc. The utility and power of this approach is yet to be realised in full as it is an emerging area of current research.

In this review, we first discuss the delay embedding technique in the next section followed by the conventional and complex network based approaches in Sects. 2.3 and 2.4 respectively. We then show in Sect. 2.5 how the methods and measures have been utilized for the analysis of real data with examples from three different areas. An overview and conclusion are presented in Sect. 2.6.

2.2 Delay Embedding: Reconstructing the Dynamics

The whole of NTSA rests on the ability of reconstructing the dynamics from a single time series through delay coordinate embedding. Here, a series of past (or future) values of a single scalar measurement from a dynamical system are used to form a vector that defines a point in the reconstructed space. In practice, a set of suitably chosen values of a scalar time series $u(t_i)$ with a delay time τ is used as coordinates to represent the vector $\mathbf{x_i}$ in the reconstructed space of dimension M:

$$\mathbf{x_i} = [u(t_i), u(t_i + \tau), \ldots, u(t_i + (M-1)\tau)] \tag{2.1}$$

here, the time delay τ is an important parameter and should be chosen properly. From the original embedding theorem, the basic condition for choosing τ is that it should be sufficiently large so that the reconstructed vectors are not correlated. If τ is small, the attractor will not unfold properly and will shrink into the diagonal line. The delay cannot be too large either which may result in insufficient vectors in the embedded space, especially in higher dimension. Even though several methods have been suggested in the literature (Liebert and Schuster 1989; Fraser and Swinney 1986; Aberbanel et al. 1993; Schreiber 1999) for choosing τ depending on the type of time series and the nature of noise involved, the generally accepted norm is to use a τ value corresponding to the first minimum of auto correlation.

It should be noted that there are other methods related to delay embedding, such as derivative delay embedding (DDE), where intrinsic characteristics of the data are preserved as recursive patterns and used as modeling and classification scheme (Lainscsek 2011; Lainscsek et al. 2013) and is not directly related to the analysis that we consider here.

Once the attractor is constructed, several dynamical measures characterizing the invariant set representing the underlying attractor can be computed: the fractal dimension related to the geometry of the set, the Kolmogorov entropy (Ott 1993) which measures the rate of information loss as the attractor evolves, the spectrum of Lyapunov exponents (Sano and Sawada 1985) indicating the stability with respect to infinitesimal perturbations, and so on. However, the computation of the latter measures is known to be much more involved and difficult compared to that of dimension. As such, they are rarely used in practice, especially for the the analysis of real data. Details regarding their computation can be found elsewhere (Ott 1993; Sano and Sawada 1985; Wolf et al. 1985). Here we limit our discussion to the computation of dimension, as it is the most commonly used measure in NTSA and also the least error-prone among the measures that can be derived from time series data.

There are, in fact, two algorithmic approaches for computing the fractal dimension of the embedded attractor. The first one is through partitioning of the state space: the number of boxes N_ϵ of size ϵ needed to cover the fractal set with dimension D_0 scales with box size ϵ as ϵ^{-D_0}. Direct application of this box counting method to the reconstructed attractor is possible, but is sensitive to data length and requires significant memory. Instead of the simple box counting, the correlation between the trajectory points in an attractor has been shown to be a more efficient and robust estimator of dimension. Hence this method called the Grassberger–Procaccia algorithm (Grasberger and Procaccia 1983) is employed in practice, which uses the scaling of the *correlation sum* as a function of distance. For this, the first step is to choose a threshold distance R in the embedding space. One then counts the number of points within the distance R from a randomly chosen (ith) data point and normalize it with respect to the total number of reconstructed vectors $N_v$to get:

$$p_i(R) = \lim_{N_v \to \infty} \frac{1}{N_v} \sum_{j=1, j\neq i}^{N} H(R - |\mathbf{x_i} - \mathbf{x_j}|) \tag{2.2}$$

here, H is the Heaviside step function. This quantity is then averaged over the total number of centers N_c to get the correlation sum:

$$C_M(R) = \frac{1}{N_c} \sum_{i}^{N_c} p_i(R) \tag{2.3}$$

To get the correlation dimension D_2, the scaling of $C_M(R)$ with R in the limit $R \to 0$ is computed:

$$D_2 \equiv \lim_{R \to 0} \frac{d\log C_M(R)}{d\log(R)} \tag{2.4}$$

Though the procedure appears to be straightforward, several practical difficulties are involved in the computation, especially for real world data. For example, one does not have perfect data in real circumstances, nor does one know the dimension of the

system under study. The embedding theorem requires that the data should be evenly sampled without gaps. Otherwise, one has to get methods, such as interpolation, to get a mix of real and interpolated data. The choice of τ is also not straightforward. As mentioned above, though the traditional practice of choosing τ is the first minimum of auto correlation (ensuring minimum τ for zero correlation between components), numerous other methods have also been proposed for this. As such, there is no universal strategy for selecting τ in practice since the process is system-dependent and a τ that works well for one purpose (eg. prediction) may not work well for another (eg. computing dynamical invariants) (Bradley and Kantz 2015).

Another crucial parameter is the embedding dimension M. Ideally, one wants the "smallest" M in which the attractor unfolds completely to avoid unnecessary over-embedding. There are basically two approaches here, one based on the false nearest neighbour (FNN) algorithm (Kennel et al. 1992) and the other termed *asymptotic invariant approach*. In the former, one computes the nearest neighbours to each point increasing the embedding dimension. Typically, the number reduces with M. If the number remains constant for two consecutive M values, the minimum of this is taken as the correct M value. The latter method is more commonly used for the computation of D_2, where the computation is done starting from $M = 1$ to a maximum value M_{max} and look for the M value where D_2 saturates.

Even after the proper choice of the above parameters, there are still certain inherent algorithmic pitfalls which are to be taken care of in the computation of D_2. For example, if R is small, $p_i(R)$ will be correspondingly small and would be affected by noise. On the other hand, as R becomes large, the M-spheres can go beyond the size of the attractor leading to the *edge effect*. This, in turn, makes the computed value of $C_M(R)$ to saturate to unity. To avoid these effects, a suitable linear part in the variation of $\log C_M(R)$ with $\log R$ is taken as the *scaling region* whose slope is computed as D_2.

This is illustrated in Fig. 2.1 (left panel) where scaling regions corresponding to embedding dimensions from 1 to 4 for the Rössler attractor are shown. As M is increased (from left to right), the slope of the scaling region gets saturated to provide the saturated correlation dimension D_2^{sat} for the Rössler attractor Fig. 2.1 (right panel). Note that the range of saling region depletes as M increases.

The above discussion implies that the computation has to be necessarily subjective with the scaling region needs to be identified by looking at the correlation sum for each embedding dimension. Such an exercise severely affects the utility of the method, especially in the case of surrogate analysis where the data and the surrogates are to be subjected, in principle, to the same algorithmic conditions. An alternative approach which makes this possible (without requiring subjective evaluation of the scaling region) has been proposed in the literature whose details can be found elsewhere (Harikrishnan et al. 2006). In this non-subjective approach, the scaling region is identified algorithmically without requiring any subjective evaluation of the correlation sum and the scheme has been applied for the analysis of synthetic as well as real world data (Misra et al. 2006; Harikrishnan et al. 2009).

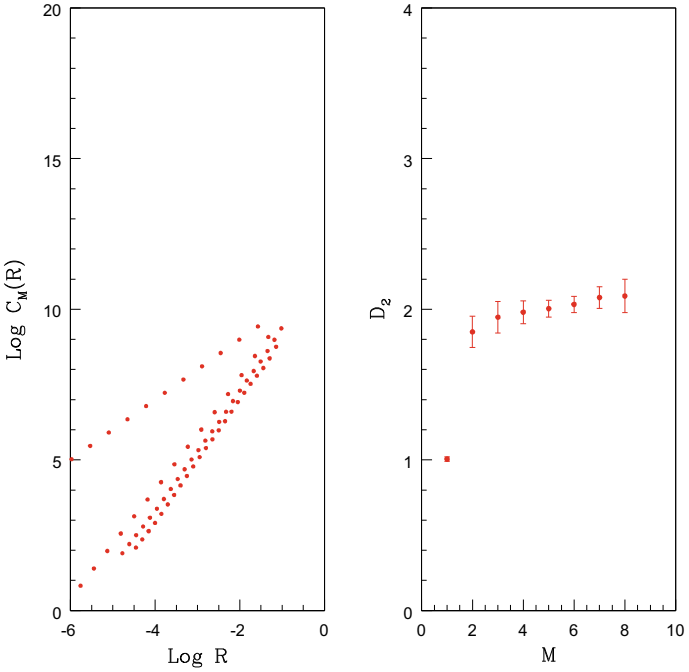

Fig. 2.1 The scaling region in the correlation sum $C_M(R)$ versus R for the Rössler attractor for the first four values of M (left panel). The variation of D_2 (the slope of the scaling region) with M is shown with error bar in the right panel, which saturates with M

2.3 Generalized Dimensions and Multi-fractal Spectrum

It is very well accepted that the chaotic attractor is not a simple fractal, but a multi-fractal since the distribution of the trajectory points and the scaling in different regions of the attractor are different. Hence the full geometric characterization of a chaotic attractor requires the computation of the generalized dimensions (Hentschel and Procaccia 1983) and the associated singularity spectrum called the $f(\alpha)$ spectrum (Halsey et al. 1986; Jensen et al. 1985). Many authors have discussed the mathematical details of multi-fractality in detail (Halsey et al. 1986; Jensen et al. 1985; Falconer 1994; Paladin and Vulpiani 1987) and we briefly summarize the main results below.

The attractor is first partitioned into M dimensional cubes of side length r. Let $N(r)$ being the number of cubes required to cover the attractor. We then find the probability that the trajectory passes through the jth cube, denoted as $p_j(r) = N_j/N_t$. Here N_j is the number of points within the jth cube and N_t the total number of points on the attractor. It is then assumed that $p_j(r)$ satisfies a scaling relation

$$p_j(r) \propto r^{\alpha_j} \tag{2.5}$$

where α_j is the scaling index for the jth cube. Considering the variation of α to be continuous, we compute how many cubes have scaling index within α and $\alpha + d\alpha$. Scaling of this number, say $g(\alpha)d\alpha$, with r is determined as

$$g(\alpha) \propto r^{-f(\alpha)} \tag{2.6}$$

with $f(\alpha)$ some characteristic exponent. Since $f(\alpha)$ behaves as a dimension, it is taken as the fractal dimension of the set of points with scaling index α. Since the scaling on different parts of a chaotic attractor is, in general, different, one uses a spectrum of dimensions D_q (Hentschel and Procaccia 1983) to represent it. It can be shown that the transformation from D_q to $f(\alpha)$ is a Legendre transformation (Grassberger et al. 1988). If $f(\alpha)$ is plotted as a function of α, one gets a one hump curve with the maximum corresponding to the box counting dimension of the attractor D_0.

To compute $f(\alpha)$ from a time series, the D_q spectrum is first determined. Then the equations of Legendre transformation are used for the computation of $f(\alpha)$:

$$\alpha = \frac{d}{dq}[(q-1)D_q] \tag{2.7}$$

$$f(\alpha) = q\alpha - (q-1)D_q \tag{2.8}$$

Eventhough the procedure, in principle, appears straightforward, its practical implementation is extremely difficult. The error in the D_q values is usually large and moreover, the negative part of the D_q spectrum often remains incomplete due to the finiteness of the data set. Thus, a smoothing and extrapolation is often required to get the complete D_q curve which makes the exact computation of the $f(\alpha)$ spectrum even more difficult.

An algorithmic approach to overcome these difficulties and compute the complete spectrum from the time series for any dimension has been proposed by Harikrishnan et al. (2009). The main idea behind this approach is that the typical convex profile of the $f(\alpha)$ curve can be fitted by an analytic function which contains four independent parameters. The D_q curve obtained by inverting this function using the Legendre transformation equations is compared with the D_q spectrum computed from the time series. The spectrum is fitted with the D_q curve and the statistically best fit D_q curve is found by adjusting the parameters. The final $f(\alpha)$ spectrum is determined from the dest fit D_q curve. An advantage of this scheme is that the whole procedure is *automated*. In other words, once the time series is given, the D_q and $f(\alpha)$ spectrum can be obtained for the particular embedding dimension without any intermediate subjective analysis.

The details of the scheme are discussed here briefly. As the first step, the spectrum of the generalized dimensions D_q is computed from the time series after delay embedding. The generalised correlation sum $C_q(R)$ for any M is given by the relative number of data points within a distance R from a particular (ith) data point ($p_i(R)$,

as in Eq. (2.2) raised to the power of $(q-1)$ and averaged over N_c randomly selected centres:

$$C_q(R) = \frac{1}{N_c} \sum_{i}^{N_c} p_i(R)^{q-1} \tag{2.9}$$

Then the spectrum of dimensions is then given by

$$D_q \equiv \frac{1}{q-1} \lim_{R \to 0} \frac{\log\ C_q(R)}{\log\ R} \tag{2.10}$$

To compute the $f(\alpha)$ spectrum, one makes use of the fact that the $f(\alpha)$ curve is single valued between the limits of α_{min} and α_{max}, having a single maximum in betweeen. Also, the values at the extreme points are zero, while the slopes at these points tend to ∞. A simple function which can satisfy all these properties is

$$f(\alpha) = A(\alpha - \alpha_{min})^{\gamma_1}(\alpha_{max} - \alpha)^{\gamma_2} \tag{2.11}$$

where A, γ_1, γ_2, α_{min} and α_{max} are a set of parameters characterizing a particular $f(\alpha)$ curve.

Differentiating Eq. (2.8), one gets

$$q = \frac{d}{d\alpha} f(\alpha) \tag{2.12}$$

Substituting for $f(\alpha)$ from above and simplifying one can show that

$$q = f(\alpha) \left[\frac{\gamma_1}{\alpha - \alpha_{min}} - \frac{\gamma_2}{\alpha_{max} - \alpha} \right] \tag{2.13}$$

Imposing the conditions on the $f(\alpha)$ curve, one finds that the range of γ_1 and γ_2 have to remain within the unit interval [0, 1]:

$$0 < \gamma_1, \gamma_2 < 1 \tag{2.14}$$

Corresponding to $q = 1$, there is a value of $\alpha(\equiv \alpha_1)$ and $f(\alpha)(\equiv f(\alpha_1))$ such that

$$D_1 = \alpha_1 = f(\alpha_1) \tag{2.15}$$

Putting $q = 1$ in Eq. (2.13), we get

$$\alpha_1 \left[\frac{\gamma_1}{\alpha_1 - \alpha_{min}} - \frac{\gamma_2}{\alpha_{max} - \alpha_1} \right] = 1 \tag{2.16}$$

This equation is first used to compute γ_2 with others as input parameters. Taking the inputs from the D_q spectrum for α_{min} and α_{max}, the parameter A can be calculated

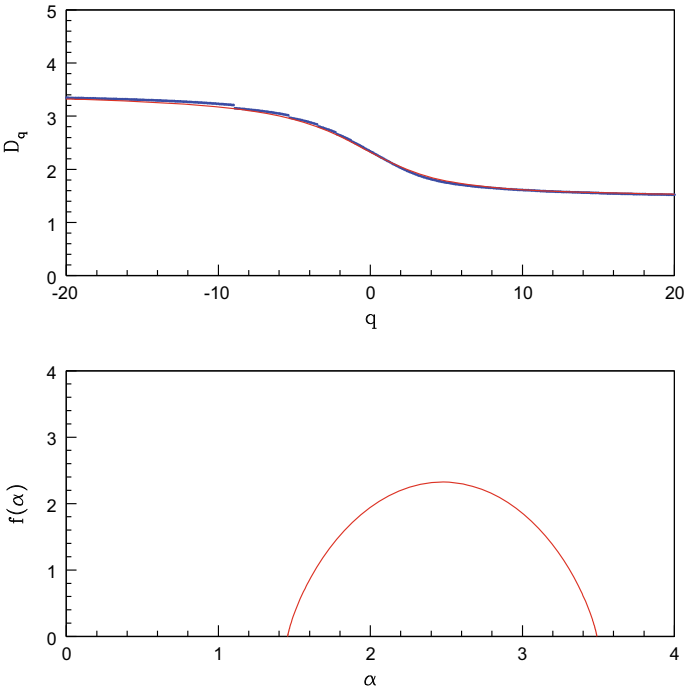

Fig. 2.2 The top panel gives the D_q spectrum of the Rössler attractor computed using scheme discussed in the text along with its best fit curve (solid line). The $f(\alpha)$ curve of the Rössler attractor computed from the best fit D_q curve is shown in the bottom panel

from the original $f(\alpha)$ fit. This provides the $f(\alpha)$ curve from which the D_q curve can be obtained. More details regarding the scheme and its practical aspects of implementation can be found in Harikrishnan et al. (2009).

The scheme is illustrated in Fig. 2.2 by applying it to the time series from the Rössler attractor. The D_q spectrum is first computed from the time series and its best fit curve is determined. Both are shown in Fig. 2.2 (top panel), with the solid line representing the best fit curve. The final $f(\alpha)$ curve computed from the best fit D_q curve is also shown in Fig. 2.2 (bottom panel). The scheme has been utilized for the analysis of synthetic as well as real world data whose details are given in Sect. 2.5.

2.4 Complex Network Approach to Nonlinear Time Series Analysis

Analysis of time series for the characterization of underlying dynamics utilizing complex network measures has become an important area of research over the last one decade. This has allowed addressing some fundamental questions regarding

the structural properties of chaotic attractors as well as the successful treatment of a variety of applications from a broad range of disciplines. Here we provide an overview of the existing techniques of network based NTSA focusing mainly on the phase space based recurrence network analysis.

The field of complex networks and its applications has evolved independently over the last two decades following the discovery of scale free topology (Barabasi and Albert 1999) in most real networks as compared to the classical random topology (Erdos and Renyi 1960). The renewed interest in complex network analysis has lead to a variety of "non conventional" applications apart from its classical areas of research, such as, social networks, communication networks, ecological networks, etc. The most important among these is the analysis of dynamical systems utilizing the network based concepts and measures.

Here the emphasis is on systems (represented by time series) suspected to have deterministic nonlinearity to extract information through network based measures on the structure of the underlying attractor, which is otherwise unable to get using existing methods of time series analysis. The basic idea here is to map the information inherent in an embedded attractor on to the domain of a complex network using a suitable scheme. One then uses the statistical measures of the complex network to characterize this information specific to the underlying attractor.

It should be noted that the attractor and the network are two different entities. While the former has a dynamical measure involving a metric defined in a state space, the latter has only nodes and connections defined in an abstract space and just a static structure. As such, one should expect a certain loss of information (especially regarding dynamics) during this mapping which also involves parameters whose selection is based on certain criteria. However, one presumes that, with a proper mapping, the characteristic geometric properties of the attractor are preserved in the resulting network and reflected in the network measures, though these measures are not directly related to the dynamic measures of the attractor.

Several methods have been suggested in the literature to transform a time series into the corresponding complex network. Examples are cycle networks (Zhang and Small 2006), visibility graphs (Lacasa et al. 2008), transition networks (Nicolis et al. 2005) and recurrence networks (RN) (Marwan et al. 2009). The RNs can be constructed in different ways, namely, the correlation networks (Yang and Yang 2008), k-nearest neighbour networks Xu et al. (2008) and ϵ-recurrence networks (Donner et al. 2011). Different methods of network generation are used for different types of applications. A detailed discussion of these methods and their comparison can be found elsewhere (Zou et al. 2019). The method that we focus here is the one based on ϵ - recurrence since it is the most popular having a number of practical applications. From now on, we simply call it recurrence networks (RN).

In fact, RN is the network analogue of the recurrence plot (RP), a visualization tool introduced by Eckmann et al. (1987). It is a two dimensional graphical representation of the trajectory of a dynamical system in the form of a binary, symmetric matrix $\mathcal{R}$ where $R_{ij} = 1$ if the state $\mathbf{x_j}$ is a neighbour of $\mathbf{x_i}$ in phase space and $R_{ij} = 0$, otherwise. The neighbourhood is defined through a certain recurrence threshold ϵ. To construct the RP from the scalar time series, one uses the delay embedding procedure discussed

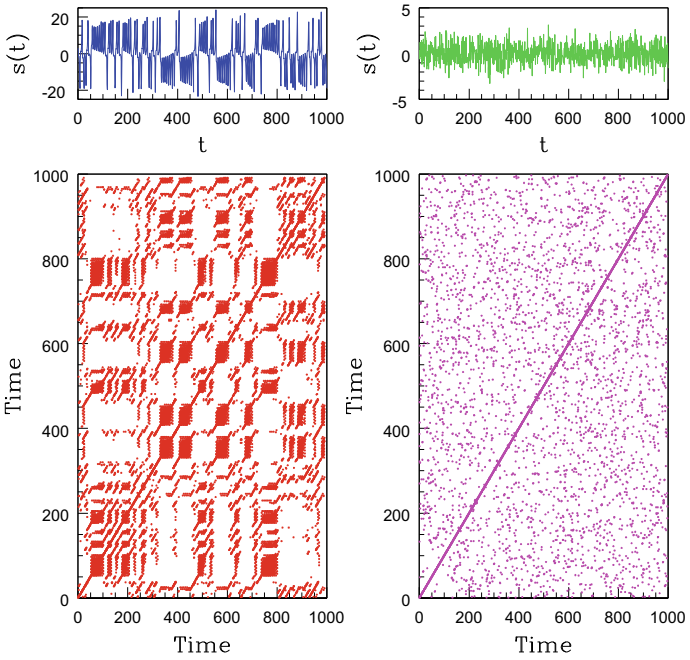

Fig. 2.3 The time series from the Lorenz attractor and the RP generated from this time series are shown in the left panel. The same for white noise is shown in the right panel

in Sect. 2.2. As an example, the RPs constructed from the Lorenz attractor time series and white noise are shown in Fig. 2.3. The difference between the two is evident as the diagonal lines (indicating recurrence of trajectory) is missing in the case of white noise.

There are several quantifying measures (Marwan et al. 2007; Schinkel et al. 2009) associated with the RP and used for the analysis of data. Two of the important measures frequently used are the recurrence rate (RR) and the determinism (DET) which can be computed from the following equations:

$$RR = \frac{1}{N^2} \sum_{i,j} R_{ij} \tag{2.17}$$

$$DET = \frac{\sum_{l \geq l_{min}}^{l_{max}} lp(l)}{\sum_{l=1}^{l_{max}} lp(l)} \tag{2.18}$$

The former is a measure of the overall probability that a certain state recurs while the latter is a measure based on the distribution of the diagonal structures $p(l)$ and reflects how predictable the system is. The larger diagonal structures are an indication that two trajectories evolve closer for long time intervals. For random data,

the diagonal structures are missing while for a periodic data, all the points fall on diagonal lines. Hence these measures are directly related to the nature of dynamics on the attractor.

From the RP, one can easily construct the RN. It is the network form of RP after removing the self loop, namely, the diagonal elements. The elements of the adjacency matrix $\mathcal{A}$ of the RN is given by

$$A_{ij} = R_{ij} - \delta_{ij} \tag{2.19}$$

where δ_{ij} is the Kronecker delta. Each point on the reconstructed attractor now becomes a node in the RN and a reference node is connected to another node if the distance between the corresponding points on the attractor is $\leq \epsilon$.

For the construction of the RN, the key parameters are ϵ and M. If ϵ is large, the specific small scale properties of the attractor cannot be revealed and if ϵ is too small, the network breaks into disuaded nodes due to lack of connections. In general, for each embedded attractor, the value of ϵ has to be determined seperately as it varies with the size of the attractor. Two criteria are usually employed (Eroglu et al. 2014) to select ϵ. The first and the primary one is that there should be a giant component for the resulting RN which sets a lower bound for ϵ. By giant component, it is meant that there exists a single connected network involving more than 95% of the nodes in the whole network connected to it. In order to ensure that the resulting network is not over connected, the upper bound for ϵ is usually set in such a way that the link density (the ratio of actual connections to all possible connections in the network) is only a small fixed fraction of the maximum possible value. This provides a small range $\Delta\epsilon$ for threshold for each system where the resulting network is considered to be a proper representation of the time series.

To illustrate the importance of choosing the proper threshold, we show in Fig. 2.4, the RNs constructed from the Lorenz attractor time series with four different values of ϵ. Here ϵ increases from (a) to (d). When ϵ is small (as in (a) and (b)), the network is broken into smaller components and when its value is higher, the network becomes over connected. In between, for a small range of ϵ, the network is considered to be a proper representation of the attractor.

Recently, a uniform framework for the choice of ϵ applicable to different systems independent of the size of the embedded attractor has been proposed by Jacob et al. (2016). Here, the time series is first transformed into a uniform deviate so that the size of the attractor always remains within the unit cube. To find the lower bound for ϵ, the standard criterion that the network turns into a single giant component is used. However, the upper bound is determined by the condition that the characteristic path length (which describes the global connectivity of the network) of the RN from a chaotic attractor is significantly different from that of white noise data. Due to uniform deviate transformation, the scheme provides an approximately identical range $\Delta\epsilon$ for constructing RN from different chaotic time series for a given embedding dimension M.

Once the network is constructed, one can make use of statistical measures used in complex network analysis for the characterization of the attractor. The complex

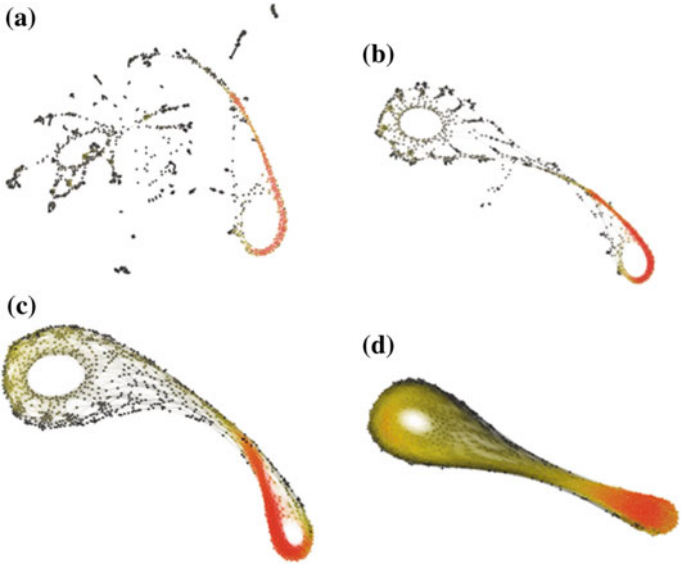

Fig. 2.4 The RNs constructed from the Lorenz attractor time series for four different values of ϵ, namely, **a** 0.06, **b** 0.08, **c** 0.10 and **d** 0.14, with the size of the attractor rescaled into the unit cube. The number of points in the time series is 2000 and and the embedding dimension used is $M = 3$. It is evident that only the case (**c**) can properly characterize the attractor. The colour of the node represents its degree which increases from blue to red

network measures commonly employed in NTSA are the degree distribution, the characteristic path length (CPL) and the average clustering coefficient (CC). The degree distribution is a statistical measure which tells how many nodes n_k among the total number of nodes N have a given degree k. The probability $p(k) = \frac{n_k}{N}$ is plotted as a function of k. To define CPL, one considers the shortest path l_s between two nodes g and h in the network. It is the minimum number of intermediate nodes needed to reach h from g. The average value of l_s for all the pair of nodes in the whole network is taken as CPL and can be determined from the equation:

$$CPL = \frac{1}{N(N-1)} \sum_{g,h}^{N} l_s \tag{2.20}$$

To get the average clustering coefficient CC of a network, we first define a local clustering index c_q. It tells how many of the nodes connected to a reference node q are also mutually connected:

$$c_q = \frac{\sum_{g,h} A_{qg} A_{gh} A_{hq}}{k_q(k_q - 1)} \tag{2.21}$$

Taking the average of c_q for the whole network, we get CC:

$$CC = \frac{1}{N}\sum_q c_q \tag{2.22}$$

There are many reviews on network measures (Albert and Barabasi 2002; Boccaletti et al. 2006) as well as some excellent books (Newman 2010; Watts 2003) which provide more details regarding all the network measures.

It can be shown that, if properly constructed, all the statistical measures of the RN discussed above are characteristic of the attractor from which it is constructed (Jacob et al. 2016). The measures can also discriminate between a chaotic attractor and pure white noise. As an example, we show the CPL and CC values of the RNs from 3 standard chaotic attractors and white noise in Fig. 2.5. These measures can also be used as discriminating measures for hypothesis testing using surrogate data.

There are two aspects of the RN that make them special for the analysis of time series data. Firstly, since the network measures can be derived reasonably accurately using a small number of nodes in the network, the method is suitable for the analysis of short and non-stationary data. Secondly, they generally preserve the structure of the embedded attractor and hence the structural changes in the underlying attractor due

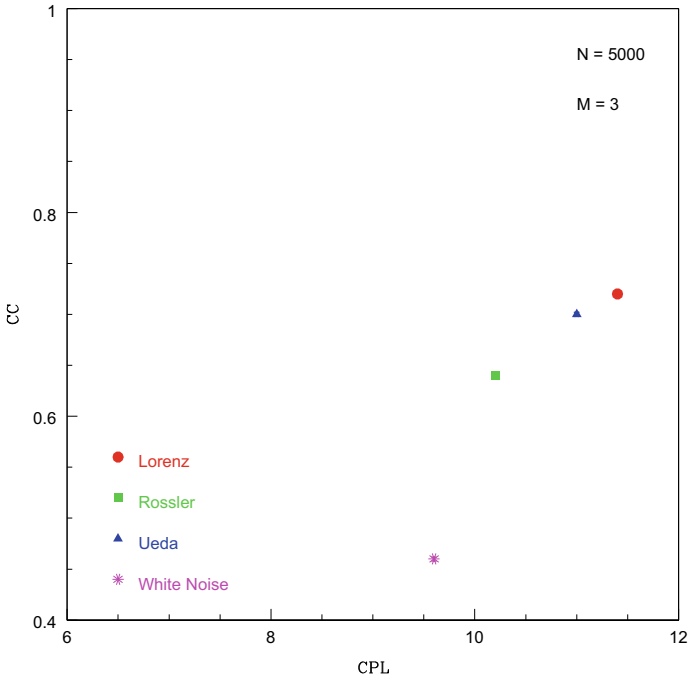

Fig. 2.5 The CPL-CC plane indicating the corresponding values of the RNs from 3 standard chaotic attractors and white noise. It is clear that the white noise can be distinguished from the rest

to, say, noise addition is also reflected in the corresponding RN. Hence the network measures can be effectively used to study how the structure of a chaotic attractor is affected by increasing levels of noise contamination (Jacob et al. 2016).

2.5 Examples of Real Data Analysis

Nonlinear time series analysis is actually an interface between the developments of the concepts and ideas in nonlinear dynamics (or the so called chaos theory) and their practical applications. The aims of NTSA can be broadly classified (but not limited to) as: (1) system characterization from a single time series (2) identifying quantitative changes in system behavior with respect to changes in a control parameter (3) discrimination between a given signal and some other signals (4) classification of different time series from a dynamical perspective (5) testing for deterministic nonlinearity in a signal (6) identifying nature and amount of noise based on the variation of characteristic measures (7) nonlinear prediction and control of system behavior espicially in many engineering applications and (8) to help in developing the nonlinear model equations underlying the dynamics. Here we briefly discuss three main areas of applications of the methods and measures presented in previous sections, namely, astrophysical, engineering andbio-medical.

2.5.1 Applications in Astrophysical Data

One of the earlier attempts on the application of NTSA techniques was on astrophysical data. Light curves from different groups of variable stars were analyzed to search for deterministic nonlinearity in their temporal variations. Several studies were done in this regard (Serre et al. 1996; Lindner et al. 2015; Moskalik et al. 2015) and is still continueing (George et al. 2017) with more accurate data sets now available from Kepler archive. Another category of data that have been exhaustively analized using measures of nonlinear dynamics are the X-ray light curves from certain black hole systems. Especially, a prominent black hole GRS1915+105 has been analized in great detail. The light curves from this black hole system have been classified into 12 spectroscopic classes based on RXTE observations by Belloni et al. (2000). The nature of the lightcurves changes completely as the system flips from one temporal state to another. Evidently, pure stochastic process cannot account for such qualitative changes in the light curves, leading many to suspect the presence of some deterministic nonlinear processes underlying the generation of these light curves.

A detailed analysis of the light curves have been done by Harikrishnan et al. using both dimension measures (Misra et al. 2006; Harikrishnan et al. 2011) and network measures (Jacob et al. 2018) discussed above. The authors have reported evidence for deterministic nonlinearity in the temporal behavior of a few states by applying surrogate analysis using D_2 as well as CPL as discriminating statistic. They have

also analysed the nature of noise contamination in these light curves and classified the light curves into 3 groups based on the temporal behavior and the nature and amount of noised involved.

2.5.2 Applications in Engineering Problems

In many engineering problems, controlling the system to operate at desired states introduces various forms of feedback mechanisms.These result in nonlinearities in the system behavior with a very small change in the control parameter leading to undesirable outputs. Accordingly, one has to go beyond the linear models and methods and hence techniques from nonlinear dynamics are increasingly being employed for the prediction and to control such instabilities in system output.

A typical example where such a control feedback phenomenon plays a crucial role is a practical combustion system (Kabiraj and Sujith 2012). This includes industrial gas turbines, rocket motors, furnaces, etc., which often face the problem of high amplitude pressure oscillations that appear due to thermo-accoustic instability within the system. These can induce structural vibrations within the combustor, leading to reduced life span, reduced efficiency and even complete system failure in specific cases.

Time series data of pressure fluctuations from such systems clearly indicate (Kabiraj and Sujith 2012) limit cycle, quasiperiodic and intermittent oscillations with respect to changes in control parameters. The reconstructed phase space from the time series also show the presence of an underlying strange attractor. Several studies based on NTSA (Murugesan and Sujith 2015; Kabiraj et al. 2015; Christodoulou et al. 2016) have been undertaken in this regard that highlight the importance of nonlinear and network based measures in understanding, predicting and controlling such systems.

2.5.3 Applications in Bio-medical Data

An area where the techniques from NLTA have been constantly employed right from the beginning is in the analysis of bio-medical data. The complexity of many physiological rhythms originate from the nonlinear control processes taking place inside the human body (Glass 2001; Karma 2013; Qu et al. 2014). The different levels of this complexity and their variations, if properly analysed, will be useful in understanding the abnormalities that lead to many pathological cases (Go 2014). A mathematical representation of such a complexity using dynamical equations is most often not realizable due to the many interacting variables and uncertain parameters involved (Bruggerman and Westerhoff 2007; Lillacci and Khammash 2010). Hence the only possibility to study the underlying dynamics is to rely on information that can be deciphered from signals that can be obtained from these systems (Lehnertz

and Elger 1998; Richman and Moorman 2000). Over the last four decades, several such physiological signals like ECG, EEG, fMRI etc have been subjected to different techniques from NLTA.

As a typical example, Shekatkar et al. (2017) have undertaken a detailed analysis of ECG data combining dimension analysis, surrogate analysis and multi-fractal analysis using techniques discussed in Sects. 2.2 and 2.3. The authors have used 129 data sets from Physio Bank Archive for the analysis involving healthy and unhealthy subjects with different types of health anomalies. The results obtained reveal that the attractor underlying the dynamics of the heart has multi-fractal structure and the variations in the resultant multi-fractal spectra can clearly separate healthy subjects from unhealthy ones. The increased variability observed in the unhealthy cases can be a clinically meaningful diagnostic tool for detecting the abnormal dynamics of the heart.

2.6 Conclusion

In this review, we tried to present an overview of various techniques commonly used for the nonlinear analysis of time series data. These techniques are based on the concepts of dynamical systems theory by reconstructing the underlying dynamics in a higher dimension from a scalar time series. It is not possible to present all the different methods and measures of NTSA developed over the last four decades in a short review like this. Nor could we address all the different aspects regarding the practical implementation of these techniques available in a vast volume of literature. Here, we have mainly focused on the computation of dimension and multi-fractal spectrum and a specific method on the complex network based analysis of time series.

Finally, it should be reminded that NLTA is a powerful technique, but has its own limitations and also various possible sources of error in its practical implementation. This is especially important while applying to practical data analysis. These limitations can be of different origin, say, related to data (uneven sampling, finiteness, gap, etc), related to uncertainties in the choice of computational parameters (delay, threshold, etc) due to external factors (contamination by different types of noise) or due to algorithmic and computational limitations (edge effects, choice of scaling region, finite precision arithmatic, etc). One has to be aware of them in order to report meaningful results. As such, it requires a certain amount of expertise and experience on the part of the user in applying these methods and more so in interpreting the results.

References

Aberbanel HDI, Brown R, Sidorowich JJ, Tsimring LS (1993) Rev Mod Phys 65:1331
Albert R, Barabasi AL (2002) Rev Mod Phys 74:47
Andrzejak RG, Lehnertz K, Mormann F, Ricke C, David P, Elger CE (2001) Phys Rev E 64:061907

Barabasi AL, Albert R (1999) Science 286:509
Belloni T, Klein-Walt M, Mendez M, van der Klis M, Paradjis J (2000) Astron Astrophys 355:271
Boccaletti S, Latora V, Moreno Y, Chavez M, Hwang DU (2006) Phys Rep 424:175
Bradley E, Kantz H (2015) CHAOS 25:097610
Bruggerman FJ, Westerhoff HV (2007) Trends Microbiol 15:45
Casdagli M, Eubank S, Farmer JD, Gibson J (1991) Phys D 51:52
Christodoulou L, Kabiraj L, Saurabh A, Karimi N (2016) CHAOS 26:013110
Donner RV, Small M, Donges JF, Marwan M, Zou Y, Xiang R, Kurths J (2011) Int J Bifurc Chaos 21:1019
Donner RV, Zou Y, Donges JF, Marwan N, Kurths J (2010) New J Phys 12:033025
Donner RV, Heitzig J, Donges JF, Zou Y, Marwan N, Kurths J (2011) Eur Phys J B 84:653
Eckmann JP, Ruelle D (1992) Phys D 56:185
Eckmann JP, Kamphorst SO, Ruelle D, Ciliberto S (1986) Phys Rev A 34:4971
Eckmann JP, Kamphorst SO, Ruelle D (1987) Europhys Lett 4:973
Erdos P, Renyi A (1960) Publ Math Inst Hung Acad Sci 5:17
Eroglu D, Marwan N, Prasad S, Kurths J (2014) Nonlinear Proc Geophys 21:1085
Falconer KJ (1994) J Theor Prob 7:681
Fraser A, Swinney H (1986) Phys Rev A 33:1134
George SV, Ambika G, Misra R (2017) Nonlinear Dyn 89:465
Glass L (2001) Nature 410:277
Go AS (2014) Circulation 129:1
Grasberger P, Procaccia I (1983) Phys D 9:189
Grassberger P (1988) Phys Lett A 128:369
Grassberger P, Badii R, Politi A (1988) J Stat Phys 51:135
Halsey TC, Jensen MH, Kadanoff LP, Procaccia I, Shraiman BI (1986) Phys Rev A 33:1141
Harikrishnan KP, Misra R, Ambika G, Kembhavi AK (2006) Phys D 215:137
Harikrishnan KP, Misra R, Ambika G (2009) Comm Nonlinear Sci Num Sim 14:3608
Harikrishnan KP, Misra R, Ambika G, Amritkar RE (2009) CHAOS 19:043129
Harikrishnan KP, Misra R, Ambika G (2011) Res Astron Astrophys 11:71
Hentschel HGE, Procaccia I (1983) Phys D 8:435
Hilborn RC (1994) Chaos and nonlinear dynamics. Oxford University Press, Oxford
Jacob R, Harikrishnan KP, Misra R, Ambika G (2016) Phys Rev E 93:012202
Jacob R, Harikrishnan KP, Misra R, Ambika G (2016) Comm Non Sci Num Sim 41:32
Jacob R, Harikrishnan KP, Misra R, Ambika G (2018) Comm Non Sci Num Sim 54:84
Jensen MH, Kadanoff LP, Lichaber A, Procaccia I, Stavos I (1985) Phys Rev Lett 55:2798
Kabiraj L, Sujith RI (2012) J Fluid Mech 713:376
Kabiraj L, Saurabh A, Karimi N, Sailor A, Mastorakos E, Dowling AP, Paschereit CO (2015) CHAOS 25:023101
Karma A (2013) Ann Rev Condens Matter Phys 4:313
Kennel MB, Brown R, Aberbanel HDI (1992) Phys Rev A 45:3403
Lacasa L, Luque B, Ballesteris F, Luque J, Nuno JC (2008) Proc Natl Acad Sci USA 105:4972
Lainscsek C (2011) Phys Rev E 84:046205
Lainscsek C, Hernandez ME, Weyhenmeyer J, Sejnowski TJ, Poizner H (2013) Front Neurol 4:200
Lehnertz K, Elger CE (1998) Phys Rev Lett 80:5019
Liebert W, Schuster H (1989) Phys Lett A 142:107
Lillacci G, Khammash M (2010) PLoS Comput Biol 6:e1000696
Lindner JF, Kohar V, Kia B, Hippke M, Learned JG, Ditto WL (2015) Phys Rev Lett 114:054101
Mandelbrot BB (1982) The fractal geometry of nature. Freeman, New York
Marwan N, Romano MC, Thiel M, Kurths J (2007) Phys Rep 438:237
Marwan N, Donges JF, Zou Y, Donner RV, Kurths J (2009) Phys Lett A 373:4246
Misra R, Harikrishnan KP, Mukhopadhyay B, Ambika G, Kembhavi AK (2004) Astrophys J 609:313
Misra R, Harikrishnan KP, Ambika G, Kembhavi AK (2006) Astrophys J 643:1114
Moskalik P, Smolec R, Kolenberg K, Molnar L, Kurtz DW (2015) MNRAS 447:2348

Murugesan M, Sujith RI (2015) J Fluid Mech 772:225
Newman MEJ (2010) Networks: an introduction. Oxford University Press, Oxford
Nicolis G, Cantu G, Nicolis C (2005) Int J Bifurc Chaos 15:3467
Ott E (1993) Chaos in dynamical systems. Cambridge University Press, Cambridge
Packard N, Crutchfield J, Farmer JD, Shaw R (1980) Phys Rev Lett 45:712
Paladin G, Vulpiani A (1987) Phys Rep 156:147
Qu Z, Hu G, Garfinkel A, Weiss JN (2014) Phys Rep 543:61
Raidl A (1996) Czechoslovak J 46:293
Richman JS, Moorman JR (2000) Am J Physiol Heart Circ Physiol 278:H2039
Sander T, Wubbelar G, Lueschow A, Cuno G, Trahms L (2002) IEEE Trans Biomed Eng 49:345
Sano M, Sawada Y (1985) Phys Rev Lett 55:1091
Sauer T, Yorke J, Casdagli M (1991) J Stat Phys 65:579
Scheiber T, Schmitz A (1996) Phys Rev Lett 77:635
Schinkel S, Marwan N, Dimigen O, Kurths J (2009) Phys Lett A 373:2245
Schreiber T (1999) Phys Rep 308:1
Schreiber T, Schmitz A (2000) Phys D 142:346
Serre T, Kollath Z, Buchler JR (1996) Astron Astrophys 311:833
Shekatkar SM, Kotriwar Y, Harikrishnan KP, Ambika G (2017) Nat Sci Rep 7:15127
Shuster H, Just W (2005) Deterministic chaos. Wiley, New York
Silva C, Pimentel IR, Andrada A, Fored JP, Soares ED (1999) Brain Topogr 11:201
Takens F (1981) Detecting strange attractors in fluid turbulence. In Rand D, Young LS (eds) Dynamical systems and turbulence. Springer, Berlin
Theiler J, Eubank S, Longtin A, Galdrikian B, Farmer JD (1991) Phys D 58:72
Watts DJ (2003) Six degrees: the science of a connected age. Norton, New York
Wolf A, Swift J, Swinney H, Vastano J (1985) Phys D 16:285
Xu X, Zhang J, Small M (2008) Proc Natl Acad Sci USA 105:19601
Yang Y, Yang H (2008) Phys A 387:1381
Zhang J, Small M (2006) Phys Rev Lett 96:238701
Zou Y, Donner RV, Marwan N, Donges JF, Kurths J (2019) Phys Rep 787:1

Chapter 3
Unfolding Nonlinear Characteristics of Noise-Contaminated Real-World Data

Sirshendu Mondal and Achintya Mukhopadhyay

Abstract The success of dynamic characterization of a system mostly depends on how far the nonlinear structure of the data is identified. In most of the practical systems, the dynamic behaviour is to some extent dominated by stochastic processes. In such a scenario, unfolding the hidden determinism and nonlinearity from the real world data which is acquired from a complex physical phenomenon is a challenging task. The tools from nonlinear time series analysis facilitate a systematic investigation of complex dynamics mostly observed in real life phenomena. The present chapter proposes a survey on different such tools which are used for the dynamic characterization of experimental time series. To take the first step in this course, detecting noise contamination in the time series data is discussed, highlighting the tests for determinism such as local flow test (Kaplan-Glass test), translation error, correlation dimension, and correlation entropy. Once the determinism of a time series is identified, figuring out the nonlinear nature is the next concern. There are a few direct tests such as Lyapunov exponent, correlation dimension to confirm chaos, however, they have their inherent limitations while analysing experimental data contaminated with noise. In such a situation, a statistical test popularly known as surrogate test is adopted. The test is based on different (null) hypotheses and examining their validity through any discriminating statistics such as translation error, permutation entropy. Permutation spectrum can further be used to characterize the dynamic nature of the time series. Other aspects which help further understanding of the data sets in hand are the fractal features and the predictability. The fractal features of a time series are identified by using singularity spectrum. Finally, the role of local predictor such as Sugihara-May algorithm for forecasting the dynamics of a deterministic system is discussed.

S. Mondal (✉)
Department of Mechanical Engineering, National Institute of Technology Durgapur, Durgapur 713209, India
e-mail: sirshendumondal13@gmail.com

A. Mukhopadhyay
Department of Mechanical Engineering, Jadavpur University, Jadavpur, Kolkata 700032, India
e-mail: achintya.mukho@gmail.com

A. Mukhopadhyay et al. (eds.), *Dynamics and Control of Energy Systems*,
Energy, Environment, and Sustainability,
https://doi.org/10.1007/978-981-15-0536-2_3

3.1 Introduction

Time series which is one major form of the measured data is essentially a discrete sequence of observations acquired in time (Box et al. 2015). We encounter time series data in many different fields such as physical, biological and social sciences, stock market, meteorology, ecology. One of the major concerns of time series analysis is to understand the underlying mechanism that produces the observed time series. Most often, certain features of the time series are identified by evaluating different nonlinear measures so that the dynamical transition of the phenomenon is captured. Towards that, many measures based on dynamical systems theory such as translation error (Wayland et al. 1993), Hurst exponent (Nair and Sujith 2014), correlation dimension (Grassberger and Procaccia 1983; Harikrishnan et al. 2006) find their application in nonlinear analysis of the measured data observed in the diverse fields. These measures are indicative for the change between periodic and aperiodic time series. However, an aperiodic time series can be deterministic or stochastic. Therefore, identifying the deterministic nature of a time series or, in other words, quantifying the noise contamination (which is inevitable in the real-world data) should be the first step towards understanding the dynamics.

There are several methods to confirm determinism in a time series data; local flow test (Kaplan 1993) is one of them. The method is originally devised for continuous dynamical system by Kaplan and Glass (1992). The points in the phase space (reconstructed phase space for the case of single variable measurement) are evolved in time. For a deterministic signal, such points which are close to each other evolve in the same direction whereas, they evolve in arbitrary direction for stochastic signals. Capturing this feature, the vectors connecting initial and final points are constructed, normalized and averaged for a short duration. The process is further repeated for several time durations. These average vectors takes higher values for deterministic signals. The detailed procedure for the local flow test is given in Sect. 3.3.1.

We discuss another metric, called Translation error which is also a quantitative measure of determinism present in a time series (Wayland et al. 1993). The method is centered on the idea that neighbouring trajectories in phase space align in similar directions for the deterministic case. The detailed procedure is discussed in Sect. 3.3.2.

Sometimes, using multiple measures of determinism is found to produce more accurate information regarding the noise contamination. An example is the combined use of correlation dimension (D_2) and correlation entropy (K_2) proposed by Harikrishnan et al. (2009). This is a modified version of Grassberger-Proccacia algorithm (1983). By evaluating D_2, the presence of white noise can be quantified where K_2 is a better measure to detect colored noise in the measured data (Sect. 3.3.3). Once the determinism of a time series is identified, figuring out the nonlinear nature of the measured data is our next concern.

There are several measures and methods prescribed in literature, which can detect nonlinearity in the time series. These measures are used to recognize regular (periodic), chaotic and hyperchaotic dynamics. Among these, showing the evidence of

chaos remains the primary concern in analysing experimental time series. Towards that, Lyapunov exponent is a fundamental measure. For a deterministic dynamical system, the sensitive dependence of initial conditions is the fundamental property which is implemented to prove the chaotic nature of a time series (Pikovsky 1992). The Lyapunov exponent essentially quantifies the same by evaluating exponential divergence of nearby trajectories of an attractor in the phase space. If any one or more Lyapunov exponents become positive, the system is considered to be chaotic. The detailed procedure for calculating Lyapunov exponents is given in Sect. 3.4.1. This measure, however, find difficulty for identifying chaos for the noise contaminated experimental data.

Another direct measure which can detect the chaotic nature of a time series is correlation dimension (Grassberger and Procaccia 1983; Harikrishnan et al. 2006, 2009; Datta et al. 2009). The standard algorithm of Grassberger and Proccacia (1983) is generally adopted to compute correlation dimension. The procedure of finding correlation dimension involves identification of a scaling region by visual inspection (explained in Sect. 3.3.3). This becomes even challenging for the practical data contaminated with high levels of noise. Considering the limitations of aforementioned tests, the evidence of chaos and nonlinearity in the real-world data cannot therefore solely proved by the tests mentioned above. The remedy is pursuing a statistical test, known as surrogate test (Theiler et al. 1992; Schreiber and Schmitz 2000).

As a first step of surrogate test, a linear process is assumed as a so-called null hypothesis and the process is claimed to be the origin of the data under consideration. Next, surrogate data sets are generated from the original data following the null hypothesis. A discriminating statistic (any suitable nonlinear statistic) is then computed for both original and the surrogate data sets. If the value of the statistic for the original data is significantly different from the values obtained for the surrogate data sets, the null hypothesis (a linear process) can be rejected and nonlinearity is confirmed (Theiler et al. 1992). However, the hypothesis is rejected in a probabilistic sense and therefore, the number of surrogate data sets generated is predetermined to assure the required confidence level (Theiler et al. 1992). The detailed procedures for generating different types of surrogates (Schreiber and Schmitz 2000) are described in Sect. 3.4.2. As said earlier, any nonlinear statistic can be adopted for this statistical test. Here, we discuss one such statistic, namely, permutation entropy (also permutation spectrum). The degree of randomness/complexity in the time series is captured through permutation entropy which is easy to calculate for all types of time series such as regular, chaotic and noisy (Bandt and Pompe 2002). A symbolic approach is adopted wherein a time series is partitioned into groups. The measure has been shown to be similar to Lyapunov exponents, however, produces meaningful results for even noise contaminated real-world data (Bandt and Pompe 2002).

Apart from the features such as determinism and nonlinearity of a time series data, other aspects which help further understanding of the data sets in hand are the fractal features and forecasting. A self-similar structure is identified in a chaotic time series leading to the patterns of non-integer dimensions called fractals and the non-integer dimension is known as fractal dimension. A fractal time series is significantly different from a stochastic time series which does not hold any pattern (Gotoda et al.

2012; Nair and Sujith 2014). The fractal features are identified through a measure called singularity spectrum (Nair and Sujith 2014). However, this measure is not sufficient to claim the chaotic nature of a time series. This is due to the fact that a correlated noise might possess fractal features similar to that of a chaotic signal.

Another characteristic feature of a chaotic signal is short-term predictability and long-term unpredictability. This is again a consequence of the sensitive dependence of initial conditions. Therefore, nonlinear forecasting is able to quantify the complexity in the time series by updating the library data in phase space. Forecasting has been shown to satisfactorily distinguish between deterministic and stochastic data. In the present chapter, we discuss Sugihara-May algorithm (1990) as a local nonlinear predictor and its extended version proposed by Gotoda et al. (2015).

The rest of the chapter is organized as follows. Phase space reconstruction from a experimental time series will be discussed in Sect. 3.2. In Sect. 3.3, a few tests for determinism such as local flow test, translation error and correlation entropy will be described. Testing for nonlinearity of a time series will be discussed in Sect. 3.4. Fractal features of time series and nonlinear forecasting are discussed in Sects. 3.5 and 3.6, respectively. Application and limitations of different measures are summarized in Sect. 3.7.

3.2 Phase Space Reconstruction

A phase space or a state space is a space in which all the states of a system is reprented by its coordinates. As the system evolves in time, a path in the phase space is traced, know as phase space trajectory. The phase space or the attractor in phase space needs to be obtained before computing any nonlinear measure. Therefore, to construct the phase space, we require the time series of many variables. However, most often, the experimental data available consists of a single variable, if fortunate, a few. In such a situation, dynamics of any system/phenomenon can be visualized by constructing the mathematical phase space from a single time series data. The methodology is known as Takens' delay-embedding (Takens 1981). In this construction, the time series in hand is converted into a set of delay vectors. Consider a variable, $x(t)$ which is the only variable from the system under study. Now, we can construct the vectors such a way that these vectors collectively provide us the maximum information on the system dynamics. The vectors, $\mathbf{x}_i(d)$ are constructed as:

$$\mathbf{x}_i(d) = [x(t_i), x(t_i + \tau), x(t_i + 2\tau), \ldots x(t_i + (d-1)\tau)] \tag{3.1}$$

The elements of such vectors are the co-ordinates in the d-dimensional phase space and any vector, say $\mathbf{x}_i(d)$ is a point in the d-dimensional phase space at the time instant t_i. Two crucial parameters for accomplishing an appropriate reconstruction are the optimum time delay, τ and the least embedding dimension, d. A proper evaluation of τ and d is pivotal so that the full structure of the attractor is unfolded in the phase space.

A proper choice (optimum value) of the time delay is important. A very small value of the time delay may not unveil all the details of the dynamic characteristics (as the neighbouring points become highly correlated), while a very large value may introduce spurious features (as neighbouring points become mostly uncorrelated). There are a few methods to find the value of optimum time day for a given time series data (Abarbanel et al. 1993). In this chapter, we discuss a couple of them. The optimum time delay can be determined as the time when the *linear autocorrelation function* (LAF) first crosses zero (Abarbanel et al. 1993; Hilborn et al. 2000). As the name suggests, this is a linear measure, however, produces a reliable estimate for time delay. The LAF is given as,

$$C_L(\tau) = \frac{\frac{1}{N}\sum_{m=1}^{N}[x(m+\tau)-\bar{x}][x(m)-\bar{x}]}{\frac{1}{N}\sum_{m=1}^{N}[x(m)-\bar{x}]^2}, \tag{3.2}$$

where,

$$\bar{x} = \frac{1}{N}\sum_{m=1}^{N} x(m). \tag{3.3}$$

Here, $x(m)$ denotes the instantaneous measurement at $t = t_0 + m\tau_s$, where t_0 and τ_s are initial and sampling time, respectively. m, an integer, is a count for the time steps and N is the total number of data available in x. For a good choice of τ, one should look for the time lag when $C_L(\tau)$ first passes through zero. However, finding τ through such linear measure makes two observations, say $x(t)$ and $x(t+\tau)$ only linearly independent. Application of LAF for evaluating optimum time delay can be found in Datta et al. (2009), Mondal et al. (2014, 2015), Ghosh et al. (2010). Although, the linear independence may serve the purpose, nonlinear independence can be sought for, through the concept of *average mutual information* (Abarbanel et al. 1993).

The idea behind this method is how much information of a measurement at one time instant we can extract from a measurement of another time instant. The value of τ is found when the average mutual information (AMI) between the delay vectors reaches the first minimum. The AMI of a signal $x(m)$ is given by,

$$I(\tau) = \sum_{m=1}^{N} P(x(m), x(m+\tau)) \log_2 \left[\frac{P(x(m), x(m+\tau))}{P(x(m))P(x(m+\tau))}\right], \tag{3.4}$$

where, $P(x)$ denotes the probability of event x. AMI is essentially a measure of the amount of information shared by two sets of data. Therefore, for minimum value of AMI, the τ corresponds to two vectors which provide more information about the system than the individual vector can provide (Nair et al. 2013). Application of AMI for evaluating optimum time delay can be found in Gotoda et al. (2012, 2014), Nair et al. (2013). Once the optimum time delay is evaluated either by LAF or AMI, next step is to find a suitable (minimum) embedding dimension, d.

We discuss here Cao's method (1997) for finding a proper embedding dimension in which the dynamics of an attractor can be fully unfolded. This is an optimized version of well-known False Nearest Neighbors (FNN) method (Abarbanel et al. 1993). The FNN method is subjective in some sense and different embedding dimensions can be obtained for different value of parameter involved in that method (Cao 1997). The Cao's method overcomes the shortcoming of FNN. A false nearest neighbor to a point moves away as the embedding dimension is increased. Therefore, in these methods, one follows the nearest neighbors as the dimension is increased.

With optimum time lag, a measure $a(i, d)$ can be estimated as,

$$a(i, d) = \frac{||\mathbf{x}_i(d+1) - \mathbf{x}_{n(i,d)}(d+1)||}{||\mathbf{x}_i(d) - \mathbf{x}_{n(i,d)}(d)||}, \tag{3.5}$$

where, $i = 1, 2, \ldots, (N - d\tau)$ and $n(i, d)$ is the index of nearest neighboring point to the point $\mathbf{x}_i(d)$. $||\cdot||$ is the Euclidean norm between two points in phase space. Important to note that the nearest neighbors, $n(i, d)$ in $(d + 1)$-dimension should be same as those chosen in d-dimension, and if $\mathbf{x}_{n(i,d)}(d)$ equals to $\mathbf{x}_i(d)$, then one should consider the next neighbor. Here, appropriate dimension means there does not exist any false neighbor. Now, to avoid the dependency of index i, an average value of $a(i, d)$ is computed as,

$$E(d) = \frac{1}{N - d\tau} \sum_{i=1}^{N-d\tau} a(i, d), \tag{3.6}$$

where, $E(d)$ is a function of only d and τ. Now, the variation of $E(d)$ is obtained by defining $E_1(d)$ as,

$$E_1(d) = \frac{E(d+1)}{E(d)}. \tag{3.7}$$

$E_1(d)$ saturates beyond a value of d which is considered to the embedding dimension of the system. This happens for a deterministic signal, however, $E_1(d)$ always increases with increasing d for random signals. An additional measure $E_2(d)$ is also calculated to clearly distinguish between deterministic and stochastic signals.

$$E_2(d) = \frac{E^*(d+1)}{E^*(d)}, \tag{3.8}$$

where,

$$E^*(d) = \frac{1}{N - d\tau} \sum_{i=1}^{N-d\tau} |x(i + d\tau) - x(n(i, d) + d\tau)|. \tag{3.9}$$

Now, $E_2(d)$ is independent of d for random signals and equals to 1 whereas, for deterministic signal, it is a function of d and there must exist some values of

embedding dimension for which $E_2(d) \neq 1$. Having discussed the methodologies for phase space reconstruction, we turn to the tests of determinism in a measured time series.

3.3 Tests for Determinism

There are several metrics prescribed in literature to quantify the deterministic nature of a time series. In the present chapter, we discuss local flow test, translation error and correlation entropy.

3.3.1 Local Flow Test

Kaplan and Glass proposed a method for detecting determinism in continuous-time dynamical systems (Kaplan and Glass 1992). The method is then extended for discrete-time dynamical systems by Kaplan (1993). We discuss here the discrete version of it which is applicable for any measured time series. Once the phase space is reconstructed from a time series, the d-dimensional phase space needs to be filled with non-overlapping hypercubes (i.e. d-dimensional cubes). Let us say, jth hypercube consists of n_j points in the phase space with time indices $t_{j,1}, t_{j,2}, t_{j,3}, \ldots, t_{j,n_j}$. After a short time interval, knows as translation horizon (δ), the change in state for kth time instant ($k = 1, 2, \ldots, n_j$) in jth hypercube, i.e. $t_{j,k}$ to $t_{j,k} + \delta$ is given by,

$$\Delta \mathbf{x}_{j,k} = \mathbf{x}(t_{j,k} + \delta) - \mathbf{x}(t_{j,k}). \tag{3.10}$$

Note that the points which are at the edge of the cloud in the phase space tend to be connected to the points at center of the cloud for stochastic systems, leading to the directional bias of $\Delta \mathbf{x}_{j,k}$ (Kaplan 1993). For eliminating this bias, the modified method to calculate $\Delta \mathbf{x}_{j,k}$ is,

$$\begin{aligned}\Delta \mathbf{x}_{j,k} = \Bigg[&\sin\Big(2\pi \frac{x(t_{j,k} + \delta) - x(t_{j,k})}{\lambda}\Big), \sin\Big(2\pi \frac{x(t_{j,k} + \delta - \tau) - x(t_{j,k} - \tau)}{\lambda}\Big), \\ &\sin\Big(2\pi \frac{x(t_{j,k} + \delta - 2\tau) - x(t_{j,k} - 2\tau)}{\lambda}\Big), \cdots, \\ &\sin\Big(2\pi \frac{x(t_{j,k} + \delta - (d-1)\tau) - x(t_{j,k} - (d-1)\tau)}{\lambda}\Big)\Bigg]\end{aligned} \tag{3.11}$$

where, λ is the characteristic length of the cloud in the phase space and τ and d are the parameters for the phase space reconstruction. Now, a resultant vector ($\mathbf{V}_j$) is computed by summing up all the vectors in jth hypercube as,

$$\mathbf{V}_j = \frac{1}{n_j} \sum_k \frac{\Delta \mathbf{x}_{j,k}}{||\Delta \mathbf{x}_{j,k}||}. \tag{3.12}$$

The direction of $\mathbf{V}_j$ yields the information about the dynamics, however, the length of the vector, $|\mathbf{V}_j|$ is what we are interested in. Combining the values of $|\mathbf{V}_j|$ for all hypercubes in which $n_j = n$ and $n \geq 2$, a set of values, V_n (the average norm of all $|\mathbf{V}_j|$) are produced. We now define a measure, Λ for quantifying the local flow in the phase space as,

$$\Lambda = \left\langle \frac{V_n^2 - c_d^2/n}{1 - c_d^2/n} \right\rangle. \tag{3.13}$$

Here, c_d is a constant defined as (Kaplan and Glass 1992),

$$c_d = \sqrt{\frac{2}{d}} \frac{\Gamma(\frac{d+1}{2})}{\Gamma(\frac{d}{2})}, \tag{3.14}$$

where, Γ is a gamma function. The measure Λ approaches 1 for deterministic signal whereas it has values close to 0 for stochastic signals (Kaplan and Glass 1992; Kaplan 1993). Note, the characteristic length, λ is chosen as twice the standard deviation (2σ) of the data which is normally distributed. Several examples of this methods are illustrated in Kaplan and Glass (1992), Kaplan (1993). Apart from this, the method is utilized to explore determinism in combustion noise data (Nair et al. 2013) and physiological data (Glass and Kaplan 1993).

3.3.2 Translation Error

Next, we discuss the Wayland method to extract determinism in the time series. This is "*computationally simple variant*" on Kaplan-Glass method (Wayland et al. 1993). Let us choose arbitrarily a vector, $\mathbf{x}(t_i)$ from the reconstructed phase space of a given time series and find k nearest neighbors, $\mathbf{x}(t_j)$ ($j = 1, 2, \ldots, k$), of it. Now, projecting all the neighboring vectors after a suitable time interval T, $\mathbf{x}(t_j)$ becomes $\mathbf{x}(t_j + T)$. Therefore, the translation vectors are calculated as $\mathbf{V}(t_j) = \mathbf{x}(t_j + T) - \mathbf{x}(t_j)$.

Now, the spread of the displacements of the neighboring points yields to the diversity of the direction of neighboring trajectories ($\mathbf{V}(t_j)$ approximates the tangential vectors of the trajectories) and the same is calculated in terms of translation error, E_{trans} as,

$$E_{trans} = \frac{1}{k+1} \sum_{j=1}^{k} \frac{||\mathbf{V}(t_j) - \bar{\mathbf{V}}||}{||\bar{\mathbf{V}}||}, \tag{3.15}$$

where,

$$\bar{\mathbf{V}} = \frac{1}{k+1} \sum_{j=1}^{k} \mathbf{V}(t_j). \tag{3.16}$$

$||\cdot||$ represents the Euclidean distance between the vectors. Here, important to note that division by the length of $\bar{\mathbf{V}}$ ensures that the measure is insensitive to the overall scaling of the time series data. More the determinism is there in the time series (the trajectories being more parallel), the value of E_{trans} becomes more close to 0. For a stochastic signal, the value of E_{trans} approaches 1. Further, to reduce the stochastic error while evaluating translation error, one should compute medians of P sets of q randomly chosen $\mathbf{x}(t_i)$ and calculating average of P medians (Wayland et al. 1993; Miyano et al. 2008; Gotoda et al. 2010, 2014).

3.3.3 Correlation Entropy

We now turn our attention to the modified version of Grassberger-Procaccia algorithm (1983) to extract the stochastic component in the measured time series. The modified version is developed by Harikrishnan et al. (2009) for calculating correlation dimension, D_2 and correlation entropy, K_2. This method is more accurate identifying different types of noise (white and color) present in the time series data. By computing D_2, one can identify the presence of white noise, whereas the colored noise can be better detected by evaluating K_2. In the scheme proposed by Harikrishnan et al. (2009), the scaling region in the correlation sum is algorithmically determined, reducing the human error. Therefore, utilizing both D_2 and K_2 in combination eventually results in a more efficient analysis of time series.

Once the delay vectors are constructed using the values of delay time, τ (discussed above) and embedding dimension, d (variable here) from a time series, the next step is to calculate correlation sum $C_i^d(\epsilon)$ for any randomly chosen point in the phase space as,

$$C_i^d(\epsilon) = \frac{1}{N_v} \sum_{j=1, j\neq 1}^{N_v} H\big(\epsilon - ||\mathbf{x}(t_i) - \mathbf{x}(t_j)||\big), \tag{3.17}$$

where, H is a Heaviside function and N_v is the total number of reconstructed vectors (i.e. $N - (d-1)\tau$). $C_i^d(\epsilon)$ essentially counts the neighboring vectors of $\mathbf{x}(t_i)$ within a d-dimensional hypersphere of radius ϵ. Averaging this quantity over N_c randomly selected vectors, $\mathbf{x}(t_i)$, the correlation function appears to be

$$C^d(\epsilon) = \frac{1}{N_c} \sum_{i=1}^{N_c} C_i^d(\epsilon). \tag{3.18}$$

The correlation dimension (D_2) is then defined as,

$$D_2 \equiv \lim_{\epsilon \to 0} \frac{d(\log C^d(\epsilon))}{d(\log \epsilon)}, \tag{3.19}$$

and the correlation entropy, K_2 is defined as,

$$C^d(\epsilon) \propto \exp(-dK_2 \Delta t), \tag{3.20}$$

where, Δt is the time step between two successive measurement of the given data. The scaling region in Eq. (3.19) is conventionally identified by visual inspection. However, an algorithmic approach can be adopted for better computation (refer Harikrishnan et al. 2006). The measure, correlation dimension has been applied in the time series data of several systems such as pulse combustor (Datta et al. 2009; Mondal et al. 2014), swirl flames (Gotoda et al. 2009), fluid flows (Nakabayashi et al. 2005). Further, correlation entropy has been implemented to explore the noise contamination in different fields such as candle flame oscillations (Ghosh et al. 2010), combustion (Tony et al. 2015), astrophysics (Harikrishnan et al. 2011).

3.4 Tests for Nonlinearity

In nonlinear time series analysis, there are several measure to confirm nonlinearity in the measured data. Here, we discuss a measure, called Lyapunov exponent which is based on the fundamental properties of a chaotic time series. Considering the limitations of such measure, we further discuss surrogate test for nonlinearity. In the connection with surrogate data method we describe permutation entropy as a metric which can be used as a discriminating statistic.

3.4.1 Lyapunov Exponent

Lyapunov exponents essentially quantify the exponential convergence or divergence of the initially close trajectories in phase space. For all practical purposes, it is sufficient to know the largest/maximal Lyapunov exponent (LLE/MLE). We discuss here the method developed by Rosenstein et al. (1993). Alternative methods for calculating Lyapunov exponents are available in the literature (refer Kanz et al. 1994) which is an improved version of Wolf's method (1985).

The algorithm of Rosenstein et al. (1993) is widely accepted method for calculating maximal Lyapunov exponent, λ_{max} or λ_1. Once phase space is reconstructed, a reference vector, $\mathbf{x}(t_i)$ and its nearest neighbor vector, $\mathbf{x}(t_k)$ are found by searching the minimum distance between them as follows,

$$d_i(0) = \min_{\mathbf{x}(t_k)} ||\mathbf{x}(t_i) - \mathbf{x}(t_k)||, \tag{3.21}$$

where, $d_i(0)$ is the initial separation distance between the reference vector and it nearest neighbor. Now, if the distance between them after T time steps is $d_i(T)$, the follow relation hold true.

$$d_i(T) = d_i(0)e^{\lambda_1(T\Delta t)}, \tag{3.22}$$

where Δt is the sampling time period of $x(t)$. Therefore, maximal (largest) Lyapunov exponent is estimated as the gradient of the linear part of $\langle \ln d_i(T) \rangle$ against $T\Delta t$. Here, $\langle \ln d_i(T) \rangle$ is the average value of $\ln d_i(T)$ over all values of i.

Apart from Lyapunov exponent, correlation dimension (D_2, discussed above) can be used as a nonlinearity measure. However, these measures may not work for the measured data which are contaminated with noise. In other words, the application of these techniques are limited to noise free data. The alternative is a statistical test, called surrogate tests.

3.4.2 Surrogate Test

As a first step of surrogate test, a linear process is defined as null hypothesis. For example, we presume that an uncorrelated random process is the source of the measured data. This is an assumption and we next generate surrogate data sets which is consistent with this null hypothesis. Therefore, depending upon the types of null hypothesis we define there are different methods for generating surrogate data sets. Let us first discuss different null hypothesis and their corresponding method of generating surrogate data sets.

The most commonly used methods for surrogate data generation include (a) random shuffling of original time series, (b) Fourier transformed (FT) surrogates and (c) amplitude adjusted Fourier transformed (AAFT) surrogates, against which the original time series might be compared (Theiler et al. 1992).

The simplest way of generating surrogates is random shuffling or random permutation (RP). Thereby, the linear correlation present, if any, in the original time series is destroyed. However, the amplitude distribution of the original time series is preserved in the generated time series data. The null hypothesis defined for such surrogate data sets is that *an uncorrelated random process is the source of the data in hand*. If such hypothesis is rejected at the end of this test, we conclude that the measured data has temporal correlations.

Next step is to check whether *the measured data is generated from linearly correlated Gaussian process*. According to this hypothesis, the mean and the covariance of the surrogate data sets should match with that of original time series. Towards that, Fourier transformed (FT) surrogates are used. The phases of the Fourier transformed data is randomized with a uniform distribution of $[0, 2\pi]$ while maintaining

the amplitude spectrum of the original time series. In this method, phases are randomized because the useful information of a linear Gaussian process completely lies in mean and autocovariance function and not in Fourier phases (Schreiber and Schmitz 2000). Further, the autocovariance of the original time series is maintained in the surrogate data sets by maintaining the power spectrum (Wiener-Khinchin theorem (Chatfield 2016)).

If the data is contaminated with observational or measurement noise, the nonlinearity detected in the surrogate tests discussed above can be a consequence of the measurement noise. This is due to the fact that the probability distribution of the data generated from a linear Gaussian process may not be normal distribution if the data contains observational noise. In such a situation, the null hypothesis is defines as *the data is originated from a linear Gaussian process and also modified by a nonlinear measurement function* (Dolan and Spano 2001). Corresponding method of generating surrogate data is known as amplitude adjusted Fourier transformed (AAFT) surrogate. If $x(t_i)$ is the measured time series, according to null hypothesis, $x(t_i) = h(s(t_i))$, where h is the nonlinear measurement function and $s(t_i)$ is the outcome of a linear Gaussian process. The process of generating AAFT surrogates are as follows:

1. The measurement function is inverted to obtain a Gaussian/normal distribution of the original data. In other words, the original data is re-scaled to a normal distribution. This is done by assigning a rank to all the elements in the time series. A white noise data is then is rearranged to obtain the same rank structure.
2. A phase randomized surrogates of the rearranged data (from step 1) are then constructed.
3. Finally, the surrogate data sets are scaled to the distribution of original data such that the order the original data matches with that of the resultant surrogates.

By this method, the distribution and also the power spectrum of original time series are preserved (Dolan and Spano 2001). However, the method can lead to incorrect outcome if the distribution of the original data possess singularities or sharp transitions. Note that the outcome of the test is accurate if the original time series is long and the measurement function is almost an identity function meaning that the distribution of original data is close to Gaussian.

Once the surrogate data sets are generated, we need to compute any suitable nonlinear statistic (say, T) for both original and surrogate data. If the value of this statistic, also known as discriminating statistic, calculated for original data significantly differs from that evaluated for surrogates data sets, the null hypothesis can be rejected or one can conclude that the data is not generated from the process defined in the respective null hypothesis. Now, the rejection is carried out with some significance level depending upon the number of surrogate data is generated. The rejection region is found out at the tail of the distribution of T values calculated from the surrogate data sets and the significance level (s_L) is evaluated by the following equation.

$$s_L = \frac{|T - \langle T \rangle_{surrogate}|}{\sigma_{surrogate}}, \tag{3.23}$$

where, T is the value of the statistic considered, $\langle T \rangle_{surrogate}$ is the mean value of the statistic calculated for the surrogate data sets, and $\sigma_{surrogate}$ is the standard deviation of the statistic evaluated for the surrogate data sets. If any time series data is passed through the rejection of random shuffling, FT and AAFT surrogate test, one can conclude that the measured signal exhibits nonlinearity. As said earlier, any nonlinear statistic can be considered as deterministic statistic. Here in the next section, we discuss permutation entropy as an example of the same.

3.4.3 Permutation Entropy

Permutation entropy is one of the complexity measures of a time series. It is easy to calculate, computationally fast and gives meaningful results even if the data is contaminated with observational or dynamical noise (Bandt and Pompe 2002). This measure is based on ordinal pattern statistics (Parlitz et al. 2012). In this approach, a time series is partitioned by comparing the neighboring values. In other words, the method essentially maps a continuous time series onto a symbolic sequence.

Let us start with a time series, $x(t_i), i = 1, 2, 3, \ldots N$ and vectors in reconstructed phase space, $\mathbf{x}_i(d) = [x(t_i), x(t_i + \tau), x(t_i + 2\tau), \ldots x(t_i + (d-1)\tau)]$ where, τ and d are the optimum time delay and embedding dimension (discussed in Sect. 3.2), respectively. Essentially, the delay vectors, $\mathbf{x}_i(d)$ are the subsets (of length d) of the original time series and the elements are separated by τ. For any sequence (or delay vector, $\mathbf{x}_i(d)$) of length d, there can be $d!$ permutations.

Now, the order of the elements in any arrangement (permutation) is found by comparing the the relative values of the elements. The elements with the smallest and largest value are assigned the rank "1" and "d" (i.e. d distinct symbols), respectively. In other words, any point in the d-dimensional phase space of index i can be mapped onto one of the $d!$ permutations (Cao et al. 2004). If each such permutation is considered as a symbol (order of the ranks, also called ordinal pattern), the phase space becomes a symbol sequence and the maximum number of distinct symbols is $d!$. If the probability distribution (or relative frequency) of the distinct symbols are $P_1, P_2, \ldots, P_l$, where $l \leq d!$, permutation entropy is defined as the Shannon entropy of l distinct symbols as,

$$h_p = -\frac{\sum_{i=1}^{l} P_i \log_2 P_i}{\log_2 d!}. \tag{3.24}$$

The value of h_p lies between 0 and 1. For a regular time series, h_p approaches 0 whereas for a random time series, it becomes 1. Foe small values (say, 1 or 2) of d the method does not work, as there are very few number of permutations. Bandt and Pompe (2002) recommend d between 3 and 7.

3.5 Test for Fractal Features

For examining the fractal features of the phase space constructed from the time series, multifractal analysis is conducted. As said earlier, this is to evaluate the degree of self-similarity which is characterized by a spectrum, known as singularity spectrum (Gotoda et al. 2012; Nair and Sujith 2014). Here we discuss the method of evaluating singularity spectrum from a time series, developed by Harikrishnan et al. (2009).

Once the phase space is reconstructed from the given time series data, the generalized dimension D_q is computed. D_q is defined for any $q \geq 0$. The generalized correlation sum, $C_q(\epsilon)$ is computed by the following equations.

$$C_i(\epsilon) = \frac{1}{N_v} \sum_{j=1, j\neq 1}^{N_v} H\big(\epsilon - ||\mathbf{x}(t_i) - \mathbf{x}(t_j)||\big), \tag{3.25}$$

and

$$C_q(\epsilon) = \frac{1}{N_c} \sum_{i=1}^{N_c} C_i(\epsilon)^{q-1}, \tag{3.26}$$

where, N_v is the total number of vectors in the phase space and N_c is the number of randomly chosen centers. Next, the spectrum of the generalized dimensions is given by

$$D_q \equiv \frac{1}{q-1} \lim_{\epsilon \to 0} \frac{\log C_q(\epsilon)}{\log \epsilon}. \tag{3.27}$$

Again, The scaling region in Eq. (3.27) is conventionally identified by visual inspection. However, an algorithmic approach developed by Harikrishnan et al. (2006) can be adopted as a nosubjective approach. Once spectrum of generalized dimensions, D_q is found, singularity spectrum or $f(\alpha)$ spectrum is estimated.

Conventionally, $f(\alpha)$ spectrum can be determined analytically using Legendre transformation between from D_q to $f(\alpha)$ spectrum by the following equations.

$$\alpha = \frac{d}{dq}[(q-1)D_q], \tag{3.28}$$

$$f(\alpha) = q\alpha - (q-1)D_q. \tag{3.29}$$

However, computing $f(\alpha)$ using Eqs. (3.28) and (3.29) is considered to be difficult as it involves the smoothing of D_q curve and the Legendre transformation. Therefore, a different approach is prescribed by Harikrishnan et al. (2006), which is discussed below.

$f(\alpha)$ is defined as a function given as,

$$f(\alpha) = A(\alpha - \alpha_{min})^{\gamma_1}(\alpha_{max} - \alpha)_2^{\gamma}, \tag{3.30}$$

where, $A, \gamma_1, \gamma_2, \alpha_{min}$ and α_{max} are the characteristic parameters to produce $f(\alpha)$ curve. $f(\alpha)$ is defined such a particular way that the equation satisfies the following facts.

1. $f(\alpha)$ is a function of α only, within the limits α_{min} and α_{max}.
2. The derivative of $f(\alpha)$ that is $f'(\alpha) = df(\alpha)/d\alpha = q$ is also a function of α only.
3. $f(\alpha)$ curve has a single extremum (or maximum). $f(\alpha_{min}) = f(\alpha_{max}) = 0$ and $f'(\alpha_{min}) \to \infty$ and $f'(\alpha_{max}) \to -\infty$.

Harikrishnan et al. (2006) showed that out of the five parameters, only four ($\alpha_1 (\equiv D_1)$, $\alpha_{min} (\equiv D_\infty)$, $\alpha_{max} (\equiv D_{-\infty})$, and γ_1) can independently produce $f(\alpha)$ curve (γ_1 and A can be calculated from the four parameters (Harikrishnan et al. 2006)). Note that D_1 or α_1 is used as one of the input parameters, which can be obtained from D_q spectrum evaluated from the time series. There is another popular method to calculate D_q and $f(\alpha)$ spectrum in the literature (Ihlen 2012). These spectra help identifying the fractal features. As said earlier, such measure is not sufficient to ensure the chaotic nature of the time series.

3.6 Test for Predictability

Short-term predictability is another characteristic feature of a chaotic time series. Such a decay of predictability with time is caused by the fundamental characteristics of any chaotic data, sensitive dependence of initial conditions. Here, we present the Sugihara-May algorithm (1990) as a local nonlinear predictor.

A time series is initially divided into two parts (each consists of exactly half of the total data points). The first part is used as a source for generating predicted data set while the second part is used as a reference data to compare the predicted time series. The next step is to construct a phase space (as discussed in Sect. 3.2).

Once the phase space is reconstructed ($\mathbf{x}_i(d)$ from $x(t)$, Eq. 3.1), the final point of the trajectory ($\mathbf{x}_p$) is chosen where, $p = N - \tau(d-1)$. In phase space, k number of neighboring vectors ($\mathbf{x}_j$ where $j = 1, 2, 3, \ldots, k$) of $\mathbf{x}_p$ are found out. The neighboring points are chosen to form a minimal neighborhood such that $\mathbf{x}_p$ is enclosed d-dimensional polytope of minimum diameter.

If the value of $\mathbf{x}_i$ is to be predicted after T time steps (i.e. $\mathbf{x}_{p+T\Delta t}$), one needs to find out the location of the neighboring points after T time steps (i.e. $\mathbf{x}_{j+T\Delta t}$). From the new positions of the neighbors, $\mathbf{x}_{p+T\Delta t}$ is predicted using the exponential weights depending upon the original distances ($d_j = ||\mathbf{x}_j - \mathbf{x}_p||$) from the neighbors ($\mathbf{x}_j$) to the point, $\mathbf{x}_p$ by the following equation.

$$\mathbf{x}_{p+T\Delta t} = \frac{\sum_{j=1}^{k} \exp(-d_j)\, \mathbf{x}_{j+T\Delta t}}{\sum_{j=1}^{k} \exp(-d_j)}. \tag{3.31}$$

Equation 3.31 is called the local predictor as it depends on k nearest neighbor in the phase space. Minus sign in the weight indicates that neighbor of minimum distance has the maximum contribution to the predicted value. T can be varied from 1 to T_{max} where,

$$T_{max} = \frac{p - max(t_j)}{\Delta t}, \tag{3.32}$$

t_j being the time stamp of jth neighbor.

The library data is updated with predicted values to predict the longer time series with high accuracy. The idea is to update the source data library (in phase space, $\mathbf{x}_i(d)$) by adding number of predicted values from the previous step and removing the same number of vectors from the beginning of the trajectory (Gotoda et al. 2011, 2012). Once the predicted values are calculated, time series reconstruction is done from the predicted vectors.

As a final step, a comparison between predicted time series and reference time series (2nd part of the original time series) can be made by calculating Pearson correlation coefficient (Benesty et al. 2009; Mondal et al. 1995).

3.7 Summary

Detection of nonlinearity and other dynamical features in real-world data is one of the most important issues in physical, medical, engineering, and economic sciences. Meteorology demands a quantitative spatiotemporal description of different variables for accurate weather forecasting whereas in medical science, precise identification of transitions from a normal to an abnormal state enhance the quality of diagnosis and treatment. Other important applications include earthquake prediction and detection of anomalous events leading to power outages in power grids or financial crashes.

We discuss several measures and methods to unfold the nonlinear features of real-world data. As there can be dynamic as well as observational noise in the practical time series data, it is critical to quantify the amount of noise contamination and also to develop the measures which can extract information from the data set irrespective of noise contamination. Nonlinear time series analysis finds its application in diverse fields including energy systems.

References

Abarbanel HD, Brown R, Sidorowich JJ, Tsimring LS (1993) Rev Mod Phys 65(4):1331

Bandt C, Pompe B (2002) Phys Rev Lett 88(17):174102

Benesty J, Chen J, Huang Y, Cohen I (2009) Noise reduction in speech processing. Springer, pp 1–4

Box GE, Jenkins GM, Reinsel GC, Ljung GM (2015) Time series analysis: forecasting and control. Wiley

Cao L (1997) Phys D Nonlinear Phenom 110(1–2):43
Cao Y, Tung WW, Gao J, Protopopescu VA, Hively LM (2004) Phys Rev E 70(4):046217
Chatfield C (2016) The analysis of time series: an introduction. Chapman and Hall/CRC
Datta S, Mondal S, Mukhopadhyay A, Sanyal D, Sen S (2009) Combust Theory Model 13(1):17
Dolan KT, Spano ML (2001) Phys Rev E 64(4):046128
Ghosh S, Mondal S, Mondal T, Mukhopadhyay A, Sen S (2010) Int J Spray Combust Dyn 2(3):267
Glass L, Kaplan D (1993) Med Prog Technol 19:115
Gotoda H, Asano Y, Chuah KH, Kushida G (2009) Int J Heat Mass Transf 52(23–24):5423
Gotoda H, Miyano T, Shepherd IG (2010) Phys Rev E 81(2):026211
Gotoda H, Shinoda Y, Kobayashi M, Okuno Y, Tachibana S (2014) Phys Rev E 89(2):022910
Gotoda H, Pradas M, Kalliadasis S (2015) Int J Bifurc Chaos 25(05):1530015
Gotoda H, Amano M, Miyano T, Ikawa T, Maki K, Tachibana S (2012) Chaos Interdiscip J Nonlinear Sci 22(4):043128
Gotoda H, Ikawa T, Maki K, Miyano T (2012) Chaos Interdiscip J Nonlinear Sci 22(3):033106
Gotoda H, Nikimoto H, Miyano T, Tachibana S (2011) Chaos Interdiscip J Nonlinear Sci 21(1):013124
Grassberger P, Procaccia I (1983) Phys D Nonlinear Phenom 9(1–2):189
Harikrishnan K, Misra R, Ambika G, Kembhavi A (2006) Phys D Nonlinear Phenom 215(2):137
Harikrishnan K, Misra R, Ambika G (2009) Commun Nonlinear Sci Numer Simul 14(9–10):3608
Harikrishnan K, Misra R, Ambika G (2011) Res Astron Astrophys 11(1):71
Harikrishnan K, Misra R, Ambika G, Amritkar R (2009) Chaos Interdiscip J Nonlinear Sci 19(4):043129
Hilborn RC et al (2000) Chaos and nonlinear dynamics: an introduction for scientists and engineers. Oxford University Press on Demand
Ihlen EAFE (2012) Front Physiol 3:141
Kantz H (1994) Phys Lett A 185(1):77
Kaplan DT (1993) Int J Bifurc Chaos 3(03):617
Kaplan DT, Glass L (1992) Phys Rev Lett 68(4):427
Miyano T, Moriya T, Nagaike H, Ikeuchi N, Matsumoto T (2008) J Phys D Appl Phys 41(3):035209
Mondal S, Mukhopadhyay A, Sen S (2014) Combust Sci Technol 186(2):139. https://doi.org/10.1080/00102202.2013.851078
Mondal S, Mukhopadhyay A, Sen S (2015) Pramana 84(3):443
Mondal S, Mukhopadhyay A, Sen S (1995) In: 10th Asia-Pacific conference on combustion, Beijing, China, 19–22 July 1995
Nair V, Sujith R (2014) J Fluid Mech 747:635
Nair V, Thampi G, Karuppusamy S, Gopalan S, Sujith R (2013) Int J Spray Combust Dyn 5(4):273
Nakabayashi K, Sha W, Tsuchida Y (2005) J Fluid Mech 534:327
Parlitz U, Berg S, Luther S, Schirdewan A, Kurths J, Wessel N (2012) Comput Biol Med 42(3):319
Pikovsky AS (1992) Phys Lett A 165(1):33
Rosenstein MT, Collins JJ, De Luca CJ (1993) Phys D Nonlinear Phenom 65(1–2):117
Schreiber T, Schmitz A (2000) Phys D Nonlinear Phenom 142(3–4):346
Sugihara G, May RM (1990) Nature 344(6268):734
Takens F (1981) Dynamical systems and turbulence, Springer, Warwick, pp 366–381
Theiler J, Eubank S, Longtin A, Galdrikian B, Farmer JD (1992) Phys D Nonlinear Phenom 58(1–4):77
Tony J, Gopalakrishnan E, Sreelekha E, Sujith R (2015) Phys Rev E 92(6):062902
Wayland R, Bromley D, Pickett D, Passamante A (1993) Phys Rev Lett 70(5):580
Wolf A, Swift JB, Swinney HL, Vastano JA (1985) Phys D Nonlinear Phenom 16(3):285

Part II
Dynamics and Control of Nuclear and Phase Change Systems

Chapter 4
Dynamics of Flow in Natural Circulation Systems

Kannan Iyer

Abstract This chapter addresses the stability behavior of closed diabatic loops. The focus is on the prediction of stability boundaries for both single-phase and two-phase systems with minimum numerical distortion. As a means to check the performance of numerical schemes, several analytical solutions using method of characteristics have been evolved. These are then used to demonstrate the superiority of the characteristics based numerical method that is evolved systematically. Once the power is demonstrated, stability boundary is evolved for both single phase and two phase natural circulation in a closed rectangular loop. The method is demonstrated to satisfactorily predict the linear stability results obtained in single phase and experimental data generated in a two phase system.

Keywords Natural circulation · Thermosyphon · Linear stability · Non-linear stability

4.1 Introduction

Natural Circulation based systems have variety of applications in many engineering fields such as Chemical, Solar, Geothermal, Nuclear, etc. To appreciate the very many applications, the reader is directed to the review papers (Basu et al. 2014; Nayak and Vijayan 2008). Due to their inherently passive mode of operation, they are finding an increasingly bigger role in the new generation of nuclear plants. Two IAEA publications (2005, 2012) have a comprehensive compilation of the advantages, disadvantages and important issues arising in natural circulation systems. One of the important considerations in the design of natural circulation system is its dynamic characteristics. In these systems, the flow can change from a steady behavior to an oscillatory behavior, which is not desirable. The flow is called unstable if it oscillates. Hence, all engineered systems have to be assessed for their stability behavior. This

K. Iyer (✉)
Department of Mechanical Engineering, Indian Institute of Technology, Bombay, Mumbai 400076, India
e-mail: kiyer@iitb.ac.in

A. Mukhopadhyay et al. (eds.), *Dynamics and Control of Energy Systems*,
Energy, Environment, and Sustainability,
https://doi.org/10.1007/978-981-15-0536-2_4

assessment can be done mathematically using both linear and non-linear stability analysis. While the classical linear stability analysis is well established, the same cannot be said for the non-linear stability analysis.

In spite of several approaches that have been proposed for the non-linear stability analysis, there has always been a major hurdle in ascertaining the accuracy of the predictions. This is attributed to the inherent numerical dissipation and dispersion that creeps in due to the truncation errors inevitably present due to the approximations of the schemes proposed to solve the system of differential equations (Pletcher et al. 2013). In particular, the solution of energy equation that turns out to be a hyperbolic partial differential equation, if done incorrectly, leads to spurious prediction of the temporal response and stability boundaries. The boundaries are found to be sensitive to the spatial and temporal discretization. There have been many different approaches that have evolved in the literature to minimize numerical diffusion (Ambrosini and Ferreri 2003; Ferreri and Ambrosini 2002; Ambrosini and Ferreri 1998). While most authors who perform non-linear stability analysis and compare their results with the corresponding linear analysis, seldom have ventured to demonstrate the performance of their schemes against problems whose analytical solutions can be obtained.

In the present chapter, a characteristic based method that is most suitable for hyperbolic equations is systematically evolved and comparisons are made with problems that have analytical solutions in duct flows. Upon satisfactory comparison of temporal responses for simple cases, the method is then used to analyze the stability of the system and the boundaries are identified. Parametric results on the effect of grid sizes are also presented to demonstrate the robustness of the method. The methods cover both single-phase and two-phase natural circulation.

4.2 Governing Equations

In the development of the analysis, first, the equations are identified assuming a homogeneous two-phase fluid. Then, the case of all liquid is considered and its analysis is carried out separately before two-phase flow is considered. In the development, the following approximations have been made

1. The flow is incompressible in single-phase (refer item-5 for a more clear explanation). When two-phases are encountered, each phase is assumed to have a constant density. Thus, while the average density changes, the phase densities are constant.
2. The loop components are rigid and do not change their shape;
3. One dimensional area averaged equations are adequate to predict the system behavior. In case of two-phase flow, homogeneous equilibrium model is adequate;
4. Wall friction can be expressed adequately by a suitable friction factor. In case of two-phase flows homogeneous multiplier can be applied. It may, however, be noted that the major uncertainty in modelling real systems is the correct

representation of the friction factor. As this is not the focus of the present chapter, no further reference is made to this aspect;
5. Boussinessq approximation is valid when the fluid in the entire loop is in single-phase. This implies that the density may be treated as variable only in the body force term of the momentum equation; and
6. The following properties viz., cp and μ are assumed to be constant.

The conservation of mass may be written as,

$$\frac{\partial(\rho_m A)}{\partial t} + \frac{\partial(\rho_m A u_m)}{\partial s} = 0, \tag{4.1}$$

where, ρ_m, u_m and A represent the mixture density, velocity and cross sectional area for the flow, and s represents the running co-ordinate along the initial flow direction. At the junctions where different streams split or merge, the mass balance may be written as,

$$\sum \dot{m}_i = 0, \tag{4.2}$$

where, $\dot{m}_i$ represents mass flow rate of individual streams meeting at the junction. The flow coming into a junction is treated as positive and those leaving are taken as negative.

The conservation of momentum for the fluid may be written as,

$$\frac{\partial(\rho_m A u_m)}{\partial t} + \frac{\partial\left(\rho_m A u_m^2\right)}{\partial s} = -A\frac{\partial p}{\partial s} - \tau_w P_{hy} - \rho_m A g \sin\theta \tag{4.3}$$

where, P_{hy} is the hydraulic perimeter, θ is the inclination of the flow direction with the gravity vector and τ_w is the wall shear stress. The value of wall shear stress may be expressed in terms of the friction factor, f, as,

$$\tau_w = f_l \frac{\rho u_m^2}{2} \tag{4.4}$$

The closing relation used for the friction factor in ducts is,

$$f_l = CRe^{-n}, \text{ and, } Re = \frac{\rho_m u_m d_{hy}}{\mu_l} \tag{4.5}$$

where, μ_l is the viscosity of the liquid and d_{hy} is the hydraulic diameter. The values for C and n are (typically) 16 and 1 or 0.079 and 0.25 respectively, depending on whether the flow is laminar or turbulent

The conservation of energy may be written as,

$$\frac{\partial(\rho_m A h_m)}{\partial t} + \frac{\partial(\rho_m A u_m h_m)}{\partial s} = q'_w, \tag{4.6}$$

where, h_m is specific enthalpy of the mixture and q'_w is the heat generated per unit length at the wall. If the entire fluid is in single phase, then the linearized equation of state for ρ in the present analysis is taken as,

$$\rho = \rho_R(1 - \beta(T - T_R)), \tag{4.7}$$

where, β is the volumetric expansion coefficient and subscript R indicates the reference condition. In case of phase change, the phase densities are assumed to be constant at their saturation values and mixture density is taken as,

$$\rho_m = \frac{1}{v_m} = \frac{1}{v_f + x\left(v_g - v_f\right)}, \tag{4.8}$$

where, v represents the specific volume, the subscripts f and g stand for liquid and gas phases respectively, and x represents the thermodynamic quality. The equation of state for the specific enthalpy of mixture is taken as the thermodynamic definition,

$$h_m = h_f + x(h_g - h_f) \tag{4.9}$$

Thus, we have a closed system of equations and we can solve for u_m, ρ_m, h_m and p variations along the length of a closed heated and cooled loop.

4.3 Analysis of Single-Phase Systems

The loops can operate either fully in single-phase, or there can be boiling and condensation in the loop. The treatment has to be a bit different for the two cases mentioned above. This arises from the fact that if phase change is absent, the velocity in a constant area duct remains constant and hence the analysis can be simplified. However, this would not be the case when boiling occurs as the fluid accelerates while boiling and decelerates while cooling, thus making the analysis more detailed. To begin with, let us assume that phase change is absent.

Since, the system is rigid and Boussinessq approximation is invoked, the density and area in the transient term of Eq. (4.1) are constant. Hence, for a constant area duct, the velocity must be constant along the length. If the system is divided into a series of constant area links, then integration of Eq. (4.3) for a link of length, L, with Boussinessq approximation would lead to,

$$-\Delta p = \frac{4f\dot{m}^2 L}{2\rho_R d_{hy}} + g\int \rho_R(1 - \beta(T - T_R))dH + \frac{L}{A}\frac{d\dot{m}}{dt}, \tag{4.10}$$

where Δp is the pressure difference between the inlet and exit of the link and H is the elevation from a reference datum. Summing the pressure difference over the entire

loop will amount to,

$$\sum \Delta p = 0. \tag{4.11}$$

Using Eq. (4.8) in Eq. (4.9) we get,

$$\frac{4\dot{m}^2}{2\rho_R} \sum_{\substack{\text{All}\\\text{Links}}} \frac{f_i L_i}{d_i A_i^2} + g \oint_{\substack{\text{All}\\\text{Links}}} [\rho_R(1 - \beta(T - T_R))dH] + \frac{d\dot{m}}{dt} \sum_{\substack{\text{All}\\\text{Links}}} \frac{L_i}{A_i} = 0. \tag{4.12}$$

The second term can be simplified and Eq. (4.12) can be rewritten as,

$$\frac{4\dot{m}^2}{2\rho_R} \sum_{\substack{\text{All}\\\text{Links}}} \frac{f_i L_i}{d_i A_i^2} + \frac{d\dot{m}}{dt} \sum_{\substack{\text{All}\\\text{Links}}} \frac{L_i}{A_i} = g\beta\rho_R \oint_{\substack{\text{All}\\\text{Links}}} TdH. \tag{4.13}$$

Thus, the integral momentum equation can be solved, only when the temperature variation is obtained. Substituting the equation of state for enthalpy of a single-phase fluid,

$$dh = c_p dT, \tag{4.14}$$

into Eq. (4.6) leads to the following result for a duct of constant area,

$$\frac{\partial(T)}{\partial t} + u\frac{\partial(T)}{\partial s} = \frac{q'_w}{\rho c_p A}. \tag{4.15}$$

To put down Eqs. (4.13) and (4.15) in non-dimensional form, it is illustrative to look at the steady state form of the equations. Without loss of generalization, a rectangular loop of constant diameter studied by Mousavian et al. (2004) shown in Fig. 4.1 is considered for illustration of the concepts. It consists of 4 legs with the

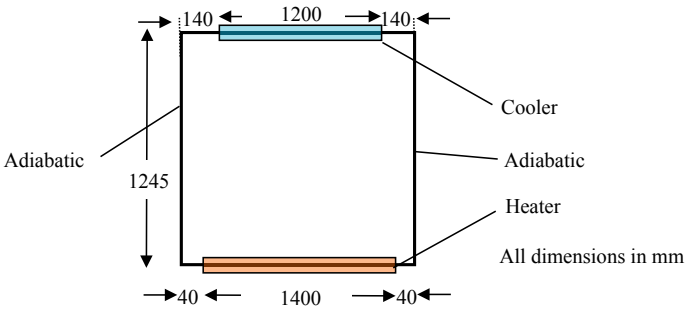

Fig. 4.1 Schematic representation of a closed rectangular loop

top leg (link 2) being the cooler and the bottom leg (link 4) the heater. The links 1 and 3 can be called the hot leg and cold legs respectively.

It should be quite clear that the term on the right hand side of integral momentum equation, viz., Eq. (4.13) will have contributions only from links that are vertically oriented. Thus, for the system shown in Fig. 4.1, the contributions will arise only from the hot and cold legs. At steady state, if the temperatures in the hot and cold legs are T_H and T_C respectively, then we can write,

$$\oint_{\substack{\text{All}\\\text{Links}}} TdH = H(T_H - T_C) \tag{4.16}$$

Thus, Eq. (4.13) can be written as

$$\frac{4\dot{m}^2}{2\rho_R A^2}\left(\frac{f_i L_{tot}}{d}\right) = g\beta\rho_R H(T_H - T_C) \tag{4.17}$$

$$\Rightarrow \left(\frac{f_i L_{tot}}{d}\right) = \frac{g\beta\rho_R H(T_H - T_C)2\rho_R A^2}{4\dot{m}^2} \tag{4.18}$$

On simplification, we can write the above equation as

$$\Rightarrow \left(\frac{f_i L_{tot}}{d}\right) = \frac{2gH\beta(T_H - T_C)}{4u^2} \tag{4.19}$$

Steady state energy balance would imply,

$$\rho A u c_p (T_H - T_C) = Q, \tag{4.20}$$

where, Q is the total heat transferred. Thus, we can rewrite Eq. (4.19) as

$$\Rightarrow \left(\frac{f_i L_{tot}}{d}\right) = \frac{2gH\beta Q}{4u^3\rho_R A c_p} \tag{4.21}$$

Thus, we can state that N_F (Friction number) is a function of Ri_m (Modified Richardson Number), where,

$$N_F = \left(\frac{f_i L_{tot}}{d}\right), \text{ and } Ri_m = \frac{gH\beta Q}{u^3\rho_R A c_p} \tag{4.22}$$

Since both N_F and Ri_m are unknowns, the same can be rewritten as,

$$\Rightarrow Re = \left(\frac{2}{4C}\frac{d}{L_{tot}}Gr_m\right)^{\frac{1}{3-n}}, \tag{4.23}$$

where,

$$Gr_m = \frac{gH\beta Qd^3\rho_R^2}{A\mu^3 c_p} \tag{4.24}$$

Thus, Reynolds number is a unique function of modified Grashoff number.

While the results have been derived for the special case of rectangular channel, to make the results applicable for a complex loop that will consist of several links with differing diameters, we shall manipulate the integral momentum equation to get results in a similar form as obtained for a rectangular channel. For this purpose, we shall choose a reference channel in the loop and call its length as L_R and its diameter as d_R. It is possible that in reactor systems, there can be several parallel channels carrying fluid in the loop and so, the flow area would be equal to the total area of all the parallel channels. In such a case the total mass flow rate can be expressed as

$$\dot{m} = N_R a_R \rho_R u_R = A_R \rho_R u_R = N_i a_i \rho_R u_i = A_i \rho_R u_i \tag{4.25}$$

where subscript i denotes any channel, R denotes reference channel and 'a' and 'A' represent the flow areas of one channel and the total flow area of all N channels put together respectively. Since friction factor for the reference and any arbitrary channel can be represented as,

$$f_R = CRe_R^{-n}, \text{ and } f_i = CRe_i^{-n}, \tag{4.26}$$

It is straight forward to write the following relations for circular pipes,

$$\frac{f_i}{f_R} = \left(\frac{Re_i}{Re_R}\right)^{-n} = \left(\frac{u_i d_i}{u_R d_R}\right)^{-n} = \left(\frac{N_R a_R d_i}{N_i a_i d_R}\right)^{-n} = \left(\frac{N_R d_R}{N_i d_i}\right)^{-n}. \tag{4.27}$$

Thus, Eq. (4.13) can be written as,

$$\frac{4\dot{m}^2}{2\rho_R A_R^2}\frac{f_R L_R}{d_R}\sum_{\substack{\text{All}\\\text{Links}}}\frac{L_i}{L_R}\left(\frac{N_R}{N_i}\right)^{2-n}\left(\frac{d_R}{d_i}\right)^{5-n} + \frac{d\dot{m}}{dt}\frac{L_R}{A_R}\sum_{\substack{\text{All}\\\text{Links}}}\frac{A_R}{A_i}\frac{L_i}{L_R} = g\beta\rho_R \oint_{\substack{\text{All}\\\text{Links}}} TdH \tag{4.28}$$

Before generalization into a meaningful form, it is pertinent to point that the integral term on the right hand side, as one moves around the loop, will give negative values while going up and positive values while moving down the loop. Thus, it is justifiable to write this term as,

$$\oint_{\substack{\text{All}\\\text{Links}}} TdH = \Delta T_{Ref} H_{Ref}. \tag{4.29}$$

This may become more clear as one looks at this term for the special case of the rectangular loop as given in Eq. (4.16). It would be logical to choose the reference temperature as the one across the heater under steady state and define it such that,

$$\Delta T_{Ref} = \frac{Q}{\dot{m}c_p}, \tag{4.30}$$

where Q is the total heat transferred. Thus, H_{ref} will get defined as,

$$H_{Ref} = \frac{\dot{m}c_p}{Q} \oint_{\substack{All\\Links}} TdH. \tag{4.31}$$

Physically H_{Ref} represents the vertical distance between the thermal centers between the two vertical legs. With the substitution of Eq. (4.29) in Eq. (4.28), it takes the form,

$$\frac{4\dot{m}^2}{2\rho_R A_R^2}\frac{f_R L_R}{d_R}\sum_{\substack{All\\Links}}\frac{L_i}{L_R}\left(\frac{N_R}{N_i}\right)^{2-n}\left(\frac{d_R}{d_i}\right)^{5-n} + \frac{d\dot{m}}{dt}\frac{L_R}{A_R}\sum_{\substack{All\\Links}}\frac{L_i}{L_R}\frac{A_R}{A_i} = \frac{g\beta\rho_R\Delta T_{Ref}Q}{\dot{m}c_p}. \tag{4.32}$$

Substituting for the mass flow rate in terms of reference conditions as given in Eq. (4.25), and expressing u_R and f_R in terms of Reynolds number, and rearranging the terms, we get,

$$Re_R^{3-n} + Re_R\frac{d(Re_R)}{d\tau}\frac{2\Sigma_2}{4c\Sigma_1} = Gr_m\frac{D_R}{L_R}\frac{2}{4c\Sigma_1}, \tag{4.33}$$

where, $\Sigma_1 = \sum_{\substack{All\\Links}}\frac{L_i}{L_R}\left(\frac{N_R}{N_i}\right)^{2-n}\left(\frac{d_R}{d_i}\right)^{5-n}$, $\Sigma_2 = \sum_{\substack{All\\Links}}\frac{L_i}{A_i}$, $\tau = \frac{t}{D_R^2/\nu}$, and

$$Gr_m = \frac{g\beta\rho_R^2 H_{Ref}Qd_R^3}{c_p A_R\mu^3}. \tag{4.34}$$

At steady state, the integral momentum equation can be expressed by dropping the transient term as,

$$Re_R = \left(Gr_m\frac{D_R}{L_R}\frac{2}{4C\Sigma_1}\right)^{\frac{1}{3-n}}. \tag{4.35}$$

It is fairly straight forward to compare Eq. (4.35) with Eq. (4.23) for the steady state by dropping the second term, and realizing that for the special case, N_i and N_R shall be 1 and d_i and d_R will be replaced with d and $L_R\Sigma_1$ will be replaced with L_{tot}, the summation of all lengths.

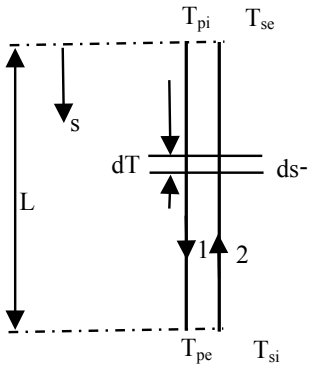

Fig. 4.2 Schematic view of a counter flow heat exchanger

It must however be clear that H_{Ref}, as defined in Eq. (4.31), can be evaluated for a general problem, only when the temperature profile is evaluated. In order to determine this profile, we need to integrate Eq. (4.15) for each link. Thus, it becomes necessary to specify a boundary condition at any arbitrary location. This anchoring of the fluid boundary condition in real systems is done at the cooling link which is usually cooled by an external fluid. It may, however, be noted that for a constant property (μ, c_p) system, the boundary condition has no effect on the circulation rate as it is the differential weight between the rising and falling columns that determines the flow and not the absolute weight. In other words, shifting of the temperature profile by a constant term would not cause a shift in circulating flow rate. Further, it is also interesting to point out that if the heating and cooling is carried out in horizontal links of a rectangular closed loop, then even the power profile will not alter the circulating flow rate, so long as the total power is preserved. This will, however, not be the case if the heating and cooling is carried out in vertical links.

To provide this boundary condition for an externally cooled system, consider a vertical link. To facilitate a simple solution, it is assumed to be a part of a one pass heat exchanger (assumed counter-flow) with a constant overall heat transfer coefficient. The energy balance at steady state for a differential element shown in Fig. 4.2 can be written as

$$-\dot{m}_p c_{pp} dT_p = UP_h(T_p - T_s)ds = \dot{m}_s c_{ps} dT_s, \tag{4.36}$$

where, subscript 'p' and 's' refers to primary and secondary streams that exchange heat, U is the overall heat transfer coefficient and P_h is the perimeter over which heat transfer occurs.

$$\Rightarrow \frac{dT_p}{ds} = -\frac{UP_h(T_p - T_s)}{\dot{m}_p c_{pp}} \text{ and } \frac{dT_s}{ds} = \frac{UP_h(T_p - T_s)}{\dot{m}_s c_{ps}}; \tag{4.37}$$

$$\Rightarrow \frac{d(T_p - T_s)}{ds} = -UP_h(T_p - T_s)\left\{\frac{1}{\dot{m}_p c_{pp}} + \frac{1}{\dot{m}_s c_{ps}}\right\}. \tag{4.38}$$

Using the boundary condition, $(T_p - T_s)$ at $s = 0$ is $(T_p - T_s)_0$, we can write,

$$\Rightarrow (T_p - T_s)_s = (T_p - T_s)_0 e^{-St\frac{s}{L}}, \text{ where } St = UP_hL\left\{\frac{1}{\dot{m}_p c_{pp}} + \frac{1}{\dot{m}_s c_{ps}}\right\}. \quad (4.39)$$

Using the above profile, the total heat exchanged from stream 1–2 can be shown to be,

$$Q_{ps} = \frac{UP_hL(T_p - T_s)_0}{St}\left(1 - e^{-St}\right). \quad (4.40)$$

If the total heat generated Q (= Q_{ps} at steady state), all fluid properties, geometry of the exchanger, and fluid parameters for secondary stream are known, then the temperature of primary stream at the inlet can be given expressed in terms of the mass flow rate of primary stream, by rearranging Eq. (4.40) as,

$$T_{p0} = T_{s0} + \frac{Q\left\{\frac{1}{\dot{m}_p c_{pp}} + \frac{1}{\dot{m}_s c_{ps}}\right\}}{\left(1 - e^{-St}\right)}. \quad (4.41)$$

This completes the specification of the boundary condition. The heat transferred per unit length at any given distance 's' from the inlet can be computed as,

$$q' = UP_h(T_p - T_s)_0\left(1 - e^{-St\frac{s}{L}}\right). \quad (4.42)$$

Further, integrating the first differential equation in the set of equations given in Eq. (4.37) after using Eq. (4.39) to eliminate the term $(T_p - T_s)$ with the boundary condition $T_p = T_{p0}$ at $s = 0$, we get,

$$T_p(s) = T_{p0} - \frac{UP_h}{\dot{m}_p c_{pp}}(T_p - T_s)_0\left(s + \frac{L}{St}\left\{e^{-St\frac{s}{L}} - 1\right\}\right). \quad (4.43)$$

The above equation can be rewritten by eliminating T_{p0} and $(T_p - T_s)_0$ by using Eq. (4.41) as,

$$T_p(s) = T_{s0} + \frac{Q\left\{\frac{1}{\dot{m}_p c_{pp}} + \frac{1}{\dot{m}_s c_{ps}}\right\}}{1 - e^{-St}}\left[1 - \frac{UP_h}{\dot{m}_p c_{pp}}\left(s + \frac{L}{St}\left\{e^{-St\frac{s}{L}} - 1\right\}\right)\right]. \quad (4.44)$$

Thus, the temperature profile of the primary fluid has been obtained in terms of the primary and secondary mass flow rates. Later in this work, the case of high secondary flow is considered for obtaining the stability boundaries. For this particular case, the Stanton number definition, $St_{s\infty}$ (the subscript denotes that the secondary flow is very large), can be given as,

$$St_{s\infty} = UP_hL\left\{\frac{1}{\dot{m}_p c_{pp}}\right\}. \tag{4.45}$$

Using this definition, Eq. (4.44) can be rearranged to express it in the non-dimensional form as,

$$\frac{T_p(s) - T_{s0}}{\left\{\frac{Q}{\dot{m}_p c_{pp}}\right\}} = \frac{1}{1 - e^{-St_{s\infty}}}\left[1 - St_{s\infty}\left(\frac{s}{L} + \frac{1}{St_{s\infty}}\left\{e^{-St_{s\infty}\frac{s}{L}} - 1\right\}\right)\right]. \tag{4.46}$$

Thus, Stanton number is the non-dimensional parameter that affects the temperature profile and will become a control parameter in the transient analysis.

4.3.1 Transient Analysis

Generally, steady state analysis seldom causes difficulties. It is the transient solutions which tend to get erroneous due to improper solution of the resulting hyperbolic energy equation. The main source of error is due to the numerical diffusion that results on account of the nature of finite difference algorithm that is used. The purpose of this section is to develop an algorithm and benchmark the same.

The governing equations for the transient analysis are the integral momentum equation and the energy equation as given in Eqs. (4.12) and (4.15) respectively. These form a set of non-linear equations. For engineering analysis, one prefers to deal with dimensional parameters. Hence all the discussions are limited to the dimensional form of the equation. However, for the purpose of comparing the final result with those of other authors, non-dimensional form is resorted to.

For the purpose of simplicity of representation and for later application to two-phase flows, Eq. (4.12) is rewritten as,

$$\frac{d\dot{m}}{dt}\sum_{\substack{\text{All}\\\text{Links}}}\frac{L_i}{A_i} = -\Delta p_{fric} - \Delta p_{grav}, \tag{4.47}$$

where,

$$\Delta p_{fric} = \frac{4\dot{m}^2}{2\rho_R}\sum_{\substack{\text{All}\\\text{Links}}}\frac{1}{A_i^2}\left(\frac{f_i L_i}{d_i} + \frac{K_i}{4}\right) \text{ and } \Delta p_{grav} = g\oint_{\substack{\text{All}\\\text{Links}}}[\rho_R(1 - \beta(T - T_R))dH]. \tag{4.48}$$

It may be noted that in the frictional term, a loss coefficient (K_i) has been added to account for irreversible junction loss. Thus, the governing equations for determining the transient flow in the system are Eq. (4.47) and Eq. (4.15). While, Eq. (4.47) is an Ordinary Differential Equation (ODE) with an integral term, Eq. (4.15) is a Partial

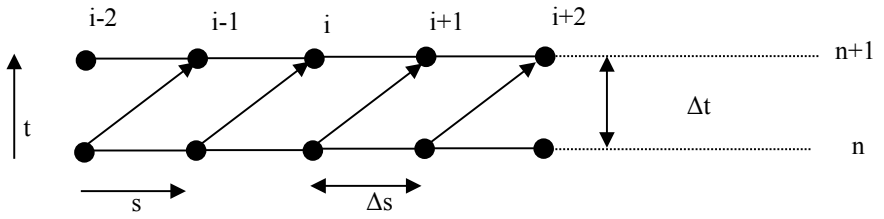

Fig. 4.3 Schematic representation of the grids and the characteristic direction

Differential Equation (PDE) of the hyperbolic type. These coupled equations can now be solved numerically.

Numerical Solution. The solution of hyperbolic equations is best obtained by characteristics based method as this introduces minimum numerical errors. In this method, characteristic direction along which information propagates is identified and numerical calculations are performed along the characteristic direction. The PDE given in Eq. (4.15) is split into two ODEs as follows,

$$\frac{dT}{dt} = \frac{q'_w}{\rho c_p A}, \text{ along } \frac{dt}{ds} = \frac{1}{u}. \tag{4.49}$$

The direction given by the second ODE in Eq. (4.49) is the characteristic direction. For single-phase flow in a duct of constant area, u is constant along its length, and the solution plane can be represented as shown in Fig. 4.3. The arrows in the figure point to the characteristic directions. The figure depicts that the information from the grid point $(i - 1)$ at level (n) is just passed on to the grid point (i) at level $(n + 1)$. In such a case,

$$\frac{\Delta t}{\Delta s} = \frac{1}{u}, \text{ or } \frac{u\Delta t}{\Delta s} = 1. \tag{4.50}$$

If this condition is satisfied and we compute the temperatures at level $(n + 1)$ using the relation,

$$\frac{T_i^{n+1} - T_{i-1}^{n}}{\Delta t} = \frac{q'_w}{\rho c_p A}, \tag{4.51}$$

then, the solution is exact, if the parameters on the right hand side of Eq. (4.51) are constant.

Errors in solution creep, if the condition in Eq. (4.50) cannot be satisfied at every node. This can arise in when there are several links of lengths L_i, whose cross sectional areas are A_i (if there are parallel links, then this represents the total area) and the velocities are u_i. For such a system, the mass balance would imply,

$$u_i = \frac{u_R A_R}{A_i}, \tag{4.52}$$

where, subscript 'r' refers to the reference link and 'i' refers to any link. To obtain exact solutions, at all points for a given Δt, the condition to be satisfied is,

$$\frac{u_i \Delta t}{\Delta s_i} = 1 = \frac{u_R \Delta t}{\Delta s_R}. \tag{4.53}$$

This implies that,

$$\Delta s_i = \frac{u_i \Delta s_R}{u_R}. \tag{4.54}$$

Thus, for a given Δt, Δs_R, that have been chosen to satisfy Eq. (4.53), Δs_i, will be constrained by Eq. (4.54). Thus, for a given length of the links L_i, the number of nodes given by $L_i/\Delta s_i$ may turn out to be a non-integer. In such an event, one would be forced to choose the number of nodes to be truncated to the nearest lower integer. It should be understood that by choosing the number of grids more than this value would lead to numerical instability. Thus, the numerical information would have to be interpolated, leading to numerical diffusion. The classical upwind scheme, to be described later is a scheme that interpolates using linear interpolation. One way to avoid this is to adjust the length to the links to satisfy the condition such that the number of nodes is an integer.

To demonstrate the degree of distortion that is introduced by interpolation, consider the idealised equation,

$$\frac{\partial \phi}{\partial t} + u \frac{\partial \phi}{\partial s} = S. \tag{4.55}$$

In the above equation, u and S are assumed to be constants. The numerical solution using the upwind scheme with u in the positive x direction would be (refer Fig. 4.3),

$$\frac{\phi_i^{n+1} - \phi_i^n}{\Delta t} + u \frac{\phi_i^n - \phi_{i-1}^n}{\Delta s} = S, \text{ or, } \phi_i^{n+1} = \phi_i^n - C\left(\phi_i^n - \phi_{i-1}^n\right) + S\Delta t, \tag{4.56}$$

with

$$C = \frac{u \Delta t}{\Delta s}, \tag{4.57}$$

where, C is called the Courant number. When $C = 1$, it is the exact form of the characteristic based method with no interpolation. The necessary condition for stability of the numerical scheme being $C \leq 1$, it can be shown that even a 30% reduction in Courant Number can have a substantial addition of numerical diffusion.

To demonstrate this, let us assume that the initial and boundary condition for Eq. (4.55) be,

$$\phi(s, 0) = \phi_{to}(s), \text{ and } \phi(0, t) = \phi_{so}(t). \tag{4.58}$$

The analytical solution for the above is

$$\phi(s, t) = \phi_{to}(s_0) + S(t - t_0), \text{ with, } s_0 = s - ut, \ t_0 = 0, \text{ for the condition } s > ut, \tag{4.59}$$

and

$$\phi(s, t) = \phi_{to}(s_0) + S(t - t_0), \text{ with, } s_0 = 0, \ t_0 = t - s/u, \text{ for the condition } s \leq ut. \tag{4.60}$$

To demonstrate the solution for oscillating conditions, for a domain of $0 < s < 10$, $0 < t < 20$ with $S = 1$ and with,

$$\phi_{to}(s) = s/10, \text{ and } \phi_{so}(t) = \sin t, \tag{4.61}$$

the comparisons of analytical and numerical solutions for $C = 1.0$, 0.9 and 0.7 are shown in Fig. 4.4 and 4.5. It may be observed that at $C = 1.0$, the solution is exact, whereas deviation is substantial at $C = 0.7$. The errors at $C = 0.9$ appears tolerable for the present parameters. Thus, while a small variation in Courant Number (up to 10%) is probably acceptable, a deviation of 30% brings about serious dissipation error.

It is now apparent that we can get very accurate solutions, if we can keep the Courant Number close to 1 at all points. Whenever we are predicting transients, it is necessary to understand the implications as the velocity varies with time. Since the positions of nodes have been fixed based on the initial data, the time step at every instant has to be adjusted to satisfy the Courant Number criterion. The influence of this on the accuracy has to be investigated. For this an analytical solution based on MOC (Method of Characteristics) is evolved and compared. Since the primary interest is on the stability analysis, the velocity is assumed to vary sinusoidally with time. The governing equation chosen is,

$$\frac{\partial \phi}{\partial t} + (C - \sin(\omega t))\frac{\partial \phi}{\partial s} = 0, \tag{4.62}$$

subject to initial and boundary condition,

$$\phi(s, 0) = \phi_{to}(s), \text{ and } \phi(0, t) = \phi_{so}(t). \tag{4.63}$$

For a domain of $0 < s < 10$, $0 < t < 50$ and with,

$$\phi_{to}(s) = s/10, \text{ and } \phi_{so}(t) = \sin 2t, \tag{4.64}$$

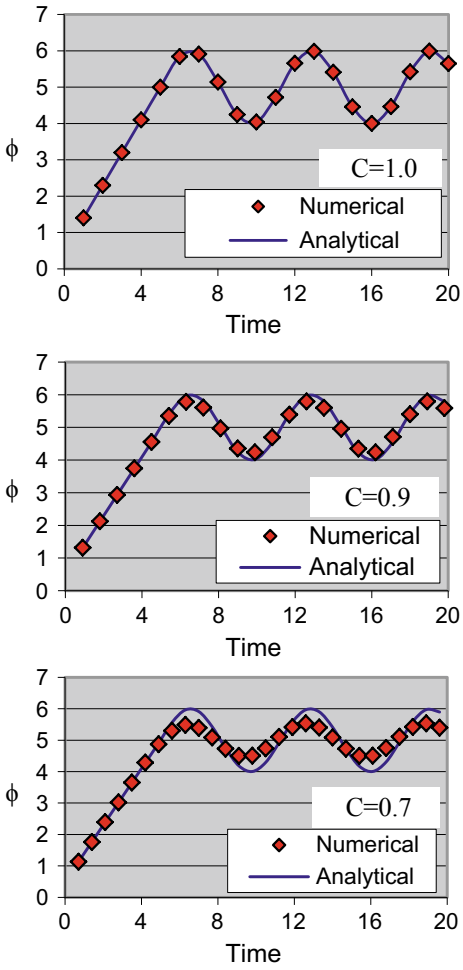

Fig. 4.4 Comparisons of numerical and analytical solutions at s = 5 for C = 1.0, 0.9 and 0.7

the analytical solution for this case can be expressed as

$$\phi(s, t) = \phi_{to}(s_0), \text{ for the condition } s \geq s^* \tag{4.65}$$

and

$$\phi(s, t) = \phi_{so}(t_0), \text{ for the condition } s < s^*, \tag{4.66}$$

where

$$s_0 = s - s^*, s^* = Ct + (\cos(\omega t) - 1)/\omega, \tag{4.67}$$

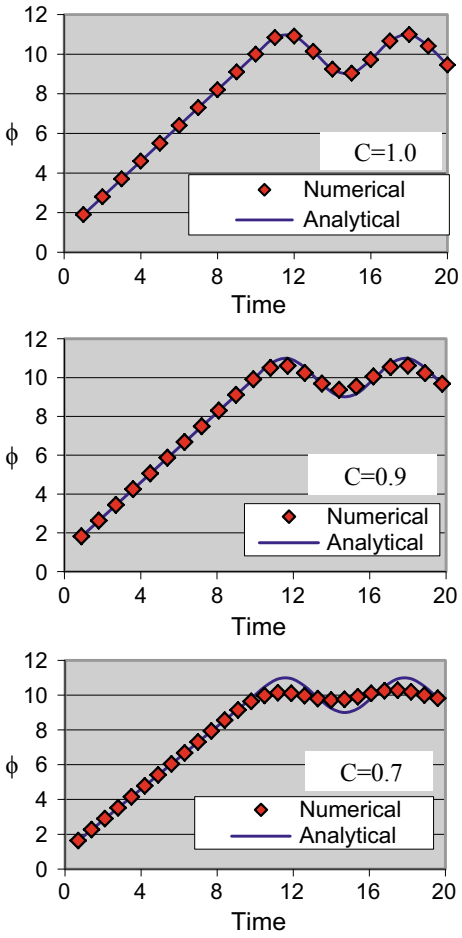

Fig. 4.5 Comparisons of numerical and analytical solutions at s = 10 for C = 1.0, 0.9 and 0.7

and t_0 is the root of the equation,

$$s - C(t - t_0) - (\cos(\omega t) - \cos(\omega t_0))/\omega = 0 \tag{4.68}$$

The analytical solution is now compared with the numerical solution for C = 3 and $\omega = 5$. The Numerical and analytical solutions at the mid point and at the two ends are shown in Fig. 4.6. In Fig. 4.6a the velocity variation with time is also sketched for visualisation. It may be observed that the method has been able to capture the analytical solution almost exactly. Having established the accuracy of the method, the same is now applied to predict the stability boundary of the loop used by Mousavian et al. (2004).

The solutions for stability in the loop shown in Fig. 4.1 was investigated by Mousavian et al. (2004) by finite difference method. They observed that the predictions for

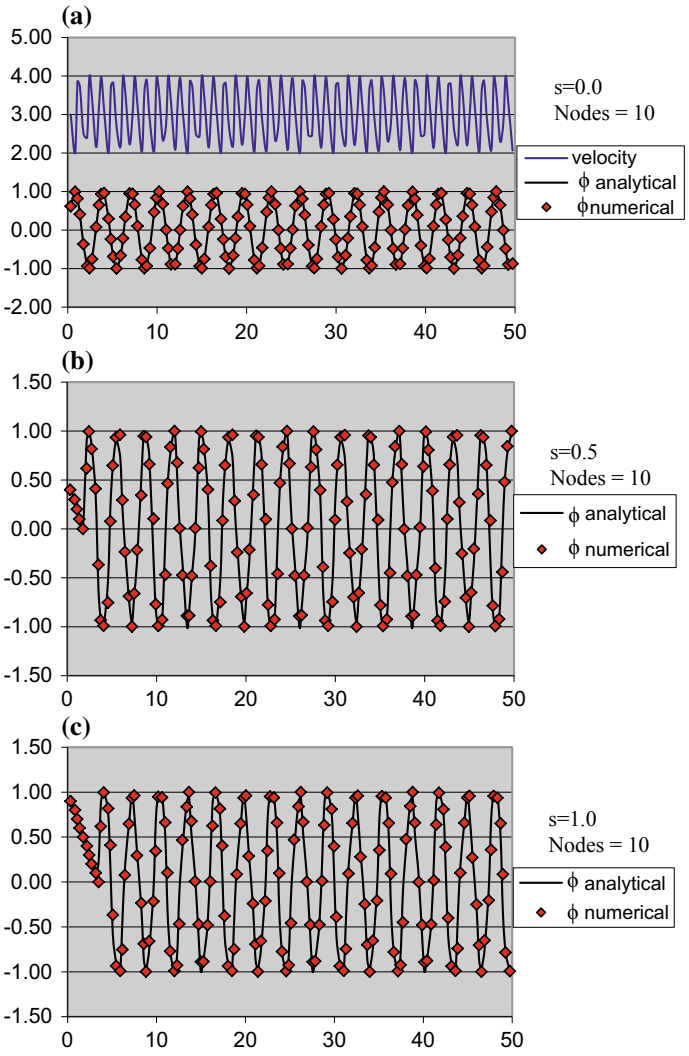

Fig. 4.6 Comparisons of numerical and analytical solutions at s = 0.5

the onset of stability was dependent on the grid size and had to resort to fine nodalisations. Similar observations are expressed by Ambrosini and Ferreri (2003). Further, the linear stability solution and the non-linear stability solution presented by Mousavian et al. (2004) apparently do not agree. For instance, they presented a non-linear solution to be unstable below a critical Gr_m of 2.8×10^{10} at $St_m = 8$, whereas, their linear solution predicts that for $St_m > 6.7$, the flow is always stable. Thus, their linear and non-linear solutions have been wide apart. The reason for this discrepancy is probably the inaccuracies that are introduced in the non-linear model. It is believed

that the characteristics based method discussed above, that uses adaptive time step, would be more accurate. The loop given in Fig. 4.1 was simplified to get rid of the small links next to heater and was accommodated as a part of the heater. The Fanning friction factor, f, was taken to be,

$$f = 0.079\,Re^{-0.25}, \tag{4.69}$$

and the stability analysis was performed. The analysis was carried out with an initial perturbation of 1% of the steady state velocity. The results are shown in Fig. 4.7. It may be observed that there is only a small difference seen between linear and non-linear solutions and this may be attributed to the non-linear effects. The above calculations were done with a minimum node size of 35 mm. Just to show the power of the method, the temporal variation of the velocity using a node spacing of 70 mm for the case of $Gr_m = 10^9$ and $St_m = 7.1$ is compared with the temporal result with 35 mm spacing in Fig. 4.8. It may be observed that the transients are almost identical. Thus, the method is relatively insensitive to node sizes and can be used with coarse meshes.

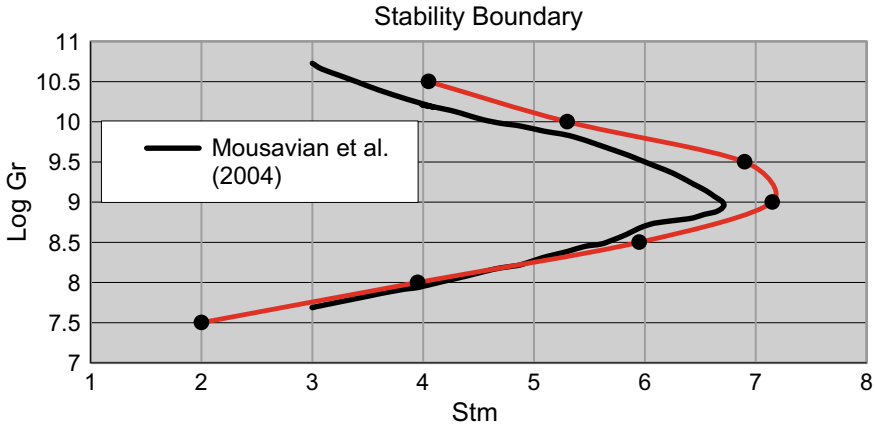

Fig. 4.7 The stability plot for the loop shown in Fig. 4.1

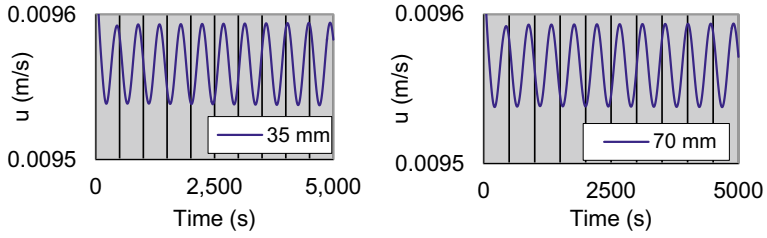

Fig. 4.8 Effect of node size on the temporal response

4.3.2 Conclusions from Single-Phase Studies

A computational procedure is developed for the steady state and transient analysis of flow in diabatic loops. The characteristics based numerical method is demonstrated to be an efficient and reliable method to capture the transients with almost no numerical diffusion. The method is found to be a robust one for the analysis of stability of thermosyphon loops and does not require excessive nodes. This method can be logically extended to two-phase systems. This will be discussed in the next few sections.

4.4 Analysis of Two Phase Systems

For loops in which boiling may occur, the treatment of stability analysis is a bit different. The main difference is that the variation of density is a much stronger function of position in the heated link, which makes the essential assumption in single-phase, viz., Boussinessq approximation, where density varies only in the body force term of momentum equation, invalid. As density rapidly decreases with vapour generation, the fluid accelerates in the heated link, thereby making lumping of the acceleration term impossible. As done earlier, the analysis of steady state is presented prior to the transient analysis.

4.4.1 Steady State Analysis

The governing equations have already been summarised in Sect. 4.2 (Eqs. (4.1)–(4.9)). However, the manipulation of the equations is slightly different. Particularly, since the temperature does not vary during phase change, it is customary to handle enthalpies instead. The state of the fluid is also expressed in terms of thermodynamic quality, which can be defined as,

$$x = \frac{h_m - h_f}{h_{fg}}. \tag{4.70}$$

Note that x would be negative, for sub-cooled fluid. Usually the fluid at the entry to the heated link will be sub-cooled. As in the single-phase loops, the inlet sub-cooling to the heater will be anchored by the secondary coolant. Since the primary purpose of this section is to develop the methodology for stability analysis, this boundary condition is assumed to be known as h_{in} and the treatment to compute this value is deferred for the time being. The non-dimensional representation of this state is called the sub-cooling number defined by,

$$N_s = \frac{h_f - h_{in}}{h_{fg}} \frac{v_{fg}}{v_f}. \tag{4.71}$$

Considering the steady state mass balance (Eq. (4.1)) can be stated as,

$$\frac{d\dot{m}}{ds} = 0 \text{ or } \dot{m} = \text{constant}. \tag{4.72}$$

Thus, mass flow rate across any link at steady state is independent of position and hence we can write,

$$\dot{m} = N_R a_R \rho_R u_R = A_R \rho_R u_R = N_i a_i \rho_i u_i = A_i \rho_i u_i. \tag{4.73}$$

The energy equation (Eq. (4.6)) at steady state can be written as,

$$\dot{m} h_{fg} \frac{dx}{ds} = N_H q'_w, \tag{4.74}$$

where, N_H represents number of heated channels. The above equation can be integrated for the heated link and can be written as,

$$\dot{m} h_{fg} (x_e - x_{in}) = N_H \int_0^{L_H} q'_w ds = Q. \tag{4.75}$$

Equation (4.75) can be rewritten in non-dimensional form as,

$$x_e \frac{v_{fg}}{v_f} = N_Z - N_s, \tag{4.76}$$

where, N_z is the Zuber number defined as,

$$N_Z = \frac{Q}{\dot{m} h_{fg}} \frac{v_{fg}}{v_f} \tag{4.77}$$

The momentum equation (Eq. (4.3)) can be restated for steady state as,

$$-\frac{\partial p}{\partial s} = \frac{1}{A^2} \frac{\partial (\dot{m}^2 / \rho_m)}{\partial s} + \frac{\tau_w P_{hy}}{A} + \rho_m g \sin\theta. \tag{4.78}$$

The three terms on the right are the accelerational, frictional and gravitational pressure gradients. If a link is adiabatic, then the accelerational gradient is zero. Thus, it has contributions only from the heater and cooler links. Integration of Eq. (4.78) for single-phase link can be written as,

$$-\Delta p = \Delta p_f + \Delta p_g, \tag{4.79}$$

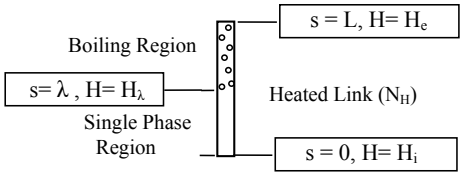

Fig. 4.9 The schematic representation of a heated link

where,

$$\Delta p_f = \frac{4f\dot{m}^2 L}{2\rho_f d_{hy} A^2} \text{ and } \Delta p_g = \rho_f g \Delta H. \tag{4.80}$$

In case of a heated link, the value of the local coordinate s where boiling starts, is denoted by λ. This is schematically shown in Fig. 4.9. In the figure, the local s coordinate value and the elevations are also marked at select locations of interest. Integration of the momentum equation for the two-phase portion of the heated link can be written as,

$$-\Delta p = \Delta p_a + \Delta p_f + \Delta p_g, \tag{4.81}$$

Since the component of each of the pressure drop would depend on the heat flux profile, analytical expressions are derived for the constant heat flux case. These are summarized below:

$$\Delta p_a = \frac{\dot{m}^2 v_{fg} x_e}{A_H^2}, \tag{4.82}$$

$$\Delta p_f = \frac{\dot{m}^2}{2\rho_f A_H^2} 4\left(\frac{f(L_H - \lambda)}{d_H} + \frac{k_H}{4}\right)\overline{\phi_{lo}^2}, \quad \text{where } \overline{\phi_{lo}^2} = \left(1 + \frac{x_e}{2}\frac{v_{fg}}{v_f}\right), \tag{4.83}$$

and

$$\Delta p_g = \rho_f g\left(H_e - H_\lambda \frac{\ln(1 + x_e v_{fg}/v_f)}{x_e v_{fg}/v_f}\right). \tag{4.84}$$

In Eq. (4.83), $\overline{\phi_{lo}^2}$ stands for the mean two-phase multiplier. The local ϕ_{lo}^2 by definition represents the ratio of local pressure gradient in two-phase flow in the pipe to the pressure gradient in the pipe with the same mass flow rate of single phase liquid (Todreas and Kazimi 2011).

Similar components for adiabatic two-phase links can be written as,

$$-\Delta p = \Delta p_f + \Delta p_g, \tag{4.85}$$

where,

$$\Delta p_f = \frac{4\dot{m}^2}{2\rho_f A_i^2}\left(1 + \frac{x_e v_{fg}}{v_f}\right)\left(\frac{f_i L_i}{d_i} + \frac{k_i}{4}\right), \tag{4.86}$$

$$\Delta p_g = \rho_e g \Delta H, \tag{4.87}$$

where,

$$\rho_e = \rho_f\left(1 + \frac{x_e v_{fg}}{v_f}\right)^{-1}. \tag{4.88}$$

Integration of the momentum equation (Eq. (4.78)) over the entire loop will amount to,

$$\sum \Delta p = 0. \tag{4.89}$$

To illustrate this for a specific case, the loop shown in Fig. 4.1 is employed. For simplicity, it is assumed that the heater and cooler impose constant heat flux. Using the expressions for the various pressure drops as derived above, the integral momentum equation for the entire loop may be written as,

$$\frac{4\dot{m}^2}{2\rho_f A^2}\frac{fL}{d}\left[\left(1 + 2\frac{\lambda}{L}\right) + 2\left(1 - \frac{\lambda}{L}\right)\left(1 + \frac{x_e v_{fg}}{2v_f}\right) + \left(1 + \frac{x_e v_{fg}}{v_f}\right)\right] - \rho_f g H\left(1 - \frac{\rho_e}{\rho_f}\right) = 0 \tag{4.90}$$

The factor 2 in the first and second terms inside the square parenthesis account for identical frictional pressure drops in the cooler and the heater. The same in non-dimensional form using conventional definitions can be written as,

$$N_F\left[\left(1 + 2\frac{N_s}{N_Z}\right) + 2\left(1 - \frac{N_s}{N_Z}\right)\left(1 + \frac{N_Z - N_s}{2}\right) + (1 + N_Z - N_s)\right] - \frac{2}{4N_{Fr}}\left(1 - \frac{1}{1 + N_Z - N_s}\right) = 0 \tag{4.91}$$

While, the definitions of N_Z and N_s have already been given in Eqs. (4.71) and (4.77), the definitions of Froude number, N_{Fr}, and the friction Number, N_F, are given by,

$$N_{Fr} = \left(\frac{\dot{m}}{\rho_f A}\right)^2 \frac{1}{gH}, \text{ and } N_F = \frac{fL}{d}. \tag{4.92}$$

It is pointed out that mass flow rate, which is to be solved for, appears directly in the definitions of Zuber and Froude numbers and indirectly in friction number. While, many times friction factor is assumed to be a constant, if it is assumed to be varying as given in Eq. (4.5), the friction number can be expressed in terms of Froude Number as,

$$N_F = C\left(\frac{\rho_f \sqrt{gH} d}{\mu_l}\right)^{-n} \frac{N_{Fr}^{-0.5n}}{d}. \tag{4.93}$$

Further, we can also eliminate mass flow rate and define, heat source number N_Q as,

$$N_Z^2 N_{Fr} = \left(\frac{Qv_{fg}}{Ah_{fg}}\right)^2 \frac{1}{gH} = N_Q^2. \tag{4.94}$$

As Zuber number and friction number can be expressed as functions of Froude number and heat source number, the integral momentum equation (Eq. (4.91)) can be viewed as a non-linear equation expressing Froude number in terms of sub-cooling number and heat source number. Thus, for a given loop, we can solve for Froude number in terms of heat source number and sub-cooling number. In terms of dimensional parameters, this amounts to determination of circulation flow rate for given inlet sub-cooling and the power.

4.4.2 Transient Analysis

As pointed out earlier, the treatment of transient analysis in two-phase systems is different owing to the fluid acceleration/deceleration during phase change. Particularly, for the case where the individual phases can be treated as incompressible, a major simplification results in the spatial variation of the mixture velocity. To put the physics of the problem in perspective, the governing equations are manipulated as follows. First the continuity equation given in Eq. (4.1) is expanded for a duct of constant area to be written as,

$$\frac{\partial \rho_m}{\partial t} + u_m \frac{\partial \rho_m}{\partial s} + \rho_m \frac{\partial u_m}{\partial s} = 0. \tag{4.95}$$

Now the energy equation for constant area duct can be expanded and simplified using the continuity equation as,

$$\frac{\partial h_m}{\partial t} + u_m \frac{\partial h_m}{\partial s} = \frac{q'_W}{A\rho_m}. \tag{4.96}$$

To simplify algebra, we can rewrite the above two equations using substantial derivative as,

$$\frac{D\rho_m}{Dt} = -\rho_m \frac{\partial u_m}{\partial s}, \tag{4.97}$$

and

$$\frac{Dh_m}{Dt} = \frac{q'_w}{A\rho_m}. \tag{4.98}$$

Using the equations of state for ρ_m and h_m as given in Eqs. (4.8) and (4.9), Eqs. (4.97) and (4.98) can be written as,

$$\frac{Dx}{Dt} = \frac{v_m}{v_{fg}} \frac{\partial u_m}{\partial s}, \tag{4.99}$$

and

$$\frac{Dx}{Dt} = \frac{q'_W}{h_{fg} A \rho_m}. \tag{4.100}$$

Since the left hand side of the above two equations are same, we can equate the right hand side of the same and rewrite it to give a differential equation for the axial velocity distribution for the mixture velocity as,

$$\frac{\partial u_m}{\partial s} = \frac{q'_W v_{fg}}{A h_{fg}}. \tag{4.101}$$

Thus, the spatial velocity variation at any instant can be obtained by integrating the above equation, if the heat flux variation is known. This major simplification has resulted by treating the saturation properties as constant, which is very much applicable at pressure levels reactors operate. Thus, the governing equations that will be used in the analysis are Eqs. (4.3), (4.96) and (4.101). The solution procedure for this set of equations is discussed in the following sections. It may be noted that for a constant wall heat flux, the velocity varies linearly even during transient in the two-phase portion of the link.

Numerical Solution. We have previously seen in the transient analysis of single-phase system that the solution for a hyperbolic equation such as Eq. (4.96) carried out by characteristics procedure produces minimum error, when the information from a given node at a given time step is passed on to the adjacent node at the next time step as shown in Fig. 4.3. This could easily be achieved in single-phase systems as the velocity of the fluid is constant in a constant area duct. However, in two-phase systems, where the fluid accelerates during phase change, the nodes have to be appropriately spaced to satisfy the criterion mentioned above. For the present, the concepts are developed for a constant heat flux system in which the velocity varies linearly. The procedure to divide the domain is discussed next.

Consider the case in which the velocity varies linearly in the domain. The assumed form of the velocity is,

$$u = a\,s + b. \tag{4.102}$$

A schematic view of the discretisation is shown in Fig. 4.10. It may be observed that as the velocity increases with s, the slope of the characteristic direction will decrease with s. The objective therefore, is to divide the spacing such that information

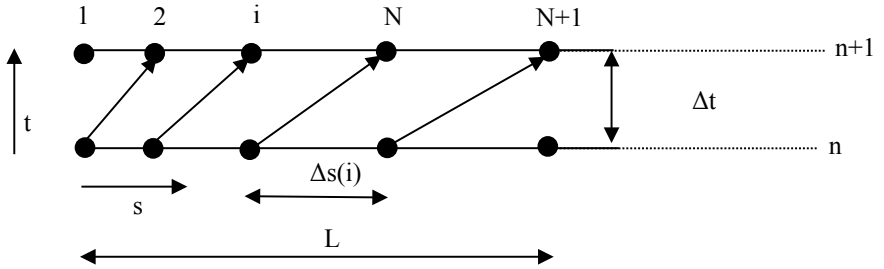

Fig. 4.10 Schematic view of the nodalization for a linearly varying velocity

from one node passes into the adjacent node at the next time as shown. The distribution of nodes can be arrived at as follows.

To begin with, it is assumed that the velocity varies linearly only as a function of space and it does not vary with time. Assuming that there are N + 1 nodes or N divisions in the domain whose length is L, we can write,

$$\Delta t = \frac{\Delta s(1)}{u(1)} = \frac{\Delta s(i)}{u(i)} = \frac{\Delta s(N)}{u(N)} \tag{4.103}$$

Further,

$$L = \sum_{i=1}^{N} \Delta s(i) = \Delta t \sum_{i=1}^{N} u(i). \tag{4.104}$$

As the velocity linearly varies in space as given in Eq. (4.102), we can write

$$\frac{\partial u}{\partial s} = a = \frac{\Delta u}{\Delta s}. \tag{4.105}$$

With reference to Fig. 4.10, use of Eq. (4.104) leads to,

$$u(2) = u(1) + a\,\Delta s(1) = u(1) + a\,u(1)\Delta t = u(1)(1 + a\Delta t), \tag{4.106}$$

$$u(i) = u(1)(1 + a\Delta t)^{i-1}, \tag{4.107}$$

and

$$u(N) = u(1)(1 + a\Delta t)^{N-1}. \tag{4.108}$$

Using the above relations, Eq. (4.110) can be written as,

$$L = u(1)\Delta t\big(1 + (1 + a\Delta t) + (1 + a\Delta t)^2 + \cdots + (1 + a\Delta t)^{N-1}\big). \tag{4.109}$$

Summing the terms in the series within the parenthesis, we can obtain,

$$\Delta t = \frac{\left(1 + \frac{La}{u(1)}\right)^{\frac{1}{N}} - 1}{a} \tag{4.110}$$

It may be observed that u(1) is equal to b, and hence for a given L, a, b and N, Δt can be computed. Then using Eq. (4.107), the velocity at every node can be obtained and subsequently, using Eq. (4.103), the node spacing can be obtained. This node structure would ideally satisfy the Courant number criterion at every node (C = 1), thereby reducing numerical diffusion.

Now a simple problem is taken to demonstrate the utility of the kind of nodalisation resorted to. Consider the governing equation,

$$\frac{\partial \phi}{\partial t} + (as + b)\frac{\partial \phi}{\partial s} = 0, \tag{4.111}$$

with the following initial and boundary conditions,

$$\phi(s, 0) = a\,s + b, \text{ and } \phi(0, t) = a\,e^{-at}. \tag{4.112}$$

The analytical solution for this special case is,

$$\phi(s, t) = (a\,s + b)e^{-at}. \tag{4.113}$$

Using the characteristic procedure, the characteristic direction of the governing equation (Eq. (4.111)) and its corresponding compatibility condition are,

$$\frac{ds}{dt} = u = a\,s + b, \text{ and } \frac{d\phi}{dt} = 0. \tag{4.114}$$

Thus, along the characteristic direction shown in Fig. 4.10, the numerical solution can be written as,

$$\frac{\phi_i^{n+1} - \phi_{i-1}^{n}}{\Delta t} = 0, \text{ or, } \phi_i^{n+1} = \phi_{i-1}^{n}. \tag{4.115}$$

The solution for the above problem was obtained numerically for a = 3, b = 1, L = 1 and N = 10. The comparison of the spatial profile between the numerical and analytical solution at three different times during the transient are shown in Fig. 4.11. Similarly, the temporal profile at the inlet, middle and the exit of the domain are shown in Fig. 4.12.

It may be observed that the numerical solutions almost exactly follow the analytical solutions Thus, the procedure has been demonstrated for a linear variation of the velocity in the axial direction, but is fixed in the time domain. When velocity varies in the time domain too, which is expected in general transients, the method

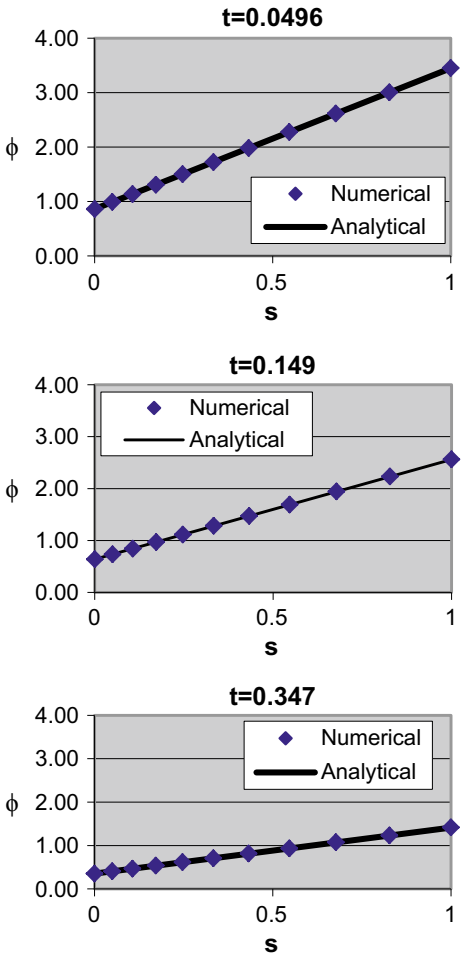

Fig. 4.11 Comparison of the spatial variation of analytical and numerical solutions

has to be modified a little bit. This is due to the fact that the spatial distribution of nodes to satisfy Courant number equal to one at a given linear velocity distribution at time, t, would no longer be valid at time $t + \Delta t$. To account for this, the solution is first obtained at the newer time step satisfying a Courant number of 1 and then interpolated to get the values at the desired locations, where the spatial distribution at the new time step would satisfy the condition derived earlier. Both linear and second order interpolations have been tried with little variation in results. To demonstrate the methodology, the governing equation chosen is

$$\frac{\partial \phi}{\partial t} + (as + b)(C - \sin(\omega t)\frac{\partial \phi}{\partial s} = S, \tag{4.116}$$

subject to initial and boundary condition,

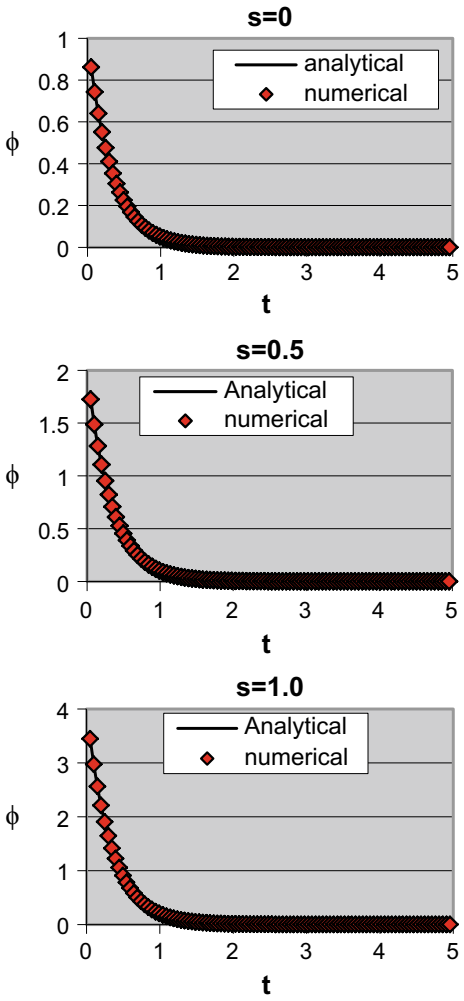

Fig. 4.12 Comparison of the temporal variation of analytical and numerical solutions

$$\phi(s, 0) = \phi_{to}(s), \text{ and } \phi(0, t) = \phi_{so}(t). \tag{4.117}$$

For a domain of $0 < s < 10$, $0 < t < 50$ and with,

$$\phi_{to}(s) = s/10, \text{ and } \phi_{so}(t) = \sin 2t. \tag{4.118}$$

The analytical solution for this case can be expressed as,

$$\phi(s, t) = \phi_{to}(s_0) + St, \text{ for the condition } s \geq s^*, \tag{4.119}$$

where, s^* is given by,

$$s^* = \frac{b}{a}\left(e^{(aCt+a(\cos(\omega t)-1)/\omega)} - 1\right), \tag{4.120}$$

and

$$s_0 = \left(\frac{(as+b)}{e^{(aCt+a(\cos(\omega t)-1)/\omega)}} - b\right)\frac{1}{a}, \tag{4.121}$$

and,

$$\phi(s,t) = \phi_{so}(t_0) + S(t-t_0), \text{ for } s < s^*, \tag{4.122}$$

where t_0 is the root of,

$$\ln\left(\frac{as+b}{b}\right) - aC(t-t_0) - a(\cos(\omega t) - \cos(\omega t_0))/\omega = 0. \tag{4.123}$$

The analytical solution is now compared with the numerical solution for $a = 0.1$, $b = 1$, $C = 3$, $S = 3$ and $\omega = 5$. Ten nodes and numerical interpolation were used in the numerical computation. The spatial behaviours of the numerical and analytical solutions are shown at three chosen times in Fig. 4.13. The temporal behaviours at the mid-section and at the two ends of the domain are shown in Fig. 4.14. It may be observed that the method has been able to capture the analytical solution almost exactly.

Now to benchmark the solution towards predicting the stability boundaries in a two-phase system, the experimental data of Solberg (1966) (as quoted in Ishii 1971) is considered. The system under consideration is schematically shown in Fig. 4.15. It consists of a test section of diameter d and length L with two orifices, one at the inlet and one at the exit of the test section. The orifice coefficients at the inlet and exit are denoted by K_i and K_e respectively. To be consistent with the definitions used in Eq. (4.48), viz.,

$$K = \frac{\Delta p}{0.5\rho u^2}, \tag{4.124}$$

the orifice coefficients given in the reference have been doubled. This is because the author does not use the factor, 0.5, in the definition of K (Eq. (4.124). The stability boundaries are established for a given steady state mass flow rate. For every inlet sub-cooling, there exists a critical power after which the system becomes unstable. Since the mass flow rate is specified, the Froude number is fixed. The stability can then be expressed as a plot between the Zuber number and the sub-cooling number.

The numerical solution procedure for this kind of a system would use all the principles that have been developed earlier. However, as the problem involves both the single-phase and two-phase regions, the treatment requires few more details. First, the steady state solution and the position of the interface where boiling boundary begins is obtained. Once the transient is initiated, the boiling boundary is continuously

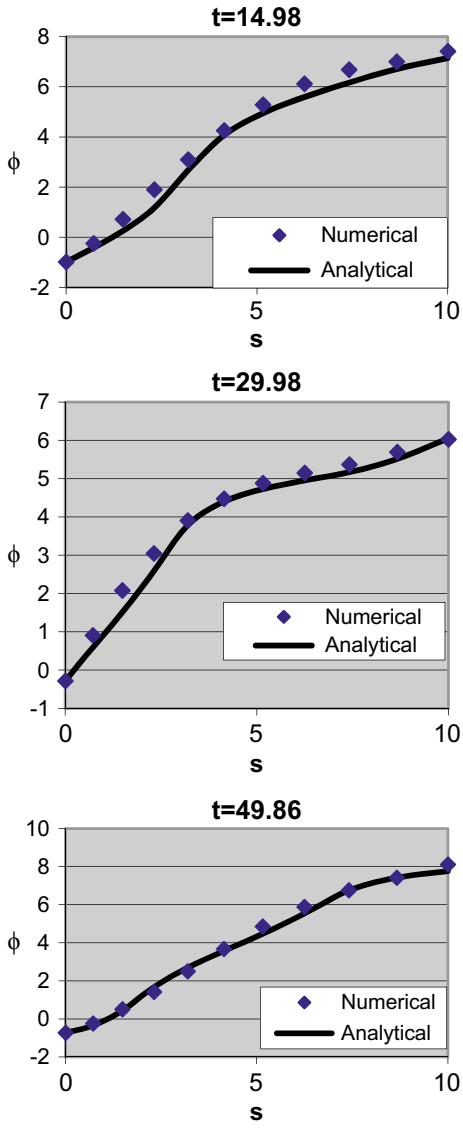

Fig. 4.13 Comparison of the spatial variation of analytical and numerical solutions

tracked and the single-phase and two-phase regions are being continuously adapted. These details are discussed next.

The general governing equations of interest are Eqs. (4.3), (4.96) and (4.101) along with the equations of state Eqs. (4.8) and (4.9). Integration of Eq. (4.101) for the present case would lead to a composite velocity profile. With reference to Fig. 4.15, the velocity would be constant in the single-phase region ($0 \leq s \leq \lambda$), whereas, in the two-phase region ($\lambda \leq s \leq L$), it would increase linearly. Since it

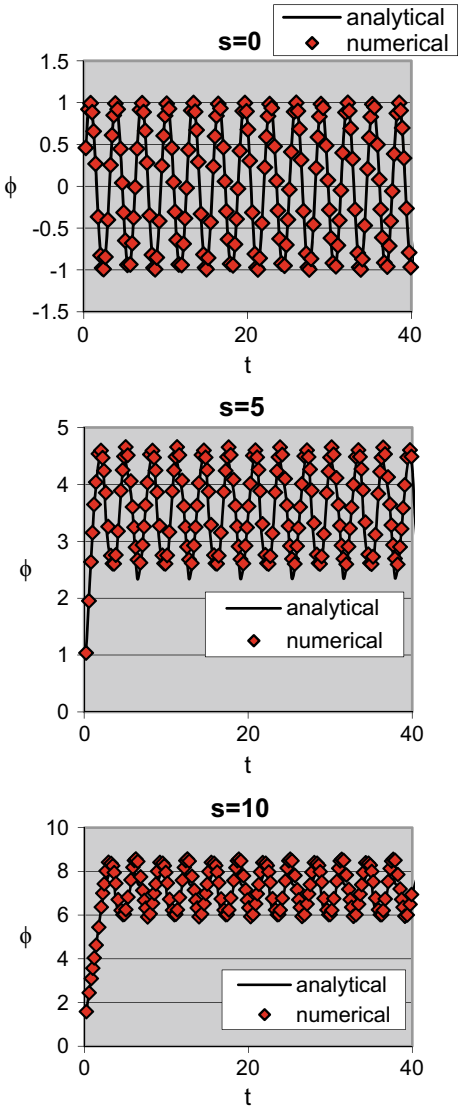

Fig. 4.14 Comparison of the temporal variation of analytical and numerical solutions

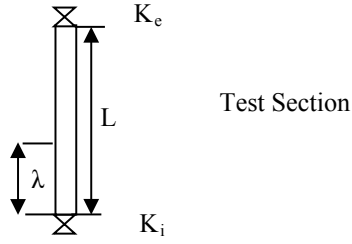

Fig. 4.15 Schematic view of the domain for the benchmark problem

is intended that all the variables in all the nodes during numerical computation be available at the same time, the time step increment and the node spacing distribution have a distinct relationship.

Earlier, it was pointed out that the Δt in the region where the velocity varies linearly gets fixed once the coefficients a, b, number of nodes, N, and length of the two-phase region is known, as given in Eq. (4.110). Thus, for the given problem, once the initial conditions are specified, which is usually the steady state condition, the single-phase length (λ), velocity at the inlet (u_{fi}), and the velocity distribution in two-phase length are all known. It is fairly straight forward to visualize that the velocity distribution at any time can be written by integrating Eq. (4.101) for the present problem

$$u(s,t) = u_{fi} + \frac{q'_W v_{fg}}{h_{fg} A_m} s = u_{fi} + \xi s, \tag{4.125}$$

where,

$$\xi = \frac{q'_W v_{fg}}{h_{fg} A}, \tag{4.126}$$

It is pertinent to point that in Eq. (4.125), $s = 0$ refers to the front where boiling begins. Thus, for a chosen number of segments in the two-phase region (NB), length of the two-phase region ($L - \lambda$), and the coefficients ($a = \xi$, $b = ufi$), the time increment can be computed using Eq. (4.110). To ensure Courant number to be close to 1 in the single-phase region, the number of segments can be obtained as given in Eq. (4.127). $N_S i$ is truncated to the nearest integer.

$$N_{Si} = \frac{\lambda u_{fi}}{\Delta t} \tag{4.127}$$

Having discussed the nodalization procedure, attention is now shifted to the integration of the momentum equation. When Eq. (4.43) is integrated over the length of the channel, we get,

$$\int_0^L \frac{\partial(\rho_m u_m)}{\partial t} ds = -\Delta p + \Delta p_a + \Delta p_f + \Delta p_g = -\Delta p_{net}, \tag{4.128}$$

where, $-\Delta p$ is the applied pressure drop across the channel and others are the accelerational, frictional and gravitational pressure drops respectively. The evaluation of the individual components in the single-phase and two-phase regions has already been discussed previously in Eqs. (4.80)–(4.84). Prior to discussion of the integration of the momentum equation, it is useful to summarise the overall numerical procedure for identifying the stability limits. The steps are:

(i) Nodalize the channel as described above for a given number of segments in the two-phase portion of the channel and estimate the time step size Δt.
(ii) Perturb the inlet velocity by a small amount.
(iii) Advance the enthalpy equation by one step maintaining Courant number at every node to be 1 and store them at these temporary locations. Also locate the new boiling front.
(iv) Renodalize the channel and get the new velocity distribution and location of the new grids. The time step for the next computation is also obtained and kept ready for next evaluation
(v) Now carry out linear interpolation to get the enthalpy at the chosen locations.
(vi) Use integral momentum equation to update the new velocity at the first node. This is discussed in the following paragraphs.
(vii) Repeat steps (i)–(vi) till the time of interest. If the perturbation grows, then the original steady state is unstable, otherwise it is stable.

Thus, the essential purpose of integrating the momentum equation is to update the new entrance velocity. The methodology adopted is the numerical analogue of the analytical work of Calusse and Lahey (1991). Since the upper and lower limits are invariant with time, the left hand integral in Eq. (4.128) can be written as,

$$\int_0^L \frac{\partial(\rho_m u_m)}{\partial t} ds = \frac{d}{dt} \int_0^L (\rho_m u_m) ds. \tag{4.129}$$

Using a first order method, and the above equation, Eq. (4.128) can be written as,

$$\int_0^L (\rho_m u_m) ds \Big|_{t+\Delta t} = \int_0^L (\rho_m u_m) ds \Big|_t - \Delta p_{net} \Delta t. \tag{4.130}$$

As the distributions of ρ_m and u_m at time step t, as well as Δp_{net} are fully known, the integral on the left hand side of Eq. (4.130) can be computed. Using this value, the updated value of u_{fi} can be extracted as given below.

$$\begin{aligned} \int_0^L (\rho_m u_m) ds &= \int_0^\lambda (\rho_m u_m) ds + \int_\lambda^L (\rho_m u_m) ds \\ &= \rho_f u_{fi} \lambda + \int_0^{L-\lambda} \frac{(u_{fi} + \Omega s)}{v_m} ds \\ &= \rho_f u_{fi} \lambda + u_{fi} \int_0^{L-\lambda} \frac{1}{v_m} ds + \int_0^{L-\lambda} \frac{\Omega s}{v_m} ds \end{aligned} \tag{4.131}$$

Table 4.1 Data for simulation of two-phase natural circulation

Pressure	80 bar
Fluid	Water
Reynolds number at inlet	47,800
K_i	35.6[a]
K_e	0.06[a]
Length of test section (L)	2.9 m
Orientation	Vertical
Diameter of test section (d)	0.00525 m
Friction factor in two-phase	$2f_{single\text{-}phase}$

[a]The values quoted in the table are double that in the reference as explained in the text

As the enthalpy distribution has already been updated at every new node location, the integral can be replaced by summation using trapezoidal rule and Eq. (4.130) can be written as,

$$\int_0^L (\rho_m u_m) ds = \rho_f u_{fi} \lambda + u_{fi} \sum_{i=1}^{N_B} \overline{\frac{1}{v_m}} \Delta s_i + \sum_{i=1}^{N_B} \overline{\frac{\Omega s}{v_m}} \Delta s_i \tag{4.132}$$

The only unknown in the above equation is u_{fi} and can be computed.

The simulation was carried on the basis of the steps outlined above. The relevant input is summarised in Table 4.1. The stability map generated is shown in Fig. 4.16. In the same figure the experimental data is also compared. The comparison is fairly good. The sensitivity of the stability boundary to the number of nodes is also demonstrated in the same figure. It may be seen that nodalisation is fine enough to consider the simulation adequate. Thus the procedure gets benchmarked.

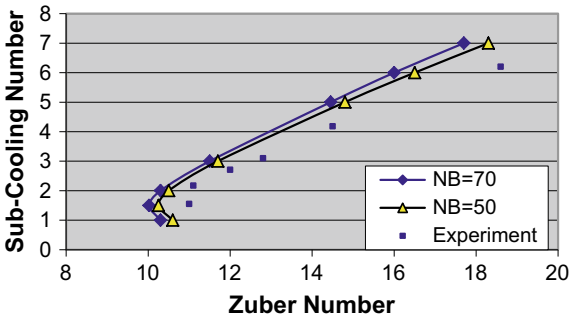

Fig. 4.16 Comparison of numerical stability map with experimental data

4.4.3 Conclusions from Two-Phase Studies

The computational procedure that has been developed based on the method of characteristics has been able to capture the oscillations satisfactorily for several simple cases for which the analytical solutions were generated. It has also been successful in obtaining the stability boundary for an experimental loop, and the results closely follow the experimental data. However, the number of nodes required to resolve the boundary is fairly on the higher side as first order method is used for integration of momentum equation. Hence there is scope to improve the proposed method.

References

Ambrosini W, Ferreri JC (1998) The effect of truncation error on the numerical prediction of linear stability boundaries in a natural circulation single-phase loop. Nucl Eng Des 183:53–76

Ambrosini W, Ferreri JC (2003) Prediction of stability of one-dimensional natural circulation with a low diffusion numerical scheme. Ann Nucl Energy 30:1505–1537

Basu DN, Bhattacharyya S, Das PK (2014) A review of modern advances in analyses and applications of single-phase natural circulation loop in nuclear thermal hydraulics. Nucl Eng Des 280, 326–348 (2014)

Calusse T, Lahey T (1991) The analysis of periodic and strange attractors during density-wave oscillations in boiling flows. Chaos, Solitons Fractals 1(2):167–178

Ferreri JC, Ambrosini W (2002) On the analysis of thermal-fluid-dynamic instabilities via numerical discretization of conservation equations. Nucl Eng Des 215:153–170

IAEA Publication: Natural circulation in water cooled nuclear power plants. IAEA-TECDOC-1474 (2005)

IAEA Publication: Natural circulation phenomena and modelling for advanced water cooled reactors. IAEA-TECDOC-1677 (2012)

Ishii M (1971) Thermally induced flow instabilities in two-phase mixtures in thermal equilibrium. Ph.D. thesis, Georgia Institute of Technology

Mousavian SK, Misale M, D'Auria F, Salehi MA (2004) Transient and stability analysis in single-phase natural circulation. Ann Nucl Energy 31:1177–1198

Nayak AK, Vijayan PK (2008) Flow instabilities in boiling two-phase natural circulation systems: a review. Sci Technol Nucl Install 1–15

Pletcher RH, Tannehill JC, Anderson DA (2013) Computational fluid mechanics and heat transfer, 3rd edn. CRC Press, Boca Raton

Solberg K (1966) Results des essais d'instabilites sur la boucle culine et comparisons avec un code de calcul', C.E.N.G., note 225, Centre d'Etudes Nucleaires de Grenoble, France

Todreas NE, Kazimi M (2011) Nuclear systems-I—thermal hydraulics fundamentals, 2nd edn. CRC Press, Boca Raton

Chapter 5
An Overview of the Dynamics of Supercritical Natural Circulation Loops

Tanuj Srivastava, Pranab Sutradhar, Dipankar Narayan Basu and Lin Chen

Abstract The concept of supercritical natural circulation loops (scNCLs) is only a recent one, with the pioneering research being publicized only in 2001. But the favorable heat transport properties and large volumetric expansion of the supercritical fluids make them ideal for natural circulation based cooling applications, and hence is gaining increased popularity in several applications, particularly for reactor core cooling. The unique nature of the supercritical fluid ensures distinct thermal hydraulic and stability characteristics of scNCLs, widely different than other fluid-driven loops. Only a small temperature variation is sufficient to induce drastic changes in the density of the supercritical fluid, leading to substantial local buoyancy and radial motion. Therefore, a thorough understanding of both thermal hydraulic and stability behavior of an scNCL is mandatory before full-scale industrial applications. However, the knowledge base is reasonably thin and some of the reported observations are also not in consensus, making it difficult for the beginners to grasp the initial concepts, particularly with the contrasting standards adopted by various research groups around the world. That prepares the backdrop of the present chapter, with the basic aim being to introduce a reader with basic engineering knowledge into the field of scNCL and primarily into the dynamics of such systems. Starting with a brief state-of-the-art review of the technology, both experimental and theoretical studies are discussed, in order to summarize the stability responses of such loops. Considering the increasing popularity, the comprehensive discussion present in this chapter will definitely help in consolidating the concerned knowledge for the future researchers.

T. Srivastava · P. Sutradhar · D. N. Basu (✉)
Department of Mechanical Engineering, Indian Institute of Technology Guwahati, Guwahati 781039, India
e-mail: dnbasu@iitg.ac.in

L. Chen
Institute of Engineering Thermophysics, Chinese Academy of Sciences, Beijing 100190, China
e-mail: chenlinpkucoe@gmail.com

School of Aeronautics and Astronautics, University of Chinese Academy of Sciences, Beijing 100049, China

A. Mukhopadhyay et al. (eds.), *Dynamics and Control of Energy Systems*,
Energy, Environment, and Sustainability,
https://doi.org/10.1007/978-981-15-0536-2_5

Keywords Supercritical · Natural circulation · Stability

Nomenclature

Abbreviations

sc	Super critical
NCL	Natural Circulation Loop
FiHTD	Flow induced Heat transfer deterioration
pc	Pseudo critical
in	Inlet
cr	Critical
HHHC	Horizontal heater horizontal cooler
HHVC	Horizontal heater vertical cooler
VHVC	Vertical heater vertical cooler
VHHC	Vertical heater horizontal cooler

Non-dimensional numbers

N'_{TPC}	Trans pseudo critical number
N_{SUBPC}	Sub pseudo critical number
ρ^*	Non-dimensional density
h^*	Non-dimensional enthalpy
$\mathrm{St_m}$	Modified Stanton number

Symbols

Δp_d	Pressure difference by gravity
Δp_r	Pressure difference by frictional resistance
$\dot{m}$	Mass flow rate (kg/s)
Q	Power (MW)
β	Thermal expansion coefficient ($\mathrm{K^{-1}}$)
$\mathrm{L_t}$	Total length
w	Velocity (m/s)
C_p	Specific heat capacity (kJ/kg K)
Π_h	Heated Perimeter
h	Enthalpy (J/kg)
q''	Heat flux ($\mathrm{W/m^2}$)
ρ	Density ($\mathrm{kg/m^3}$)
0	Reference value
D	Diameter (m)

5.1 Introduction to Natural Circulation Loop

The term "circulation" primarily refers to the movement of fluid through a closed circuit by virtue of some driving potential. When this potential is the resultant of a density differential, we employ the terminology "Natural circulation loop". It can be viewed as one of the most efficient option of transporting energy from a source to a sink, without their direct interaction. The absence of any driving machinery also leads to a reduction in the overall expenses and an enhancement in the reliability of the operation. Consequently the natural circulation loops (NCLs) have found applications in numerous engineering fields, encompassing electronic chip cooling (Kim et al. 2008), solar heaters (Close 1962), geothermal systems (Kreitlow et al. 1978; Torrance 2010) and nuclear reactors (Dimmick et al. 2002; Chatoorgoon et al. 2005a), just to name a few.

A favorable density gradient, conventionally known as the buoyancy, can be generated inside the flow domain of an NCL either by introducing a secondary lighter phase or through suitable thermal interactions. While the former has its utility in certain chemical industries, the latter is conventionally referred as the NCL, and hence will be the only one considered under the purview of the present chapter. The thermally-developed density field requires an energy source and an energy sink, with the sink being located mandatorily at a higher elevation. On receiving energy from the source, the fluid experiences an increase in the temperature level and consequent reduction in the density, enforcing it to rise upwards. The reverse is true for the sink section, leading to a downward motion of the cooler, heavier fluid. Therefore, a suitable orientation of the source and sink along a closed loop can easily set up the circulation, while facilitating proficient energy transport from the high-temperature source to the low-temperature sink. The loop can be of any shape to accommodate the system requirement, as long as the development of a favorable buoyancy field can be warranted, thereby providing design simplicity and flexibility, while being comparatively inexpensive. Such loops however, suffer from the constraint of lower flow rates and heat fluxes, compared to their forced flow counterpart. Possibility of flow reversals leading to instability and the absence of direct controlling options are other major concerns.

As the circulation rate in an NCL and subsequent heat transfer characteristics are directly dependent on the nature of density variation, selection of working fluid is of utmost importance in such systems. Single-phase, primarily liquid-based, loops offer good heat transport capability in a compact system, but are restricted by the constraint of the saturation temperature. Two-phase boiling loops, on the contrary, are capable of large energy transport and substantial volumetric expansion. But they are also prone to static and dynamic instabilities, and possible deteriorations in heat transfer. Supercritical phase of the working substance provides an opportunity of combining the superior heat transport characteristics of the single-phase version with the large density differential achievable in the two-phase loops. But such systems have their own issues, particularly in relation with the requisite working conditions. Water is the most common working fluid, owing to its availability and non-toxic behavior.

But extreme critical point values ($P_{cr} = 22.064$ MPa and $T_{cr} = 647.1$ K) makes it non-suitable for most of the industry-level appliances. In this precise context, carbon dioxide ($P_{cr} = 7.377$ MPa and $T_{cr} = 304.13$ K) has gained increased popularity over last couple of decades as the possible working fluid in scNCLs. Along with the noticeably-low critical temperature, it is also environment-friendly, non-flammable and chemically stable over a wide temperature range (Blackburn et al. 2001; Ochsner 2008). Certain synthetic refrigerants have also been explored by researchers in recent times, such as R134a, which has much lower critical pressure ($P_{cr} = 4.059$ MPa and $T_{cr} = 374.2$ K). But their chemical stability at elevated temperatures and compatibility with structural material remain issues to be sorted out.

Several research groups are intensely working on scNCL over last couple of decades, with the aim of harnessing its immense potential as a heat transport system over wide range of scales, leading to decent volume of literature. However, many of these observations are not in consensus with each other, making it difficult for the beginners to grasp the fundamental concepts. That prepares the backdrop of this chapter, which is focusing on the judicial amalgamation of the most relevant concepts associated with the dynamic behavior of scNCL and its stability performance. A brief summary of the steady-state characteristics is presented to begin with, subsequently moving into the transient and stability consideration.

5.2 General Dynamic Behavior of NCLs

Before engaging into a detailed discussion on the stability aspects and dynamic behavior of scNCL, it is only prudent to have a brief overview of the generalized dynamic response of single-phase and two-phase loops. Gross operation of single-phase loops can be classified into three categories, namely, (a) steady state, (b) stable oscillatory flow and (c) flow reversal. Depending on the state of the system, if heater power is in oscillatory zone, then amplitude of temperature difference or mass flux increases with increase in the heater power (Saha et al. 2018). Similar phenomenon has also been observed in the flow reversal regime. Loop dynamics are also strongly dependent on the loop orientation. With a vertical heater, flow initiation is almost instantaneous, while it requires a finite time with horizontal heating. HHVC orientation, in general, leads to stable behavior with clockwise motion, characterized by downward flow through the cooler. The VHVC configuration is commonly the most stable one (Vijayan et al. 2007). Vijayan et al. (2008) in their experiments and analytical study found that small diameter loops were more stable and larger L_t/D is important factor for stability. Applicability of various codes (ATHLET, CATHARE2, RELAP5/Mod3.2, and computational fluid dynamic) for single phase NCL has been verified by many investigators to investigate the different aspect like inside diameter (Vijayan et al. 1995) wall frictions (Ambrosini et al. 2004), heater and cooler orientations (Pilkhwal et al. 2007), effect of power step (Kudariyawar et al. 2016), aspect ratio (height to width) (Chen 1985). Hashemi-Tilehnoee et al. (2019) investigated the effect of asymmetric heater and found response of CFD code to be different to

RELAP5 and experiments, in terms of the oscillatory behaviour which depends on imposed power level.

Significant research volume is available for two-phase loops, following both analytical and experimental route. Wissler et al. (1956) was the first to report the instability in two-phase system. Song (2012) experimentally applied the simplified pressure drop condition (gravity and friction drop) and found little sign of static instability, while there was potential for density wave oscillation (discussed in Sect. 5.4.1), which is of dynamic-type. Hence two phase system is more prone to dynamic instability. Fichera and Pagano (2003) incorporated a proportional-derivative control in their study for the inlet velocity and temperature difference at the heater section, and found that to be useful in stabilizing the system dynamics. In two phase CO_2, for lower fill ratio (volume of filled space/total volume) the system is likely to fluctuate under small heat inputs (Tong et al. 2016). Sukchana and Pratinthong (2017) investigated the dependency of thermal performance on the bending and inclination of loop up to a certain limit with higher evaporation temperature, pressure and optimum filling ratio. Slight horizontal tilting caused poor performance and vice versa for slight vertical tilting. Using anodic oxidation on the inner surface of the loop makes it more porous and hydrophilic which enhances evaporator heat transfer coefficient, reduces evaporator wall temperature and total thermal resistance for different orientations of the loops (Solomon et al. 2015).

5.3 Steady-State Behavior of ScNCL

When state parameters are independent of time, the system is in steady-state, which demands a balance between buoyancy and friction for any NCL. Steady-state characteristics of scNCLs have been explored both experimentally and analytically, among which Chatoorgoon (2001) was the first to develop the analytical model using SPORTS code for HHHC loop. In the steady state analysis for UDL and non-UDL, modified Grashof number was found to have linear relationship with the steady state Reynolds number (Vijayan 2002). Behavior of supercritical fluid is similar to two-phase at higher power as there is reduction in the mass flow rate due to drastic variation near the pseudo critical point. Investigation of Sharma et al. (2010) using NOLSTA code shows the consequences of various loop parameters like diameter (large diameter, high flow) and loop height (large height, high flow). Various orientations of the heat source and heat sink were also tested, among which HHHC showed the maximum flow rate among all and VHVC the lowest. Computational simulation showed that CO_2 loop exhibit higher velocity, but is asymmetric in nature.

Limited literature revealed that out of all combination of orientation of heater and cooler, HHHC is more prone to flow reversal and instability than any other. Increased inclination angle leads to decrease in buoyancy, leading to affect mass flow and Nusselt number with effect more pronounced at low heat flux (Chen et al. 2013) and at high heat flux, effect of inclination angle is less. Drastic increment and decrement was observed in Nusselt number with increased loop diameter and high

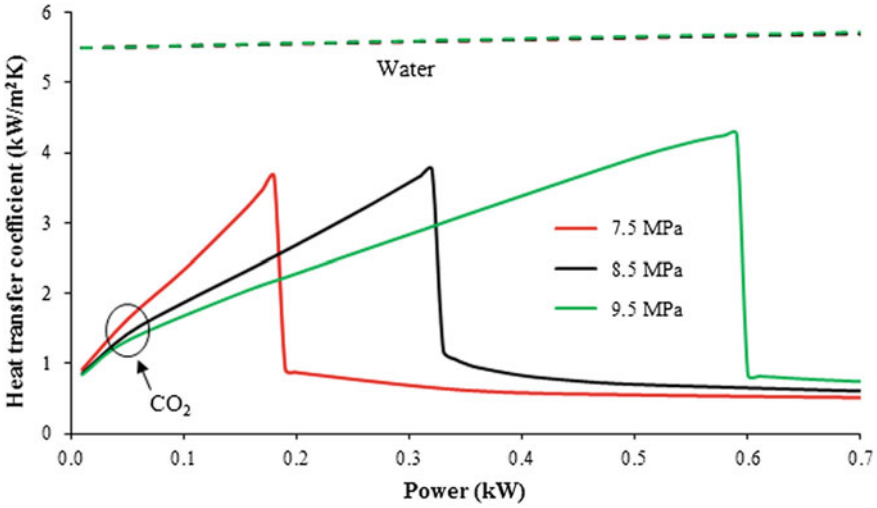

Fig. 5.1 Variation in steady-state heat transfer coefficient with heater power at different pressure levels with supercritical CO_2 as the working fluid (Sarkar and Basu 2016)

heating wall temperature respectively, with better heat transfer coefficient in cooler section. Probability of flow reversal is less in larger loop diameter. To maintain the same condition with large loop diameter, high heat flux is required to overcome the increased friction.

Owing to property variation near pseudocritical temperature, undesirable heat transfer deterioration takes place leading to poor performance in terms of rapid reduction is mass flow and heat transfer as shown in Fig. 5.1 (Sarkar and Basu 2016). The power level corresponding to the appearance of FiHTD can be increased by raising the pressure, lowering sink temperature and increasing diameter. It is interesting to observe that the power level corresponding to the initiation of FiHTD is insensitive to any inclination angle of the NCL. Moreover, it was reported that inclination provided at Y-Z plane on the NCL leads to more driving flow potential than the inclination provided in X-Y plane.

5.4 Introduction to Stability

Current scenario of nuclear reactor is focused upon improving the overall plant efficiency. In this queue of development, supercritical natural circulation consideration on primary side has shown promising outcomes due to its capabilities of proposing higher thermal efficiency. Supercritical water reactor is one of the suggested modifications of light water reactors under the Gen-IV initiative, which promises a thermal efficiency of the order of 45%. Due to high coefficient of volumetric expansion and

heat transfer features, using supercritical fluids as coolant in advanced nuclear reactor offers key advantages like exclusion of steam generator and recirculator pump, compact size and high thermal efficiency, because of elimination of phase change phenomenon and hence critical heat flux. Due to the safety issues, however, it cannot be used at any random operating condition. Henceforth proper investigation for stable steady state is mandatory. Otherwise it can lead to power oscillation and vibrations in the mechanical modules and this may lead to system catastrophe. A good natural circulation loop will be the one that guarantees a sufficient mass flux for the intended applications, while avoiding the instabilities as much as possible.

This is the reason that it is imperative to explore the possibilities of safety issues in scNCLs. In closed loop operation of nuclear reactor, thermal fatigue may occur due to repetitive cycle of wall temperature. This fatigue may cause mechanical breakdown, and in the vilest circumstance discharge of radioactive material (Kakac and Bon 2008). The key reason associated with the above stated occurrence is due to drastic variation of thermophysical properties near pseudo-critical temperature (Swapnalee et al. 2012), leading to flow oscillations when temperature passes through pseudocritical temperature. Hence instability must be predicted and avoided through cautious means. Flow instability for supercritical region has not been studied thoroughly because most of the reactors operate at subcritical region.

Before moving further, it is imperative to understand what instability is. Because of the disturbance, if the system after diverting

(a) returns to the original state, it is called stable.
(b) keeps on oscillating with new amplitude, neutrally stable.
(c) oscillates with growing amplitude, unstable.

The oscillation of the system cannot go to indefinite value, but is limited by nonlinearities and limit cycle oscillations. Oscillations with amplitude more than $\pm 10\%$ of the mean value (or $\pm 30\%$) imparts itself to instability.

5.4.1 Classification of Flow Instabilities in Thermal-Hydraulic Systems

Zuber (1966) was the first one to analytically state that instability in supercritical flow are similar to two-phase instabilities. Based on analytical method, instabilities are classified into two categories.

(a) Static instability
(b) Dynamic instability

Static instability can have multiple steady state solution, whereas for dynamic instability, transient governing equations are solved to identify the threshold. Figure 5.2 demonstrates the general categorization of the thermal hydraulic instabilities. There are instabilities which are common for both static and dynamic which have been described later in this chapter.

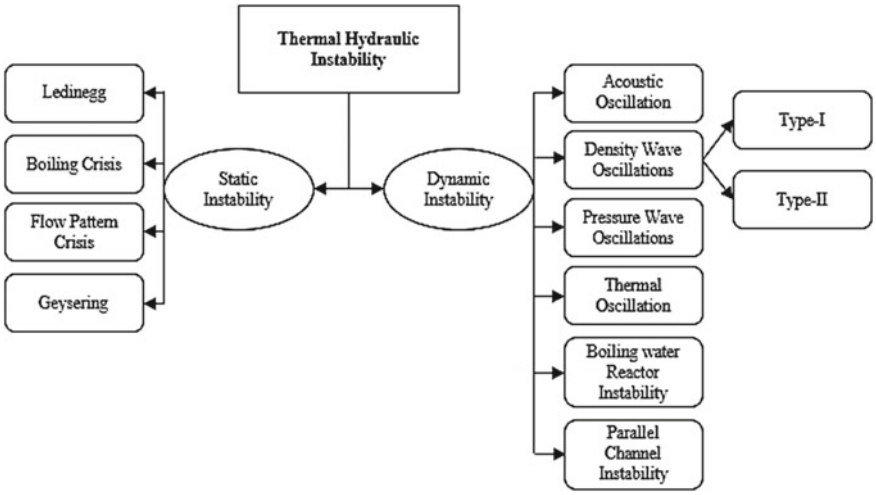

Fig. 5.2 A generalized classification of instabilities in thermal-hydraulic systems

NCL flow instability are inherently more unstable as compared to boiling heated channel. The attribution goes to non-linear nature of NCL. It is fairly intricate phenomenon as it is governed by both gravitational and frictional resistances. Depending on the conditions enforced either of the two dominates (Fig. 5.3).

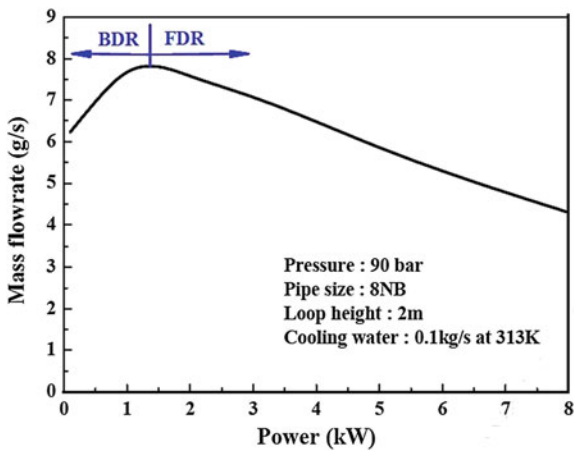

Fig. 5.3 Buoyancy and friction-dominated regimes of NCL operation (Sadhu et al. 2017)

5.4.2 Thermal-Hydraulic Instabilities in ScNCL

Zhao et al. (2005) suggested that there exist a resemblance between boiling channel and scNCL. As in the case of boiling under subcritical conditions, there exist single-phase vapor region, single phase liquid region and the two phase region. Similarly, for scNCL, there exist light fluid region, dense fluid region and mixture region. So instabilities that are found in subcritical boiling region are probable to ensue under supercritical region as well, which can be identified following either linear or nonlinear approaches.

Linear approach solves linearized versions of the time-dependent equations in frequency domain, after imposing infinitesimally small perturbation, while in nonlinear approach, disturbance is imposed on the steady-state solutions and resultant transient traces are followed. The drawback with linear approach is that, it can only predict threshold boundary, but fails to capture limit cycles and nature of instabilities. On the contrary, nonlinear approach can accurately envisage the transients, it is generally more time consuming and computationally expensive (Sharma et al. 2010). Nonlinear approach encourages implications of more practical aspect and hence leads to better resolution of actual scenario.

In case of supercritical fluid generally three type of instabilities are significant and those are the followings.

(i) **Ledinegg instability (Flow excursion)**: In this type of instability when disturbance is imparted, system undergoes the oscillation and either settles down to a different steady-state or exhibits periodic behavior, without returning to the initial state, subsequently leading to flow excursion (Boure et al. 1973). The required condition for this to occur is

$$\frac{\partial(\Delta p_d)}{\partial \dot{m}} \leq \frac{\partial(\Delta p_r)}{\partial \dot{m}} \tag{5.1}$$

where Δp_d is, the driving pressure drop and Δp_r is the resistance pressure drop. Determination of Ledinegg-type instability can be done without the use of time dependent equations and can be theoretically explained.

(ii) **Pressure drop oscillations (PDOs)**: It is a dynamic type instability triggered by static instability. It is found to be on the negative slope of pressure drop—mass flow curve. This type of instability was not very much noteworthy in natural circulation with supercritical pressures and mainly occurs in two-phase system or subcritical system. Thorough explanation of this can be found in Kakac and Bon (2008), Welander (1967).

(iii) **Density wave oscillations (DWO)**: It comes under the dynamic-type instability and requires time dependent equations to analyze. It occurs in the positive slope region of pressure drop- mass flow curve. Supercritical DWO have been observed both experimentally and numerically (Fukuda and Kobori 1979) and can be of two types depending upon the operating conditions.

(a) Type-I occurs at low power and high inlet subcooling temperature, in which pressure drop through gravity governs the characteristics.
(b) Type-II rather occurs at high power and low fluid density, in which frictional pressure drop plays the dominant role.

5.5 Stability Behavior of ScNCL

One of the basic necessities for understanding the steady state and stability behavior of NCLs is the availability of generalized dimensionless groups (or scaling parameters) which are not loop-specific. Such dimensionless groups are useful in comparing the performances of different loops and to extend data from small scale loops to the prototype. Investigations, both analytically and experimentally for different loop configurations [rectangular loop (Welander 1967), Toroidal Loop (Creveling et al. 2016)] have been done by many researchers, however the facts have gained momentum in the recent decade only. Most of the results may be observed analytically but are skipped out while observing experimentally. Boundary conditions and structure of loop have effect on steady state and stability behavior (Chen et al. 2014). Due to dependencies on Equation of States (EOS) of the properties and transient nature, stability is rather complex phenomenon.

5.5.1 Theoretical and Numerical Analyses

Welander (1967) have predicted that flow oscillations in a single phase NCL occurs in small amplitudes which later on increases until the flow is completely reversed from the original direction. Chen (1985) investigated that in a single phase rectangular loop the aspect ratio (width/height) of the rectangular loop affects the modified Grash of number (associated with Buoyancy) which in turn affects the stability of the loop. The loop is only stable if the Grashof number is above a critical value. Cammarata et al. (2003) showed that a single phase NCL flowing in square loop is the least stable, while slender loops were the most stable. Slender loops are not only stable but are also less sensitive to modifications or perturbations in the operating conditions. This fact was considered in many investigations for supercritical NCL done by Chen and Zhang (2011) with CO_2 as operating fluid.

Pioneering work for the stability analysis of supercritical fluid was done by Chatoorgoon (2001). He analyzed a simple NCL with water as the working fluid, assuming no effect of temperature on wall film thermal conductivity and operating conditions 25 MPa, 350 °C with uniform heat addition and removal. The case was imposed and solved by numerical code Special Prediction Of Reactor Transients and Stability (SPORTS) (Chatoorgoon 1986). SPORTS was found suitable at those regions where

liquid to vapor variation takes place. STEAM property package was used for calculation of properties. It was found that positive slope of flow-power characteristics defines the stable operating regions. After this, instability starts amplifying, which was captured roughly by the SPORTS code, as can be seen in Fig. 5.4, the reason for divergence was approximations considered while solving.

To verify the authenticity of the code, a theoretical model was also developed. To make the code simpler, point source and sink was considered instead of taking uniform heat flux, so that equations become linear and relatively easier to solve skipping the complications arising from non-linear nature of temperature and density near critical points. The results obtained from above conditions were in good agreement with SPORTS. Similar to two-phase flow, approximate stability boundary criterion was developed and that was a major breakthrough at that time.

$$\frac{\partial(flow)}{\partial Q} = 0 \tag{5.2}$$

Non-dimensional group for uniform diameter proposed by Vijayan and Austregesilo (1994) was used by Vijayan (2002) for linear stability model in non-uniform diameter loop. In their study, non-linear conservation equations were linearized. System was considered to be unstable if there exist any real root of the equation. To envisage the instability there is a vital role to the modified Grashof number and modified Stanton number. Parametric studies were done with three different diameter

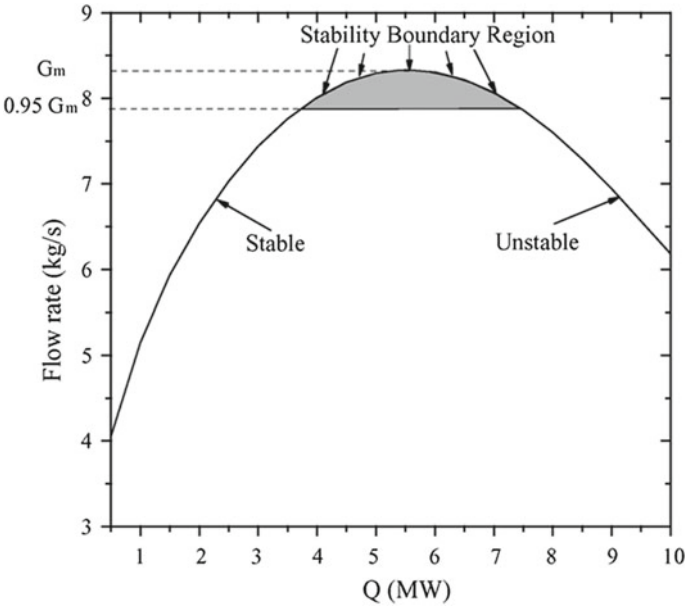

Fig. 5.4 Steady-state profile of flow rate, demonstrating stable and unstable regimes, and the stability boundary region (Chatoorgoon et al. 2005a)

loops (6, 11 and 23.2 mm). It was observed that, at the particular Stanton number, as the fraction of L_t/D increases, unstable zone shifts up as shown in Fig. 5.5. The key conclusion considering the real life situation, the ratio of L_t/D is quite high for nuclear reactor, so no stability of this kind was found to be detected. Considering the same loop configuration when $St_m > 9.7$, no instability was observed. But it is important to note that special care for calculation of St_m should be given, as it changes with loop diameter. So it is recommended to increase L_t/D or St_m to suppress the instability.

Earlier proposed non-dimensional numbers for supercritical flow in NCL were examined by Chatoorgoon (2001) and Chatoorgoon et al. (2005b) in large number of simulations for H_2O, CO_2 and H_2 using SPORTS code. Dimensionless numbers nicely predicted the stability boundary within 95% of maximum mass flux.

Zhao et al. (2005) attempted to improvise the correlations used in boiling channels for supercritical fluid case. Earlier there were phase change numbers and subcooling numbers for boiling channels. Their study was taken further by Ambrosini and Sharabi (2008) and proposed apparent trans-pseudo critical number N'_{TPC} and sub-pseudo-critical number N_{SUBPC} for supercritical pressure.

$$N'_{TPC} = \frac{q''_0 \Pi_h L}{\rho_{pc} w_0 A} \frac{\beta_{pc}}{C_{p,pc}} \tag{5.3}$$

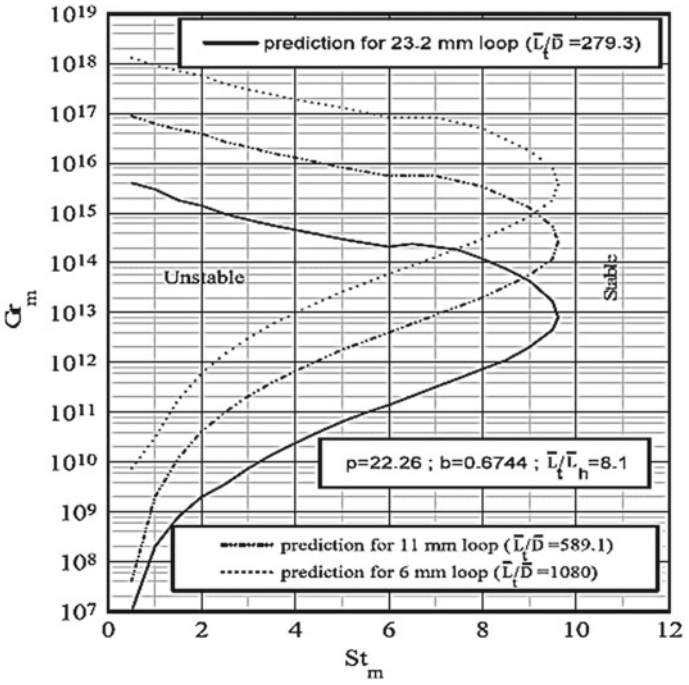

Fig. 5.5 Stability map evaluation for three rectangular loops (Vijayan 2002)

$$N_{SUBPC} = \frac{\beta_{pc}}{C_{p,pc}}\left(h_{pc} - h_{in}\right) \tag{5.4}$$

The present work was favored by (Ambrosini and Ferreri 1998) and was made a convenient tool for linear and non-linear stability analysis. Stability prediction was made with the help of RELAP5/MOD3.3 which shows the confidence in the applicability of the proposed model for supercritical fluids. However, the prime drawback of the study was the inconsideration of problems in supercritical fluids like momentum transfer across pseudo critical point.

Jain and Rizwan-uddin (2008) developed a computer code FIASCO (Flow Instability Analysis Under Supercritical Operating Conditions) in FORTRAN90 to analyze transient stability of supercritical water and CO_2 in NCL. The equations were solved by implicit finite difference method. Supercritical properties were determined using NIST/STEAM 2.21 (Harvey and Lemmon 2013) and NIST/REFPROP7 (Lemmon et al. 2002) respectively for water and CO_2. Results obtained in this investigation always predict the stability threshold to be in the positive slope region of the (steady state) flow-power curve. Using time step 0.02 s and grid size 0.1 m leads to stability zone quite early (Fig. 5.6). But results proposed that the stability threshold of a natural circulation loop with supercritical fluid is not confined to the near-peak region of the (steady state) flow-power curve, which contradict the threshold stability result of Chatoorgoon and Upadhye (2005).

Simulation results undoubtedly showed the significance of time step used. Consideration of larger time step and implicit scheme, leads to more dissipative nature leading to stability. Reducing time step to half and quarter from 0.0875 s leads to sustaining and growing oscillations at 1 MW power while grid size has insignificant effect. Increasing the pressure stretches the threshold of stability towards higher flow rate. For small sub cooling, stable zone diminishes but for higher sub-cooling

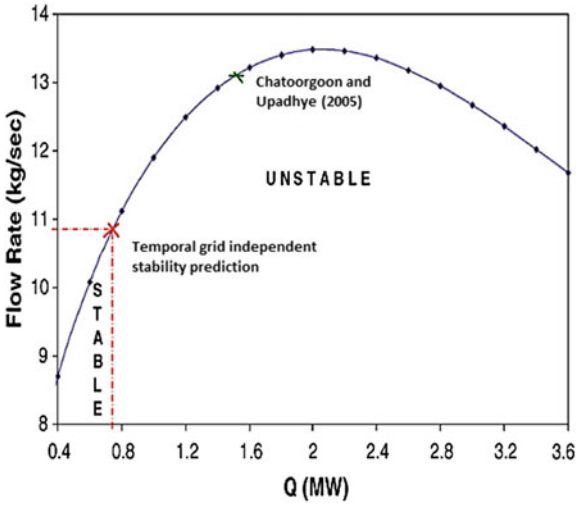

Fig. 5.6 Comparison of stability predictions of (Ambrosini and Sharabi 2008) with previous investigations (Chatoorgoon and Upadhye 2005)

it enlarges again. The results clearly remark that stability threshold does not always stick near the peak value of mass flow which manifests the prediction of (Jain and Corradini 2005).

A linear stability code named SUCLIN, was developed by Sharma et al. (2010) for sc water. Assuming initial mass flow and heat rejected to be equal to heat added, small disturbance in flow rate, specific, enthalpy and pressure was given. Required properties of water were calculated using International Association for the Properties of Steam (IAPS) formulation 1984. SUCLIN was found suitable for analysis after successful validation from previous literature (Chatoorgoon 2001; Jain and Corradini 2005). For the inlet temperature of 350 °C and 25 MPa, Nyquist plot was verified with that of Chatoorgoon (2001) who used SPORTS code and showed that loop was stable for 4 MW but unstable for 4.5 MW, while the SUCLIN code, predicts the threshold to be 4.2 MW as shown in Fig. 5.7. This difference has been attributed to the stability assessments made with different techniques and assumptions. The trend of results however remains similar in both the investigations. With increase of heater inlet temperature above 300 °C the lower threshold power of instability increases mildly but the upper threshold of power reduces expressively.

Parametric study was done for various loop diameters (7, 14, 20.7, 28 mm) at 25 MPa with varying heater inlet temperature. Stability maps obtained from the investigation shows that the instability zone increases with the increase in diameter. However, there exists a specific heater inlet temperature beyond which no instability is observed, and the value of that specific temperature decreases with the increase in loop diameter. Moreover, when the inlet temperature increases beyond the pseudo-critical temperature, the mass flow rate decreases significantly but that could be avoided by increasing the system pressure as, high system pressure has stabilizing effect. The loop height if increased, the instability in the scNCL also increases.

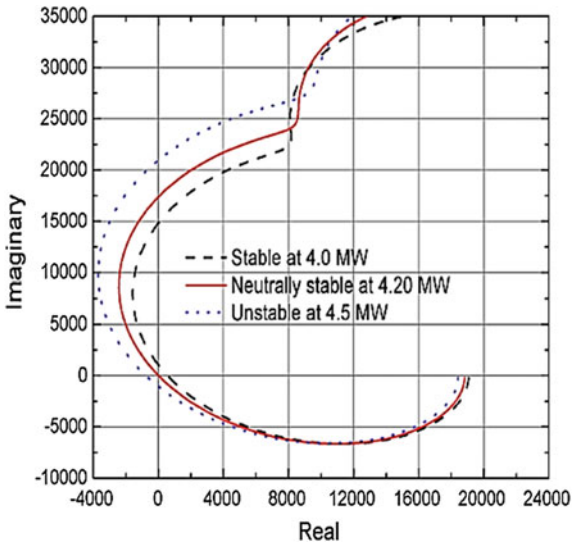

Fig. 5.7 Linear stability map predicted by SUCLIN code (Sharma et al. 2010)

However, slender loops have better buoyancy effect on the loop which provides a healthy steady state mass flow rate. These results could be of great importance in designing aspects of the NCL.

Chen et al. (2010) investigated the stability of $scCO_2$ NCL, at an average loop temperature higher than pseudo-critical range of 375 K, the 'second-critical' point which varies with pressure. The effect of increasing the diameter has been found stabilizing, while for smaller diameters it will depend on the heater input. When the heat flux is increased from a stable condition, both the velocity and temperature increased linearly without fluctuations, but then fluctuations develop and the oscillation amplifies and repetitive flow reversals occurs. When the power is again restored to previously stable point, other parameters also recover to stable conditions very fast. This is a very desirable feature for operational safety.

Debrah et al. (2012) was the first one to analyze the role of heating structure. Nodalization of CIAE (China Institute of Atomic Energy) VHHC loop was done and solved using RELAP5. When heating structures were considered, it was found that instability in water based loop arises at much higher power as compared to earlier studies. When cooler heating structures were considered, the threshold comes early. So in order to understand the phenomenon better non-dimensional numbers proposed by Ambrosini and Sharabi (2008) were compared between RELAP5 results and in-house code (without heating structure) for stability response. For in-house code two different number of nodes, namely 168 and 336, were selected and it was seen that courser mesh predicts comparatively large stable zone. RELAP5 approves the predictions made earlier. RELAP5 also precisely predicts the effects of surface roughness and fouling factors. But, comparing with the real life situation, code results with heating structure over envisages the stable behavior (Fig. 5.8). This can be attributed to the reason of having different geometry and boundary conditions.

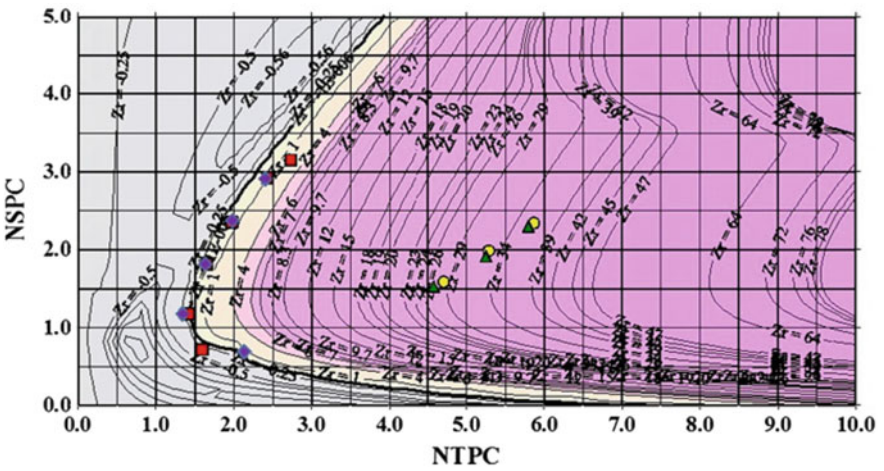

Fig. 5.8 Stability map developed by Debrah et al. (2012) showing the effect of heat structures in RELAP5 calculations (red square: no heating structure; blue diamond: only cooler structure; yellow circle: only heater structure; green triangle: both heater and cooler structures)

In computation study of Ledinegg and density wave oscillations of water, Rai et al. (2018) found that under operating condition of 25 MPa and 300 kJ/kg inlet enthalpy, there was no sign of Ledinegg instability for power range up to 230 kW. In the operating range of density wave oscillations at 58.11 kW power, system reaches on the verge of the instability for inlet enthalpy of 1623.89 kJ/kg. With increasing diameter, stability boundary shifts towards higher power attributed to higher mass flow. Increasing pressure, decreases stability boundary and with increase in loss coefficient, there is small drop in stability boundary, but later on drastic drop was seen.

Archana et al. (2015) modified a 2D axisymmetric code NAFA-loop (Numerical Analysis of Flows in Axis-symmetric geometries) considering CO_2 as working fluid and other parameters such as pressure, inlet coolant temperature and coolant flow rate were kept constant at 80.4 bar, 8 °C and 56 lpm. A heat transfer deterioration is predicted at around 1300 W owing to the fact that the inlet and outlet temperature of the heated section is above pseudo-critical temperature, which agrees with the results from Sharma et al. (2013). The code also predicts that the wall temperature increases sharply compared to the bulk flow temperature.

The results of Tilak and Basu (2015) for the stability dependence of scH_2O NCL on time step and grid size were in agreement with Chatoorgoon et al. (2005) and Sharma et al. (2013). In the investigation Step, ramp, exponential and sinusoidal excitations were imposed on the system where step rise in heater power introduced instability into the system and had the most destabilizing influence. System takes longer time to regain steady-state, if the final power is within stability boundary. Ramp and exponential profiles were found to provide favorable response during both power upsurge and down-surge, however exponential transition is preferable from stability's perspective. Longer period of transition allows the system to suppress unstable fluctuations in a better way. Application of sinusoidal transition results in distorted periodic response while attempting to follow the imposed signal only after sufficient time since application shows periodic signal. Fast Fourier transform of resultant discrete data series exhibits two distinct peaks, with the larger one corresponding to the imposed sinusoid and the other one signifying the natural frequency of the system as shown in Fig. 5.9. The natural frequency is a characteristics of the loop and remains invariant of the frequency of the imposed signal. On imposing impulse signal, a stable system exhibits large-amplitude oscillations while, an unstable system may suffer from flow reversal.

5.5.2 Experimental Investigations

Lomperski et al. (2004) in their experiment studied the two types of configurations, one with the base case and other with an orifice in hot leg. Orifice creates flow disturbances, effect of which can be seen as the heater outlet temperature rises quickly

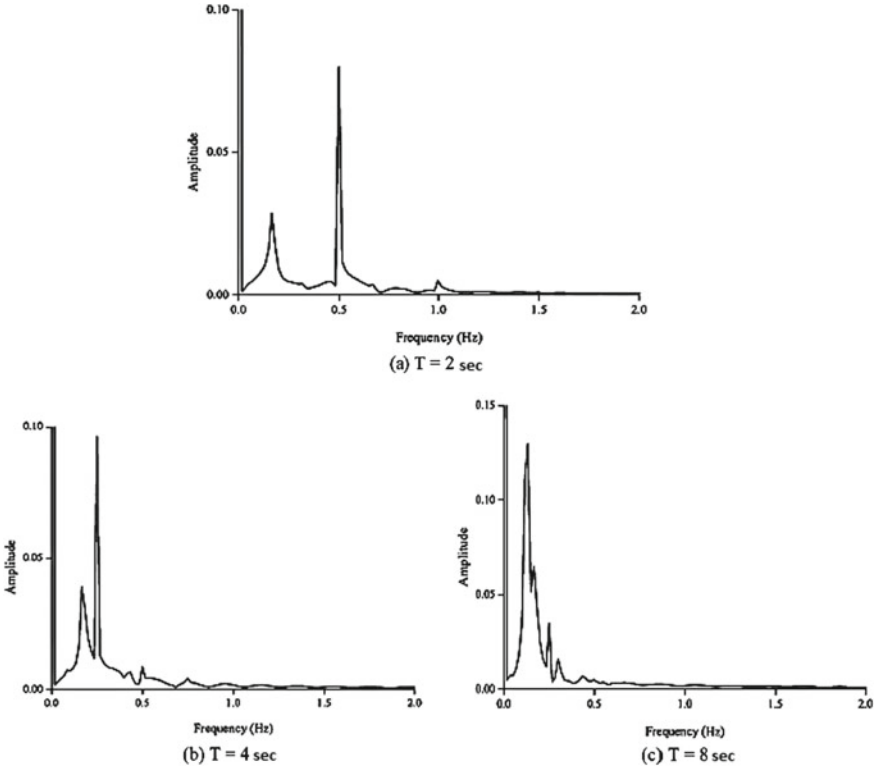

Fig. 5.9 Variation of amplitude with frequency under FFT of transient response for sinusoidal variation of heater power with three different time periods (Tilak and Basu 2015)

at lower powers as compared to base arrangement and correspondingly mass flow peak occurs early. The possible reason could be the dominance of friction losses over driving head. Experimentally no signs of instabilities were seen. As far as the stability is concerned, the parameter $\partial m/\partial \rho$ showed great significance, as Chatoorgoon (2001) mentioned about the peak power for instability. When the slope of $\partial m/\partial \rho$ is negative, the disturbance gets neutralized by rise in mass flow. While when the slope is positive, outlet temperature would increase and amplify the disturbance. Operating the loop for inlet/outlet temperature 20–30 °C/40–85 °C and pressure 75–95 bar, the system was found to be stable in both the regions of power (Fig. 5.10), which was completely contrary to the numerical analysis. Numerical analysis showed that beyond the certain power level, system did not stabilize. This discrepancy was suggested to be analyzed through further experimentation.

Jain and Corradini (2005) found divergences between the results of instability for $scCO_2$ in experimental study (stable) at Argonne National Laboratory (ANL) and 1-D transient analysis using FORTRAN code (unstable) at University of Wisconsin, Madison. Stability of water loop depends upon the accuracy of EOS. EOS2 captures

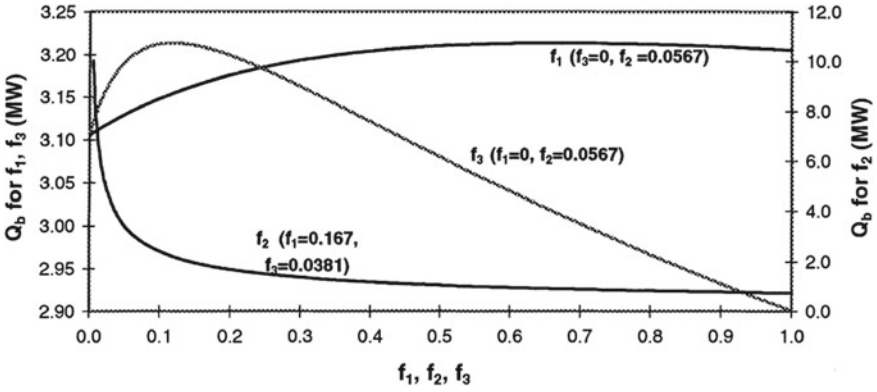

Fig. 5.10 Effect of friction factors on the bounding power (Chatoorgoon 2001)

the maximum temperature (821 K) within its specified range (655–850 K), while EOS1 had the range (630–820 K) below the maximum temperature range. Thus EOS2 yields more accurate results, which is in consensus with the experimental results.

In case of $scCO_2$, results from experimental analysis depicts stable behavior while linearized transient analysis depicts the unstable behavior. The main reason for these discrepancies could be either due to the uncertain nature of the distribution of friction factor along the flow path or improper application of constant heat flux or both. Following modifications were suggested to void these discrepancies.

(1) Using closed loop geometry which actually resembles the experimental facility. Open loop was made in order to validate the linearized code with previous works.
(2) Applying more practical boundary conditions like constant flow rate and inlet temperature on secondary side fluid.

Yu et al. (2011) conducted stability analysis experiments in supercritical water. The results were verified with the numerical code, emphasizing on the Ledinegg type instability. Analytical code was run over wide range of powers. For a particular input temperature (Fig. 5.11), till the mass flow reaches 0.066 kg/s, system is stable. As the condition for Ledinegg instability does not hold true, instability arises. In the range of experiments conducted, no Ledinegg instability was found. To operate the system at higher mass flow rate without occurrence of instability, author recommended to use system at low inlet temperature because operating at low inlet temperature, leads system to higher flow rate, thus causing delay in instability.

In the past literatures, correlations were available for sub-critical conditions only, which due to drastic change of properties near pseudo-critical temperature, cannot be applied for super-critical fluids. Using earlier correlations (Ambrosini and Sharabi 2008), efforts were made by Swapnalee et al. (2012), to find out the generalized explicit correlations for super critical fluids and were validated with experiments with

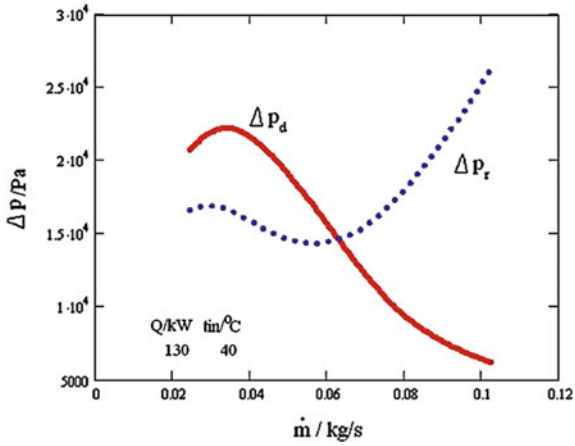

Fig. 5.11 Pressure drop variation with mass flow rate predicted by Yu et al. (2011)

water and CO_2. Relationships developed were based on the dimensionless density and enthalpy.

$$\rho^* = \frac{\rho}{\rho_{pc}} \tag{5.5}$$

$$h^* = \beta_{pc}\left(h - h_{pc}\right) \tag{5.6}$$

Experiments were performed with all possible horizontal and vertical orientations of heater and cooler. In order to capture the Ledinegg instability (static) for CO_2, analytical method was adopted and equation capturing different losses were derived and no sign of multiple steady states were found as shown in Fig. 5.12. In case of

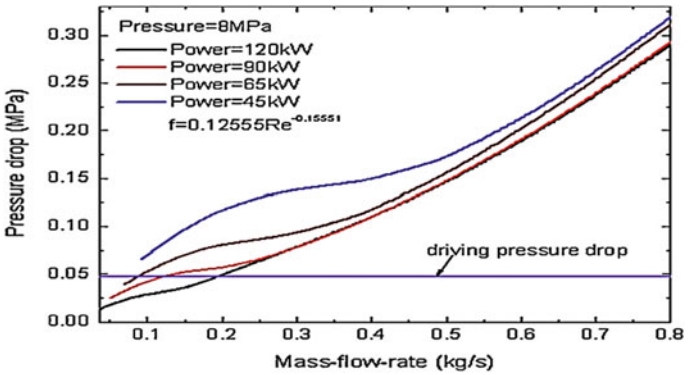

Fig. 5.12 Identification of instability with mass flow versus pressure drop (Swapnalee et al. 2012)

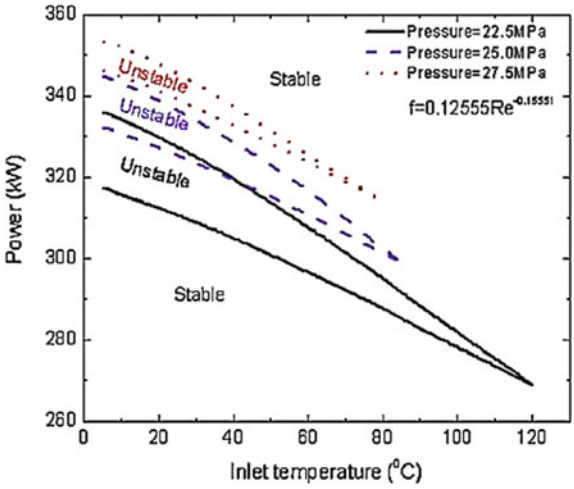

Fig. 5.13 Stability map with respect to power variation (Swapnalee et al. 2012)

water it was observed that for high powers, excursive instability was observed at high sub-pseudo critical number N_{SUBPC} (Ambrosini 2007) and unstable zone gets narrower with the rise in pressure (Fig. 5.13).

Chen et al. (2013) investigated the effect of inclination angle on a $scCO_2$ NCL. Horizontal loop setting is found to have highest thermal resistance while vertical loop is preferred for heat transfer characteristics. Still, complex heat transfer behaviors are found for 15° to 75° inclination angles. Judging from both the numerical and experimental results, larger inclination angles will have higher circulation rate and better heat transfer behavior.

Liu et al. (2017) have confirmed oscillations similar to pressure drop oscillations. The effect of inlet temperature also shows that when the pressure increases, the density variation slope is less steep, showing better stability (Fig. 5.14). It also approves

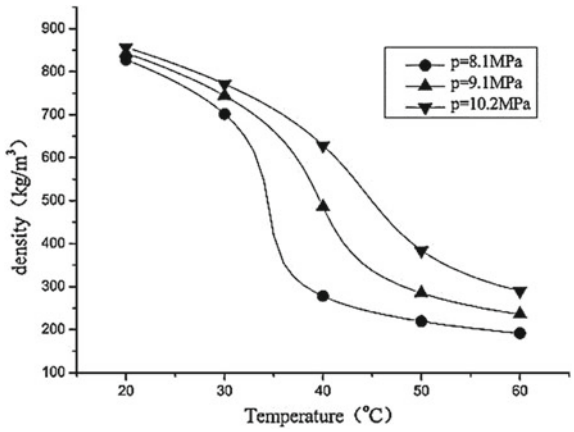

Fig. 5.14 Effect of inlet temperature of the heater on the threshold power (Liu et al. 2017)

that the wall temperature increases sharply than the bulk temperature (Archana et al. 2015). When the low-temperature fluid particle contacts the hot wall, it significantly expands owing to the temperature sensitivity of density near the pseudo-critical point, and then move away from the hot wall. Finally, it would contract in the bulk flow. The obvious variation of the volume of the fluid particle leads to pressure fluctuation in the loop. The experiments also affirm that increasing the system pressure has a stabilizing effect on the NCL which is in agreement with (Sharma et al. 2010). It is also to be noted that when the local resistance of heat sink section is increased the loop stabilizes but at the same time if the local resistance increases for heat source section then the loop becomes susceptible to instabilities. In the subsequent experimental study of Liu et al. (Liu et al. 2016) with vertical heating and horizontal cooling with CO_2, effect of system pressure and intel temperature was seen having no effect on stable behavior, while inlet temperature do have effect on mass flow rate and effect becomes noteworthy when it is in the range of pseudo-critical limit. Sharma et al. (Sharma et al. 2013) also experimentally investigated a rectangular $scCO_2$ NCL. The instability in the loop was observed in the pseudo-critical temperature range of operation where the volumetric expansion coefficient of the fluid is the highest. Experiments also affirms on the decrease of mass flow rate predicted by NOLSTA.

Few studies have been done with heat exchanger on both end. Yadav et al. (2017) focused their transient experimental study with CO_2 (hot heat exchanger 323–353 K and cold heat exchanger 305 K for water). It was seen that the system reaches steady state faster with high system pressure. Tilt angle and inlet temperature both have effect on impact on steady state characteristics of the loop, but system was found to be stable. Cooling of CO_2 by air instead of water does not cause problems for stability point of view (Sadhu et al. 2017).

5.6 Recommendation

After comprehensive analysis on different aspects of steady state and stability of super-critical natural circulation loop, it is now clear that using super critical fluid imposes remarkable advantages over forced flow system. But as far as safety is concern, it is primary duty of design engineer to thoroughly investigate the stability aspects from the design point of view as well as imparted condition. From the beginning of 21st century, this technology has been accelerated and is improving progressively. Most of the stability related work has been done analytically or theoretically with lesser experimental verification with many contradictions in the results. Drawback with the analytical analysis is that to solve complex non-linear equations, certain assumptions are needed to make it easily solvable, thus moving away from real conditions. Operating the system in stable zone is mandatory for which quite a few suggestions can be listed to expand the stable zone.

(i) Maximum L_t/D ratio.

(ii) For scH_2O cooled reactor, large diameter is stable and unstable zone disappear at high inlet temperature.
(iii) High Slenderness loop.
(iv) Operating at high pressure.
(v) Higher inclination angle in YZ plane.

It is advisable to operate at the power input so that pseudo-critical temperature range crosses within heater to get substantial flow rate. To avoid the FiHTD

(i) High system pressure
(ii) Lower sink temperature
(iii) Large diameter
(iv) Increased Loop Height
(v) Longer Heat Sink Length.

Multidimensional computer simulations based on finite volume is recommended over 1-D finite difference method as it can lead to less accurate behavior of heat transfer characteristics. Apart from this, selection of turbulence model and meshing is important to capture the actual phenomenon. EOS plays crucial role for calculation of property variation as complete desirable output of the loop depends upon thermal hydraulics of loop.

5.7 Conclusion

Supercritical NCL is approved to be a potent technology whose application could be found in: cooling of nuclear reactors, electronic chip cooling, solar heaters, etc. Once fully acknowledged its power could lead many other fields as well. Decent number of analytical work has been done in the recent past, however very few experiments have been carried out. Crucial phenomenon associated with NCL have been correctly predicted but at the same time contradictory results were also observed. Lack of experimental work also makes it difficult to decipher and confirm the mechanisms behind the phenomenon.

This chapter deals with the dynamics of NCL and hence much emphasis has been put on the stability aspects of the NCL. Different models of analysis as well as computational models have been developed to study the steady state and transient analysis of scNCL. 1-D analysis on codes such as FIASCO, NOLSTA, SPORTS, RELAP5, SUCLIN while, 2-D dimensional analysis was done in NAFA-Loop code. The codes' predictions and results were compared with experimental observations on same and different investigations. The relevance of choice of fluid have and the effects of both geometric and parametric were also discussed. This chapter includes the findings of various investigations and briefly summarized them. Finally, a few recommendations have been provided for future research as more work needs to be done to increase the knowledge base of this unusual yet interesting field.

References

Ambrosini W (2007) On the analogies in the dynamic behaviour of heated channels with boiling and supercritical fluids. Nucl Eng Des 237:1164–1174. https://doi.org/10.1016/j.nucengdes.2007.01.006

Ambrosini W, Ferreri JC (1998) The effect of truncation error on the numerical prediction of linear stability boundaries in a natural circulation single-phase loop. Nucl Eng Des 183:53–76. https://doi.org/10.1016/s0029-5493(98)00157-5

Ambrosini W, Sharabi M (2008) Dimensionless parameters in stability analysis of heated channels with fluids at supercritical pressures. Nucl Eng Des 238:1917–1929. https://doi.org/10.1016/j.nucengdes.2007.09.008

Ambrosini W, Forgione N, Ferreri JC, Bucci M (2004) The effect of wall friction in single-phase natural circulation stability at the transition between laminar and turbulent flow. Ann Nucl Energy 31:1833–1865. https://doi.org/10.1016/j.anucene.2004.05.011

Archana V, Vaidya AM, Vijayan PK (2015) Numerical modeling of supercritical CO_2 natural circulationloop.pdf. Nucl Eng Des 293:330–345 (2015). https://doi.org/10.1016/j.nucengdes.2015.07.030

Blackburn JM, Long DP, Cabañas A, Watkins JJ (2001) Deposition of conformal copper and nickel films from supercritical carbon dioxide. Science 294:141–145. https://doi.org/10.1126/science.1064148

Boure JA, Bergles AE, Tong LS (1973) Review of two-phase flow instability. Nucl Eng Des 25:165–192. https://doi.org/10.1016/0029-5493(73)90043-5

Cammarata L, Fichera A, Pagano A (2003) Stability maps for rectangular circulation loops. Appl Therm Eng 23:965–977. https://doi.org/10.1016/S1359-4311(03)00027-9

Chatoorgoon V (1986) SPORTS—a simple non-linear thermal hydraulic stability code. Nucl Eng Des 93:51–67. https://doi.org/10.1016/0029-5493(86)90194-9

Chatoorgoon V (2001) Stability of supercritical fluid flow in a single-channel. Int J Heat Mass Transf 44:1963–1972. https://doi.org/10.1016/S0017-9310(00)00218-0

Chatoorgoon V, Upadhye P (2005) Analytical studies of supercritical flow instability in natural convection loops. In: 11th international topical meeting on nuclear reactor thermal-hydraulics (NURETH-11), Avignon, France, Oct 2–6, Avignon, France (2005)

Chatoorgoon V, Voodi A, Fraser D (2005a) The stability boundary for supercritical flow in natural convection loops: part I: H_2O studies. Nucl Eng Des 235:2570–2580. https://doi.org/10.1016/j.nucengdes.2005.06.003

Chatoorgoon V, Voodi A, Upadhye P (2005b) The stability boundary for supercritical flow in natural-convection loops: Part II: CO_2 and H_2. Nucl Eng Des 235:2581–2593. https://doi.org/10.1016/j.nucengdes.2005.06.004

Chen K (1985) On the oscillatory instability of closed-loop thermosyphons. J Heat Transfer 107:826–832. https://doi.org/10.1115/1.3247510

Chen L, Zhang XR (2011) Simulation of heat transfer and system behavior in a supercritical CO_2 based thermosyphon: effect of pipe diameter. J Heat Transfer 133:1–8. https://doi.org/10.1115/1.4004434

Chen L, Zhang XR, Yamaguchi H, Liu ZS (2010) Effect of heat transfer on the instabilities and transitions of supercritical CO_2 flow in a natural circulation loop. Int J Heat Mass Transf 53:4101–4111. https://doi.org/10.1016/j.ijheatmasstransfer.2010.05.030

Chen L, Zhang XR, Deng BL, Jiang B (2013) Effects of inclination angle and operation parameters on supercritical CO_2 natural circulation loop. Nucl Eng Des 265:895–908. https://doi.org/10.1016/j.nucengdes.2013.06.037

Chen L, Zhang X-R, Jiang B (2014) Effects of heater orientations on the natural circulation and heat transfer in a supercritical CO_2 rectangular loop. J Heat Trans 136:1–12. https://doi.org/10.1115/1.4025543

Close DJ (1962) The performance of solar water heaters with natural circulation. Sol Energy 6:33–40. https://doi.org/10.1016/0038-092X(62)90096-8

Creveling HF, De Paz JF, Baladi JY, Schoenhals RJ (2016) Stability characteristics of a single-phase free convection loop. J Fluid Mech 67: 65–84 (2016). https://doi.org/10.1017/s0022112075000171

Debrah SK, Ambrosini W, Chen Y (2012) Discussion on the stability of natural circulation loops with supercritical pressure fluids. Ann Nucl Energy 54:47–57. https://doi.org/10.1016/j.anucene.2012.10.015

Dimmick GR, Chatoorgoon V, Khartabil HF, Duffey RB (2002) Natural-convection studies for advanced CANDU reactor concepts. Nucl Eng Des 215:27–38. https://doi.org/10.1016/S0029-5493(02)00039-0

Fichera A, Pagano A (2003) Modelling and control of rectangular natural circulation loops. Int J Heat Mass Transf 46:2425–2444. https://doi.org/10.1016/S0017-9310(02)00543-4

Fukuda K, Kobori T (1979) Classification of two-phase flow instability by density wave oscillation model classification of two-phase flow instability by density wave oscillation model. J Nucl Sci Technol 16:95–108. https://doi.org/10.1080/18811248.1979.9730878

Harvey AH, Lemmon EW (2013) NIST/ASME Steam Properties—STEAM-Version 3.0. *S.* Department of Commerce's National Institute of Standards Reference Data Program Gaithersburg, Maryland 20899 (2013)

Hashemi-tilehnoee M, Sahebi N, Dogonchi AS, Masoud S, Tashakor S (2019) Simulation of the dynamic behavior of a rectangular single-phase natural circulation vertical loop with asymmetric heater. Int J Heat Mass Transf 139:974–981. https://doi.org/10.1016/j.ijheatmasstransfer.2019.05.076

Jain PK (2008) Rizwan-uddin: numerical analysis of supercritical flow instabilities in a natural circulation loop. Nucl Eng Des 238:1947–1957. https://doi.org/10.1016/j.nucengdes.2007.10.034

Jain R, Corradini ML (2005) A linear stability analysis for natural-circulation loops under supercritical conditions. Nucl Technol 155:312–323. https://doi.org/10.13182/nt06-a3764

Kakac S, Bon B (2008) A Review of two-phase flow dynamic instabilities in tube boiling systems. Int J Heat Mass Transf 51:399–433. https://doi.org/10.1016/j.ijheatmasstransfer.2007.09.026

Kim DE, Kim MH, Cha JE, Kim SO (2008) Numerical investigation on thermal-hydraulic performance of new printed circuit heat exchanger model. Nucl Eng Des 238:3269–3276. https://doi.org/10.1016/j.nucengdes.2008.08.002

Kreitlow DB, Reistad GM, Miles CR, Culver GG (1978) Thermosyphon models for downhole heat exchanger applications in shallow geothermal systems. J Heat Transfer 100: 713–719 (1978). https://doi.org/10.1115/1.3450883

Kudariyawar JY, Vaidya AM, Maheshwari NK, Satyamurthy P (2016) Computational study of instabilities in a rectangular natural circulation loop using 3D CFD simulation. Int J Therm Sci 101:193–206. https://doi.org/10.1016/j.ijthermalsci.2015.11.003

Lemmon EW, McLinden MO, Huber ML (2002) NIST Standard Reference Database 23: Reference Fluid Thermodynamic and Transport Properties, version 9.0. Natl Inst Stand Technol Gaithersbg. (2002)

Liu G, Huang Y, Wang J, Lv F, Leung LKH (2016) Experiments on the basic behavior of supercritical CO_2 natural circulation. Nucl Eng Des 300:376–383. https://doi.org/10.1016/j.nucengdes.2016.01.021

Liu G, Huang Y, Wang J, Lv F, Liu S (2017) Experimental research and theoretical analysis of flow instability in supercritical carbon dioxide natural circulation loop. Appl Energy 205:813–821. https://doi.org/10.1016/j.apenergy.2017.08.132

Lomperski S, Cho D, Jain R, Corrandini ML (2004) Stability of a natural circulation loop with a fluid heated through the thermodynamic pseudocritical point. In: Proceedings of ICAPP '04 Pittsburgh, PA USA, June 13–17, 2004 Paper ID 4268. pp 1–6, Pittsburgh, PA USA

Ochsner K (2008) Carbon dioxide heat pipe in conjunction with a ground source heat pump (GSHP). Appl Therm Eng 28:2077–2082. https://doi.org/10.1016/j.applthermaleng.2008.04.023

Pilkhwal DS, Ambrosini W, Forgione N, Vijayan PK, Saha D, Ferreri JC (2007) Analysis of the unstable behaviour of a single-phase natural circulation loop with one-dimensional and computational fluid-dynamic models. Ann Nucl Energy 34: 339–355 (2007). https://doi.org/10.1016/j.anucene.2007.01.012

Rai SK, Dutta G, Sheorey T (2018) Stability analysis of supercritical water natural circulation loop with vertical heater and cooler. In: Proceedings of the 24th national and 2nd international ISHMT-ASTFE heat and mass transfer conference (IHMTC-2017). Begellhouse, Connecticut, pp 607–611 (2018)

Sadhu S, Ramgopal M, Bhattacharyya S (2017a) Steady-state analysis of a high-temperature natural circulation loop based on water-cooled supercritical CO_2. J Heat Transfer 140:062502. https://doi.org/10.1115/1.4038541

Sadhu S, Ramgopal M, Bhattacharyya S (2017b) Experimental studies on an air-cooled natural circulation loop based on supercritical carbon dioxide—part b: transient operation. Appl Therm Eng 133:809–818. https://doi.org/10.1016/j.applthermaleng.2017.10.016

Saha R, Mukhopadhyay Achintya KG, Sen S (2018) Dynamic characterization of a single phase square natural circulation loop. Appl Therm Eng 128:1126–1138. https://doi.org/10.1016/j.applthermaleng.2017.09.092

Sarkar MKS, Basu DN (2016) Numerical comparison of thermal hydraulic aspects of supercritical carbon dioxide and subcritical water-based natural circulation loop. Nucl. Eng. Technol. 49:1–10. https://doi.org/10.1016/j.net.2016.09.007

Sharma M, Pilkhwal DS, Vijayan PK, Saha D, Sinha RK (2010) Steady state and linear stability analysis of a supercritical water natural circulation loop. Nucl Eng Des 240:588–597. https://doi.org/10.1016/j.nucengdes.2009.10.023

Sharma M, Vijayan PK, Pilkhwal DS, Asako Y (2013) Steady state and stability characteristics of natural circulation loops operating with carbon dioxide at supercritical pressures for open and closed loop boundary conditions. Nucl Eng Des 265:737–754. https://doi.org/10.1016/j.nucengdes.2013.07.023

Solomon AB, Roshan R, Vincent W, Karthikeyan VK, Asirvatham LG (2015) Heat transfer performance of an anodized two-phase closed thermosyphon with refrigerant as working fluid. Int J Heat Mass Transf 82:521–529. https://doi.org/10.1016/j.ijheatmasstransfer.2014.11.034

Song JH (2012) Performance of a two-phase natural circulation in a rectangular loop. Nucl Eng Des 245:125–130. https://doi.org/10.1016/j.nucengdes.2012.01.006

Sukchana T, Pratinthong N (2017) Effect of bending position on heat transfer performance of R-134a two-phase close loop thermosyphon with an adiabatic section using flexible hoses. Int J Heat Mass Transf 114:527–535. https://doi.org/10.1016/j.ijheatmasstransfer.2017.05.133

Swapnalee BT, Vijayan PK, Sharma M, Pilkhwal DS (2012) Steady state flow and static instability of supercritical natural circulation loops. Nucl Eng Des 245:99–112. https://doi.org/10.1016/j.nucengdes.2012.01.002

Tilak AK, Basu DN (2015) Computational investigation of the dynamic response of a supercritical natural circulation loop to aperiodic and periodic excitations. Nucl Eng Des 284:251–263. https://doi.org/10.1016/j.nucengdes.2014.12.028

Tong Z, Liu X, Li Z, Jiang Y (2016) Experimental study on the effect of fill ratio on an R744 two-phase thermosyphon loop. Appl Therm Eng 99:302–312. https://doi.org/10.1016/j.applthermaleng.2016.01.065

Torrance KE (2010) Open-loop thermosyphons with geological applications. J Heat Transfer 101: 677–683 (2010). https://doi.org/10.1115/1.3451056

Vijayan PK (2002) Experimental observations on the general trends of the steady state and stability behaviour of single-phase natural circulation loops. Nucl Eng Des 215:139–152. https://doi.org/10.1016/S0029-5493(02)00047-X

Vijayan PK, Austregesilo H (1994) Scaling laws for single-phase natural circulation loops. Nucl Eng Des 152:331–347. https://doi.org/10.1016/0029-5493(94)90095-7

Vijayan PK, Austregesilo H, Teschendorff V (1995) Simulation of the unstable oscillatory behavior of single-phase natural circulation with repetitive flow reversals in a rectangular loop using the computer code ATHLET. Nucl Eng Des 155:623–641

Vijayan PK, Sharma M, Saha D (2007) Steady state and stability characteristics of single-phase natural circulation in a rectangular loop with different heater and cooler orientations. Exp Therm Fluid Sci 31:925–945. https://doi.org/10.1016/j.expthermflusci.2006.10.003

Vijayan PK, Nayak AK, Saha D, Gartia MR (2008) Effect of loop diameter on the steady state and stability behaviour of single-phase and two-phase natural circulation loops. Sci Technol Nucl Install 2008:1–17. https://doi.org/10.1155/2008/672704

Welander P (1967) On the oscillatory behaviour of a differentially heated fluid loop—Welander. J Fluid Mech 29:17–30. https://doi.org/10.1017/S0022112067000606

Wissler EH, Isbin HS, Amundson NR (1956) Oscillatory behavior of a two-phase natural-circulation loop. Am Inst Chem Eng J 2:157–162. https://doi.org/10.1002/aic.690020206

Yadav AK, Ramgopal M, Bhattacharyya S (2017) Transient analysis of subcritical/supercritical carbon dioxide based natural circulation loop with end heat exchangers: experimental study. Heat Mass Transf und Stoffuebertragung. 53:2951–2960. https://doi.org/10.1007/s00231-017-2038-z

Yu J, Che S, Li R, Qi B (2011) Analysis of Ledinegg flow instability in natural circulation at supercritical pressure. Prog Nucl Energy 53:775–779. https://doi.org/10.1016/j.pnucene.2011.04.001

Zhao J, Saha P, Kazimi MS (2005) Stability of supercritical water-cooled reactor during steady-state and sliding pressure start-up conditions. In: International topical meeting on nuclear reactor thermal hydraulics (NURETH 11); Avignon (France); 2–6 Oct 2005, France (2005)

Zuber N (1966) An analysis of thermally induced flow oscillations in the near-critical and supercritical thermodynamic region

Chapter 6
Dynamics and Control of a Load-Following Nuclear Power Plant for Grid with Intermittent Sources of Energy

Areai Nuerlan and Rizwan-uddin

Abstract Intermittent renewable energy sources such as solar and wind are still in their early stages of market penetration. However, fraction of electricity coming from these sources continues to increase, putting pressure on the stability of the new grid, which is best characterized as a hybrid energy system (HES). Generation II nuclear power plants (NPPs) were designed to supply base load to the grid, making it necessary for the new generation of NPPs to have some level of load following capability to respond to the needs of the new grid with varying load and frequency needs. NPPs that can follow load need new kind of hardware and control strategy. One of the newer reactors, AP1000, is designed to load follow, thus permitting its easy integration into a modern HES electricity grid. The advanced Mechanical Shim (MSHIM) control system is used in the AP1000 reactor design to regulate power. This control system consists of two separate rod controllers that control the core reactivity and axial power distribution using the "gray and black M control banks" (M-banks) and the "axial offset control bank" (AO-bank), respectively. In this chapter, past works on the development of the modeling of AP1000 will be reviewed first. This will include nodal model for reactor, pressurizer and UTSG dynamics, and corresponding models for their control. This will be followed by a discussion of load following capability of AP1000 with original MSHIM strategy and a revised one.

Keywords Grid with intermittent energy sources · AP1000 · MSHIM · Load following · Modeling and control

A. Nuerlan (✉)
School of Nuclear Science and Technology, Xi'an Jiaotong University, No. 28, Xianning West Road, 710049 Xian, People's Republic of China
e-mail: rizwan@illinois.edu

Rizwan-uddin
Department of Nuclear, Plasma, and Radiological Engineering, University of Illinois at Urbana-Champaign, 104 S Wright St., 61801 Urbana, IL, USA

A. Mukhopadhyay et al. (eds.), *Dynamics and Control of Energy Systems*,
Energy, Environment, and Sustainability,
https://doi.org/10.1007/978-981-15-0536-2_6

6.1 Introduction

Multi-input, multi-output hybrid energy systems (HESs) can be designed to operate flexibly based on thermal and/or electrical energy demands while accommodating multiple, time-varying input streams (Carelli and Ingersoll 2015). Those input streams could be a combination of sources such as nuclear reactors, hydro-electric dams, wind turbines or solar farms. While nuclear power plants can provide a base load to the HES, it is desirable for the nuclear reactor integrated in the HES to be able to participate in the load regulation operation. This requires the nuclear reactor to be able to load follow. The Westinghouse AP1000 is an advanced Generation pressurized water reactor (PWR) based on the concept of passive nuclear safety (Wan et al. 2015). Mechanical shim (MSHIM) based control, adopted in the AP1000, makes it able to operate under load following scenarios (Wang et al. 2014). The AP1000 nuclear steam supply system (NSSS) contains the reactor core and the reactor coolant system (RCS). The RCS consists of two heat transfer circuits, each with a vertical U-tube steam generator (UTSG) and a single hot leg and two cold legs. In addition, the RCS also includes a pressurizer, interconnecting pipes, and the valves and instrumentation necessary for operational control and the actuation of safeguards (Westinghouse Electric Company 2005). In response to changing plant conditions as well as to time-varying load, the NSSS is equipped with reactor power control system, pressurizer pressure control system, pressurizer water level control system, and feedwater control system to automatically regulate the operating conditions in the plant (Wan et al. 2015). To investigate the ability of AP1000 to operate in the load following mode when connected to a HES grid, it is important to first review all the features of the control systems of the key plant components such as reactor core, pressurizer and UTSG.

Mechanical Shim (MSHIM) system to regulate core power is one of the advanced components used in the AP1000, originally developed as an evolutionary reactor control concept that would improve transient control capabilities. Existing GEN-II reactors depend largely on chemical shim to achieve fine control. On the other hand, MSHIM system utilizes low worth (gray) control rod banks as ‘mechanical shim’. In this control strategy, two independently moving Rod Cluster Control Assemblies (RCCA) are respectively used to control reactor power and axial power distribution for a wide range of operational scenarios (Drudy et al. 2009). The first RCCA uses a sequence of low worth control rod banks (M-banks), and the second one consists of a single, high worth bank (axial offset or AO-bank). Priority in these two control circuits is given to the M-banks. Movement of the M-banks does not significantly impact the axial power distribution, making it possible to decouple the control of reactor power and axial offset. This control procedure with two different RCCAs allows automatic control of reactivity in response to rapidly changing power demand, eliminating the need for chemical shim adjustments during power maneuvers (Drudy et al. 2009; Onoue et al. 2003).

By increasing the size of the pressurizer in the AP1000, the transient margin is increased and unplanned reactor shutdowns are reduced. This also enhances the load following capability of the plant. The pressure and water level in the pressurizer reflect the state of the primary side. Hence, the two parameters are crucial for the control of the average temperature Tavg and to maintain pressure in the primary side. Pressurizer pressure and water level can be controlled by two separate controllers. AP1000 employs Δ125 U type steam generator. The UTSG serves as the major heat sink, transferring the heat generated in the reactor core it to the circulating water on the secondary side. The water level in the secondary side of the UTSG must be maintained at a pre-determined value to ensure proper heat transfer from the reactor coolant to the secondary system as well as for satisfactory operation of steam-drying equipment. This is achieved by controlling the feedwater flow.

The original MSHIM bank overlap scheme is beneficial as it can provide both positive and negative reactivity insertion capability in the event of an operational transient. It also allows compensation for fuel depletion through the slow withdrawal of the M-banks during base load operation. However, Drudy et al. (2009) proposed a revised version of the M-banks overlap configuration considering that the original insertion sequence would cause large perturbations to the core power distribution when the M-banks are withdrawn or inserted from the reference position because the effective lead bank is of high worth. Simulation results show that the revised overlap scheme is beneficial, reducing the power distribution perturbations caused by the motion of the lead M-bank.

In this chapter, past work on the development of the control system of AP1000 including reactor control subsystem, UTSG water level control subsystem and pressurizer pressure control subsystem will be reviewed. This will start with the description of each plant component model, which is the necessary first step for designing control systems. Improvements in the model of the reactor core and UTSG are also reviewed. This is followed by a discussion of load following capabilities of AP1000 with original and revised version of MSHIM control strategy in complex operational conditions.

6.2 AP1000 Nuclear Steam Supply System Model

The schematic diagram of the nuclear steam supply system (NSSS) is depicted in Fig. 6.1. AP1000 consists of a reactor core and two loops. Each loop contains a Δ125 U type steam generator, two shielded motor pumps, two cold section main pumps and one hot section main pump. Model of each component of the NSSS are needed to complete the design of the controllers. A nodal core model, a non-equilibrium two-regions/three-volumes pressurizer model, a lumped parameter dynamic steam generator model with moving boundary, and the relevant pipe and plenum models were proposed by Wan et al. (2015) based on the fundamental conservation of mass, energy and momentum. These are described below.

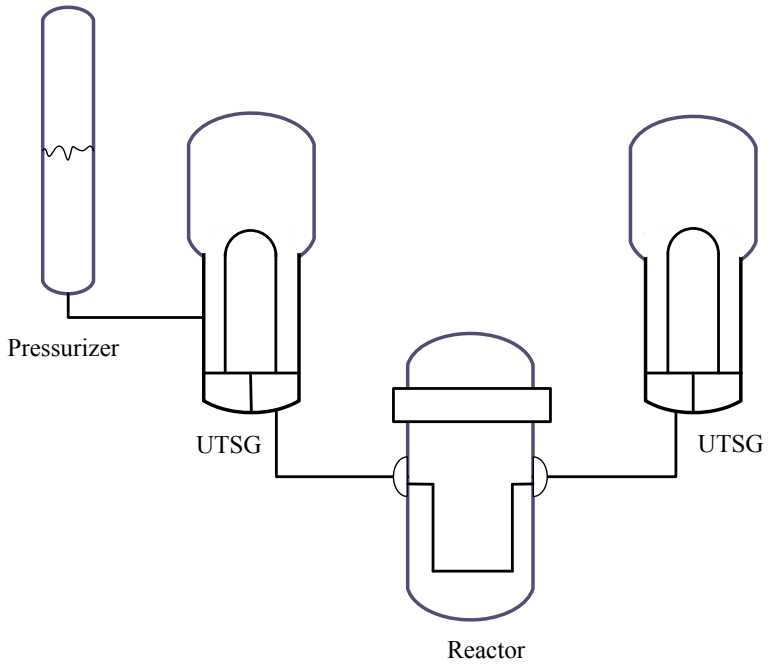

Fig. 6.1 Schematic diagram of the NSSS

6.2.1 Reactor Core Model

The large volume and height-to-diameter ratio of AP1000 core and the mechanical shim (MSHIM) control system can lead to a phenomenon called "flux tilt." Because of this, the commonly used point kinetics model for reactor power is not appropriate to model the AP1000 reactor core. To model and simulate the space–time neutron kinetics of AP1000 reactor, the nodal approach was adopted for its effectiveness and simplification (Wan et al. 2015). In this approach, the reactor core is divided into a number of relatively large size nodes in the axial direction. The nodal core model of the AP1000 reactor for the neutron kinetics, thermal–hydraulics and xenon-iodine dynamics can be written as:

Point kinetics equations with six-group delayed neutrons:

$$\begin{cases} \frac{dN_i}{dt} = \left(\frac{\rho_i - \beta}{\Lambda_i} - \frac{D_i \upsilon}{\Delta H_i d_{i,i-1}} - \frac{D_i \upsilon}{\Delta H_i d_{i,i+1}} \right) N_i + \sum_{k=1}^{6} \frac{\beta_k}{\Lambda_i} C_{k,i} + \frac{D_i \upsilon n_{i-1}(0)}{\Delta H_i d_{i,i-1} n_i(0)} N_{i-1} + \frac{D_i \upsilon n_{i+1}(0)}{\Delta H_i d_{i,i+1} n_i(0)} N_{i+1} \\ \frac{dC_{k,i}}{dt} = \lambda_k (N_i - C_{k,i}) \end{cases} \tag{6.1}$$

Core-fuel-to-coolant heat transfer equations:

$$\begin{cases} \frac{dT_{fi}}{dt} = \frac{f_f P_{i0}}{\mu_{fi}} N_i - \frac{\Omega_i}{\mu_{fi}} T_{fi} + \frac{\Omega_i}{\mu_{fi}} T_{ci} \\ \frac{dT_{ci}}{dt} = \frac{(1-f_f) P_{i0}}{\mu_{ci}} N_i + \frac{\Omega_i}{\mu_{fi}} T_{fi} - \frac{\Omega_i + 2M_i}{\mu_{ci}} T_{ci} + \frac{2M_i}{\mu_{ci}} T_{ci,in} \end{cases} \tag{6.2}$$

Xenon-iodine dynamics:

$$\begin{cases} \frac{dI_i}{dt} = \lambda_I (N_i - I_i) \\ \frac{dX_i}{dt} = \frac{\lambda_X + \sigma_{a,i}^X \phi_{i0}}{\gamma_I + \gamma_X} (\gamma_X N_i + \gamma_I I_i) - (\lambda_X + \sigma_{a,i}^X \phi_{i0}) X_i \end{cases} \tag{6.3}$$

Reactivity feedbacks due to fuel and coolant temperature variations:

$$\rho_i = \rho_{ri} + \alpha_{fi}(T_{fi} - T_{fi,0}) + \alpha_{ci}(T_{ci} - T_{ci,0}) + \alpha_{Xi}(X_i - X_{i,0}) \tag{6.4}$$

where subscript i has been used to denote the i-th node, and n is the number of axial nodes in the reactor core. Other variables are described in the Nomenclature section.

6.2.2 *Pressurizer model*

The water level in the pressurizer should be above a threshold to make sure that the electrical heating plates are always submerged during any system transients. The steam pressure in the pressurizer determines the system pressure on the primary side, and is another key variable in the operation of PWRs to maintain the primary side pressure at a fixed value. A two-regions/three-volumes pressurizer model is proposed based on the three fixed control volumes denoted by 1, 2 and 3 (Wan et al. 2015). A schematic diagram of the pressurizer and the three control volumes is shown in Fig. 6.2.

The fundamental one dimensional, mass and energy conservation equations can be expressed as:

$$\frac{\partial \rho}{\partial t} + \frac{1}{A} \frac{\partial W}{\partial z} = 0 \tag{6.5}$$

$$\frac{\partial \rho h}{\partial t} + \frac{1}{A} \frac{\partial W h}{\partial z} = \frac{\partial P}{\partial t} + \frac{qU}{A} \tag{6.6}$$

Integrating Eqs. (6.5) and (6.6) over a fixed boundary control volume shown in Fig. 6.3, yields:

$$V \frac{d\bar{\rho}}{dt} = W_{in} - W_{out} \tag{6.7}$$

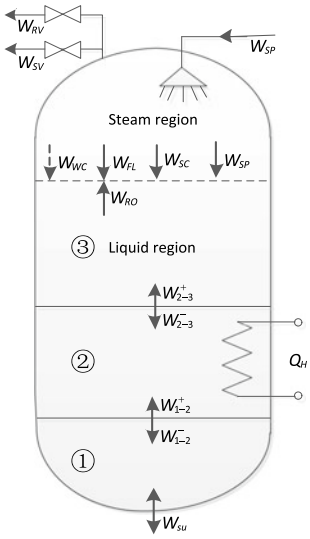

Fig. 6.2 Schematic diagram of the two-regions/three-volumes pressurizer model (Wan et al. 2015)

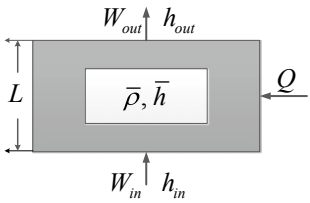

Fig. 6.3 Schematic diagram of a control volume

$$V\frac{d\bar{\rho}\bar{h}}{dt} = W_{in}h_{in} - W_{out}h_{out} + V\frac{dP}{dt} + Q \tag{6.8}$$

where, $\bar{\rho}$ and V are the average density and volume of the fluid in the control volume respectively, W_{in} and W_{out} are the inlet and outlet flowrate of the fluid, h_{in}, h_{out} and $\bar{h}$ are the inlet, outlet and average fluid enthalpy in the control volume respectively, P is the fluid pressure in the control volume, and Q is the heat transfer between the control volume and external environment.

Volumes 1 and 2 in the pressurizer are filled with liquid. The third control volume is divided into two regions—one for steam and one for liquid—with a moving boundary between them. The pressurizer model is based on the following assumptions: (1) pressure inside the pressurizer is uniform; (2) the thermodynamic parameters inside a region are uniform; (3) flashing and condensation occurs only at saturation conditions. The dynamic characteristics of the pressurizer can be described by the mass and energy balance equations for the three control volumes:

$$V_1\frac{d\rho_1}{dt} = W_{su} - W_{1-2} \tag{6.9}$$

$$V_2 \frac{d\rho_2}{dt} = -W_{2-3} + W_{1-2} \tag{6.10}$$

$$\frac{d(V_{3L}\rho_{3L})}{dt} = W_{RO} - W_{FL} + W_{SC} + W_{WC} + W_{SP} + W_{2-3} \tag{6.11}$$

$$\frac{d(V_{3V}\rho_{3V})}{dt} = W_{FL} - W_{RO} - W_{SC} - W_{WC} - W_{SV} - W_{RV} \tag{6.12}$$

$$V_1 \frac{d(\rho_1 h_1)}{dt} = W_{su} h_{su} - W_{1-2} h_{1-2} + V_1 \frac{dP}{dt} \tag{6.13}$$

$$V_2 \frac{d(\rho_2 h_2)}{dt} = -W_{2-3} h_{2-3} + W_{1-2} h_{1-2} + V_2 \frac{dP}{dt} + Q_h \tag{6.14}$$

$$\frac{d(V_{3L}\rho_{3L}h_{3L})}{dt} = W_{RO} h_f - W_{FL} h_g + (W_{SC} + W_{WC}) h_g + W_{SP} h_{SP} + W_{2-3} h_{2-3} + V_{3L} \frac{dP}{dt} \tag{6.15}$$

$$\frac{d(V_{3V}\rho_{3L}h_{3V})}{dt} = W_{FL} h_g - W_{RO} h_f - (W_{SC} + W_{WC}) h_g - (W_{SV} + W_{RV}) h_{3V} + V_{3V} \frac{dP}{dt} \tag{6.16}$$

where $h_{su} = h_{hot}$, $h_{1-2} = h_1$, $h_{2-3} = h_2$ for positive fluctuation and $h_{su} = h_1$, $h_{1-2} = h_2$, $h_{2-3} = h_3$ for negative fluctuation. Other variables are described in the *Nomenclature* section.

Flashing occurs when saturation conditions are reached in the liquid region of volume 3 during the depressurization with $h_{3L} = h_f$ and

$$\frac{dh_{3L}}{dt} = \frac{\partial h_f}{\partial P} \frac{dP}{dt} \tag{6.17}$$

Similarly, condensation occurs in the steam region of volume 3 under saturation condition with $h_{3V} = h_g$ and

$$\frac{dh_{3V}}{dt} = \frac{\partial h_g}{\partial P} \frac{dP}{dt} \tag{6.18}$$

W_{FL} and W_{RO} as unknown variables under saturation conditions are obtained by substituting Eq. (6.17) or Eq. (6.18) into the energy balance equations, respectively. W_{FL} and W_{RO} are equal to zero under subcooled and superheated conditions, respectively.

6.2.3 Steam Generator Model

The UTSG is the major equipment in which thermal energy generated in the core is removed from the primary coolant and transferred to the secondary side circulating water. High pressure steam is generated for steam turbines enabling them to convert

thermal energy to mechanical energy, which is then converted to electricity. The water in the secondary side of UTSG must be maintained at the desired level to ensure adequate heat transfer from the primary coolant to the secondary system and for satisfactory operation of steam-drying equipment. A schematic diagram of a UTSG is shown in Fig. 6.4. The heat transfer mechanism between the tube wall and

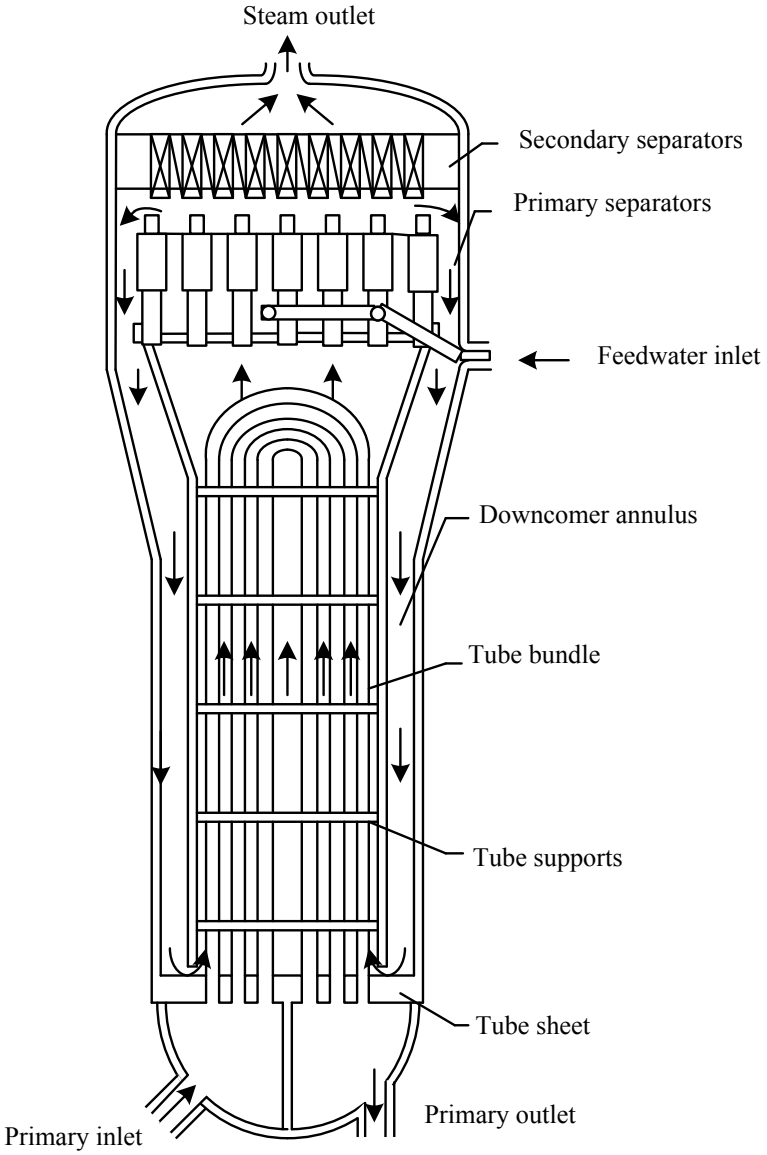

Fig. 6.4 Schematic view of the UTSG (Westinghouse Electric Company 2009)

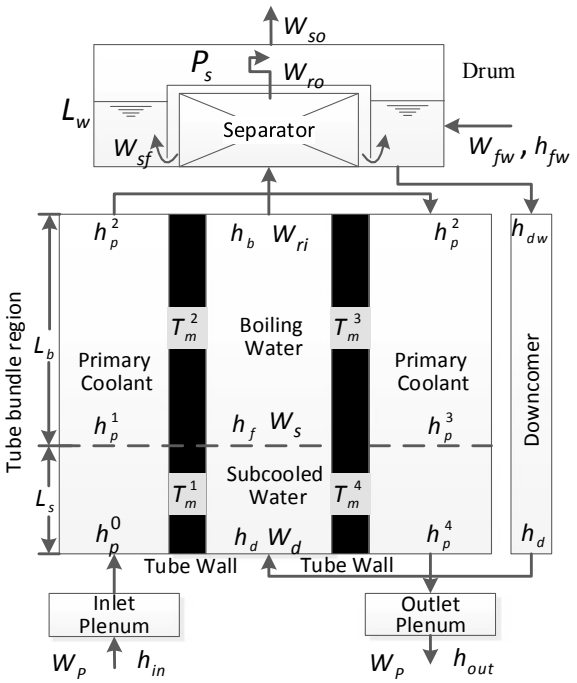

Fig. 6.5 Schematic diagram of the UTSG sections (Wan et al. 2015)

the secondary fluid varies along the tube length due to the changing temperature along the tube's axial direction. Hence, the tube bundle part of the UTSG is divided into a subcooled heat transfer section and a boiling heat transfer section, with a dynamic boundary between the two sections. This results in four primary fluid sections and four tube metal sections in the tube bundle region, as shown in Fig. 6.5. The length of the subcooled section is determined by the amount of thermal energy necessary to raise the fluid temperature of the secondary fluid from T_d to T_{sat}. Moreover, the inlet and outlet plena of the primary coolant, the downcomer, and the equivalent drum divided into the riser/separator volume, drum water volume and drum steam volume above the tube bundle also need to be modeled (Wan et al. 2015).

Following assumptions are made in developing the UTSG model:

(1) Both primary and secondary fluids are treated as one-dimensional flow;
(2) No heat transfer takes place between the tube bundle region and the downcomer;
(3) The axial conductive heat transfer for the U-type tube and fluids is negligible.

To develop a dynamic model with moving boundaries for the SG, the fundamental one dimensional mass and energy conservation equations are integrated using Leibniz rule within a control volume, shown in Fig. 6.2.

Recall the Leibniz rule for integration over domain with time-dependent boundaries is:

$$\int_{L_i(t)}^{L_{i+1}(t)} \frac{\partial F(z,t)}{\partial t} dz = \frac{d}{dt} \int_{L_i(t)}^{L_{i+1}(t)} F(z,t) dz - F(L_{i+1},t) \frac{dL_{i+1}}{dt} + F(L_i,t) \frac{dL_i}{dt} \tag{6.19}$$

Therefore,

$$\frac{d(\bar{\rho} L)}{dt} - \rho_{out} \frac{dz_{out}}{dt} + \rho_{in} \frac{dz_{in}}{dt} = \frac{(W_{in} - W_{out})}{A} \tag{6.20}$$

$$\frac{d(\bar{\rho} \bar{h} L)}{dt} - \rho_{out} h_{out} \frac{dz_{out}}{dt} + \rho_{in} h_{in} \frac{dz_{in}}{dt} - L \frac{dP}{dt} = \frac{W_{in} h_{in} - W_{out} h_{out} + Q}{A} \tag{6.21}$$

Moreover, for incompressible fluid, mass conservation equation can be rewritten as $W_{in} = W_{out}$. Omitting the term LdP/dt in Eq. (6.21), the lumped energy conservation equation can be obtained as

$$\frac{L}{2} \left(\frac{dh_{in}}{dt} + \frac{dh_{out}}{dt} \right) + \frac{h_{in} - h_{out}}{2} \left(\frac{dz_{out}}{dt} + \frac{dz_{in}}{dt} \right) = \frac{W_{in}(h_{in} - h_{out}) + Q}{A \bar{\rho}} \tag{6.22}$$

where P and Q respectively denote the pressure and heat transfer from the fluid to the tube wall, and other variables are described in the *Nomenclature* section.

Primary Side. Only two levels of headings should be numbered. Lower level headings remain unnumbered; they are formatted as run-in headings.

Applying Leibniz rule (Eq. 6.19) to the four primary fluid sections in the primary heat exchange region yields the following lumped equations:

$$\frac{L_i}{2} \left(\frac{dh_p^{i-1}}{dt} + \frac{dh_p^i}{dt} \right) + f_i \frac{(h_p^{i-1} - h_p^i)}{2} \frac{dL_s}{dt} = \frac{W_p (h_p^{i-1} - h_p^i) + Q_p^i}{A_p \rho_p^i}, \quad i = 1, 2, 3, 4 \tag{6.23}$$

where

$$L_1 = L_4 = L_s, L_2 = L_3 = L_b, f_1 = f_2 = 1, f_3 = f_4 = -1 \tag{6.24}$$

and W_p and A_p denote the coolant mass flow rate and the flow area of primary loop. Other variables are described in the *Nomenclature* section.

Secondary Side. Similarly, the energy balance equation for the subcooled section on the secondary side can be written as (Wan et al. 2015)

$$\frac{L_s}{2} \left(\frac{dh_d}{dt} + \frac{\partial h_f}{\partial P_s} \frac{dP_{sg}}{dt} \right) + \frac{(h_d - h_f)}{2} \frac{dL_s}{dt} = \frac{W_d (h_d - h_f) + Q_s^1 + Q_s^4}{A_s \rho_s} \tag{6.25}$$

Applying Eqs. (6.20) and (6.21) to the saturated boiling section on the secondary side yields the following lumped equations (Wan et al. 2015):

$$\frac{d(\rho_b L_b)}{dt} + \rho_f \frac{dL_s}{dt} = \frac{W_d - W_{sep}}{A_s} \tag{6.26}$$

$$\frac{d(\rho_b h_b L_b)}{dt} + \rho_f h_f \frac{dL_s}{dt} - L_b \frac{dP_{sg}}{dt} = \frac{W_d h_f - W_{si} h_{si} + Q_s^2 + Q_s^3}{A_s} \tag{6.27}$$

The secondary fluid in the saturated boiling section is considered to be a homogeneous steam-water mixture with an average quality x_b, density ρ_b and enthalpy h_b expressed as

$$x_b = \frac{x_e}{2},\ \rho_b = \frac{1}{v_f + x_b v_{fg}},\ h_b = h_f + x_b h_{fg} \tag{6.28}$$

Substituting Eq. (6.28) in Eqs. (6.26) and (6.27), and defining

$$k_2 = x_b \frac{\partial v_{fg}}{\partial P_{sg}} + \frac{\partial v_f}{\partial P_{sg}},\ k_3 = \left(\frac{\partial h_f}{\partial P_{sg}} + x_b \frac{\partial h_{fg}}{\partial P_{sg}}\right) \tag{6.29}$$

the lumped mass and energy conservation equations for the boiling section on the secondary side are obtained

$$\frac{(\rho_b - \rho_f)}{L_b} \frac{dL_s}{dt} + \frac{\rho_b^2 v_{fg}}{2} \frac{dx_e}{dt} + \rho_b^2 k_2 \frac{dP_{sg}}{dt} = \frac{W_{sep} - W_d}{A_s L_b} \tag{6.30}$$

$$\frac{(\rho_f h_f - \rho_b h_b)}{L_b} \frac{dL_s}{dt} + (\rho_b k_3 - h_b \rho_b^2 k_2 - 1) \frac{dP_{sg}}{dt} + \frac{(\rho_b h_{fg} - h_b \rho_b^2 v_{fg})}{2} \frac{dx_e}{dt} = \frac{Q_s^2 + Q_s^3 + W_d h_f - W_{si} h_{si}}{A_s L_b} \tag{6.31}$$

where $v_{fg} = v_g - v_f$, and Q_s^i $(i = 1, 2, 3, 4)$ denotes the heat transfer rate between the ith node in the tube and the secondary coolant.

Metal Tube. The energy balance equation (conduction only) for the metal tube can be written as:

$$\rho_m C_{pm} A_m \frac{\partial T_m}{\partial t} = \dot{q}_p - \dot{q}_s \tag{6.32}$$

After applying Leibniz rule, the above equation can be written for the four tube metal sections as

$$L_i \frac{dT_m^i}{dt} + g_i \frac{dL_s}{dt} = \frac{Q_p^i - Q_s^i}{A_m C_{pm} \rho_m},\ g_1 = g_2 = \frac{T_m^1 - T_m^2}{2},\ g_3 = g_4 = \frac{T_m^4 - T_m^1}{2},\ i = 1, 2, 3, 4 \tag{6.33}$$

where T_m^i $(i = 1, 2, 3, 4)$ denotes the average temperature in the i-th tube metal node, and ρ_m and C_{pm} respectively denote the density and specific heat capacity of the tube material.

Drum. The dynamics of the drum, where the feedwater mixes with the saturated water recirculated from the separators, is governed by the mass and energy conservation equations (Wan et al. 2015):

$$A_{dw}\rho_{dw}\frac{dL_{dw}}{dt} = (1 - x_e)W_{ro} + W_{fw} - W_d \tag{6.34}$$

$$A_{dw}\rho_{dw}(L_{dw}\frac{dh_{dw}}{dt} + h_{dw}\frac{dL_{dw}}{dt}) = (1 - x_e)W_{ro}h_g + W_{fw}h_{fw} - W_d h_{dw} \tag{6.35}$$

The riser/separator volume and volume of the steam in the drum can be modeled using mass balances

$$\frac{d(V_r\rho_r)}{dt} = W_{ri} - W_{ro} \tag{6.36}$$

$$\frac{d(V_{ds}\rho_g)}{dt} = x_e W_{ro} - W_g \tag{6.37}$$

Substituting the steam volume in the drum

$$V_{ds} = V_{dr} - A_{dw}L_{dw} \tag{6.38}$$

into Eq. (6.36) and the fluid density in the riser/separator volume

$$\rho_r = \frac{1}{v_f + x_e v_{fg}} \tag{6.39}$$

into Eq. (6.37), we have:

$$-\rho_g A_{dw}\frac{dL_{dw}}{dt} + V_{ds}\frac{\partial\rho_g}{\partial P_{sg}}\frac{dP_{sg}}{dt} = x_e W_{ro} - W_{so} \tag{6.40}$$

$$-V_r\rho_r^2(v_{fg}\frac{dx_e}{dt} + x_e\frac{\partial v_{fg}}{\partial P_{sg}}\frac{dP_{sg}}{dt}) = W_{ri} - W_{ro} \tag{6.41}$$

Downcomer, plenum and recirculation flow. Assuming that the coolants in the inlet plenum, outlet plenum and downcomer are adiabatic and well mixed, energy balance equations are given by

$$M_{ip}\frac{dh_p^0}{dt} = W_p(h_{in} - h_p^0) \tag{6.42}$$

$$M_{op}\frac{dh_{out}}{dt} = W_p(h_p^4 - h_{out}) \tag{6.43}$$

$$M_d\frac{dh_d}{dt} = W_d(h_{dw} - h_d) \tag{6.44}$$

where M_{ip}, M_{op} and M_d denote the coolant mass in the inlet plenum, outlet plenum and downcomer, respectively.

Integrating the momentum conservation equation along the secondary recirculation loop, we obtain

$$\frac{dW_s}{dt}\oint\frac{dz}{dA} = -\oint\rho g dz - \Delta P_f - \Delta P_{loc} \tag{6.45}$$

where ΔP_f and ΔP_{loc} denote the frictional pressure loss and local pressure loss, respectively.

Main feedwater flow. The feedwater flow rate is determined by the main control valve position. Integrating the momentum conservation equation from the deaerator to the steam generator, we obtain:

$$\begin{aligned}\frac{dW_{fi}}{dt}\oint\frac{dz}{A_f} &= \left(P_{dea} + \Delta P_{mfp} - P_{sg}\right) - \rho_{mfw}g\Delta H_{mds} - \frac{1}{2}\rho_{mfw}\left(v_{sg}^2 - v_{dea}^2\right) - \Delta P_{mfrv} \\ &\quad - \Delta P_{mfiv} - \Delta P_{mfcv} - \left(\frac{k_{hph}}{2\rho_{mfw}A_{hph}^2} + \frac{1}{2\rho_{mfw}}\oint\frac{f_{mfw}}{A_{mfw}^2 D_{mfw}}dz\right)|W_{fi}|W_{fi}\end{aligned} \tag{6.46}$$

where P_{dea} denotes the deaerator pressure, ΔP_{mfp} denotes the main feedwater pump head, ΔP_{mfrv}, ΔP_{mfiv} and ΔP_{mfcv} denote the pressure differences across the control valve, isolating valve and check valve in the main feedwater line, respectively.

6.2.4 Modified Reactor Core and UTSG Model

The core heat transfer model in the core model given in Sect. 6.2.1 is rather simplified and can be improved. Specifically, the heat conduction model in the fuel can be improved.

Reactor core. Wang et al. (2013) proposed a nodal core model which divides the reactor core into a number of nodes in the axial direction, and fuel pellet in the radial direction as shown in Fig. 6.6. Each node can be treated as a "small" reactor core, linked with other "cores" by coupling coefficients. They also investigated the optimal number of nodes in both axial direction and for fuel pellet in the radial direction. This modified nodal core model of the AP1000 reactor including the neutron kinetics, thermal–hydraulics and xenon iodine dynamics can be written as:

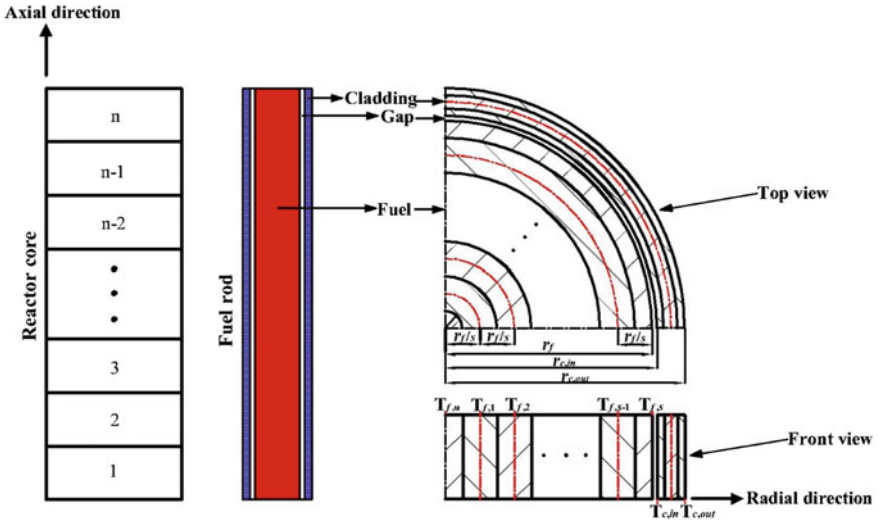

Fig. 6.6 Division of the active region of the AP1000 reactor core (Wang et al. 2013)

Point kinetics equations with six-group delayed neutrons:

$$\begin{cases} \frac{dN_i}{dt} = w_{i,i-1}N_{i-1} + w_{i,i+1}N_{i+1} + \sum_{k=1}^{6} \frac{\beta_k}{\Lambda_i} D_{k,i} + \frac{N_i}{\Lambda_i}(\rho_i - \beta) - N_i w_{ii},\ i = 1, 2, \ldots, n \\ \frac{dD_{k,i}}{dt} = \lambda_k (N_i - D_{k,i}),\ k = 1, 2, \ldots, 6 \end{cases} \tag{6.47}$$

Core-fuel-to-coolant heat transfer equations:

$$\begin{cases} \frac{dT_{fi,u}}{dt} = \frac{4s^2\lambda_{fi}}{\rho_{fi}C_{fi}r_f^2}(T_{fi,1} - T_{fi,u}) + \frac{F_q f_f P_{i0} N_i}{\rho_{fi}C_{fi}N_R \pi r_f^2 \Delta H_i} \\ \frac{dT_{fi,j}}{dt} = \frac{s^2\lambda_{fi}}{\rho_{fi}C_{fi}r_f^2}[(1+\frac{1}{2j})T_{fi,j+1} - 2T_{fi,j} + (1-\frac{1}{2j})T_{fi,j-1}) + \frac{F_q f_f P_{i0} N_i}{\rho_{fi}C_{fi}N_R \pi r_f^2 \Delta H_i},\ j = 1,2,...,s-1 \\ \frac{dT_{fi,s}}{dt} = \frac{s(2s-1)\lambda_{fi}}{\rho_{fi}C_{fi}r_f^2}(T_{fi,s-1} - T_{fi,s}) + \frac{sh_{fc,i}(r_f + r_{c,in})}{\rho_{fi}C_{fi}r_f^2}(T_{c,in} - T_{fi,s}) + \frac{F_q f_f P_{i0} N_i}{\rho_{fi}C_{fi}N_R \pi r_f^2 \Delta H_i} \\ \frac{dT_{ci,n}}{dt} = \frac{2h_{fc,i}(r_f + r_{c,in})}{r_{c,in}(r_{c,out} - r_{c,in})\rho_{ci}C_{ci}}(T_{fi,s} - T_{ci,in}) + \frac{2\lambda_{c,i}(r_{c,out} + 3r_{c,in})}{r_{c,in}(r_{c,out} - r_{c,in})^2 \rho_{ci}C_{ci}}(T_{ci,cen} - T_{ci,in}) \\ \frac{dT_{ci,cen}}{dt} = \frac{2\lambda_{c,i}(r_{c,out} + 3r_{c,in})}{(r_{c,out} + r_{c,in})(r_{c,out} - r_{c,in})^2 \rho_{ci}C_{ci}}(T_{ci,in} - T_{ci,cen}) + \frac{2\lambda_{c,i}(3r_{c,out} + r_{c,in})}{(r_{c,out} + r_{c,in})(r_{c,out} - r_{c,in})^2 \rho_{ci}C_{ci}}(T_{ci,out} - T_{ci,cen}) \\ \frac{dT_{ci,out}}{dt} = \frac{2\lambda_{c,i}(3r_{c,out} + r_{c,in})}{r_{c,out}(r_{c,out} - r_{c,in})^2 \rho_{ci}C_{ci}}(T_{ci,cen} - T_{ci,out}) - \frac{4h_{cn,i}}{(r_{c,out} - r_{c,in})\rho_{ci}C_{ci}}(T_{ci,out} - T_{mi}) \\ \frac{dT_{mi}}{dt} = \frac{(1-f_f)P_{i0}}{\mu_{mi}}N_i + \frac{2\pi r_{cq}\Delta H_i h_{cm,i}}{\mu_{mi}}T_{ci,out} - (\frac{2\pi r_{cq}\Delta H_i h_{cm,i} + 2M_i}{\mu_{mi}})T_{mi} + \frac{2M_i}{\mu_{mi}}T_{mi,in} \end{cases} \tag{6.48}$$

Xenon-iodine dynamics:

$$\begin{cases} \frac{dI_i}{dt} = \lambda_I (N_i - I_i) \\ \frac{dX_i}{dt} = \frac{\lambda_X + \sigma_{ai}^X \phi_{i0}}{\gamma_I + \gamma_X} (\gamma_X N_i - \gamma_I I_i) - (\lambda_X + \sigma_{ai}^X \phi_{i0} N_i) X_i \end{cases} \tag{6.49}$$

Reactivity feedbacks due to fuel and coolant temperature variations:

$$\rho_i = \rho_{ri} + \alpha_{fi}(T_{fi} - T_{fi,0}) + \alpha_{mi}(T_{mi} - T_{mi,0}) + \alpha_{Xi}(X_i - X_{i0}) + \rho_{i0} \tag{6.50}$$

where subscript i has been used to denote the i-th node, n is the number of nodes in the axial direction, and other variables are described in the *Nomenclature* section. For the hot channel of the AP1000 reactor, the F_q in the 18 months equilibrium cycle is taken as 1.75 with all the uncertainties taken into consideration. w_{ii} can be considered as the coupling coefficient of the i-th axial node to itself, $w_{i,i+1}$ and $w_{i,i-1}$ are the coupling coefficients between the i-th axial node and its adjacent nodes. For the node at the top of the reactor core, $w_{i,i+1} = 0$, and for that at the bottom, $w_{i,i-1} = 0$. The coupling coefficient between a node and a nonadjacent node is assumed to be zero.

To determine the number of nodes along the core axial direction and the number of nodes in the fuel pellet in the radial direction that balance the need for satisfactory accuracy and fast computational speed, three suitable performance indices–mean square error (MSE), maximum absolute error (MAE), and total training time (TRT)—were used (Wang et al. 2013).

UTSG. Although, the UTSG model given in the previous section is suitable for the UTSG water level controller design for AP1000, some simplifications in it for the secondary side and for the tube model can be relaxed, thus making it more accurate. Improved models for the UTSG are given by Wan et al. (2017). The following assumptions are made in the development of this model:

(1) flow in both primary and secondary sides is assumed to be one-dimensional. Conduction in the axial direction in the U-tube is ignored. Axial conductive heat transfer for the U-type tube and fluids is negligible;
(2) the primary side coolant is considered to be incompressible;
(3) the secondary fluid properties are evaluated at a reference pressure;
(4) steam leaving the steam generator is assumed to be saturated;
(5) no heat transfer takes place between the secondary tube bundle region and down comer;
(6) the heat capacity in the steam generator except that of the U-tubes is ignored;
(7) linear profiles for volume weighted specific volume and specific enthalpy are used on the secondary side of the tube bundle region.

Subcooled region. The subcooled heat transfer region on the secondary side is treated as compressible fluid in this modified model. Integrating Eqs. (6.5) and (6.6) along the z-axis yields the following equations,

$$A_s \frac{d}{dt} \int_0^{L_s} \rho_s(z) dz - \rho_f A_s \frac{dL_s}{dt} = W_d - W_s \tag{6.51}$$

$$A_s \frac{d}{dt} \int_0^{L_s} \rho_s(z) h_s(z) dz - A_s \rho_f h_f \frac{dL_s}{dt} - A_s L_s \frac{dP_s}{dt} = W_d h_d - W_s h_f + \dot{Q}_{s1} + \dot{Q}_{s4} \tag{6.52}$$

The specific volume and specific enthalpy in the subcooled region are assumed to vary linearly, and therefore can be expressed as

$$\frac{1}{\rho_s(z)} = \left(\frac{1}{\rho_f} - \frac{1}{\rho_d}\right) \frac{z}{L_s} + \frac{1}{\rho_d} \qquad 0 < z < L_s \tag{6.53}$$

$$h_s(z) = \left(h_f - h_d\right) \frac{z}{L_s} + h_d \qquad 0 < z < L_s \tag{6.54}$$

The mass and enthalpy in the subcooled region can then be written as

$$m_s = A_s \int_0^{L_s} \rho_s(z) dz = \frac{A_s L_s \rho_d \rho_f}{\rho_d - \rho_f} \ln \frac{\rho_d}{\rho_f} \tag{6.55}$$

$$H_s = A_s \int_0^{L_s} \rho_s(z) h_s(z) dz = m_s \left[\frac{h_f - h_d}{\ln(\rho_d / \rho_f)} + \frac{\rho_d h_d - \rho_f h_f}{\rho_d - \rho_f} \right] \tag{6.56}$$

both m_s and H_s depend only on the values of the length of the subcooled region and fluid properties at the inlet and outlet, which can be uniquely determined with the state variables: the secondary side system pressure, P_s; the subcooled liquid inlet specific enthalpy, h_d; and the length of the subcooled region L_s. Substituting the time derivatives of m_s and H_s in Eqs. (6.51) and (6.52) and applying the chain rule, the resulting mass balance and energy balance equations for the secondary subcooled heat transfer region can be obtained

$$\frac{\partial m_s}{\partial h_d} \frac{dh_d}{dt} + \left(\frac{m_s}{L_s} - A_s \rho_f\right) \frac{dL_s}{dt} + \frac{\partial m_s}{\partial P_s} \frac{dP_s}{dt} = W_d - W_s \tag{6.57}$$

$$\frac{\partial H_s}{\partial h_d} \frac{dh_d}{dt} + \left(\frac{H_s}{L_s} - A_s \rho_f h_f\right) \frac{dL_s}{dt} + \left(\frac{\partial H_s}{\partial P_s} - A_s L_s\right) \frac{dP_s}{dt} = W_d h_d - W_s h_f + \dot{Q}_{s1} + \dot{Q}_{s4} \tag{6.58}$$

Boiling region. Unlike the former model in Sect. 6.2.3.2 given by Eqs. (6.30) and (6.31), in which the density and enthalpy values at the exit of the volumetric region were used as the average value over the entire volume, the mean density and specific enthalpy at the outlet of secondary tube bundle are now calculated as the volume weighted average, similar to the approach used for the subcooled region,

$$\bar{\rho}_b = (1 - \alpha_b) \rho_f + \alpha_b \rho_g \tag{6.59}$$

$$\bar{h}_b = \left[(1 - \alpha_b) \rho_f h_f + \alpha_b \rho_g h_g\right] / \bar{\rho}_b \tag{6.60}$$

Assuming linear distributions of volume weighted specific volume and volume weighted specific enthalpy, the mean density and mean specific enthalpy of two phase mixture can be expressed as

$$\frac{1}{\bar{\rho}_s(z)} = \left(\frac{1}{\bar{\rho}_b} - \frac{1}{\rho_f}\right)\frac{z - L_s}{L_b} + \frac{1}{\rho_f} \qquad L_s < z < L_s + L_b \tag{6.61}$$

$$\bar{h}_s(z) = \left(\bar{h}_b - h_f\right)\frac{z - L_s}{L_b} + h_f \qquad L_s < z < L_s + L_b \tag{6.62}$$

The total mass and enthalpy in the two-phase region are given by

$$m_b = A_b \int_{L_s}^{L_s+L_b} \bar{\rho}_s(z)dz = \frac{A_b L_b \rho_f \bar{\rho}_b}{\rho_f - \bar{\rho}_b} \ln\frac{\rho_f}{\bar{\rho}_b} \tag{6.63}$$

$$H_b = A_b \int_{L_s}^{L_s+L_b} \bar{\rho}_s(z)\bar{h}_s(z)dz = m_b\left[\frac{\bar{h}_b - h_f}{\ln(\rho_f / \bar{\rho}_b)} + \frac{\rho_f h_f - \bar{\rho}_b \bar{h}_b}{\rho_f - \bar{\rho}_b}\right] \tag{6.64}$$

Integrating Eqs. (6.5) and (6.6) along the z-axis and substituting the total time derivatives of m_b and H_b, the final mass and energy balance equations for the saturated boiling heat transfer region on the secondary side can be obtained:

$$\frac{\partial m_b}{\partial \alpha_b}\frac{d\alpha_b}{dt} - \left(\frac{m_b}{L_b} - A_b\rho_f\right)\frac{dL_s}{dt} + \frac{\partial m_b}{\partial P_s}\frac{dP_s}{dt} = W_s - W_{ri} \tag{6.65}$$

$$\frac{\partial H_b}{\partial \alpha_b}\frac{d\alpha_b}{dt} - \left(\frac{H_b}{L_b} - A_b\rho_f h_f\right)\frac{dL_s}{dt} + \left(\frac{\partial H_b}{\partial P_s} - A_b L_b\right)\frac{dP_s}{dt} = W_s h_f - W_{ri} h_b + \dot{Q}_{s2} + \dot{Q}_{s3} \tag{6.66}$$

The specific enthalpy at the outlet of the two-phase fluid region, h_b, can be written as:

$$h_b = (1 - x_b)h_f + x_b h_g \tag{6.67}$$

where the flow quality x_b is calculated using the Bankoff-Jens correlation (Li and Zhang 2010).

Tube-wall metal. Wall temperatures at the interfaces between two nodes in the tube-wall metal are calculated using the following weighted mean equations

$$g_1 = g_2 = \frac{1}{L_b + L_s}(L_b T_{m1} + L_s T_{m2}) \tag{6.68}$$

$$g_3 = g_4 = \frac{1}{L_b + L_s}(L_s T_{m4} + L_b T_{m4}) \tag{6.69}$$

6.3 Control System Design

The function of the AP1000 control systems is to establish and maintain the plant operating conditions within prescribed limits. Control of the AP1000 is divided up into sub control systems. The reactor coolant temperature, and power level and distribution are regulated by *reactor power control system*. The reactor coolant system pressure and pressurizer water level are maintained by *pressurizer control system*. The steam generator water level is regulated by *feedwater control system*. These sub control systems are briefly described here.

6.3.1 Reactor Power Control System

Two control modes of GEN-II PWRs, the Mode A and Mode G, lead to strong coupling between reactor power level control and axial offset control and depend largely on soluble boron concentration. They also rely on manual regulation under full load operation. Thus these control modes reduce possibilities of automation in GEN-II PWRs. An advanced control strategy is developed for AP1000 to give it more flexibility and load following capability. Note that three quantities that need to be controlled are reactor power level, core exit average temperature, and core axial offset. The control strategy, named MSHIM, employs separate, independent control rod banks M-bank and AO-bank for respectively controlling T_{avg} (core exit) and axial offset within corresponding deadbands. Most importantly, the control system satisfies most of the control demands automatically, without human intervention. Thus, this novel control method enhances the PWRs' load following capability, flexibility and safety.

AP1000 reactor core and MSHIM control strategy. The AP1000 reactor core has a matrix of 157 fuel assemblies, along with various control and structural elements. These fuel assemblies consist of 264 fuel rods in a 17 $\times$ 17 square array with an active fuel stack length of 14 feet (426.7 cm) (Fetterman 2009). The 69 Rod Cluster Control Assemblies (RCCA) are divided into two categories: 37 of them for control, and other 32 assemblies for shutdown. The control group consists of 16 Gray RCCAs in the MA through MD-banks, 12 Black RCCAs in the M1 and M2-banks, and 9 Black RCCAs in the AO-bank. The shutdown group has 32 Black RCCAs in the S1 through S4-Banks. The distribution of RCCAs in the reactor core is depicted in Fig. 6.7 (Drudy et al. 2009; Onoue et al. 2003). Only quarter of the core is shown here. The core RCCA distribution is symmetric.

The M-banks, consisting of MA through M2, are used to control the core reactivity or reactor core coolant average temperature. The AO bank is used to control the axial power distribution. It normally stays at the top of the core, with only a small part inserted. Due to its high worth, it is very effective in controlling the axial power distribution even by short movements. The M-banks move with a fixed overlap to minimize the impact on the axial offset while retaining the T_{avg} to meet the desired

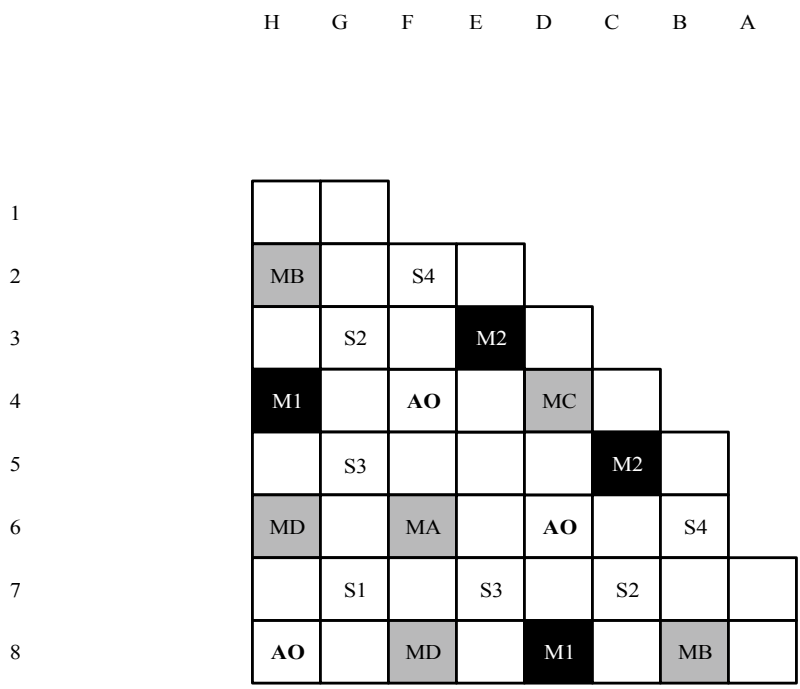

Bank ID	Group Association	Cluster Type	# of Clusters
MA	MSHIM Control	Gray	4
MB			4
MC			4
MD			4
M1		Black	4
M2			8
AO	Axial Offset Control		9
S1	Shutdown		8
S2			8
S3			8
S4			8

Fig. 6.7 AP1000 control rod configuration (Drudy et al. 2009)

load changes. These two control loops constitute the main feature of the MSHIM control strategy to achieve the two desired set points: power/T_{avg}; and axial offset. The M-banks in the control logic have priority over the AO-bank. That is AO-bank does not operate until the core power is within its dead-band or M-banks stop. This is achieved by the interlocking design, explained below, between the two banks.

The MSHIM control strategy is designed to provide extensive load following operational capability to AP1000 without the need to adjust the soluble boron concentrations during power regulation maneuvers (Drudy et al. 2009; Onoue et al. 2003). The MSHIM control strategy has the following advantages:

(1) The power reactivity compensation with grey rods, and less reliance on boron dilution allows fast load following;
(2) The axial power distribution is controlled automatically by the AO-bank, which can reduce the possibility of undesirable events caused by humans during reactor operation;
(3) During power regulations and other transient conditions, this control strategy can ensure that the power distribution is not distorted and there are no core hot spots, thus ensuring the safety of the fuel assembly.

The M-Banks are designed such that there is an overlap between them when they move. This is shown in Fig. 6.8. Movement of the M-banks is synchronized, driven by a single goal (criticality). The first two Banks, MA and MB, operate together with 100% overlap between them. MA+MB and MC operate with 10% core height overlap, and MC through M2 banks operate with an overlap of 33% core height. Besides, the similarity between the MA+MB-Bank and MC+MD-Bank provides the capability for the interchanging of these banks during operation. This option would mitigate burnup-shutdown effects due to long term insertion of the MA and MB-Banks. Interchanging also reduces the magnitude of the rod stepping duty on the same control rod drive mechanisms (Onoue et al. 2003). To keep the axial offset within a target band using only the AO-Bank (independent of the M-Bank), the AP1000 utilizes a Constant Axial Offset Control (CAOC) strategy (Morita 1974).

AP1000 reactor core control logic. Figure 6.9a and b show the schematic diagram of the M-banks and AO-bank control systems, respectively (Wang et al. 2014). Central to the MSHIM control strategy is the advanced dual-loop, digital rod control system, which incldues the T_{avg} controller and the AO controller that independently maintain the reactivity and axial offset. In the T_{avg} control system, the sum of the T_{avg} error (T_{err}) and the power error derivative (dP_{err}), with appropriate gains, is used as control signal to drive the M-banks automatically. This is shown in Fig. 6.9a (Wang et al. 2014).

The T_{err} is the difference between the measured T_{avg} and the reference temperature (T_{ref}). The T_{avg} signal passes a compensation circuit including the following components:

$$G_1 = \frac{1}{T_1 s + 1} \tag{6.70}$$

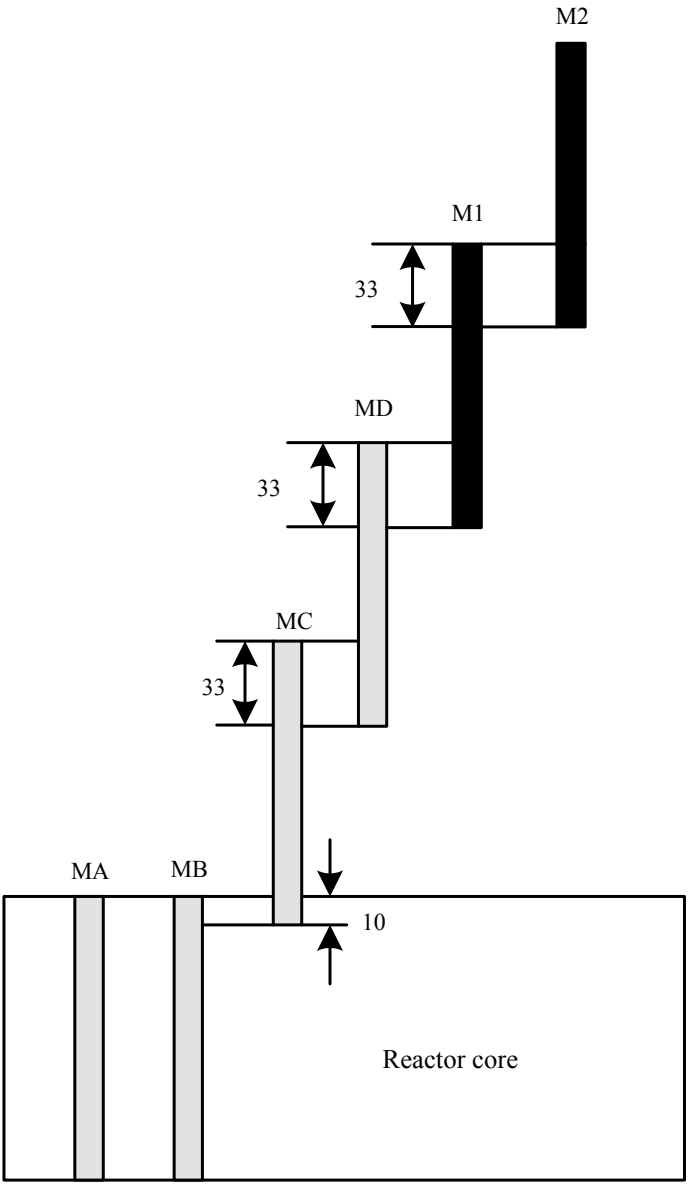

Fig. 6.8 AP1000 M-banks insertion sequence (Onoue et al. 2003)

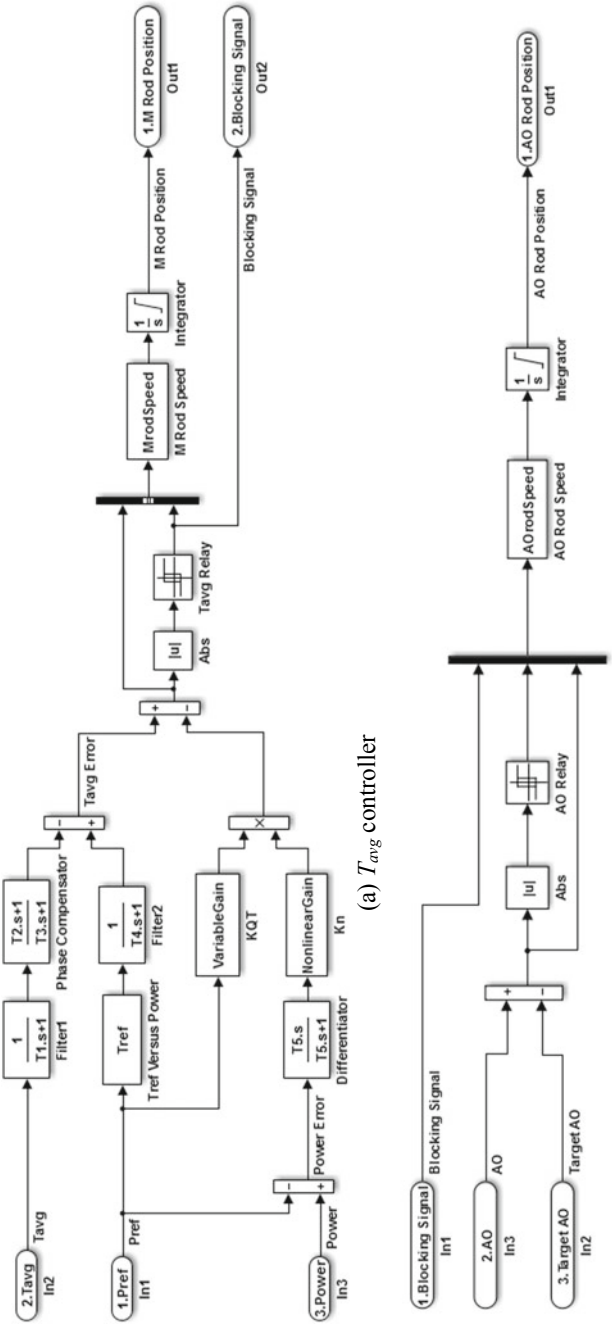

Fig. 6.9 Simulation platform of the MSHIM control strategy in MATLAB/SIMULINK (Wang et al. 2014)

$$G_2 = \frac{T_2 s + 1}{T_3 s + 1} \tag{6.71}$$

where T_1 is the lag time constant, T_2 and T_3 are the lead time constant and lag time constant, respectively, and T_2 is larger than T_3. The compensation circuit compensates for the delay of response caused by the heat capacity of the temperature sensor or of the coolant system and makes phase-advance compensation to improve control responses. The reference temperature T_{ref} is set as a function of the turbine load signal (P_{ref}), which can be expressed as follows:

$$T_{ref} = \begin{cases} 291.7 + 9.2\mathrm{P}_{ref}, & 0 \le \mathrm{P}_{ref} \le 1 \\ 300.9, & \mathrm{P}_{ref} > 1 \end{cases} \tag{6.72}$$

The corresponding T_{ref} is added to the control signal after a phase lag compensation as follows:

$$G_3 = \frac{1}{T_4 s + 1} \tag{6.73}$$

where T_4 is the lag time constant. The power error signal is added to the control signal through the differential circuit and the nonlinear gain. Then the power reference signal is multiplied with the above signal through the variable gain. The differential circuit includes the following component:

$$G_5 = \frac{T_5 s}{T_5 s + 1} \tag{6.74}$$

where T_5 is the derivative time constant. The variable gain K_{QT} and nonlinear gain K_n can be respectively expressed as follows (Wang et al. 2014):

$$K_{QT} = \begin{cases} 4, & 0 \le \mathrm{P}_{ref} < 0.25 \\ 1/\mathrm{P}_{ref}, & 0 \le \mathrm{P}_{ref} < 1 \\ 1, & \mathrm{P}_{ref} \ge 1 \end{cases} \tag{6.75}$$

$$K_n = \begin{cases} 0.17 d\,P_{err}, & -0.02 \le d\,P_{err} < 0.02 \\ 0.83 d\,P_{err}, & d\,P_{err} \le -0.02 \text{ or } d\,P_{err} > 0.02 \end{cases} \tag{6.76}$$

The rod speed of the M-banks varies over the range of 5–45 inches per minute (8–72 steps per minute) depending on the input signal level (Wang et al. 2014). This variable speed drive provides the ability to insert small amounts of reactivity at low speeds to give fine control of reactor coolant average temperature, as well as to control at high speeds to correct larger temperature transients (Wang et al. 2014).

The axial power distribution control is achieved by the AO control system working with the high worth AO-bank. The axial offset AO can be described using the parameters ΔI and I:

$$AO = \frac{\Delta I}{I} \tag{6.77}$$

where

$$\Delta I = P_T - P_B \tag{6.78}$$

$$I = P = P_T + P_B \tag{6.79}$$

where P_T and P_B are the power of the reactor's top half and bottom half, respectively. ΔI is the axial flux difference (AFD), the absolute difference between the power generated in the top and bottom halves of the reactor core. When AO value is not within the target band (a reference band defined around a set value), the AO-bank is inserted into or withdrawn from the core. When AO exceeds in the positive direction, the AO-bank is to be inserted into the core to move the power peak value toward the bottom, and vice versa. Since the AO-bank is of high worth, it moves with a fixed low speed of approximately 5 inches per minute (8 steps per minute). This minimizes the impact on the global power of the reactor. The control logic for the rod drive speed for the M and AO banks both have a dead zone to avoid continuous movement of the control rods under steady state conditions.

6.3.2 Pressurizer Control System

The pressurizer control system is designed to provide stable and accurate control of the RCS pressure, and to maintain it at its predetermined setpoint during the normal operation. Fine pressure control to the desired setpoint is accomplished by controlling a bank of proportional heaters and four banks of backup heaters as well as the pressurizer spray. The heaters are located in the bottom head of the pressurizer. The pressurizer spray is located in the top head of the pressurizer, and is used to condense steam. Illustrated in Fig. 6.10 is the schematic diagram of the pressure control system. The proportional-plus-integral (PI)-compensated deviation between the measured pressure and the target value is used to modulate the proportional heaters and the proportional spray. The proportional heater control is used to compensate "small" drops in the pressure. Drops in pressure larger than that lead to the actuation of the backup heaters to generate even more steam and thus increase the pressure. Pressure increases are controlled by actuating the pressurizer spray (Wan et al. 2015).

The pressurizer level control system maintains the water level in the pressurizer at its set point to prevent damage to the heaters. The schematic diagram of the pressurizer level control system is shown in Fig. 6.11 (Wan et al. 2015). Intermittent control of charging and letdown is achieved by setting a deadband around the programmed pressurizer level setpoint. When the pressurizer water level reaches the lower limit of the deadband the charging system will be actuated and continue to operate until the level returns to a limit above the nominal program value. The letdown to the

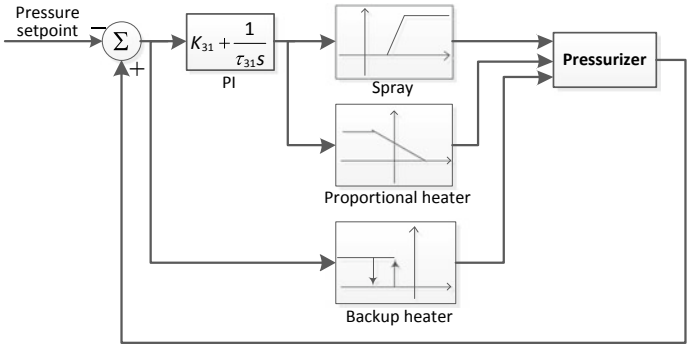

Fig. 6.10 Schematic diagram of pressurizer pressure control system (Wan et al. 2015)

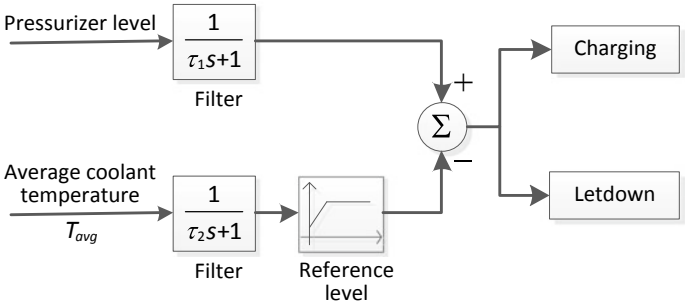

Fig. 6.11 Schematic diagram of pressurizer water level control system (Wan et al. 2015)

liquid waste processing system will be actuated to release excessive water when the water level reaches the upper limit of the deadband.

6.3.3 Main Feedwater Control System

The main feedwater control system maintains a prescribed water level in the shell side of the steam generator, and limits the water shrink and swell during normal plant operation (Wan et al. 2015). The main feedwater control system includes high power control mode and low power control mode, as demonstrated in Fig. 6.12 In the high power control mode, the feedwater flow is regulated by a three-element feedwater controller in response to: (1) changes in steam flow; and (2) deviation in the feedwater-temperature-compensated steam generator narrow-range water level from its setpoint. The three signals, water level error signal, the steam flow rate signal, and the feedwater flow rate signal, determine the valve position. In the low-power control mode, the feedwater flow is regulated in response to changes in steam generator wide-range water level and PI-compensated steam generator narrow-range

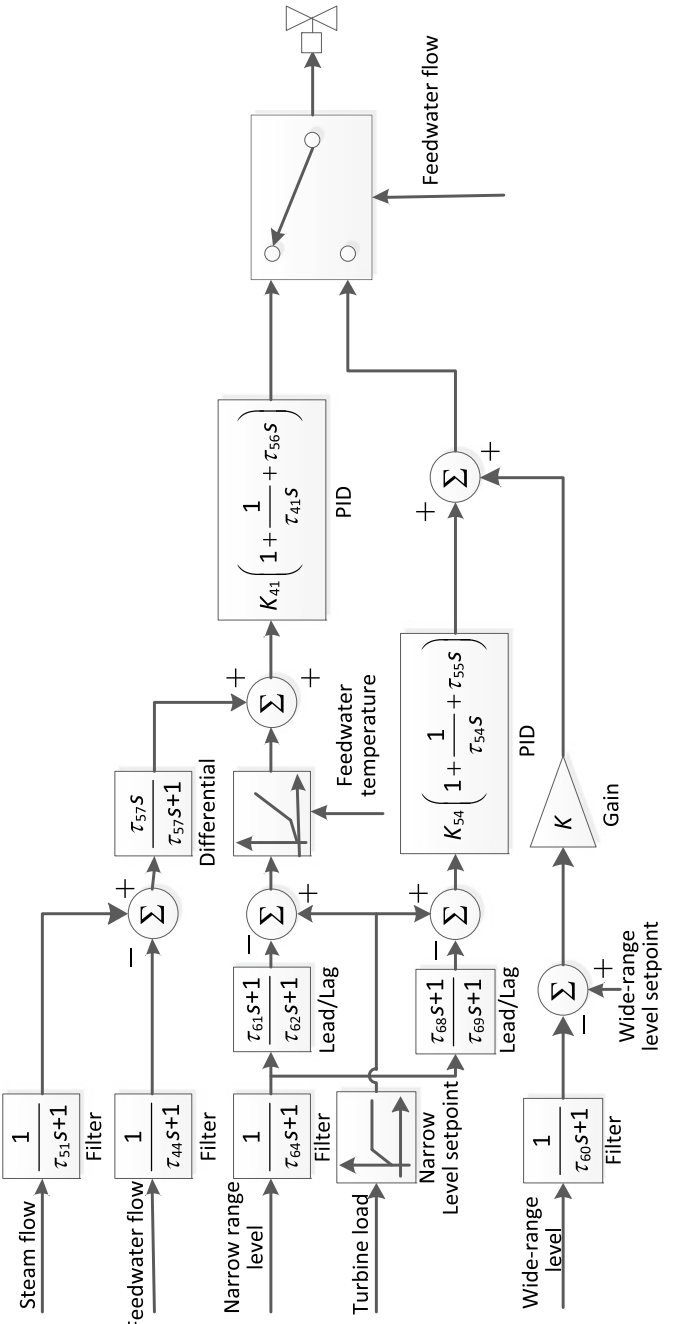

Fig. 6.12 Schematic diagram of feedwater control system (Wan et al. 2015)

water level deviation from setpoint. is initiated on the basis of The filtered high-range feedwater flow signal serves to initiate the transition from the low to the high-power control mode. With the feedwater flow demand from the main feedwater control system, the main feedwater valve lift is then computed on the basis of the estimated pressure difference across the feedwater control valve and the characteristic curve of the valve (Wan et al. 2015).

6.4 AP1000 Load Following Capability and Revised MSHIM Control Strategy

6.4.1 MSHIM Load Following Capability

While most of the nuclear plants, with a few notable exceptions, operate only as base load power providers, some utilities around the world do operate nuclear power stations in load regulation mode (or for grid frequency control) (Drudy et al. 2009). This type of operation is characterized by rapid, nearly random oscillations in reactor power level (Drudy et al. 2009). Typically, these power swings are as large as 10% of rated thermal power (RTP), with power ramp rates as high as 5% per minute (Drudy et al. 2009). "Load regulation" operation is analogous to "load follow" operation, but only on a smaller (and more rapid in time) scale (Drudy et al. 2009). It is expected that the MSHIM strategy would be ideal for handling load regulation. This is because the MSHIM strategy utilizes control rods for automatic reactor control, resulting in rapid power change capability with the added benefit of stable control of axial power distribution (Drudy et al. 2009).

Simulations of load regulation scenarios have demonstrated that the MSHIM control strategy provides superior control capability (Drudy et al. 2009; Onoue et al. 2003). In most instances, it was shown that transition from base-load to load regulation requires no change in AFD target or M-bank positioning. Simulations showed that load regulation (or frequency control) could be easily performed using MSHIM control (Drudy et al. 2009; Onoue et al. 2003). Onoue et al. (2003) evaluated core characteristics—such as core average axial power distribution, M-Bank and AO-Bank position, and critical boron concentration—and showed that acceptable MSHIM load follow operation in the AP1000 without the need to change boron concentration is achievable for up to 95% of cycle life. Drudy et al. (2009) confirmed that the M-banks would be able to accommodate the 5%/min power ramp rates that may be needed in rapid succession.

One potential area of concern in load regulation operation was the impact on long term control rod duty that could be accumulated if a plant was to operate in this mode for most of its life. If rod duty calculations were performed near constant load regulation operation over an AP1000's 60-year lifetime, it was shown that this would result in unacceptable duties being accumulated on the control rod drive mechanisms (Drudy et al. 2009). A plant operator could select a separate rod control

system mode if desired, in order to mitigate the duties accumulated during load regulation operation. In this mode of operation, the control dead-bands and the time compensation logic on the rod controllers would be relaxed so as to reduce the amount of rod motion during operation. Load regulation operation could still be performed with adequate control of the core reactivity and axial offset without excessive use of the rod control system in this condition.

6.4.2 Revised MSHIM and Its Robustness

As mentioned above, the MSHIM operation and control strategy is based on M-bank insertion sequence given in Fig. 6.8. In the original design, the MA and MB banks are supposed to work together with 100% overlap like a single bank, designed to remain nearly fully inserted during normal operation (Drudy et al. 2009). This strategy benefits the reactor by providing both positive and negative reactivity insertion during an operational transient. It also compensates fuel depletion that occurs as the reactor operates through the slow withdrawal from the core. However, this duplication of MA and MB banks is of relatively high worth and might cause large perturbations to the core power distribution when they are withdrawn or inserted from the reference height. In order to address this issue, Drudy et al. (2009) proposed a modified M-banks overlap configuration. This is shown in Fig. 6.13. In this modified overlap scheme, the MB-bank is no longer fully inserted into the core, instead all M-banks are set to follow in an overlap of approximately 33% of the core height.

Simulations by Drudy et al. (2009) for a standard set of nine transient scenarios (these transient scenarios represent a wide range of possible operational conditions and are meant to challenge the control capability of the MSHIM strategy) show that this overlap scheme not only retains the two advantages of the original scheme in load regulation, but also significantly reduces the power distribution perturbations caused by the motion of the fully overlapped MA and MB banks. Moreover, it also results in an almost flat axial offset response to the insertion of subsequent M-banks. The only notable exception to this conclusion is that the new MSHIM base load operational strategy allows M-banks to periodically cycle through a range of positions. Given the position of the M-banks at the initiation of a transient, an initial boron dilution may be necessary in order to insert the M-banks and provide for fully automatic rod control throughout the ensuing reactor transient (Drudy et al. 2009).

As for the load following capability of the revised MSHIM strategy, Drudy et al. (2009) compared the results of the two strategies under a typical transient condition. The comparison of the results confirms that the revised strategy maintains the required core control capabilities similar to the original strategy. Also, no boron dilution change is required in this process, except for an initial dilution to insert the M-banks from their nearly withdrawn initial position. During the ensuing transient, the M-banks fully control core reactivity throughout the transient. Furthermore, results also show that AFD is strictly controlled by the AO-bank, and that ample margins to thermal limits are maintained throughout the transient.

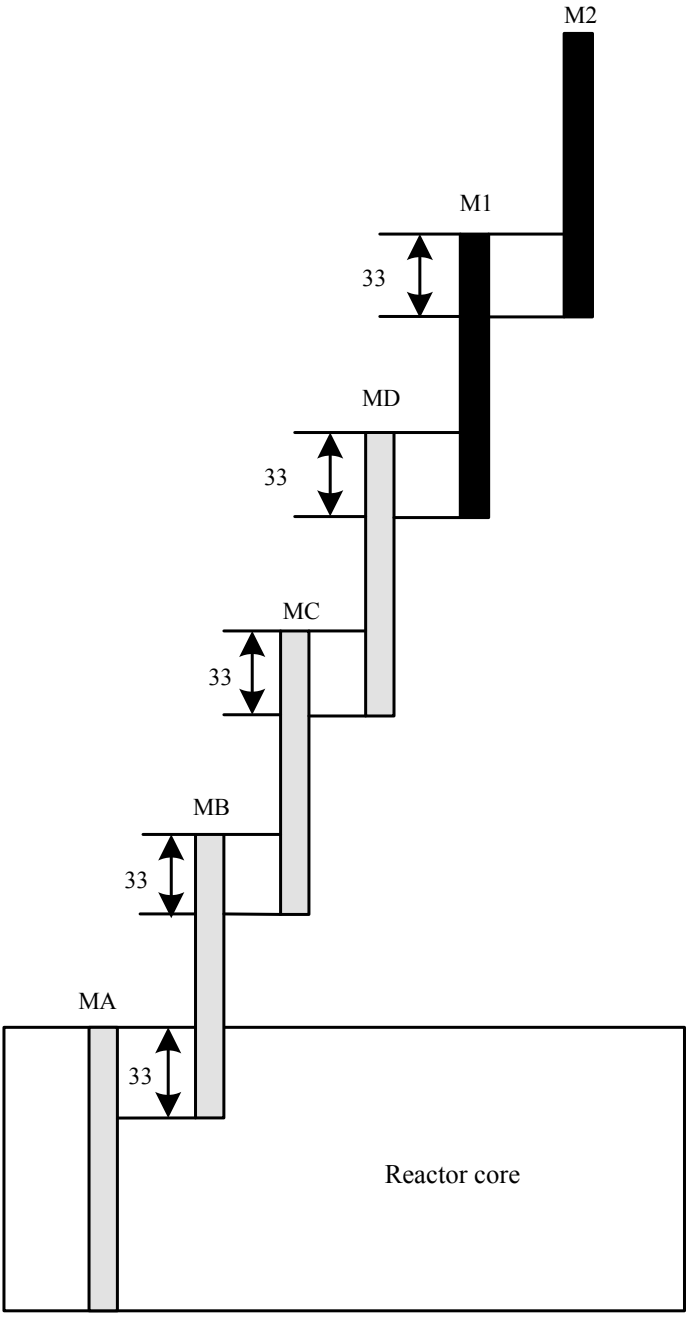

Fig. 6.13 Revised insertion sequence of the M-banks (Drudy et al. 2009)

It was estimated that the load regulation operation could easily be accomplished through automatic rod control based on the MSHIM control strategy. As mentioned previously, this is because load regulation operation consists basically of short, rapid power swings that occur at nearly random intervals. Considering the size of the power swings involved, it was concluded that the M-banks would be able to accommodate the 5%/min power ramp rates that may be needed in rapid succession (Drudy et al. 2009).

6.5 Summary and Conclusions

Control of nuclear power plants that are connected to Hybrid Energy Systems grid fed by intermittent energy sources such as solar and wind requires load following capabilities. AP1000 is equipped with an advance MSHIM core power control strategy that should allow this reactor design to follow load demand. In this control strategy, core reactivity (or coolant average temperature) control and axial power distribution (or axial offset) control are achieved using two separate control rod groups called M-banks and AO-banks. M-banks consist of four grey rods banks and two high worth banks. AO bank is a single high worth bank, designed to control the AO with small movements. The interlock design between the two banks allows the power level and AO to be independently controlled. MSHIM control strategy also allows rapid response to large power change demands. The control of pressurizer pressure and water level and the water level of steam generator are also important for the regulation of the plant during the load following scenarios. Mathematical modeling of the components of the AP1000 is important for the controller design and simulation. In this chapter we have reviewed modeling approaches for the reactor core, pressurizer and UTSG. Controllers for pressurizer and UTSG are also reviewed.

Based on past experience of the MSHIM control for load regulation (or frequency control), and results of simulation exercises reported in literature, it can be concluded that MSHIM control can be used in load following operation, without the need to change boron concentration, for up to 95% of life cycle. Moreover, the M-banks would be able to accommodate the 5%/min power ramp rates that may need to be accommodated in AP1000 connected to grid with substantial input from intermittent sources of energy.

Appendix

See Tables 6.1 and 6.1.

Table 6.1 Nomenclature

A	Volume cross-sectional area
A_p	Flow area of primary loop
C_k	Relative precursor concentration group k
C_{fi}	Fuel specific heat node i
C_{ci}	Fuel cladding specific heat node i
C_{mi}	Specific heat of the coolant node i
D	Diffusion coefficient
$D_{k,i}$	Relative precursor concentration group k node i
f_f	Fraction of the core power generated in the fuel
F_q	Total peaking factor
h_1	Specific enthalpy in volume 1
h_2	Specific enthalpy in volume 2
h_{3L}	Specific enthalpy of liquid region in volume 3
h_{3V}	Specific enthalpy of liquid region in volume 3
h_g	Saturated steam enthalpy
h_f	Saturated water enthalpy
$\bar{h}$	Mean enthalpy
h_{in}	Control volume inlet enthalpy
h_{out}	Control volume outlet enthalpy
h_p^i	Primary side outlet enthalpy node i
h_{fg}	Latent heat of vaporization
$h_{cm,i}$	Heat transfer coefficient between the fuel cladding and the coolant node i
I	Iodine relative concentrations
I_i	Iodine concentrations node i
L	Volume length
L_i	Length of node i
L_s	Length of the subcooled section
L_b	Length of the boiling section
$n_i(0)$	Neutron concentration at rated power-level node i
N	Relative neutron concentration
N_i	Relative neutron concentration node i
N_R	Number of fuel rods
P_{i0}	Rated reactor thermal power node i
P	Pressure
Q	Heat transfer from fluid to tube metal
Q_p^i	Heat transfer from the primary coolant to the tube metal node i
r_f	Fuel pellet radius

(continued)

Table 6.1 (continued)

A	Volume cross-sectional area
$r_{c,in}$	Fuel cladding inner radius
$r_{c,out}$	Fuel cladding outer radius
r_{fj}	Radial distance between the center line of the jth radial node and the center line of the fuel pellet
T_{avg}	Average coolant temperature
T_{fi}	Fuel average temperature node i
T_{ci}	Coolant average temperature node i
$T_{ci,in}$	Coolant inlet temperature node i
$T_{fi,0}$	Fuel steady-state value node i
$T_{ci,0}$	Coolant steady-state value node i
$T_{fi,s}$	Fuel pellet outer surface temperature node i
$T_{ci,in}$	Cladding inner surface temperature node i
$T_{ci,out}$	Fuel cladding outer surface temperature
T_{mi}	Coolant average temperature node i
$T_{fi,u}$	Fuel pellet central temperature node i
$T_{fi,j}$	Fuel pellet jth radial node temperature ith node
$T_{ci,cen}$	Fuel cladding center temperature node i
$T_{mi,0}$	Coolant initial average temperature node i
V_1	Volume of volume 1
V_2	Volume of volume 2
V_{3L}	Volume of liquid region in volume 3
V_{3V}	Volume of liquid region in volume 3
W_{RV}	Discharge rate of relief valve
W_{SV}	Discharge rate of safety valve
W_{SC}	Condensation rate due to spray
W_{SP}	Spray flow rate
W_{1-2}, W_{2-3}	Exchange mass flow rates between two adjacent control volumes
W_{WC}	Condensation rate on vessel wall
W_{FL}	Flashing mass flow rate of liquid into steam
W_{RO}	Rainout mass flow rate of steam into liquid
W_{in}	Control volume inlet flow
W_{out}	Control volume outlet flow
W_p	Coolant mass flow rate
X	Xenon relative concentrations
X_{i0}	Relative xenon concentration steady-state value node i
X_i	Xenon concentrations node i

(continued)

Table 6.1 (continued)

A	Volume cross-sectional area
α_f	Fuel reactivity coefficient
α_c	Coolant reactivity coefficient
α_{X}	Xenon reactivity coefficient
β_k	Delayed neutron fraction group k
γ_I	Fission yields of iodine
γ_X	Fission yields of xenon
ΔH_i	Height of node i
$\Delta \mathrm{r_f}$	Fuel pellet radial node width
$\Delta \mathrm{r_c}$	Fuel cladding radial node width
λ_k	Decay constant group k
λ_{fi}	Fuel heat conductivity node i
λ_{ci}	Fuel cladding heat conductivity node i
λ_I	Decay constants of iodine
λ_{X}	Decay constants of xenon
Λ	Average neutron generation time
Λ_i	Average neutron generation time node i
μ_f	Heat capacity of the fuel
μ_c	Heat capacity of the coolant
v_f	Specific volume of saturated water
v_g	Specific volume of saturated steam
ρ_r	Control rods' reactivity
ρ_{i0}	Initial nodal reactivity node i
ρ_1	Density in volume1
ρ_2	Density in volume2
ρ_{3L}	Density of liquid region in volume3
ρ_{3V}	Density of liquid region in volume3
$\bar{\rho}$	Mean density
ρ_{in}	Control volume inlet density
ρ_{out}	Control volume outlet density
ρ_p^i	Primary side mean density node i
ρ_f	Saturated steam density
ρ_g	Saturated water density
ρ_i	Reactivity node i
ρ_{fi}	Fuel density node i
ρ_{ci}	Fuel cladding density node i
ρ_{ri}	Reactivity contributed by the control rods node i

(continued)

Table 6.1 (continued)

A	Volume cross-sectional area
$\sigma_{a,i}^{X}$	Xenon absorption cross section node i
σ_{ai}^{X}	Xenon microscopic cross section for absorption node i
ϕ_{i0}	Neutron flux at rated power-level
φ_{i0}	Neutron flux at rated power node i
Ω	Transfer coefficient between the fuel and coolant

Table 6.2 Selected AP1000 technical parameters (Westinghouse Electric Company 2005)

Parameter	Value
Reactor thermal power	3400 MWt
Reactor pressure	15.41 MPa
Reactor coolant inlet temperature (FP)	280.7 °C
Reactor coolant outlet temperature (FP)	321.1 °C
Average coolant temperature (FP)	300.9 °C
UTSG steam pressure	5.61 MPa
UTSG steam temperature	271 °C
Feedwater temperature	226.7 °C

References

Carelli DM, Ingersoll TD (2015) Handbook of small modular nuclear reactors. Elsevier

Drudy KJ, Morita T, Connelley BT (2009) Robustness of the MSHIM operation and control strategy in the AP1000 design. In: Proceedings of the 17th international conference on nuclear engineering (ICONE17), pp 893–904. ASME, Brussels, Belgium

Fetterman RJ (2009) Advanced first core design for the Westinghouse AP1000. In: Proceedings of the 17th international conference on nuclear engineering (ICONE17). ASME, Brussels, Belgium

Li L, Zhang Z (2010) Application of water properties table lookup method to development of thermal-hydraulic analysis code in real-time for plate type fuel reactor. In: Asia-Pacific power and energy engineering conference (APPEEC). IEEE, pp 1–4

Morita T (1974) Topical report—power distribution control and load following procedures, WCAP-8403

Onoue M, Kawanishi T, Carlson WR, Morita T (2003) Application of MSHIM core control strategy for Westinghouse AP1000 nuclear power plant. GENES4/ANP, pp 15–18, Kyoto, Japan

Wan J, Song H, Yan S, Sun J, Zhao F (2015) Development of a simulation platform for dynamic simulation and control studies of AP1000 nuclear steam supply system. Ann Nucl Energy 85:704–716

Wan J, Wu S, Nuerlan A, Zhao F (2017) Dynamic modeling of AP1000 steam generator for control system design and simulation. Ann Nucl Energy 109:648–657

Wang P, Liu Y, Jiang B, Wan J, Zhao F (2013) Nodal dynamics modeling of AP1000 reactor for control system design and simulation. Ann Nucl Energy 62:208–223

Wang P, Wan J, Chen Z, Sun J, Zhang R, He Z, Zhao F (2014) Dynamic simulation and study of Mechanical Shim (MSHIM) core control strategy for AP1000 reactor. Ann Nucl Energy 72:49–62

Westinghouse Electric Company (2005) AP1000 design control document Rev (2005)

Westinghouse Electric Company (2009) AP1000 Steam Generator design specification APP-MB01-Z0-101 Rev 2

Chapter 7
Robust Control of Nuclear Reactors with Proportional—Integral-Derivative (PID) Controllers: The Fractional Order (FO) and Interval Approaches

Amitava Gupta

7.1 Introduction

Control of a nuclear reactor poses a challenge to a control-system designer due to the inherent nonlinear and a time varying nature of the associated dynamics which changes with the power level and the depletion level of the radio-active fuel in the reactor core. A constraint on the rate of rise of reactor power poses an additional challenge restricting the operation of a Nuclear Power Plant (NPP) mostly as a base load station. Conventional reactor control approaches aim to achieve a stable reactor period around a designated reactor power level—which is usually 100% Full Power (FP), with refinements like flux-tilt control and zonal power level variations within a narrow range using reactivity devices distributed across the reactor core. A bulk power controller is invoked either to raise the reactor power to a steady operational level or during a sharp reduction, known as a *step-back* and seldom in a demand following mode.

While a nonlinear controller approach can be employed to achieve control of reactor power over the entire operating regime, such methods are plagued by complexities of the controllers and additional complexities in analyses imposed by multiple rate and saturation constraints. On the other hand, a robust control approach is necessary to achieve reliable control in presence of different uncertainties e.g. those associated with estimation of the neutron flux or the reactor power or for that matter in the estimation of coolant channel temperatures and concentration of neutron absorbers and delayed neutron precursors. Thus, standard robust control approaches like H_∞ control, sliding mode control, periodic output feedback etc. have been proposed by contemporary researchers—their applicability being heavily restricted by the complexity in realization of the controllers.

A. Gupta (✉)
Department of Power Engineering and School of Nuclear Studies and Applications, Jadavpur University, Kolkata, India
e-mail: amitava.gupta@jadavpuruniversity.in

A. Mukhopadhyay et al. (eds.), *Dynamics and Control of Energy Systems*,
Energy, Environment, and Sustainability,
https://doi.org/10.1007/978-981-15-0536-2_7

It is a well known fact that 90% of the industrial controllers are Proportional-plus-Integral-plus Derivative (PID) controllers-marked by their simple structure, excellent tracking, good disturbance rejection and reasonable noise immunity. While PID controllers can be designed to achieve desired stability robustness in terms of specified gain and phase margins either by explicit analytical design techniques or by a standard technique like the Linear Quadratic Regulator (LQR), applicability of such a controller to nuclear reactor control is again restricted to a specific power level due to the inherent dependency of such techniques on a linearized model of a reactor. As a natural corollary, it follows that if a PID design methodology that ensures a certain level of stability robustness is augmented with add-ons that ensure parametric robustness, such a controller can be used for controlling the reactor over a wide range of varying reactor power and also in absence of uncertainties in sensor parameters.

The proposed book chapter surveys some recent works that extend the robust PID controller design methodology to achieve enhanced parametric robustness with Fractional Order (FO) elements and with Interval Techniques. The techniques are demonstrated using a standard 540 MWe Pressurized Heavy Water Reactor (PHWR), used extensively in Indian NPPs. Both the methodologies are demonstrated with PID controllers. For demonstrating the effectiveness of FO elements, the 540 Me PHWR is considered under a condition of a step-back where the bulk power of the reactor is reduced with a large stepped reduction in the demand power set-point. It is shown that an active step-back system can be devised for a PHWR with *a single controller* designed to control the reactor at a certain base power level—either with *Phase Shaping* by augmenting a PID controller with a FO phase shaper, or by using a FO PID controller known by the acronym FOPID. The control under a varying power regime using a single controller is possible because of the enhanced parametric robustness introduced by the FO elements viz. the FO phase shaper and the FO PID controller.

With the advent of mathematical tools for solving interval problems in engineering, in the recent past, it has been attempted by some researchers to apply some of these techniques to define systems with whose parameters are assumed to vary within known bounds as interval systems and design robust control systems accordingly. The parametric variations may arise due to nonlinearities that affect a linearized approximation of the system or uncertainties or both. In this Chapter, one such interval based methodology has been presented which shows that a PHWR can indeed be used in a limited load-following mode with a single PID controller.

The rest of the Chapter is organized as follows. The enabling concepts that are essential in understanding FO systems, phase shapers and controllers are introduced first. These concepts are then illustrated with practical applications viz. active step-back in a PHWR, in the next section, with credible MATLAB simulation. Parametric robustness achieved with an interval approach is presented next and demonstrated with MATLAB simulation of load-following operation of a PHWR. The concluding section presents an assessment of the methodology presented and points to further aspects of these methodologies which need to be studied for a full appreciation of the subject.

7.2 FO Approximation of Physical Systems and FO Controllers

Figure 7.1 shows the schematic representation of an infinite transmission line comprising a ladder of a series resistance R and a shunt capacitance C.

It can be shown that the Laplace Transform of the equivalent impedance of the network can be expressed as

$$Z(s) = \sqrt{\frac{R}{C}} s^{-0.5} \tag{7.1}$$

Equation (7.1) above shows that the long transmission line is ideally a FO system which can be approximated by a higher order system for all practical purposes by truncating the line.

The advantage offered by an FO approximation of a dynamic system and the efficacy of an FO controller for controlling the same can be understood if one examines the time response of the system:

$$G(s) = \frac{1}{0.1s^{0.5} + 1} \tag{7.2}$$

due to step input $U_{-1}(t)$ which is shown in Fig. 7.2.

The transfer function (7.2) could represent the transfer characteristics of a *Resistance-Fractance* (R-Q) (Das 2008) circuit shown in Fig. 7.3 represented by the FO differential equation:

$$v_i(t) = \frac{R}{Q} \frac{d^{\alpha} v_o(t)}{dt^{\propto}} + v_o(t) \tag{7.3}$$

with $\frac{R}{Q} = 1$ and $\alpha = 0.5$

Next, with the system (7.2) simulated in MATLAB using the CRONE (http://archive.ims-bordeaux.fr/CRONE/toolbox/pages/accueilSITE.php?guidPage=home_page) tool box, it is attempted to identify the system with

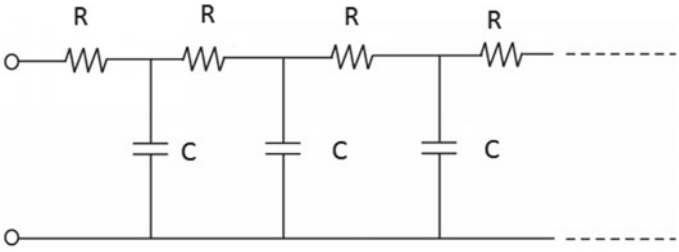

Fig. 7.1 An infinite transmission line

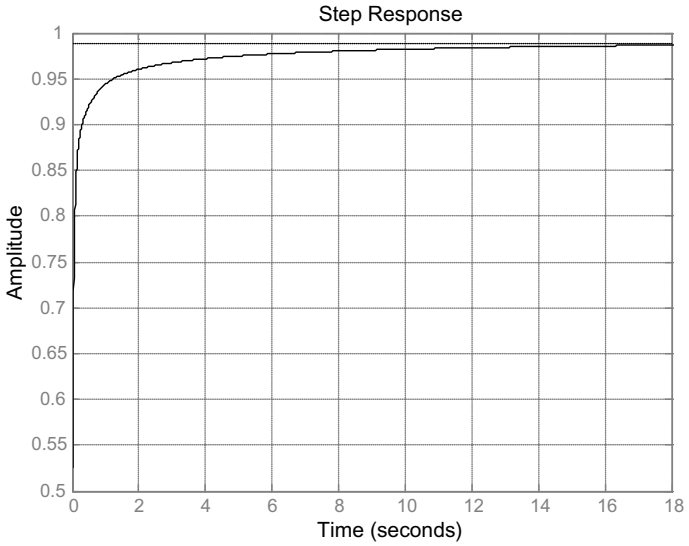

Fig. 7.2 Step response of the system (7.2)

Fig. 7.3 A resistance-fractance network

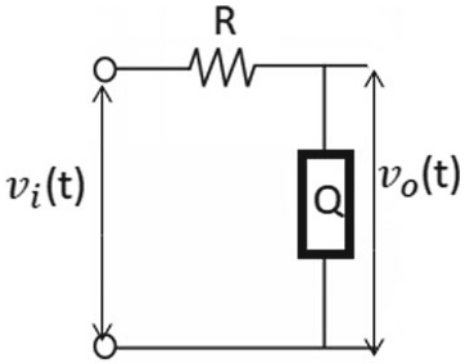

input-output relationships starting with a simple first order template and the approximated systems identified by the MATLAB's *ident* function and the corresponding percentage best fits are enumerated in Table 7.1.

Now, approximating $s^{0.5}$ using the Carlson Approximation (Das 2008) for $H(s) = s^{0.5}$ and iteratively defining

$$H_i(s) = H_{i-1}(s)\frac{(q-m)\left[H_{i-1}(s)\right]^2 + (q+m)P(s)}{(q+m)\left[H_{i-1}(s)\right]^2 + (q-m)P(s)} \tag{7.4}$$

where $P(s) = s$, $H_0(s) = 1, \alpha = 0.5, q = \frac{1}{\alpha}$ and $m = \frac{q}{2}$ yields

Table 7.1 Integer order approximation of (7.2)

Sl.	Identified system transfer function	% best fit
1	$G(s) = \frac{0.9718}{0.2156s+1}$	62.19
2	$G(s) = \frac{0.667s+4.504}{s+4.634}$	62.19
3	$G(s) = \frac{s^2+25.98s+20.06}{1.858s^2+29.40s+20.486}$	92.45
4	$G(s) = \frac{s^3+34.88s^2+91.02s+26.02}{1.92s^3+42.23s^2+97.64s+26.65}$	99.38
5	$G(s) = \frac{s^4+36s^3+126.04s^2+84.03s+8.99}{1.9s^4+44.42s^3+138.6s^2+87.88s+9.103}$	100.0

$$G(s) = \frac{1}{\left(0.1s^{0.5}+1\right)} = \frac{s^4+36s^3+126s^2+84s+9}{1.9s^4+44.4s^3+138.6.s^2+87.6s+9.1} \tag{7.5}$$

It is seen that the transfer function defined by (7.5) tallies very closely with the transfer function in Sl. No. 5 in Table 7.1. Further, from Table 7.1, it is seen that if this system is controlled by a controller $G_c(s)$ such that $G_c(s)G(s)$ is a low-pass filter to achieve good-tracking with acceptable output disturbance and measurement noise rejection, a higher order controller would be better suited and the controller design methodology would be cumbersome due to the orders of the polynomials involved. A compact FO controller, on the other hand, will lead to a more compact form of a controller in the FO domain, provided, appropriate techniques for FO controller design are available. An intuitive argument for the use of an FO controller for an FO system arises from the fact, that such a controller would allow better cancellation of system poles and zeros which might otherwise not be possible with a lower, integer order controller such as a PID Controller.

However, it is to be noted that in most cases, for analysis purposes, systems in process control applications are integer order and can be represented either by a First Order Plus Time Delay (FOPTD) or a Second Order Plus Time Delay (FOPTD) template. Further, a majority of controllers used in industrial control are PID controllers. Such controllers are extremely popular because of their simple structure, excellent tracking, robustness and noise and disturbance rejection. While PID controllers can be designed to produce specified gain and phase margins (Astrom and Wittenmark 1997) parametric robustness cannot be guaranteed. Robustness to system gain variations, for example, cannot be guaranteed. With a PID controller, this can be done by using a phase shaping approach which aims at a flat phase curve around the gain crossover frequency w_{gc} Achieving enhanced parametric robustness by using either a FOPID controller or a phase shaper with a PID controller is extremely significant from the application point of view as this often produces a controller that is resilient to gain changes and robust to parametric variations, often associated with a changing operating regime of the plant and/or with ageing.

Phase shaping has been approached by contemporary researchers in a number of ways. Chen et al. (2004) have proposed optimization based techniques to achieve this. On the other hand Saha et al. in (2010a, b) have proposed an analytical method based on Bode's Integral. These methods assume an integer order system.

To understand the efficacy of a FO element as a phase shaper, it is first attempted to understand the phase contribution due to a fractional semi-differentiator $s^{0.5}$ as shown in Fig. 7.4 with progressively higher order Carlson approximation.

From Fig. 7.4, it is seen that the semi-differentiator acts as a compensator with the frequency spread depending on the order of approximation. Now, if a frequency shift is added, the phase contribution can be localized at a target frequency which is usually the Gain Crossover Frequency (GCF). In general, a phase shaper defined by

$$G_{ph}(s) = (s+\beta)^{\pm q} \tag{7.6}$$

approximated using a template

$$(s+\beta)^{\pm q} = \frac{s+\alpha+\beta}{\alpha s+1+\alpha\beta}, \alpha \in R^{+} \tag{7.7}$$

With the First Order Carlson's First Order Approximation (7.7) and (7.6) is actually a phase compensator with

$$\omega_r = \sqrt{\frac{(1+\alpha\beta)(\alpha+\beta)}{\alpha}} \tag{7.8}$$

and

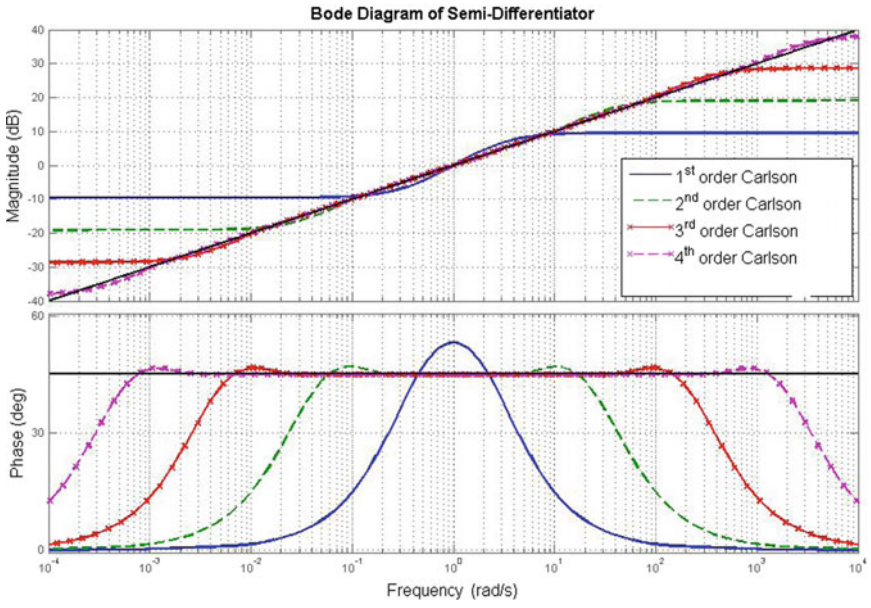

Fig. 7.4 Frequency spread of a fractional semi-differentiator

$$\varphi_m = \tan^{-1}\left(\frac{1-\alpha^2}{2\alpha\omega_r}\right) \tag{7.9}$$

For any system $G_o(s) = G_c(s)G(s)$, representing the plant with its controller in open-loop, in order that a phase shaper $G_{ph}(s)$ produces a flat phase region in the phase curve around its GCF ω_{gc} to achieve parametric robustness, the following condition must be satisfied:

$$\frac{d}{d\omega}\angle G(j\omega) + \frac{d}{d\omega}\angle G_{ph}(j\omega) \approx 0 \tag{7.10}$$

for a frequency band $\Delta\omega$ around ω_{gc}.

The FO differ-integrator $G_{ph}(s)$ is designed to act as a phase-shaper such that the resultant closed-loop system exhibits iso-damped response to step changes in input over a range of gain variations. The design methodology for the phase shaper aims to maximize the width of $\Delta\omega$ allowing maximum variation in system gain. This ensures a constant phase margin and hence gain independent overshoot (iso-damped) for the time response of the system.

$$G_{ol}(s) = G_o(s)G_{ph}(s) \tag{7.11}$$

in closed-loop. The transfer function $G_{ol}(s)$ in (7.11), therefore, represents the open-loop plant with its controller and phase shaper.

Design of a FO phase shaper using Bode's integral formulae has been proposed in (Saha et al. 2010a, b) which has been found to work with a wide variety First Order plus Time Delay (FOPTD) and Second Order plus Time Delay (SOPTD) plants. This methodology assumes that the controller $G_c(s)$ ensures a certain minimum phase margin for $G_o(s)$.

Using Bode's phase integral, it can be shown, that for a stable, minimal phase system in the neighborhood of any specified ω,

$$\omega\frac{d\angle G_o(j\omega)}{d\omega} = \angle G_o(j\omega) + \frac{2}{\pi}[\ln|k_g| - \ln|G_o(j\omega)|] \tag{7.12}$$

where k_g is the static gain of $G_o(s)$.

Substituting $\omega = \omega_{gc}$ in Eq. (7.12) yields

$$\frac{d\angle G_o(j\omega)}{d\omega}\Big|_{\omega=\omega_{gc}} = \frac{\phi_m - \pi}{\omega_{gc}} + \frac{2}{\pi\omega_{gc}}\ln|k_g| \tag{7.13}$$

where

ϕ_m is the phase margin of $G_0(s)$

For a FOPTD or a SOPTD system, $\frac{d\angle G_o(j\omega)}{d\omega}\big|_{\omega=\omega_{gc}}$ is negative and therefore, for (7.10) to be valid in the neighborhood of ω_{gc}, $\frac{d}{d\omega}\angle G_{ph}(j\omega)\big|_{\omega=\omega_{gc}}$ should be positive.

This can be achieved by using a phase shaper of the form

$$G_{ph}(s) = (1 + \beta s^q) \tag{7.14}$$

$$\text{with} \frac{1}{\beta} \leq \omega_{gc}^q \tag{7.15}$$

$$\text{and } 0 \leq q \leq 1 \tag{7.16}$$

In order that the phase shaper $G_{ph}(s)$ does not introduce any change in the magnitude of the original plant, the phase shaper described by Eq. (7.14) must be modified as

$$G_{ph}(s) = \frac{(1 + \beta s^q)}{s^q} \tag{7.17}$$

With the phase shaper represented by Eq. (7.17), a flat-phase curve for any ω in the neighborhood of ω_{gc} can be achieved if

$$\frac{\phi_m - \pi}{\omega_{gc}} + \frac{2}{\pi \omega_{gc}} \ln|k_g| + \frac{\beta q \omega^q sin\frac{q\pi}{2}}{\omega(1 + 2\beta\omega^q cos\frac{q\pi}{2} + \beta^2\omega^{2q})} = 0 \tag{7.18}$$

Now, the addition of $G_{ph}(s)$ alters the phase of $G_o(s)$ and the net phase of $G_{ol}(s)$ at ω_{gc} can be expressed as

$$\phi|_{\omega=\omega_{gc}} = \phi_m - \pi - \frac{q\pi}{2} + \tan^{-1}\left(\frac{\beta\omega^q sin\frac{q\pi}{2}}{1 + \beta\omega^q cos\frac{q\pi}{2}}\right) \tag{7.19}$$

From Eq. (7.19) it follows that the phase of $G_{ol}(s)$ at ω_{gc} is less than the phase of $G_o(s)$ at the same frequency. Since the phase shaper flattens the phase curve of $G_{ol}(s)$ around ω_{gc}, it follows that the phase margin may reduce with the introduction of the phase shaper. Thus if the minimum desired phase margin with the phase shaper be ϕ_{md}, then it follows that the constraint must be satisfied.

$$\phi_{md} - \phi_m + \frac{q\pi}{2} - \tan^{-1}\left(\frac{a\omega^q \sin\frac{q\pi}{2}}{1 + a\omega^q \cos\frac{q\pi}{2}}\right) \leq 0 \tag{7.20}$$

The parameters (q, a) for the phase shaper $G_{ph}(s)$ maximizing the value of $|\omega - \omega_{gc}|$ and satisfying the constraints (7.20) using MATLAB's Optimization Toolbox function *fmincon* (https://www.mathworks.com/help/optim/).

As an illustrative example, the system

$$G(S) = \frac{1}{1.11s + 1} e^{-0.105s} \tag{7.21}$$

may be assumed to be controlled by a PI controller

$$G_c(s) = 7.73 + \frac{10.5}{s} \tag{7.22}$$

and a phase shaper

$$G_{ph}(s) = \frac{1 + 1.3104 s^{0.7895}}{s^{0.7895}} \tag{7.23}$$

Figure 7.5 shows the frequency response of the resultant system with and without the phase shaper.

As seen from Fig. 7.5, introduction of the phase shaper produces a flat-phase region around the GCF and the system is expected to exhibit iso-damping if the gain is varied. This is validated by Fig. 7.6 where the time response of the closed-loop system is presented with varying open-loop static gain with and without the phase shaper

It is seen that the introduction of the phase shaper (7.23) reduces the system's rise time with the same controller as the gain is increased progressively to 2 times its original value while preserving the value of damping, as evident from the overshoot. The system with the controller alone tends to become oscillatory for the same variation is system gain.

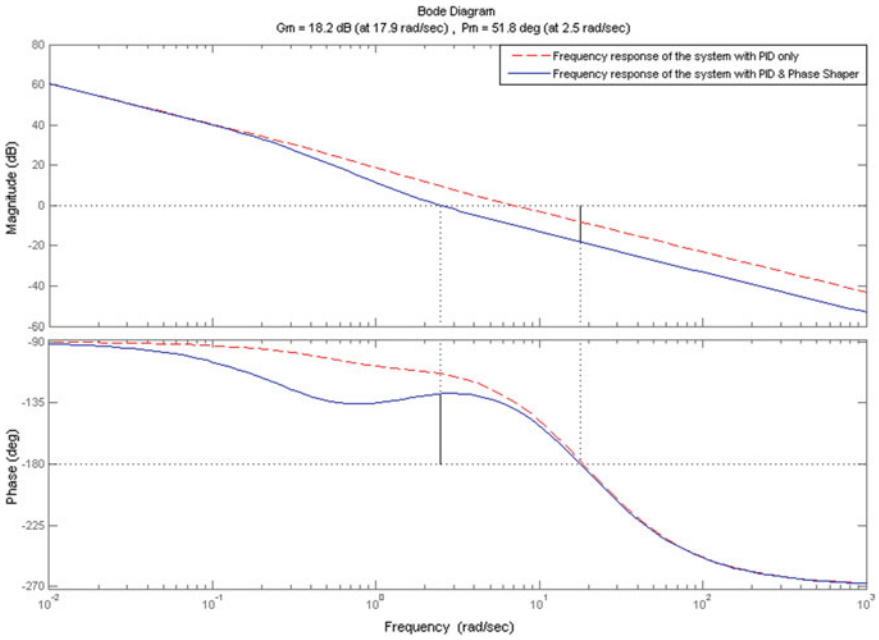

Fig. 7.5 Frequency response of the system (7.21) with controller (7.22) with and without phase shaper (7.23)

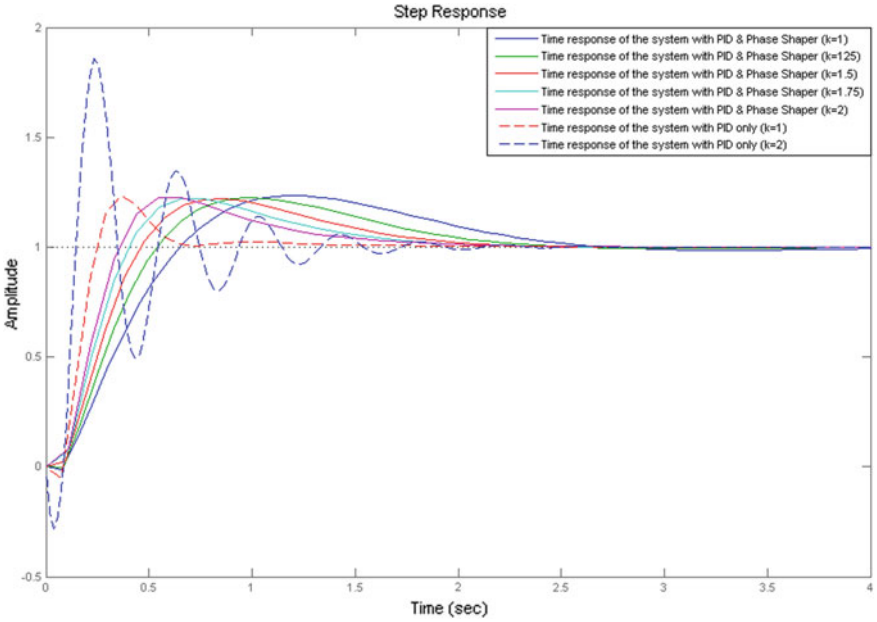

Fig. 7.6 Time response of the system (7.21) with controller (7.22) with and without phase shaper (7.23) under varying gain

While a FO phase shaper is used in conjunction with a standard PID controller, robustness through phase shaping can also be achieved for an integer order system using a FOPID controller. This follows from the fact that a standard PID controller defined by

$$G_c(s) = (k_p + \frac{k_i}{s} + sk_d) \tag{7.24}$$

In conjunction with the phase shaper (7.17) can be expressed as

$$\begin{aligned} G_c(s) \cdot G_{ph}(s) &= (k_p + \frac{k_i}{s} + sk_d).\frac{(1+\beta s^q)}{s^q} \\ &= \beta k_p + s^{-q}(k_p + \frac{\beta k_i}{s^{1-q}} + \frac{k_i}{s}) + s^{1-q}(k_d + s^q \beta k_d) \end{aligned} \tag{7.25}$$

The Eq. (7.25) can be approximated as

$$G_c(s).G_{ph}(s) = \widehat{k}_p + \frac{\widehat{k}_i}{s^\lambda} + \widehat{k}_d s^\mu \tag{7.26}$$

which is actually a FOPID controller.

From Eqs. (7.25) and (7.26), it follows therefore that a FOPID controller can approximate the function of a PID controller in conjunction with a phase shaper to achieve desired parametric robustness. Thus, some contemporary researchers (Chen et al. 2004; Das et al. 2012) have proposed the use of a FOPID controller as an alternative to a PID controller with a FO phase shaper.

An approach using a FOPID controller is usually offline and tuning employs a constrained optimization to derive the parameters $\{k_p, k_i, k_d, \lambda, \mu\}$ satisfying the following specifications:

(i) *Gain crossover frequency specification*:

$$\left|G_c(j\omega_{gc})G(j\omega_{gc})\right| = 1 \tag{7.27}$$

(ii) *Phase margin specifications*

$$Arg[G_c(j\omega_{gc})G(j\omega_{gc})] = -\pi + \phi_m \tag{7.28}$$

(iii) *Parametric robustness specification (flatness of phase curve)*

$$\left(\frac{d}{d\omega}(Arg[G_c(j\omega)G(j\omega)])\right)_{\omega=\omega_{gc}} = 0 \tag{7.29}$$

(iv) *Complementary Sensitivity Specification (High Frequency Noise rejection)*

$$|T(j\omega)| = \left|\frac{G_c(j\omega)G(j\omega)}{1 + G_c(j\omega)G(j\omega)}\right|_{dB} \leq AdB \forall \omega \geq \omega_t \, rad/s \tag{7.30}$$

(v) *Sensitivity Specification (Output Disturbance rejection*

$$|S(j\omega)| = \left|\frac{1}{1 + G_c(j\omega)G(j\omega)}\right|_{dB} \leq BdB \forall \omega \leq \omega_s rad/s \tag{7.31}$$

Tuning of a FOPID controller is mostly achieved by an offline constrained optimization as in (Das et al. 2012). However, a relay based auto-tuning technique for FOPID controllers has been presented by Monje et al. in (Monje et al. 2008). Moreover, since the controller equation involves FO poles and zeroes, it follows as an intuitive argument that a FOPID controller would perform better for a FO system, rather than an Integer Order system. The performance of both are compared with a standard plant viz. a 540 MWe PHWR.

7.3 Robust Control of a Nuclear Reactor with a Phase Shaper and FOPID Controller

The methodologies of robust control using FO elements introduced in the previous sections are demonstrated using a practical application viz. stepped power reduction in a PHWR which is popularly know as a step-back. Bulk reduction in a nuclear reactor is done under load following operations (Das et al. 2006) or under some abnormal operating conditions. To reduce reactor power, the control rods are inserted to a specified level with gradual lowering of the demand power set-point. Modern PHWRs with passive safety features rely on gravity to drive the control rods which are held above the reactor by electromagnetic clutches against a spring force. These are released during a step-back and also automatically, in case of a power failure. During a step-back, the clutches are de-energized to release the rods and then again energized to grip them once the rods have dropped by a designated amount. But this passive step-back mechanism in addition creates a power undershoot while also producing a very sluggish response which are unacceptable as reported in (Park and Cho 1993). Detailed description of a PHWR's power control mechanism or the Reactor Regulating System (RRS) can be found in (Das et al. 2006).

Saha et al. in (2010a, b) and Das et al. in (2012) have proposed a motor driven active step-back mechanism which is motor driven, the motor is assumed to be controlled by a PID controller with a phase shaper as in (Saha et al. 2010a, b) or by a FOPID controller as in (Das et al. 2012).

In Saha et al. (2010a, b) have identified a PHWR during a step-back using a series of FOPTD and SOPTD templates, with a 30% step-back initiated at 100%. 90, 80 and 70% FP as reported in (Saha et al. 2010a, b). The FOPTD transfer functions are (Saha et al. 2010a, b):

$$G^1_{100}(s) = \frac{384.6}{s+2}e^{-0.5s} \tag{7.32}$$

$$G^1_{90}(s) = \frac{355.1}{s+2}e^{-0.5s} \tag{7.33}$$

$$G^1_{80}(s) = \frac{316.7}{s+2}e^{-0.5s} \tag{7.34}$$

$$G^1_{70}(s) = \frac{272.6}{s+2}e^{-0.5s} \tag{7.35}$$

while the corresponding SOPTD transfer functions are:

$$G^2_{100}(s) = \frac{192.3}{s^2+2s+1}e^{-0.5s} \tag{7.36}$$

$$G^2_{90}(s) = \frac{177.6}{s^2+2s+1}e^{-0.5s} \tag{7.37}$$

$$G_{80}^{2}(s) = \frac{158.4}{s^2 + 2s + 1} e^{-0.5s} \tag{7.38}$$

$$G_{70}^{2}(s) = \frac{136.4}{s^2 + 2s + 1} e^{-0.5s} \tag{7.39}$$

The transfer functions enumerated above are established from practical plant data as detailed in (Saha et al. 2010a, b; Das et al. 2012) with sub-optimal order reduction. It is seen that the static gain of the individual FOPTD and SOPTD plants enumerated above depend on the initial power at which a step-back is initiated and delay and the open-loop poles remain same. Thus, this is an ideal application where an enhanced parametric robustness can provide a mechanism for using a single PID controller to manage a step-back. A flat phase around the GCF for the plant for a particular power level, controlled by a single controller will then ensure sufficient parametric robustness to tackle a change in system gain at varying power levels.

As reported in (Saha et al. 2010a, b) the controller and the phase shapers designed for the plant defined by the set of Eqs. (7.32)–(7.35) under a step-back are:

$$G_{c}^{1}(s) = 0.0059 + \frac{0.0019}{s} + 0.00082s \tag{7.40}$$

and

$$G_{ph}^{1}(s) = \frac{(1 + 1.3419s^{0.6181})}{s^{0.6181}} \tag{7.41}$$

Again, the controller and phase shaper for the SOPTD transfer functions represented by (7.36)–(7.39) are

$$G_{c}^{2}(s) = 0.0039 + \frac{0.001}{s} + 0.002s \tag{7.42}$$

and

$$G_{ph}^{2}(s) = \frac{(1 + 5s^{0.75})}{s^{0.75}} \tag{7.43}$$

Figure 7.7 shows the time response of the PHWR under a step-back represented by the set of Eqs. (7.32)–(7.35) and (7.36)–(7.39) with the corresponding controllers and the phase shaperd. The response without the phase shaper is also presented along with response with the original RRS in the same figure.

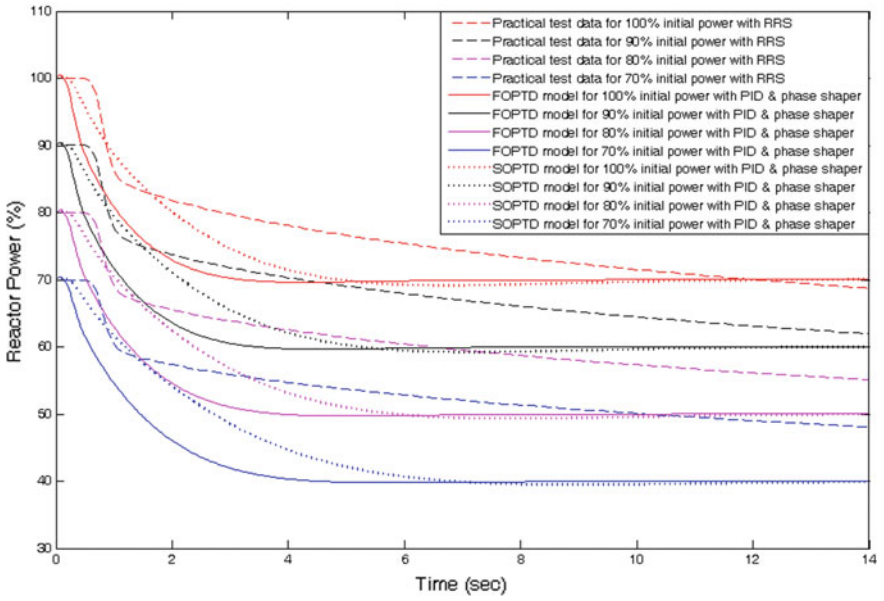

Fig. 7.7 Simulated step-back of a PHWR with RRS only and with a PID controller and phase shaper (https://www.mathworks.com/help/optim/)

Das et al. in (2012) have approached the problem with an alternate approach viz. using a FOPID controller and as enumerated in [reference] the FOPTD and the SOPTD templates correspond to the

(i) *One Non-integer Order Plus Time Delay (NIOPTD-I)* template defined as

$$G(s) = \frac{K}{Ts^{\alpha} + 1} e^{-Ls} \tag{7.44}$$

and the

(ii) *Two Non-integer Order Plus Time Delay* (*NIOPTD-II*) template defined as

$$G(s) = \frac{K}{s^{\alpha} + 2\zeta\omega_n s^{\beta} + \omega_n^2} e^{-Ls} \tag{7.45}$$

Original plant data reported in (Saha et al. 2010a, b; Das et al. 2012) is used to deduce the higher order reactor transfer functions which are used to obtain the reduced order plants in the NIOPTD-I and NIOPTD-II templates using the minimization of the H_2-norm of the identified and the fractional order NIOPTD models (Das et al. 2011). The corresponding reactor transfer functions are enumerated as follows, as reported in (Das et al. 2012):

(i) NIOPTD-I models:

$$G^1_{100}(s) = \frac{195.0736}{1.0006s^{1.057} + 1} e^{-0.0934s} \tag{7.46}$$

$$G^1_{90}(s) = \frac{175.5107}{1.0084s^{1.0559} + 1} e^{-0.0937s} \tag{7.47}$$

$$G^1_{80}(s) = \frac{156.5649}{0.99866s^{1.0566} + 1} e^{-0.0928s} \tag{7.48}$$

$$G^1_{70} = \frac{136.0175}{0.99724s^{1.0546} + 1} e^{-0.0932s} \tag{7.49}$$

(ii) NIOPTD-II models

$$G^2_{100}(s) = \frac{1522.8947}{s^{2.0971} + 8.1944s^{1.0036} + 7.7684} e^{-2.0043\times10^{-12}s} \tag{7.50}$$

$$G^2_{90}(s) = \frac{1359.2345}{s^{2.0972} + 8.1906s^{1.0036} + 7.7075} e^{-1.5968\times10^{-9}s} \tag{7.51}$$

$$G^2_{80}(s) = \frac{1027.3027}{s^{2.0163} + 6.7859s^{0.99388} + 6.5268} e^{-2.5346\times10^{-5}s} \tag{7.52}$$

$$G^2_{70}(s) = \frac{1074.396}{s^{2.0961} + 8.2663s^{1.0037} + 7.8641} e^{-3.1431\times10^{-10}s} \tag{7.53}$$

The corresponding FOPID controller as reported in (Das et al. 2012), for the NIOPTD-II plant with the plant (7.50) taken as the basis is

$$G^2_c(s) = 0.0006 + \frac{0.0052}{s^{1.0137}} + 0.0049s^{0.1067} \tag{7.54}$$

The response under a step-back condition is presented in Fig. 7.8 reproduced from (Das et al. 2012).

It is seen that the response of the PHWR under step-back, as represented in Figs. 7.7 and 7.8 are similar. However, the advantage of using a FOPID controller can be understood if one examines the simulation presented in Fig. 7.9 using the data

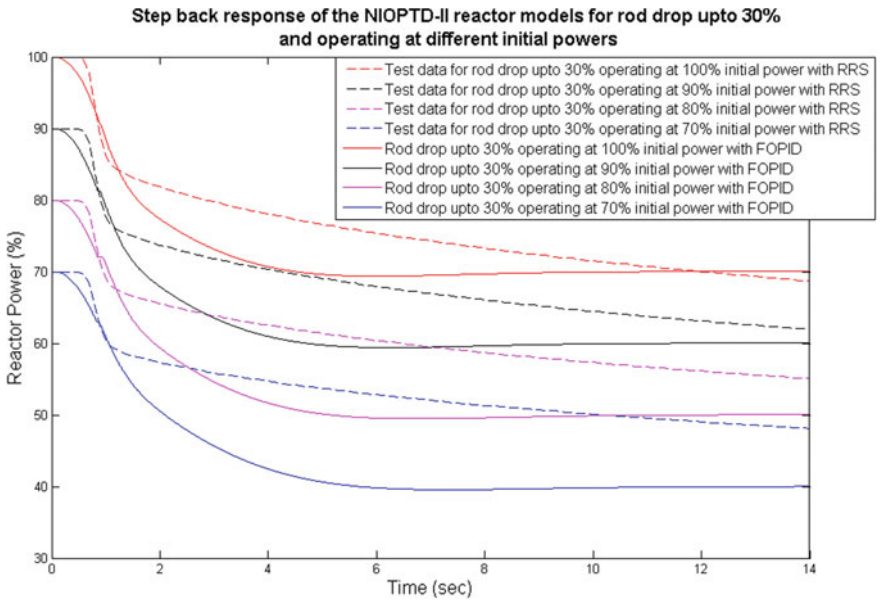

Fig. 7.8 Simulated step-back of a PHWR with RRS and a FOPID controller (Das et al. 2012)

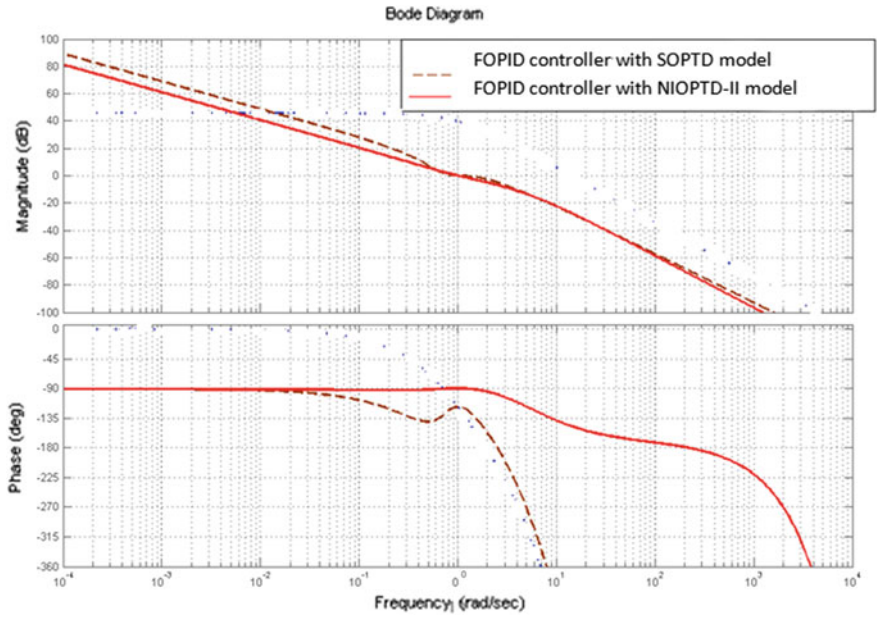

Fig. 7.9 Frequency response of the PHWR with FOPID controller applied to an Integer Order and non-integer order model

presented in (Das et al. 2012).

The systems used for comparison in Fig. 7.9 correspond to (7.36) and (7.50) and the controller equation is assumed to be defined by (7.54). From Fig. 7.9 it is clearly seen that the extent of flatness of the phase curve achievable with a FOPID controller controlling a plant described by a FO (referred to as NIOPTD) model is much more compared to that achievable with the same FOPID controller controlling an Integer Order describing the same plant. The finding tallies with the postulate that a FOPID controller allows a better cancellation of FO poles and zeroes in the original plant. A direct corollary that follows from this finding is the possibility of a faster step-back with a FOPID plant as the allowable controller gain variation is large owing to a larger flat-phase region.

7.4 Robust Control of a Nuclear Reactor Using an Interval Approach

As seen from the set of Eqs. (7.32)–(7.35) and (7.36)–(7.39), the parameters of the reactor transfer function show a polytopic variation with reactor power. Thus, if one assumes that these vary in an interval corresponding to an interval of reactor power $[\underline{P}, \bar{P}]$, where $\underline{P}$ represents the *infimum* of the interval and $\bar{P}$ represents the *supremum* of the *interval variable* $P \in [\underline{P}, \bar{P}]$, then it follows that the general form of representation of a reactor's transfer function relating variation of reactor power P to the external reactivity ρ_{ext} introduced by the reactivity control mechanism of the reactor, around an operating power level, can be expressed as and *interval plant*

$$\left.\begin{aligned} G(s, \mathbf{p}) &= \frac{f_0 + f_1 s^m + \ldots + f_m s^m}{g_0 + g_1 s + \ldots + g_n s^n} \\ \mathbf{p} &= [f_0, f_1, \ldots, f_m; g_0, g_1, \ldots, g_n]; \end{aligned}\right\} \tag{7.55}$$

where $\mathbf{p}$ represents the set of all interval variables in $G(s, \mathbf{p})$.

Normally, stability of such a system (plant) can be analyzed using the *Kharitonov's Polynomial Theorem* which states that an interval plant $G(s, \mathbf{p})$ shall be Hurwitz stable, with all poles in the left half of the s plane provided the following four polynomials known as Kharitonov's polynomials are Hurwitz stable:

$$\begin{aligned} q_1(s) &= \underline{g}_0 + \underline{g}_1 s + \bar{g}_2 s^2 + \bar{g}_3 s^3 + \underline{g}_4 s^4 + \underline{g}_5 s^5 \ldots \\ q_2(s) &= \bar{g}_0 + \bar{g}_1 s + \underline{g}_2 s^2 + \underline{g}_3 s^3 + \bar{g}_4 s^4 + \bar{g}_5 s^5 \ldots \\ q_3(s) &= \underline{g}_0 + \bar{g}_1 s + \bar{g}_2 s^2 + \underline{g}_3 s^3 + \underline{g}_4 s^4 + \bar{g}_5 s^5 \ldots \\ q_4(s) &= \bar{g}_0 + \underline{g}_1 s + \underline{g}_2 s^2 + \bar{g}_3 s^3 + \bar{g}_4 s^4 + \bar{g}_5 s^5 \ldots \end{aligned} \tag{7.56}$$

The Eq. (7.56) forms the basis of stability analyses under parametric variations arising out of change in reactor power and/or uncertainties in measurement and subsequent design of robust controllers as reported in (Lee and Na 2002) for a Pressurized Water Reactor (PWR) and in (Banerjee et al. 2015) for a 540 MWe PHWR, unlike small modular reactor in (Lee 1997), where a nonlinear model has been used for interval analysis.

A 540 Mwe PHWR consists of 14 zones, each of which is controlled by a Liquid Zone Control System (LZCS) as detailed in (Das et al. 2006). The *global power* of the reactor is the sum of the powers produced by each zone. Each zone of the PHWR has a Liquid Zone Compartment (LZC) which can be filled with light water. The height of the water column in the LZC compartment alters the neutron absorption in that zone and hence the *reactivity* ρ_{ext} input to the zone to alter its power. At steady state, when the reactor operates at a steady power the nett reactivity ρ_{nett} which is the algebraic sum of the nett internal reactivity ρ_{int} and the external reactivity ρ_{ext} introduced by the LZCS should be zero. A change $\Delta\rho_{ext}$ is therefore necessary either to change the power produced by the zone or to balance the change in internal reactivity $\Delta\rho_{int}$ caused by internal factors such as change in temperature with reactor power etc. The LZCS controller, therefore, alters this reactivity by varying the water level in the corresponding LZC in response to the change in the demand power set-point for the concerned zone. In (Banerjee et al. 2015), a control scheme has been proposed which achieves power control using one PID controller for each zone, the output of which controls the water level in the corresponding LZC, and the set-point for which is derived from the global power set-point.

In (Banerjee et al. 2015) each zone of the reactor has been modelled as an interval plant (7.55) expressible as

$$G(s, p) = \frac{K}{s(s+a)} K \in \left[\underline{K}, \bar{K}\right], a \in \left[\underline{a}, \bar{a}\right] \tag{7.57}$$

corresponding to a reactor power variation in the interval [60, 100%] FP as represented in Table 7.2 with the *nominal plant*

Table 7.2 The interval and nominal plant transfer functions of 540 MWe PHWR

Zone	Interval plant	Nominal plant
1, 8	$\frac{[0.0051,0.0084]}{s(s+[1.53,1.56])}$	$\frac{0.0064}{s(s+1.56)}$
2, 9	$\frac{[0.005,0.0082]}{s(s+[1.54,1.56])}$	$\frac{0.0063}{s(s+1.55)}$
3, 10	$\frac{[0.0053,0.0093]}{s(s+[1.51,1.53])}$	$\frac{0.0072}{s(s+1.53)}$
4, 11	$\frac{[0.0068,0.0115]}{s(s+[1.53,1.55])}$	$\frac{0.0089}{s(s+1.55)}$
5, 12	$\frac{[0.0053,0.0093]}{s(s+[1.51,1.53])}$	$\frac{0.0072}{s(s+1.53)}$
6, 13	$\frac{[0.0051,0.0084]}{s(s+[1.53,1.56])}$	$\frac{0.0064}{s(s+1.56)}$
7, 14	$\frac{[0.005,0.0082]}{s(s+[1.54,1.56])}$	$\frac{0.0063}{s(s+1.55)}$

$$G_0(s) = \frac{K_0}{s(s + a_0)} \tag{7.58}$$

representing the zone's transfer function at 80% FP.

Now, if it is attempted to control the power of each zone of the reactor for the entire interval [60, 100%] FP, with a single controller, then the controller must be able to control each interval plant enumerated in Table 7.2. In (Banerjee et al. 2015), it is attempted to control each interval plant with a single PID controller designed for the corresponding nominal plant and this is referred to as the *nominal controller*.

In (Banerjee et al. 2015) the nominal controller is designed by casting the PID controller design problem as an optimal Full State Feed-back Controller (FSFC) design using an LQR approach. For this purpose, the following state variable formulation is adopted:

$$\begin{aligned} x_1 &= \int \Delta P(t)dt \\ x_2 &= \Delta P(t) = \dot{x}_1 \\ x_3 &= \dot{x}_2 \end{aligned} \tag{7.59}$$

which yields

$$\begin{bmatrix} \dot{x}_1 \\ \dot{x}_2 \\ \dot{x}_3 \end{bmatrix} = \begin{bmatrix} 0 & 1 & 0 \\ 0 & 0 & 1 \\ 0 & 0 & -a_0 \end{bmatrix} \begin{bmatrix} x_1 \\ x_2 \\ x_3 \end{bmatrix} + \begin{bmatrix} 0 \\ 0 \\ L_0 \end{bmatrix} \Delta\rho_{ext}(t) \tag{7.60}$$

where $\Delta P(t)$ denotes the change in reactor power around an operating point corresponding to 80% FP of the zone and $\Delta\rho_{ext}(t)$ is the change in reactivity introduced by the LZCS. The corresponding matrices for the nominal plant become

$$A_0 = \begin{bmatrix} 0 & 1 & 0 \\ 0 & 0 & 1 \\ 0 & 0 & -a_0 \end{bmatrix}, B_0 = \begin{bmatrix} 0 \\ 0 \\ K_0 \end{bmatrix}, C_0 = \begin{bmatrix} 0 & 1 & 0 \end{bmatrix} and\ D_0 = [0]. \tag{7.61}$$

It is clear that with a PID controller, the control law can be expressed as

$$\Delta\rho_{ext} = \begin{bmatrix} k_i, k_p, k_d \end{bmatrix} \begin{bmatrix} x_1 \\ x_2 \\ x_3 \end{bmatrix} \tag{7.62}$$

with $K = \begin{bmatrix} k_i, k_p, k_d \end{bmatrix}$ obtained as $\mathbf{K} = \mathbf{R}^{-1}\mathbf{B}_0^T\mathbf{P}_0$, where $\mathbf{P}_0 = \mathbf{P}_0^T > \mathbf{0}$ is the unique solution of the Algebraic Riccati Equation (ARE)

$$\mathbf{A}_0^T\mathbf{P} + \mathbf{P}\mathbf{A}_0 - \mathbf{P}\mathbf{B}_0\mathbf{R}_0^{-1}\mathbf{B}_0^{\mathrm{T}}\mathbf{P} + \mathbf{Q}_0 = 0 \tag{7.63}$$

using $\mathbf{R} = r > 0$ and

$$\mathbf{Q}_0 = \begin{bmatrix} q_{10} & 0 & 0 \\ 0 & q_{20} & 0 \\ 0 & 0 & q_{30} \end{bmatrix} \tag{7.64}$$

are the corresponding weight matrices.

The closed-loop poles of the resultant system with the PID controller can be tailored by choosing the diagonal elements q_{10}, q_{20}, q_{30} in (7.64) which may be expressed as functions of a_0, K_0, r, the closed- loop damping ξ_0 and the closed-loop frequency ω_0 following the methodology detailed in (Banerjee et al. 2015).

It is clear that the matrices in (7.61) correspond to specific values of interval matrices expressible as

$$\mathbf{A} \subset \begin{bmatrix} 0 & 1 & 0 \\ 0 & 0 & 1 \\ 0 & 0 & -\left[\underline{a}, \bar{a}\right] \end{bmatrix}, \mathbf{B} \subset \begin{bmatrix} 0 \\ 0 \\ \left[\underline{K}, \bar{K}\right] \end{bmatrix}, \mathbf{C} = \begin{bmatrix} 0 & 1 & 0 \end{bmatrix} \text{and} \, \mathbf{D} = [0]. \tag{7.65}$$

An inspection of Table 7.2 reveals that the matrix pair $(\mathbf{A}, \mathbf{B})$ remains stabilizable throughout the intervals $[\mathbf{A}, \mathbf{A}]$ $\left[\underline{\mathbf{A}}, \bar{\mathbf{A}}\right]$ and $\left[\underline{\mathbf{B}}, \bar{\mathbf{B}}\right]$. Thus, if the matrices $\mathbf{A}, \mathbf{B}$ are expressed as

$$\begin{aligned} \mathbf{A} &= \mathbf{A}_0 + \Delta\mathbf{A} \\ \mathbf{B} &= \mathbf{B}_0 + \Delta\mathbf{B} \end{aligned} \tag{7.66}$$

then the ARE

$$\begin{aligned} &(\mathbf{A}_0 + \Delta\mathbf{A})^{\mathrm{T}}(\mathbf{P}_0 + \Delta\mathbf{P}) + (\mathbf{P}_0 + \Delta\mathbf{P})(\mathbf{A}_0 + \Delta\mathbf{A}) \\ -&(\mathbf{P}_0 + \Delta\mathbf{P})(\mathbf{B}_0 + \Delta\mathbf{B})\mathbf{R}_0^{-1}(\mathbf{B}_0 + \Delta\mathbf{B})^{\mathrm{T}}(\mathbf{P}_0 + \Delta\mathbf{P}) + \mathbf{Q} = \mathbf{0} \end{aligned} \tag{7.67}$$

shall always yield a unique positive definite solution

$$\mathbf{P} = \mathbf{P}_0 + \Delta\mathbf{P} \tag{7.68}$$

If the interval matrix

$$\mathbf{Q} = \begin{bmatrix} q_{10} + \Delta q_{10} & 0 & 0 \\ 0 & q_{20} + \Delta q_{20} & 0 \\ 0 & 0 & q_{30} + \Delta q_{30} \end{bmatrix} \tag{7.69}$$

always remains positive semi-definite within an interval $\left[\underline{\mathbf{Q}}, \bar{\mathbf{Q}}\right]$ specified a priori with specified intervals of open-loop and closed-loop parameters. It is clear that a positive semi-definite $\mathbf{Q}$, in this case, automatically ensures that the pair $\left(\mathbf{A}, \sqrt{\mathbf{Q}}\right)$

always remains detectable and hence (7.67) will always produce a unique positive definite solution. In (Banerjee et al. 2015) results based on bounds of Eigen values of interval matrices is used to ensure the positive semi-definiteness of the interval matrix **Q**.

The existence of a unique solution of (7.67) implies that as the reactor power changes from 80% FP and varies in the interval [80, 100%] FP, Moreover, if it can be proved, as in (Banerjee et al. 2015) that since the interval plant (7.57) does not contain any open-loop zeroes, it is always possible to find a solution $\mathbf{P} = \mathbf{P}_0 + \Delta\mathbf{P}$ of (7.67) such that the relationship

$$(\mathbf{B}_0 + \Delta\mathbf{B})^T(\mathbf{P}_0 + \Delta\mathbf{P}_0) = \mathbf{B}_0^T\mathbf{P}_0 \tag{7.70}$$

The satisfaction of (7.67) and (7.70) essentially means that the nominal PID controller, designed for the nominal plant, will be able to control the interval plant within a specified regime of operation with varying controller effort and with closed-loop poles placed within specified regions in the s plane. Figure 7.10, as reported in (Banerjee et al. 2015) illustrates this. The cases shown in Fig. 7.10 illustrate a scenario where the global power set-point for the reactor is reduced at constant rate of 0.5% FP *per sec.* and then held constant at that level, with the reactor operating at 60, 80 and 100% FP, the controller being the nominal controller designed for the nominal plant enumerated in Table 7.2. It is seen that the nominal controller which is designed to control the reactor at around 80% FP is robust to parametric variations, as conceived in its design.

Robust control of nuclear reactors has been attempted by contemporary researchers using a variety of methodologies e.g. the classical H_∞ (Lee 1997; Suzuki et al. 1993) and sliding mode control (Ansarifar and Rafiei 2015) approaches. But

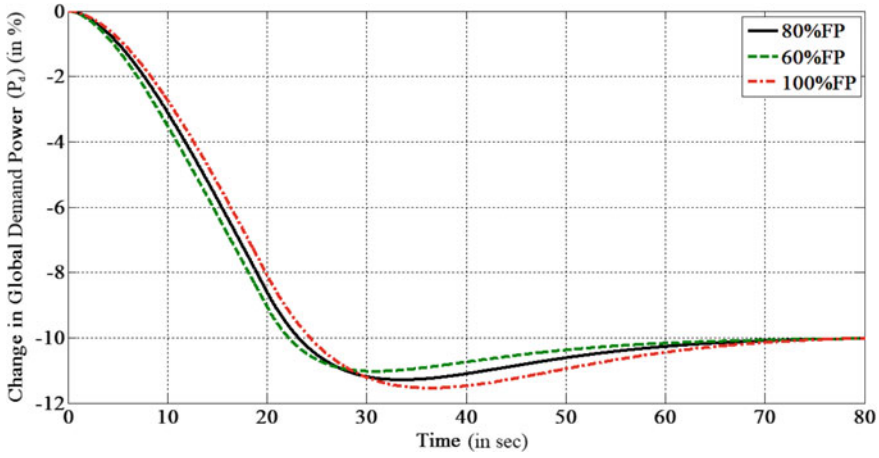

Fig. 7.10 Performance of the nominal controller at different power levels (Banerjee et al. 2015)

the effectiveness of the methodology presented in this section lies in the fact that it is based on the omni-present PID controller which makes it ready to use.

7.5 Conclusion

The methodologies presented in this chapter augment the performance of PID controller with enhanced parametric robustness with simple mechanisms like a FO phase shaper and more effectively with a FOPID controller. Such controllers are shown to derive enhanced parametric robustness due to the unique iso-damping nature of closed-loop response introduced by an FO element. This translates to a faster response of the system with almost gain independent overshoot or undershoot- a feature that is found to be extremely useful in implementing an active rapid power reduction mechanism in a nuclear reactor.

Measurement, in an industrial environment, is almost always associated with uncertainties. Further, the parameters of any physical system change with time, or if the system is nonlinear and is linearized about an operating point, the parameters change with the operating regime. This is particularly true for a nuclear reactor. The interval based approach of controller design presented in this chapter allows a single PID controller to be used for controlling such a reactor within a power regime and also with measurement uncertainties.

Implementation aspects of FO elements and FOPID controllers as well as interval techniques to assess controllability and observability of interval systems in state-variable form are left as a scope for self-study for interested readers.

Acknowledgements The author acknowledges the support received from his former doctoral students Dr. Suman Saha, Dr. Saptarshi Das and Dr. Shohan Banerjee in preparing the material presented in this chapter. The MATLAB codes developed by Dr. Saha and Dr. Das have been used extensively for producing the Figs. 7.4, 7.6 and 7.9. The author also acknowledges the support from IEEE for the permission to reproduce Figs. 7.7 and 7.8 and 10 from the sources referenced in the respective figures.

References

Ansarifar GR, Rafiei M (2015) Second-order sliding-mode control for a pressurized water nuclear reactor considering the xenon concentration feedback. Nucl Eng Technol 47(1):94–101

Astrom KJ, Wittenmark B (1997) Computer-controlled systems theory and design. Tsinghua University Press, Prentice Hall

Banerjee S, Halder K, Dasgupta S, Mukhopadhyay S, Ghosh K, Gupta A (2015) An interval approach for robust control of a large PHWR with PID controllers. IEEE Trans Nucl Sci 62(1):281–292

CRONE Tool Box. http://archive.ims-bordeaux.fr/CRONE/toolbox/pages/accueilSITE.php?guidPage=home_page

Chen YQ, Moore KL, Vinagre BM, Podlubny I (2004) Robust PID controller autotuning with a phase shaper. In: Proceedings of the first IFAC symposium on fractional differentiation and its application (FDA04), Bordeaux, France

Das S (2008) Functional fractional calculus. Springer, Berlin. ISBN 978-3-642-20545-3

Das M, Ghosh R, Goswami B, Gupta A, Tiwari AP, Balasubramanian R, Chandra AK (2006) Networked control system applied to a large pressurized heavy water reactor. IEEE Trans Nucl Sci 53(5):2948–2956, Part 2

Das S, Saha S, Das S, Gupta A (2011) On the selection of tuning methodology for FOPID controllers for the control of higher order processes. ISA Trans 50(3):376–388

Das S, Das S, Gupta A (2012) Fractional order modeling of a PHWR under step-back condition & control of its global power with a robust $PI^{\lambda}D^{\mu}$ controller. IEEE Trans Nucl Sci 58(5):2431–2441

Lee YJ (1997) H-infinity robust controller design of reactor power control system. J KNS 29(4):280–290

Lee YJ, Na MG (2002) Robust controller design of nuclear power reactor by parametric method. J KNS, 34(5):436–444

Monje CA, Vinagre BM, Feliu V, Chen YQ (2008) Tuning and auto-tuning of fractional order controllers for industry applications. Control Eng Pract 16(7):798–812

Optimization Toolbox Documentation. https://www.mathworks.com/help/optim/

Park MG, Cho NZ (1993) Time-optimal control of nuclear reactor power with adaptive proportional-integral-feedforward gains. IEEE Trans Nucl Sci 40(3):266–270

Saha S, Das S, Ghosh R, Goswami B, Balasubramanian R, Chandra AK, Das S, Gupta A (2010a) Design of a fractional order phase shaper for iso-damped control of a PHWR under step-back condition. IEEE Trans Nucl Sci 57(3):1–11

Saha S, Das S, Ghosh R, Goswami B, Balasubramanian R, Chandra AK, Das S, Gupta A (2010b) Fractional order phase shaper design with Bode's integral for iso-damped control system. ISA Trans 49(2):196–206

Suzuki K, Shimazaki J, Shinohara Y (1993) Application of H-infinity control-theory to power-control of a nonlinear reactor model. Nucl Sci Eng 115(2):142–151

Part III
Dynamics and Control of Aeroelastic and Fluid Dynamic Systems

Chapter 8
Intermittency in a Pitch-Plunge Aeroelastic System

J. Venkatramani, Sunetra Sarkar and Sayan Gupta

Abstract This chapter focuses on investigating the phenomenon of intermittency in the dynamical behavior of aeroelastic systems. To that end, a classical two degree-of freedom pitch plunge aeroelastic system is considered as the representative aeroelastic model. Investigations are first carried out on the route to aeroelastic flutter in fluctuating flow conditions through wind tunnel experiments. The recurring nature of intermittent periodic bursts observed in the pre-flutter response are subsequently utilized to develop quantitative measures using time series based tools, that can serve as precursors to flutter instability. To gain further insights into the experimental observations, numerical investigations are carried out using a well known two degree-of-freedom pitch plunge mathematical model for the aeroelastic system. A stochastic bifurcation analysis is also carried out that provide insights into the noise induced dynamical stability characteristics. Finally, a detailed study is undertaken to investigate the physical mechanisms that lead to the appearance of intermittency. Particularly, the effect of time scales of the flow fluctuations are investigated.

8.1 Introduction

The subject of aeroelasticity focuses on studying the effect of aerodynamical forces on elastic structures. Aeroelastic oscillations in elastic structures are sustained by the effect of the aerodynamic forces induced by the structural movement itself. Flutter is

J. Venkatramani (✉)
Department of Mechanical Engineering, Shiv Nadar University,
Greater Noida 201314, India
e-mail: j.venkatramani@snu.edu.in

S. Sarkar
Department of Aerospace Engineering, Indian Institute of Technology Madras,
Chennai 600020, India
e-mail: sunetra@iitm.ac.in

S. Gupta
Department of Applied Mechanics, Indian Institute of Technology Madras,
Chennai 600020, India
e-mail: sayan@iitm.ac.in

A. Mukhopadhyay et al. (eds.), *Dynamics and Control of Energy Systems*,
Energy, Environment, and Sustainability,
https://doi.org/10.1007/978-981-15-0536-2_8

an aeroelastic phenomenon in which a wing or control surface subjected to oncoming air stream can manifest sustained or growing oscillations beyond a critical value of the wind speed. Flutter oscillation is also referred to as self-induced oscillation as there are no external forcing agencies involved in the coupled fluid-structure system. In the presence of nonlinearities, the sustained oscillations are also known as limit cycle oscillations (LCOs). The appearance of LCOs in aeroelastic systems is considered undesirable, as it can induce fatigue damage in the structural components and affect the structural integrity, posing a threat to the structural safety (Schijve 2009). A wide range of aeroelastic systems like wind turbines, helicopter rotors, bridge-decks, array of panels etc are susceptible to flutter. This has made the study of flutter analysis and prediction an important area of research.

Estimating the flutter velocity essentially requires the stability analysis of the underlying fluid-structure interaction problem and has been studied thoroughly in the literature (Hauenstein et al. 1992; Dowell et al. 1995; Alighanbari and Price 1996; Lee et al. 1999; Dowell and Tang 2002; Patil and Hodges 2004; Sarkar and Bijil 2008). These studies are primarily aimed towards developing an understanding of the underlying dynamical system, linear or nonlinear. However, accounting for the nonlinearities that are ubiquitously present are challenges that these studies encounter (Abdelkefi et al. 2012). For example, estimation of system damping to predict flutter boundaries were carried out in Kehoe (1985), Dowell et al. (1995). However, the practicability of this technique in the presence of nonlinearities, measurement noise and in cases involving abrupt transitions to flutter is elusive. Using dynamic stability criteria, the Zimmermann-Weissenburger Methodology (ZWM) (Zimmerman and Weissenburger 1964) used a stability criterion to derive the flutter margin of a linear, two dof aeroelastic system under the assumption of quasi-steady aerodynamics. The aeroelastic equations of motion were cast into the form of an eigenvalue problem resulting in a fourth order characteristic equation. Routh's stability criterion was applied to this characteristic equation. The underlying principle in Routh's criterion is that a linear system is stable if the coefficients of its characteristic equation are positive. Subsequently, ZWM was employed to estimate flutter boundaries for aeroelastic systems with higher degrees of freedom as well (Price and Lee 1993). To predict nonlinear flutter responses such as LCOs, an "expert system" was developed in Popescu et al. (2009). The methodology was tested with airfoil response data acquired from both experiments and numerical simulations. The technique was developed in the presence of freeplay nonlinearity in the pitch dof. The nonlinear stiffness from the experimental setup was estimated and updated at regular intervals using a Kalman filter approach.

It should be noted that the model based prediction approaches are strongly dependent on the accuracy of the underlying models. With time, due to ageing and wear and tear, model parameters may change, thereby affecting the accuracy of the predictions. Regular updating of the models and the associated parameters are crucial in order to make model based tools effective. One can alternatively use time series analysis of measurement data for identifying flutter onset. Indeed, the use of time series methodologies and in turn time histories of the responses, captures the inherent changes in the system due to ageing effects. This approach avoids the need for

cumbersome task of regular model updating using inverse problems. However, such model free approaches to developing precursors to aeroelastic flutter has remained elusive.

Another key concern in aeroelastic problems is discerning the dynamical signature(s) and route to flutter. The flutter prediction techniques discussed in earlier parts are based on the assumption that the input flow is deterministic. However, in field conditions the flow is invariably accompanied by temporal fluctuations about a mean wind velocity. These fluctuations in the flow appear to lead to qualitatively different dynamical behavior in these aeroelastic systems. Consequently, the hitherto aeroelastic literature has devoted considerable attention towards gaining insights on the dynamical stability characteristics of the aeroelastic system in the presence of fluctuating flows.

Hitherto studies on the behaviour of stochastic dynamical systems have been shown to modify the bifurcation characteristics in comparison to their deterministic counterpart (Arecchi et al. 1985; Kim et al. 1997). Consequently, different metrics than those applied for deterministic systems are required for bifurcation analysis of stochastic dynamical systems and its interpretation (Horsthemke and Lefever 1984; Arnold and Crauel 1991; Ariaratnam 1994; Schenk-Hoppé 1996; Arnold 1998). By tracking the long-time behaviour of the response trajectories, using the largest Lyapunov exponent (LLE), the stability characteristics of deterministic systems are investigated. A change in the stability of the dynamical system is monitored through a change in the sign of the LLE (Wolf et al. 1985) and is accompanied by an abrupt change in the topology associated with the phase space of the system. This abrupt change in the topology is referred to in the literature as dynamical or D-bifurcation. For stochastic dynamical systems, the computation of the LLE is suitably modified to incorporate the average effect of the long-term behaviour of the trajectories.

For stochastic nonlinear dynamical systems, one also resorts to quantifying the long term behaviour of the trajectories is through the stationary joint probability density function (pdf) associated with the state variables. By tracking the topological changes in the structure of the pdf associated with the state variables, as a bifurcation parameter is varied, the long term behaviour of the dynamical system is qualitatively characterized. This is called as phenomenological or P-bifurcation. P- and D-bifurcations are dissimilar measures of the behaviour of stochastic nonlinear dynamical systems as time evolves. Consequently, the occurrence of these bifurcations need not be concurrent (Baxendale 1986; Crauel and Flandoli 1998). Hence, a necessity to develop an understanding of the behaviour of the bifurcation characteristics of such systems and interpret their long-term behaviour exists.

From the parlance of pitch-plunge aeroelastic systems, a series of numerical studies was undertaken by Poirel and Price (1997, 2007), Poirel (2001), to examine the response dynamics of a structurally nonlinear pitch-plunge airfoil in randomly fluctuating flows. A cubic hardening type of nonlinearity in the pitch dof was considered. The mean wind speed was taken to be the bifurcation parameter. The response dynamics and stability were described using the concepts of stochastic bifurcations. In the presence of random flow fluctuations, the response registered low amplitude oscillations with a noisy signature at wind speeds below the critical speed. The post

flutter LCOs showed fluctuations as well and were called random LCOs (Poirel 2001). Most importantly, unlike in the uniform flow conditions, where the response transitions to LCOs (flutter) at a well identifiable critical speed U_{cr}, under flow fluctuations the system transitions gradually. Along the way to fully grown LCOs, the response showed a tendency to both dynamical states (low amplitude noise as well as LCO), giving rise to a qualitatively distinct dynamical state that was not seen in uniform flow condition.

In order to analyse the different dynamical states, Poirel and Price (2001) investigated the system in terms of phenomenological (P-type) and dynamical (D-type) bifurcations. A P-bifurcation was said to occur when the joint-probability density function (j-pdf) of the response and its instantaneous derivative underwent a topological change in their structure, as the mean flow speed was changed. D-bifurcation, on the other hand, was said to occur when sign of the largest Lyapunov exponent (LLE) changes as the mean flow speed is varied. LLE is a measure of the long time behaviour of the response trajectories. A change in the sign of the LLE is indicative of a change in the stability of the dynamical system (Wolf et al. 1985) and is accompanied by an abrupt change in the topology associated with the phase space of the system. In the presence of longitudinal flow fluctuations, it was observed that the change in the sign of the LLE occurred at mean flow speeds lower than the corresponding uniform flow case (Poirel 2001; Poirel and Price 2001). On the contrary, the presence of fluctuations along the vertical direction alone revealed no change in the sign of the LLE at similar mean velocity regimes, indicating that the instability was suppressed (Poirel and Price 2007). These observations were supported by the findings of Zhao et al. (2009) as well.

Inability to interrelate the occurrence of P- and D- bifurcations result in difficulties in interpreting the dynamical behaviour of aeroelastic systems subjected to input flow fluctuations and in turn identifying their stability regimes. In uniform flow conditions, the transition in response dynamics from one state to the other occurs abruptly at a well identifiable flow velocity U_{cr} (critical speed). However, the presence of flow fluctuations can result in the system exhibiting dynamical signatures whose characteristics are distinctly different from their deterministic counterparts at flow speed regimes near the vicinity of U_{cr}. In particular, noisy flow fluctuations appear to result in a regime of intermittent oscillations that appear before the LCO regime (Poirel and Price 2001; Poirel et al. 2008; Andrianne and Dimitriadis 2019; Korbahti et al. 2011; Kalmár-Nagy et al. 2016). Investigating the response dynamics of aeroelastic systems subjected to input flow fluctuations therefore demand a systematic investigation.

Indeed, observations of noise-induced observations “on-off” type intermittency were encountered in the pre-flutter regime of an aeroelastic system subjected to noisy input flows (Poirel 2001). The presence of noisy flow fluctuations yielded in irregularly occurring windows of periodic-looking oscillations and was referred to as “on-off" intermittency. Such intermittent oscillations were also observed in wind tunnel experiments in Poirel et al. (2008) when bluff bodies were placed ahead of the wing. Qualitatively distinct intermittencies were experimentally observed in other types of aeroelastic systems as well, such as in bridge deck

flutter (Andrianne and Dimitriadis 2019) and in delta wing oscillations (Korbahti et al. 2011). It was observed from these experiments that the aeroelastic response was comprised of high-amplitude periodic bursts amidst low-amplitude aperiodic fluctuations and were encountered before the onset of fully developed LCOs. However, the physical reasoning behind the formation of two qualitatively different intermittency behaviors has not been addressed in the existing literature.

From the above discussion of the relevant literature, certain broad areas can be identified that demand further research attention that are examined in the following.

- The very first topic of practical interest to the aeroelastic community is the development of a robust prediction methodology for flutter. Substantial research attention has been devoted in the literature towards this direction. However, as was presented in the review of the literature, most studies investigate this under the uniform flow conditions. From a practical point of view, a sterile input flow is probably unrealistic and thereby puts a strong assumption on the overall analysis. Suitable tools that can accommodate the inherent fluctuations in the input need to be proposed.
- The next important issue is the resolution of the dynamics. In the presence of inherent fluctuations in the input wind model, the resulting dynamical behavior is largely unknown. Previous studies from the literature (Poirel 2001; Andrianne and Dimitriadis 2019; Korbahti et al. 2011) indeed suggest qualitatively different dynamical behavior in the presence of input fluctuations. This alters the route to flutter from a uniform flow situation. However, a detailed investigation of this modified dynamics has not been taken up in the existing literature. In order to predict and forewarn LCOs in a nonlinear system under input fluctuations, it is crucial to develop an in-depth understanding of the underlying dynamical characteristics.
  As discussed earlier, in the presence of input noise, a dynamical system can manifest noise induced intermittency behavior. This has been reported for aeroelastic systems as well. However, to the best of the knowledge of the authors, their dynamical characteristics have not been analyzed in details, nor their prognostic capabilities were investigated. The dynamics of intermittency observed in the pre-flutter regime requires a systematic investigation.
- It is also important to investigate the effect of the time scales (compared to the system time scales) present in the input fluctuations. It is intuitive that input fluctuations can occur across very different time scales due to various physical mechanisms like localized obstructions or seasonal effects. This variation can potentially affect the output dynamics and flutter onset, both qualitatively and quantitatively. To the best of the knowledge of the authors, this aspect has hardly been probed in the aeroelastic literature.
- Another important point of concern is the development of suitable models for the prediction of flutter (under fluctuating flow conditions). It is obvious that the accuracy of flutter prediction depend in turn on the accuracy of the mathematical model. This implies that one needs to estimate the parameters in the model accurately. This is not easy especially in the presence of nonlinearities. Moreover, for a structure that is already in use, fatigue and other ageing effects lead to the system parameters changing with time. This in turn implies that the mathematical model

should consider such effects into the equations. Alternatively, the parameters need to be estimated at regular intervals by solving an inverse problem. This can be computationally expensive and a tedious task. Therefore, a model free approach to flutter warning and prediction is a more desirable alternative. Such approaches can use the response data directly and develop qualitative or quantitative measures for the prediction. Use of dynamical tools such as those based on time series analysis can be utilised. This can provide effective model free approaches to flutter warning and prediction. This possibility has not been exploited by the aeroelastic community, to the best of the knowledge of the authors.

- In the presence of random input fluctuations, the bifurcation analysis of the underlying stochastic aeroelastic system (in order to predict the dynamical changes) may require alternative tools and interpretations. The available literature characterise stochastic bifurcations in terms of D- and P- bifurcations. D-bifurcation involves identifying stability regimes based on the change in sign of LLE. Typically, an abrupt cross over of LLE over one sign to another is an indicator of underlying change in the stability of the dynamical system. An additional metric to interpret the bifurcation of noisy systems is the inspection of the joint-pdf of the state variables, a qualitative change in it is called as P-bifurcation. This analysis is based on visual inspection and the stability regime qualitatively identified using P-bifurcation could be different from that obtained using the LLE (Poirel and Price 2007). Therefore, identifying changes in the response dynamics using P-bifurcation analysis could become difficult. Hence, developing alternative quantitative measures is required.

Recent studies by the authors Venkatramani et al. (2016, 2017a, b, 2018a, b) were focused towards obtaining answers to these open questions. These studies examined the dynamics of noisy aeroelastic system through a classical pitch-plunge aeroelastic system with cubic hardening nonlinearity in the plunge degree of freedom. The input flow fluctuations are assumed to exist in the in-plane, longitudinal direction and the aeroelastic responses are obtained by varying the mean flow speed as the bifurcation parameter. An overview of the methodology undertaken for the aeroelastic analysis, followed by a discussion on the findings from these studies are presented in this chapter.

The rest of this chapter is organized as follows. Section 8.2 presents the experimental methodology and the route to flutter in noisy case. Insights into the experimental findings are obtained through numerical simulations and the details of the same are presented in Sect. 8.3. A suite of measures that exploits the characteristic features of intermittency and can be used to forewarn flutter instability are introduced in Sect. 8.4. The intermittency route to flutter is examined in the light of stochastic bifurcations and the corresponding P- and D- bifurcation behavior are presented in Sect. 8.5. The physical mechanism for the appearance of intermittent bursts of oscillations in the pre-flutter responses are investigated in Sect. 8.6. The key findings from this study are summarized in Sect. 8.7.

8.2 Experimental Methodologies and Route to Flutter

An experimental frameware that permits pitch-plunge oscillations of an airfoil is developed and placed in a low speed wind tunnel available in the Biomimetics and Dynamics laboratory, Department of Aerospace engineering, IIT Madras. The tunnel can be operated in both suction and blow-down mode. In the latter, the air stream is made to approach the test section directly from the fan without passing through the honeycomb structure (the honeycomb helps in straightening the stream). The aeroelastic setup is based on the principle of a spring-cam mechanism as reported in O'Neil and Strganac (1998). However, indigenous changes to the bearing arrangements and plunging movements are made to reduce the moving mass and consequently minimize the frictional dissipations. The source of structural nonlinearity in the system arises due to the cubic nonlinear behavior of the springs being used along the plunge degree of freedom. A photograph and schematic of the experimental setup in the wind tunnel is shown in Fig. 8.1. A pair of Wenglor opto NCDT type laser sensors having a 300 mm measurement range and one micron resolution is used to acquire the pitch (α) and plunge (y) responses.

The wind tunnel experiments are conducted by operating the wind tunnel in the blowing conditions, and hence the flow is accompanied by irregular fluctuations about its mean value. The mean flow speed (U_m) is taken to be the control parameter. The experiments were initiated with U_m well below the flutter speed and the corresponding time histories of the plunge response is shown in Fig. 8.2. At $U_m = 4$ m/s, the response time history is observed to have low-amplitude oscillations; see Fig. 8.2a. As U_m is increased to 6 m/s, bursts of periodic oscillations amidst segments of low-amplitude oscillations are observed; see Fig. 8.2b. This phenomenon of the response alternating between two distinct dynamical behavior is called as intermittency. On further increasing U_m, the duration of periodic oscillations as well as their amplitude were observed to increase significantly; see Fig. 8.2c. Finally, at $U_m = 7.2$

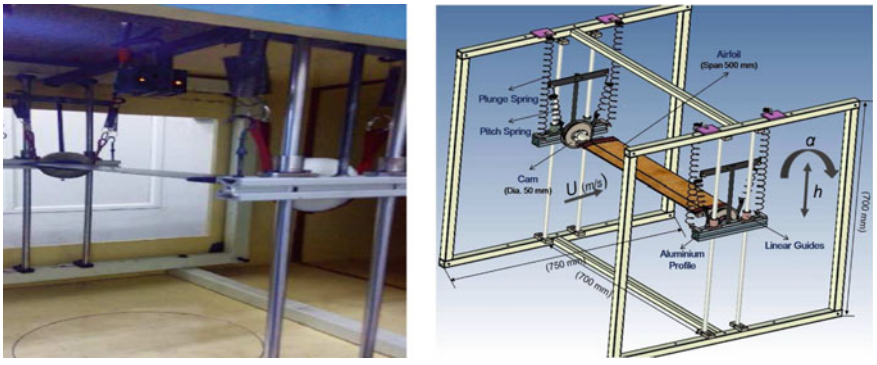

Fig. 8.1 Developed pitch-plunge experimental setup placed in the open loop wind tunnel. To the left the photograph of the setup is shown and its corresponding schematic is shown in the right hand side image. Reproduced with permission from Venkatramani et al. (2016)

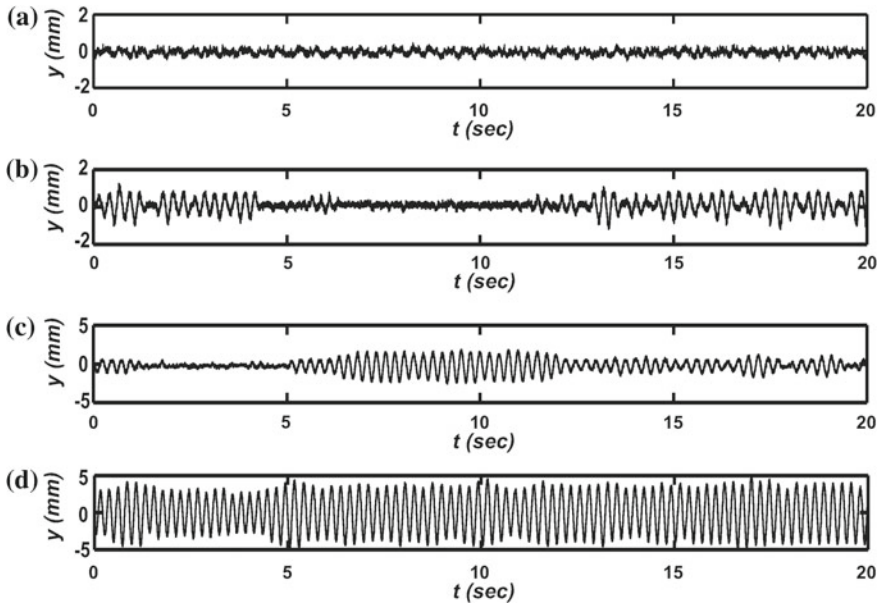

Fig. 8.2 Experimentally obtained plunge responses, $y(mm)$, of airfoil for mean flow speed **a** U_m = 4 m/s, **b** U_m = 6 m/s, **c** U_m = 6.6 m/s and **d** U_m = 7.2 m/s. Reproduced with permission from Venkatramani et al. (2016)

m/s, the response transitions to a fully developed LCO; see Fig. 8.2d. This intermittency route to flutter is not present in aeroelastic systems in uniform flow, where the system transitions from a fixed point to LCO via a supercritical Hopf bifurcation without the appearance of any intermittency.

8.3 Numerical Investigation

The experimental observations are validated through numerical investigations using a well known two degree-of-freedom pitch plunge mathematical model for the aeroelastic system (Fung 1955). However, some modifications are made to account for the contribution of moving mass along the pitch and plunge modes due to the fixtures in the experimental setup. The total mass of the system consists of three parts: m_1 is the additional mass in plunge corresponding to the moving frame, m_2 is the mass of the pitching mechanism and m_3 is the mass of the airfoil; see the schematic diagram of the airfoil presented in Fig. 8.3.

The total moving mass in plunge is $m_y = m_1 + m_2 + m_3$ and the total moving mass in pitch is $m_\alpha = m_2 + m_3$. The equations of motion along the plunge and the pitch degrees of freedom are given below in nondimensional form Marsden and Price (2007).

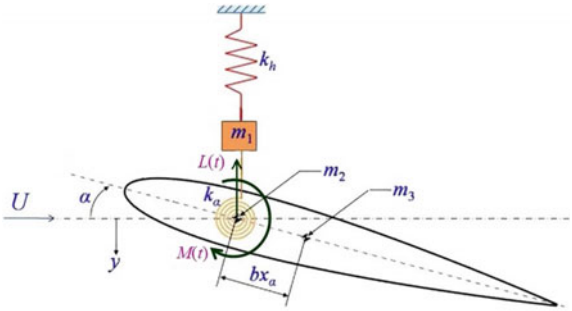

Fig. 8.3 Schematic of airfoil section model. Reproduced with permission from Venkatramani et al. (2016)

$$\epsilon'' + \frac{m_3}{m_y} x_\alpha \alpha'' + 2\zeta_\epsilon \frac{\overline{\omega}}{V} \epsilon' + \left(\frac{\overline{\omega}}{V}\right)^2 (\epsilon + \beta_\epsilon \epsilon^3) = -\frac{1}{\pi\mu} C_L(\tau), \tag{8.1}$$

$$m_3 b^2 \frac{x_\alpha}{I_\alpha} \epsilon'' + \alpha'' + 2\frac{\zeta_\alpha}{V} \alpha' + \frac{1}{V^2}(\alpha) = \frac{2}{\pi\mu {r_\alpha}^2} C_M(\tau). \tag{8.2}$$

Here, $\epsilon = y/b$ is the non-dimensional plunge displacement, b is the semichord of the airfoil, α is the pitch angle, $\mu = (m_y/\rho\pi b^2)$ is the total reduced mass of the airfoil per unit span, I_α is the moment of inertia about the elastic axis such that $I_\alpha = m_\alpha r_\alpha^2 b^2$, V is the nondimensional flow speed defined as $V = (U/b\omega_\alpha)$, U is the dimensional flow speed, $\overline{\omega}$ denotes the ratio of plunge (ω_y) to pitch (ω_α) natural frequencies, given by, $\overline{\omega} = (\omega_y/\omega_\alpha)$, τ is nondimensional time defined as $\tau = Ut/b$, t denotes the dimensional time, ζ_ϵ and ζ_α are the damping ratios in plunge and pitch respectively, β_ϵ is the nondimensional coefficient of nonlinear plunging stiffness, a_h is the nondimensional distance between elastic axis and midchord and x_α is the nondimensional distance between the center of mass and the elastic axis. Also, $(')$ refers to differentiation with respect to non dimensional time τ. The terms $C_L(\tau)$ and $C_M(\tau)$ respectively represent the aerodynamic lift and moment coefficients, and are represented as a set of coupled second order differential equations (Lee et al. 1999) of the following form

$$\begin{aligned} C_L(\tau) = {} & \pi(\epsilon''(\tau) - a_h\alpha''(\tau) + \alpha'(\tau)) + 2\pi[\alpha(0) + \epsilon'(0) + (0.5 - a_h)\alpha'(0)]\phi(\tau) \\ & + 2\pi \int_0^\tau \phi(\tau - \sigma)[\alpha'(\sigma) + \epsilon''(\sigma) + (0.5 - a_h)\alpha''(\sigma)]\mathrm{d}\sigma, \end{aligned} \tag{8.3}$$

$$\begin{aligned} C_M(\tau) = {} & \pi(0.5 + a_h)[(\alpha(0) + \epsilon'(0) + (0.5 - a_h)\epsilon'(0))]\phi(\tau) \\ & + \pi(0.5 + a_h) \int_0^\tau \phi(\tau - \sigma)[\alpha'(\sigma) + \epsilon''(\sigma) + (0.5 - a_h)\alpha''(\sigma)]\mathrm{d}\sigma \\ & + \tfrac{\pi}{2} a_h(\epsilon''(\tau) - a_h\alpha''(\tau)) - (0.5 - a_h)\tfrac{\pi}{2}\alpha'(\tau) - \tfrac{\pi}{16}\alpha''(\tau). \end{aligned} \tag{8.4}$$

Here, $\phi(\tau)$ is the Wagner's function. Equations (8.3)–(8.4) represent the unsteady aerodynamic model which takes into account the effect of a trailing wake behind the

airfoil. A canonical model for the input flow fluctuation is assumed of the form

$$V(\tau) = V_m + f(\tau), \tag{8.5}$$

where, $f(\tau) = \sigma V_m \sin(\tau\omega_r(\tau))$, V_m is the nondimensional mean wind speed, σ is the amplitude of the fluctuating component taken to be of $\mathcal{O}(1)$, ω_r is the frequency of the sinusoid, adjusted such that, $\omega_r(\tau) = \omega_0 + \kappa R(\tau)$, κ is a constant of $\mathcal{O}(\omega_0)$ and R is a uniformly distributed random number in [0, 1].

The time histories of the nondimensional plunge response are obtained from numerical integration for various values of V_m and are shown in Fig. 8.4. As expected periodic bursts appear with an increase in V_m and is qualitatively consistent with the observations from the wind tunnel experiments. Finally, well developed LCOs are obtained on further increasing V_m; see Fig. 8.4d. In the absence of input flow fluctuations, *i.e.,* when $f(\tau) = 0$, and $V(\tau) \equiv V_m \equiv V$, the route to flutter occurs via a supercritical Hopf bifurcation as shown in Fig. 8.5.

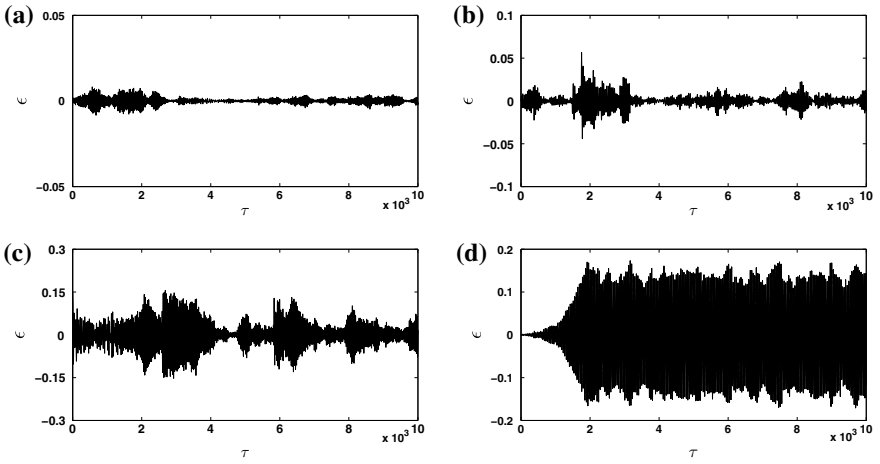

Fig. 8.4 Plunge response from numerical model; **a** $V_m = 2.96$, **b** $V_m = 3.4$, **c** $V_m = 4.4$ and **d** $V_m = 5.1$. Note that these mean flow speeds in the dimensional values correspond to those presented in Fig. 8.2. Reproduced with permission from Venkatramani et al. (2018b)

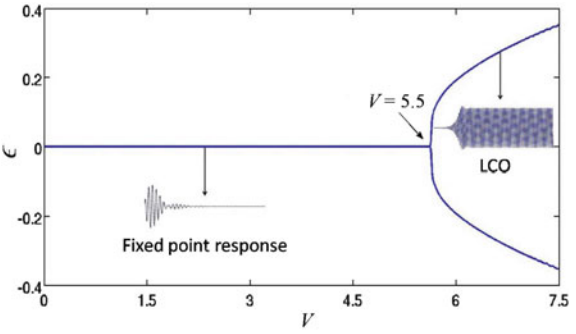

Fig. 8.5 Transformation of the plunge response into sustained LCOs via a supercritical Hopf-bifurcation as V is varied. The onset of flutter is at $V = 5.5$ and corresponds to a dimensional value of 7.45 m/s. Reproduced with permission from Venkatramani et al. (2018b)

8.4 Precursors to Aeroelastic Flutter

The intermittent oscillations that presage fully developed LCOs in aeroelastic systems is next exploited to develop precursors for predicting flutter. A suite of time series analysis based measures are developed as potential precursors. The development of these measures are based on (i) recurrence quantification analysis, (ii) scaling structures, such as, generalised Hurst exponents, (iii) statistical entropy based measures, such as, Approximate and Sample entropy, and (iv) complexity based measures, such as Lempel-Ziv complexity (Yan and Gao 2007).

The underlying principle of recurrence quantification analysis, involves quantifying the Euclidean distance of nearest neighbours in the phase space (Marwan et al. 2007) and developing measures based on (a) the trapping time τ_0 of the trajectories within a domain in the phase space, and (b) Shannon entropy H_s for the length of the lines in the recurrence plots. We commence our precursor measure development first from recurrence plots. Sample recurrence plots for a few cases of time histories of the plunge response are shown in Fig. 8.6. Note that at $U_m = 4$ m/s, the response consists of a low-amplitude aperiodic fluctuations and the corresponding recurrence plot shown in Fig. 8.6a comprises of grainy black dots spread out irregularly over the domain. Increasing U_m to 6 m/s intermittent bursts of periodic oscillations can be noticed in the response dynamics. This leads to the recurrence plot exhibiting more regular characteristics as seen in Fig. 8.6b. Finally at $U_m = 7.2$ m/s, large amplitude periodic oscillations (LCOs) are encountered. Correspondingly, one can observe the recurrence plot to comprise of clear regular patterns of diagonal lines parallel to one another; see Fig. 8.6c.

An alternative precursor based on the multifractality of the oscillations have been derived. Scaling structures in a signal are indicative of the growth in fluctuations of different amplitudes in different segments of a time signal. The presence of different scaling structures in a time series is an indication of a multifractal signature (Kantelhardt et al. 2001) and is quantified using generalised Hurst exponents H_q.

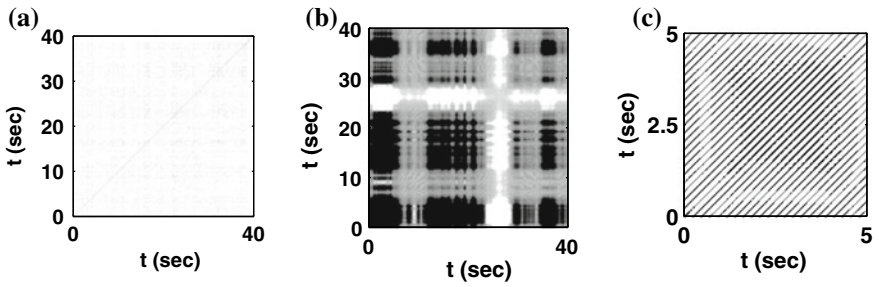

Fig. 8.6 Recurrence plots corresponding to the transformation of the response from a state of aperiodic to LCOs via intermittency is shown. The cases correspond to mean flow speed of **a** U_m = 4 m/s **b** U_m = 6.6 m/s and **c** U_m = 7.2 m/s. Reproduced with permission from Venkatramani et al. (2018a)

The Shannon entropy—which is a statistical measure of the disorder in a signal—can also be used to quantify the different regimes of dynamical behavior in these systems. Here, Shannon entropy based measures, such as the Approximate entropy H_{AE} and Sample entropy H_{SE} have been used as precursor measures. Complexity measures, such as Lempel-Ziv complexity (LZC) quantifies the rate of emergence of new patterns in a time signal (Lempel and Ziv 1976). Note that the term of complexity refers to the presence of unpredictable or irregular patterns in a time series. All these measures have been shown to be useful in capturing the change in the dynamics from an aperiodic state to a periodic one via intermittency; see Fig. 8.7. The theory and computational details of these measures are detailed in Venkatramani et al. (2018a) and are not repeated here.

The measures shown in Fig. 8.7 are computed using the time histories of the response obtained from the wind tunnel experiments. It is evident that all these measures undergo a smooth change in magnitude in the intermittency regime, and approaches a stable value as U_m is increased beyond flutter. The ability of these measures to manifest a change in their trends well in advance, before the appearance of LCOs, highlights that these measures can serve as robust precursors to aeroelastic

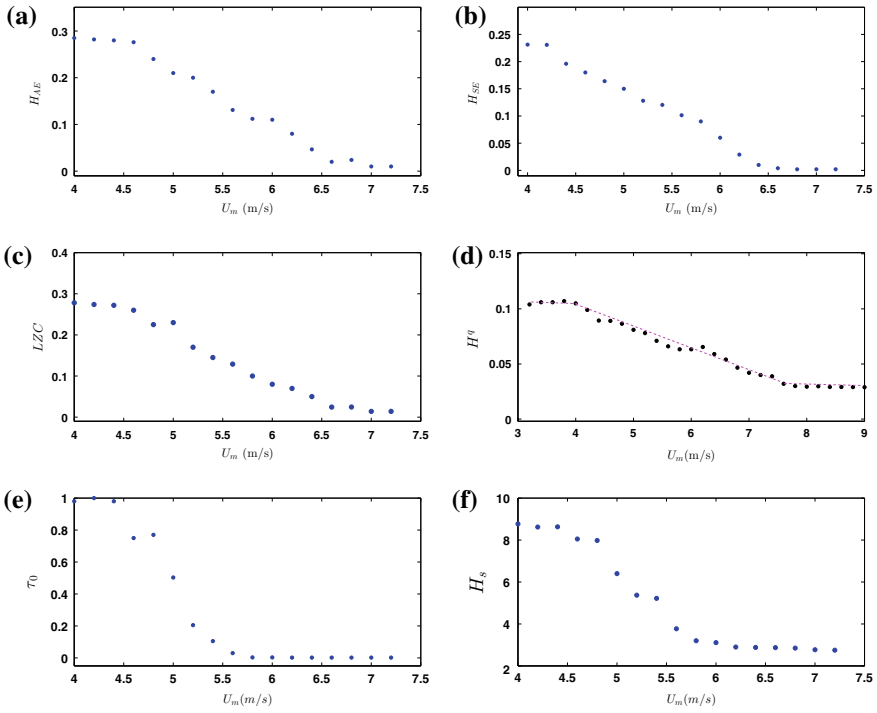

Fig. 8.7 Variation of **a** H_{AE}, **b** H_{SE}, **c** LZC, **d** H^q, **e** τ_0 (trapping time from recurrence plot) and **f** H_s (Shannon entropy from recurrence plot), with U_m. Reproduced with permission from Venkatramani et al. (2018a)

Table 8.1 Time taken (in seconds) to compute the precursor measures

Measure	τ_0	H_s	H^q	H_{AE}	H_{SE}	LZC
Time for computation	95	95	324	218	16.9	8.5

flutter. These precursor measures are based on time series analysis of experimentally measured data and do not require the development of an equivalent mathematical model. Thus, these methods are more useful for online health monitoring in comparison to model based methods which require periodic model updating to take into account the material degradation that invariably occur due to ageing and the consequent changes in the dynamical stability boundaries.

The utility of these measures as structural health monitoring tools is investigated based on their dependence on the length of the time signal and the computational cost associated in estimating these measures. Estimating the precursor measures discussed in the previous section using every fourth data point from the experimentally measured time histories of the response showed that the quantitative values and trends get affected in measures, such as, H_{AE} and H_q, indicating their dependence on the data size. On the other hand, measures such as LZC and H_{SE} showed minimal qualitative or quantitative change. The computational time required to estimate these measures are presented in Table 8.1. It can be seen that the LZC and H_{SE} require the least computational time. Coupled with the fact that they do not place heavy demands on the size of the data set, LZC and H_{SE} were found to be most suitable for online health monitoring strategies.

8.5 Identifying Stability Regimes Using Stochastic Bifurcations

A bifurcation analysis of the system is carried out next to identify the dynamical stability regimes. Since the flow is accompanied by random fluctuations, the bifurcation analysis of the stochastic system requires alternative tools and interpretations. To that end, we compute the LLE and track its sign change as the mean flow speed is varied. In the case of input fluctuations, the mathematical expression for LLE is suitably modified and is estimated as

$$\lambda_{\max} = \max\left\{ \lim_{\tau \to \infty} \mathrm{E}\left[\frac{1}{\tau} \ln \frac{||\mathbf{u}(\tau)||}{||\mathbf{u}(0)||} \right] \right\}, \tag{8.6}$$

where, E[·] is the expectation operator and $\mathbf{u}(\tau) : \tau \geq 0$ are the solution trajectories of the linearized form of Eqs. (8.1)–(8.2). Figure 8.8 presents the variation of the LLE (computed from the numerical model results) with V_m (nondimensional mean flow speed) as the bifurcation parameter. An inspection of Fig. 8.8 shows that at $V_m \approx 5.1$

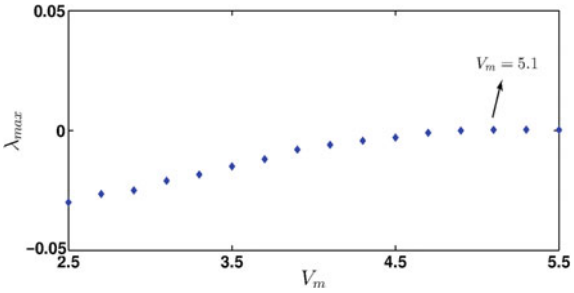

Fig. 8.8 Evolution of LLE as V_m is varied. At about $V_m = 5.1$, a change in the sign of LLE is observed. Reproduced with permission from Venkatramani et al. (2018b)

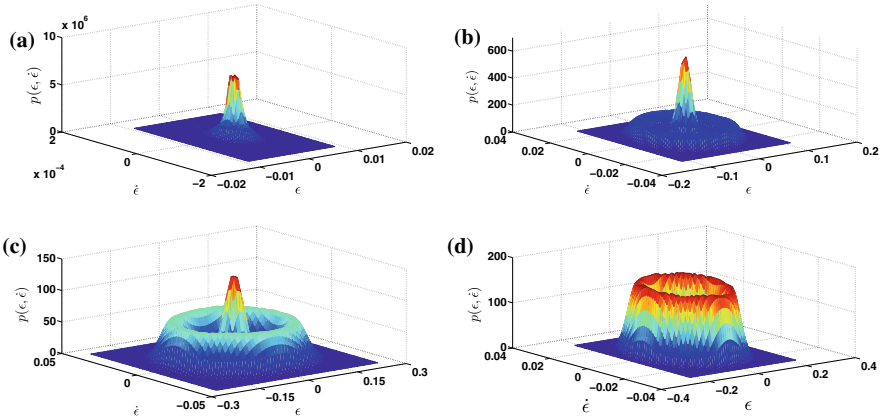

Fig. 8.9 Stationary joint probability density function of plunge response and its instantaneous derivative $p_{\epsilon,\dot{\epsilon}}(\epsilon, \dot{\epsilon})$ for V_m = **a** 2.96, **b** 3.4, **c** 4.4 and **d** 5.1. Reproduced with permission from Venkatramani et al. (2018b)

the LLE undergoes a sign change. As the Hopf bifurcation occurred at $V = 5.5$ in uniform flow conditions as shown in Fig. 8.5, it indicates that fluctuations in the flow leads to the system losing dynamical stability at V_m lower than that in uniform flow conditions. This finding is in-line with that presented in the aeroelastic literature (Poirel 2001; Zhao et al. 2009).

Next, we conduct a P-bifurcation analysis, by visually inspecting topological changes in $p(\epsilon, \dot{\epsilon})$ as V_m is varied. Figure 8.9 shows representative joint pdfs $p(\epsilon, \dot{\epsilon})$ at specific values of V_m. A visual inspection of $p_{\epsilon,\dot{\epsilon}}(\epsilon, \dot{\epsilon})$ show that at $V_m = 2.96$, the topology represents that of a unimodal structure centered about the origin; see Fig. 8.9a. As V_m is increased to 3.4, as shown in Fig. 8.9b, the j-pdf structure shows that a peak at the origin continues to exists, albeit with lower strength, along with a ring like structure appears to form around the peak at the origin. An increase in V_m results in formation of complete crater like structure indicating fully developed LCOs. A visual inspection of the j-pdfs reveal that with change in V_m, a topological

change in the probability structure exist, qualitatively indicating the occurrence of a P-bifurcation.

An inspection of D- and P-bifurcation regimes clearly reveal that they do not occur simultaneously. This is not surprising as these are different measures. Moreover, identification of the P-bifurcation boundaries are essentially based on visual inspection and is therefore qualitative. In this study, the P-bifurcation regime is quantified using a newly developed quantitative measure (Kumar et al. 2016). This involves defining an envelope process A, defined as $A = \sqrt{(\epsilon^2 + \dot{\epsilon}^2)}$. A essentially quantifies the volume of the attractors in the state space. The probability distribution function $F_A(a)$ can be evaluated numerically from the joint pdf as

$$F_A(a) = \int \int_{\sqrt{(\epsilon^2+\dot{\epsilon}^2)} \leq a} p_{\epsilon,\dot{\epsilon}}(\epsilon, \dot{\epsilon}) \mathrm{d}\epsilon \mathrm{d}\dot{\epsilon}. \tag{8.7}$$

A numerical differentiation of $F_A(a)$ yields the corresponding marginal pdf $p_A(a)$. Figure 8.10 shows the corresponding 1-D pdfs. A simple quantitative measure that captures the qualitative changes occurring in the pdf structure of $p_A(a)$ is the Shannon entropy measure defined as Shannon (2001)

$$H(x,t) = -\int_{-\infty}^{\infty} p(x,t) \log_b p(x,t) \mathrm{dx} \tag{8.8}$$

Figure 8.11 shows the computed Shannon entropy for $p_A(a)$ as a function of V_m. Kumar et al. (2016) suggested that the crossing of the Shannon entropy $H(a)$, across the zero level from below can be identified as the onset of P-bifurcation and a crossing of the zero level from above as the completion of P-bifurcation. However, the choice of the datum level is arbitrary. Instead a new datum level is selected here based on the entropy measure prior to the onset of intermittency. An inspection of Fig. 8.11 reveals that $H(a)$ is almost identical for the first two data points. The corresponding entropy value is thus considered to be the datum (shown as a dashed line in Fig. 8.11). It can be observed from Fig. 8.11 that this leads to identifying the onset of P-bifurcation to be at $V_m \approx 2.8$ and is completed at $V_m \approx 4.8$. These values closely resemble the onset of intermittency and the onset of fully developed LCOs observed from the time histories of the response.

8.6 Physical Mechanism of Intermittency

The physical mechanisms that lead to intermittent oscillations in the presence of fluctuating flows is investigated next. Preliminary investigations reveal that the time scales of the fluctuations play an important role in the appearance of intermittency. To investigate the role of time scales of the fluctuations, two qualitatively different input fluctuating flow models are considered (a) flows that involve long time scales having a large correlation length and (b) rapidly fluctuating flows whose correlation

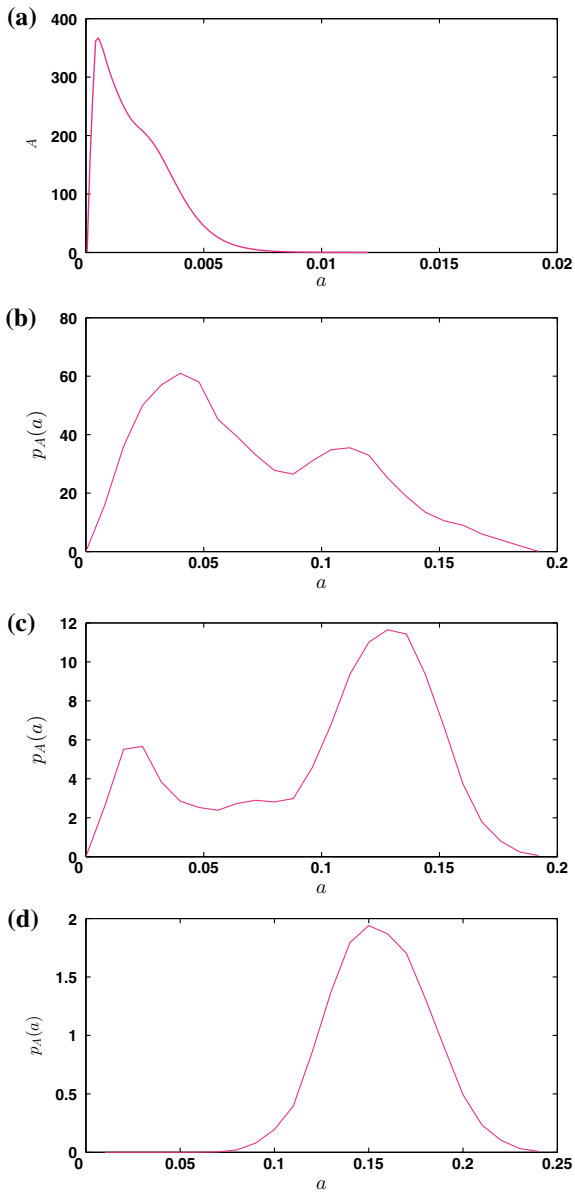

Fig. 8.10 Probability density function $p_A(a)$ for **a** $V_m = 2.96$, **b** $V_m = 3.4$, **c** $V_m = 4.4$ and **d** $V_m = 5.1$. Reproduced with permission from Venkatramani et al. (2018b)

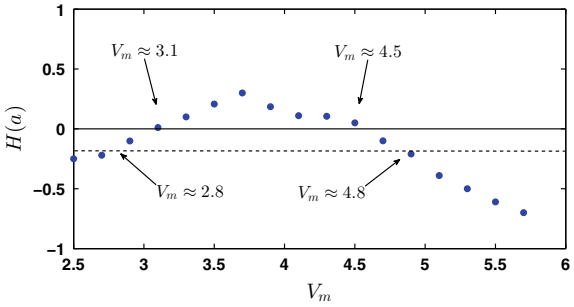

Fig. 8.11 Evolution of $H(a)$ as V_m is varied. Reproduced with permission from Venkatramani et al. (2018b)

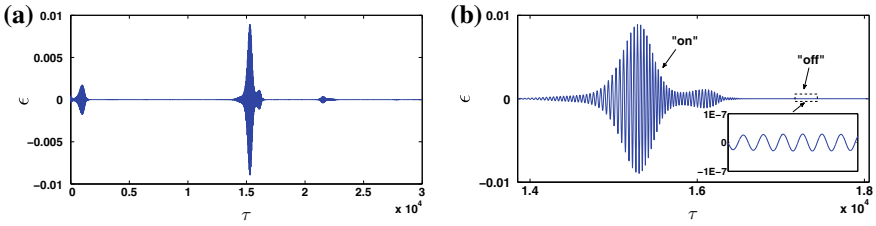

Fig. 8.12 "On-off" intermittency encountered at **a** $V_m = 2.96$, **b** zoomed view of **a**, **c** $V_m = 4.4$ and (d) $V_m = 5.1$. The flows possess long time scale fluctuations. Reproduced with permission from Venkatramani et al. (2017b)

length appears as a Dirac-delta function in comparison to the time scales of the system response. Defining the system time scale τ_{sys} as the reciprocal of the flutter frequency, fluctuations are defined to be of long time scales if $\tau_c \gg \tau_{sys}$ and when $\tau_c \ll \tau_{sys}$, the fluctuations are said to possess short time scale fluctuations.

As a first step, the flow is assumed to fluctuate with long time scales and is provided as input to Eqs. (8.1)–(8.2). A typical response time history for $V_m = 2.96$ is shown in Fig. 8.12a. In Fig. 8.12b an enlarged section of the same is shown for clearer visualization. The time history of the response is observed to consist of well defined states of "rest" interspersed by segments of amplitude modulated oscillations. A zoomed view of the "off" state as shown in inset in Fig. 8.12b reveals fluctuations of $\mathcal{O}(10^{-7})$ even in the "off" state. However, for all intents and purposes, these fluctuations are small enough to be negligible. Note that these intermittency behavior is qualitatively different from those observed from the wind tunnel experiments (Fig. 8.2). This dynamical behavior conforms to the "on-off" type intermittency (Platt et al. 1993).

On the other hand, use of short time scale flow fluctuations, result in the time histories as shown in Fig. 8.13. It is obvious that the intermittent time history looks qualitatively close to the experimental observations but very different from the "on-off" intermittency shown in Fig. 8.12a. The response comprises of periodic bursts

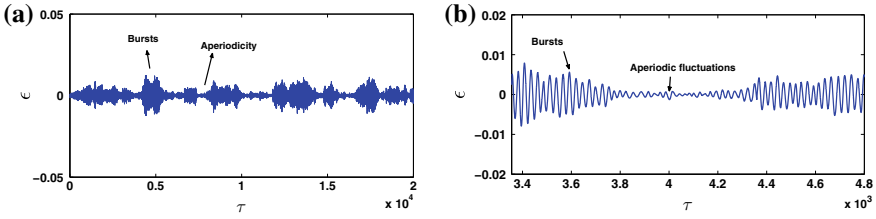

Fig. 8.13 "Burst" type intermittency encountered at **a** $V_m = 2.96$. A zoomed view of **a** is shown in **b**. The corresponding input flow possesses short time scale fluctuations. Reproduced with permission from Venkatramani et al. (2017b)

of relatively high amplitude modulated oscillations and low amplitude aperiodic oscillations occurring irregularly. A zoomed response of Fig. 8.13a is shown in Fig. 8.13b. A comparison of the response behavior shown in Figs. 8.12 and 8.13 indicates that though intermittency can occur in the presence of fluctuating flows, their qualitative characteristics depend on the time scales of the fluctuations. In this study, this switching between two qualitatively different and irregularly occurring response windows as observed in Fig. 8.13 is referred to as "burst" type intermittency, in order to distinguish the behavior from the "on-off" type intermittency observed in Fig. 8.12.

The mechanism of "on-off" intermittency can be explained using the dynamical systems theory (Platt et al. 1993). When the flow $V(\tau)$ stays over the critical speed V_{cr} for sufficient durations, the system displays an oscillatory behavior or the "on" state. Similarly, when $V(\tau) < V_{cr}$ for sufficiently large time windows, a damped response or "off" state is observed in the system. Repetition of this process over time yields an "on-off" type intermittent behavior (Platt et al. 1993). An illustration of the mechanism of "on-off" intermittency, a zoomed section of the "on-off" states along with the corresponding input flow fluctuation is shown in Fig. 8.14. Here, the time segments for which the instantaneous flow velocity exceeds the critical value ($V(\tau) > V_{cr}$) is denoted as τ_u^i, where i indicates the i^{th} such window in a time history. Likewise, the time segments corresponding to $V(\tau) < V_{cr}$ is represented as τ_l^j. From Fig. 8.14, one observes that when the stay of $V(\tau)$ over V_{cr} is for sufficiently large durations (τ_1^i), a corresponding increase in the amplitude of the response is noticed. Note that a time lag between the commencement of τ_1^i and the manifestation of a fully "on" state can be observed as well. Similar observations can be made on the stay of $V(\tau)$ below V_{cr} for the decay of the response. This substantiates the notion that the stay of $V(\tau)$ over and below V_{cr} for sufficient durations can give rise to an "on-off" type intermittency. For the appearance of the "burst" type intermittency (under short time scale flows) is not trivial to present mechanisms as it was in the case of an "on-off" type intermittency. Owing to the rapid input flow fluctuations, it is unlikely that the system dynamics stays above or below the critical value for durations considerable enough for the system time scales to become predominant. As per this argument, the aeroelastic response should not manifest intermittent oscillations at all.

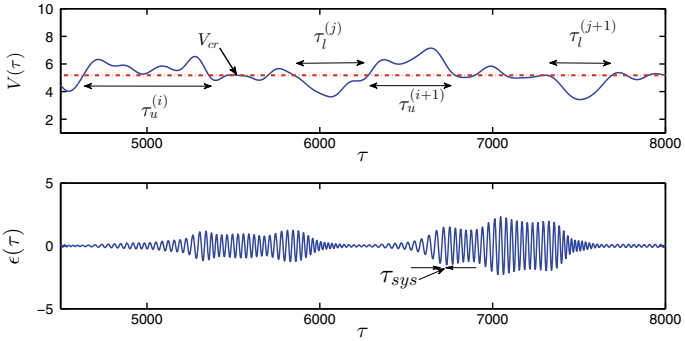

Fig. 8.14 Illustration of the mechanism of "on-off" intermittency. Reproduced with permission from Venkatramani et al. (2017b)

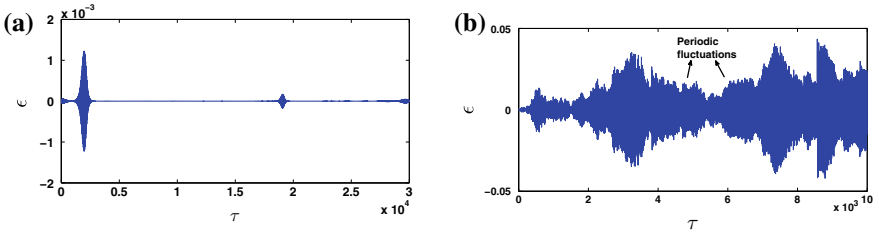

Fig. 8.15 Airfoil response with quasi-steady aerodynamics formulation. **a** "on-off" intermittency is observed to exist under predominantly long scales in input fluctuations. **b** A modulated periodic response is encountered when the flow is rapidly fluctuating. Reproduced with permission from Venkatramani et al. (2017b)

Therefore, it likely that an ancillary mechanism that slows down the input fluctuations to result in intermittency must exist. It is possible that the wake model (present in Eqs. 8.3 and 8.4) is a potential candidate for ensuring the same. To investigate the role of the unsteady wake, a quasi-steady aerodynamics model that ignores the wake effect is considered. It is observed that the long time scale flow fluctuations are still able to generate "on-off" type intermittency behavior. However, the short time scale case does not manifest the same "burst" type intermittency. This supports the conjecture that the unsteady wake does play a key role in developing intermittency in the aeroelastic system; see Fig. 8.15. More details on these investigations can be found in Venkatramani et al. (2017b).

Next, we resort to investigating the time frequency content the observed intermittent signals. To that end, a continuous wavelet transform for both "on-off" and "burst" type intermittency is carried out and the obtained scalograms are presented in Figs. 8.16 and 8.17 respectively. From the scalogram in Fig. 8.16, one can observe that the "on" regime exhibits oscillations with nondimensional frequency of about 0.03. Note that as shown in the inset these oscillations are periodic. The oscillations

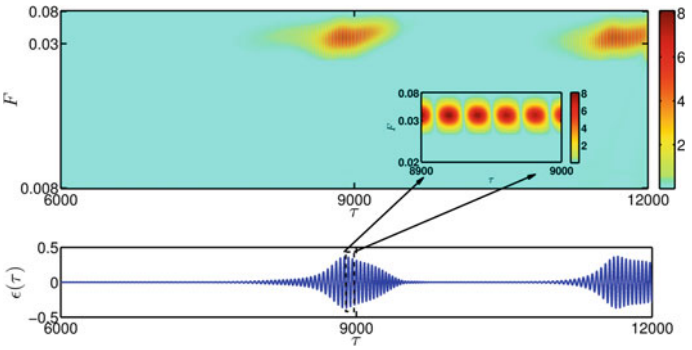

Fig. 8.16 Time-frequency content for "on-off" intermittency at $V_m = 4.4$. Reproduced with permission from Venkatramani et al. (2017b)

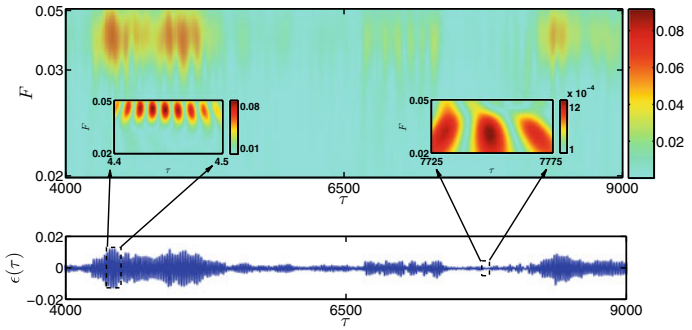

Fig. 8.17 Time-frequency content for "burst" type intermittency at $V_m = 2.96$. Reproduced with permission from Venkatramani et al. (2017b)

corresponding to the "off" regime, (as can be seen in Fig. 8.12b) are of $\mathcal{O}(10^{-7})$ and are hence negligible and therefore not visible in the scalogram.

Visually inspecting Fig. 8.17, one observes that during the "burst" type intermittency, oscillations in the aperiodic regimes exists. For clearer visualization, inset images are shown. From the same, it is obvious that the burst regime possesses oscillations with relatively larger amplitude and with a nondimensional frequency of about 0.03 along with some smaller frequencies. Typically, the smaller frequencies can arise from variations in the time histories of the responses. On the other hand, one can observe from the inset that during the aperiodic regime, different scales co-exist and that these regimes are defined through a broad band of frequencies with lower relative strength—with the broadband nature arising due to the aperiodicity.

8.7 Summary and Concluding Remarks

This study focused on characterizing intermittency observed in the response of nonlinear pitch plunge aeroelastic system in the presence of input fluctuating flows. Wind tunnel experiments conducted on a NACA 0012 profile under input flow fluctuations showed that the onset of sustained LCOs is presaged by an intermediate regime of oscillations called intermittency. It was observed that the regime of intermittency possessed an irregular switching between low-amplitude aperiodic oscillations and large amplitude periodic burst oscillations. Increasing the mean flow speed systematically resulted in a frequent appearance of the periodic bursts with larger amplitude. Further increase in the mean flow speed led to the development of large amplitude periodic oscillations marking the onset of flutter. Probing into the underlying dynamical structure of intermittency showed that scales of different order are present indicating a multifractal signature. The extent of multifractality diminished as the mean flow speed approaches the flutter boundary. At the onset of LCOs, it was observed that there is a total collapse of the multifractal signature, indicating the emergence of a predominant scale.

Exploiting the characteristic features of intermittency, a suite of model free measures to forewarn aeroelastic flutter were developed. The recurring nature of burst oscillations were utilized to provide early warning signals to an impending flutter using recurrence quantification analysis. The gradual decay of extent of multifractality was quantified using representative measures such as Hurst exponents. The Hurst exponent measure was demonstrated to successfully warn flutter well in advance, from the regime of intermittency itself. Entropy based measures such as approximate entropy and sample entropy and complexity based measure such as Lempel-Ziv complexity were also developed to forewarn flutter by utilizing the characteristic features of intermittency. It was shown that each of these measures can successfully forewarn an impending flutter well before its onset. Investigations were carried out to draw the relative merits of the proposed precursor measures. It was found that the Lempel-Ziv complexity measure is more practically viable for the purpose of on-line health monitoring of aeroelastic structures. A corresponding numerical investigation revealed that in the absence of flow fluctuations, the aeroelastic response transforms itself into sustained LCOs via a supercritical Hopf bifurcation. However, the presence of noisy input flow fluctuations, modelled using a canonical representation, results in the formation of intermittency in the pre-flutter responses. The numerically obtained time responses also displayed a qualitatively similar multifractal behavior that collapsed as LCOs were set in the aeroelastic system.

A stochastic bifurcation analysis in terms of P- and D- bifurcations were carried out. D-bifurcation involved identifying stability regimes based on the sign change in LLE. It was found that LLE of the noisy system underwent a change in sign earlier in comparison to its deterministic counterpart. This implies that the input flow fluctuations can influence the stability regimes. P-bifurcation analysis was carried out by visually inspecting the topological changes in the joint-pdf of the state variables. Since this analysis is qualitative, identifying stability regimes based on P-bifurcation

analysis becomes a difficult task. A quantitative measure based on Shannon entropy was used to estimate the boundaries of P-bifurcation. It was observed that the boundaries of P-bifurcation coincided with the flow regimes in which intermittency was observed in the aeroelastic response.

To gain insights into the physical mechanisms of intermittency in aeroelastic responses, the role of time scales in the input flow fluctuations were investigated. Two isolated cases of flow fluctuations were considered, namely, one involving very long time scales and another involving extremely short time scales as input to the aeroelastic system. It was found that flows with predominantly long time scales gave rise to "on-off" type intermittency in the aeroelastic responses. These responses were characterized by the sporadic appearance of large amplitude periodic oscillations interspersed amidst states of rest. On the other hand, the short time scale input fluctuations gave rise to a qualitatively different intermittency ("burst" type intermittency) characterized by switching of response dynamics between periodic "bursts" and aperiodic fluctuations. It was shown that manifestation of "on-off" intermittency is due to the traverse of the response over and below the critical speed for sufficient durations. However, the mechanism for the "burst" type intermittency was found to require an ancillary mechanism that slows down the effect of rapid input fluctuations and result in the appearance of intermittency. An investigation into the aerodynamic forces suggested that the unsteady wake effects could provide the necessary slow down effects in the case of short time scale input fluctuations. Suppressing the unsteady wake effects using a quasi-steady aerodynamic model and using short time scale fluctuations resulted in the absence of intermittency confirming the key role played by unsteady wake effects in the manifestation of intermittency. A set of measures were used to provide a quantitative distinction to the qualitatively different intermittency, namely, measures from recurrence plots, fractional occupation time and time-frequency representation using wavelets. These measures provided quantitative evidence that during "on-off" intermittency, a periodic "on" state and a region of rest state ("off") exists and during "burst" intermittency, an irregular switch over between the periodic bursts and aperiodic oscillations occur.

Disclaimer The figures and tables used in this chapter are reproduced with permission from Venkatramani et al. (2016, 2017a, b, 2018a, b). Excerpts from parts of Venkatramani et al. (2017b, 2018a, b) are also re-used here with appropriate permissions.

References

Abdelkefi A, Vasconcellos R, Marques F, Hajj M (2012) Modeling and identification of free play nonlinearity. J Sound Vib 331:1898–1907

Alighanbari H, Price SJ (1996) The post-hopf-bifurcation response of an airfoil in incompressible two-dimensional flow. Nonlinear Dyn 10:381–400

Andrianne T, Dimitriadis G (2019) Experimental analysis of the bifurcation behavior of a bridge deck undergoing across-wind galloping. In Proceedings of the 8th international conference on structural dynamics, EURODYN, Leuven Belgium. ISBN 978-90-760-1931-4

Arecchi F, Badii R, Politi A (1985) Generalized multistability and noise-induced jumps in a nonlinear dynamical system. Phys Rev A 32:402
Ariaratnam A (1994) Some illustrative examples of stochastic bifurcations. In Nonlinearity and chaos in engineering dynamics. Wiley, New York (1994)
Arnold L (1998) Random dynamical systems. Springer, New York
Arnold L, Crauel H (1991) Random dynamical systems. Lecture notes in mathematical, vol 1486, pp 1–22
Baxendale PH (1986) Asymptotic behaviour of stochastic flows of diffeomorphisms: two case studies. Probab Theory Relat Fields 73:51–85
Crauel H, Flandoli F (1998) Additive noise destroys a pitchfork bifurcation. J Dyn Differ Equs 10:259–274
Dowell E, Tang D (2002) Nonlinear aeroelasticity and unsteady aerodynamics. AIAA J 40:1697–1707
Dowell EH, Crawley EE, Curtiss HC Jr, Peters DA, Scanlan RH, Sisto F (1995) A modern course in aeroelasticity. Kluwer Academic Publishers, Dordrecht
Fung Y (1955) An introduction to the theory of aeroelasticity. Wiley, New York
Hauenstein A, Zara J, Eversman W, Qumei I (1992) Chaotic and nonlinear dynamic response of aerosurfaces with structural nonlinearities. AIAA J 92
Horsthemke W, Lefever R (1984) Noise-induced transitions in physics, chemistry, and biology, noise-induced transitions: theory and applications in physics, chemistry, and biology, pp 164–200
Kalmár-Nagy T, Csikja R, Elgohary TA (2016) Nonlinear analysis of a 2-DOF piecewise linear aeroelastic system. Nonlinear Dyn 85:739–750
Kantelhardt J, Kosciekny-Bunde E, Rego H, Havlin S, Bunde A (2001) Detecting long-range correlations with detrended fluctuation analysis. Phys A 295:441–454
Kehoe M (1985) A historical overview of flight flutter testing, NASA TM-4270
Kim S, Park SH, Ryu CS (1997) Noise-enhanced multistability in coupled oscillator systems. Phys Rev Lett 78:1616
Korbahti B, Kagambage E, Andrianne T, Razak N, Dimitriadis G (2011) Subcritical, nontypical and period-doubling bifurcations of a delta wing in a low speed wind tunnel. J Fluids Struct 27:408–426
Kumar P, Narayanan S, Gupta S (2016) Investigations on the bifurcation of a noisy Duffing-van der Pol oscillator. Probabilistic Eng Mech 45:70–86
Lee B, Price S, Wong Y (1999) Nonlinear aeroelastic analysis of airfoils: bifurcations and chaos. Prog Aerosp Sci 35:205–334
Lempel A, Ziv J (1976) On the complexity of finite sequences. IEEE Trans Inf Theory 22:75–81
Marsden CC, Price SJ (2007) Transient and limit cycle simulation of a nonlinear aeroelastic system. J Aircr 44:60–70
Marwan N, Romano MC, Thiel M, Kurths J (2007) Recurrence plots for the analysis of complex systems. Phys Rep 438:237–329
O'Neil T, Strganac T (1998) Aeroelastic response of a rigid wing supported by nonlinear springs. J Aircr 35:616–622
Patil MJ, Hodges DH (2004) On the importance of aerodynamic and structural geometrical nonlinearities in aeroelastic behavior of high-aspect-ratio wings. J Fluids Struct 19:905–915
Platt N, Spiegel E, Tresser C (1993) On-off intermittency: a mechanism for bursting. Phys Rev Lett 70:279–282
Poirel D (2001) Random dynamics of a structurally nonlinear airfoil in turbulent flow, PhD thesis, McGill University, Montreal, Canada
Poirel DC, Price SJ (1997) Post-instability behavior of a structurally nonlinear airfoil in longitudinal turbulence. J Aircr 34:619–626
Poirel DC, Price SJ (2001) Structurally nonlinear fluttering airfoil in turbulent flow. AIAA J 39:1960–1968

Poirel D, Price S (2007) Bifurcation characterstics of a two-dimensional structurally nonlinear airfoil in turbulent flow. Nonlinear Dyn 48:423–435
Poirel D, Harris Y, Benaissa A (2008) Self-sustained aeroelastic oscillations of a NACA0012 airfoil at low-to-moderate Reynolds numbers. J Fluids Struct 24:700–719
Popescu C, Wong Y, Lee B (2009) An expert system for predicting nonlinear aeroelastic behavior of an airfoil. J Sound Vib 319:1312–1329
Price SJ, Lee BHK (1993) Evaluation and extension of the flutter-margin method for flight flutter prediction. J Aircr 30:395–402
Sarkar S, Bijil H (2008) Nonlinear aeroelastic behavior of an oscillating airfoil during stall induced vibration. J Fluids Struct 24:757–777
Schenk-Hoppé KR (1996) Bifurcation scenarios of the noisy duffing-van der pol oscillator. Nonlinear Dyn 11:255–274
Schijve J (2009) Fatigue damage in aircraft structures, not wanted, but tolerated? Int J Fatigue 31:998–1011
Shannon CE (2001) A mathematical theory of communication. ACM SIGMOBILE Mob Comput Commun Rev 5:3–55
Venkatramani J, Nair V, Sujith R, Gupta S, Sarkar S (2016) Precursors to flutter instability by an intermittency route: a model free approach. J Fluids Struct 61:376–391
Venkatramani J, Nair V, Sujith R, Gupta S, Sarkar S (2017a) Multi-fractality in aeroelastic response as a precursor to flutter. J Sound Vib 386:390–406
Venkatramani J, Kumar SK, Sarkar S, Gupta S (2017b) Physical mechanism of intermittency route to aeroelastic flutter. J Fluids Struct 75:9–26
Venkatramani J, Sarkar S, Gupta S (2018a) Investigations on precursor measures for aeroelastic flutter. J Sound Vib 419:318–336
Venkatramani J, Sarkar S, Gupta S (2018b) Intermittency in pitch-plunge aeroelastic systems explained through stochastic bifurcations. Nonlinear Dyn 92:1225–1241
Wolf A, Swift JB, Swinney HL, Vastano JA (1985) Determining Lyapunov exponents from a time series. Phys D: Nonlinear Phenom 16:285–317
Yan R, Gao RX (2007) Approximate entropy as a diagnostic tool for machine health monitoring. Mech Syst Signal Process 21:824–839
Zhao D, Zhang Q, Tan Y (2009) Random flutter of a 2-DOF nonlinear airfoil in pitch and plunge with freeplay in pitch. Nonlinear Dyn 58:643–654
Zimmerman N, Weissenburger J (1964) Prediction of flutter onset speed based on flight testing at subcritical speeds. J Aircr 1:190–202

Chapter 9
Nonlinear Dynamics of Circular Cylinders Undergoing Vortex Induced Vibrations in Presence of Stochastic Noise

M. S. Aswathy and Sunetra Sarkar

Abstract Vortex induced vibrations (VIV) is a widely explored fluid-structure interaction problem with immense applications ranging from heat exchanger tube arrays, power transmission lines to offshore structures. VIV of circular cylinders stands as one of the classical problems in this area, wherein the cylinder undergoes high amplitude vibrations due to the 'lock-in' phenomenon. The dynamics of the structure and flow field are well studied in the literature for a varied range of flow and structural parameters. However, real-life situations can be characterized by the presence of 'noise', which are fluctuations or uncertainties associated with the incoming flow or geometrical parameters of the system. The dynamical characteristics of the VIV system in the presence of such stochastic fluctuations are a relatively lesser-explored domain of research and not much documentation on this subject is available. In this chapter, we aim to present a comprehensive review of stochastic dynamics of VIV systems, especially we will highlight the presence of novel dynamical states and its implication on the coupled system behaviour that have been reported recently by us. It is known from experimental studies that free-stream noise can increase the response amplitudes of the structure and thus acts as a source of negative aerodynamic damping. Analytical works which model turbulence in experiments as stochastic processes use asymptotic expressions of Lyapunov exponents to determine the stability boundaries of VIV systems. Studies based on mathematical models investigating stochastic dynamics have modelled noise as additive and parametric, in the equations governing the VIV system. The current chapter mainly reviews the literature on stochastic VIV studies based on mathematical models that include wake oscillator models, single degree of freedom and force decomposition models, from a nonlinear dynamics perspective. Brief reviews on previous numerical studies using uncertainty quantification techniques in high fidelity solvers and key experimental results emphasizing the role of free-stream noise are also presented.

M. S. Aswathy (✉)
Indian Institute of Technology Madras, Chennai 600036, India
e-mail: aswathymek@gmail.com

S. Sarkar
Department of Aerospace Engineering, Indian Institute of Technology Madras, Chennai, India
e-mail: sunetra.sarkar@gmail.com

A. Mukhopadhyay et al. (eds.), *Dynamics and Control of Energy Systems*,
Energy, Environment, and Sustainability,
https://doi.org/10.1007/978-981-15-0536-2_9

9.1 Introduction

Vortex induced vibrations of a circular cylinder is an extensively studied fluid-structure interaction problem. The schematic of such a VIV system, where a circular cylinder of mass m, damping c and stifness k undergoing transverse vibrations $y(t)$, where t is the time, is shown in Fig. 9.1 (Aswathy and Sarkar 2018). Firstly, we discuss the dynamics of circular cylinders undergoing vortex induced vibrations in a deterministic environment. Extensive reviews on this topic, covering experimental, mathematical and numerical studies are already available in the literature. Usually, the vortex shedding frequency of the fixed cylinder is based on its Strouhal number, as $St = \frac{f_v D}{U}$, where f_v is the vortex shedding frequency of the fixed cylinder, D is its diameter, U is the incoming flow velocity. The Strouhal number is found to be constant with a value of 0.2, for the subcritical range of Reynolds number ($300 - 2 \times 10^5$) (Gabbai and Benaroya 2005). In the case of a cylinder allowed to vibrate freely, an important phenomenon called synchronisation or lock-in occurs. In the non-synchronised regimes, the vortex shedding frequency follows the Strouhal relation mentioned above. However, for a range of velocities where the value of f_v gets closer to the natural frequency of the cylinder (f_n), the Strouhal relationship is no longer followed. During this range, the vortex shedding frequency gets locked onto f_n and hence the name 'lock-in' for this regime. Lock-in is a well studied phenomenon in VIV mainly because of the high amplitude oscillation exhibited by the cylinder in this regimethe and its identification and prediction is considered important in design and implementation of VIV systems. It has been observed that the transition from the low amplitude to a high amplitude oscillation regime can be characterised by hysteresis (Sarpkaya 2003). A typical response bifurcation diagram for a freely vibrating circular cylinder is described by Feng (1968). As the velocity is increased, the low amplitude region transits into a high amplitude regime, again transiting back to low amplitude regime. Hysteresis region can be observed for a range of reduced velocities. Also seen is the frequency of vibration and the vortex shedding frequency being aligned with the natural frequency of cylinder during lock-in. Additionally, it is reported that there is a phase lag between the cylinder displacement and fluid forces as the jumps occur. There are numerous factors which the vibration of the cylinder is dependent upon such as the Reynolds number(Re), structural damping, added mass effect etc. In experimental studies, one such important parameter which is known to produce two types of response bifurcation diagrams, is the mass-ratio, m^* defined as $4m/\pi\rho D^2 L$, where m is the mass of the cylinder, ρ is the density of the fluid and L is its spanwise length. Khalak and Williamson (1996) have done experiments with a cylinder of low mass ratio and low damping ratio ζ. The m^* value used was 2.4 and the combined mass-damping parameter $m^*\zeta$ used was 0.13. The response amplitude plotted versus the reduced velocity is shown in Fig. 9.2 by the ■ symbol. The response is characterised by three different branches, the initial branch, the upper branch (high amplitude branch) and the lower branch (moderate amplitude branch). Hysterisis is reported between the transition from the lower branch to upper branch. The classical experiments by Feng (1968) are performed for a high

mass ratio $m^* = 248$ and high mass-damping parameter $m^*\zeta = 0.36$ (Feng 1968) and shows different types of response bifurcation diagram as in Fig. 9.2 with $\diamond$ symbols. As mentioned previously, unlike the previous case, they are characterised by just two branches of response, an initial branch and a lower branch, between which a hysteritic transition is known to happen. Also, as seen from the figure, the amplitude of response has decreased substantially in this case. Lower values of the mass ratio are associated with larger amplitude of vibration and larger regime of lock-in. In terms of the flow dynamics, each of these jumps or transition to another branch is associated with a change in the vortex shedding mode/pattern. Since we focus on discussing mainly the structural dynamics in this chapter, further discussions on these vortex shedding modes shall not be made here and the readers are referred to Khalak and Williamson (1999). The above-mentioned studies were done at high Reynolds number range ($5000 < Re < 16000$). The experimental studies of low Reynolds number VIV in the laminar vortex shedding regimes are relatively less compared to studies at high Reynolds number flows. Anagnostopoulos and Bearman (1992) have performed experiments for VIV systems with Re between 90 and 150. They report that the maximum amplitude occurs in the middle of the locked-in region and the frequency of oscillation is slightly higher than the cylinder's natural frequency during lock-in. Later, wake oscillator models became popular owing to their capacity in predicting the response amplitudes, range of lock-in and various other qualitative features of the VIV system effectively. In these models, the cylinder motion is made to interact with a self-excited, self-limited oscillator, called as the wake oscillator. The wake oscillator models are generally developed, assuming two-dimensional flow around the cylinder and do not give much information on the flow dynamics. The most popular among the wake oscillator models is that based on Bishop and Hassan's (1964) where the vortex shedding around the cylinder is represented through a Van der Pol equation. Later Hartlen and Curie (1970) gave a modification to this model by modelling the forcing term in the flow equation which couples the structure and flow dynamics, as a term dependent on cylinder velocity. Several modifications discussing the choice of coupling terms, empirical parameters etc. came about later, many of them being able to predict different features of VIV (Ng et al. 2001; Griffin et al. 1973; Iwan and Blevins 1974). It should be noted that some of them even produced contradictory results. For example, the experimental results of Feng (1968) show that the cylinder's vibration frequency outside lock-in is its natural frequency, but the models by Hartlen and Curie (1970) and Skop and griffin (1973) don't predict so. Apart from wake oscillator models, another class of semi-empirical model used to study VIV dynamics is the single degree of freedom oscillator model, where a single ordinary differential equation is used to describe the structural oscillator. The general form given by Goswami et al. (1993) is:

$$m(\ddot{x} + 2\zeta\omega_n\dot{x} + \omega_n^2) = F(x, \dot{x}, \ddot{x}, \omega_s t) \tag{9.1}$$

Here, overdots represent differentiation with respect to time. Also, m is the mass of the cylinder, x is the transverse displacement, ω_s is the vortex shedding frequency, F

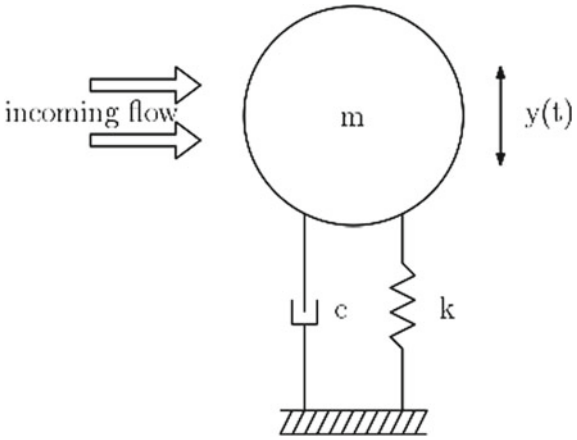

Fig. 9.1 Schematic of a circular cylinder undergoing vortex induced vibrations. Reproduced with permission from Aswathy and Sarkar (2018)

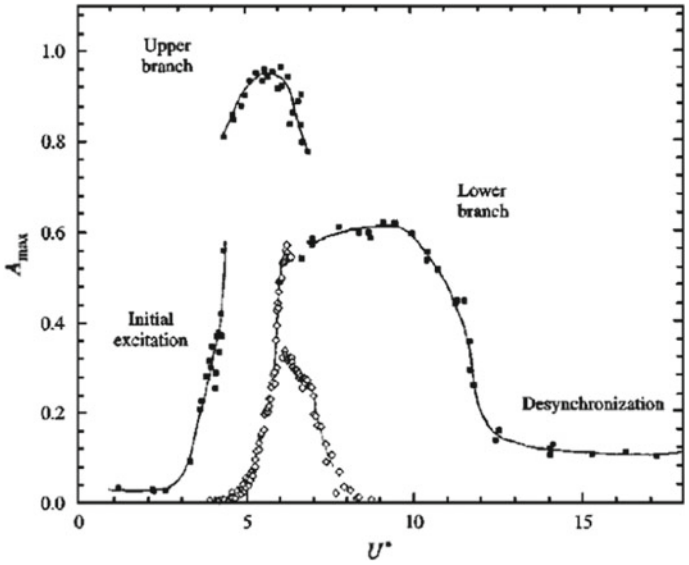

Fig. 9.2 Maximum amplitude of response for $m* = 2.4$(■) and $m* = 248$(◇). Reproduced with permission from Gabbai and Benaroya (2005)

is the aeroelastic forcing term incorporating the wake dynamics and the appropriate modelling of this is significant in capturing the correct dynamics.

Force decomposition models are another class of semi-empirical models, where, the lift force acting on the cylinder is represented as a combination of components arising from two different mechanisms. Sarpkaya (1978), in his force decomposition model, represented the lift force as a sum of those arising from the fluid inertia

(as a function of cylinder displacement) and fluid damping (a function of cylinder displacement) and later through a parametric study, confirmed that the mass-damping parameter is crucial in determining the maximum response amplitudes. Griffin and Koopman (1977) modelled the fluid force as the sum of an excitation part and a reaction part. The latter incorporates all the forces related to the movement of the cylinder. Force decomposition models were even applied in the case of two degree of freedom models where Euler Bernoulli equations were used to model the cylinder vibration (Wang et al. 2003). The two degree of freedom models have been useful in proving that streamwise oscillations have a prominent effect on transverse vibrations and the overall dynamics (Zhou et al. 1999).

Numerical studies using Navier Stokes solver to solve the flow equations are also important to substantiate and extend the results from experiments and low order methods. Numerical studies for VIV of cylinders have been done using Direct Numerical Simulation based on spectral element methods, finite element methods, finite volume methods, vortex cell methods etc. The modelling of the cylinder vibration, modelling the flow field, coupling the flow and structure and data analysis are major issues to be dealt with here (2005). Most of the numerical studies in low Re range (Leontini et al. 2006; Blackburn and Henderson 1996; Prasanth and Mittal 2008) also report three regions of dynamics as the reduced velocity is increased: a low amplitude region characterised by the vortex shedding frequency, which transits into a high amplitude region characterised by the structural frequency again transiting into a low amplitude region. It is also reported in these studies that the amplitude difference between the low and high amplitude regions are not considerably huge compared to the high Reynolds number cases. The flow patterns along all these branches are reported to be pre-dominantly in 2S mode (Leontini et al. 2006). Depending on the blockage ratio, the high amplitude region can be characterised by C(2S) pattern also, where the single vortices coalesce farther downstream (Prasanth and Mittal 2008). Based on such modes of vortex shedding, the response during the transition between the low and high amplitude branch is reported to be having hysteresis or intermittent responses (Leontini et al. 2006; Prasanth and Mittal 2008).

In the next section, we will discuss the influence of noise on the dynamics of VIV systems. The report is organised as follows: Sect. 9.2 discusses the experimental, semi-empirical and numerical studies discussing the effect of noise on VIV dynamics. In Sect. 9.3, the overall conclusions are drawn and summarised.

9.2 Dynamics of Vortex-Induced Vibrations of Circular Cylinders in the Presence of Noise

A general review of the structural dynamics of VIV systems was discussed in the previous section. In this section, we discuss significant works in literature where the effect of stochasticity or noise has been presented. Noise is defined as any type of uncertainty associated with the system parameters, primarily reflected as random

temporal fluctuations of the concerned system parameter. This can also be the inherent fluctuations associated with the local flow field or the fluctuations associated with the external environment (Horsthemke and Lefever 1984). In nonlinear systems, noise brings in substantial qualitative and quantitative dynamical changes. For example, in many physical, chemical and biological systems, the presence of noise is known to change the onset of bifurcation (Crauel and Flandoli 1998; Crauel and Gundlach 1999), stabilise the system (Ariaratnam 1996) and change the probability extremes, which leads to triggering new dynamical states (Horsthemke and Lefever 1984). In systems with electrohydrodynamic instabilities (Brand et al. 1985), noise is reported to delay the transition to turbulence, which they define as a loss of coherence in space and time (Brand et al. 1985). The frequency characteristics of the dynamical system can also be altered by noise as in the studies by Arecchi et al. (1985), where noise manifests as a low-frequency component in the output. Numerous studies have also discussed the qualitative changes in the output behaviour through the so-called stochastic bifurcations (Xu et al. 2011; Zakharova et al. 2010). The effect of noise on the dynamical stability of the responses is investigated in coupled systems such as aeroelastic systems (Poirel and Price 2001, 2007; Zhao et al. 2009; Venkatramani et al. 2016). It is clear that noise has a prominent effect on any kind of nonlinear dynamical systems. In this context, we do a review of experimental, mathematical and numerical works which have investigated the effect of noise/gust on the vortex-induced vibrations of circular cylinders. More emphasis is given to the works based on semi-empirical methods.

9.2.1 Experiments

In this section, we review in detail the experimental studies reporting the influence of gust/noise on VIV systems. In this review, the results are discussed mainly for the structural responses of the system.

Although there is a large number of experimental studies investigating VIV dynamics, those studying the effect of gust are relatively rare. Due to the same reason, the few existing numbers of experiments studying the effect of noise prove to be detrimental for comparison with numerical and analytical models. One such experimental work which we identify as important by So et al. (2008). They have performed experiments on a circular cylinder undergoing cross flow oscillations in the Re range of 5×10^3 to 4×10^4 and analysed the amplitude responses and the frequency spectra. Noise in this context refers to homogeneous, isotropic turbulence in the flow velocity generated using a turbulence grid. The authors mention that the power spectral density of the turbulent flow reveals a low frequency, wide banded random process, thus signifying the fact this is a signal which can be defined in a statistical sense.

The main effect of noise on the system is reported to be in the cylinder's vibration amplitudes, which is reported to increase almost four times than that of the cylinder's amplitude in uniform flow. This is explained based on an energy analysis, where they

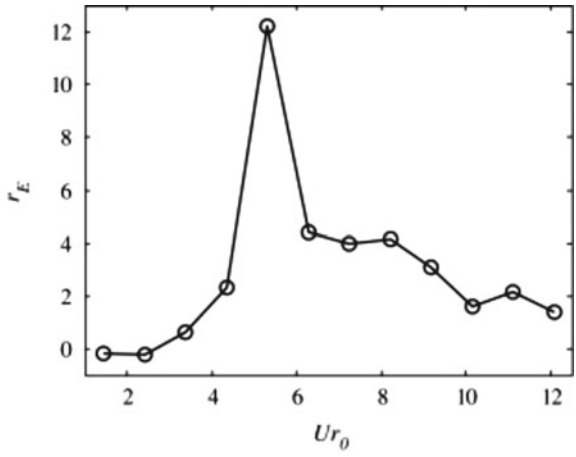

Fig. 9.3 Ratio of energy increment in the cylinder due to noise, U_{ro} represents the reduced velocity. Reproduced with permission from So et al. (2008)

calculate the energy increments in the pre-lock-in, lock-in and post-lock-in regimes. The total energy increment r_E of the system is defined as

$$r_E = \frac{\int_0^{f_{max}} S_t(f)df - \int_0^{f_{max}} S_u(f)df}{\int_0^{f_{max}} S_u(f)df} \tag{9.2}$$

Here, f represents frequency and f_{max} is the upper-frequency limit for integration and is decided based on the sampling frequency of the experiment. $S_u(f)$ and $S_t(f)$ represent the power spectral density functions for the uniform and noisy cases at the same U. Figure 9.3 shows the ratio of energy increment of the cylinder due to noise as a function of reduced velocity. As is evident from the figure, free-stream noise feeds energy into the fluid-cylinder system approximately by a factor of 12. This increment is maximum during lock-in. The vibration data of the pre and the regimes are also subject to this energy increments with frequency contributions coming from the vortex shedding forces and fluid-damping forces. In this particular range of Reynolds number, the authors report the post-lock-in regimes to have a higher contribution from a negative fluid-damping force in the presence of free-stream noise. In other words, noise enhances a negative fluid-damping in the fluid cylinder system, which increases vibration amplitude of the cylinder in the post-lock-in regime. However, the overall system dynamics remain stable, as seen from the phase plots (not shown here) where the cylinder experiences limit-cycle oscillations. In summary, this work concludes that free-stream noise doesn't have much effect on the lock-in range and frequency of the body; however the amplitudes of the structural response and the power of the frequency components are significantly affected by it.

9.2.2 Semi-empirical Models

The semi-empirical models in the literature are generally classified into three (Gabbai and Benaroya 2005), namely the wake oscillator models, single degree of freedom models and force decomposition models. As discussed previously, wake oscillator models are coupled models where there will be separate equations for both wake and structure and these equations will be coupled. In single degree of freedom models, there will be a single equation describing the motion of the structure and the right-hand side representing the forcing from the aeroelastic terms. In the force decomposition models, the forces on the structure are classified into various components occurring due to various mechanisms. In this section, we review these categories of work which have incorporated stochastic modelling.

9.2.2.1 Wake-Oscillator Models

Krenk and Nielsen (1997) investigated the stochastic response based on a double oscillator model (Krenk and Nielsen 1999). Noise has been modelled as a random process R in the non-dimensional set of equations. It is modelled as a stationary random process whose covariance is defined by an Ornstein-Uhlenbeck process as

$$K_{RR}(\tau) = {\sigma_R}^2 exp(-|\tau|/\tau_c) \tag{9.3}$$

Here, σ_R is the standard deviation and τ_c is the correlation time scale. The noise intensity is defined as $\sigma_R/2$. The process $R(t)$ is simulated from an Ito differential equation,

$$dR(t) = \frac{-1}{\tau_c} R(t)\, dt + \sqrt{\frac{2}{\tau_c}} \sigma_R\, dW(t) \tag{9.4}$$

where $W(t)$ signifies a Wiener process. The governing equations along with Eq. 9.4 are integrated using fourth order Runge-Kutta method. In this work, the authors discuss the response characteristics for two different noise intensities, low noise intensity and high noise intensity. The probability density functions of the response at various frequency ratios (ω_s/ω_0) corresponding to various mean speeds are plotted and discussed by the authors for two different noise intensity cases. From their discussions, it is seen that the pdfs show a bimodal behaviour and the response shows two harmonic responses near the lock-in regime. This behaviour is similar to the deterministic behaviour and hence, the authors conclude that low noise intensity does not have much effect on the response. On the other hand, when the noise intensity becomes high, all the responses are characterised by unimodal pdf Also, the upper lock-in branches destabilise and the responses turn into narrow banded stochastic responses in this case.

One of the very recent works which reported the effects of noise in VIV systems is the study by Aswathy et al. (2018, 2019). In this work, the authors have simulated the time histories of the structural responses during different regimes such as pre lock-in, lock-in and post lock-in and given exclusive focus on understanding the dynamical characteristics of the system. This is one among the few works where the dynamics is investigated based on bifurcation analysis of the system and the time series analysis of the responses, along with examining the frequency spectrum. The details are as follows.

The deterministic wake oscillator model used is based on the model by Fachinetti et al. (2004) with an additional cubic term in the structural response (Srinil and Zanganeh 2012). The structural and wake equation are as follows:

$$\ddot{y} + \left(2\zeta + \frac{\gamma \times \mathrm{St} \times U_r(t)}{\mu}\right)\dot{y} + y + \alpha y^3 = M\mathrm{St}^2 U_r(t)^2 q. \tag{9.5}$$

$$\ddot{q} + \epsilon \mathrm{St} U_r(t)(q^2 - 1)\dot{q} + \mathrm{St}^2 U_r(t)^2 q = A\ddot{y} \tag{9.6}$$

where y is the non-dimensional transverse displacement and the overdot denotes differentiation with respect to non-dimensional time t. Stochastic free-stream $U_r(t)$ is also known as the reduced velocity and the deterministic component of $U_r(t)$ is varied as the bifurcation parameter in this study. St is the Strouhal number taken as 0.2. Also, γ is the stall parameter assumed to be 0.8 and α is the nonlinear stiffness coefficient taken as 0.7. All the above parameter values have been chosen as per (Facchinetti et al. 2004; Srinil and Zanganeh 2012). Further, μ is called the dimensionless mass ratio taken as $\mu = 195.56$, also $\mu\zeta = 0.01$. The variable q at the right hand side of Eq. 9.5 is called the non-dimensional wake variable; coefficient of coupling M is represented as $M = \dfrac{Cl_0}{16\pi^2 \mathrm{St}^2 \mu}$, where Cl_0 is the lift coefficient of a stationary cylinder and taken as 0.3 (Facchinetti et al. 2004). ϵ and A are empirical constants and are taken as 0.3 and 12, respectively (Facchinetti et al. 2004). In the acceleration coupling model of Facchinetti et al. (2004), structural response y and wake output q are considered to have a phase difference, but a common angular frequency as any coupled dynamical system should demonstrate.

Noise is incorporated in this model through reduced velocity as $U_r(t) = U_{rm} + \sigma u'(t)$, where σ is the noise intensity, U_{rm} is the deterministic component and u' is the stochastic component of the wind. The process $u'(t)$ is defined as a second order stationary random process which is uniformly distributed with its limits between 0 and 1. The noise process, which has been generated using Nataf's transformation, is assumed to have an exponential correlation function of the form $exp(-\beta\tau^2)$. This chosen form ensures that the process is mean square differentiable and the process has a finite correlation time, which leads the authors in using the standard Runge Kutta algorithm for integrating the governing equations.

The deterministic time series and spectrum analysis show that the structural responses are single frequency responses with the frequency of oscillation being the structural natural frequency outside lock-in and vortex shedding frequency dur-

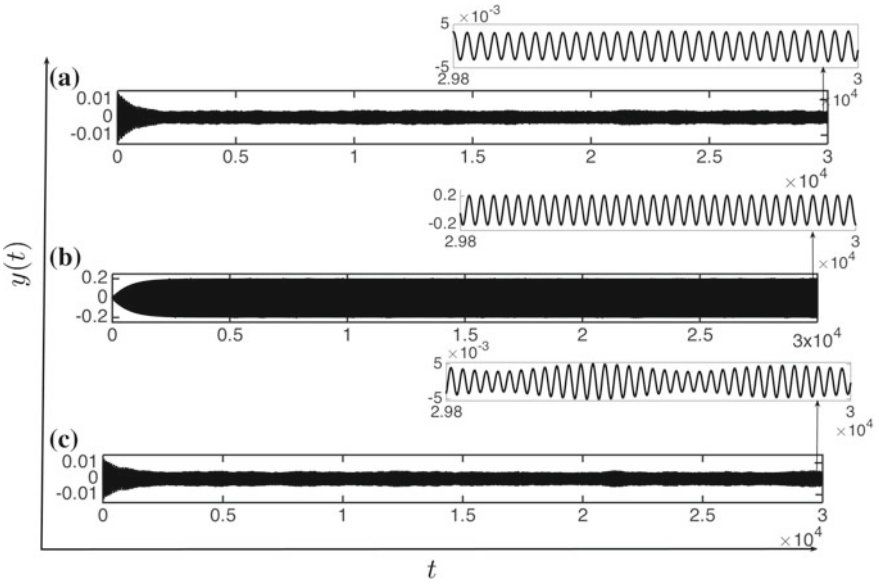

Fig. 9.4 Time histories for σ= 0.1 at U_{rm} values of **a** 4.6 (before lock-in) **b** 5 (lock-in) **c** 5.4 (immediately after lock-in). Reproduced with permission from Aswathy and Sarkar (2019)

ing lock-in. The authors analyse the responses for two different noise intensities ($\sigma = 0.1$ and $\sigma = 1$) and investigate how noise can change the spectrum of the system. Firstly, for a low noise intensity case ($\sigma = 0.1$), they find that noise excites the structural natural frequency (f_n) in addition to the shedding frequency (f_v) in the non lock-in regimes as shown in Figs. 9.4 and 9.5. This results in the periodic responses in the non lock-in regimes of deterministic case, showing dynamic characteristics of a quasi-periodic like behaviour outside lock-in. These are shown by time series analysis of the responses, wherein the non lock-in responses show a torroidal like structure outside lock-in and closed loops during lock-in(not shown here). Recurrence plots of the responses (shown in Fig. 9.6) show broken parallel diagonal lines in the pre and post lock-in regimes and parallel diagnol lines during lock-in.

When the noise intensity becomes high ($\sigma = 1$), the dynamical characteristics of the response change considerably. First of all, the change is reflected in the time histories and frequency characteristics (Figs. 9.7, 9.8). The frequency spectrum is still composed of two frequencies but the relative dominance of the two changes. That is, the structural frequency is stronger than the vortex shedding frequency at low values of reduced velocity, at $U_{rm} = 3$. As the bifurcation parameter is increased and lock-in is approached, at $U_{rm} = 4.1$, a new dynamical state is observed wherein the response shows a tendency to shuttle between the non lock-in and lock-in states. This transition state, named as Noise Induced Intermittency (NII) is solely induced due to the presence of noise and has been highlighted due to its scope of being precursors to the impending instability in flutter systems as well (Venkatramani et al.

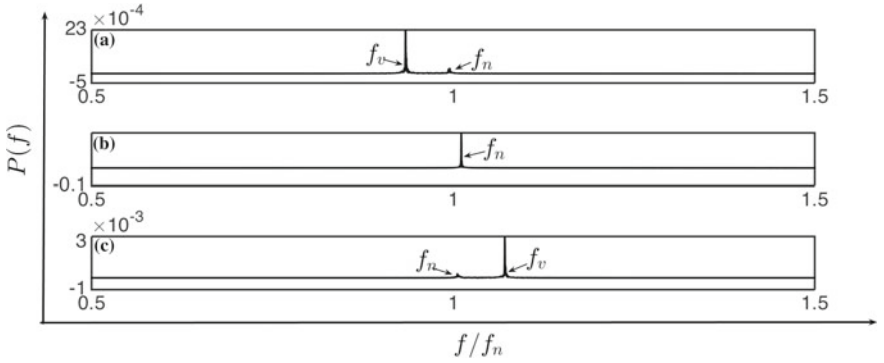

Fig. 9.5 Frequency spectra for $\sigma = 0.1$ for U_{rm} value of **a** 4.6 (before lock-in) **b** 5 (lock-in) **c** 5.4 (immediately after lock-in). Reproduced with permission from Aswathy and Sarkar (2019)

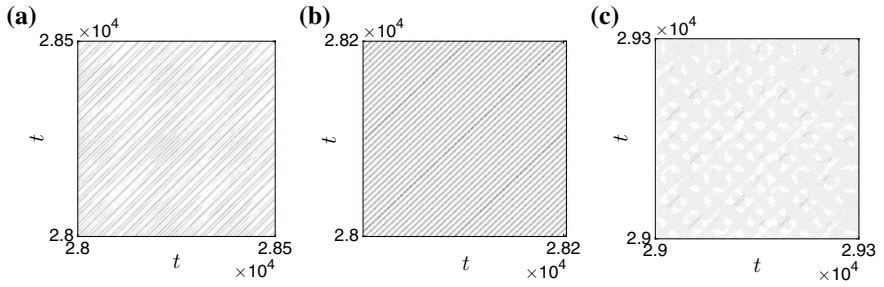

Fig. 9.6 Recurrence plots for $\sigma = 0.1$ at U_{rm} values of **a** 4.6 (before lock-in) **b** 5 (lock-in) **c** 5.4 (immediately after lock-in). Reproduced with permission from Aswathy and Sarkar (2019)

2016). During lock-in ($U_{rm} = 4.6$), the response still resembles the deterministic behaviour. Again, post lock-in, the intermittent response is followed ($U_{rm} = 5$) by a response similar to the low intensity case, at $U_{rm} = 10$. These dynamics are reflected in the recurrence plots also Fig. 9.9, which show windows of black and white dots at $U_{rm} = 4.1$, which becomes prominent at $U_{rm} = 4.6$, signifying the fact that the amplitude shuttles above and below the threshold intermittently. Further, the RP at lock-in is characterised by parallel diagnol lines ($U_{rm} = 4.6$). Post lock-in, RPs with characteristics of intermittency is seen again ($U_{rm} = 5$). Further at $U_{rm} = 10$, quasiperiodic-like dynamics is revealed in the RPs. In summary, the paper discusses the role of noise in introducing new dynamical states and altering the frequency characteristics of the stochastic VIV system. The presence of additional system frequencies and an enhancement in their strengths due to the presence of noise is also reported by previous literature, as in the experiments by So et al. (2008). The discussions of So et al. (2008) and Aswathy and Sarkar (2019) regarding frequencies also show that noise can bring in a negative aerodynamic damping and can hence excite the structural frequency component also. The qualitative differences in

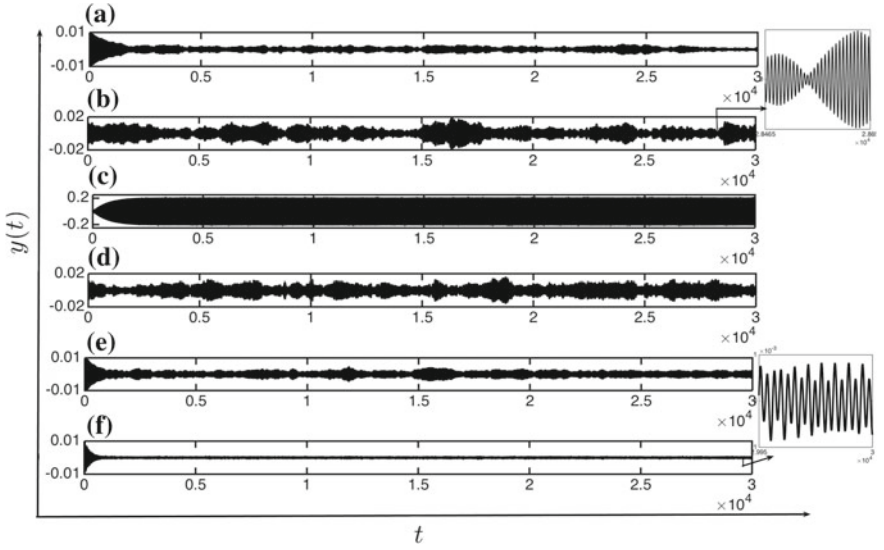

Fig. 9.7 Time histories for $\sigma = 1$ at U_{rm} values of **a** 3 (pre lock-in) **b** 4.1 (immediately before lock-in) **c** 4.6 (lock -in) **d** 5 (immediately after lock-in) **e** 6 (post lock-in) **f** 10 (post lock-in). Reproduced with permission from Aswathy and Sarkar (2019)

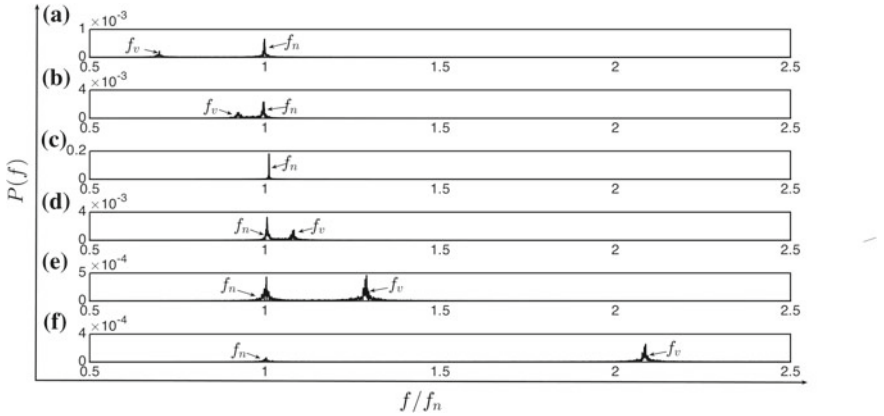

Fig. 9.8 Frequency spectra for $\sigma = 1$ for U_{rm} value of **a** 3 (pre lock-in) **b** 4.1 (immediately before lock-in) **c** 4.6 (lock-in) **d** 5 (immediately after lock-in) **e** 6 (post lock-in) **f** 10 (post lock-in). Reproduced with permission from Aswathy and Sarkar (2019)

dynamics are also analysed by means of the joint probability density functions of the responses, which show topological changes in their structures. Hence the stochastic system is reported to undergo Phenomenological bifurcations, since a qualitative change in probability density functions is attributed to P/stochastic bifurcations.

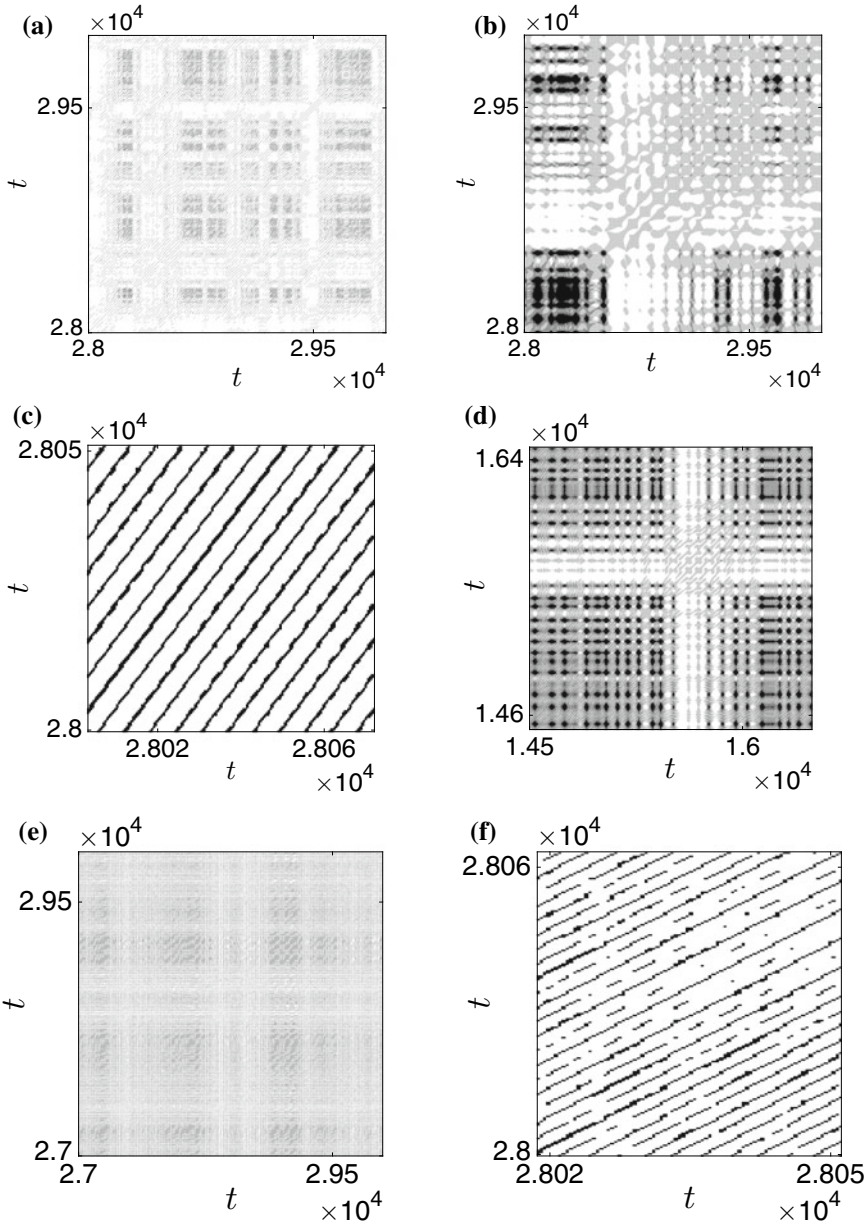

Fig. 9.9 Recurrence plots for $\sigma = 1$ at **a** $U_{rm} = 3$ **b** $U_{rm} = 4.1$ **c** $U_{rm} = 4.6$ **d** $U_{rm} = 5$ **e** $U_{rm} = 6$ **f** $U_{rm} = 10$. Reproduced with permission from Aswathy and Sarkar (2019)

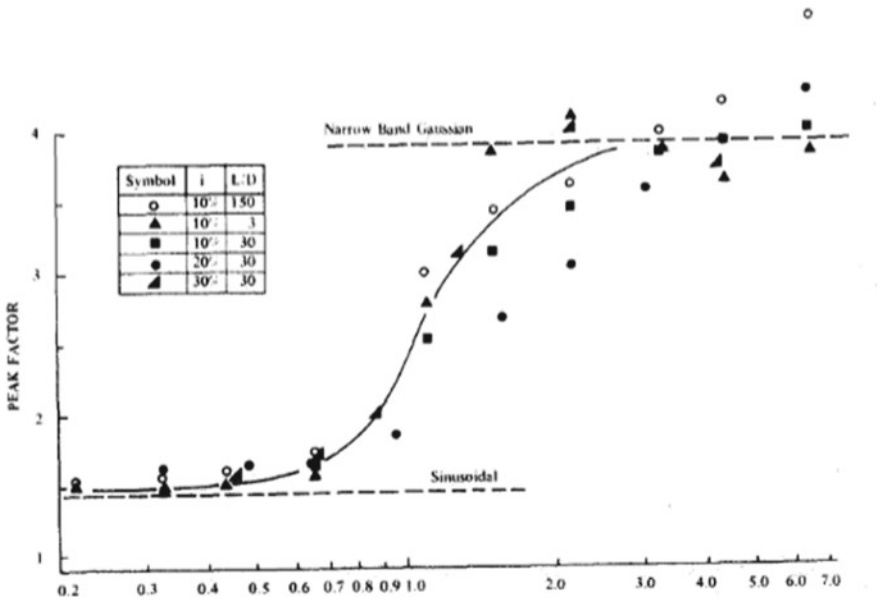

Fig. 9.10 Peak factor as a function of K_s/K_a. Reproduced with permission from Vickery and Basu (1983)

9.2.2.2 Force Decomposition Models

One of the prominent force decomposition models discussing stochastic VIV is the model developed by Vickery and Basu (1983). In this model, all the motion-dependent phenomenon is represented by a negative aerodynamic forcing. On the other hand, the lift force on the cylinder is the effective of sum of vortex shedding forces and those arising due to the fluid-structure interaction phenomenon. The latter, called as motion-dependent phenomenon, is said to be dependent on a negative aerodynamic damping coefficient, which is a function of Reynolds number, amplitude of vibration and the ratios of system frequencies. The representation for motion-induced forces are developed in the framework of random vibration theory. Based on the empirical equation and its numerical simulation, the authors successfully show that the ratio of the structural damping (K_s) to the aerodynamic damping (K_a) determines the type of responses. When $K_s/K_a > 1$, low amplitude Gaussian type of responses occur and when $K_s/K_a < 1$, *i.e*, the negative aerodynamic damping dominates, sinusoidal responses which are high amplitude locked-in oscillations occur. The author also discusses that the transition regime ($K_s/K_a = 1$) is characterised by moderate amplitude oscillations. The peak factor in these three cases are shown in Fig. 9.10 and the corresponding time histories are also shown in Fig. 9.11.

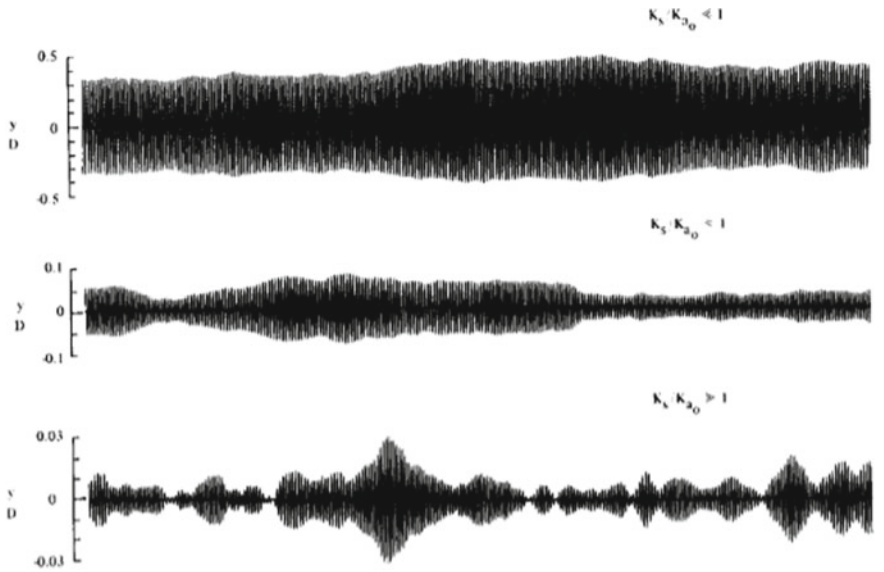

Fig. 9.11 Computed displacement time histories for high, moderate and low damping. Reproduced with permission from Vickery and Basu (1983)

We infer that the idea of negative aerodynamic damping and its relation with noise is a common interest discussed in many of the works. Also, the moderate and low amplitude time histories discussed in Fig. 9.11 resemble the intermittent time histories discussed by Aswathy et al. (2019) and highlights the presence of new dynamics in the transition regimes.

Zhu et al. (2008) investigate the flow induced vibration of a single cylinder in cross flow under bounded noise excitation. The motion of the cylinder is represented by a spring-mass equation and the forces on it are assumed to be due to the contributions from vortex induced forces and motion-dependent forces. The motion-dependent forces are assumed to be composed of the added mass forces, fluid-damping forces and fluid stiffness forces. The equation of motion of the cylinder is written as

$$\ddot{Y} + 2\zeta\omega_0\dot{Y} + \omega_0^2 Y = F_v + F_M \tag{9.7}$$

where F_v and F_M are the vortex shedding and motion dependent forces respectively. After invoking quasi-steady and small angle approximations, the final non-dimensional equation of motion becomes

$$\ddot{Y} + [\beta + A(\tau)]\dot{Y} + Y = B(\tau) \tag{9.8}$$

Here β is a term related to the system parameters and is always positive. The terms $A(\tau)$ and $B(\tau)$ are related to the system parameters and can be positive or negative

based on the same. $B(\tau)$ is essentially representative of the vortex induced forces and is represented as a narrow banded stochastic process instead of a simple sinusoidal function. This is the term responsible for the lock-in phenomenon. An additional reason that the authors discuss as a reason for instability is the term $A(\tau)$, which is also a bounded stationary random process. As mentioned earlier, depending on the parameters involved in this term, it can become positive or negative. If it becomes negative, a negative damping induced instability or 'parametric instability' is induced as the authors call it. The conditions for instability are derived and the dynamic stability of the responses are examined using their moment Lyapunov exponents. This is one of the important works which have focused on the relevance of parametric excitations in causing/enhancing instability other than the usual lock-in phenomenon.

Additionally, similar to the single degree of freedom model, a two degree of freedom model has been developed by Namachivaya et al. (2000). They examine the stability boundaries of a smooth circular cylinder having two degree of freedom, in the wake of another fixed circular cylinder. This work uses the moment Lyapunov exponents and the maximal Lyapunov exponents to discuss the dynamic stability and to find the instability onset. One of the major results of this work is that noise brings stabilisation to the system. The set of two degree of freedom equations that the authors analyse have one critical eigenvalue and one stable eigenvalue. They add noise through the free-stream velocity field as $V = V_0 + \epsilon f(\zeta(t))$, where $f(\zeta(t))$ is a stochastic process generated through a filter method, with the mean field as V_0. The addition of this noise tends to stabilise the critical eigenvalue and the overall instability boundaries alter in the presence of noise. Figure 9.12 shows this shift in the bifurcation onset in the presence of noise at various k, which is the ratio of natural frequencies in the transverse direction y and the streamwise direction x of the cylinder respectively (w_y/w_x). It is seen that noise narrows down the instability regime and this is further enhanced as the value of k decreases.

9.2.3 Numerical Models

There have been few works using full fidelity CFD solvers to solve for the flow field instead of an oscillator equation. Since the inviscid approximations are avoided and the fluid-forces at every time instant is recorded and fed into the cylinder, these solvers involve huge computational time. Due to the same reason, studies investigating stochastic stability by solving the Navier Stokes equations deserves due credit. Geraci et al. (2015) have examined the stochastic stability of two cylinders placed in a tandem configuration, by considering the vertical (L_y) and horizontal distance (L_x) between the centre of the cylinders as an uncertain quantity modelled as a uniformly distributed random variable (Fig. 9.13). The stochastic setting is mainly done using a Polynomial chaos approach wherein the probability of occurrence of three quantities of interest are studied, which are, the maximum displacement of the front and rear cylinder and the maximum vertical separation between them, which are useful design conditions while encountering tandem configurations. For example, as seen in

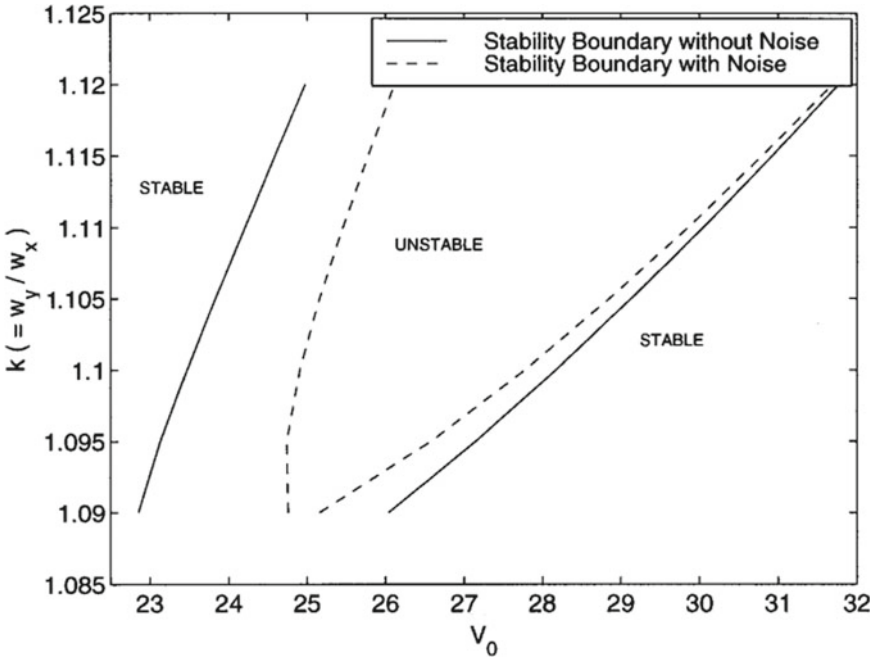

Fig. 9.12 Stability boundaries with and without noise in the system. Reproduced with permission from Namachchivaya and Vedula (2000)

Fig. 9.14, the authors claim that there exists a non-negligible probability that the front cylinder exhibits larger amplitude oscillations than the rear cylinder, except for very high reduced velocities. This is contradicting the observation of Borazjani (2009) that the rear cylinder exhibits large amplitude of oscillations. On the other hand, Geraci et al. (2015) claim that this can happen only at nominal conditions and if the distance between the cylinders is uncertain, the probability can change. Further, the differences in amplitudes of the front cylinder and an isolated cylinder subjected to the same flow are examined. The confidence interval for the oscillation of the front cylinder is given with an isolated cylinder for all reduced velocities and the results are plotted in Fig. 9.14. Their results also show that although the probability of larger oscillations of front cylinder compared to the isolated cylinder is higher, this is enhanced only in higher velocity ranges. The authors point out that, during practical situations, there is a need to account for the non-negligible probability of higher oscillations being exhibited by the isolated cylinder.

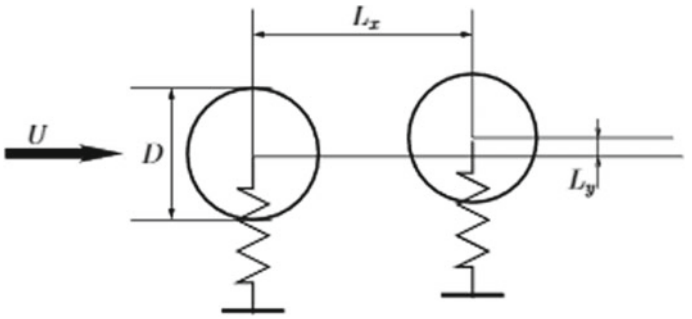

Fig. 9.13 Schematic representation of the cylinders in tandem configuration. Reproduced with permission from Geraci et al. (2015)

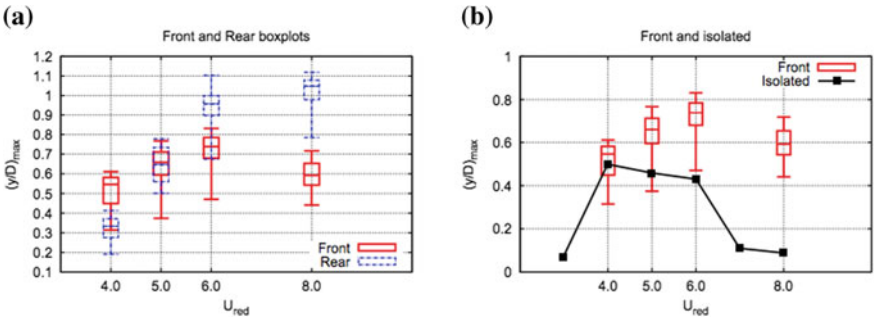

Fig. 9.14 **a** Box plots for the response of front and rear cylinder. **b** Comparison of maximum amplitude of front cylinder with that of an isolated cylinder. Reproduced with permission from Geraci et al. (2015)

9.3 Conclusion

This is a brief review on the vortex-induced vibrations(VIV) of circular cylinders in the presence of stochastic noise. The uncertainties associated with the incoming flow or any other system parameters is an important factor which can control the dynamics of nonlinear systems. Selected papers discussing the effect of noise in VIV systems are discussed in this review report. The strong dependence of VIV systems to noise has been emphasised through experimental, semi-empirical and numerical works. The role of noise in acting as a source of negative aerodynamic damping, altering the frequency characteristics are some of the major results discussed in many of the works. Also, studies based on various wake oscillator models have shown different structural dynamics for low and high noise intensity cases. An energy increment for the structure often manifests as an intermittent type of response, which has been shown in a few of the works. It is to be noted that the majority of the works in stochastic VIV analysis have been carried out based on semi-empirical models rather than experimental and numerical methods. Also, the fluctuations associated

with the incoming velocity is the most commonly considered type of uncertainty discussed in the literature. In the future, the investigation of the dynamics considering the uncertainties associated with more system parameters needs to be undertaken. Stochastic modelling and uncertainty quantification by using Navier Stokes solvers can also enhance the scope and implementation of this subject largely.

References

Anagnostopoulos P, Bearman PW (1992) Response characteristics of a vortex-excited cylinder at low reynolds numbers. J Fluids Struct 6(1):39–50

Arecchi FT, Badii R, Politi A (1985) Generalized multistability and noise-induced jumps in a nonlinear dynamical system. Phys Rev A 32(1):402

Ariaratnam ST (1996) Stochastic stability of viscoelastic systems under bounded noise excitation. In: IUTAM symposium on advances in nonlinear stochastic mechanics. Springer, Berlin, pp 11–18

Aswathy MS, Sarkar S (2018) Manifestation of additional frequencies in vortex induced vibrations in the presence of noise. In: MATEC web of conferences, vol 148. EDP Sciences, p 08003

Aswathy MS, Sarkar S (2019) Effect of stochastic parametric noise on vortex induced vibrations. Int J Mech Sci 153:103–118

Bishop RED, Hassan AY (1964) The lift and drag forces on a circular cylinder oscillating in a flowing fluid. In: Proceedings of the royal society of london a: mathematical, physical and engineering sciences, vol 277. The Royal Society, pp 51–75

Blackburn H, Henderson R (1996) Lock-in behavior in simulated vortex-induced vibration. Exp Therm Fluid Sci 12(2):184–189

Borazjani I, Sotiropoulos F (2009) Vortex-induced vibrations of two cylinders in tandem arrangement in the proximity-wake interference region. J Fluid Mech 621:321–364

Brand HR, Kai S, Wakabayashi S (1985) External noise can suppress the onset of spatial turbulence. Phys Rev Lett 54(6):555–557

Crauel H, Flandoli F (1998) Additive noise destroys a pitchfork bifurcation. J Dyn Differ Equ 10(2):259–274

Crauel H, Gundlach M (1999) Stochastic dynamics. Springer Science & Business Media

Facchinetti ML, De Langre E, Biolley F (2004) Coupling of structure and wake oscillators in vortex-induced vibrations. J Fluids Struct 19(2):123–140

Feng CC (1968) The measurement of vortex induced effects in flow past stationary and oscillating circular and d-section cylinders. PhD thesis, University of British Columbia

Gabbai RD, Benaroya H (2005) An overview of modeling and experiments of vortex-induced vibration of circular cylinders. J Sound Vib 282(3–5):575–616

Geraci G, de Tullio MD, Iaccarino G (2015) Stochastic analysis of vortex-induced vibrations of two oscillating cylinders in the proximity-wake interference region. In: Annual research briefs, Stanford, CA: Stanford University, Center for Turbulence Research. pp 197–210

Goswami I, Scanlan RH, Jones NP (1993) Vortex-induced vibration of circular cylinders. ii: new model. J Eng Mech 119(11):2288–2302

Griffin OM, RSkop RA, Koopmann GH (1973) The vortex-excited resonant vibrations of circular cylinders. J Sound Vib 31(2):235–IN3

Griffin OM, Koopmann GH (1977) The vortex-excited lift and reaction forces on resonantly vibrating cylinders. J Sound Vib 54(3):435–448

Hartlen RT, Currie IG (1970) Lift-oscillator model of vortex-induced vibration. J Eng Mech Div 96(5):577–591

Horsthemke W, Lefever R (1984) Noise-induced transitions: theory and application in physics, chemistry, and biology, vol 15. Springer, Berlin

Iwan WD, Blevins RD (1974) A model for vortex induced oscillation of structures. J Appl Mech 41(3):581–586
Khalak A, Williamson CHK (1996) Dynamics of a hydroelastic cylinder with very low mass and damping. J Fluids Struct 10(5):455–472
Khalak A, Williamson CHK (1999) Motions, forces and mode transitions in vortex-induced vibrations at low mass-damping. J Fluids Struct 13(7–8):813–851
Krenk S, Nielsen SRK (1999) Energy balanced double oscillator model for vortex-induced vibrations. J Eng Mech 125(3):263–271
Leontini JS, Thompson MC, Hourigan K (2006) The beginning of branching behaviour of vortex-induced vibration during two-dimensional flow. J Fluids Struct 22(6–7):857–864
Ng L, Rand RH, Wei T, Keith WL (2001) An examination of wake oscillator models for vortex-induced vibrations. Technical report, Naval Undersea Warfare Center Newport Div ri
Nielsen SRK, Krenk S (1997) Stochastic response of energy balanced model for vortex-induced vibration. Aalborg University, Denmark, Technical report, Dept. of Building Technology and Structural Engineering
Poirel DCM, Price SJ (2001) Structurally nonlinear fluttering airfoil in turbulent flow. AIAA J 39(10):1960–1968
Poirel DCM, Price SJ (2007) Bifurcation characteristics of a two-dimensional structurally non-linear airfoil in turbulent flow. Nonlinear Dyn 48(4):423–435
Prasanth TK, Mittal S (2008) Vortex-induced vibrations of a circular cylinder at low reynolds numbers. J Fluid Mech 594:463–491
Sarpkaya T (2003) A critical review of the intrinsic nature of viv. In: IUTAM symposium on integrated modeling of fully coupled fluid structure interactions using analysis, computations and experiments. Springer, Berlin, pp 159–161
Sarpkaya T (1978) Fluid forces on oscillating cylinders. Nasa Sti/Recon Tech Rep A 78:275–290
Skop RA, Griffin OM (1973) A model for the vortex-excited resonant response of bluff cylinders. J Sound Vib 27(2):225–233
So RM, Wang XQ, Xie W-C, Zhu J (2008) Free-stream turbulence effects on vortex-induced vibration and flow-induced force of an elastic cylinder. J Fluids Struct 24(4):481–495
Sri Namachchivaya N, Vedula L (2000) Stabilization of linear systems by noise: application to flow induced oscillations. Dyn Stab Syst 15(2):185–208
Srinil N, Zanganeh H (2012) Modelling of coupled cross-flow/in-line vortex-induced vibrations using double duffing and van der pol oscillators. Ocean Eng 53:83–97
Venkatramani J, Nair V, Sujith RI, Gupta S, Sarkar S (2016) Precursors to flutter instability by an intermittency route: a model free approach. J Fluids Struct 61:376–391
Vickery BJ, Basu RI (1983) Across-wind vibrations of structures of circular cross-section. part i. development of a mathematical model for two-dimensional conditions. J Wind Eng Ind Aerodyn 12(1):49–73
Wang XQ, So RMC, Chan KT (2003) A non-linear fluid force model for vortex-induced vibration of an elastic cylinder. J Sound Vib 260(2):287–305
Xu Y, Gu R, Zhang H, Xu W, Duan J (2011) Stochastic bifurcations in a bistable Duffing-Van der Pol oscillator with colored noise. Phys Rev E 83(5):056215
Zakharova A, Vadivasova T, Anishchenko V, Koseska A, Kurths J (2010) Stochastic bifurcations and coherence like resonance in a self-sustained bistable noisy oscillator. Phys Rev E 81(1):011106
Zhao D, Zhang Q, Tan Y (2009) Random flutter of a 2-dof nonlinear airfoil in pitch and plunge with freeplay in pitch. Nonlinear Dyn 58(4):643–654
Zhou CY, So RMC, Lam K (1999) Vortex-induced vibrations of an elastic circular cylinder. J Fluids Struct 13(2):165–189
Zhu J, Wang XQ, Xie WC, So RMC (2008) Flow-induced instability under bounded noise excitation in cross-flow. J Sound Vib 312(3):476–495

Chapter 10
Vibration Energy Harvesting in Fluctuating Fluid Flows

S. Krishna Kumar, Sunetra Sarkar and Sayan Gupta

Abstract Ambient energy harvesting for power supply to low power hardware, like sensors in inaccessible environments, has garnered sustained interest over the last two decades. Common sources of ambient energy include vehicle vibrations and natural fluid flow. The latter is also proposed as a possible quiet alternative to conventional renewable energy systems like horizontal and vertical axis wind turbines. Various forms of flexible structures have been proposed and tested over years and found to be comparable to conventional systems on an energy density basis. These harvesters often rely on instability of the fluid-structure coupled system at increasing flow velocities. Thus, the design of these harvesters requires an understanding of the complex fluid-structure interaction inherent in them, which may include nonlinear effects. The inclusion of an electric circuit to scavenge the vibratory energy further transforms it into a three-way coupling problem. Despite laboratory scale verification of the potential of these systems, practical deployment has been deterred by the fluctuating nature of the natural fluid flows. Recent researches have sought to develop adaptive harvesters for such scenarios. Some progress has also been made in exploiting the spatio-temporal flow fluctuations beneficially for enhancing harvested power. This chapter summarizes the state-of-the-art in this regard and classifies the various approaches to tackling flow fluctuations.

S. K. Kumar
Indian Institute of Technology Madras, Chennai 600036, India
e-mail: skk.89@hotmail.com

S. Sarkar
Department of Aerospace Engineering, Indian Institute of Technology Madras, Chennai, India
e-mail: sunetra.sarkar@gmail.com

S. Gupta (✉)
Department of Applied Mechanics, Indian Institute of Technology Madras, Chennai, India
e-mail: gupta.sayan@gmail.com

A. Mukhopadhyay et al. (eds.), *Dynamics and Control of Energy Systems*,
Energy, Environment, and Sustainability,
https://doi.org/10.1007/978-981-15-0536-2_10

10.1 Introduction

The rapid growth of electricity consumption over the last few decades and concurrent rapid depletion of non-renewable resources for power generation have stimulated widespread research efforts into renewable energy technologies. While solar and wind energy production has progressively improved in terms of yield and efficiency, such sources are not useful in all scenarios of power consumption. For example, the ubiquitous use of small sized sensors across critical infrastructure, urban monitoring systems, aerospace applications have necessitated development of reliable ultra low power (ULP) sources. In many cases, like structural health monitoring of bridges, the sensors operate in remote locations and are wireless (Park et al. 2008). The difficulty in providing sustained power from ground station over time has motivated standalone energy harvesters tapping abundantantly available ambient energy in the environment. Further, portable electronic systems like sensors are often small in size, i.e., centimeter-scale to micro-scale. Ambient energy harvesters help replace batteries as power sources for such systems since batteries are often of unwieldy size and require repeated maintenance. Prominent sources of ambient energy are base excitation as in an oscillator placed on a bridge or a moving vehicle, acoustic energy and energy from fluid flows.

Various vibration based energy harvesters (VEH) exploiting base excitation and external forcing have been developed over the past few decades (Pellegrini et al. 2013; Williams and Yates 1996; Stephen 2006). Early models of VEH considered linear oscillators which would undergo substantial vibration due to resonant conditions. Optimal energy harvesting would then require that the VEH was tuned to resonate with the ambient energy source. However, this imparted a restriction on the practical use of such harvesters as the ambient energy source could have varying frequencies over time and space. In other words, the ambient source is characterized by a wide frequency spectra. Linear harvesters perform poorly away from the resonant frequency, even for small mistuning. While automated tuning of VEH has been attempted with some success, a better solution to this problem exists in the form of nonlinear energy harvesting. As nonlinear systems possess multiple equilibria- both stationary and oscillatory- rich dynamical behaviour ranging from inter-well oscillations in systems with double well potential to limit cycle oscillations can be expected. Since the nonlinear systems permitted significant oscillation even in non-resonant conditions, along with the emergence of superharmonic and subharmonic frequencies in the response due to nonlinearity, it improves the frequency range over which substantial energy can be harvested. Most nonlinear harvesters, like those of the double well potential type, typically are designed to operate in noisy or random environment conditions. The interaction of noise and nonlinearity has been found to widen the frequency band suitable for energy harvesting, leading to what is known as broadband energy harvesting.

Broadband energy harvesting has been applied to both linear and nonlinear systems. Adhikari et al. (2009) studied a stack based base-excited energy harvester with a stationary Gaussian white noise energy source. Stochastic differential equa-

tions based on a single degree-of-freedom model for the harvester were obtained and solved using theory of linear random vibrations. Optimal values of mechanical damping, electromechanical coupling and natural frequency of the electrical circuits were obtained. Kim et al. (2011) studied a proof mass attached to two cantilever beams. While their numerical model was linear and yielded broadband harvesting, the experiments revealed that the bandwidth was enhanced by presence of nonlinearities. A similar improvement in energy harvesting performance was observed in a bistable inertial harvester comprising of two permanent magnets and a piezo-electric cantilever beam by Stanton et al. (2009). Daqaq (2012) studied the effect of stiffness nonlinearities on monostable or bi-stable piezoelectric Duffing-type harvesters subjected to white Gaussian noise. Conditions for optimal performance of harvester were derived and contrasted with the performance of linear harvesters. Further, He and Daqaq (2014) studied nonlinear energy harvesters with asymmetric potential functions and excited by white noise. It was noticed that the asymmetry leads to degradation of performance for low and moderate noise intensities. For higher noise intensities, it seemed that the effects of asymmetry were marginal. Tang et al. (2010) discuss multiple strategies to increase the bandwidth of energy harvesting for both linear and nonlinear harvesters.

Atmospheric wind flow is one of the prominent and virtually limitless sources of broadband energy. In many systems, like unmanned air vehicles (Anton and Inman 2008), micro-air-vehicles and morphing wings (Erturk and Inman 2008; Abdelkefi and Ghommem 2013), flow induced vibrations may also be the only mechanisms available for energy harvesting. The possibility of harnessing energy from flow induced vibrations in such cases has stimulated numerous investigations into the same (Young et al. 2014; Xiao and Zhu 2014; Abdelkefi 2016). These systems attempt to harvest the enormous untapped energy available in wind flows and are easily extended to energy harvesting from other fluid flows, for example, oceanic flows. Early implementation of flow energy harvesters assumed a steady freestream flow, often causing an oscillatory instability in a flexible structure. A common structure which has been considered for such a harvester is the oscillating or 'flapping foil' (Young et al. 2014). Periodic oscillations obtained in such a system for a range of flow velocities have been found to be suitable for energy harvesting (Peng and Zhu 2009). Such flapping foils may be 'passive', i.e. oscillating purely due to the fluid forces acting on them, or 'active' when a pitching or heaving motion is externally imparted to the airfoil (Zhu and Peng 2009). An early implementation of flapping foil harvester was by McKinney and DeLaurier (1981), taking inspiration from fish motion. The pitching-heaving airfoil was termed 'oscillating wingmill' and the average power and efficiency were found to be peak with an optimal phase difference between the two oscillations. Jones et al. (1999) showed, through numerical experiments, that the efficiency of these harvesters can be improved further through a proper choice of their configurations.

Thus, the flutter or instability based harvesters involve oscillation of elastic structures under fluid forces. Energy harvesters exploiting flow induced vibrations require these vibrations to be augmented to yield reasonable quantity of power. The oscillations could be self-excited, as in the case of an elastically mounted cylinders

(Mehmood et al. 2013), airfoils (Xiao and Zhu 2014), or flat plates (Tang et al. 2009; Jamshidi et al. 2015; Onoue et al. 2014). In other cases, the oscillations of the harvester could be due to unsteady flow caused by an upstream bluff body (Allen and Smits 2001; Akaydın et al. 2010; Shi et al. 2013). Comprehensive reviews of general flow energy harvesters can be found in Young et al. (2014), Abdelkefi (2016), Xiao and Zhu (2014).

Most of the harvesters discussed hitherto assume a steady freestream flow. However, realistic flows are more often unsteady, turbulent and hence, timevarying. A classic example is the case of flexible plate or airfoil placed in the wake of a bluff body, as in Allen and Smits (2001), Akaydın et al. (2013), Shi et al. (2013). At higher Reynolds numbers, the flow behind a bluff body is turbulent. Thus, a flexible foil harvester placed in the wake of bluff body encounters unsteady upstream flow. For the standalone-foil-harvesters placed in atmospheric boundary layer, i.e. close to earth surface, the freestream flow itself is turbulent. Similarly harvesters placed over buildings in urban environment are likely to be impinged by turbulent freestream flow due to interfering buildings. In fact, most real life flows are time-varying and fluctuating, if not turbulent. Thus, fluctuating flows are both realistic as well as advantageous for robust flow energy harvesting. The rest of the chapter presents a brief review of the state of the art in different kinds of fluctuating flow energy harvesters. A cursory summary of the modelling of wind fluctuations is elucidated, followed by a review of different classes of energy harvesters based on fluctuating flow.

10.2 Aeroelastic Flow Fluctuations

Typically, turbulence is characterised by a broad frequency spectrum, comprising of a range of spatial and temporal scales, and can serve as a broadband power source. Fluctuating flows are ubiquitous in nature. The atmospheric flow closer to earth's surface is largely fluctuating, and the fluctuations are often considered simply as horizontal and vertical components. In aerospace parlance, velocity fluctuations in these components are called gusts. Real life fluid flows possess gusts of different temporal and spatial scales. Typically, in fluid-elastic problems, the fluctuations are modelled as discrete gusts- i.e., discrete impulses for computation of design loads. However, a continuous type of fluctuations is preferred when the interaction between nonlinearity and fluctuations are studied from a dynamics perspective (Poirel and Price 1997). Further, the freestream fluctuations are generally considered to be independant of structural deformations, since these do not originate from the flexible-body motion and are often called "external noise" in physics literature. Hence, the flow fluctuations are modelled in this study as a purely temporal irregular fluctuations, i.e., a stochastic process, under the assumption of isotropy, stationarity and homogeneity (Poirel and Price 1997). This implicitly assumes chordwise uniformity of the flow fluctuations. As the responses of elastic systems are often dominated by a long time scale or low frequencies in a fluctuating flow, such an assumption is found permissible (Poirel and Price 1997). Further, atmospheric fluctuating flows have often been found

to conform to a Gaussian distribution (Taylor 1965; Rice 1944). Even in the presence of non-Gaussian or even non-stationary components of fluctuations, existence of a Gaussian continuous fluctuation background has been found to be reasonable (Hoblit 1988), especially when the fluctuations are strong. The frequency spectra for such a Gaussian process is often based on the Dryden spectrum or the Von-Kárman spectrum, which can essentially be treated as filtered Gaussian noise (Hoblit 1988). Common aero-elastic fluctuation spectra have predominant low frequencies, with most energy transferred between the fluid and the solid at such frequencies (Taylor 1965). Further insights on modelling turbulent flows, for energy harvesting as well as other aero-elastic applications, can be obtained from elsewhere (Hoblit 1988; Poirel and Price 1997). In addition to turbulent flows, periodic flow fluctuations have also been exploited for low power energy extraction. Real life periodic flows include fluctuations behind a bluff body for Reynolds numbers lower than the turbulent-critical value and airflow across rotor blades. A plain sinusoidal fluctuation model often suffices for such flow fluctuations. The rest of the chapter provides a short summary of energy harvesters based on fluctuating flows. The list of harvesters described here are only representative of diverse efforts in the literature towards energy harvesting from fluctuating flows and not exhaustive. Comprehensive reviews of aeroelastic harvesters, including some of the harvesters based on fluctuating flows can be found in Young et al. (2014), Xiao and Zhu (2014).

10.3 Bluff Body and Tandem Harvesters

A well known source of turbulence, studied extensively by fluid mechanicians, is the turbulence caused by obstruction of a fluid flow by a 'bluff' body. The flow past a bluff body, which is laminar for low fluid velocities, turns turbulent at higher velocities. Large eddies or coherent structures are formed behind the bluff body. The fluctuating wake has been identified as a suitable source of energy. For example, a flexible foil placed in the wake of a bluff body undergoes oscillations at lower velocities than the critical velocity at which standalone foil would exhibit substantial vibrations. The vibration of the harvester could then be considered to be a result of a combination of movement induced instability and an extraneously induced instability (Allen and Smits 2001; Naudascher and Rockwell 2012). The downstream flexible harvesters are usually called membranes or foils, and oscillate due to the unsteady fluid forcing acting on them. When the foil motion is well coupled to the vortex shedding, characterised by the foil oscillating at the frequency corresponding to Strouhal number, remarkable oscillations happen facilitating power extraction (Allen and Smits 2001).

Taylor et al. (2001) developed energy harvesting eel using a PVDF bimorph made to undergo a wavy vibration due to upstream bluff body. When flapping frequency matched the shedding frequency, maximum power output was obtained. The electric subsystem was optimised and upto 37% conversion from mechanical to electrical energy was achieved. Allen and Smits (2001) experimentally studied the flutter

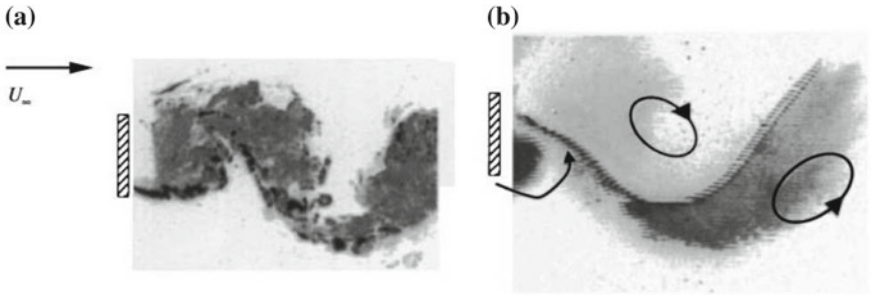

Fig. 10.1 **a** Particle image velocimetry results from the experiments in Allen and Smits (2001), which show the interaction between alternating wake coherent structures and the flexible foil; **b** Clockwise and counter-clockwise coherent structures highlighted. Reproduced with permission from Allen and Smits (2001)

characteristics of this system in detail (see Fig. 10.1). Results from particle image velocimetry showed the interaction between the flexible harvester and the coherent structures in the wake. One of the key parameters, the ratio of gap s between the bluff body and foil and the length scale D of the bluff body was fixed to be 1. Later investigations have shown that the gap plays a crucial role in the wake-foil interaction and optimal values have to be identified for efficient energy harvesting Lau et al. (2004), Kumar et al. (2017).

Pobering and Schwesinger (2004) conducted experiments on two models: PVDF flag placed behind a rectangular cylinder and a cantilever bimorph. The PVDF flag exhibited substantial energy harvesting potential and possessed an energy density of 11–32 W/m^2. It was noted that a large scale array of generators can exhibit 68 W/m^2 power compared to 34 W/m^2 of wind turbines, and could be developed as a hydro power plant. However proximity effects or mutual interaction of harvesters were ignored. It must be noted that in these harvesters, the upstream body remained static under the action of fluid forces. Alternate systems, where the upstream body can also contribute to energy output, have also been developed in the form of tandem harvesters. Depending on the freestream flow velocity, the wake of an upstream vibrating harvester can possess strong flow fluctuations, periodic or turbulent. Taking inspiration from fish shoal and bird flock motion, it has long been expected that the downstream harvesters can improve their aero-elastic performance in the presence of an upstream fluctuating harvester. Bryant and Garcia (2011) studied tandem operation of two airfoil-beam-flap harvesters. The upstream harvester performance was found to be unaffected by the downstream one. However, for the downstream harvester, presence of upstream counterpart improved performance by 30%. Streamwise gap was found to be optimal at twice the length scale of upstream harvester but the cross stream separation was found to have no effect. Four tandem harvesters were also tested with a zero gap and were found to yield more power than the individual cases. The harvesters flapped at the same frequency. The wake interaction in the tandem

Fig. 10.2 Tandem harvesters comprising of flexible beams with a tip flap tested in Bryant et al. (2012). Reproduced with permission from Bryant et al. (2012)

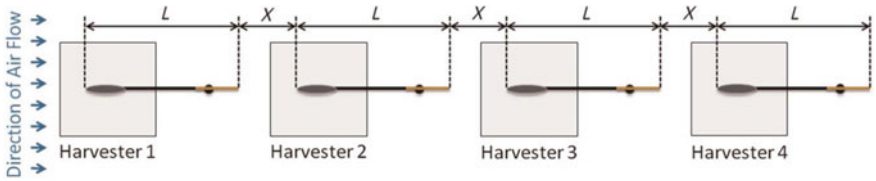

Fig. 10.3 Tandem harvesters comprising of four flexible beams with a tip flap tested in Bryant et al. (2012). Here, X refers to the streamwise gap between harvesters and L refers to the length of the harvesters. Reproduced with permission from Bryant et al. (2012)

airfoil harvester scheme was further studied by Bryant et al. (2012) (see Figs. 10.2 and 10.3). The results indicated that the tandem scheme with closely spaced array of harvesters outperformed the performance of independant harvesters. The turbulent wake structure, dependent on the streamwise and cross-stream separation of the harvesters, was found to have significant effect on the power output of the system. Optimal separation distances along cross-stream and streamwise directions were identified and frequency locking between the harvesters was observed for harvesters with identical flutter frequency.

Similarly, Abdelkefi et al. (2014) studied a cantilever beam with a rectangular tip mass placed in a fluctuating flow (see Fig. 10.4). Two cases were studied: the harvester placed in the wake of another harvester and a single harvester placed in a grid-generated freestream turbulence. Optimal spacing for the tandem harvester case and optimal turbulence scales for the grid-generated turbulence were identified and the harvesters showed power enhancement over the steady flow. Note that the bluff body-wake foil harvesters and tandem foil harvesters do not require the freestream to be fluctuating. As a corollary, the effects of freestream flow fluctuations on the

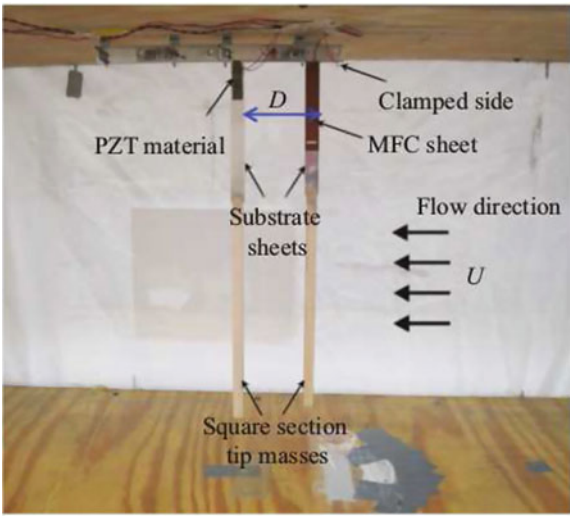

Fig. 10.4 Tandem cantilever beams with rectangular tip masses studied in Abdelkefi et al. (2014). Reproduced with permission from Abdelkefi et al. (2014)

harvesting performance of these multi-body harvesters are less known. Since real wind flows often possess substantial freestream turbulence, significant efforts have been made over years towards harvesting energy directly from it.

10.4 Freestream Pulsating Flow

The effect of upstream flow fluctuations on aero-elastic systems attracted significant interest in the early days of manned flight. Often, the focus was limited to vertical or cross-stream fluctuations, though sporadic efforts on streamwise or horizontal flow fluctuations have been made from time to time. In recent times, the development of Micro-air-vehicles (MAVs) and the need to control their flight as well as to provide persistent source of power has motivated the study of upstream flow effects at this size scale. Micro-air-vehicles are generally operated at low altitudes, in atmospheric boundary layer (Lundström and Krus 2012). Additionally, use of MAVs in urban surroundings necessitates the consideration of turbulence. Thus, substantial efforts have been made by the aero-elastic community over the last century to understand energy extraction from flow fluctuations. The first part of the review presented next deals with the pulsating or periodic flows often considered to model freestream fluctuations. The second part discusses energy harvesting research considering continuous freestream turbulence.

Katzmayr (1922) conducted one of the earliest investigations into energy extraction during aircraft flight in pulsating flow. It was shown through wind tunnel experiments that a pulsating flow caused reduction in both drag and lift for thin airfoils. On the contrary, for thick airfoils, a negative drag with positive lift was observed

indicating a forward ascending flight. This is often known as the 'Katzmayr effect'. It was also noted that the aircraft performance improved with increase in the amplitude of the pulsating flow. The frequency of the pulsating flow was seen to have a less significant effect, though an optimal low frequency was also reported for certain airfoil sections. Phillips (1975) developed a simple analysis of the propulsive effect caused by gusts encountered by aircraft. A Dryden spectrum based model of vertical gusts was used, along with assumptions of constant airspeed and constant pitch angle. It was shown that the thrust improvements were insignificant for aircrafts, for example soaring gliders, fighters, transport and light airplanes, encountering moderate turbulence. Langelaan (2009) proposed the biomemetic exploitation of short duration gusts by aircrafts for performance enhancement, in comparison to earlier efforts to exploit long duration vertical air motions, thermals and dynamic soaring. The study noted that such gusty flows are highly probable in urban environments and may provide performance benefits at the size-scale of micro-air-vehicles, which operate in such environments. A closed loop control architecture was developed for energy extraction and the gust-soaring controller was shown to have advantages over a constant-air-speed controller. Cutler et al. (2010) investigated the flight performance of UAVs using ridge lift based energy harvesting, enabling persistent imaging of a stationary target. The flow past the ridge and the closed loop trajectory of the UAV effectively causes a periodically fluctuating flow. Optimal position and trajectory of the UAV for low use of external supplied power were identified.

Pozzi et al. (2012) investigated the strain levels in an aircraft wing with a piezoelectric skin caused during and after a gust event. The gust was modelled using 1-Cosine profile and a range of gust frequencies were studied to yield insight into realistic air turbulence. It was found through finite-element based numerical simulations that the energy generation was higher when the gust frequency was closer to the natural frequency of the wing. In general, higher gust frequencies yielded better energy output than lower frequencies. Also, large and thin PZT patches were seen to improve energy output. The gust based harvesting technique was also noted to be useful during taxiing of aircrafts and during long flights.

Bruni et al. (2014) studied the response of three wing models to discrete gust loads for the purpose of gust alleviation and energy harvesting. Three different gust models were employed- sinusoidal, constant and linear. The numerical simulations suggested that significant energy output could be harvested from the gusts and was preferable to flutter based energy harvesting due to the fatigue effects caused by the latter.

Chen et al. (2017) examined the effects of a sinusoidal gust on the energy harvesting performance of NACA0012 airfoil with imposed heaving and pitching motions (see Figs. 10.5 and 10.6). It was observed that the energy harvesting efficiency varies with the phase difference between the gust and airfoil pitching motions and peaked at optimal values of phase difference. Energy efficiency was found to be less sensitive to changes in gust frequency. However the sensitivity of energy efficiency towards gust amplitude was found to depend on the gust frequency. At lower gust frequencies, monotonic decrease in efficiency with increase in gust amplitude was

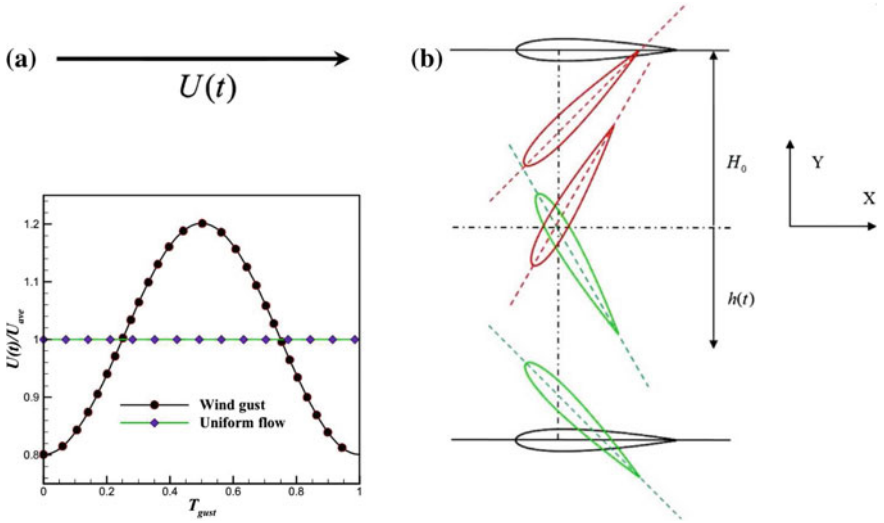

Fig. 10.5 **a** Sinusoidal flow fluctuations and **b** the kinematics of pitching-heaving airfoil in Chen et al. (2017). Reproduced with permission from Chen et al. (2017)

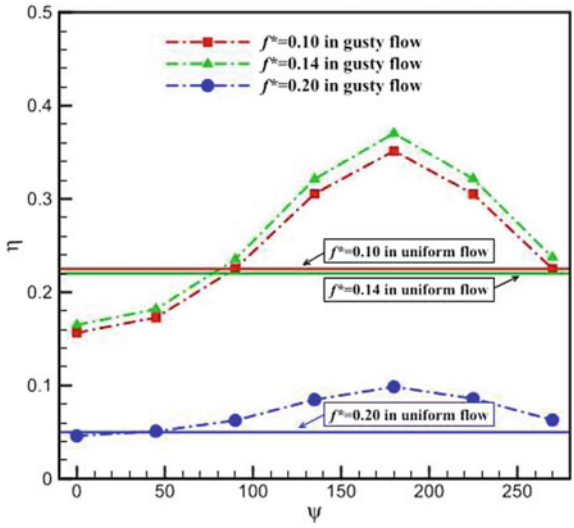

Fig. 10.6 Variation of harvester efficiency η with variation in the phase difference Ψ between the gust and the pitch Chen et al. (2017). Reproduced with permission from Chen et al. (2017)

observed. In contrast, at higher frequencies, the efficiency has a peak value at an optimal amplitude.

Xiang et al. (2015) studied aeroelastic energy harvesting from a piezo-electric wing under a 1-Cosine discrete gust through a coupled aero-electro-elastic model. They optimized the energy harvester for a given gust through a parametric study for energy efficiency and energy output density. It was noted that maximum efficiency

and maximum output density occur at different optimal size of transducers. Bruni et al. (2017) note that in the pre-flutter regime, flutter based harvesters are typically subjected to unsteady and time-varying fluid forces. These are similar to broadband and impulsive excitations studied for general vibration based energy harvesters. They considered 1-Cosine and square gusts as idealization of continuous vertical turbulence. The gusts were deemed to be comparable if they had equal area under the curve defining the gust profiles. It was found that the square gust acted like a step input to the system and the response was transient decay of oscillations during and after the active period of the gust. For the 1-Cosine gust, the scenario was different. During the active period of the gust, the response had the same cosine profile as the gust, except for a time-lag. Beyond this period, the response was found to be transient decay. It was found that the power generated during the cosine gust was lesser than that generated from the transient decay after the gust. The power from the transient decay was also found to be dependant on the value of response at the termination of the gust. Both the gust profiles were found to produce more power after the gust than during it. The power generated during the square gust was found to be higher than that during the 1-Cosine gust. Note that the gust, being a cross-stream fluctuation acts akin to an external forcing on the system. The interesting observation of this study was that the power generated after the termination of the forcing was higher than that during the forcing. Since the discrete gust profiles themselves are idealizations of continuous turbulence, it is unclear how these insights would translate for continuous gust. In such a case, the transient decay would not be largely existent and the increased power expected could be absent (Fig. 10.7).

Bruni et al. (2017) also studied the variation in the power output with variation in the gust gradient. It was observed that during the square gust, the peak power increased with increase in gust gradient. In contrast, a decrease in peak power was observed with increase in gust gradient for the 1-Cosine gust. Likewise, the average power output after the termination of the gust was found to increase with increase in the gust gradient for the square gust. However, for post-termination response corresponding to the 1-Cosine gust, an optimal gradient existed beyond which both the peak instantaneous power and the average power decreased with increase in gust gradient. Additionally, it was found that for both the gust profiles, an optimal electrical resistance of the harvesting circuit existed beyond which the gust seemed to

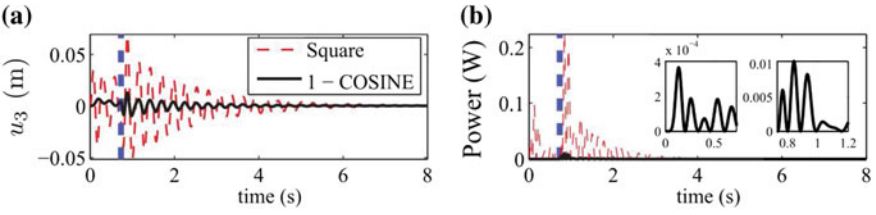

Fig. 10.7 **a** Displacement and **b** instantaneous power output of the harvester for square and cosine gust studied in Bruni et al. (2017). The blue dashed line marks the end of the active period of the gust. Reproduced with permission from Bruni et al. (2017)

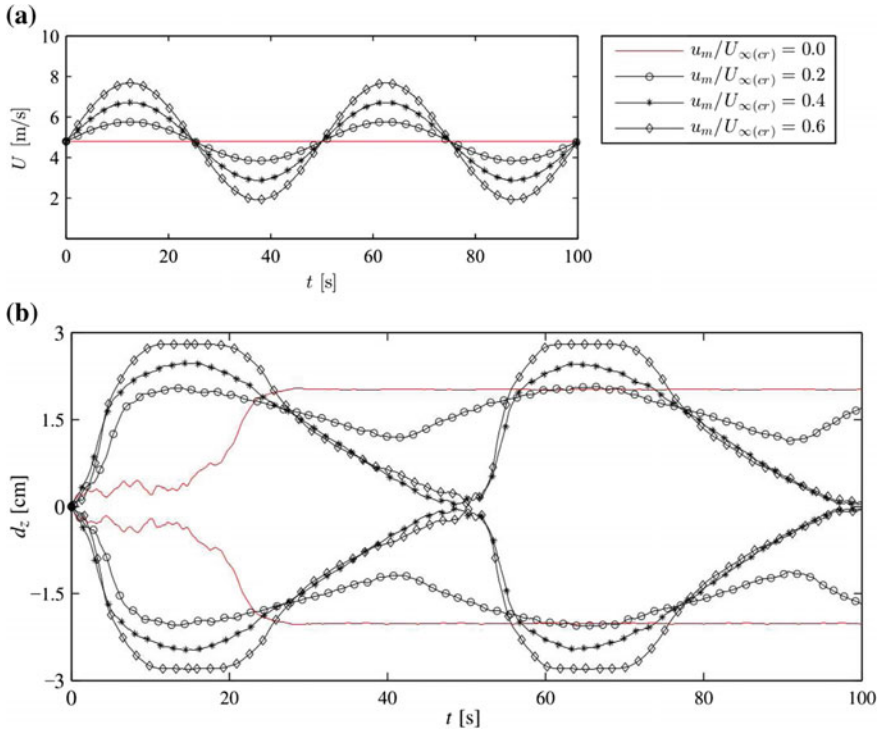

Fig. 10.8 Flow velocity fluctuations and displacment time histories for different non-dimensional amplitude of imposed fluctuations in Chawdhury et al. (2018). Reproduced with permission from Chawdhury et al. (2018)

have no effect on the wing. Chawdhury et al. (2018) numerically studied the effect of a pulsating flow on a T-shaped flutter based energy harvester through a single degree of freedom model coupled with a vortex particle method based fluid solver (see Fig. 10.8). Periodic streamwise flow velocity fluctuations were superimposed on a mean flow. The fluctuations were chosen to have low frequency for computational convenience as well as to model larger eddies present in natural fluid flows. They noted that the flow fluctuations caused a change in the onset of flutter. An early commencement of unstable motion was observed, though amplitude of the resulting oscillations was observed to be smaller than the corresponding steady flow case. These two effects were attributed to effective negative aerodynamic damping occurring when instantaneous flow velocity was lesser than the mean velocity and effective positive aerodynamic damping when it was otherwise. They compared the two damping effects using flutter derivatives and concluded that the net effect was

effectively that of a negative damping. However the study was restricted to modelling of fluid-structure interaction and the effects of pulsating flow on the power output wasn't investigated.

10.5 Freestream Turbulence

Though the 1-Cosine pulses and periodic streamwise flows enable easy exploration of effects of freestream flow fluctuations, they do not capture the complete effects of turbulence. For instance, these models do not account for the co-existence of different spatial and temporal scales in turbulent flows and their simultaneous interaction with the harvester. This necessitates the need to study realistic turbulence and its effects on the flow energy harvesters. A short summary of recent research on this front is presented next. Fei et al. (2012) proposed a wind belt based harvester designed to operate under low mean-wind-speed random flow conditions. The harvester performed better under higher mean velocities when the spring constant was higher, enabling better aero-elastic coupling. A peak output of 7mW at mean flow velocity of 2m/s was observed. Such randomly fluctuating flows can result from boundary layers of objects or inherent turbulence in the freestreamflow. Andreopoulos et al. (2015) investigated the effect of size and strength of turbulent eddies on energy harvesters (see Figs. 10.9 and 10.10). Two scenarios were experimentally studied- an inhomogenous turbulent field in a boundary layer and a homogenous grid-generated turbulence. They noted that turbulent flow degraded the performance of resonance based energy harvesting. It was found that the power harvested varied nonlinearly with change in turbulence length scales.

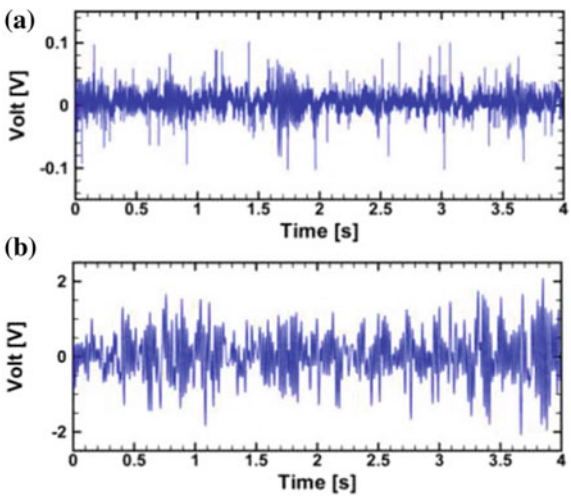

Fig. 10.9 Votage time histories for **a** boundary layer turbulence and **b** grid-generated turbulence for the harvester in Andreopoulos et al. (2015). Reproduced with permission from Andreopoulos et al. (2015)

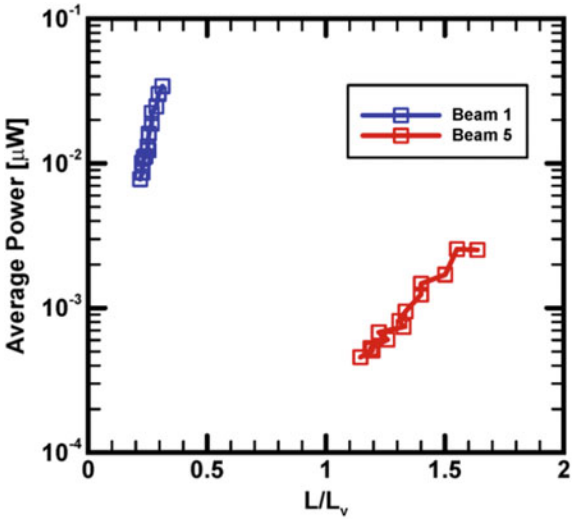

Fig. 10.10 Variation of average power output with the length scale of turbulence for the harvester studied in Andreopoulos et al. (2015). Reproduced with permission from Andreopoulos et al. (2015)

St. Clair et al. (2010) used the pressure fluctuation in a cavity to harvest energy from a piezo-electric beam (see Fig. 10.11). The design was inspired from air-flow induced oscillations inside harmonicas. A supercritical Hopf bifurcation was found to occur and limit cycle oscillations yielded sustained power output of the range 0.1–0.8 mW in the flow velocity range of 7.5–12.5 m/s. An electro-mechanical model and a Galerkin discretization based reduced order model for the harvester was later developed by Bibo et al. (2011). Akaydın et al. (2010) tested a harvester under pure freestream turbulence and obtained 0.06 μW at 11 m/s. This was lesser than 4 μW obtained at 11 m/s behind a cylinder. Hobeck and Inman (2012) studied inverted/vertical cantilever beam arrays, termed as 'piezo-electric grass' (Figs. 10.12 and 10.13). They attempted to harvest energy from low velocity high turbulence flows as in rivers. The experiments used a bluff body upstream with mean freestream velocity of 7 m/s and turbulence intensity of 25% impinging on the 'grass'. A power output of 1 mW was observed for PVDF patch and PZT Quickpacks(TM).

Lundström and Krus (2012) performed a flight testing of a MAV in real turbulent atmospheric flow. Effect of turbulence on the performance of MAV was found to be negligible, though the MAV flight itself was heavily disturbed by the unsteady effects caused by turbulence. However it was noted that turbulence seemed to offset drag increase due to yaw oscillations expected for a steady aerodynamics. Similar investigations have also been carried out by Emmanuel Bénard's group (Bonnin et al. 2015; Gavrilovic et al. 2017, 2018, 2019). Zhu (2012) performed numerical simulations of a flapping foil placed in a shear flow. The foil was found to undergo sustained periodic oscillations for low shear rates and optimal parameter values for energy harvesting were identified. The region in the parameter space over which

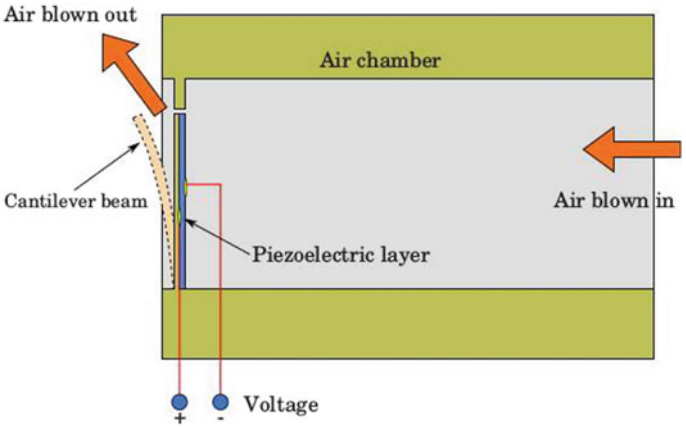

Fig. 10.11 A schematic of the cavity based harvester in St. Clair et al. (2010). Reproduced with permission from St. Clair et al. (2010)

Fig. 10.12 A schematic of harvester studied in Hobeck and Inman (2012). Reproduced with permission from Hobeck and Inman (2012)

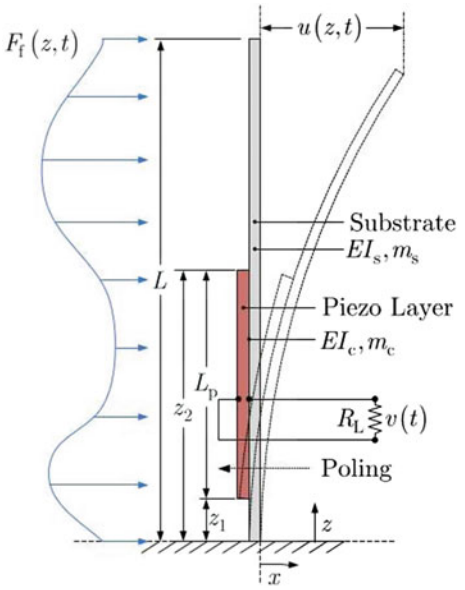

periodic oscillations occurred were observed to be bigger than that for uniform flows. However, for large shear rates, such regions completely disappeared and irregular oscillations less suitable for energy harvesting were also observed. Kwuimy et al. (2012) explored energy harvesting from a magneto-piezo-elastic Duffing oscillator placed in a turbulent flow (see Figs. 10.14 and 10.15). A periodic forcing with a Gaussian distributed random phase was used to simulate turbulent airflow. The energy output, from inter-well oscillations that occur once the potential barrier was

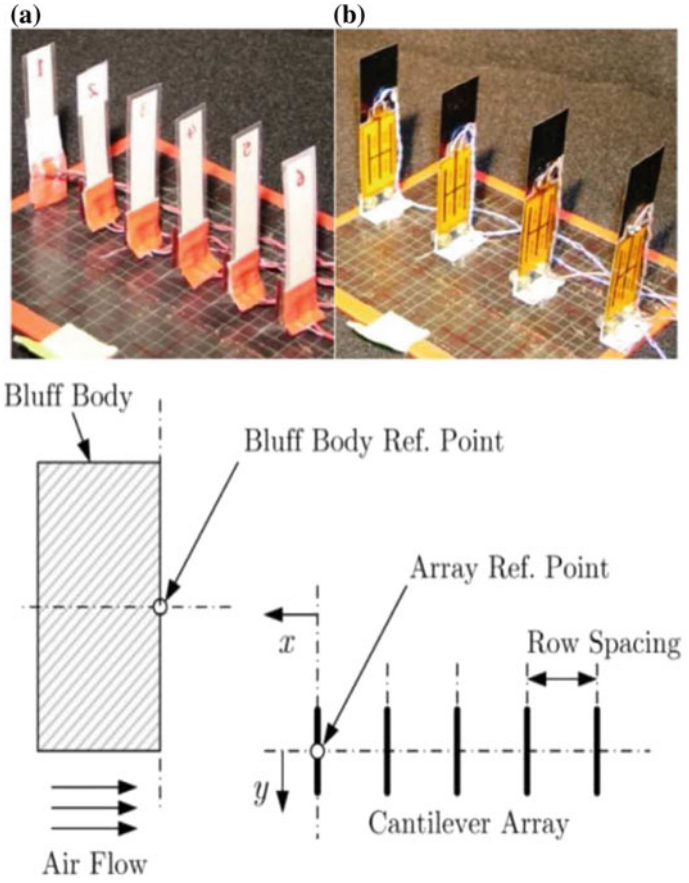

Fig. 10.13 Array of harvestors forming the piezo-electric 'grass' proposed in Hobeck and Inman (2012): **a** using PVDF patches and **b** using PZT Quickpacks. (**c**) Schematic of the placement of the harvesters. Reproduced with permission from Hobeck and Inman (2012)

overcome, were maximum when the noise intensity was such that the system was closer to stochastic resonance.

Wang and Inman (2013a, b) designed a multi-functional wing spar for energy harvesting and gust alleviation in UAV flight. They considered a filtered Gaussian noise with a Dryden PSD spectrum. Variation of gust scale length was imparted by using a gust gain factor in the frequency domain. The model was supposed to mimic clear sky flight with cumulus cloud gusts. Their theoretical and numerical investigations indicated that active gust alleviation was feasible through self-powered piezoelectric wafers. The harvested power was observed to be higher for longer active length of the spar. McCarthy et al. (2015) studied a triangular polymeric leaf attached through a hinge to a PVDF stalk which itself is fixed to a cylindrical base (see Figs. 10.16 and 10.17). In wind tunnels experiments, they replicated atmospheric

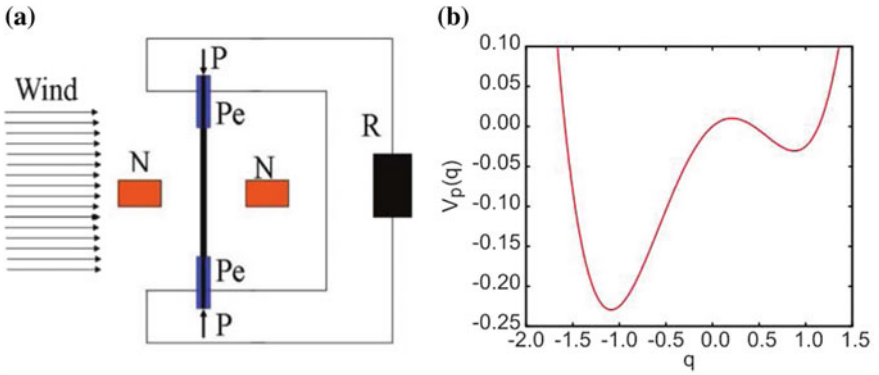

Fig. 10.14 **a** Schematic of harvesters studied in Kwuimy et al. (2012) and **b** the corresponding potential well. Reproduced with permission from Kwuimy et al. (2012)

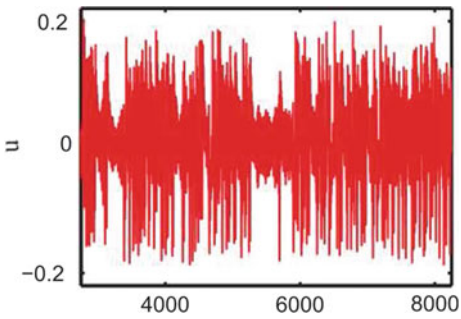

Fig. 10.15 Harvester response near stochastic resonance with prominent inter-well oscillations for the harvester in Kwuimy et al. (2012). Reproduced with permission from Kwuimy et al. (2012)

boundary layer flow using an upstream grid and placed the harvester at sufficient distance downstream to cause a well mixed turbulence. They found that turbulence is generally detrimental to energy harvesting for bluff body- wake foil harvesters. However at high incidence angles of the harvesters, turbulence improved the power output. Increase in power was noted to be possibly due to increased higher frequency contributions. In contrast, at small pitch and yaw angles, turbulence in the flow was noted to dampen the harvester response and acted as a dynamic damping mechanism. Goushcha et al. (2015) experimentally tested the energy harvesting potential of thin flexible cantilever beam piezo-electric harvesters placed in a turbulent boundary layer (see Fig. 10.18). It was seen that the power output increased with higher mean horizontal flow velocity and the optimal position was a region close to the wall.

These studies indicate that both periodic and turbulent fluctuations in fluid flows possess ample potential for energy harvesting. However, it must be noted that the efforts towards a practical flow fluctuation energy harvester is still in nascent stages. Note that significant focus along these ideas have occurred only over the last decade, in contrast to four decades of flow energy harvesting. In addition to the inherent complexity of the flow fluctuations, issues in appropriately modelling and testing them respectively through numerical models and experiments aggravate the slow pace of

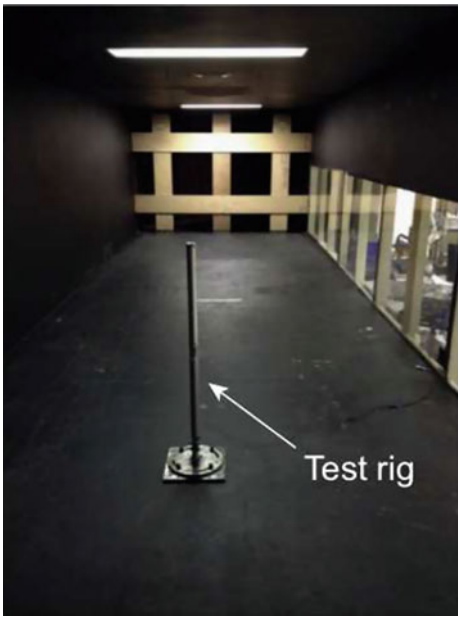

Fig. 10.16 Setup for grid turbulence and test rig for the harvester studied in McCarthy et al. (2015). Reproduced with permission from McCarthy et al. (2015)

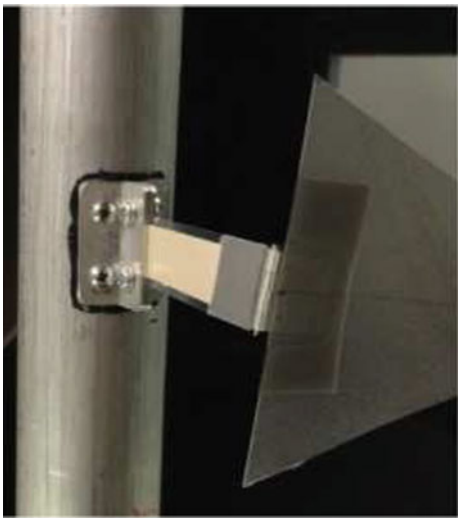

Fig. 10.17 A close view of the piezo-electric leaf harvester in McCarthy et al. (2015). Reproduced with permission from McCarthy et al. (2015)

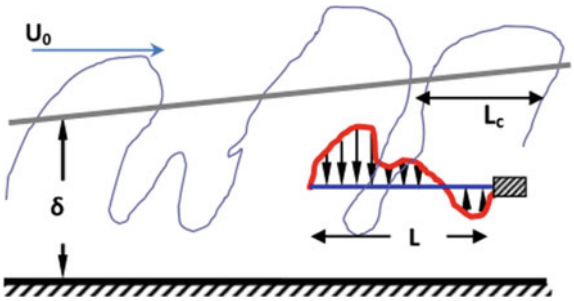

Fig. 10.18 Schematic of harvester in boundary layer turbulence in Goushcha et al. (2015). Reproduced with permission from Goushcha et al. (2015)

progress. Despite four decades of research, hardly any low power flow energy harvester has successfully been commercialised. Flow fluctuations based energy harvesting presents a possible solution to this conundrum, and also significant research challeges.

10.6 Conclusion

This chapter provided a brief background of flow energy harvesting and the necessity and use of considering the fluctuations inherent in the flow. A cursory description on modelling of flow fluctuations has been provided. The chronological development of research on energy extraction from pulsating, periodic and turbulent flow has been provided. Significant emphasis has been given to recent developments in this regard. While a significant body of research has emerged on energy harvesting from flow fluctuations, many aspects of the problem are still scantily explored. While most studies have focussed on effects of fluctuations on a particular harvester configuration, more generic studies akin to fundamental studies on generic nonlinear broadband harvesters need to be conducted. Likewise, little attention has been paid on suitably designing the electrical subsystem of the harvester which needs to be resilient to the irregular or fluctuating nature of the power generated in most of these harvesters. As natural fluid flows are often fluctuating, investing research effort along these lines can be extremely rewarding as the field of flow energy harvesting matures further.

References

Abdelkefi A (2016) Aeroelastic energy harvesting: a review. Int J Eng Sci 100:112–135

Abdelkefi A, Ghommem M (2013) Piezoelectric energy harvesting from morphing wing motions for micro air vehicles. Theor Appl Mech Lett 3(5):052004

Abdelkefi A, Hasanyan A, Montgomery J, Hall D, Hajj MR (2014) Incident flow effects on the performance of piezoelectric energy harvesters from galloping vibrations. Theor Appl Mech Lett 4(2):022002

Adhikari S, Friswell MI, Inman DJ (2009) Piezoelectric energy harvesting from broadband random vibrations. Smart Mater Struct 18(11):115005

Akaydın HD, Elvin N, Andreopoulos Y (2010) Wake of a cylinder: a paradigm for energy harvesting with piezoelectric materials. Exp Fluids 49(1):291–304
Akaydın HD, Elvin N, Andreopoulos Y (2013) Flow-induced vibrations for piezoelectric energy harvesting. In: Advances in energy harvesting methods. Springer, Berlin, pp 241–267
Allen JJ, Smits AJ (2001) Energy harvesting eel. J Fluids Struct 15(3–4):629–640
Andreopoulos Y, Danesh-Yazdi AH, Goushcha O, Elvin N (2015) The effects of turbulence length scale on the performance of piezoelectric harvesters. In: ASME (Oct. 2015), p V002T22A005
Anton SR, Inman DJ (2008) Vibration energy harvesting for unmanned aerial vehicles. In: The 15th international symposium on: smart structures and materials and nondestructive evaluation and health monitoring. International Society for Optics and Photonics, pp 692824–692824
Bibo A, Li G, Daqaq MF (2011) Electromechanical modeling and normal form analysis of an aeroelastic micro-power generator. J Intell Mater Syst Struct 22(6):577–592
Bonnin V, Bénard E, Moschetta J-M, Toomer CA (2015) Energy-harvesting mechanisms for uav flight by dynamic soaring. Int J Micro Air Veh 7(3):213–229
Bruni C, Cestino E, Frulla G, Marzocca P (2014) Development of an aeroelastic wing model with piezoelectric elements for gust load alleviation and energy harvesting. In: ASME 2014 international mechanical engineering congress and exposition. American Society of Mechanical Engineers, pp V001T01A057–V001T01A057
Bryant M, Garcia E (2011) Modeling and testing of a novel aeroelastic flutter energy harvester. J Vib Acoustics 133(1):011010
Bryant M, Mahtani RL, Garcia E (2012) Wake synergies enhance performance in aeroelastic vibration energy harvesting. J Intell Mater Syst Struct 23(10):1131–1141
Chen Y, Zhan J, Wu J, Wu J (2017) A fully-activated flapping foil in wind gust: energy harvesting performance investigation. Ocean Eng 138:112–122
Claudia B, James G, Giacomo F, Enrico C, Pier M (2017) Energy harvesting from aeroelastic vibrations induced by discrete gust loads. J Intell Mater Syst Struct 28(1):47–62
Cutler M, McLain T, Beard R, Capozzi B (2010) Energy harvesting and mission effectiveness for small unmanned aircraft. In: AIAA guidance, navigation, and control conference, p 8037
Daqaq MF (2012) On intentional introduction of stiffness nonlinearities for energy harvesting under white gaussian excitations. Nonlinear Dyn 69(3):1063–1079
Erturk A, Inman DJ (2008) A distributed parameter electromechanical model for cantilevered piezoelectric energy harvesters. J Vib Acoustics 130(4):041002
Fei F, Mai JD, Li WJ (2012) A wind-flutter energy converter for powering wireless sensors. Sens Actuators A: Phys 173(1):163–171
Gavrilovic N, Benard E, Pastor P, Moschetta JM (2017) Performance improvement of small unmanned aerial vehicles through gust energy harvesting. J Aircraft 55(2):741–754
Gavrilovic N, Bronz M, Moschetta J-M, Benard E (2019) Bioinspired energy harvesting from atmospheric phenomena for small unmanned aerial vehicles. In: AIAA Scitech 2019 Forum, p 0570
Gavrilovic N, Mohamed A, Marino M, Watkins S, Moschetta J-M, Bénard E (2018) Avian-inspired energy-harvesting from atmospheric phenomena for small uavs. Bioinspiration Biomimetics 14(1):016006
Goushcha O, Akaydin HD, Elvin N, Andreopoulos Y (2015) Energy harvesting prospects in turbulent boundary layers by using piezoelectric transduction. J Fluids Struct 54:823–847
He Q, Daqaq MF (2014) Influence of potential function asymmetries on the performance of nonlinear energy harvesters under white noise. In: ASME 2014 international design engineering technical conferences and computers and information in engineering conference. American Society of Mechanical Engineers, pp V006T10A060–V006T10A060
Hobeck JD, Inman DJ (2012) Artificial piezoelectric grass for energy harvesting from turbulence-induced vibration. Smart Mater Struct 21(10):105024
Hoblit FM (1988) Gust loads on aircraft: concepts and applications. American Institute of Aeronautics and Astronautics

Jamshidi S, Dardel M, Pashaei MH, Alashti RA (2015) Energy harvesting from limit cycle oscillation of a cantilever plate in low subsonic flow by ionic polymer metal composite. Proc Inst Mech Eng Part G: J Aeros Eng 229(5):814–836

Jinwu X, Yining W, Daochun L (2015) Energy harvesting from the discrete gust response of a piezoaeroelastic wing: modeling and performance evaluation. J Sound Vib 343:176–193

Jones KD, Davids ST, Platzer MF (1999) Oscillating-wing power generation. In: 3rd ASME/JSME joint fluids engineering conference. San Francisco, CA

Katzmayr R (1922) Effect of periodic changes of angle of attack on behavior of airfoils

Kim I-H, Jung H-J, Lee BM, Jang SJ (2011) Broadband energy-harvesting using a two degree-of-freedom vibrating body. Appl Phys Lett 98(21):214102

Kumar SK, Bose C, Ali SF, Sarkar S, Gupta S (2017) Investigations on a vortex induced vibration based energy harvester. Appl Phys Lett 111(24):243903

Kwuimy CAK, Litak G, Borowiec M, Nataraj C (2012) Performance of a piezoelectric energy harvester driven by air flow. Appl Phys Lett 100(2):024103

Langelaan JW (2009) Gust energy extraction for mini and micro uninhabited aerial vehicles. J Guid Control Dyn 32(2):464–473

Lau YL, So RMC, Leung RCK (2004) Flow-induced vibration of elastic slender structures in a cylinder wake. J Fluids Struct 19(8):1061–1083

Lundström D, Krus P (2012) Testing of atmospheric turbulence effects on the performance of micro air vehicles. Int J Micro Air Veh 4(2):133–149

McCarthy JM, Watkins S, Deivasigamani A, John SJ, Coman F (2015) An investigation of fluttering piezoelectric energy harvesters in off-axis and turbulent flows. J Wind Eng Ind Aerodyn 136:101–113

McKinney W, DeLaurier J (1981) Wingmill: an oscillating-wing windmill. J Energy 5(2):109–115

Mehmood A, Abdelkefi A, Hajj MR, Nayfeh AH, Akhtar I, Nuhait AO (2013) Piezoelectric energy harvesting from vortex-induced vibrations of circular cylinder. J Sound Vib 332(19):4656–4667

Naudascher E, Rockwell D (2012) Flow-induced vibrations: an engineering guide. Courier Corporation

Onoue K, Song A, Strom BW, Breuer KS (2014) Cyber-physical energy harvesting through flow-induced oscillations of a rectangular plate. In: 32nd ASME wind energy symposium, p 0712

Park G, Rosing T, Todd MD, Farrar CR, Hodgkiss W (2008) Energy harvesting for structural health monitoring sensor networks. J Infrastruct Syst 14(1):64–79

Pellegrini SP, Tolou N, Schenk M, Herder JL (2013) Bistable vibration energy harvesters: a review. J Intell Mater Syst Struct 24(11):1303–1312

Peng Z, Zhu Q (2009) Energy harvesting through flow-induced oscillations of a foil. Phys Fluids 21(12):123602

Phillips WH (1975) Propulsive effects due to flight through turbulence. J Aircraft 12(7):624–626

Pobering S, Schwesinger N (2004) A novel hydropower harvesting device. In: 2004 international conference on MEMS, NANO and smart systems (ICMENS'04). IEEE, pp 480–485

Poirel DC, Price SJ (1997) Post-instability behavior of a structurally nonlinear airfoil in longitudinal turbulence. J Aircraft 34(5):619–626

Pozzi M, Guo S, Zhu M (2012) Harvesting energy from the dynamic deformation of an aircraft wing under gust loading. In: Health monitoring of structural and biological systems 2012, vol 8348. International Society for Optics and Photonics, p 834831

Rice SO (1944) Mathematical analysis of random noise. Bell Syst Tech J 23(3):282–332

Samir C, Dario M, Guido M (2018) Modeling of pulsating incoming flow using vortex particle methods to investigate the performance of flutter-based energy harvesters. Comput Struct 209:130–149

Shi S, New TH, Liu Y (2013) Flapping dynamics of a low aspect-ratio energy-harvesting membrane immersed in a square cylinder wake. Exp Thermal Fluid Sci 46:151–161

St. Clair D, Bibo A, Sennakesavababu VR, Daqaq MF, Li G (2010) A scalable concept for micropower generation using flow-induced self-excited oscillations. Appl Phys Lett 96(14):144103

Stanton SC, McGehee CC, Mann BP (2009) Reversible hysteresis for broadband magnetopiezoelastic energy harvesting. Appl Phys Lett 95(17):174103
Stephen NG (2006) On energy harvesting from ambient vibration. J Sound Vib 293(1–2):409–425
Tang L, Païdoussis MP, Jiang J (2009) Cantilevered flexible plates in axial flow: energy transfer and the concept of flutter-mill. J Sound Vib 326(1):263–276
Tang L, Yang Y, Soh CK (2010) Toward broadband vibration-based energy harvesting. J Intell Mater Syst Struct 21(18):1867–1897
Taylor GW, Burns JR, Kammann SA, Powers WB, Welsh TR (2001) The energy harvesting eel: a small subsurface ocean/river power generator. IEEE J Oceanic Eng 26(4):539–547
Taylor J (1965) Manual on aircraft loads. Technical report, advisory group for aeronautical research and development Paris (France)
Wang Y, Inman DJ (2013a) Simultaneous energy harvesting and gust alleviation for a multifunctional composite wing spar using reduced energy control via piezoceramics. J Compos Mater 47(1):125–146
Wang Y, Inman DJ (2013b) Experimental validation for a multifunctional wing spar with sensing, harvesting, and gust alleviation capabilities. IEEE/ASME Trans Mechatron 18(4):1289–1299
Williams CB, Yates RB (1996) Analysis of a micro-electric generator for microsystems. Sens Actuators A: Phys 52(1–3):8–11
Xiao Q, Zhu Q (2014) A review on flow energy harvesters based on flapping foils. J Fluids Struct 46:174–191
Young J, Lai JCS, Platzer MF (2014) A review of progress and challenges in flapping foil power generation. Prog Aerosp Sci 67:2–28
Zhu Q (2012) Energy harvesting by a purely passive flapping foil from shear flows. J Fluids Struct 34:157–169
Zhu Q, Peng Z (2009) Mode coupling and flow energy harvesting by a flapping foil. Phys Fluids 21(3):033601

Part IV
Dynamics and Control of Combustion Systems

Chapter 11
Syngas Combustion Dynamics in a Bluff-Body Turbulent Combustor

Nikhil A. Baraiya and S. R. Chakravarthy

Abstract Future energy needs that are supplemented by combustion require alternate fuel sources derived from both fossil and non-fossil sources. In this regard, syngas provides a relatively clean and large-scale resource. However, contrasted to conventional gaseous fuels, syngas poses challenges along both static and dynamic stability of flames owing to source dependent composition changes. These often result in altered global flame stabilization and dynamics when compared to its constituents being individually combusted. The present chapter deals with dynamic challenges is syngas combustion, when its static component, i.e., flame stabilization, is taken to be sufficiently addressed by resorting to non-premixed combustion. The chapter is descriptive of the combustion dynamics of syngas combustion across varying compositions in a turbulent bluff-body combustor, with focus on numerous aspects that need to be accounted to explain the vastly different behavior that syngas combustion dynamics display. The differences in the dynamic behavior of syngas compared to fuels that have been sought to "mimic" syngas like hydrogen-enriched hydrocarbon include-1. Excitation of higher modes across similar parameter change and most significantly 2. Presence of two heat release rate zones as a result of differing diffusion and chemical time-scales. Time-resolved pressure, velocity and OH* and CO_2* imaging reveal that peculiarities arising in syngas combustion dynamics are a result of various steady and unsteady processes viz. fuel to air momentum ratio, the effect of the same on mean flame stabilization, baroclinic torque, shear layer stabilization and the offset between peak OH* and CO_2* concentrations. The foresaid processes are aided by the time-lag between acoustic quantities that result in excitation of various modes as seen from a simple theoretical model. The chapter thus explains the unique nature of syngas combustion from a multitude of well-established combustion theories that are required to understand and control the dynamic challenges of syngas combustion.

N. A. Baraiya (✉) · S. R. Chakravarthy
Department of Aerospace Engineering, National Centre for Combustion Research and Development, Indian Institute of Technology Madras, Chennai 600036, India
e-mail: nikhildwivedi77@gmail.com

A. Mukhopadhyay et al. (eds.), *Dynamics and Control of Energy Systems*,
Energy, Environment, and Sustainability,
https://doi.org/10.1007/978-981-15-0536-2_11

Keywords Syngas · High-frequency combustion instability · OH* chemiluminescence · CO_2* chemiluminescence

11.1 Introduction

The gasification of coal is an efficient way to use it as a fuel source in thermal power plants, due to clean combustion properties. Gasification of coal produces syngas, also called as town gas, consisting of hydrogen and carbon monoxide as its main constituents, and traces of methane, nitrogen and carbon dioxide. The composition of the syngas is dependent on the nature of coal and the process of the production. This results in significant variation of combustion properties like flame stability, flame-speed, ignition delay, etc. Furthermore, differences in characteristic flame time scales of syngas constituents, associated with both chemistry and transport, results in different modes of flame stabilization in turbulent flows (Lieuwen et al. 2008). In addition to steady-state and limit phenomena, the dynamic nature of syngas combustion is also dependent on the composition and the manner of operation (Lieuwen et al. 2009). In this context, under certain conditions, the positive feed-back between pressure and heat release rate oscillations can lead to large scale oscillations in the flow-flame quantities in the system, that can lead to flame flash-back, blow-off or even structural damage. The focus of the present chapter is on uncovering and addressing dynamic aspects of syngas combustion, in the sense of thermo-acoustic stability.

The role of combustion in exciting acoustics in a system is well known since Rayleigh (1945) and, comprehensive literature has been devoted towards flame-acoustic coupling (Dowling and Stow 2003; Zinn and Lieuwen 2005; Sé et al. 2003; Candel 2002; Lieuwen 2012; Chakravarthy et al. 2017). From these studies, we can broadly classify the studies into—(1) Identification of mechanisms responsible for combustion instability (2) Identification of conditions, that can excite combustion instability based on linear/non-linear stability theories (Chakravarthy et al. 2017; Dowling 1999; Kim et al. 2010; Palies et al. 2011; Han et al. 2015), (3) development of computational/experimental methodologies to obtain the stability map and (4) development of time-series analysis methods to characterize states of stable and unstable combustion (Han et al. 2015; Gotoda et al. 2011; Kabiraj et al. 2012). In general, the above broad classification distinguishes between stable and unstable combustion at fixed base states and fuel compositions. However, considering the wide range of composition that constitutes syngas, there have been relatively few direct and indirect attempts to identify key parameters influencing the dynamic stability of syngas combustion. Natarajan et al. (2007) have reported the effect of syngas composition on its flame speed, which is in-turn seen to influence the dynamic stability of the system. Similar Studies have been attempted on partially and non-premixed flames for similar fuel composition (Lee et al. 2013; Park et al. 2009). Dynamic processes like thermo-acoustic instability, auto-ignition, and blow-off/flashback have been studied in Lieuwen et al. (2008) that have been related to changes in limit phenomena and flame speed. Focusing on the main constituents of syngas, the presence of CO is

seen to dampen the acoustics (Lee et al. 2010, 2012), and hence has not been considered as a reactant in several studies, e.g. Park and Lee (2016) that have studied the thermo-acoustic nature of syngas. However, as seen from Baraiya and Chakrvarthy (2019), the amplitude, as well as spectra of oscillations in the non-premixed turbulent combustor, is drastically different for syngas (CO–H_2) compared to H_2–CH_4 combustion. The observed differences drive the need to understand the reasons for the difference in thermo-acoustic behavior and the role of CO in dictating them. The role of the other major constituent H_2 is reflected in another facet of combustion instability-mode shifts between various unstable states. In addition to the stable-unstable classification discussed above, the phenomena governing mode shifts in combustor are equally important but are far less studied. Most studies on mode shifts are based on flame describing functions (Palies et al. 2011; Han et al. 2015; Gotoda et al. 2011; Kabiraj et al. 2012; Natarajan et al. 2007; Lee et al. 2010, 2012, 2013; Park and Lee 2016; Park et al. 2009; Baraiya and Chakrvarthy 2019; Noiray et al. 2008), that identify the length of combustor as well as the incident velocity amplitudes to dictate mode shifts. However, such studies are confined to single fuel and hence do not account for the role of the fuel composition. In the context of Hydrogen added fuel compositions, mode shifts at different operating conditions viz. equivalence ratio and fuel composition has been studied in Park and Lee (2016), Yoon et al. (2015, 2017), Choi and Lee (2016), Balachandran et al. (2008), Altay et al. (2009), Hong et al. (2013), Chakravarthy et al. (2007). In general, the higher Hydrogen content is seen to excite higher harmonics, even skipping intermediate ones. Choi and Lee (2016) have ascribed this to the lowering of the convective length scale, based on flame length, that in-turn modifies the phase between pressure and heat release rate oscillations. Ghoniem and co-investigators (Taamallah et al. 2015a, b; Shanbhogue et al. 2016) have reported on the effect of H_2/CH4 ratio on flame macrostructures in sustaining different modes of combustion instability. The studies indicate the role of fuel-composition on flame topology, whether length or macrostructure to dictate the stability and mode of a multi-fuel combustion. Considering the fore-mentioned effects of CO and H_2 addition on combustion dynamics, a study involving the combined effect of combustion of both the fuels presents a considerable challenge to the present understanding of combustion dynamics.

The present chapter is dedicated to the study of mode shifts in a turbulent non-premixed combustor for syngas combustion and is an extension of (Baraiya and Chakrvarthy 2018, 2019a, b; Baraiya et al. 2017). The chapter is broadly divided into three parts: 1. Effect of fuels on combustion dynamics, 2. Effect of syngas composition on combustion dynamics and 3. theoretical analysis transition from low-frequency instability to high-frequency instability. The chapter begins with an investigation on the role of *Re* in determining the excitation of combustion instability, for a fixed flame-holder location. Subsequently, a bifurcation plot or stability map is illustrated to identify zones of different types of stability/instability across different fuels. We further discuss the excitation of the fundamental mode at low *Re*, followed by a stable zone and subsequently to a high-frequency instability for syngas, which is not seen for hydrocarbon-based or pure hydrogen combustion. Such transitions are hard to describe by a single phenomenon, e.g. changes in flame topology or

stabilization and will be seen to be a result of the total of various processes like fuel-air diffusion, mean flame. On the other hand, changing *Re* presents an effect, which is a sum total of various processes like fuel-air diffusion, flame stability, and position, as well as response to flow structures that modulate a flame. In the course of the chapter, we also reveal that unlike other gaseous fuels that have been investigated in the past syngas flame structure does not display drastic changes across the various zone. The peculiar nature of syngas combustion instability is revealed to be a result of the presence of two heat release rate zones. This is a new result, derived from rigorous experimentation. It will be seen, over the course of this chapter, on how the presence of the two heat release rate zones, as well as their separation, results in excitation of higher harmonics. Further, a simple theoretical model is formulated to explain the role of time/phase lags in promoting/suppressing the observed acoustic modes.

In summary, the chapter is aimed at a comprehensive understanding of mode shifts in syngas combustion in bluff-body from the perspective of subtle changes in flame structure and phase lag between acoustic variables.

11.2 Experimental Setup

The experimental setup for the turbulent bluff-body combustor is as illustrated in Fig. 11.1. The combustor (Fig. 11.1) consists of four main components—1. settling chamber, 2. inlet duct, 3. primary combustor with optical access window, and 4. extension ducts. The inlet duct, primary combustor, and extension ducts are cumulatively 1970 mm in length. The settling chamber has a diameter of 280 mm followed by a sudden contraction, leading to a duct of 60×60 mm^2 cross-section. Air enters the primary combustor through the settling chamber and arrangement of honeycomb and wire meshes ensure uniform inlet conditions, whereby it is fed inside the inlet ducts by an annulus of width 13 mm. Subsequently, the flow is expanded from the annulus to the entire cross-section of the primary combustor (zoomed in Fig. 11.1). The annulus is terminated by four zero degree vanes positioned at 90° for supporting the fuel supply line, placed along the central axis of the combustor.

The fuel line is a 2000 mm long stainless steel tube ID of 9 mm, and thickness 1.5 mm, that provides sufficient length for internal mixing. The downstream end of the fuel pipe is fastened to a stainless steel disc of thickness 15 mm height and diameter of 30 mm. This disc acts as the flame holder. The circumference of the disc is drilled with 16 equally spaced holes of diameter = 1.5 mm to deliver fuel. The upstream end of the fuel line is fastened to a Y shaped joint that is connected to hydrogen and carbon monoxide feed line from the respective cylinders.

The fuel (Hydrogen and Carbon monoxide) and air are regulated and metered using mass flow controllers (Alicat make) with an uncertainty of 0.8% of full scale and ±0.2% of measured reading.

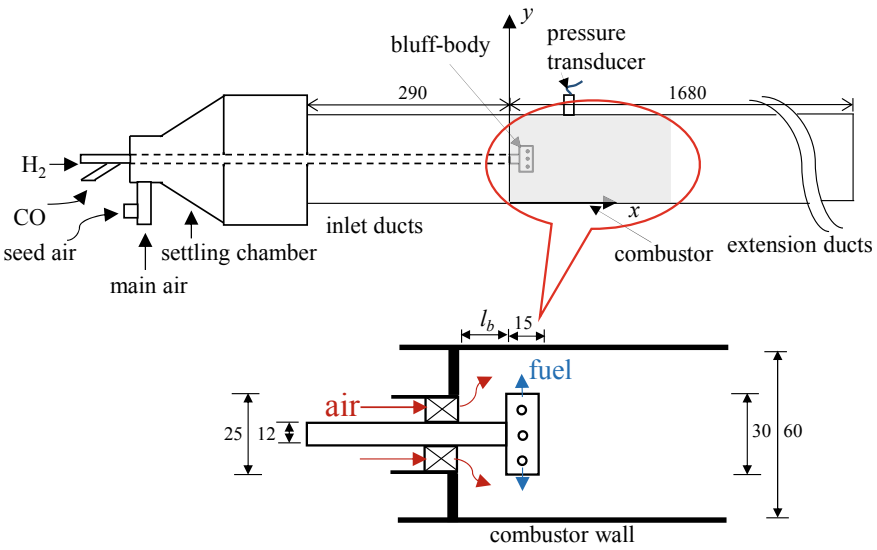

Fig. 11.1 Schematic of bluff body stabilized non-premixed turbulent combustor (all dimensions are in mm). Reprinted from Baraiya and Chakravarthy (2019), 15598–15609, with permission from Elsevier

Measurements and Operating Conditions.
The stability map of the combustor is mapped by measurement of dynamic pressure by piezoelectric pressure transducers (103B02 model, PCB make, the sensitivity of 225 mV/kPa), at eight axial locations as adopted in our previous work (Baraiya and Chakrvarthy 2019). The range of *Re* and tested, for the stability mapping is tabulated in Table 11.1. The pressure fluctuations are measured by keeping the bluff-body location (l_b) and the fuel flow rate as constant and varying the *Re*, for given fuel mixtures viz. three syngas compositions, synthesis natural gas (SNG) and pure hydrogen (PH) as illustrated in Table 11.1. The sampling rate is 9 kHz for a duration of 3 s at each condition. The diameter of the bluff body is taken as length scale, and velocity of the air at sudden expansion to the combustor is used for the *Re* calculations.

Table 11.1 List of operating conditions

Gas name	Composition (% vol.)			*Re* of air	l_b
	H_2	CO	CH_4		
SG-1	25	75	0	2200–8000 in step of ~600	10 mm
SG-2	50	50	0		
SG-3	75	25	0		
SNG	75	0	25		
PH	100	0	0		

The second set of experiments combine simultaneous time-resolved OH*, and CO_2*/CH* chemiluminescence imaging (Phantom make, model V611) mounted in opposite directions and focused on the same plane. The cameras are used at their full frame resolution of 1280 × 800 pixels. For OH* chemiluminescence, a 100 mm UV lens is used along with a Lambert intensifier and a filter of transmitivity 310 ± 5 nm. For CO_2*/CH* chemiluminescence, a 50 mm Nikor lens with a filter centered around 430 nm is used. The OH* and CO_2*/CH* high-speed chemiluminescence imaging is performed at a framing rate of 4000 frames per second (fps) over 1 s.

In the next set of imaging experiments, high-speed PIV and OH* chemiluminescence imaging are performed with high-speed cameras mounted on opposite sides and focused on the same plane. The cameras are used at their full frame resolution of 1280 × 800 pixels^2 with a FOV of 104.9 × 65.57 mm^2. For PIV imaging, a 100 mm Tokina lens with a 527 nm band-pass filter is used. Nd:YLF laser (Litron make) at a wavelength of 527 nm is used as an illumination source for Mie-scattering of alumina seeding particle. Synchronization and simultaneous triggering of laser, cameras, intensifier, and pressure transducer are done with BNC model 575 pulse/delay generator. The dynamic pressure measurement and OH* chemiluminescence is done at a framing rate of 6 kHz, whereas the PIV is recorded at 3 kHz. The delta time for all cases is 15 μs. The post-processing of the raw PIV images is done by software package PIV view taking interrogation window of 32 × 32 pixels with window overlap of 75%, and the overall correlation coefficient was ensured to be always above 0.5.

11.3 Results and Discussion

11.3.1 Effect of Fuels on Combustion Dynamics

Acoustic Characterization

It is observed that by sweeping the *Re* in the range of 2200–8000, in steps described earlier, we can observe the shift in dominant frequency of pressure oscillations for different fuels, as shown in Fig. 11.2a. The dominant frequency is evaluated from the Fourier transform (FFT) of the underlying time-series. We first focus on the three syngas compositions (SG-1, SG-2, and SG-3). It is seen that irrespective of the syngas composition variation, the dominant frequency is ~130 Hz until $Re < 4000$. This frequency corresponds to the fundamental duct acoustic mode, confirmed by the impedance tube technique (Baraiya and Chakrvarthy 2019). For $Re > 4000$, we can observe the shift in dominant frequency from ~130 to ~500 Hz for all syngas compositions. The frequency ~500 Hz is seen to be the third harmonic of the duct acoustic mode. The dominant frequency is ~480 Hz for the composition with least hydrogen (SG-1) ~ 520 Hz for the composition with highest Hydrogen content (SG-3) and ~500 Hz for composition with intermediate Hydrogen content (SG-2) between $4000 < Re < 6000$. The minor difference in the high-frequency values are a result

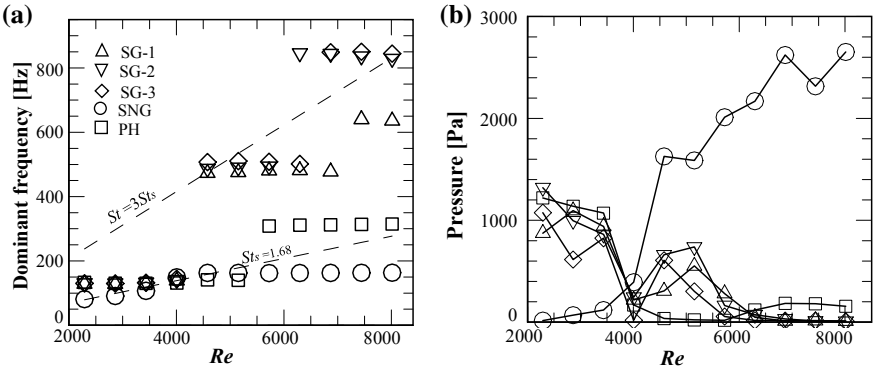

Fig. 11.2 Variation of **a** acoustic frequency and **b** corresponding acoustic amplitude over the test range of *Re* for three different syngas compositions, pure hydrogen and synthesis natural gas. Reprinted from Baraiya and Chakravarthy (2019), 15598–15609, with permission from Elsevier

of the differences in the combustion product temperature of different compositions illustrated in Table 11.2 (obtained by using the ANSYS Chemkin Pro 18.1® using OPPDIFF model and Davis H_2/CO (Davis et al. 2005) mechanism). On the further increase of *Re* from 6000 to 8000, the composition with highest and intermediate hydrogen composition display dominant frequencies ~800 Hz and the composition with least hydrogen at ~650 Hz. The PH case displays a frequency shift from fundamental acoustic mode (~130 Hz) to the first harmonic (~280 Hz) at $Re > 5000$. For SNG the linear increasing trend is observed in the frequency from ~87 Hz at $Re < 5000$, after which it remains constant ~160 Hz.

The linear rise in the frequency with *Re* for SNG necessitates the investigation on the role of flow instabilities in sustaining combustion instability. This has been reported earlier by Chakravarthy et al. (2007), whereby the duct acoustics locks-on to a dominant flow structure. The latter is seen to shed at a constant Strouhal number, whose value depends on the nature of flow instability. In the present work, the Strouhal number, *Sts* corresponding to the linearly increasing frequency of SNG combustion was seen to be = 1.68. This value describes the separated shear layer frequency for flow past circular disc (Berger et al. 1990; Zhong et al. 2014). In the range of low *Re* (<4000) we could observe that SNG and PH follows the constant *Sts* = 1.68, whereas all three syngas compositions follow the constant Strouhal number line, whose slope is thrice that of *Sts*. This observations clearly signify the presence

Table 11.2 Adiabatic flame temperature variation across syngas composition

Composition (% by vol.)	Adiabatic flame temperature (K)
SG-1	2027
SG-2	2155
SG-3	2250

of the flow-acoustic lock-on between the shear layer mode in the hydrodynamic field downstream of the bluff-body and longitudinal natural acoustic mode of the combustor.

The corresponding pressure amplitudes, evaluated at the dominant frequency, are shown in Fig. 11.2b. The pressure amplitudes for all syngas compositions display a trend of high amplitude at low *Re*, followed by a sudden drop at *Re* ~ 4000, and then an increase with *Re* till *Re* ~ 5100. Beyond *Re* ~ 5100, the pressure amplitudes are significantly lower, although they possess coherent spectral content (higher harmonics). Hence, with an increase in *Re*, the transition of the dynamical system from the low-frequency instability (high-pressure amplitude) to high-frequency instability (low-pressure amplitudes) at *Re* ~ 4000 is observed. Such an abrupt shift in the nature of oscillations has been seldom reported in turbulent combustors. For PH, a similar trend of peaks in the pressure amplitude is observed for the range of tested *Re*, as seen in syngas mixtures. However, for PH, the second peak in pressure amplitude is observed at much higher *Re* (>6000), and the amplitude is ~200 Pa. Further, pressure amplitude drops after *Re* > 7000. SNG shows the continuous rise in the pressure with *Re*, which almost saturates for *Re* > 7000. The dominant frequency is also seen to attain constant value, which implies the onset of the classical definition of combustion instability.

Similar to the exercise carried out for Fig. 11.2, FFT is performed on the heat release rate for all the fuel compositions. This is shown in Fig. 11.3. The heat release rate here represents the integrated pixel intensity values performed across all the time instants from OH* chemiluminescence imaging. It is clear from Fig. 11.3, that the heat release rate has a spectral content identical to the one derived from unsteady pressure. This confirms that the heat release rate oscillations are the source of acoustics in the present system, and thereby confirming the thermo-acoustic nature of the same. Further, the dominant spectral content matches that of the duct natural modes, thereby negating other modes of instabilities like Helmholtz resonance, intrinsic flame instabilities, etc.

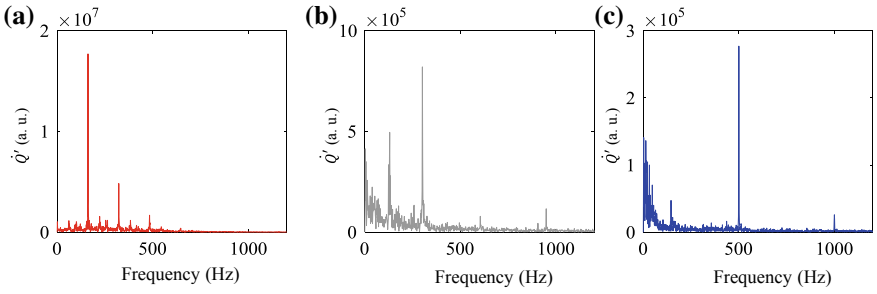

Fig. 11.3 Amplitude spectrum of total heat release rate (OH* chemiluminescence images) for **a** SNG at *Re* ~ 8000 **b** PH at *Re* ~ 6900 and **c** SG-3 at *Re* ~ 4600. Reprinted from Baraiya and Chakravarthy (2019), 15598–15609, with permission from Elsevier

Here, SG-3 is taken to be representative of all the syngas compositions. This is justified in view of all syngas compositions displaying identical global dynamics. The subtle differences amongst syngas compositions in dictating their combustion dynamics will be discussed later in the chapter. From Fig. 11.3, one can observe that SNG has a heat release rate oscillations that are two orders of magnitude higher compared to both PH and SG. We further observe that SNG displays harmonics at ~320 and ~480 Hz, which are likely to be a result of non-linear interactions resulting in the generation of higher harmonics. In contrast, PH displays a dominant peak at the first harmonic and a secondary peak at the fundamental mode, which is representative of period-2 oscillations. SG displays a strong peak at the third harmonic, with a small contribution seen from the fundamental mode. Figure 11.3 conclusively establishes that SG combustion dynamics is significantly different from that of PH or SNG. In fact, the spectral content clearly points out to the role of CO in determining it, and hence to play a significant role in describing syngas combustion dynamics.

The following sections in the chapter will pertain to explaining the role of CO in specific and its relation to hydrogen combustion, to describe the peculiarities in syngas combustion. As a first step, we resort to an analysis of flame chemiluminescence images in the forthcoming section.

Time-Resolved Flame Dynamics Across the Fuel Mixtures

Flame dynamics across fuel mixtures Fig. 11.4 shows the time-resolved OH* chemiluminescence images, corresponding to the instants marked over the pressure cycle shown above the flame images for all the fuel mixtures. The conditions corresponding to the images are listed in the figure caption. The *Re* is chosen, such that it subscribes to the condition of maximum pressure.

From Fig. 11.4a we can observe that for SNG, large-scale modulation of the flame is seen across the pressure cycle instants (Fig. 11.4a (i–iv)). The large scale modulation results in the high magnitude of OH* chemiluminescence oscillations at the listed frequency shown in Fig. 11.3. These large-scale flame modulations are seen to involve flame lift-off and flashback, which cause significant variations in the total heat release rate across a pressure cycle. It is also clear that the flow structures resulting in such bulk flame modulation are of the order of the disk diameter. Whereas, seen from Fig. 11.3b, c the PH and SG-3 flames are seen to be modulated by small scale bluff-body shear layer structures, which result in lower pressure amplitude. This is because of the stabilization of these flames, extending from the injection holes towards the separated shear layer of the circular disk. This will be discussed later. Also, it is seen that SG-3 exhibits serrations, which are equally spaced as seen from the flame images. These correspond to the excitation of shear layer vortices at their third harmonic. Such a feature is not seen prominently in PH combustion. This is a result of hydrogen combustion happening in the vicinity of the injection holes as will be seen later.

The difference in amplitude of combustion instability for low and high *Re* for PH and SG combustion is seen to correlate with shorter flames at the former condition (Baraiya and Chakravarthy 2019) (not shown in the present chapter). This necessitates

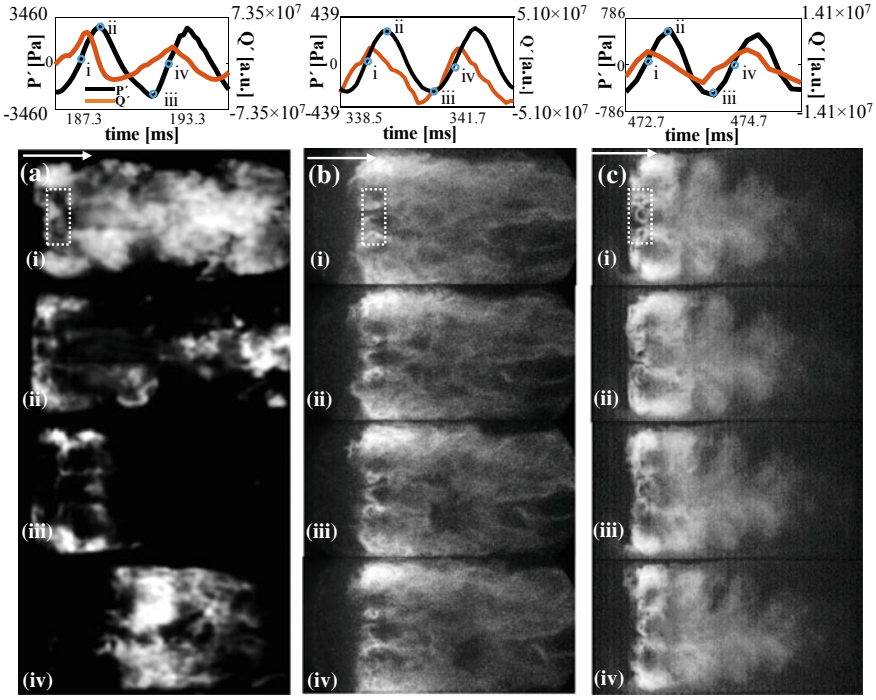

Fig. 11.4 Time-resolved OH* chemiluminescence images corresponding to pressure cycle marked ((o)) from i–iv for **a** SNG at *Re* ~ 8000 **b** PH at *Re* ~ 6900 and **c** SG-3 at *Re* ~ 4600. Reprinted from Baraiya and Chakravarthy (2019), 15598–15609, with permission from Elsevier

us to probe the role of flame stabilization in dictating the amplitude and spectral content across *Re*. This is addressed next.

Mean Flame Dynamics Across the Fuel Mixtures

The mean flame structure across the fuel mixtures is analyzed by averaging the instantaneous flame images across all the time-instants and is shown in Fig. 11.5. From the figure, it is clear that the location of the peak heat release rate are different

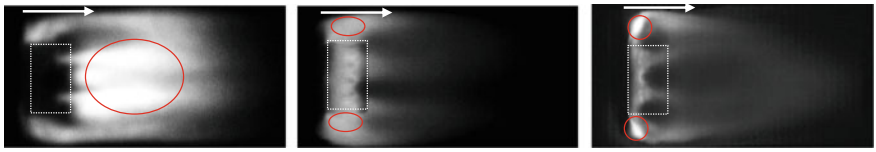

(a) 75%H_2-25%CH_4 at *Re* ~ 8000 (b) 100% H_2 at *Re* ~ 6900 (c) 75%H_2-25%CO at *Re* ~ 4600

Fig. 11.5 Time-averaged OH* chemiluminescence images for three different fuels. The red circles in images indicates the regions of maximum intensity. Reprinted from Baraiya and Chakravarthy (2019), 15598–15609, with permission from Elsevier

across the fuel mixtures. Considering that at high *Re*, the global effect of diffusion can be neglected, the observed differences are a result of the fuel-cross jet and the incoming air. Thus, the observed flame stabilization is a result of the combined effects of 1. the equivalence ratio, which dictates the extent of OH* radicals formed and 2. The fuel-jet turning, which is dependent on the momentum flux ratio of the fuel and incoming air.

In the case of SNG, we observe that the bulk of flame as well as region of maximum intensity is present in the wake (marked by a red circle) of the bluff body. This is a result of the low momentum ratio of the fuel to air jet, owing to a lower molecular mass of the individual constituents. For the case of pure hydrogen, the most luminous regions are in the vicinity of the fuel injection holes. This is a result of high local diffusivity and reactivity of hydrogen that leads to combustion as soon as it is injected into the air stream. SG-3 combustion follows an intermediate pattern between the PH and SNG combustion. It is seen that the diffusivity and reactivity of hydrogen is reduced as a result of lower concentration gradient with the incoming air. This is marked by the relatively low luminosity in the neighborhood of the injection holes. Further, the high momentum flux of the fuel jet (high molecular weight of CO) results in the flame stabilizing in the shear layer as opposed to in the wake of the bluff body, shows the bright regions of the intensity in the shear layer of the bluff-body as the momentum of the fuel to air is obviously lower but still considerable due to which the flame is anchored in the shear layer of the flame.

As a result of the mean flame stabilization of the fuel mixtures, SNG tends to promote large scale modulation by flow structures, due to promotion by virtue of baroclinic torque as seen in Fig. 11.4a. For the other fuels (SG-3 and PH), large scale wake vortices formation is inhibited by the baroclinic torque, which has now reversed its orientation due to the peak heat release rate happening in the shear layer. Next, we focus our discussion on observations that were reported from Fig. 11.4. This is motivated by the observation that SG displays flame modulations that are entirely different from PH and SNG combustion. To explain the observed behavior, we resort to joint analysis of the CO_2*/CH* and OH* chemiluminescence images. Analysis of mean Flame structure through CO_2*/CH* and OH* chemiluminescence.

Time-Averaged Spatial Intensity Variation (SIV) Plots

Although several methods exist to identify regions in flame, that are markers of peak reactivity, an elegant and simple manner to estimate the same is derived by summing the intensity across "pixel strips" for each axial pixel location. These integrated pixel intensity values for both the radical emissions, when normalized by the peak integrated intensity, are represented as spatial intensity variation (SIV) plots. The SIV plots of OH* and CO_2* radicals are also useful to gain insights into attributes of the flame structure such as flame stabilization point, flame length, growth, and convection. Along with the SIV plots, a plot displaying the grey-scale OH* chemiluminescence images overlapped by CO_2*/CH* chemiluminescence is shown. The CO_2* radical is formed in the fuel containing only H_2 and CO, whereas in the presence of the hydrocarbon fuels, the CH* is also formed (Ning et al. 2017; Shih and

Hsu 2012). Thus the visible intensity captured in the range of 400–500 nm by a camera with a filter having peak around 440 nm is due to continuum blue emission from CO_2* for the three syngas mixtures and CH* predominantly in the case of SNG.

One can observe, that for SNG flames (Fig. 11.6a), the OH* and CH* chemiluminescence, and SIV, exactly overlaps indicating that the location of peak OH* and CO_2* concentrations is nearly overlapping, resulting in the presence of a unified or single reaction zone. Also, the SIV is seen to peaking the region of the wake of the bluff body, which agrees with our previous observations. Figure 11.6b shows the presence of OH* emission for PH combustion. The peak concentration is seen to be near the fuel injection holes. However, while observing SG-3 flame at *Re* ~ 4600 (Fig. 11.6c), we note that peak OH* location has significant spatial stagger compared to peak CO_2* location, which is seen downstream of OH*. This indicates the presence of two-reaction zones in the case of SG combustion. The presence of more than one reaction zone, which is not a result of staging, illustrates the role of chemical kinetics to understand such flames. The result is of paramount importance and is the central premise of the present work.

In addition to chemical kinetics, it is also important to note that the transport of methane is faster than carbon-monoxide owing to lower molecular mass and hence will aid in the formation of a single reaction zone. We next describe the presence of the two heat release rate zones, as a result of competing and symbiotic chemistry among the two fuels.

Chemical Kinetics of Syngas

The reactions that govern the combustion kinetics of syngas as per Rahnama et al. (2017) are as follows.

$H_2 + M = H + H + M$	(R1)
$H_2 + O_2 = HO_2 + H$	(R2)
$H + O_2 = O + OH$	(R3)
$O + H_2 = H + OH$	(R4)
$OH + H_2 = H + H_2O$	(R5)
$H + O_2 + M = HO_2 + M$	(R6)
$HO_2 + H_2 = H_2O_2 + H$	(R7)
$H_2O_2 + M = OH + OH + M$	(R8)
$HO_2 + HO_2 = H_2O_2 + O_2$	(R9)
$HO_2 + H = OH + OH$	(R10)
$HO_2 + O = OH + O_2$	(R11)
$CO + OH = CO_2 + H$	(R12)
$CO + O_2 = CO_2 + O$	(R13)
$O_2 + M = O + O + M$	(R14)
$O + H_2O = OH + OH$	(R15)

(continued)

(continued)

$H_2 + M = H + H + M$	(R1)
$CO + HO_2 = CO_2 + OH$	(R16)

Reaction R1 and R2 are two main initiation reactions, in which hydrogen molecules are being dissociated. The chain branching reactions R3 and R4 take place with the production of OH* radical.

Formation of H_2O terminates the reaction due to it is non-reactive nature. Reactions R6–R8 occur only at high pressure. Reactions R9–R11, are important at high temperature. Reactions R12 and R13 show the oxidation reactions of CO. For the oxidation of CO, the presence of OH* radical is very important, as the activation energy required by reaction R12 is much less when compared to R13. Reactions R14 and R15 accelerate CO oxidation. Reaction R16 takes place at elevated pressure. The key point from the above reactions is that, for the oxidation of CO, the presence OH* is crucial.

Returning back to our observations from Fig. 11.6c, the first peak in SIV plots of OH* chemiluminescence figure is due to the oxidation of H_2 molecules (shown in above reaction steps), which forms the OH radicals (R1–R3) (Rahnama et al. 2017; Chaos and Dryer 2008). For the oxidation of CO, the OH* radicals are required as the activation energy for reaction R13 is much higher than R12 (Kéromnès et al. 2013; Joshi and Wang 2006). Thus, the majority of CO_2* is formed after the production of OH*. With an increase in the H_2 content in syngas, the higher concentration of OH* radicals is generated, leading to significant oxidation of CO to form CO_2*. This is further seen from Fig. 11.6c, whereby we see a direct correlation between the value of the second OH* peak and the extent of CO_2* radicals emission. The excessive production of OH* radicals initiates quicker CO oxidation leading to significant detection of CO_2* SIV plot close to the peak OH* SIV plot at higher H_2 content as well as a large extent downstream of the bluff-body. The afore-mentioned processes result in the presence of two reaction zones which behave like two oscillators, a result seldom reported earlier.

The SIV plots are further extended to the time-resolved images and used to compute the convective velocity by tracing the peaks of CO_2* SIV across the time instants. The value was found to be 13.17 m/s. The average stagger obtained from time-resolved OH* and CO_2* SIV is seen to be 31.33 mm. From these values, the time lag between the two heat release rate locations was computed to be 2.38 ms. This was found to be matching the acoustic time scales at high-frequency instability, having a time period of 2 ms. This leads to uncovering a central mechanism of the excitation of high frequency in SG combustion, i.e., the time-lag associated with the stagger being equal to the third harmonic of the duct acoustic mode. This time-lag is seen to be a characteristic of SG combustion, as other fuels do not possess this attribute. After analyzing and establishing the differences in SG combustion with other fuel, next, we shift to the next section of the chapter, whereby we focus on the role of syngas composition in altering the combustion dynamics characteristics among them.

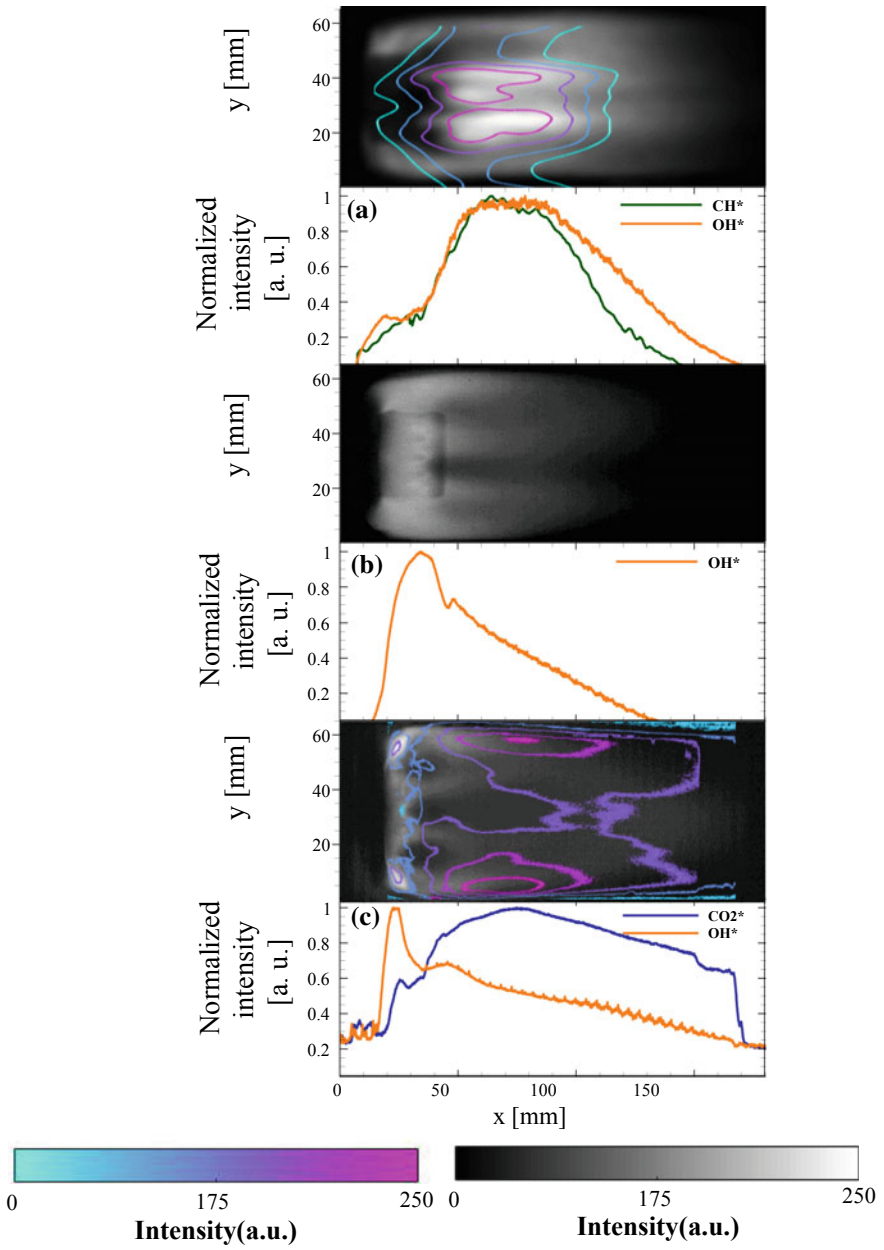

Fig. 11.6 Time-averaged OH* chemiluminescence image (in gray scale) superposed by CH*/CO_2* color line contour followed by corresponding spatial intensity variation plots for **a** SNG at *Re* ~ 8000 **b** PH at *Re* ~ 6900 and **c** SG-3 at *Re* ~ 4600. Reprinted from Baraiya and Chakravarthy (2019), 15598–15609, with permission from Elsevier

11.3.2 *Effect of Syngas Composition on Combustion Dynamics*

In the present section, we will exclusively compare the fluid mechanics, flame dynamics of various syngas compositions and their interaction.

Time-Averaged Flame and Flow Field Across Syngas Composition

Figure 11.7 shows the comparison of time-averaged images of PIV, OH* and CO_2* chemiluminescence for all the three syngas compositions at high *Re*. The increase in the hydrogen content in the fuel mixture of syngas is seen to increase the chemiluminescent intensities of both the radicals. The axial length over which the chemiluminescence is prominent also increases, relative to the SNG-1 (Fig. 11.7I), where the flame is seen to be quite compact. These observations are due to the presence of enhanced hydrogen, which in-turn increases carbon monoxide oxidation. This results in increased heat release rate (He et al. 2014), and longer flame length. We can observe the flame jet-turning angle to increase with the percentage of the hydrogen in the syngas fuel mixture due to lower jet momentum flux associated with higher hydrogen content.

In a bid to understand the role of flow-field in dictating the mean flame behavior, the mean velocity field corresponding to different syngas compositions is shown in

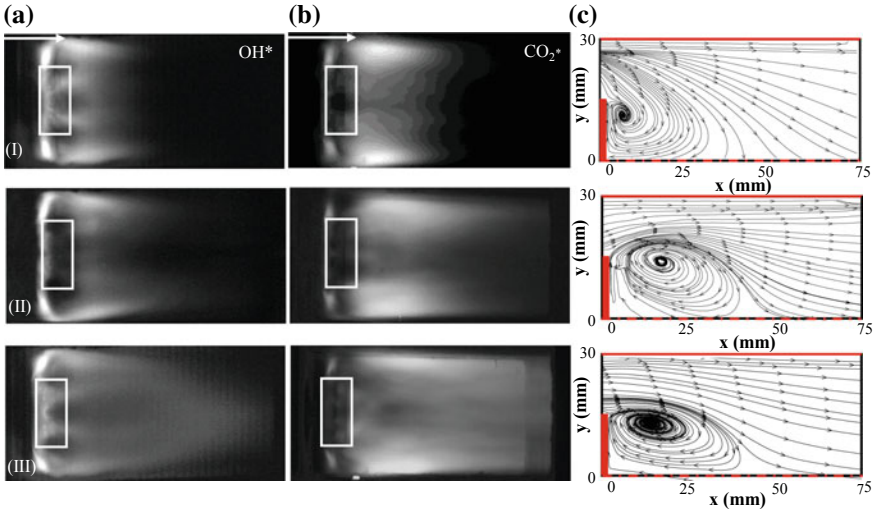

Fig. 11.7 Time-averaged **a** OH* chemiluminescence images, **b** CO_2* chemiluminescence images and **c** mean flow structures for three different syngas compositions with increase in the percentage of hydrogen content(top to bottom) in syngas mixture viz; (I) SG-1 at *Re* ~ 5100 (II) SG-2 at *Re* ~ 5100 and (III) SG-3 at *Re* ~ 4600. The flow direction is from left to right. The half plane is shown for PIV images owing to bilateral symmetry. The bluff body is marked as the solid red block in the lower left corner in PIV images. Reprinted from Baraiya and Chakravarthy (2019), 15598–15609, with permission from Elsevier

Fig. 11.7c. The classical mean flow field of a bluff body is seen, namely features like a central recirculation zone. However, it is clearly seen that syngas composition plays major role in dictating the extent of recirculation zone, as seen from the mean velocity field. The span of vortex bubble is seen to increase with an increase in hydrogen content, which could be due to higher temperature induced expansion as also reported in Lee et al. (2013). These subtle changes in the mean flow-flame field can impact the frequency of oscillations that is seen to vary across syngas compositions. This can be further understood by examining the mean flame images, whereby higher hydrogen flames are seen to occupy more area and are more luminous, resulting in higher average temperature in the system. This would result in the speed of sound to be marginally higher across compositions with higher hydrogen. Following the analysis of time-averaged fields, we resort to SIV based analysis, similar to what was performed for various fuel mixtures, but with a slightly altered objective of estimating the extent of fluctuations in the SIV field.

SIV Fluctuations Across Syngas Compositions

The spatio-temporal evolution of the time-resolved SIV from time-resolved OH* and CO_2* chemiluminescence is shown in grey contour in Fig. 11.8. The local maxima at individual time instants are represented by the dotted line superposed on the contour map. From these peak SIV displacement, we again reinforce that OH* peak SIV fluctuations are in the neighborhood of the fuel injection holes. While CO_2* peak SIV fluctuations are seen to fluctuate much downstream of the fuel injection holes as a result of the previously described sequential oxidation. This observation hold true for all syngas compositions.

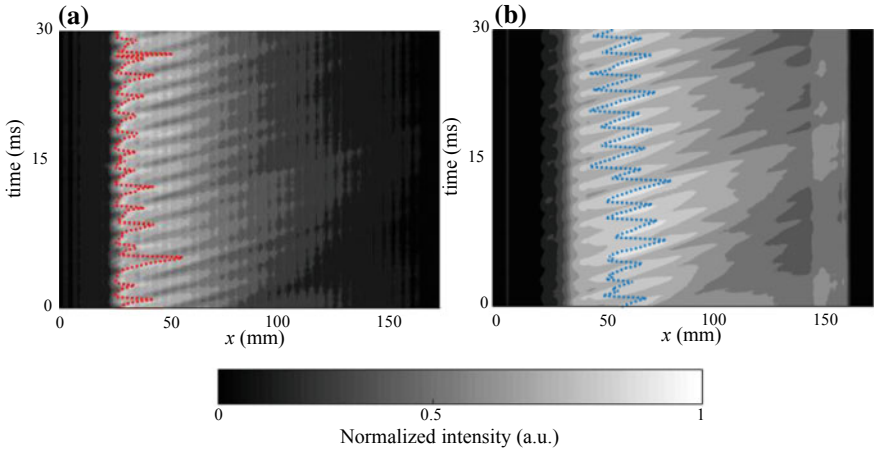

Fig. 11.8 Spatio-temporal evolution of the SIV contour in gray scale derived from **a** OH* chemiluminescence overlaid by local maximum peak in red dotted line and **b** CO2* chemiluminescence overlaid by local maximum peak in blue dotted line for SG-3. Reprinted from Baraiya and Chakravarthy (2019), with permission from Elsevier

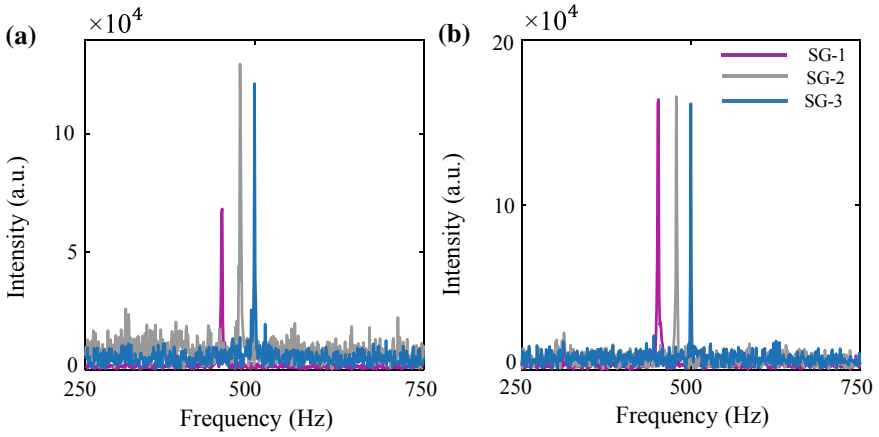

Fig. 11.9 Amplitude spectra from **a** OH* chemiluminescence and **b** CO_2* chemiluminescence images for different composition of syngas from SIV peak fluctuation. Reprinted from Baraiya and Chakrvarthy (2019), with permission from Elsevier

The amplitude spectra of the time series corresponding to the peak SIV value fluctuations for OH* and CO_2* chemiluminescence images are shown in Fig. 11.9. The corresponding frequencies for SG-1 are ~450 Hz, for SG-2 is ~480 and ~500 Hz for SG-3 from both OH* and CO_2* data, corresponds exactly to the dominant acoustic pressure frequency. This is expected in the light of the fact that SIV represents integrated flame characteristics, similar to the heat release rate spectra obtained in Fig. 11.3. The fluctuations in the displacement of peak SIV of either radicals imply the modulation of regions having instantaneously high luminosity values by convection, whose time-scales correspond to acoustic time-scales. From the spectra plots, it is also clear that SG-2, the composition with intermediate hydrogen concentration has the highest pressure amplitude as a result of larger displacement, particularly of that of OH* SIV. A higher displacement of the peak SIV values implies larger flame motion along the longitudinal direction, resulting in substantial energy addition to the acoustic field if the Rayleigh condition is satisfied. This aspect is discussed next.

Rayleigh Index Map Across Syngas Composition

The spatial Rayleigh index mappings for the various syngas fuel compositions are shown in Fig. 11.10. The map is obtained by performing a cycle average of the unsteady pressure and heat release rate oscillation at the dominant acoustic frequency. The spatial map is obtained by considering each pixel in the camera image to be a flame element. The images at the top correspond to OH* chemiluminescence, whereas the bottom side panel depicts CO_2* chemiluminescence. As evident from the images, the driving, as well as damping regions of flame, are sharp and discrete that display the presence of shear layer vortex train and the flame being modulated by these vortices. One can observe, that as the hydrogen content is increased, the structure of the driving/damping regions becomes significantly altered. At higher H_2,

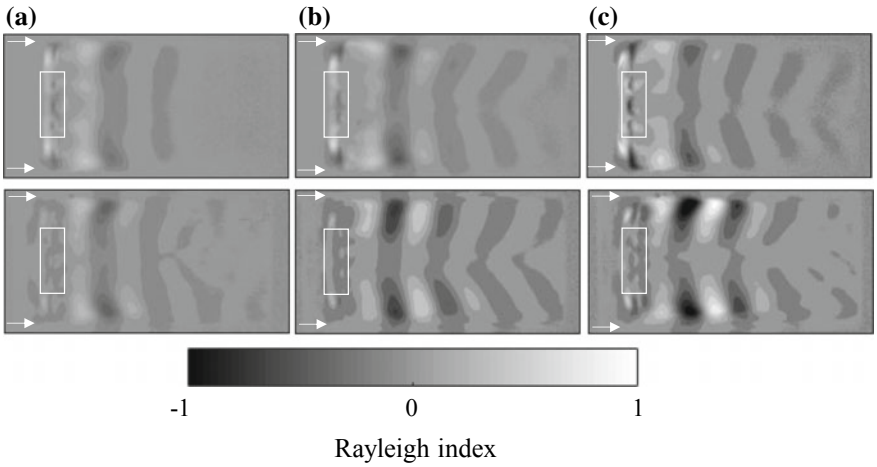

Fig. 11.10 Rayleigh index map for **a** SG-1 at *Re* ~ 5100 **b** SG-2 at *Re* ~ 5100 and **c** SG-3 at *Re* ~ 4600, from time-resolved OH* chemiluminescence images (top row) and CO_2* chemiluminescence images (bottom row). White rectangles indicate the bluff body and arrows indicate the flow direction from left to right. Reprinted from Baraiya and Chakrvarthy (2019), with permission from Elsevier

we observe that the CO_2* chemiluminescence displays clearly demarcated driving and damping regions, as contrasted to low H_2 condition.

Also, one can note that across all the compositions, that the region just downstream of the bluff-body is a driving region for both the OH* and CO_2* chemiluminescence, or both the heat release zones. This might be a result of the exodus of OH* radicals formed, which ensure rapid oxidation of the CO fuel in the mixture, resulting in near simultaneous excitation of the pressure fluctuation by the two heat release rate contributors (OH* and CO_2*). Subsequently, we see a damping region that is a result of the flame being modulated during negative pressure fluctuation or rarefaction. We can observe, that although the CO_2* map displays in driving that is co-linear with OH* map as described earlier, the peak driving regions corresponding to CO_2* are actually further downstream, which is a corroboration of the chemical kinetics scheme described earlier. Subsequently, the reactions, that are getting completed, result in them playing little role in exciting acoustics, as shown by the Rayleigh index map in far downstream of the bluff body. To summarize, the rich dynamics of syngas combustion across different compositions in a bluff body combustor is seen to be a result of numerous factors viz. mean flame stabilization, interaction or presence of flame in shear layer, the role of hydrogen in aiding CO combustion and most importantly—the presence of two heat release rate zones with optimal extent of stagger.

Next, we analyze the excitation of both low and high-frequency instability seen in syngas combustion from a theoretical perspective. The role of a time-delay between acoustic pressure and unsteady heat release rate as well as the contribution of two heat release rate zones in determining the time-delay are discussed in the same context.

11.3.3 Theoretical Analysis of Excitation of Multiple Modes in Syngas Combustion

The theoretical formulation to explain the observed behavior in the syngas is based on Crocco's $n-\tau$ model (McManus et al. 1993), whereby the flame is modeled to per purely modulated by acoustic velocity and is compact. The pictorial representation of the same is shown in Fig. 11.6. Considering the low Mach number limit, existing in the present study and the wavelength of acoustics at all the desired frequencies significantly larger than the flame extent, we can write the governing equations as McManus et al. (1993) (Fig. 11.11).

The flame is compact and stabilized at 'a' from the left open end. A and B are the right and left running waves upstream of the flame, and C and D represent the same downstream.

$$p'_{up} = \left(Ae^{ik_1(x-a)} + Be^{-ik_1(x-a)}\right)e^{-i\omega t} \tag{11.1}$$

$$p'_{ds} = \left(Ae^{ik_1(x-a)} + Be^{-ik_2(x-a)}\right)e^{-i\omega t} \tag{11.2}$$

where, p'_{up} is the upstream pressure oscillation and p'_{ds} is the downstream pressure oscillation. $k_1 = \frac{\omega}{c_{up}}$ and $k_2 = \frac{\omega}{c_{ds}}$ The boundary conditions assuming open-open mode are—

$$p'_{up}(x = 0, t) = 0,\ p'_{up}(x = a + b, t) = 0 \tag{11.3}$$

The unsteady pressure is continuous across the flame, stabilized at 'a' and the velocity jump across the flame is related to the unsteady heat release rate. The unsteady heat release rate is modeled as a scaled and delayed version of the upstream acoustic velocity, i.e.

$$u'_{ds} - u'_{up} = (\gamma - 1)\frac{\dot{Q}'}{\rho_{up}c^2_{up}} \tag{11.4}$$

$$(\gamma - 1)\frac{\dot{Q}'}{\rho_{up}c^2_{up}} = nu'_{up}(a, t - \tau) \tag{11.5}$$

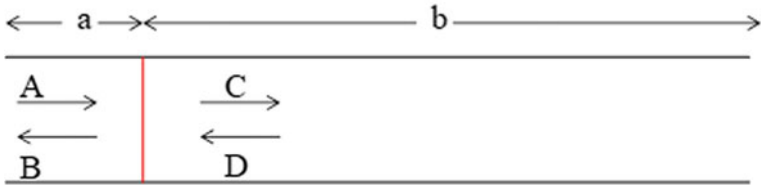

Fig. 11.11 Schematic for $n - \tau$ model

The two boundary conditions, along with the jump condition and pressure continuity can be expressed as—

$$\begin{bmatrix} e^{-ik_1a} & e^{ik_1a} & 0 & 0 \\ 0 & 0 & e^{ik_2b} & e^{ik_2b} \\ -\left(1+ne^{i\omega\tau}\right) & \left(1+ne^{i\omega\tau}\right) & \varepsilon & \varepsilon \\ 1 & 1 & -1 & -1 \end{bmatrix} [ABCD]' = 0; \tag{11.6}$$

ε is $\frac{\rho_{up}c_{up}}{\rho_{ds}c_{ds}}$ For a non-trivial solution, the determinant on the left has to vanish, which yields the following dispersion relation—

$$\tan(k_1a)\cot(k_2b) = \frac{-\varepsilon}{\left(1+ne^{i\omega\tau}\right)} \tag{11.7}$$

To solve the dispersion relation, we choose quantities by assuming that the specific gas constant and the ratio of specific heat is constant and equal to 287 J/kg K and 1.4, respectively. The specific heat C_p is taken to be 1000 J/kg K. Values of 'a' and 'b' are taken to be 285 and 1685 mm, respectively. The upstream (reactant) temperature T_{up} is chosen as 300 K and the downstream temperature is taken to be 1200 K at low *Re* (3000) and 1100 K at higher *Re* (5000). This is based on fitting a linear fit between the adiabatic flame temperature, T_f and the exhaust temperature and then calculating the mean temperature. The adiabatic flame temperature is calculated using NASA-CEA® for equilibrium combustion. The flame temperature corresponding to the low frequency instability is ~1900 and ~1800 K for the high frequency instability. The exhaust gas temperature is taken to be equal to 600 K, based on experimental data on the same setup but not as a part of the present work. To derive an estimate for the gain index, n, we use the following relations—

$$\dot{Q}' = G\bar{Q}\frac{u'}{\bar{u}} \text{ and } \bar{Q} = \dot{m}C_p\left(T_{\dot{f}} - T_{up}\right) \tag{11.8}$$

where, G is the flame transfer function, which is a complex quantity. In-fact, the magnitude of the flame transfer function is the coupling index 'n' in the $n-\tau$ model. The phase of the flame transfer function is related to the time-delay $-\tau$. Knowledge of the gain and phase of the flame transfer function requires experiments performed for different forcing frequencies or extensive computation. For significant excitation amplitudes, the majority of literature point out towards the gain to assume values between 0.3 and 1 for the majority of combustion systems. In view of the absence of flame transfer function measurements in the present work, we solve for Eq. 12 for all gain values between 0.3 and 1 in steps of 0.1. Further, people Park and Lee (2016) have derived the phase from time-scales that involve convection, reaction and propagation by assuming a single point as a representative of the entire flame. In the present work, the issue is compounded by the presence of two heat release rate zones. As we have already discussed, there exists a convective time-delay between the two heat release rate zones. The net gain is also a result of this delay between the heat

release rate zones, as the spatial Rayleigh index map represents regions of driving and damping. If one integrates the entire map, we would get the net gain or the coupling index. The issue of gain is tackled by varying the value of gain from 0.3 to 1 as stated earlier. To account for the crucial issue of time-lag/phase, we derive relation based between the OH* heat release rate measurement and the pressure. Considering that the time lag between the two heat release rate zones during high frequency instability is equal to the acoustic time scale at high, the addition of this delay in Eq. 11.7 will not alter the dispersion relation. For the low frequency instability case, we do not have reliable estimates of the time-lag. However, we have observed in the preceding sections that the flame stabilizes near the injection hole and near the combustor wall at low *Re*, which would imply that for all practical considerations, the time lag is negligible in the context of one dimensional acoustics. The dispersion relation is solved using Matlab® R 2018 using Newton-Raphson method. To estimate the stability of the dispersion relation, we examine the real and imaginary parts of ω, and if the imaginary part of ω is >0, then the mode is unstable. For the present work, we choose two values of the time delay, τ. For the low frequency instability, since the unsteady pressure and heat release rate fluctuations are in phase, the acoustic velocity would lead the heat release rate fluctuations by 3/4 T_1, where T_1 is the time period corresponding to the dominant oscillation frequency. In the present work, this is equal to 5.76 ms. The other time delay we choose corresponds to the high frequency instability, where the unsteady pressure and heat release rate fluctuations are having a phase difference of 90°, we choose the time lag to be the time period of oscillations = 2 ms. This is reasoned as follows—the unsteady heat release rate is the source of pressure fluctuations and thus leads it by 270°, This is identical to the phase difference of 90°, arrived from Fig. 11.3, but, reasoned out on the causal ground. Whereas the acoustic velocity always lags pressure by 90°, resulting in total lag to be the time period. For the listed conditions, it is seen that for both the time lags, as the gain is increased, the imaginary part (frequency) does not vary appreciably, however, the growth rate is enhanced as the gain is increased. To avoid, over prediction of growth rates, we choose a value of gain = 0.3 to calculate the growth rates and frequencies.

The complex frequencies with the real (frequency) and imaginary (growth rate) parts are listed in Table 11.3.

It is seen that the actual and predicted frequencies are close, and this also implies that the frequency at low *Re* instability is an Eigen value to the formulation with combustion. The positive growth rates imply the preference of these modes at the

Table 11.3 Frequencies and growth rates at the two unstable conditions, with listed time delays

Condition	Time delay (τ) (ms)	Predicted frequency (Hz)	Growth rate (s^{-1})
Low *Re* instability	5.76	169.8	0.00569
High *Re* instability	2	594.3	0.0393

listed conditions. It is seen that at the listed time delays, the growth rates at all other modes, other than the ones corresponding to the tabulated frequencies are negative and thus are not preferred or persist. It should be noted that the net growth is the difference between the ideal case presented here and the damping at the listed frequency. These observations illuminate us on the sensitivity of the preferred mode on the time lag between unsteady velocity and pressure.

It is worth noting that such an analysis underscores the role of physical mechanisms in generating and sustaining combustion instability. It is well known that coherent structures or purely velocity fluctuations (e.g., flame in a duct) are responsible hydro-dynamically in exciting the acoustics in the system. While conventional belief hinges on the presence/absence of these structures using stability analysis, it is further important to note that, even if the structures exist, they can excite acoustics if the time delay of interaction between them and the flame is conductive for the growth of oscillations at the particular frequency. This reasoning is critical as many coherent structures have a characteristic Strouhal number, which dictates the extent of circulation required before they shed off and hence modulate the flame (Matveev and Culick 2003). This in-turn will dictate the time-delay, and hence the stability of the system. In the present case, the shear layer coherent structures offer the critical time lag required to excite the acoustics in the system.

This also explains why the transition from low frequency to high frequency was by means of a stable route. As the *Re* is increased, the phase shifts between the acoustic velocity and pressure, and briefly enters a state whereby the damping rates at all frequencies are negative. However, during the transition, the mode with positive growth rate gets excited, resulting in oscillations at that frequency. The differential time lags associated with each of the mode of instability present a situation, where control based on predetermined feed-back might be notoriously hard to achieve. This necessitates the need to quantify the nature of instability to actuate control.

To summarize the chapter in brief, syngas provides for rich dynamical combustion behavior, which is usually not encountered in typical gas-powered combustors. The observed behavior stems from the presence of two reaction zones, largely a result of sequential oxidation and due to the phase relationship between pressure and heat release rate oscillations. The insights gained from the present work provide sufficient challenges for a rigorous understanding of syngas combustion instability that encompasses the disciplines of both chemistry and fluid mechanics based combustion. Addressing these challenges would pave the way for the development of gas turbines that focus on alternate sources.

11.4 Conclusion

The dynamic nature of syngas composition was studied to identify key physical and chemical factors affecting combustion stability characteristics. It is seen that syngas, as contrasted to pure hydrogen (PH) and hydrogen-methane (SNG) mixture excites much higher frequencies at the same *Re* range. This is explained on the basis of

mean flame stabilization, fuel chemistry and as a result-presence of more than one heat release rate zone. The stabilization of the mean flame was dictated by two flow parameters, (i) momentum ratio of the fuel to air and (ii) global equivalence ratio, which results in different flow structures, having different characteristic frequencies to interact and perturb the flame.

From the chemiluminescence images, we see that the oxidation of H_2 to form OH is necessarily followed by the oxidation of CO by the OH to form CO_2. Indeed, the reaction time scales of the former oxidation are quite smaller than that of the latter. This results in the presence of two heat release rate zones in syngas, the stagger nature of which results in the excitation of high-frequency oscillations. The same is confirmed from the spatial Rayleigh map obtained for three different composition of the syngas from OH* and CO_2* chemiluminescence imaging. Alternate driving and damping regions for all three syngas confirms the syngas combustion instability is driven by the shear layer. The driving regime of OH* is concentrated closer to the bluff body whereas for the CO_2* driving regime is much downstream to the bluff body confirms the presence of the two heat release rate zones spanned at the distance acting as two oscillator whose time lag matching the high frequency instability.

In a bid to understand the role of phase lag between the fore-mentioned unsteady quantities in driving the frequency shifts, we analyzed the same through a $n - \tau$ model for the obtained phase lags. The stability of the modes at low and high *Re* indicated, that at low *Re*, the low frequency displays positive growth rate with all other modes being damped, whereas the higher frequency mode displays this behavior at higher *Re*. This emphasized the role of phase or time lag in determining the stability of a system. In other words, even if one could have the mechanism of combustion instability at any phase, only a few phase lags would sustain combustion instability and at particular modes.

In summary, the combustion dynamics of a bluff-body stabilized non-premixed syngas flame is because of the tendency of the flame to reside in the shear layer and owing to the presence of twin reaction zones.

References

Altay HM, Speth RL, Hudgins DE, Ghoniem AF (2009) Flame-vortex interaction driven combustion dynamics in a backward-facing step combustor. Combust Flame 156:1111–1125

Balachandran R, Chakravarthy SR, Sujith RI (2008) Characterization of an acoustically self-excited combustor for spray evaporation. J Propul Power 24:1382–1389

Baraiya NA, Chakravarthy SR (2019) The role of mean flame anchoring on the stability characteristics of syngas, synthesis natural gas, and hydrogen fuels in a turbulent non-premixed bluff-body combustor. In: Proceedings of ASME Turbo Expo (Accepted)

Baraiya NA, Chakrvarthy SR (2018) Effect of chemical composition of syngas on combustion dynamics inside bluff-body type turbulent syngas combustor. In: Proceedings ASME Turbo Expo (2018)

Baraiya NA, Chakrvarthy SR (2019) Excitation of high frequency thermoacoustic oscillations by syngas in a non-premixed bluff body combustor. Int J Hydrog Energy 44(12):6299–6312

Baraiya NA, Baladandayuthapani N, Chakrvarthy SR (2017) Experimental investigation of combustion dynamics in a turbulent syngas combustor. In: Proceedings ASME Turbo Expo
Berger E, Scholz D, Schumm M (1990) Coherent vortex structures in the wake of a sphere and a circular disk at rest and under forced vibrations. J Fluids Struct 4(3):231–257
Candel S (2002) Combustion dynamics and control: Progress and challenges. Proc Combust Inst 29(1):1–28
Chakravarthy SR, Sivakumar R, Shreenivasan OJ (2007a) Vortex-acoustic lock-on in bluff-body and backward-facing step combustors. Sadhana Acad Proc Eng Sci 32:145–54
Chakravarthy SR, Sivakumar R, Shreenivasan OJ (2007b) Vortex acoustic lock-on in bluff-body and backward-facing step combustors. Sadhana 32(parts 1 & 2):145–154 (2007)
Chakravarthy SR, Sampath R, Ramanan V (2017) Dynamics and diagnostics of flame-acoustic interactions. Combust Sci Technol 189(3):395–437
Chaos M, Dryer FL (2008) Syngas combustion kinetics and applications. Combust Sci Tech 180:1053–1096
Choi O, Lee MC (2016) Investigation into the combustion instability of synthetic natural gases using high speed flame images and their proper orthogonal decomposition. Int J Hydrog Energy 41(45):20731–20743
Davis SG, Joshi AV, Wang H, Egolfopoulos F (2005) An optimized kinetic model of H_2/CO combustion. Proc Combust Inst 30(1):1283–1292
Dowling AP (1999) A kinematic model of a ducted flame. J Fluid Mech 394:51–72
Dowling AP, Stow SR (2003) Acoustic analysis of gas turbine combustors. J Propul Power 19(5):751–764
Gotoda H, Nikimoto H, Miyano T, Tachibana S (2011) Dynamic properties of combustion instability in a lean premixed gas-turbine combustor. Chaos: Interdiscip J Nonlinear Sci 21(1):013124
Han X, Li J, Morgans AS (2015) Prediction of combustion instability limit cycle oscillations by combining flame describing function simulations with a thermoacoustic network model. Combust Flame 162(10):3632–3647
He Y, Wang Z, Weng W, Zhu Y, Zhou J, Cen K (2014) Effects of CO content on laminar burning velocity of typical syngas by heat flux method and kinetic modeling. Int J Hydrog Energy (39):9534–9544
Hong S, Shanbhogue SJ, Speth RL, Ghoniem AF (2013) On the phase between pressure and heat release fluctuations for propane/hydrogen flames and its role in mode transitions. Combust Flame 160:2827–2842
Joshi AV, Wang H (2006) Master equation modeling of wide range temperature and pressure dependence of CO + OH → products. Int J Chem Kinet 38(1):57–73
Kabiraj L, Sujith RI, Wahi P (2012) Bifurcations of self-excited ducted laminar premixed flames. J Eng Gas Turbines Power 134(3):031502
Kéromnès A, Metcalfe WK, Heufer KA, Donohoea N, Das AK, Sung CJ, Herzler J, Naumann C, Griebel P, Mathieu O, Krejci MC, Petersen EL, Pitz WJ, Curran HJ (2013) An experimental and detailed chemical kinetic modeling study of hydrogen and syngas mixture oxidation at elevated pressures. Combust Flame 160:995–1011
Kim KT, Lee JG, Quay BD, Santavicca DA (2010) Spatially distributed flame transfer functions for predicting combustion dynamics in lean premixed gas turbine combustors. Combust Flame 157(9):1718–1730
Lee MC, Seo SB, Chung JH, Kim SM, Joo YJ, Ahn DH (2010) Gas turbine combustion performance test of hydrogen and carbon monoxide synthetic gas. Fuel 89:1485–1491
Lee MC, Seo SB, Yoon J, Kim M, Yoon Y (2012) Experimental study on the effect of N_2, CO_2, and steam dilution on the combustion performance of H_2 and CO synthetic gas in an industrial gas turbine. Fuel 102:431–438
Lee MC, Park S, Kim U, Kim S, Yoon J, Joo S, Yoon Y (2013) Effect of hydrogen content on the gas turbine combustion performance of synthetic natural gas. In: Proceedings of ASME turbo expo (2013)
Lieuwen TC (2012) Unsteady combustor physics. Cambridge University Press

Lieuwen T, McDonell V, Petersen E, Santavicca D (2008) Fuel flexibility influences on premixed combustor blowout, flashback, autoignition, and stability. J Eng Gas Turbines Power 130(1):011506

Lieuwen T, Yetter R, Yang V (2009) Synthesis gas combustion: fundamentals and applications. CRC Press

Matveev KI, Culick FEC (2003) A model for combustion instability involving vortex shedding. Combust Sci Technol 175(6):1059–1083

McManus KR, Poinsot T, Candel SM (1993) A review of active control of combustion instabilities. Prog Energy Combust Sci 19(1):1–29

Natarajan J, Lieuwen TC, Seitzman J (2007) Laminar flame speeds of H2/CO mixtures: Effect of CO_2 dilution, preheat temperature, and pressure. Combust Flame 151(1–2):104–119

Ning D, Fan A, Yao H (2017) Effects of fuel composition and strain rate on NO emission of premixed counter-flow H_2/CO/air flames. Int J Hydrog Energy 42(15):10466–10474

Noiray N, Durox D, Schuller T, Candel S (2008) A unified framework for nonlinear combustion instability analysis based on the flame describing function. J Fluid Mech 615:139–167

Palies P, Durox D, Schuller T, Candel S (2011) Nonlinear combustion instability analysis based on the flame describing function applied to turbulent premixed swirling flames. Combust Flame 158(10):1980–1991

Park J, Lee MC (2016) Combustion instability characteristics of H_2/CO/CH_4 syngases and synthetic natural gases in a partially-premixed gas turbine combustor: Part I Frequency and mode analysis. Int J Hydrog Energy 41(8):7484–7493

Park J, Lee MC (2016b) Combustion instability characteristics of H_2/CO/CH_4 syngases and synthetic natural gases in a partially premixed gas turbine combustor: Part II time lag analysis. Int J Hydrog Energy 41(18):1304–1312

Park J, Kim JS, Chung JO, Yun JH, Keel SI (2009) Chemical effects of added CO_2 on the extinction characteristics of H_2/CO/CO_2 syngas diffusion flames. Int J Hydrog Energy 34:8756–8762

Rahnama P, Paykani A, Bordbar V, Reitz RD (2017) A numerical study of the effects of reformer gas composition on the combustion and emission characteristics of a natural gas/diesel RCCI engine enriched with reformer gas. Fuel 209:742–753

Rayleigh L (1945) The theory of sound, vols. I and II

Sé Ducruix B, Schuller T, Durox D, Sé Candel B (2003) Combustion dynamics and instabilities: Elementary coupling and driving mechanisms. J Propuls Power 19(5):722–734

Shanbhogue SJ, Sanusi YS, Taamallah S, Habib MA, Mokheimer EMA, Ghoniem AF (2016) Flame macrostructures, combustion instability and extinction strain scaling in swirl-stabilized premixed CH_4/H_2 combustion. Combust Flame 163:494–507

Shih HY, Hsu JR (2012) Computed NOx emission characteristics of opposed-jet syngas diffusion flames. Combust Flame 159(5):1851–1863

Taamallah S, Labry ZA, Shanbhogue SJ, Ghoniem AF (2015a). Thermo-acoustic instabilities in lean premixed swirl-stabilized combustion and their link to acoustically coupled and decoupled flame macrostructures. Proc Combust Inst 35:3273–3282

Taamallah S, LaBry ZA, Shanbhogue SJ, Habib MAM, Ghoniem AF (2015b) Correspondence between "Stable" flame macrostructure and thermo-acoustic instability in premixed swirl-stabilized turbulent combustion. J Eng Gas Turbines Power 137:071505

Yoon J, Joo S, Lee MC, Kim J, Oh J, Yoon Y (2015) The effect of fuel composition on combustion instability mode occurrence in a model gas turbine combustor. In: Proceedings of ASME Turbo Expo

Yoon J, Seongpil J, Jeongjin K, Lee MC, Jong G, Yoon Y (2017) Effects of convection time on the high harmonic combustion instability in a partially premixed combustor. Proc Combust Inst 36(3):3753–3761

Zhong W, Liu M, Wu G, Yang J, Zhang X (2014) Extraction and recognization of large-scale structures in the turbulent near wake of a circular disc. Fluid Dyn Res 46(2):025507

Zinn BT, Lieuwen TC (2005) Combustion instabilities: basic concepts. Combust Instabil Gas Turbine Engines: Oper Exp Fundam Mech Model 210:3–26

Chapter 12
A Review on Noise-Induced Dynamics of Thermoacoustic Systems

Lipika Kabiraj, Neha Vishnoi and Aditya Saurabh

Abstract Practical combustion systems such as gas turbine combustors, rocket engines, industrial furnaces, and boilers are essentially thermoacoustic oscillators involving acoustic energy amplification through feedback interaction among fluctuations in the aerodynamic field, acoustic field, and the combustion process. Such systems are also noisy, in the sense that there inherently exists noise within the system. Noise may be associated with various sources–noise in fuel/air supply systems, fluctuations in the flow field, acoustic fluctuations, fluctuations in the heat release. Additionally, such noise may be correlated or uncorrelated, may have a specific spectral characteristic; but often noise will interact with/influence the feedback process. Since the importance of noise in determining the stability of the system discussed by Culick et al. (Combustion noise and combustion instabilities in propulsion systems, 1992) and group at Caltech, there have been several recent contributions to the theory of noise-induced phenomena in thermoacoustic systems–further advancements in the determination of system stability through noise-induced behaviour in the system prior to bifurcation as well as during the self-excited state, noise-induced effects in the presence of nonlinear interactions, noise-induced transitions (incl. dynamics in the bistable regime in the case of transition to self-excited oscillations via a subcritical Hopf bifurcation), as well as recent identification of interesting behaviour such as noise-induced coherence and stochastic bifurcations (stochastic P-bifurcations). The latter effects are based on new findings in the theory of dynamical systems and since reports on their influence in thermoacoustic systems are also being investigated in other aero/hydrodynamic systems such as in jets. The review will focus on the influence of developments in the theory of random noise (such as the Fokker-Plank equations), the theory of oscillators and dynamical systems on noise induced behaviour in thermoacoustic systems; experiments, modelling, and predictions on noisy thermoacoustic systems; and the implications of these findings on practical systems.

L. Kabiraj (✉) · N. Vishnoi
CDC Lab, Department of Mechanical Engineering, IIT Ropar, Rupnagar 140001, PB, India
e-mail: lipika.kabiraj@iitrpr.ac.in

A. Saurabh
Department of Mechanical Engineering, IIT Kanpur, Kanpur 208016, UP, India

A. Mukhopadhyay et al. (eds.), *Dynamics and Control of Energy Systems*,
Energy, Environment, and Sustainability,
https://doi.org/10.1007/978-981-15-0536-2_12

12.1 Introduction

A thermoacoustic system is one which involves heat transfer via combustion—as in a rocket engine motors, furnace, or gas turbine combustor[1]—or via heat exchangers such as in thermoacoustic engines (Swift 1988) or heated wires as in the Rijke tube (Feldman 1968; Raun et al. 1993); within a confinement which supports acoustic modes—planar as well as non-planar modes, with the latter associated with high-frequency instabilities (O'Connor et al. 2015). The unifying feature of such thermoacoustic systems, which is of academic and industrial interest is the establishment of a constructive feedback coupling between the acoustic field and fluctuating heat transfer referred to as *thermoacoustic instability*.

Heat transfer fluctuations feeding energy into the acoustic field in accordance with the famous Rayleigh criteria (Rayleigh 1878; Putnam 1971) given as,

$$\int_V \int_T p'_{x,t}\, \dot{q}'_{x,t}\, \mathrm{d}t\, \mathrm{d}V > 0,$$

$p'_{x,t}$ and $\dot{q}'_{x,t}$ denoting pressure and heat release rate fluctuations respectively; and the response of heat transfer (specifically heat release rate fluctuations) to acoustic fluctuations are the key elements of thermoacoustic feedback loop (Zinn and Lieuwen 2006). Furthermore, the flame response is typically low pass in nature (Candel et al. 2009) and is delayed in time. Thus implying that the instability will establish only for a favourable phase difference between pressure and heat release rate fluctuations in accordance with the Rayleigh integral above, and that an accurate description of thermoacoustic instability would necessarily involve delayed-differential equations. When combustion and flames are involved, additional complexities, characteristic to the configuration under consideration such as equivalence ratio fluctuations (Shreekrishna et al. 2013) and swirl flow and flame dynamics (Candel et al. 2014; Chakravarthy et al. 2016) must be incorporated.

To be able to predict and suppress instability is a practical necessity and research in the field has primarily focused on understanding the instability phenomenon and developing methods for prediction and control. The Rayleigh criterion is not of much help in this regard, but the latter—the flame response—allows for the determination of whether a given combustor-flame configuration may become unstable for a given set of operating conditions: the flame response in the form of the flame transfer function and the flame describing function (Dowling 1999; Noiray et al. 2008) together with input-output representations for acoustics within the combustor provides sufficient information to establish stability boundaries. The method depends on the accurate measurement of the flame response—a task which becomes increasingly difficult if the flame configuration, operating conditions, and the acoustic field expected during

[1] Among the three, the gas turbine combustor is of focus here; but most of the results and inferences discussed would apply to other systems, including thermoacoustic engines which involve heat transfer but not combustion.

the instability in modern combustors are to be exactly represented for the flame response measurements.

One of the interesting recent developments in the field was to note that, characteristic features aside, the thermoacoustic system is yet another dynamical system governed by a set of critical parameters. When fluctuations in system variables are small, the evolution is well represented by linear operators; but as the amplitude of fluctuations increases, system dynamics feature nonlinear behaviour such as amplitude saturation, bifurcations, and chaotic scenarios. The thermoacoustic system features remarkable similarities in its dynamics with a wide spectrum of nonlinear systems implying that fundamental features of thermoacoustic instability may be studied based on a class of governing equations that have been developed for generic nonlinear systems with which thermoacoustic instability shares its dynamic features. As will be discussed, this perspective has also aided in developments in our understanding of noise-induced dynamics in thermoacoustic systems.

Noise in thermoacoustic systems has on the one hand delayed the identification of bifurcations and dynamical attractors (cf. Sterling and Zukoski 1991; Kabiraj et al. 2015a) and on the other hand enabled the identification of measures of system stability. The latter has been possible because noise leads to frequent excursions of the system away from its asymptotic dynamics; and characteristics of its evolution back to the asymptotic behaviour (steady state or oscillatory states) is indicative of the system stability. Both the aspects are discussed in further detail later.

Thermoacoustic instability is highly undesirable in practical systems because of the large amplitude pressure oscillations that result in thrust oscillations, severe vibrations that interfere with control-system operation, enhanced heat transfer and thermal stresses to the combustor walls, oscillatory mechanical loads that result in fatigue of system components, and flame blow-off or flashback. These phenomena may result in premature wear of the components of the gas turbine that leads to costly shutdown or catastrophic component and/or mission failure (e.g.: the failure of America's first manned moon mission occurred due to these instabilities in F1 engine (Culick and Yang 1995). It becomes necessary either to avoid the operational regime under which these instabilities occurs or to suppress the resulting oscillations. This requires the knowledge of stability margins of a system and the understanding of the dynamics of these instabilities, which are found to be influenced by the interactions between the thermoacoustic instabilities and other processes in a combustor (Zinn and Lieuwen 2006). Emerging trends in practical combustion systems tend to make them more susceptible to this feedback phenomenon. Consequently, determination of the stability boundaries is essential and here a noisy system may lead to problems associated with noise-induced oscillations/transitions. A basic understanding of the primary (Hopf) bifurcation would help understand this effect of noise.

In a stable combustor, large amplitude coherent oscillations (consisting of one or more distinct peaks in the frequency spectra of acoustic pressure/velocity or heat release rate fluctuations from the flame) will be absent. Fluctuations may still be present due to inherent noise and these might contain small amplitude intermittent coherent oscillations. As a critical parameter is varied, large amplitude coherent oscillations will appear in one of the two possible ways: oscillations with gradually

increasing amplitude as the critical parameter is varied, or oscillations with a sudden jump in the amplitude. These two pathways are associated with the two forms of the Hopf bifurcation. Figure 12.1 presents schematics of the two forms: the supercritical and the subcritical Hopf bifurcation. The X-axis is the parameter and the Y-axis is the amplitude of oscillations. Solid lines are 'stable' asymptotic states: once the system assumes such a state it will continue to stay at that state in the absence of any large disturbance and further parameter variations. These are also known as 'attractors' because of the property that if the system is disturbed from this state via small perturbations, it will be attracted back to it. The dashed lines are also states that the system can settle on for a short time, but will eventually be repelled from this state to the closest attractor available. These are therefore 'unstable' states or 'repellers'.

Depending on the nature of the nonlinearity within a system, transition to the oscillatory state may happen via a supercritical or subcritical bifurcation (Gupta et al. 2017; Burnley and Culick 2000). For a supercritical Hopf bifurcation, the transition to the oscillatory state occurs such that beyond the critical point (also the Hopf point), x_H, the amplitude changes gradually. The role of noise for this case can be expected to be limited to excursions of the system away from the stable states induced by noise, followed by return towards the closest'attractors'.

The subcritical Hopf bifurcation is more interesting—and also more dangerous than supercritical bifurcation for practical systems. In the most fundamental case of a subcritical Hopf bifurcation, a stable (oscillator) state exists together with the stable steady state (referred to as focus) prior to the Hopf point; and the two are separated by a repeller—an unstable limit cycle. The point at which these two meet is referred to as a 'saddle-node'. The region of coexisting attractors is called 'bistable' region because of the existence of two attractors. The system will evolve on one or the other

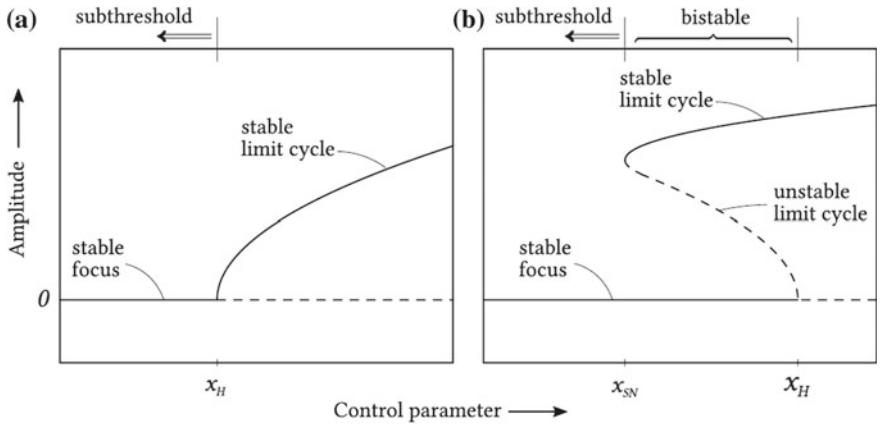

Fig. 12.1 Schematic of a supercritical (left) and subcritical (right) Hopf bifurcations (Gupta et al. 2017). x_H marks the Hopf point and, for the subcritical bifurcation, x_{SN} marks the saddle-node point

depending on the initial condition: a large enough perturbation can cause the system to switch from one to the other attractor. Such a condition is dangerous for a practical system because although the system is far away from the Hopf point—which is what may typically be obtained from linear stability analysis of the system—perturbations, including noise may 'trigger' instability (the oscillatory stable attractor).

In the 'sub-threshold' region before the bifurcations, as marked in Fig. 12.1, noise results in subtle effects that are now known and can be helpful for the practical purposes of prediction and control of the instability.

Transition due to noise is not only limited to the transition from steady to oscillatory states; it is possible for a thermoacoustic system to have multiple coexisting oscillatory states; for instance in an annular combustor both standing and rotating acoustic modes are possible during thermoacoustic instability and it has been reported that the transitions between the two, commonly observed in experiments, are likely due to noise in the system (Noiray and Schuermans 2013b).

Noise in general has also been identified to result in other more subtle effects in nonlinear systems such as stochastic resonance (SR), where a feeble external periodic forcing to the system is enhanced in the presence of noise (Benzi et al. 1981, 1982; Douglass et al. 1993; Wellens et al. 2003) coherence resonance, which similar to SR except that it does not require an external signal and internal frequencies are enhanced leading to intermittent burst of periodic behaviour (Pikovsky and Kurths 1997; Neiman et al. 1997; Kiss et al. 2003; Ushakov et al. 2005; Zakharova et al. 2010.) The term 'resonance' in both cases refers to the observation that the amplification of the external periodic signal (SR) and the coherence in noise-induced oscillations (CR) first increases with increasing noise intensity, attains a peak, and subsequently decreases monotonically—similar to a resonance curve. The particularly interesting feature of such noise-induced behaviour is the regime (control parameter range) within which it occurs: for subcritical Hopf bifurcation it occurs before the bistable region (before the saddle node point), and for supercritical bifurcation it occurs before the Hopf point. Thus, in the presence of inherent noise, such behaviour can be used as precursors, or for advance detection of the proximity of the system to the (practically dangerous) bistable (subcritical Hopf) and linearly unstable (supercritical Hopf) regimes. Only recently has coherence resonance and associated P-bifurcations been demonstrated in experiments (Kabiraj et al. 2015b; Saurabh et al. 2016) and prototypical models of thermoacoustic systems (Gupta et al. 2017).

Another important aspect concerning noise-induced dynamics is that the effects are also dependent on the nature of noise: the composition in terms of the distribution of power over frequency and whether noise appears in the parameters governing the system (parametric noise), whether noise is dependent on the state of the system (multiplicative noise), or if it is unrelated to either the state or parameters (additive noise). These are however mathematical constructs and one may find one or the other form reported in literature. The important point to note is that the different classes of noise have different effects on the system.

Briefly summarizing, noise has been identified as a major contributing factor to the complexity of thermoacoustic instabilities since the 1970s. Combustors are typically noisy environments. Considerable noise sources in practical combustion

systems include flow separation, turbulence, and combustion processes. It is expected that the presence of noise will affect in some way the amplitudes and possibly the qualitative behaviour of organized oscillations (Burnley 1996). The noise-induced dynamics in a thermoacoustic system can trigger thermoacoustic instability in the bistable regime, can be used to acquire deterministic system parameters, can modify the stability margins of the system, and can act as a noisy precursor to instability. It has been found that noisy excitation acting on thermoacoustic systems have the ability to produce coherent response in the form of acoustic oscillations (Chiu et al. 1973; Chiu and Summerfield 1974; Strahle 1978). We will take up critical effects identified in recent studies in this review.

12.2 Noise-Induced Dynamics and System Identification

It is reported that in the 1960s or even the 50's, several Russian groups were employing system identification using the statistical features of pressure fluctuations (Seywert 2001). It was however the reports published in the 80s and 90s—primarily by Culick, Zinn, and their respective groups at Caltech and Georgia tech—that made the major contributions to the theoretical investigation of nonlinear and stochastic dynamics of thermoacoustic instability. The formulations and results developed back then for liquid and solid rocket motors still have relevance for gas turbine combustors and are being employed, extended, and improved for modelling and control strategies.

This early work in particular is based on the approximate analysis for nonlinear instability in combustors developed in Culick (1971), Zinn and Powell (1971). Identifying the cause of triggering in combustors, which was observed frequently in experiments, was the major driving force behind developing a nonlinear framework involving either nonlinear gas dynamics, or nonlinear combustion, or both simultaneously; and it was realized that nonlinear combustion was important to obtain subcritical Hopf bifurcation and the associated triggering phenomenon (Burnley and Culick 1997).

Researchers were particularly interested in two questions: firstly, for noise with certain statistical features introduced into the system as multiplicative or additive noise, what are the statistical features of pressure fluctuations; and secondly, given experimental measurements of pressure fluctuations from a combustor, can the stability margins/measures of the system be inferred.

Among the first detailed studies on the effects of noise is the work by Culick et al. (1992) where the authors, building on the approximate analysis (Culick 1971; Zinn and Powell 1971), include parametric (noisy) excitation of the acoustic modes and an additive noise source in the acoustic forcing term of the form:

$$\frac{\mathrm{d}^2\eta_n}{\mathrm{d}t^2} + \omega_n^2\eta_n = F_n^a + \sum_{i=1}^{\infty}\left[\xi_i\eta_i + \xi_i^v\dot{\eta}_i\right] + \Xi_n \tag{12.1}$$

ξ_i, ξ_i^v are parametric noise amplitudes, while Ξ_n is the additive noise amplitude. Acoustic pressure and velocity are expanded as a linear summation of (classical) acoustic modes and η_n is the time-varying amplitude of the nth mode. Accordingly, the governing equations for fluctuations in the combustor appear as set of stochastic differential equations of the form of oscillators with the forcing terms containing contribution from noise. Subsequently, with the use of a two-mode approximation followed by stochastic averaging provides a simplified set of equations for the fluctuations in the modal amplitudes in the presence of noise. The corresponding Fokker-Planck equations for pressure fluctuations will provide the probability density. The authors reported a uni-modal, log-normal distribution for pressure fluctuations as the result of this formulation and the description was shown to match well with numerical simulations (Monte-Carlo) of the stochastic equations obtained earlier.

The log-normal distribution of pressure fluctuations were also reported by Clavin et al. (1994) for the special case when the combustor is close to the stability boundaries. The analysis was based on the Stuart-Landau equation with the effect of noise (specifically due to turbulence) appearing as a fluctuation of the growth rate (multiplicative noise). Furthermore, this was probably the first work to approach transitions between the stable steady and oscillatory states within the bistable region of the subcritical bifurcation due to noise. Further discussion on these transitions is postponed for the section on noise-induced transitions. The authors also pointed out that to capture noise-induced behaviour correctly, it was important to include nonlinear terms. While qualitatively the results appear to correspond to experimental observations, no further validation of the multiplicative nature of noise or a characterization of changes in the transfer function or the growth rate of the system has been attempted. Concerning multiplicative noise, additional work was more recently undertaken in Lieuwen and Banaszuk (2005) where the authors show that in the presence of fluctuations in the system damping and frequency, the stability regime shrinks (in comparison to the boundaries identified from deterministic equations).

The definitive response to the long-standing question of whether the statistical features of pressure fluctuations can give an idea about the stability margins of the system was finally given by Seywert (2001). Like the previous investigations (Culick et al. 1992; Burnley 1996), the authors simplify the governing equations to the form of an oscillator with multiplicative noise affecting the frequency and growth rates of the system; with the system itself represented by four modes. Following 'Burg's method' to curve-fit the power spectrum of the pressure fluctuations from simulations of the stochastic differential equations, they identify the frequencies and growth rates of the system and compare these to known values for the case of a linearly stable system. A very good agreement is found and the method is reported to be robust against the amplitude of noise for the case of additive noise and breaks down for large noise amplitudes for the case of multiplicative noise. More insights on the latter have been obtained in very recent experiments (Kabiraj et al. 2015b; Saurabh et al. 2016).

The authors (Seywert 2001) also applied the method to linearly unstable system but the results are not as promising. The method works only if a single mode is active during instability as it is unable to distinguish between linear and nonlinear effects

in the presence of multiple modes. The formulation may also not be accurate as the authors consider nonlinear gas dynamics but a linear flame response.

The idea that noise-induced dynamics could be used for system identification was recently revisited by Noiray and Schuermans (2013a). Unlike previous studies discussed in the last paragraphs where the authors attempted to arrive at a set of governing stochastic differential equations (Noiray and Schuermans 2013a) and follow up works (Noiray and Denisov 2017; Bonciolini et al. 2017) start with the assumption that only a single acoustic mode is active and the dynamics may be well represented by Van der Pol equations and their stochastic extensions. Noise is considered additive in nature. In Noiray and Schuermans (2013a) the authors propose four different approaches for the determination of the linear growth rate and nonlinearity coefficient—the nonlinearity being an assumed form involving a single, constant coefficient. The first of these neglects the nonlinear term and the determination of the growth rate is based on fitting the power spectrum of pressure fluctuations with a function derived for the stochastic Van der Pol equation (with additive noise). The second approach considers a weakly perturbed limit cycle oscillation of the oscillator. It involves linearization about the limit cycle oscillation for which the amplitude depends on nonlinearity coefficient and fitting of the power spectrum with the correspondingly modified functional form. The next approach is based on the Fokker-Plank equation corresponding to the amplitude and phase equations of the stochastic Van der Pol equation. An expression is obtained for the amplitude distribution (Eq. 22 in Noiray and Schuermans (2013a)) and based on fitting experimentally obtained data (Hilbert transform of the pressure oscillations given that Hilbert transform is applicable[2]) with the function. This approach relaxes the assumption of a weakly perturbed limit cycle. Finally the authors propose another approach based on the Fokker-Plank equations governing the evolution of the transient probability density. The coefficients associated with the convection and diffusion of the probability density with time can be obtained from experimental data and deterministic quantities estimated subsequently. This approach is most general and relaxes the presumption of a stochastic Van der Pol; the result may be cross-checked to identify whether the stochastic Van der Pol is a valid form for the governing equation. In the application of the method on data obtained from the combustor the authors show that for the particular case, the Van der Pol-based description largely holds. Except the first approach, the proposed strategy is applicable for the linearly unstable regime as well.

Bonciolini et al. (2017) showed that regardless of the frequency composition of noise (color of noise) linear growth rate and nonlinear saturation coefficient estimation is possible by using a band-pass filter around the oscillator eigenfrequency as a preprocessing step. This is a practically-relevant result as it is often not possible to know the noise characteristics in a real system.

Further development of the Fokker-Plank based method was presented recently in Boujo and Noiray (2017) where the authors provide a more robust estimation

[2]With the assumption of a single dominant frequency in the system, this is true.

methodology based on adjoint Fokker-Plank equations which does not suffer from problems associated with the fact that previous methods relied on band-pass filtered data.

Among the studies mentioned only Seywert (2001) has investigated the role of noise amplitude; and although the amplitude appears as a parameter in methods studied in Noiray and Schuermans (2013b) and subsequent works, it is implicitly assumed that for all cases the amplitude does not lead to variations in the general form of the power spectrum or the amplitude distribution function. As discussed below, recent experiments and associated analyses however indicate otherwise.

Kabiraj et al. (2015b) experimentally investigated the response of a model thermoacoustic system to varying amplitudes of acoustic white noise signals for a range of operating conditions prior to the bistable region. As mentioned in the introduction to this review, in this region the system is linearly stable and the steady non-oscillatory state is the sole attractor of system dynamics.

It was shown by the authors that the response to noise consists of intermittent episodes of oscillatory behaviour at the frequency which would appear if the parameter were to be changed to a value beyond the Hopf point. The episodes occurred more frequently and for a longer mean duration as the system was brought closer to the edge of the bistable region. The most important aspect concerning noise-induced dynamics was the observation that this 'coherent' behaviour was also dependent on the noise intensity; and that this dependence was not monotonous. With increasing noise amplitude the coherent response would increase and then—beyond an optimum induced coherence—decrease. The optimum also depends on the proximity of the system to the bistable region in a way that if the system is close to the bistable region, the optimum is obtained at a lower noise intensity. Such behaviour has known in the nonlinear dynamics community (cf. Zakharova et al. 2010 ; Ushakov et al. 2005) and is referred to as 'coherence resonance' due to the resonance-like dependence of the induced coherence on the noise intensity. In the presence of non-linearity, both the peak height and the width are affected by noise (Stratonovich 1967). The combined effect of noise on the spectral peak is such that the coherence factors, β, obtained from the power spectra passes through a maximum for intermediate noise levels (Neiman et al. 1997).

The investigation was further expanded in Saurabh et al. (2016) to show the presence of 'P-bifurcations': qualitative changes in the statistical characteristics of pressure fluctuations as the noise intensity is increased. The amplitude distribution functions changes from a uni-modal, log-normal distribution to a bi-modal distribution. From the characteristics of the distribution it could be inferred that the oscillatory attractor that exists in the bistable region and beyond influences the noise-induced behaviour of the system already in the 'sub-threshold' region. That such 'P-bifurcations' appear with the phenomenon of 'coherence-resonance' has also been observed in nonlinear systems (Zakharova et al. 2010).

In addition to giving insights on the stochastic features of thermoacoustic instability the observations are also practically relevant: such noise-induced behaviour and corresponding trends can be used as precursors for *advance detection of instability*.

Lately, a similar work analogous to Kabiraj et al. (2015b) was presented by Li et al. (2019). They also investigated coherence resonance and stochastic bifurcation behaviours in two modelled standing wave thermoacoustic systems (open-open and closed-open boundary conditions). They reported from the smooth transitions of the stationary probability density function (PDF) that the thermoacoustic system is destabilized via stochastic P bifurcation, as the external noise intensity was continuously increased. This was in good agreement to Kabiraj et al. (2015b). In addition, they also reported that the increased noise intensity could shift the hysteresis region, making the system more prone to quasi-periodic oscillations, but also reducing the hysteresis area possibly suggesting the presence of a multiplicative noise component (Lieuwen and Banaszuk 2005).

The phenomenon of coherence resonance was later analysed through numerical simulations in Gupta et al. (2017). The authors conducted numerical analysis of noise-induced (additive noise) dynamics in subthreshold regime for models of thermoacoustic instability—Rijke tube as well as the Van der Pol oscillator. The results reported correspond qualitatively to the observations of the experiments (Kabiraj et al. 2015b). The findings confirmed that the observed phenomenon of coherence resonance in combustion systems is intrinsic to thermoacoustic coupling. Furthermore, investigations on the Van der Pol model, which underwent bifurcation to instability via supercritical bifurcation indicated that coherence resonance is not limited to subcritical bifurcations. The trends in noise-induced coherence as the system approaches Hopf bifurcation for subcritical and supercritical Hopf bifurcations were found to be qualitatively different and indicative of the type of bifurcation. This particular result even has the potential to be used as a basis of system identification prior to the instability. The restriction of additive white Gaussian noise employed by the authors may not be accurate but the qualitative results impress the importance of considering nonlinearity and noise amplitude effects in the modelling (and use in system identification approaches) of thermoacoustic systems.

In order to summarize, the aforementioned discussions made by various researchers provided a strong theoretical modelling of the stochastic forcing in thermoacoustic systems and how the extended study of the model could be used to extract or determine the linear growth rate and non-linearity in the system. It can also be concluded that the knowledge of noise-induced linear growth/decay rates and nonlinearity coefficient could help in designing of proper damping device for dissipation of acoustic energy for a thermoacoustic system. But recent results also advocate the need for further developments in theoretical modelling and system identification approaches.

12.3 Noise-Induced Transitions

Among various practically-relevant aspects of thermoacoustic systems is the possibility of switching between or undergoing transition to different dynamical states. There are two such possibilities:

- Transitions involving thermoacoustically-stable (non-oscillatory) and oscillatory states.
- Transitions involving two oscillatory states.

In both the cases, the switch/transition may be 'triggered' by finite-amplitude disturbances, including inherent noise within the system.

Transition from the stable, non-oscillatory state to an oscillatory state (not limited to limit cycle oscillations (Kabiraj et al. 2012) is possible only for the case of a subcritical Hopf bifurcation (see Fig. 12.1). Within the bistable zone, the simultaneous existence of two attractors leads to the possibility of forcing the system to be attracted to one of them by providing an appropriate disturbance: if a disturbance causes the system to fall within the 'basin of attraction' (Nayfeh and Balachandran 1995) of the oscillatory state or the thermoacoustically-stable state, the system would be attracted to the corresponding state. Such behaviour in thermoacoustic systems was first investigated in the context of rocket engines where the triggering of thermoacoustic instability via a large amplitude pulse was referred to as hard excitation or triggering instability (Crocco and Cheng 1956). Beyond a certain 'threshold' amplitude for the disturbance, which was typically obtained through a small explosions within the combustor, instability could be triggered. Experimentally it is possible to obtain the threshold corresponding to the unstable limit cycle (Kabiraj and Sujith 2011), but only for laboratory systems.

In the context of this review it is important to discuss the fact that triggering is also possible through noise (Zinn and Lieuwen 2006). Thermoacoustic systems can be triggered by low amplitude perturbations of the order of background noise level. Noise in the system may be associated to several sources—noise in operating conditions, noise in the base flow, fluctuations leading to combustion noise, or external sources (Dowling and Mahmoudi 2015; Tam et al. 2019). It is difficult to accurately model noise solely as additive, multiplicative, or parametric noise; but this difficulty is a limitation of modelling methods. Regardless of the source or classification, it has been known for a long time that noise can induce triggering (cf. Elias 1959) and the theory of dynamical systems, in particular the subcritical Hopf bifurcation, provides us with the required framework to interpret and understand such triggering. Because noise is involved, the analysis, description, and modelling of a thermoacoustic system in the presence of noise must necessarily be probabilistic in nature.

Culick et al. (1992), Clavin et al. (1994) were among the first to capture the effects of noise in inducing repeated transitions between the stable oscillatory and stable steady states within the bistable regions. Clavin et al. (1994), in particular obtained the transformation of the amplitude distribution function from unimodal to bimodal nature—indicating the presence of transitions between the steady and oscillatory states—through the Fokker-Planck formulation of the noisy (multiplicative noise) Stuart-Landau equations that the authors argued is a simplified representation of the thermoacoustic system in the presence of turbulent fluctuations.

Of recent, there have been several reports on noisy thermoacoustic systems, specifically transitions within the bistable region, based on experiments involving prototypical setups; and numerical/analytical analysis on either the Rijke tube

formulation (Matveev and Culick 2003) with subcritical bifurcation or the Van der Pol oscillator, where transition to instability takes place via a supercritical bifurcation. The latter, due to the lack of a bistable region in the bifurcation, can not be employed to understand transition within the bistable regime; and studies have focussed mostly on the stochastic nature of pressure fluctuations within the system—without transitions between stable attractors.

Waugh and Juniper (2011) explored the mechanism of triggering a thermoacoustic system (Rijke tube) with additive noise of different spectral composition—white, blue, and pink—and different amplitudes, within the bistable region. Pink noise was identified to be the most effective in triggering instabilities. Triggering required a certain threshold amplitude of noise depending on the type of noise. If the strength of noise was increased to the point where the intensity was just enough to trigger thermoacoustic oscillations, the system would spend some time at the unstable periodic solution and eventually be attracted to the stable oscillatory solution (limit cycle) and continue oscillating. At higher noise intensities, the system would directly be attracted to the stable limit cycle. Such observation and the presence of the unstable limit cycle was also obtained in experiments involving a periodic signal input for a prototypical system within the bistable region (Kabiraj and Sujith 2011).

In a follow-up numerical study with additive noise (Waugh et al. 2011), again within the bistable region, the authors investigated the effect of noise intensity and the proximity of the system to the Hopf point on the transition dynamics. If the system is close to the Hopf point, the basin boundary for the stable oscillatory solution is closer to the steady state; and it is expected that a low amplitude disturbance will be sufficient to cause transition. This is exactly what the authors found in their study. Correspondingly, as the system is taken further away from the Hopf point, transition would require a larger noise amplitude. Alternatively, for a constant noise amplitude, transition would occur in advance (of the Hopf point); with the distance to the Hopf point for such noise-induced transition increasing for increasing noise intensities (i.e. transition would occur much in advance for a higher noise intensity). The authors investigated noise included as an additional term to the system of equations as well as being included as a perturbation of the acoustic velocity at the heater (driving the electrically-heated Rijke tube) and reported that the results are qualitatively identical. These results explain several experimental observations such as reported by Elias (1959), and recently repeated by George et al. (2016) where the transition of combustors to instability is advanced in the presence of increased noise (flow turbulence in the cited references) intensity.

In experiments, a similar study was reported by Jegadeesan and Sujith (2013), where the authors investigated the influence of perturbations in fuel flow in a diffusion flame driven combustor. The configuration is closer to being classified as a parametric noise case than an additive or multiplicative noise scenario. Within the bistable region triggering would occur and the system evolution would pass through the unstable periodic state before ending up at the stable oscillatory state as previously discussed by Waugh et al. (2011), Kabiraj and Sujith (2011). When the system was perturbed by noise (Gaussian white noise), it underwent noise induced transition (nit) which was observed when the noise intensity was just 1/8th of the triggering amplitude of the

system. The evolution along the unstable periodic orbit was found to be intermittent, with pronounced bursts of oscillatory behaviour. The authors reported that with increased fluctuation intensity, the amplitude of triggered oscillations was lower than the amplitude of the limit cycle oscillations for the configuration without noise. The authors provide an explanation for the lowered amplitude based on a previous report of the drifting of the phase between heat release rate and pressure fluctuations (thus, a constantly changed value of the Rayleigh integral) in the presence of additive noise (Lieuwen 2001); although if that was the case, the numerical investigations should have identified the effect as well. The mean amplitude in the simulations with additive noise (Waugh et al. 2011; Waugh and Juniper 2011) was the same as the limit cycle amplitude obtained without noise.

In experiments on the horizontal configuration of an electrically-heated Rijke tube, Gopalakrishnan and Sujith (2015) identified that the reduction in the hysteresis zone as a result of noise-induced transitions discussed above follows a linear trend with respect to the normalized noise intensity. Such reduction in the bistable/hysteresis zone for systems undergoing subcritical Hopf bifurcation, in the presence of noise has been observed in various other dynamical systems as well (Sastry and Hijab 1981; Coullet et al. 1985; Berthet et al. 2003). For a sufficiently high noise intensity, the system was shown to undergo repeated transitions between the stable steady and oscillatory states; because of which the bifurcation diagram for the case of subcritical bifurcation with noise-induced transitions, obtained from noisy data with a representative amplitude (in the cited work, the median of local maxima in acoustic pressure) would resemble a supercritical bifurcation.

The authors recognize that the observed qualitative change in the bifurcation is due to repeated transitions or 'flickering' as such behaviour and later in Gopalakrishnan et al. (2016) identify the observation as a stochastic P-bifurcation (Arnold 1995; Zakharova et al. 2010). The authors compare the experimental observations in terms of the transformation of the unimodal amplitude distribution function to a bimodal structure (P-bifurcations) with increased noise to the analysis (Fokker-Planck formulation) of an idealized single mode oscillator forced to undergo a subcritical Hopf bifurcation via an artificial nonlinearity, and valid as a representation of the Rijke tube under several assumptions including small heat release rate fluctuations and a small (in comparison to the oscillation time period) time-delay in the heat release rate response. On account of the assumptions, the oscillator does not feature a saddle-node bifurcation and is valid in a small vicinity of the steady state solution. For the model, the corresponding Fokker-Planck formulation gives bifurcations in the stationary probability distribution functions with variation in the bifurcation parameter and the noise intensity.

Concerning the second possibility for transitions within a thermoacoustic system, noise has also been reported to cause transition between coexisting modes of the system. Noiray and Schuermans (2013c) studied the transition between azimuthal standing and rotating modes in an annular combustor. The modal dynamics were characterized and transitions between the two modes were noted. To seek an explanation, the authors investigated the phase dynamics of a coupled stochastic oscillator system with the flame nonlinearity modelled as a cubic nonlinearity. The switch between

rotating and standing modes was a long-standing aspect frequency observed in industrial combustors and the influence of noise was found to provide the most consistent explanation for such behaviour in modern annular systems.

12.4 Conclusion

Since the breakthrough experimentation and modeling of noise in thermoacoustic systems in the 80s, several important aspects of noise, including its use for system identification and as a precursor to instability, have been uncovered. Phenomenon such as mode transitions and changes in the nature of bifurcations, which could not be answered through a deterministic framework could be explained via the inclusion of noise in the modelling approaches. Further investigation is still warranted, in particular the role of multiplicative versus additive noise; including the identification of the conditions under which the system must be described by multiplicative noise and when additive noise suffices. In future investigations, we may expect to see new results concerning developments such as coherence resonance, characteristics stochastic features of subcritical and supercritical bifurcations, and changes in the nature of bifurcations and their implications on real systems.

References

Arnold L (1995) Random dynamical systems. In: Dynamical systems. Springer Berlin Heidelberg, pp 1–43. https://doi.org/10.1007/bfb0095238

Benzi R, Sutera A, Vulpiani A (1981) The mechanism of stochastic resonance. J Phys A: Math Gen 14(11):L453

Benzi R, Parisi G, Sutera A, Vulpiani A (1982) Stochastic resonance in climatic change. Tellus 34(1):10–16

Berthet R, Petrossian A, Residori S, Roman B, Fauve S (2003) Effect of multiplicative noise on parametric instabilities. Phys D: Nonlinear Phenom 174(1–4):84–99

Bonciolini G, Boujo E, Noiray N (2017) Output-only parameter identification of a colored-noise-driven van-der-pol oscillator: thermoacoustic instabilities as an example. Phys Rev E 95(6):062217

Boujo E, Noiray N (2017) Robust identification of harmonic oscillator parameters using the adjoint fokker-planck equation. Proc Roy Soc A Math Phys Eng Sci 473(2200):20160894. https://doi.org/10.1098/rspa.2016.0894

Burnley VS (1996) Nonlinear combustion instabilities and stochastic sources. PhD thesis, California Institute of Technology

Burnley VS, Culick FEC (1997) Some dynamics of acoustic oscillations with nonlinear combustion and noise. Int J Energ Mater Chem Propul 998–1013. https://doi.org/10.1615/intjenergeticmaterialschemprop.v4.i1-6.930

Burnley VS, Culick FEC (2000) Influence of random excitations on acoustic instabilities in combustion chambers. AIAA J 38(8):1403–1410. https://doi.org/10.2514/2.1116

Candel S, Durox D, Ducruix S, Birbaud AL, Noiray N, Schuller T (2009) Flame dynamics and combustion noise: progress and challenges. Int J Aeroacoustics 8(1):1–56. https://doi.org/10.1260/147547209786234984

Candel S, Durox D, Schuller T, Bourgouin JF, Moeck JP (2014) Dynamics of swirling flames. Annu Rev Fluid Mech 46(1):147–173. https://doi.org/10.1146/annurev-fluid-010313-141300
Chakravarthy SR, Sampath R, Ramanan V (2016) Dynamics and diagnostics of flame-acoustic interactions. Combust Sci Technol 189(3):395–437. https://doi.org/10.1080/00102202.2016.1202938
Chiu H, Summerfield M (1974) Theory of combustion noise. Acta Astronaut 1(7–8):967–984
Chiu H, Plett E, Summerfield M (1973) Noise generation by ducted combustion systems. In: Aeroacoustics Conference, p 1024
Clavin P, Kim JS, Williams FA (1994) Turbulence-induced noise effects on high-frequency combustion instabilities. Combust Sci Technol 96(1–3):61–84. https://doi.org/10.1080/00102209408935347
Coullet P, Elphick C, Tirapegui E (1985) Normal form of a hopf bifurcation with noise. Phys Lett A 111(6):277–282
Crocco L, Cheng SI (1956) Theory of combustion instability in liquid propellant rocket motors. Princton Univ NJ, Tech. rep
Culick F, Paparizos L, Sterling J, Burnley V (1992) Combustion noise and combustion instabilities in propulsion systems. Tech. rep, Advisory Group for Aerospace Research and Development, North Atlantic Treaty
Culick FEC (1971) Non-linear growth and limiting amplitude of acoustic oscillations in combustion chambers. Combust Sci Technol 3(1):1–16. https://doi.org/10.1080/00102207108952266
Culick FEC, Yang V (1995) Instability phenomenology and case studies: overview of combustion instabilities in liquid-propellant rocket engines. In: Anderson WE, Yang V (eds) Liquid rocket engine combustion instability. American Institute of Aeronautics and Astronautics, pp 3–37. https://doi.org/10.2514/5.97816008663710003.0037
Douglass JK, Wilkens L, Pantazelou E, Moss F (1993) Noise enhancement of information transfer in crayfish mechanoreceptors by stochastic resonance. Nature 365(6444):337
Dowling AP (1999) A kinematic model of a ducted flame. J Fluid Mech 394:51–72. https://doi.org/10.1017/s0022112099005686
Dowling AP, Mahmoudi Y (2015) Combustion noise. Proc Combust Inst 35(1):65–100. https://doi.org/10.1016/j.proci.2014.08.016
Elias I (1959) Acoustical resonances produced by combustion of a fuel-air mixture in a rectangular duct. J Acoust Soc Am 31(3):296–304. https://doi.org/10.1121/1.1907715
Feldman KT Jr (1968) Review of the literature on Rijke thermoacoustic phenomena. J Sound Vibr 7(1):83–89
George NB, Unni V, Raghunathan M, Sujith R (2016) Effect of varying turbulence intensity on thermoacoustic instability in a partially pre-mixed combustor. In: ICSV, p 23
Gopalakrishnan E, Sujith R (2015) Effect of external noise on the hysteresis characteristics of a thermoacoustic system. J Fluid Mech 776:334–353
Gopalakrishnan E, Tony J, Sreelekha E, Sujith R (2016) Stochastic bifurcations in a prototypical thermoacoustic system. Phys Rev E 94(2):022203
Gupta V, Saurabh A, Paschereit CO, Kabiraj L (2017) Numerical results on noise-induced dynamics in the subthreshold regime for thermoacoustic systems. J Sound Vib 390:55–66
Jegadeesan V, Sujith R (2013) Experimental investigation of noise induced triggering in thermoacoustic systems. Proc Combust Inst 34(2):3175–3183
Kabiraj L, Sujith RI (2011) Investigation of subcritical instability in ducted premixed flames. In: Volume 2: combustion, fuels and emissions, Parts A and B, ASME. https://doi.org/10.1115/gt2011-46155
Kabiraj L, Saurabh A, Wahi P, Sujith RI (2012) Route to chaos for combustion instability in ducted laminar premixed flames. Chaos: Interdisc J Nonlinear Sci 22(2):023129. https://doi.org/10.1063/1.4718725
Kabiraj L, Saurabh A, Karimi N, Sailor A, Mastorakos E, Dowling AP, Paschereit CO (2015a) Chaos: Interdisc J Nonlinear Sci 25(2):023101. https://doi.org/10.1063/1.4906943
Kabiraj L, Steinert R, Saurabh A, Paschereit CO (2015b) Coherence resonance in a thermoacoustic system. Phys Rev E 92(4):042909

Kiss IZ, Hudson JL, Santos GJE, Parmananda P (2003) Experiments on coherence resonance: noisy precursors to Hopf bifurcations. Phys Rev E 67(3):035201
Li X, Zhao D, Shi B (2019) Coherence resonance and stochastic bifurcation behaviors of simplified standing-wave thermoacoustic systems. J Acoust Soc Am 145(2):692–702
Lieuwen T (2001) Phase drift characteristics of self-excited, combustion-driven oscillations. J Sound Vib 242(5):893–905
Lieuwen TC, Banaszuk A (2005) Background noise effects on combustor stability. J Propul Power 21(1):25–31
Matveev K, Culick F (2003) A study of the transition to instability in a rijke tube with axial temperature gradient. J Sound Vib 264(3):689–706. https://doi.org/10.1016/s0022-460x(02)01217-8
Nayfeh AH, Balachandran B (1995) Applied nonlinear dynamics. Wiley, pp 1–34
Neiman A, Saparin PI, Stone L (1997) Coherence resonance at noisy precursors of bifurcations in nonlinear dynamical systems. Phys Rev E 56(1):270
Noiray N, Denisov A (2017) A method to identify thermoacoustic growth rates in combustion chambers from dynamic pressure time series. Proc Combust Inst 36(3):3843–3850
Noiray N, Schuermans B (2013a) Deterministic quantities characterizing noise driven Hopf bifurcations in gas turbine combustors. Int J Non-Linear Mech 50:152–163
Noiray N, Schuermans B (2013b) On the dynamic nature of azimuthal thermoacoustic modes in annular gas turbine combustion chambers. Proc Roy Soc A Math, Phys Eng Sci 469(2151):20120535–20120535. https://doi.org/10.1098/rspa.2012.0535
Noiray N, Schuermans B (2013c) On the dynamic nature of azimuthal thermoacoustic modes in annular gas turbine combustion chambers. Proc Roy Soc A Math Phys Eng Sci 469(2151):20120535–20120535. https://doi.org/10.1098/rspa.2012.0535
Noiray N, Durox D, Schuller T, Candel S (2008) A unified framework for nonlinear combustion instability analysis based on the flame describing function. J Fluid Mech 615:139. https://doi.org/10.1017/s0022112008003613
O'Connor J, Acharya V, Lieuwen T (2015) Transverse combustion instabilities: acoustic, fluid mechanic, and flame processes. Prog Energy Combust Sci 49:1–39. https://doi.org/10.1016/j.pecs.2015.01.001
Pikovsky AS, Kurths J (1997) Coherence resonance in a noise-driven excitable system. Phys Rev Lett 78(5):775
Putnam AA (1971) Combustion-driven oscillations in industry. Elsevier Publishing Company
Raun R, Beckstead M, Finlinson J, Brooks K (1993) A review of Rijke tubes, Rijke burners and related devices. Prog Energy Combust Sci 19(4):313–364. https://doi.org/10.1016/0360-1285(93)90007-2
Rayleigh L (1878) The explanation of certain acoustical phenomena. Roy Inst Proc 8:536–542, https://ci.nii.ac.jp/naid/10029867839/en/
Sastry S, Hijab O (1981) Bifurcation in the presence of small noise. Syst Control Lett 1(3):159–167
Saurabh A, Kabiraj L, Steinert R, Paschereit CO (2016) Noise-induced dynamics in the subthreshold region in thermoacoustic systems. J Eng Gas Turbines Power 139(3):031508. https://doi.org/10.1115/1.4034544
Seywert CN (2001) Combustion instabilities: issues in modeling and control. PhD thesis, California Institute of Technology
Shreekrishna S, Acharya V, Lieuwen T (2013) Flame response to equivalence ratio fluctuations—relationship between chemiluminescence and heat release. Int J Spray Combust Dyn 5(4):329–358. https://doi.org/10.1260/1756-8277.5.4.329
Sterling J, Zukoski E (1991) Nonlinear dynamics of laboratory combustor pressure oscillations. Combust Sci Technol 77(4–6):225–238
Strahle WC (1978) Combustion noise. Prog Energy Combust Sci 4(3):157–176. https://doi.org/10.1016/0360-1285(78)90002-3
Stratonovich RL (1967) Topics in the theory of random noise, vol 2. CRC Press
Swift GW (1988) Thermoacoustic engines. J Acoust Soc Am 84(4):1145–1180. https://doi.org/10.1121/1.396617

Tam CKW, Bake F, Hultgren LS, Poinsot T (2019) Combustion noise: modeling and prediction. CEAS Aeronaut J 10(1):101–122. https://doi.org/10.1007/s13272-019-00377-2

Ushakov O, Wünsche HJ, Henneberger F, Khovanov I, Schimansky-Geier L, Zaks M (2005) Coherence resonance near a hopf bifurcation. Phys Rev Lett 95(12):123903

Waugh I, Geuß M, Juniper M (2011) Triggering, bypass transition and the effect of noise on a linearly stable thermoacoustic system. Proc Combust Inst 33(2):2945–2952

Waugh IC, Juniper MP (2011) Triggering in a thermoacoustic system with stochastic noise. Int J Spray Combust Dyn 3(3):225–241

Wellens T, Shatokhin V, Buchleitner A (2003) Stochastic resonance. Rep Prog Phys 67(1):45

Zakharova A, Vadivasova T, Anishchenko V, Koseska A, Kurths J (2010) Stochastic bifurcations and coherencelike resonance in a self-sustained bistable noisy oscillator. Phys Rev E 81(1):011106

Zinn BT, Lieuwen TC (2006) Combustion instabilities: Basic concepts. In: Lieuwen TC, Yang V (eds) Combustion instabilities in gas turbine engines. American Institute of Aeronautics and Astronautics, pp 3–26. https://doi.org/10.2514/5.9781600866807.0003.0026

Zinn BT, Powell EA (1971) Nonlinear combustion instability in liquid-propellant rocket engines. Symp (International) Combust 13(1):491–503. https://doi.org/10.1016/s0082-0784(71)80051-6

Chapter 13
Deep Learning Algorithms for Detecting Combustion Instabilities

Tryambak Gangopadhyay, Anthony Locurto, James B. Michael and Soumik Sarkar

Abstract Combustion instabilities are prevalent in a variety of systems including gas turbine engines. In this regard, the introduction of active control opens the potential for new paradigms in combustor design and optimization. However, the limited ability to detect the onset of instabilities can lead to difficulty in implementing active control approaches. Machine learning—specifically deep learning tools—may be employed to detect instabilities from various measurement and sensor data related to the combustion process. Deep learning models have recently shown remarkable potential for extraction of meaningful features from data without the need to handcraft. As one of the early studies of deep learning for combustion instability detection, we extract sequential image frames from high-speed images of a premixed, bluff-body stabilized flame which exhibits varying levels of combustion instability. Using an efficient detection framework (based on 2-D convolutional neural networks) to detect the growth of an unstable mode can lead to effective control schemes. In addition, we apply a second deep learning framework to capture the temporal correlations in the data with corresponding learned spatial features.

13.1 Introduction

Detecting the onset of critical transitions can help in implementing early warning measures and efficient control strategies in human-engineered dynamical systems. Early detection can help in preventing the occurrence of these unwanted events.

T. Gangopadhyay (✉) · A. Locurto · J. B. Michael · S. Sarkar
Iowa State University, Ames, IA 50011, USA
e-mail: tryambak@iastate.edu

A. Locurto
e-mail: alocurto@iastate.edu

J. B. Michael
e-mail: jmichael@iastate.edu

S. Sarkar
e-mail: soumiks@iastate.edu

A. Mukhopadhyay et al. (eds.), *Dynamics and Control of Energy Systems*,
Energy, Environment, and Sustainability,
https://doi.org/10.1007/978-981-15-0536-2_13

However, it is often difficult to develop models for accurate prediction of critical transition thresholds. Therefore, early warning signals are essential for improving predictions of the probability of occurrence of adverse events in complex dynamical systems across different application domains (Scheffer et al. 2009). This chapter focuses on turbulent combustors that are utilized widely in propulsion and power systems. Critical transitions can occur in these combustors, which can cause severe damage to engines and result in huge loss of revenue (Lieuwen 2012).

In a combustor, flow perturbations can cause fluctuations in the heat release rate and result in the generation of acoustic waves. If the heat release rate fluctuations are established in phase with the fluctuating acoustic pressure field, a positive feedback may be established—termed a thermoacoustic instability (Rayleigh 1878). The closed design, turbulent flowfield, and natural unsteadiness in many combustion and propulsion systems leads to a inherent risk of strong thermoacoustic feedback in many of these systems. Heat release oscillations can grow and cause an intense growth of pressure fluctuations and high heat transfer on the combustor surfaces (Dowling 1997; Culick and Kuentzmann 2006). Combustors, already operating at elevated pressure, can develop high levels of vibration due to these oscillations which may lead to structural damage and catastrophic failure resulting in huge revenue loss (Fisher and Rahman 2009). Therefore, the early detection of critical transition in combustion systems is extremely important (Gopalakrishnan et al. 2016). Characterizing combustion instability in a robust manner can lead to development of tools for early detection which in turn can result in implementation of active control approaches for optimal performance.

13.1.1 Motivation

A number of full-scale computational-fluid-dynamic (CFD) and reduced-order models have been developed in literature for the characterization of combustion instabilities. However, these models are inherently complex, and may have prohibitive computational costs, particularly when performing parametric optimization studies. Physics-based modeling of combustion instabilities have also been examined, and several important mechanisms have been identified (Palies et al. 2011; Bellows et al. 2007; Noiray et al. 2008). One mechanism determined to be important in the generation of thermoacoutic feedback is the presence of coherent fluid structures—fluid mechanical phenomena associated with the coherent phase of vorticity (Hussain 1983) which can cause large-scale velocity oscillations and overall flame shape oscillations by curling and stretch. Several methods have been proposed and successfully implemented for detection of coherent structures including proper orthogonal decomposition (POD) (Berkooz et al. 1993) and dynamic mode decomposition (DMD) (Schmid 2010). The prevalence of coherent structures in a given flowfield can be a strong indicator of instability (Chakravarthy et al. 2007), however variations in specific systems and the lack of physical understanding of the origin of these flow structures makes identification of combustion instability predictors difficult.

This challenge has been addressed in the reviews of Huang and Yang (2009) and Candel et al. (2014). In addition to exploring the origins of thermoacoustic instabilities, several studies have explored the suppression of thermo-acoustic instabilities. For example, precise control of the fuel flow rate has been shown to enable control and avoidance of combustion instabilities in engine systems (Gorinevsky et al. 2012; Banaszuk et al. 2004). In addition, dynamic data-driven application systems (Darema 2005) using time-series data have been used to characterize combustion instabilities (e.g., Nair and Sujith 2014; Nair et al. 2013; Sen et al. 2018; Ghosal et al. 2016; Gotoda et al. 2011).

Recent advances in neural network approaches have shown effective extraction of useful features from data for both automated learning and decision-making tasks. In this regard, deep learning algorithms have shown advantages in handling high-dimensional data and in extracting features (Hinton 2006). Deep learning has been mostly applied in the domains of image (or video) and speech processing. For image-based data, deep convolutional neural networks (CNNs) can be used to learn meaningful spatial patterns (Krizhevsky et al. 2012). Farabet et al. (2013) used a multi-scale convolutional neural network for scene labeling, and other applications based on CNN include gradient-based learning for character identification in handwriting, (LeCun et al. 1998), natural language processing (Collobert and Weston 2008), and low-light image enhancement (Lore et al. 2017). However, applications of deep learning in studying combustion instability is a recent research topic. In the context of combustion instability detection, a deep learning-based framework was used to extract features from high-speed flame images for early detection of combustion instability (Sarkar et al. 2015). Sarkar et al. used a neural-symbolic framework in order to first extract low-dimensional features from sequential high-speed flame images using a deep CNN. Then Symbolic Time Series Analysis (STSA) was leveraged to capture the temporal variation (Sarkar et al. 2015). Akintayo et al. also examined time dynamics through an end-to-end convolutional selective autoencoder (Akintayo et al. 2016). This enabled information about the coherent structures from unstable frames to be encoded and allowed the definition of instability metric. The 3D CNN architecture can leverage the temporal correlations among the consecutive frames and classify flame images into two classes—stable and unstable (Ghosal et al. 2017).

Recent literature (Akintayo et al. 2016) has shown that to effectively characterize combustion instabilities, which are typically found in turbulent combustion and propulsion systems, feature extraction from sequential high-speed image sequences is necessary. Robust detection of instabilities from image data is an essential step towards applying effective control strategies to minimize the occurrence of unfavorable thermoacoustic instabilities. However, the prior literature applying deep learning techniques for detection of instabilities have demonstrated success while observing test cases and training cases with similar physical mechanisms. In this chapter, we discuss our recent efforts to use an image-based detection framework which is independent of the method by which the thermoacoustic feedback drives a combustion instability. We propose an additional model to leverage the temporal correlations from sequential image frames of stable and unstable cases.

13.1.2 Detecting Instability Using 2-D Convolutional Neural Networks

Deep learning models based on 2-D convolutional neural networks can learn important spatial features from images and can therefore be successfully implemented for classifying flame images (Gangopadhyay et al. 2018). We propose a deep CNN model which is trained on sequential frames of a high-speed image sequence. We define a non-dimensional instability measure derived from the sound pressure data, which is used to apply labels. We test the model on a transient dataset where instability is induced by a different protocol (variation of fuel/air ratio) compared to that of the training set. We demonstrate the robustness of our proposed framework by successful detection of the critical transition to an unstable condition.

13.1.3 Capturing Temporal Correlations from Sequential Images

While the 2-D CNNs can capture the spatial features well, we also need to consider temporal features as instability is inherently a dynamic behavior. In this regard, Long Short Term Memory Recurrent Neural Networks (LSTM—RNNs) are effective in capturing temporal correlations from sequential data. In order to capture both the spatial and temporal information from the input sequence, we utilize the combination of 2D CNN with LSTMs. In our proposed model, the CNN captures the spatial information from each image and encodes each image into a vector. The LSTM is used on top of the CNN to capture the global temporal structure. The aim is to improve the understanding of the model using only 2D CNN.

13.2 Experimental Setup and Dataset

We begin our discussion with a description of the experimental setup and dataset preparation procedure for developing the deep learning algorithms for combustion instability detection.

13.2.1 Experimental Setup

To establish a canonical experimental testbed for study of combustion instabilities, we use a Rijke tube. Traditionally, Rijke tubes can have either a combustion or non-combustion heat source with two open ends. The system exhibits unstable behavior when a positive feedback is established between the heat release and the reflected

acoustic waves from the tube ends (Heckl 1988). We use a vertically-oriented open-ended Rijke tube setup with a turbulent, bluff-body stabilized flame as the heat source as shown in Fig. 13.1. A Pyrex glass tube of 3-inch diameter and 24-inch length is used to allow for the possibility of acoustic feedback in the system. The burner consists of a stainless steel tube (0.375-inch diameter) with a conical steel bluff body (inner diameter of 7 mm, outer diameter of 9.525 mm) with an approximate distance of 10.38 mm measured from the burner to the tip of the bluff body. The oxidizer and fuel (air and ethylene) are premixed at near-stoichiometric conditions and flowrates are controlled using mass flow controllers (Alicat M-series). A high-speed complementary metal-oxide semiconductor (CMOS) sensor is used to capture high-speed image sequences of the flame luminosity. In addition to these image sequences, an oscilloscope is used to capture synchronous sound levels from the Rijke tube combustion system.

13.2.2 Data Collection

For experimental data colleciton, the burner tip position is varied with respect to the ends of the Rijke tube (varying x/L ratio), as depicted in Fig. 13.1. The distance is

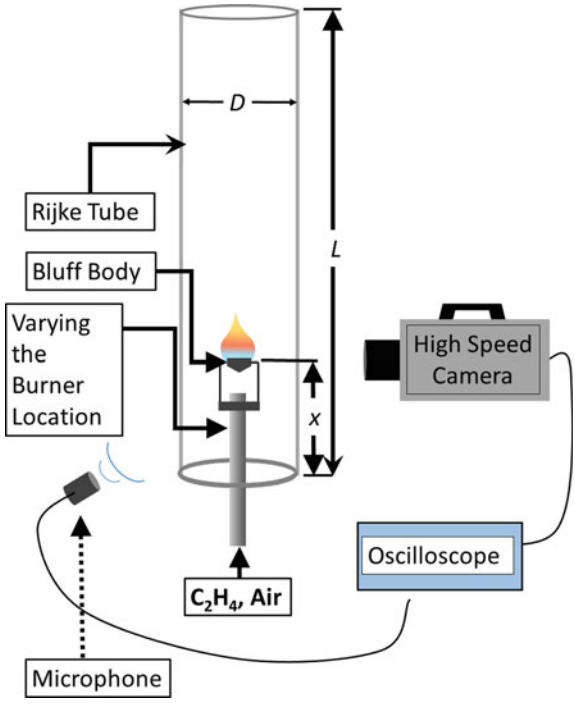

Fig. 13.1 Schematic of the Rijke tube experiment with a bluff-body stabilized premixed flame, high-speed camera, and microphone to monitor sound levels

varied from x/L of 0.125 to 0.5, while keeping the air and fuel flow rates constant at 18 SLPM and 1.5 SLPM, respectively. The instability characterization problem is posed based on the data collected at five different positions of the flame.

The high-speed camera (Photron FASTCAM SA5 1000K-M2) captures 5000 frames per second with an exposure of 1/5000 seconds and a frame size of 192×352 pixels^2 corresponding to a field of view of $19.2 \times 35.2\,\text{mm}^2$. The sound level is recorded simultaneously, with the microphone held a fixed distance away from the burner location (approximately 12-inches). To monitor the trigger signal from the camera, the acoustic signal, and the camera exposure for each frame, the oscilloscope records data for 20 seconds (Tektronix MSO 70404C, 5 MS/s, 100 million samples per channel).

Experimental runs consisted of time-series data of sound levels and 5 kHz-rate image sequences with a number of burner positions within the tube. Burner position was set from 0 to 12 inch, corresponding to x/L locations of 0 to 0.5. Data was collected 10 seconds after ignition for each flame height, to allow the flame position to stabilize.

Due to the camera memory limit, 33.88 s of data were acquired in a single time-contiguous experiment. At each flame location, we use two partitions to capture images each with a time length of 16.94 s. also, we record two separate datasets (each having 84,700 images) corresponding to every location. This data, at 5 different burner locations was used as the training input to the 2D CNN model.

A separate experiment was performed where we varied the air flow rate from 16 to 22 SLPM, decreasing the equivalence ratio of the flame from 1.5 to 0.95. The flowrates were varied every 4 s with an increase in the air flow rate by 2 SLPM for each set point. This dataset was taken for a flame position of 6 inches, or $x/L = 0.25$. These datasets are used to test the robustness of the image-based detection framework, as the level of combustion instability/acoustic feedback progressively increased during the run.

13.2.3 Data Preparation and Preprocessing

For each flame location, a total record length of 33.88 s was used, consisted of two time-continuous sets of 16.94-s duration. The chemiluminescence images were each 192×352 pixels, as shown in Fig. 13.2. Each image is cropped to use only the portions which contain signal, and reducing the cropped image to a size of 160×130 pixels^2. These cropped images are finally resized to 128×128 2D arrays to be used as input to our 2D CNN model.

Dynamic characteristics can be studied from time series data using a moving window approach (Sen et al. 2018). We fix the window length as 0.1 s (100 ms) and sequentially move the window for analysis using power spectral density plot as shown in Fig. 13.3. Each window is equivalent to 500 images as the fps of the high-speed camera is 5000. For each burner location, we consider 320 time-windows from two partitions and thus, we have a total of 1600 time windows for 5 locations.

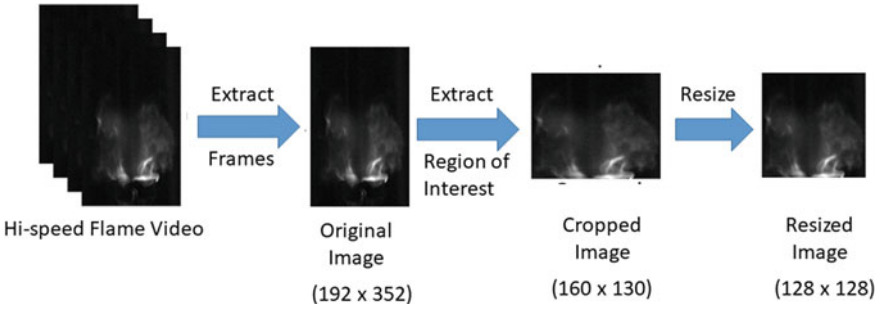

Fig. 13.2 Pre-processing of a sample image. The images are cropped to extract the region of interest and the images are then resized to dimensions of 128×128 pixels[2]

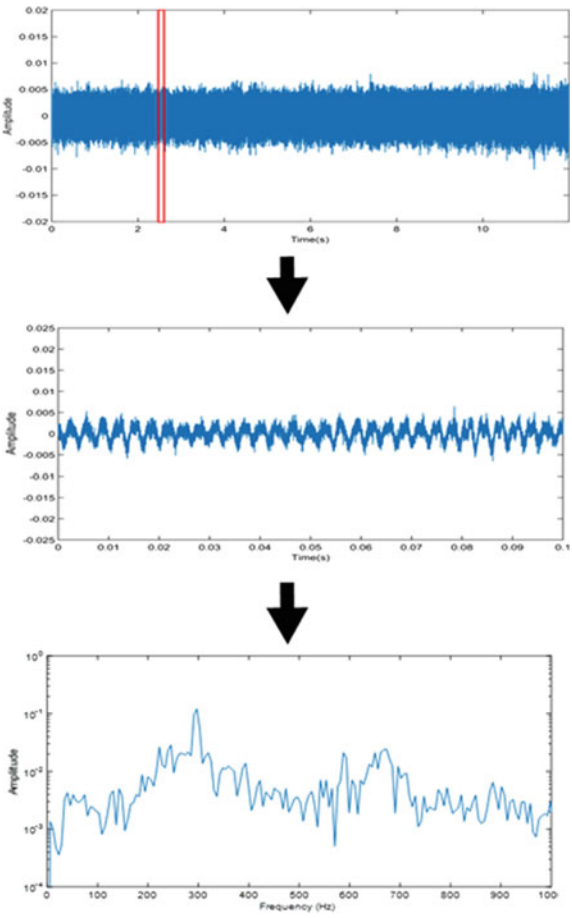

Fig. 13.3 Moving window approach is used for preprocessing the time series. The first figure shows a sample acoustic time series data from which an extracted window (length 0.1 s) is shown. The corresponding power spectral density plot of this time window is computed

13.2.4 Instability Measure and Labeling

We choose two frequency ranges (2000–5000) Hz and (200–500) Hz for computing the instability measure. We estimate noise in the selected time window by taking average of the amplitudes corresponding to the frequency range of (2000–5000) Hz. This frequency range is distant from the high amplitude zone as shown in Fig. 13.4. For our dataset, the high amplitude zone is mostly in the range of 200–500 Hz and we compute the sum of amplitudes in this range to estimate the energy content of instability in the combustion system. The instability measure (IM) is defined in Eq. (13.1).

$$IM = \frac{\sum \text{Amplitudes in the range } 200 - 500\,\text{Hz}}{\text{Mean of the amplitudes in the range } 2000 - 5000\,\text{Hz}} \tag{13.1}$$

The scatter plot (Fig. 13.5) shows that the range of IM values is 183.79–3959.30. To form 5 classes from this range, we implement maximum entropy principle (Ray 2004). We have equal number of time windows (320) in each partition which implies 160,000 images per partition. We correlate a particular time window with the corresponding images to generate labels (Table 13.1). This is an inexpensive labeling technique as it does not involve manual labeling and it is also less time consuming. This noisy labeling scheme makes our problem formulation more general as we do not perform labeling based on burner locations.

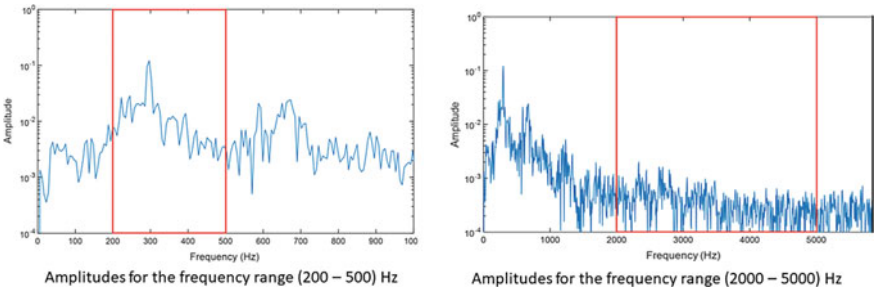

Fig. 13.4 Power spectral density plot showing the selected frequency ranges (200–500) and (2000–5000) used to compute the instability measure

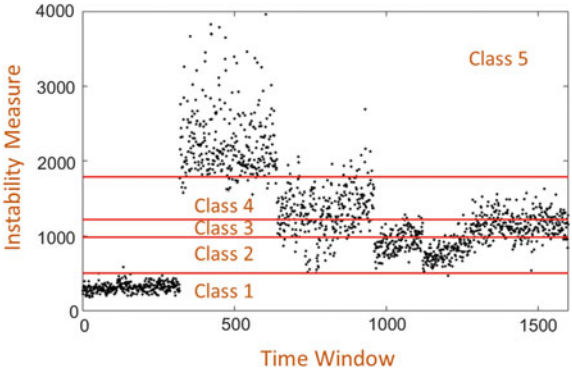

Fig. 13.5 Instability measure values for all time windows in the data; We use maximum entropy partitioning to get 5 classes

Table 13.1 The instability measure values for five classes

Range of instability measure	Class
(183.79–507.49)	1
(507.49–988.24)	2
(988.24–1223.80)	3
(1223.80–1786.60)	4
(1786.60–3959.30)	5

13.3 Detecting Instability Using 2-D Convolutional Neural Networks

13.3.1 Network Architecture

Deep learning has gained immense popularity recently and is being applied in a large variety of domains. Developments in deep learning concepts have led to advancements in research related to computer vision. For learning features from images, convolutional networks (conv. nets) have less number of trainable parameters compared to fully connected layers. Also, in fully connected layers the spatial structure of an image gets lost. There are other disadvantages such as high memory and computational requirements. Conv. nets can overcome these disadvantages by using the convolution operation. Taking input from the feature map of previous layer, the weights of the filters (kernels) of a layer get updated during the training procedure. These conv. nets are highly efficient in image recognition tasks (LeCun et al. 1998) and the feature maps in a conv. net share weights (LeCun and Bengio 1995). Apart from conv. layers, CNN may also comprise of pooling layers. By downsampling, the pooling layers have several advantages including the reduction of model overfitting and making computations more faster. Max-pooling takes the maximum value to compute the feature map and doesn't involve any learning parameters. We imple-

ment fully connected layers (using the softmax activation) before predicting the class to learn the non-linear combinations among the features.

Our proposed CNN model is demonstrated in Fig. 13.6 which is different from ones used before (Krizhevsky et al. 2012; Simonyan and Zisserman 2014). The input to the model is 128×128 grayscale image. The first two conv. layers have 32 kernels each followed by maxpooling. After that, we have a series of conv. and maxpooling layers to learn the features. The number of kernels increases as we go deeper in the network but the size of receptive field decreases from (7×7) to (3×3). We used receptive field of (2×2) for the max-pooling layers and we keep the stride as 2. For all the conv. layers we use Rectified Linear Unit (ReLU) non-linearity (Krizhevsky et al. 2012). Batch Normalization (Ioffe and Szegedy 2015) is also implemented in the model. Dropout regularization method (Hinton et al. 2012).

To prevent overfitting, we use dropout regularization (Hinton et al. 2012). We have higher dropout in the deeper layers to avoid information loss in the first few layers. We develop the model using the Keras framework (Chollet et al. 2015) with the TensorFlow backend (Abadi et al. 2016) and train the model on NVIDIA GPUs. The optimizer for our training is Adam (Kingma and Ba 2014) with learning rate of 0.001 and the batch size is 128. The loss function is categorical cross-entropy.

13.3.2 Results

We decrease the dataset size to 264,000 from 800,000 images for reducing the computation time. The training and test set (same as the validation set) comprise 250,800 and 13200 examples respectively. After training for 450 epochs, the accuracy for the training set is 98.04% and for the validation set it is 83.02%. The accuracy values are different class-wise (Table 13.2). The model shows higher accuracy values for the two extreme classes (Class 1 and Class 2). We demonstrate the performance of our model using the confusion matrix (Table. 13.3). In a confusion matrix, the probability of predicting class j given the true label is i, is represented by element (i, j) and the probabilities of correct predictions are shown in the diagonal elements (Pedregosa et al. 2011). We observe from the confusion matrix that for the classes representing intermediate values of instability, the mislabeling occurs with the nearest classes only.

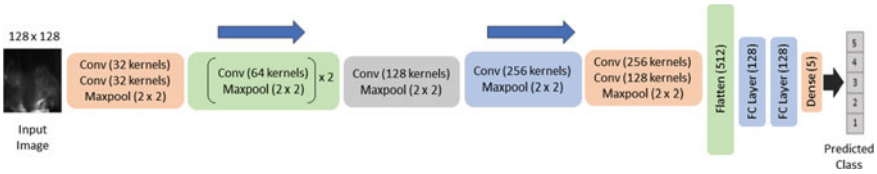

Fig. 13.6 The deep convolutional neural network architecture. It takes in input a grayscale image and predicts the class label

Table 13.2 Class accuracy values for validation/test set

Class	Accuracy (%)
1	100
2	81
3	69
4	69
5	96

Table 13.3 Normalized confusion matrix showing performance on validation/test set. The rows represent the true labels while the columns represent the predicted labels

	Class 1	Class 2	Class 3	Class 4	Class 5
Class 1	1.00	0.00	0.00	0.00	0.00
Class 2	0.00	0.81	0.13	0.05	0.00
Class 3	0.00	0.14	0.69	0.17	0.00
Class 4	0.00	0.04	0.19	0.69	0.07
Class 5	0.00	0.00	0.00	0.04	0.96

$$E = \frac{\sum_{class=1}^{5} (IM)_{class} (\text{No. of predictions})_{class}}{\sum_{class=1} (\text{No. of predictions})_{class}} \tag{13.2}$$

For early detection of the critical transition, we define Expected Instability Measure (E) as in Eq. (13.2). For a particular class, the $(\text{IM})_{class}$ is the average of the instability measure values for all samples in that class. The number of predictions for each class is also used to compute the E value. For the transient dataset, we vary the equivalence ratio from 1.5 to 0.95 by increasing the air flow rate. The fuel flow rate is kept constant. We use our trained model to predict on the images and then plot the change in the value of E (Fig. 13.7). We observe a significant increase in E which may indicate the critical transition in the system. After reaching a state of maximum instability, the value of E decreases going towards the leaner side.

13.4 Capturing Temporal Correlations from Sequential Images: CNN-LSTM Model

With the aim of improving the 2D CNN model, we propose another model using the same experimental setup for data collection and also following similar techniques for data preprocessing. After computing the instability measure values, we implement a different labeling scheme for this part of our work. We define instability measure in similar manner and thereafter we classify the dataset into two classes- stable and

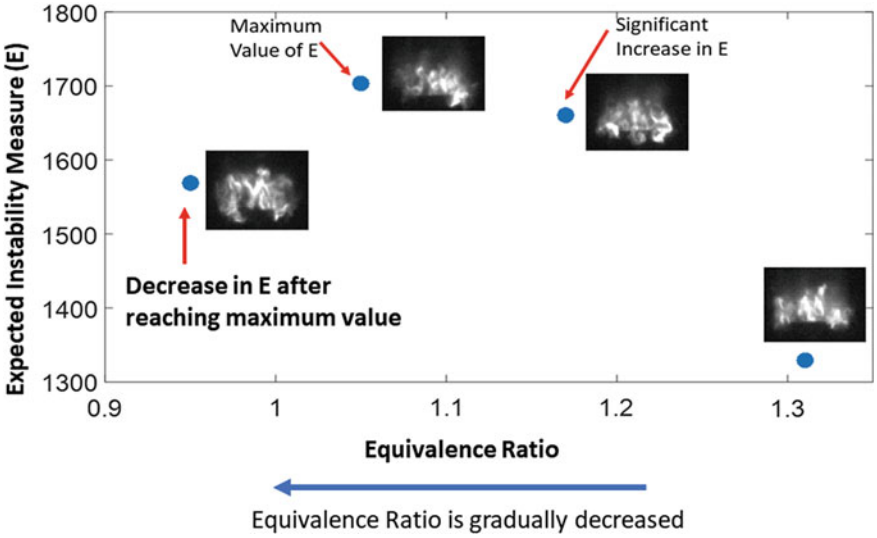

Fig. 13.7 Variation of expected instability measure (E) with decrease in equivalence ratio

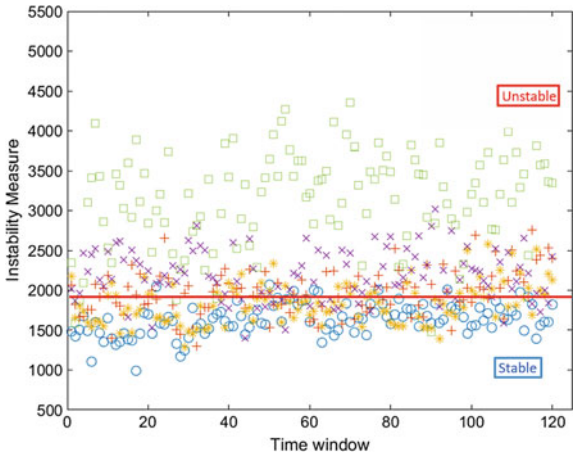

Fig. 13.8 Instability measure values for all the time windows. The partition showing the segregation between stable and unstable class

unstable. We formulate the problem as binary classification in this case to train a model in learning the temporal correlations for stable and unstable sequences.

We compute the instability measure (IM) for all the 0.1 s time windows and the results are plotted in Fig. 13.8. To separate the dataset into stable and unstable classes, we chose the median of the instability measure as the threshold (represented by the red line), where all the values above the median are considered unstable and the values below are considered stable. We correlate the image sequences with the corresponding IM values to compute the class label for each sequence.

13.4.1 Long Short-Term Memory Recurrent Neural Network

Recurrent Neural Networks (RNNs) can explicitly capture temporal correlations in sequential data and can demonstrate high accuracy outperforming the static networks by efficient learning of the temporal dependencies (Bengio 1991). Propagating the error gradients through the latent layers can result in vanishing gradients, which may cause difficulty in training the RNNs with the error backpropagation algorithm for tasks with long-range dependencies (Bengio et al. 1994). Inefficient learning can happen if the time lag is greater than 5–10 discrete time steps between relevant input events and target outputs (Gers et al. 1999). Long short-term memory (LSTM) is an RNN architecture that can overcome the error backflow problems in long-range sequential input data (Hochreiter and Schmidhuber 1997). Unlike standard RNNs, LSTM networks can demonstrate high prediction accuracy even when the interval between the relevant information in input and the output timestep becomes very large.

Forget gate layer (σ_1) is the first step of an LSTM block as illustrated in Fig. 13.9. A sigmoid layer decides the information to be erased from the cell state C_t. This operation is performed as:

$$e_t = \sigma_1(W_e \cdot [a^{<t-1>}, x^{<t>}] + b_e)$$

The next step involves replacing the erased information in the cell state with new information. The first part (information selection) is performed by a sigmoid layer (σ_2, the input gate layer), followed by a tanh layer which generates potential values for augmenting the cell state.

$$r_t = \sigma_2(W_r \cdot [a^{<t-1>}, x^{<t>}] + b_r)$$
$$\tilde{C}^{<t>} = tanh(W_C \cdot [a^{<t-1>}, x^{<t>}] + b_C)$$

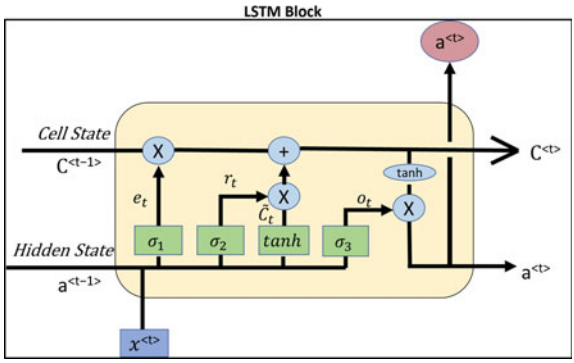

Fig. 13.9 LSTM block. The input, output and forget gates regulate whether information can be added to or removed from the cell state

By combining the outputs from the first part, we obtain the new cell state C_t:

$$C^{<t>} = e_t \times C^{<t-1>} + r_t \times \tilde{C}^{<t>}$$

After updating the cell state, the hidden state of the previous time step ($a^{<t-1>}$) is passed through the third sigmoid layer, σ_3 for filtering and selection of information. It is then combined with the new cell state filtered by the tanh layer as shown in Fig. 13.9.

$$o_t = \sigma_3(W_o \cdot [a^{<t-1>}, x^{<t>}] + b_o)$$
$$a^{<t>} = o_t \times tanh(C^{<t>})$$

The most critical components of the LSTM block are the forget gate and the output activation function and removing any of these can significantly degrade the performance (Greff et al. 2017).

13.4.2 Network Architecture

We describe the framework based on convolutional neural network, long short-term memory recurrent neural network, and a temporal attention mechanism. A proposed CNN model is used to encode the individual image in the input sequence into a 128-dimensional vector, as shown in Fig. 13.10. Our network architecture (Fig. 13.11) consists of CNN to encode each image into a vector and LSTM layers on top of that to capture the temporal correlations in the entire sequence. The combination of CNN and LSTM in the model ensures simultaneous learning of the spatial features and temporal correlations from the input sequence of images. The encoded vectors act as input for different timesteps to the LSTM layer. At timestep t the LSTM block takes in input the encoded vector $x^{<t>}$ and the hidden state from the previous timestep $a^{<t-1>}$ to compute the annotation $a^{<t>}$.

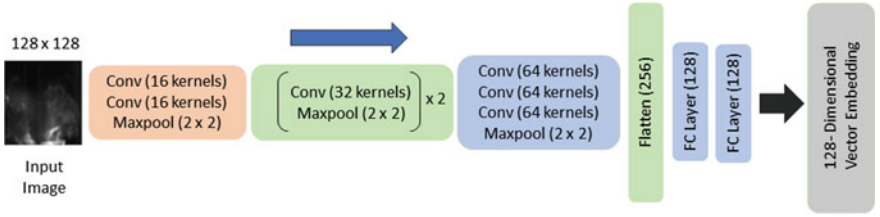

Fig. 13.10 Proposed deep CNN architecture. The network takes in input 128×128 grayscale image and encodes the image into a 128-dimensional vector. The network has 7 conv. layers and 4 max-pooling layers. The total number of trainable parameters is about 0.2 million. We use this CNN model to encode all the images individually in the input sequence

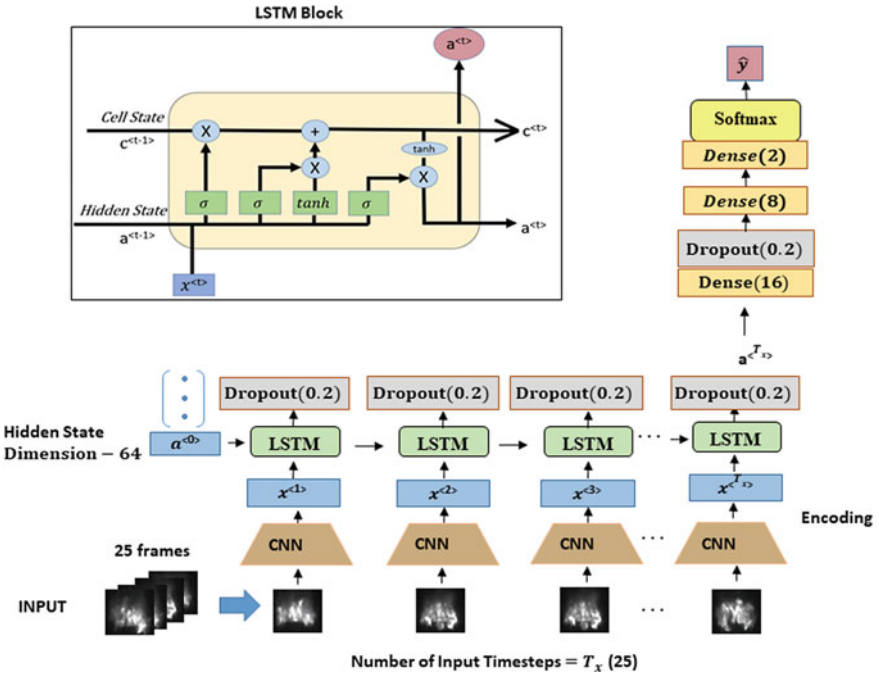

Fig. 13.11 Proposed model based on CNN and LSTM. The CNN model encodes all the images in the input sequence and the encoded 128-dimensional vectors act as the inputs for the LSTM layer. Two fully-connected layers are used before predicting the label with softmax. The total number of trainable parameters for the model is about 0.25 million and the training time is 80 secs/epoch

13.4.3 Results

The model is prone to overfitting. To get the best possible performance, we try different combinations of hyperparameters. Table 13.4 presents the training and validation accuracy with the best set of hyperparameters after optimizing the CNN-LSTM model. The model performance shows that it is robust for different lengths of input sequence. The training accuracy can reach up to 94.7% and validation accuracy of 82.9% when using a time lag of 25.

13.5 Summary and Conclusions

The turbulent flame is a source of noise generation, as is typical in many combustors. Typical high-power combustion systems use turbulent mixing and turbulent flames to achieve rapid heat release and high power density (Lieuwen 2012). In real combustors, a number of unstable modes may exist, depending on the geometry of the

Table 13.4 Training accuracy and validation accuracy for the CNN-LSTM model using different input sequence lengths

Input sequence length	Model	Training accuracy (%)	Validation accuracy (%)
5	CNN-LSTM	89.0	79.4
10	CNN-LSTM	91.0	81.5
20	CNN-LSTM	84.9	82.3
25	CNN-LSTM	94.7	82.9
50	CNN-LSTM	88.0	82.5

system. Low frequency, growling modes, are typically longitudinal acoustic modes in the combustion system. Higher-frequency modes can consist of axial acoustic modes or higher-order modes in the combustion chamber. In the experiment, the bluff-body stabilized flame acts as a source of perturbations due to the unsteady nature of the turbulent combustion process—also a source of broadband acoustic noise generation. Acoustic waves generated near the resonant frequencies of the tube are then amplified, resulting in strong thermoacoustic feedback which serves to drive heat-release oscillations in the flame at the same resonant frequency.

In this chapter, we propose deep learning frameworks to detect such combustion instability. We first develop a robust framework which is agnostic to the combustion inducing protocol and can accurately detect the transition from a state of low to high combustion instability. The CNN-based detection from images sequences is compared with the acoustic field measurements to classify the level of thermoacoustic feedback/combustion instability. Our labeling technique (using the acoustic field measurements) is based on using maximum entropy partitioning after defining an instability measure. The inducing protocols for training and test sets are different. We demonstrate the robustness of our model by showing its performance on the test set. By effective detection of critical transition, active control actions can be implemented which can eliminate the adverse effects of combustion instability.

As instability is inherently a dynamic behavior, we also propose a CNN-LSTM model which takes sequential image frames as input instead of individual frames. The CNN-LSTM model predicts a single class label for the entire input sequence. Combining 2D CNN and LSTM, this model can learn the temporal correlations in the sequence along with the spatial features in each image. By framing the problem as a binary classification problem, we achieve promising accuracy of classifying stable and unstable sequences for different lengths of input sequence.

With the typical hardware availability, implementation of image/video-based instability detection in real combustors may be challenging due to limited optical access. However, the approach shown could be modified to incorporate multiple sets of sensor data. The experiment was designed with a turbulent flame as almost all real combustors utilize turbulent mixing and combustion processes.

References

Abadi M, Barham P, Chen J, Chen Z, Davis A, Dean J, Devin M, Ghemawat S, Irving G, Isard M et al (2016) Tensorflow: a system for large-scale machine learning. OSDI 16:265–283

Akintayo A, Lore KG, Sarkar S, Sarkar S (2016) Prognostics of combustion instabilities from hi-speed flame video using a deep convolutional selective autoencoder. Int J Progn Health Manag 7(023):1–14

Banaszuk A, Ariyur KB, Krstić M, Jacobson CA (2004) An adaptive algorithm for control of combustion instability. Automatica 40(11):1965–1972

Bellows BD, Bobba MK, Forte A, Seitzman JM, Lieuwen T (2007) Flame transfer function saturation mechanisms in a swirl-stabilized combustor. Proc Combust Inst 31(2):3181–3188

Bengio Y (1991) Artificial neural networks and their application to sequence recognition. McGill University

Bengio Y, Simard P, Frasconi P (1994) Learning long-term dependencies with gradient descent is difficult. IEEE Trans Neural Netw 5(2):157–166

Berkooz G, Holmes P, Lumley JL (1993) The proper orthogonal decomposition in the analysis of turbulent flows. Annu Rev Fluid Mech 25(1):539–575

Candel S, Durox D, Schuller T, Bourgouin JF, Moeck JP (2014) Dynamics of swirling flames. Annu Rev Fluid Mech 46:147–173

Chakravarthy SR, Shreenivasan OJ, Boehm B, Dreizler A, Janicka J (2007) Experimental characterization of onset of acoustic instability in a nonpremixed half-dump combustor. J Acoust Soc Am 122(1):120–127

Chollet F et al (2015) Keras

Collobert R, Weston J (2008) A unified architecture for natural language processing: deep neural networks with multitask learning. In: Proceedings of the 25th international conference on machine learning. ACM, pp. 160–167

Culick F, Kuentzmann P (2006) Unsteady motions in combustion chambers for propulsion systems. Technical Report, NATO Research and Technology Organization, Neuilly-sur-Seine, France

Darema F (2005) Dynamic data driven applications systems: new capabilities for application simulations and measurements. In: International conference on computational science. Springer, pp. 610–615

Dowling AP (1997) Nonlinear self-excited oscillations of a ducted flame. J Fluid Mech 346:271–290

Farabet C, Couprie C, Najman L, LeCun Y (2013) Learning hierarchical features for scene labeling. IEEE Trans Pattern Anal Mach Intell 35(8):1915–1929

Fisher SC, Rahman SA (2009) Remembering the giants: Apollo rocket propulsion development

Gangopadhyay T, Locurto A, Boor P, Michael JB, Sarkar S (2018) Characterizing combustion instability using deep convolutional neural network. In: ASME 2018 dynamic systems and control conference. American Society of Mechanical Engineers, pp. V001T13A004–V001T13A004 (2018)

Gers FA, Schmidhuber J, Cummins F (1999) Learning to forget: Continual prediction with LSTM

Ghosal S, Akintayo A, Boor P, Sarkar S (2017) High speed video-based health monitoring using 3D deep learning

Ghosal S, Ramanan V, Sarkar S, Chakravarthy SR, Sarkar S (2016) Detection and analysis of combustion instability from hi-speed flame images using dynamic mode decomposition. In: ASME 2016 dynamic systems and control conference. American Society of Mechanical Engineers, pp. V001T12A005–V001T12A005

Gopalakrishnan E, Sharma Y, John T, Dutta PS, Sujith R (2016) Early warning signals for critical transitions in a thermoacoustic system. Sci Rep 6:35310

Gorinevsky D, Overman N, Goeke J (2012) Amplitude and phase control in active suppression of combustion instability. In: American control conference (ACC). IEEE, pp. 2601–2608

Gotoda H, Nikimoto H, Miyano T, Tachibana S (2011) Dynamic properties of combustion instability in a lean premixed gas-turbine combustor. Chaos Interdiscip J Nonlinear Sci **21**(1):013124

Greff K, Srivastava RK, Koutník J, Steunebrink BR, Schmidhuber J (2017) LSTM: a search space odyssey. IEEE Trans Neural Netw Learn Syst 28(10):2222–2232
Heckl MA (1988) Active control of the noise from a Rijke tube. J Sound Vib 124(1):117–133
Hinton GE, Salakhutdinov RR (2006) Reducing the dimensionality of data with neural networks. Sci **313**(5786):504–507
Hinton GE, Srivastava N, Krizhevsky A, Sutskever I, Salakhutdinov RR (2012) Improving neural networks by preventing co-adaptation of feature detectors. arXiv:1207.0580
Hochreiter S, Schmidhuber J (1997) Long short-term memory. Neural Comput 9(8):1735–1780
Huang Y, Yang V (2009) Dynamics and stability of lean-premixed swirl-stabilized combustion. Prog Energy Combust Sci 35(4):293–364
Hussain AKMF (1983) Coherent structures—reality and myth. Phys Fluids 26:2816–2850. https://doi.org/10.1063/1.864048
Ioffe S, Szegedy C (2015) Batch normalization: accelerating deep network training by reducing internal covariate shift. arXiv:1502.03167
Kingma DP, Ba J (2014) Adam: a method for stochastic optimization. arXiv:1412.6980
Krizhevsky A, Sutskever I, Hinton GE (2012) Imagenet classification with deep convolutional neural networks. In: Advances in neural information processing systems, pp. 1097–1105
LeCun Y, Bengio Y et al (1995) Convolutional networks for images, speech, and time series. Handb Brain Theory Neural Netw **3361**(10):1995
LeCun Y, Bottou L, Bengio Y, Haffner P (1998) Gradient-based learning applied to document recognition. Proc IEEE 86(11):2278–2324
Lieuwen TC (2012) Unsteady combustor physics. Cambridge University Press, New York
Lore KG, Akintayo A, Sarkar S (2017) LLNET: a deep autoencoder approach to natural low-light image enhancement. Pattern Recognit 61:650–662
Nair V, Sujith R (2014) Multifractality in combustion noise: predicting an impending combustion instability. J Fluid Mech 747:635–655
Nair V, Thampi G, Karuppusamy S, Gopalan S, Sujith R (2013) Loss of chaos in combustion noise as a precursor of impending combustion instability. Int J Spray Combust Dyn 5(4):273–290
Noiray N, Durox D, Schuller T, Candel S (2008) A unified framework for nonlinear combustion instability analysis based on the flame describing function. J Fluid Mech 615:139–167
Palies P, Schuller T, Durox D, Candel S (2011) Modeling of premixed swirling flames transfer functions. Proc Combust Inst 33(2):2967–2974
Pedregosa F, Varoquaux G, Gramfort A, Michel V, Thirion B, Grisel O, Blondel M, Prettenhofer P, Weiss R, Dubourg V, Vanderplas J, Passos A, Cournapeau D, Brucher M, Perrot M, Duchesnay E (2011) Scikit-learn: machine learning in Python. J Mach Learn Res 12:2825–2830
Ray A (2004) Symbolic dynamic analysis of complex systems for anomaly detection. Signal Process 84(7):1115–1130
Rayleigh JWS (1878) The explanation of certain acoustical phenomena. Nature 18(455):319–321
Sarkar S, Lore KG, Sarkar S (2015) Early detection of combustion instability by neural-symbolic analysis on hi-speed video. In: Proceedings of the 2015th international conference on cognitive computation: integrating neural and symbolic approaches, vol. 1583. CEUR-WS.org, pp. 93–101
Sarkar S, Lore KG, Sarkar S, Ramanan V, Chakravarthy SR, Phoha S, Ray A (2015) Early detection of combustion instability from hi-speed flame images via deep learning and symbolic time series analysis. In: Annual conference of the prognostics and health management
Scheffer M, Bascompte J, Brock WA, Brovkin V, Carpenter SR, Dakos V, Held H, Van Nes EH, Rietkerk M, Sugihara G (2009) Early-warning signals for critical transitions. Nature 461(7260):53
Schmid PJ (2010) Dynamic mode decomposition of numerical and experimental data. J Fluid Mech 656:5–28
Sen U, Gangopadhyay T, Bhattacharya C, Mukhopadhyay A, Sen S (2018) Dynamic characterization of a ducted inverse diffusion flame using recurrence analysis. Combust Sci Technol 190(1):32–56
Simonyan K, Zisserman A (2014) Very deep convolutional networks for large-scale image recognition. arXiv:1409.1556

Chapter 14
Real-Time Monitoring and Diagnostics of Anomalous Behavior in Dynamical Systems

Sudeepta Mondal, Chandrachur Bhattacharya, Najah F. Ghalyan and Asok Ray

Abstract Real-time condition monitoring of complex dynamical systems is of critical importance for predictive maintenance. This chapter focuses on data-driven techniques of fault diagnostics with an emphasis on real-time detection of anomalous behavior in combustion systems. It presents the applications of well-known statistical learning techniques such as *D*-Markov modeling and hidden Markov modeling (HMM) as possible data-driven solutions for anomaly detection in combustion systems. From the perspective of real-time monitoring and diagnostics, such statistical tools are applicable to stochastic dynamical systems in general. Both *D*-Markov and HMM algorithms have been validated on experimental data from a laboratory apparatus, which is an electrically heated Rijke tube.

14.1 Introduction

Anomaly in a dynamical system is defined as deviation of the system performance from the expected or nominal behavior. Gradual evolution of anomalies is usually a consequence of slow parametric or non-parametric changes within the system, which often leads to degraded performance and eventually premature end of the service life. Therefore, anomaly detection is considered to be essential for sustaining order and normalcy in human-engineered complex systems.

The tasks of anomaly detection and failure prediction in engineering systems can be broadly classified into two categories: model-based and dynamic data-driven. In

S. Mondal · C. Bhattacharya · N. F. Ghalyan · A. Ray (✉)
Department of Mechanical Engineering, Pennsylvania State University, State College, USA
e-mail: axr2@psu.edu

S. Mondal
e-mail: sbm5423@psu.edu

C. Bhattacharya
e-mail: czb28@psu.edu

N. F. Ghalyan
e-mail: nfg103@psu.edu

A. Mukhopadhyay et al. (eds.), *Dynamics and Control of Energy Systems*,
Energy, Environment, and Sustainability,
https://doi.org/10.1007/978-981-15-0536-2_14

the model-based category, observer-induced techniques are commonly used, where certain residuals or diagnostic signals are generated for use in (possibly) optimal or adaptive threshold functions to detect the presence of faults. Residuals are generated by estimating the system's measured variables and using a deterministic (e.g., Kwakernaak and Sivan 1972) or a stochastic (e.g., Jazwinski 1970) observer. These observers are often designed based on a linear model or a (Jacobian) linearization of the nonlinear system model at selected operating points. These linear or linearized models are constructed as reasonable approximations of local behavior of the complex system when operating under the nominal condition; however, in case of evolving anomalies, the effects of system nonlinearities may gradually become too large to be ignored or approximated. Furthermore, it may be very difficult to model an anomalous system behavior, because such anomalies (e.g., those due to incipient faults) are usually unknown and may be too complex to model by solely relying on the fundamental laws of physics. Furthermore, a fault might be entering the system in a more complex manner than as an additive disturbance. These issues have motivated the study of anomaly detection in dynamical systems using a dynamic data-driven approach, where the dependence on a physics-based system model is de-emphasized; however, the knowledge of a physics-based model, if available, may supplement the information generated from the measured time-series data. In this context, an application example is presented in this chapter.

The application addresses occurrence of thermoacoustic instabilities (TAI) in combustion systems, which are caused by spontaneous excitation of one or more natural modes of acoustic waves (Lieuwen and Yang 2005). TAI are typically manifested by large-amplitude self-sustained chaotic pressure oscillations in the combustion chamber (Matveev 2003), which may lead to damage in mechanical structures if the pressure oscillations match one of the natural frequencies of the system. The time scales of TAI are on the order of milliseconds, which must be mitigated by fast actuation of the control signals. This mandates accurate detection of instabilities from short-length sensor data. While traditional techniques for growth-rate measurement are reported in combustion literature (Noiray and Denisov 2017; Rigas et al. 2016), they are only suitable for online data-intensive computations and the lengthy observation sequences and computation time may have large delays comparable to the time scale of TAI.

Recently there has been an upsurge in the use of data-driven techniques for early detection and classification of combustion instability. Various researchers have utilised different machine learning techniques for this purpose. Simple methods such as complex networks have been used by several res archers (e.g. Sen et al. 2016; Kobayashi et al. 2015), while several others have used symbolic time series analysis (STSA) (Ray 2004; Rajagopalan and Ray 2006; Bahrampour et al. 2013; Mukherjee and Ray 2014) for the same (e.g. Chakraborty et al. 2008; Sarkar et al. 2016). Nair et al. have utilised the loss of chaos (Nair 2013) and multi-fractal analysis (Nair and Sujith 2014) for the purpose of TAI detection. Recently the use of high speed image processing has also been developed and demonstrated by researchers (e.g. Soumalya et al. 2015; Hauser et al. 2016) which utilise deep learning for detecting precursors of combustion instability. For transitions that happen in laminar combustion systems

where the system transits from a non-oscillatory to oscillatory state via a Hopf bifurcation, early warning measures based on critical slowing down are also proposed in the available literature (Gopalakrishnan et al. 2016).

This chapter focuses on formulation and validation of a decision-making algorithm for sensor-based automation (e.g., real-time monitoring and active control of dynamical systems). These algorithms have been built upon the theory of hidden Markov modeling (HMM) to extract features and classify patterns of the process behavior from short-length sensor time series. The underlying concept of the proposed HMM-based algorithms is validated on an ensemble of experimental data from a laboratory apparatus. The performance in each case is evaluated by comparison with that of symbolic time series analysis (STSA). The results show consistent improvements for the proposed HMM-based method under varying configurations. From these perspectives, the major contributions of this chapter are delineated below.

1. Development of HMM-based algorithms for feature extraction and pattern classification from short-length time series to facilitate real-time monitoring and active control of dynamical systems.
2. Experimental validation of the anomaly detection algorithms in thermoacoustic instabilities in combustors.

The rest of the chapter is organized as follows. Section 14.2 presents a brief decription of the experimental apparatus. Section 14.3 provides an introduction to the theory of hidden Markov modeling (HMM) and its usage for symbolization of time series. Section 14.4 develops a modification of traditional STSA methods for detecting anomalies in a dynamical system. Section 14.5 presents HMM-based methodologies for early detection of anomalous regimes for monitoring and control of TAI. Section 14.6 summarizes and concludes the chapter along with recommendations for future research.

14.2 Experimental Apparatus

The data used in this article has been generated from a 1.5 m long electrically heated horizontal Rijke tube with an external cross-section of $4'' \times 4''$ with a wall thickness of $0.25''$. A Parker P32E series air filter-regulator eliminates pressure fluctuations and impurities. The flow rate is controlled using a 0–1000 SLPM Alicat Mass Flow controller. The heating element is a square weave 40×40 nichrome wire mesh, placed at quarter length in the upstream end of the tube. The heating element is powered by a programmable power supply from TDK Lambda. As a safety measure to prevent accidental physical contact with the hot downstream end of the tube, the latter is insulated. The pressure data is procured by a series of 8 acoustic sensors placed inline and flushed with the inner wall of the tube. The sampling rate of the acoustic data is 8192 Hz and the data acquisition process is automated through NI Labview 2016 in conjunction with DAQ devices from National Instruments. The acquired data is filtered using a high-pass filter of cutoff frequency 40 Hz in order

to eliminate low-frequency components due to noise and acoustics in the ambient. More details about the experimental setup and data acquisition can be found in the work by Mondal et al. (2018) (Fig. 14.1).

Knowing the stability map of the system provides an operator with the prior idea of which operating conditions lead to stable and unstable operations respectively. Figure 14.3 depicts the stability map of the system at different operating conditions. The operating conditions for the different experiments are different values of airflow rate (Q) and primary heater power input (E_{in}). The current article is focused on the online detection of instabilities in the transient growth phase of thermoacoustic oscillations. Thermoacoustic instabilities occur due to subcritical Hopf bifurcations (Gopalakrishnan and Sujith 2014) in which the system transits from a stable operation to an unstable limit cycle behavior. This transient growth period is a rich source of information for developing online detection algorithms. Early detection of imminent instabilities from the transient period can provide adequate lead time for the control system to take appropriate actions in order to revert the system to a stable mode of operation. For this purpose, in way similar to the one followed by Rigas et al. (2016), E_{in} has been increased in such a fashion that the system passes through the Hopf point:

1. For every run, the air flow-rate (Q) has been set at a constant value. Different runs have been performed with flow-rates ranging from 130 LPM to 250 LPM at intervals of 20 LPM.
2. First the system has been heated to a steady state with a primary heater power input (E_{in}) of ≈200 W.
3. Then the power input has been abruptly increased to a higher value that showed limit cycle behavior.
4. Acoustic sensor data has been acquired for 30 s of operation.

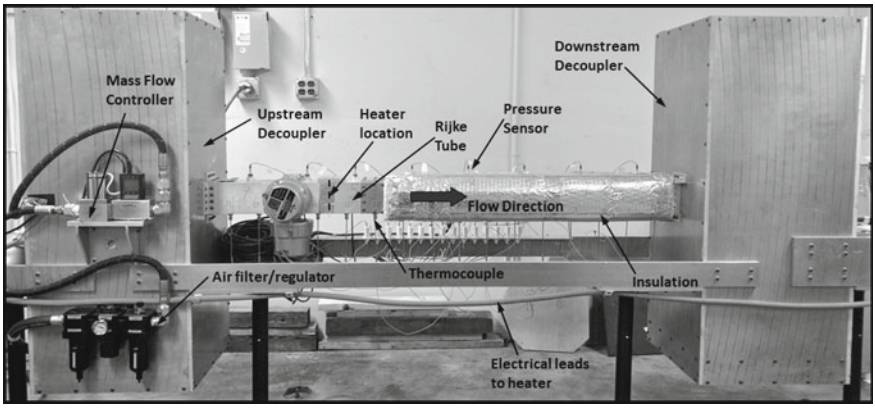

Fig. 14.1 Experimental setup: electrically heated Rijke tube (reproduced with permission from Mondal et al. (2018), Copyright: Taylor and Francis Ltd. https://www.tandfonline.com)

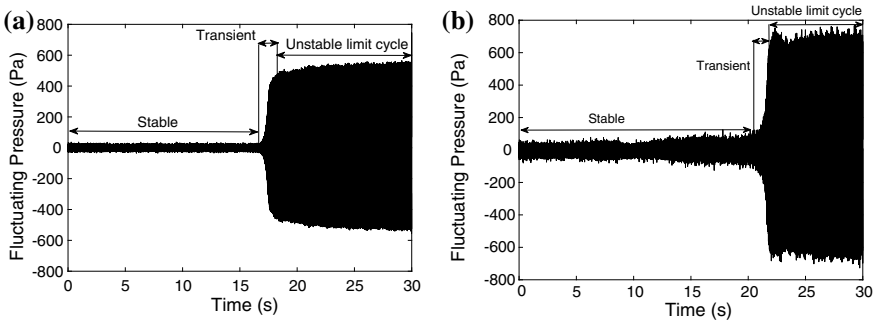

Fig. 14.2 Unsteady pressure signals showing the transience from stable fixed point to limit cycle through bifurcation. **a** E_{in} abruptly increased to 1800 W with $Q = 210$ LPM **b** E_{in} abruptly increased to 2000 W keeping $Q = 250$ LPM. (reproduced with permission from Mondal et al. (2018), Copyright: Taylor and Francis Ltd. https://www.tandfonline.com)

Within the 30 s window as mentioned above, the time series passes from stable to limit cycle regime via a transient regime. A rich source of data from each of the three regimes: stable, transient and limit cycle has been collected in this dataset, that covers a wide range of signal-to-noise ratio (SNR) due to the diferent spatial locations of the sensors used in this experiment. The typical profiles of acoustic signals are shown in Fig. 14.2. In a trial, the setup is preheated to 200 W, and then, abruptly the power input is increased to 1800 W at time ∼17 s keeping the air flow rate constant at 210 LPM. In the trial in Fig. 14.2b, the input power has been abruptly increased at time ∼17 s to 2000 W from the initial 200 W preheated condition with the air flow rate kept constant at 250 LPM. The SNR in the data is also different, as seen in the textures of the time series in Fig. 14.2a in comparison to those in Fig. 14.2b, since the sensors differ in proximity to the heating element inside the tube.

E_{in} (W) / Q (LPM)	61	72	82	92	102	112	122	132	142	152	162	172	182	191	200	210	219	228	237	246	255	264	273	281	290
2000	o	o	o	o	o	o	o	x	x	x	x	x	x	x	x	x	x	x	x	x	o	o	o	o	o
1800	o	o	o	o	o	o	o	x	x	x	x	x	x	x	x	x	x	x	x	o	o	o	o	o	o
1600	o	o	o	o	o	o	o	o	x	x	x	x	x	x	x	x	x	x	o	o	o	o	o	o	o
1400	o	o	o	o	o	o	o	o	x	x	x	x	x	x	x	x	o	o	o	o	o	o	o	o	o
1200	o	o	o	o	o	o	o	o	x	x	x	x	x	x	x	x	o	o	o	o	o	o	o	o	o
1000	o	o	o	o	o	o	o	o	x	x	x	x	x	x	o	o	o	o	o	o	o	o	o	o	o
800	o	x	x	x	x	x	x	x	x	x	o	o	o	o	o	o	o	o	o	o	o	o	o	o	o
600	o	x	x	x	x	x	x	x	o	o	o	o	o	o	o	o	o	o	o	o	o	o	o	o	o
400	o	x	x	x	x	x	o	o	o	o	o	o	o	o	o	o	o	o	o	o	o	o	o	o	o
200	o	o	o	o	o	o	o	o	o	o	o	o	o	o	o	o	o	o	o	o	o	o	o	o	o

Fig. 14.3 Stability map of the system as a function of Q and E_{in}. Emboldened box margins indicate operating conditions for which the pressure signature is depicted in Fig. 14.4 (reproduced with permission from Mondal et al. (2018), Copyright: Taylor and Francis Ltd. https://www.tandfonline.com)

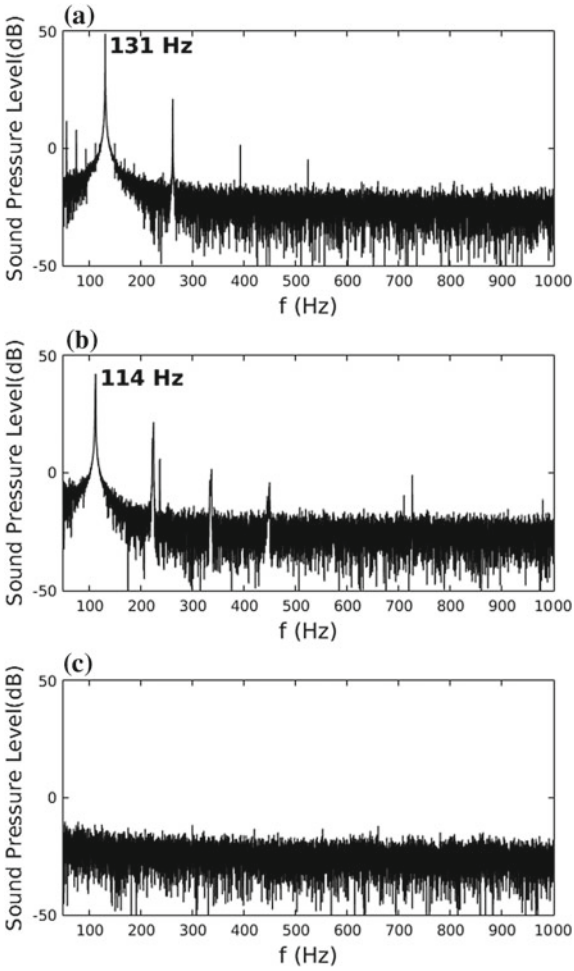

Fig. 14.4 Representative plots of fluctuating pressure amplitudes (left) and their respective power spectral densities (right) at different operating conditions. **a** E_{in}=1400 W, Q=162 LPM. **b** E_{in}=600 W, Q=112 LPM. **c** E_{in}=1400 W, Q=228 LPM. (reproduced with permission from Mondal et al. (2018), Copyright: Taylor and Francis Ltd. https://www.tandfonline.com)

Based on the initial mean temperature of the tube the steady state limit cycle amplitude can vary, since the natural frequency increases with an increase in the velocity of sound. This is depicted in Fig. 14.4. With lower initial mean temperature ∼27 °C, a lower mode of instability was excited, having a frequency ∼114 Hz. This was seen in a range of flow rates marked with '×' in un-shaded boxes in Fig. 14.3. Operating conditions when the higher frequency unstable mode (∼131 Hz) and its harmonics were excited have been indicated by shaded boxes. This corresponds to a higher initial mean temperature of ∼75 °C. The cases for which the system remains stable are marked as '○'.

14.3 Mathematical Background

This section provides the background information on Hidden Markov modeling (HMM) (Rabiner 1989) and symbolic time series analysis (STSA) (Ray 2004; Mukherjee and Ray 2014) for anomaly detection in dynamical systems[1] (Ghalyan et al. 2019).

14.3.1 Hidden Markov Modeling

Hidden Markov models (HMM) is a technique thay has been widely used for representation of long-range temporal dependencies between observations, wherein the underlying models are assumed to be probabilistic functions of the hidden states (Murphy 2012). Considering a discrete-time representation of a sequence $\mathbf{Y} = \{y_1, y_2, \ldots, y_T\}$ of T continuous (i.e., real-valued) observations, and assuming a first-order Markov property (Bishop 2007) over the observations, the joint probability density function of $\mathbf{Y}$ is obtained as:

$$p(\mathbf{Y}) = p(y_1) \prod_{t=1}^{T-1} p(y_{t+1}|y_t) \tag{14.1}$$

Although the above assumption has been widely used in practice, it may not be valid in many applications because of long-range correlations among the observations (Bishop 2007; Murphy 2012).

The HMM belongs to a class of doubly embedded stochastic processes, with a latent stochastic process of *hidden* state evolution. Although this evolution is not directly observed, it can be inferred by observing another stochastic process that produces the sequence of observations (Rabiner and Juang 1993), which captures the long-range dependencies among observations and enables the usage of HMMs as black-box density models on observation sequences. The major difference between the HMM and the standard Markov model is that the HMM does not assume the Markov property (i.e., conditionally dependence on the states and being independent of each other) for the observations themselves. Instead, the hidden state sequence $\mathbf{Z} = \{z_1, z_2, \ldots, z_T\}$ are assumed to follow Markovian dynamics, i.e. given the current state z_t, the future state z_{t+1} is independent of all the states prior to time instant t.

To formalize the mathematical structure, let a string of observations $\{y_1, \ldots., y_T\}$ be assumed to be generated by a hidden state sequence $\{z_1, \ldots., z_T\}$. An HMM is then constructed as a triplet $\lambda = \{A, B, \pi\}$ (Rabiner 1989), where:

[1] An anomaly is a deviation of the behavior of a physical process from its nominal (i.e., healthy) condition; it often evolves as a result of gradual degradation in the system characteristics (e.g., structural durability). Early detection of anomalies is essential for enhancing the system performance as well as for mitigation of potential catastrophic failures.

1. $A \triangleq [a_{ij}]$ is the $K \times K$ state-transition probability matrix:

$$a_{ij} = p(z_{t+1} = q_j | z_t = q_i) : \ q_i, q_j \in Q$$

   where $\sum_j a_{ij} = 1 \ \forall i$.
2. $B \triangleq [b_j(y_t)]$ is the probability density of the observation given the state:

$$b_j(y_t) = p(y_t | z_t = q_j)$$

3. $\pi \triangleq [\pi_i]$ is the probability distribution of the initial state z_1: $\pi_i = p(z_1 = q_i)$, where π is a $1 \times K$ vector with $\sum_i \pi_i = 1$.

Following the above model λ, the corresponding joint probability distribution of states and observations has the form:

$$p(\mathbf{Y}, \mathbf{Z}) = p(z_{1:T}) p(y_{1:T} | z_{1:T}) = \left[p(z_1) \prod_{t=1}^{T-1} p(z_{t+1} | z_t) \right] \left[\prod_{t=1}^{T} p(y_t | z_t) \right] \quad (14.2)$$

Here the HMM is assumed to have a continuous real-valued observation model, where the observations $\{y_1, \ldots, y_T\}$ are one-dimensional and their emission probability follows a Gaussian mixture model:

$$p(y_t | z_t = q_j, \lambda) = \sum_{\ell=1}^{M} c_{j\ell} \, \mathcal{N}(y_t, \mu_{j\ell}, \Sigma_{j\ell}) \quad (14.3)$$

where $\sum_{\ell=1}^{M} c_{j\ell} = 1, \forall j \in \{1, \ldots, K\}$; M is the number of Gaussian mixture components; and $\mathcal{N}(y_t, \mu_{j\ell}, \Sigma_{j\ell})$ represents Gaussian density function of y_t with mean $\mu_{j\ell}$ and covariance $\Sigma_{j\ell}$ associated with state q_j and mixture component ℓ.

Two main model parameters are, therefore, the number of hidden states (K) and the number of mixture components (M), which need to be optimally selected in the context of HMMs (Gilles and Baptiste 2008; Tobias 1995). AIC/BIC based techniques (Akaike 1974; Schwarz 1978) are most commonly used to select the optimal model parameters that maximize the likelihood of the data and minimize the model complexity, thereby balancing the goodness of fit against model complexity to alleviate data overfitting. This paper has adopted the BIC model selection function for choosing the parameters K and M. Thus, the model learning problem is to find the optimal set of parameters for $\lambda = \{A, B, \pi\}$ in order to maximize $P(\mathbf{Y}|\lambda)$. It is achieved through a commonly used iterative procedure called *Baum–Welch Algorithm* which is an application of Expectation-Maximization method for inferring HMM parameters (Rabiner 1989).

Now, given an observation sequence $\mathbf{Y} = \{y_1, y_2, \ldots, y_T\}$ and an HMM model λ, the problem at hand is to find the probability of the entire observation sequence so that it can be associated with the most likely model from a bank of pre-trained HMM models. This is expressed as:

$$p(\mathbf{Y}|\lambda) = \sum_{\mathbf{Z}} p(\mathbf{Y}|\mathbf{Z}, \lambda) p(\mathbf{Z}|\lambda) = \sum_{z_1, z_2, \ldots, z_T} \pi_{z_1} b_{z_1}(y_1) a_{z_1 z_2} b_{z_2}(y_2) \ldots a_{z_{T-1} z_T} b_{z_T}(y_T) \tag{14.4}$$

The calculation of $p(\mathbf{Y}|\lambda)$ according to the direct definition as in Eq. (14.4) has computational complexity in the order of $(2TK^T)$ which may become intractable for even small values of K and T. For numerical efficiency, the well-known *Forward Procedure* is used, which reduces computational complexity to the order of (K^2T). The relevant algorithms are briefly discussed in the following subsections.

14.3.2 The Forward Procedure

The forward variable $\alpha_t(i)$, defined as $\alpha_t(i) \triangleq p(y_1, y_2, \ldots, y_t, z_t = q_i|\lambda)$ is the probability that, provided the model λ is being followed, the partial observation sequence $\{y_1, y_2, \ldots, y_t\}$, $1 \leq t < T$ until time t ends with the state of the system being q_i at time t. This can be solved inductively as follows:

1. Initialization step: $\alpha_1(i) = \pi_i b_i(y_1), \quad 1 \leq i \leq K$ (14.5)

2. Induction step: $\alpha_{t+1}(j) = \left[\sum_{i=1}^{K} \alpha_t(i) a_{ij}\right] b_j(y_{t+1}), 1 \leq t \leq T-1, 1 \leq j \leq K$ (14.6)

3. Termination step: $p(\mathbf{Y}|\lambda) = \sum_{i=1}^{K} \alpha_T(i)$ (14.7)

where the parameters T and K are the same as defined earlier.

14.3.3 The Backward Procedure

The backward variable $\beta_t(i)$, defined as $\beta_t(i) \triangleq p(y_{t+1}, y_{t+2}, \ldots, y_T|z_t = q_i, \lambda)$, is the probability of the partial observation sequence $\{y_{t+1}, y_{t+2}, \ldots, y_T\}$ from t+1 till the end, provided that the state at time t is q_i and the model followed is λ. This can be solved inductively as follows:

1. Initialization step: $\beta_T(i) = 1, \quad 1 \leq i \leq K$ (14.8)

2. Induction step: $\beta_t(i) = \left[\sum_{j=1}^{K} a_{ij} b_j(y_{t+1}) \beta_{t+1}(j)\right], \quad t = T-1, T-2, \ldots, 1, \quad 1 \leq i \leq K$ (14.9)

where the parameters T and K are the same as defined earlier.

14.3.4 Model Learning: Baum–Welch Algorithm

The model learning problem requires the estimation of the model parameters $\lambda = \{A, B, \pi\}$ so as to maximize the likelihood $p(\mathbf{Y}|\lambda)$. Baum–Welch algorithm is a recursive estimation procedure of the HMM parameters. Given the model and the observation sequence, the intermediate variables ξ and γ are defined, for $1 \leq i \leq K$, $1 \leq j \leq K$ and $1 \leq t \leq T$, as:

$$\xi_t(i, j) \triangleq P(z_t = q_i, z_{t+1} = q_j|\mathbf{Y}, \lambda) \tag{14.10}$$

$$\gamma_t(i) \triangleq p(z_t = q_i|\mathbf{Y}, \lambda) \tag{14.11}$$

The variables γ_t and $\xi_t(i, j)$ are expressed in terms of the forward and backward variables α_t and β_t, defined earlier as:

$$\gamma_t(i) = \frac{\alpha_t(i)\beta_t(i)}{p(\mathbf{Y}|\lambda)} = \frac{\alpha_t(i)\beta_t(i)}{\sum_{i=1}^{K} \alpha_t(i)\beta_t(i)}, \quad \xi_t(i, j) = \frac{\alpha_t(i)a_{ij}b_j(y_{t+1})\beta_{t+1}(j)}{\sum_{i=1}^{K}\sum_{j=1}^{K} \alpha_t(i)a_{ij}b_j(y_{t+1})\beta_{t+1}(j)} \tag{14.12}$$

Using the above relations, and the fact that $\gamma_t(i) = \sum_{j=1}^{K} \xi_t(i, j)$, it is possible to estimate $\{A, B, \pi\}$ as:

$$\hat{\pi}_i = \gamma_1(i) \tag{14.13}$$

$$\hat{a}_{ij} = \frac{\sum_{t=1}^{T-1} \xi_t(i, j)}{\sum_{t=1}^{T-1} \gamma_t(i)} \tag{14.14}$$

$$\hat{c}_{jk} = \frac{\sum_{t=1}^{T} \tilde{\gamma}_t(j, k)}{\sum_{t=1}^{T}\sum_{k=1}^{M} \tilde{\gamma}_t(j, k)} \tag{14.15}$$

$$\hat{\mu}_{jk} = \frac{\sum_{t=1}^{T} \tilde{\gamma}_t(j, k).y_t}{\sum_{t=1}^{T} \tilde{\gamma}_t(j, k)} \tag{14.16}$$

$$\hat{\Sigma}_{jk} = \frac{\sum_{t=1}^{T} \tilde{\gamma}_t(j, k).(y_t - \mu_{jk})^2}{\sum_{t=1}^{T} \tilde{\gamma}_t(j, k)} \tag{14.17}$$

where $\tilde{\gamma}_t(j, k)$ is the probability of being in state q_j at time t with the k^{th} mixture component. That is,

$$\tilde{\gamma}_t(j, k) = \left[\frac{\alpha_t(j)\beta_t(j)}{\sum_{j=1}^{N} \alpha_t(j)\beta_t(j)}\right]\left[\frac{c_{jk}\mathcal{N}(y_t, \mu_{jk}, \Sigma_{jk})}{\sum_{k=1}^{M} c_{jk}\mathcal{N}(y_t, \mu_{jk}, \Sigma_{jk})}\right] \tag{14.18}$$

It is noted that the term $\tilde{\gamma}_t(j, k)$ generalizes to $\gamma_t(j)$ in case of a single-component Gaussian density (i.e., $M = 1$) or a (discrete) probability mass function.

The model $\hat{\lambda} = \{\hat{A}, \hat{B}, \hat{\pi}\}$ can be recursively estimated until it converges to a local maxima of the likelihood function $p(\mathbf{Y}|\lambda^*)$, where λ^* is the ML estimate of the HMM. More details on the Baum–Welch algorithm and forward-backward algorithm are available in Rabiner (1989), Hajek (2015).

14.3.5 Symbolic Time Series Analysis

The authors now provide the background for symbolic time-series analysis (STSA) and the construction of probabilistic finite state automata (PFSA) (Ray 2004; Mukherjee and Ray 2014). The time series of the measured signal is partitioned (or quantized) and then symbolized as a symbol string. In this process, the signal space is partitioned into a finite number of cells, where the number of cells is identically equal to the cardinality $|\Sigma|$ of the (symbol) alphabet Σ and a symbol from the alphabet Σ is assigned to each (signal) value corresponding to the cell to which it belongs (Rajagopalan and Ray 2006; Subbu and Ray 2008); details are reported in Mukherjee and Ray (2014). Thus, a symbol is associated with that data point when the value of a data point at a given instant of time is located within a particular cell. The following definitions, which are available in standard literature (e.g., Ray 2004; Mukherjee and Ray 2014), are recalled here for completeness of the chapter.

Definition 14.1 A finite state automaton (FSA) G, having a deterministic algebraic structure, is a triple (Σ, Q, δ) where:

- Σ is a (nonempty) finite alphabet, i.e., its cardinality $|\Sigma|$ is a positive integer.
- Q is a (nonempty) finite set of states, i.e., its cardinality $|Q|$ is a positive integer..
- $\delta : Q \times \Sigma \to Q$ is a state transition map.

Definition 14.2 A symbol block, also called a word, is a finite-length string of symbols belonging to the alphabet Σ, where the length of a word $w \triangleq s_1 s_2 \cdots s_\ell$ with $s_i \in \Sigma$ is $|w| = \ell$, and the length of the empty word ϵ is $|\epsilon| = 0$. The parameters of FSA are extended as:

- The set of all words, constructed from symbols in Σ and including the empty word ϵ, is denoted as $\Sigma^\star$.
- The set of all words, whose suffix (respectively, prefix) is the word w, is denoted as $\Sigma^\star w$ (respectively, $w\Sigma^\star$).
- The set of all words of (finite) length ℓ, where ℓ is a positive integer, is denoted as Σ^ℓ.

Remark 14.1 A symbol string (or word) is generated from a (finite-length) time series by symbolization.

Definition 14.3 A probabilistic finite state automaton (PFSA) K is a pair (G, π), where:

- The deterministic FSA G is called the *underlying FSA* of the PFSA K.

- The probability map $\pi : Q \times \Sigma \rightarrow [0, 1]$ is called the morph function (also known as symbol generation probability function) that satisfies the condition: $\sum_{\sigma \in \Sigma} \pi(q, \sigma) = 1$ for all $q \in Q$.
- The $\big(|Q| \times |\Sigma|\big)$ morph matrix Π, which is converted into the $(|Q||\Sigma| \times 1)$ morph vector ν to serve as an extracted feature in the sequel, is generated by the morph function π.

Equivalently, a PFSA is a quadruple $K = (\Sigma, Q, \delta, \pi)$.

For anomaly detection using STSA, a time series X of sensor data is first converted into a symbol string. Then, PFSAs are constructed from the symbol strings, which in turn generate low-dimensional feature vectors (Bahrampour et al. 2013) that are used for detection of anomalous patterns. The procedure is executed in the following steps.

1. *Select* a block of a time series, called the nominal block, for which the system is in a healthy condition.
2. *Construct* a partition for the nominal block and convert it into a symbol string to construct the nominal PFSA model. The features of PFSA model is computed by frequency counting (Mukherjee and Ray 2014). This yields the nominal feature vectors.
3. *Select* a new block of the time series up to the current time t and convert it into a symbol string. This yields a new PFSA with a new (quasi-)stationary feature vector o matrix of the system at time t.
4. *Compute* the anomaly at time t as the divergence between the nominal feature (F_{nom}) and current feature vectors (F_t):

$$\mu(t) = d(F_{nom}, F_t) \tag{14.19}$$

where $d(\bullet, \bullet)$ is an appropriately chosen distance norm (such as the Kullback–Leibler divergence Murphy 2012).

14.4 PFSA-Based Algorithm for Feature Extraction and Pattern Classification

In this section, the authors initially present a probabilistic finite state automaton (PFSA) approach for online feature extraction from a time-series and the subsequent pattern classification and decision making. In this section, the advantages and disadvantages of PFSA over HMM are also discussed.

14.4.1 Reconstruction of Time-Series from Symbolized Sequence

As mentioned in Sect. 14.3.5 using a PFSA involves symbolizing a segment of the time-series using a partitioning method (such as MEP or Uniform as mentioned in Sect. 14.3.5), and then generating a feature from the generated symbol string, such as the morph matrix. The naive way to generate the PFSA is using a frequency counting technique for computing the occurrence of each state and the state transition. Selecting appropriate partitioning techniques, depths and alphabet sizes greatly controls how well the PFSA captures the essential dynamics and nature of the signals. A good measure of how well the partitioning method is performing is the reconstruction error. As the symbol string is supposed to be a representation of the data, it is important to be able to reconstruct the original time series from the symbol string given the following data:

- The symbol string
- The mean value of the time series corresponding to that state (computed by taking the mean of the actual time-series values that are denoted by that state)

The L_2 (Euclidean) norm difference between the reconstructed time-series and the original time series is used as a measure of the reconstruction; normalizing the time-series makes it easier to compare the norm differences. The normalized reconstruction errors for 3 different partitioning methods, namely uniform, MEP and K-Means are tabulated in Table 14.1, with the lowest error (best reconstruction) values marked in bold font. In this analysis, the data is symbolized in a windowed fashion and the partition boundaries are recomputed for every window after normalization of the data segment. Recomputing the partitions for each segment greatly enhances the accuracy of the PFSA as compared to those methods described in the previous section. This increases computational time but by a negligible amount since the entire formulation is algebraic and computation is very simple.

This analysis has been done over 2 sets of 40 time-series obtained from the in-house Rijke tube experimental setup from 2 different pressure sensor locations, one having high signal-to-noise ratio (SNR) and the other with significantly more noise (i.e. low SNR). These signals are either initially stable and then become unstable or vice-versa. For each, different alphabet sizes ($|\Sigma|$) have been considered for demonstration purposes, while depth (D) has been maintained as $D = 1$ for brevity with only 2 cases having $D = 2, 3$. The reported values are the averaged values across all of the 40 time-series.

The K-means partitioning method proves to be the most accurate across nearly all combinations of alphabet size, depth and sensor. Also, in the given range, increasing alphabet size significantly improves performance as does increasing the depth from 1 to 2. However, increasing either of these too much causes degradation as described in the previous section.

Table 14.1 Reconstruction error for STSA

				Low SNR sensor			High SNR sensor		
$\|\Sigma\|$	D	Sampling frequency (Hz)	Data length	Uniform error ($\times 10^{-3}$)	MEP error ($\times 10^{-3}$)	K-means error ($\times 10^{-3}$)	Uniform error ($\times 10^{-3}$)	MEP error ($\times 10^{-3}$)	K-means error ($\times 10^{-3}$)
2	1	100	82 points	0.1366	0.1439	**0.1358**	0.1564	0.1683	**0.1560**
4	1	100	82 points	0.0667	0.0773	**0.0658**	0.0763	0.0837	**0.0748**
6	1	100	82 points	0.0443	0.0504	**0.0442**	0.0503	0.0574	**0.0499**
2	1	50	164 points	0.1384	0.1404	**0.1374**	0.1580	0.1610	**0.1576**
4	1	50	164 points	0.0687	0.0722	**0.0671**	0.0776	0.0840	**0.0755**
6	1	50	164 points	0.0467	0.0503	**0.0462**	0.0518	0.0572	**0.0510**
6	2	50	164 points	0.0406	0.0427	**0.0400**	0.0436	0.0470	**0.0425**
6	2	100	82 points	**0.0375**	0.0411	0.0381	0.0417	0.0461	**0.0406**

14.4.2 Online Anomaly Detection

In this subsection, 3 methods of online anomaly detection using STSA based methods are described and results presented. These methods are:

- Norm difference method
- Entropy method
- $\times$-entropy method

Norm difference method: Using the generated symbol sequence, PFSAs can be generated for each window. Using the features related to the PFSA, such as the morph matrix, we can try capture the dynamics of the system. Using this feature, classification can be done by first training a morph matrix for the nominal state by taking the mean of all the morph matrices generated from the windows corresponding to the nominal state in the training set (the ground truth). During testing, a distance function checks the distance of the morph matrix generated from the unknown data segment. If the distance is above a threshold, the generated morph matrix is said to be 'too distant' from that corresponding to the nominal state and is said to be in an anomalous state.

Entropy method: In this method, the morph matrix does not need to be computed, instead a frequency counting technique is used to compute the probability of each state, yielding a probability vector p of length equal to that of the number of states $|Q|$. The Shannon entropy of the data is then computed as $H = \Sigma_{i=1}^{|Q|} p(i) \times log(p(i))$. For the purpose of detection and classification we utilize the fact that the stable (nominal) regime is more noisy than the ordered limit cycle type behavior seen in the off-nominal conditions (Nair 2013). Thus, by definition, the entropy should have a higher value during the stable regime and a drop in the same must be an indication of a transition to the anomalous regime (Sarkar et al. 2016).

×-entropy method: Very similar to the above method, the ×-entropy or cross-entropy method uses the probability vectors from not one but 2 synchronous sensors of the same or different type. ×-entropy 'is a measure of the dynamical complexity of the temporal co-dependence from one symbol sequence to another' (Sarkar et al. 2016). As in combustion physics, a slight shift from stable combustion toward thermo-acoustic instability can be captured by an abrupt increase in the computed value of D-Markov entropy rate. The ×-entropy of 2 synchronous signals is computed as $H = \Sigma_{i=1}^{|Q|} p(i) \times log(q(i))$, where q is the probability vector of the states for the second sensor.

The following figures give the ROC curves for various trials using the PFSA norm-difference method. The data used is the same as that used in the previous subsection. Figures 14.5, 14.6 and 14.7 compare different combinations of depths (D), data-window lengths and partitioning methods for the same alphabet size of $|\Sigma| = 6$ which was found to consistently produce better results as seen in Table 14.1. The data was split into a 80:20 train-test split for this analysis.

In Fig. 14.8 the ROC curve for the entropy method is presented for a depth of 2 for various alphabet sizes, while Fig. 14.9 reports the same for the ×-entropy method. The first set of curves uses the other data set used in the previous section consisting of 145 time-series, each starting out stable and then going unstable due to a change in operating characteristics, while the one for the ×-entropy method uses the one with the 40 time-series as this data-set has values from 2 spatially-separated synchronous sensors. The uniform partitioning technique is used. The reason for choosing this is that although it does not have the highest reconstruction accuracy, it falls a very close to the K-means technique and gives better AUC values in the ROC curves as compared to the K-means technique. We do not use the MEP partitioning method,

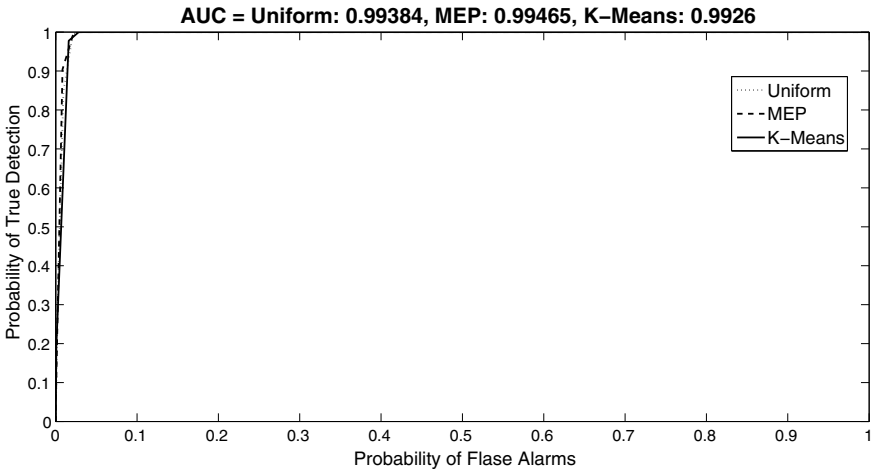

Fig. 14.5 ROC curves for combustion instability detection using PFSA having $|\Sigma| = 6$, $D = 1$, and $L = 50$ comparing various partitioning methods

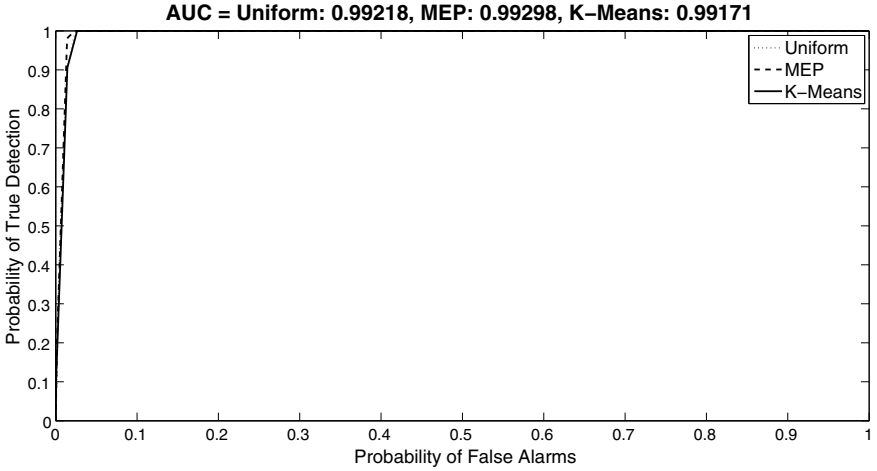

Fig. 14.6 ROC curves for combustion instability detection using PFSA having $|\Sigma| = 6$, $D = 1$, and $L = 100$ comparing various partitioning methods

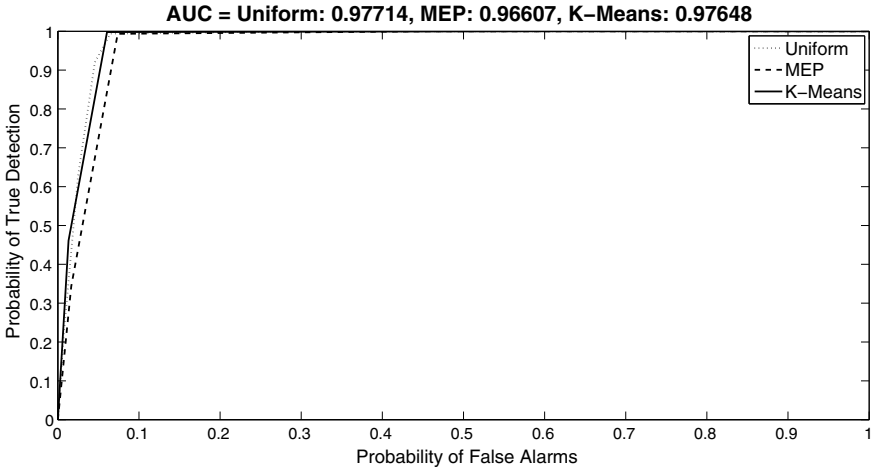

Fig. 14.7 ROC curves for combustion instability detection using PFSA having $|\Sigma| = 6$, $D = 2$, and $L = 50$ comparing various partitioning methods

as by the nature of its construction, the MEP technique yields uniform probability across all classes and the entropy information is lost.

Finally, in Fig. 14.10 a comparison is presented between the ROC curves computed for various window lengths. The depth is taken as 1, with $|\Sigma| = 6$ using the uniform partitioning technique.

PFSA methods are typically faster due to the simplicity and purely algebraic nature of the model. However, HMMs gain popularity when there are multiple regimes

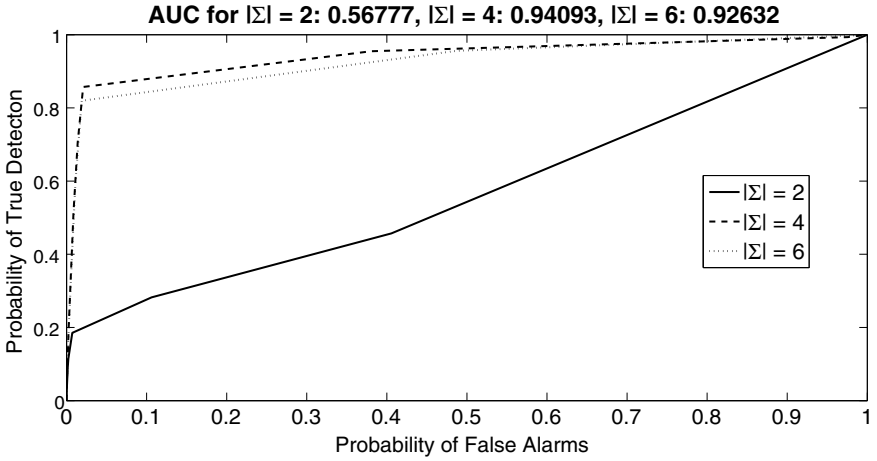

Fig. 14.8 ROC curves for combustion instability detection using Entropy based method having $D = 1$, and using uniform partitioning technique, comparing various alphabet sizes

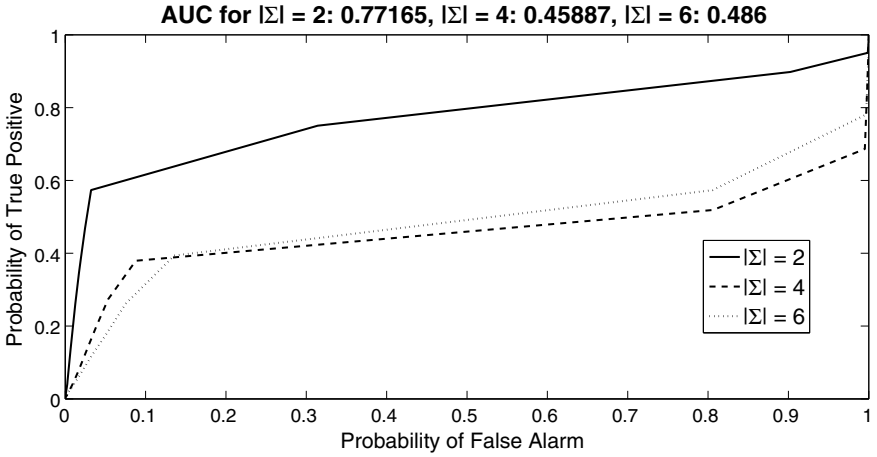

Fig. 14.9 ROC curves for combustion instability detection using $\times$-Entropy based method having $D = 1$, and using uniform partitioning technique, comparing various alphabet sizes

which are very similar to each other. For a binary classification, or for a multi-class classification that are well-separated, a PFSA based classification algorithm might work. For very small data windows, a PFSA is usable only if all the states are reached in the frequency counting, which can only be achieved by having lower alphabet size or depths, but if the dynamics is too complex, low values of $|\Sigma|$ and D might not be sufficient and that's when HMMs may be more useful. Thus HMMs tend to show more versatility.

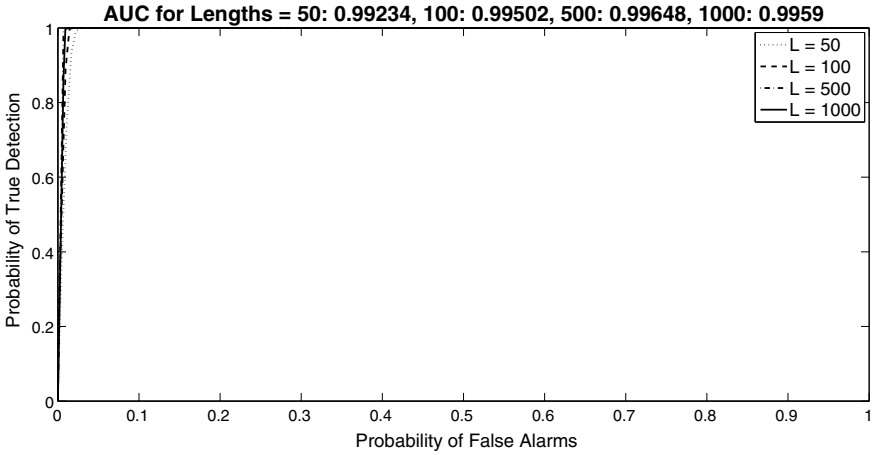

Fig. 14.10 ROC curves for combustion instability detection using PFSA having $|\Sigma| = 6$, $D = 1$, and using uniform partitioning technique, comparing various windows lengths

The subsequent section focuses on the HMM methods as a method with wider applicability, specially when the classification is ternary and the transient regime is to be separately identified and classified.

14.5 HMM-Based Early Detection of Thermoacoustic Instabilities in the Transient Regime

Early detection of instabilities is a problem that is closely related to the development of active control algorithms to augment the existing passive control systems already present in most commercial combustors. Since instabilities develop in the order of milliseconds, automated detection algorithms must be data efficient in order to detect a divergence from the nominal operation within the transient period before the system goes into the limit cycle operating mode. This is because once the limit cycle instabilities set in, the system goes into a self-driven feedback loop after which it might be too late to implement control actions. Hence, the focus in this work would be the detection of TAI with short windows of time series samples. The dataset used for this purpose comprises 145 pressure time series data samples of 30 s duration, each of which starts from a stable operation and ends in a limit cycle instability.

This dataset has been randomly divided into training and test set in the ratio 80:20. The training data provides the prior information for learning 3 HMMs: λ_1, λ_2 and λ_3. This learning phase is offline, and is performed a-priori to the online detection phase. The learnt models are representatives of the different types of data available from the system, albeit they are based on the data that has been procured by prior modeling and/or experiments. The domain knowledge of the presence of stable, transient and

the limit cycle modes of operation in the Rijke tube apparatus allows us to train λ_1 corresponding to the stable regime of operation, λ_2 corresponding to the transient growth regime and λ_3 corresponding to the limit cycle unstable regime. This step accomplishes a generative modeling of the system on the basis of the domain knowledge procured by the experiments. Although the experiments have been performed to encompass a wide range of operating conditions, it is practically unfeasible to perform experiments that cater to all the different conditions of operations that an actual combustor may be subject to. So with a sufficiently dense set of training data procured from different regimes, HMMs can be used to encapsulate the trend in the behavioral characteristics of the system in the different regimes. That is to say that λ_1, for example, serves as a representative model for all different "types" of stable behavior in the system (since the process is stochastic, no two datasets from the same regime are identical). Such a "context-based" learning makes sense in this respect because the pressure signature of the system in the limit cycle mode of operation, for example, is expected to have a deterministic nature, which is characteristically different from the noisy or chaotic nature generally exhibited in the stable regime. Learning ensemble models for each regime ensures that the modeling is robust to issues like variations in operational conditions and differences in sensor noise levels for even a single mode of operation. This indicates that the method is robust to changes in specific nominal conditions, since the learnt models already take into account a wide range of variations of the conditions based on the range of operation of the experiments.

The test data for instability detection purposes is chosen to be curtailed just before the limit cycle instability sets in, and the performance of the classifier for instability detection is based on successful online detection of the onset of the growth phase. With the pre-trained models, given a window of time series data $\{y_1, \ldots, y_T\}$, we calculate the following log-likelihood ratio (LLR):

$$\mathcal{L}_{k,1} = log\left[\frac{(p(y_{1:T})|\lambda_k)}{(p(y_{1:T})|\lambda_1)}\right] = log(p(y_{1:T})|\lambda_k) - log(p(y_{1:T})|\lambda_1) \tag{14.20}$$

where k = 2 or 3; and $(p(y_{1:T})|\lambda_k)$ denotes the probability that the observed pressure time series sequence is generated by model λ_k. This follows from the idea that as the system deviates from a stable operating mode and passes through the bifurcation point towards limit cycle instability, determinism in the form of periodicity sets in the pressure signature, which can be quantified by a greater probability of being generated from either λ_2 or λ_3 rather than λ_1. This is reflected in the log-likelihood ratio as defined in Eq. 14.20 being positive.

We focus on short time-windows of time series data for this analysis, in order to address the issues of real-time detection and control, where early detection of TAI with short data-window could provide appropriate lead-time for the actuators to implement the control action. The process involved in the analysis is described as follows:

1. First an appropriate window-size is chosen. In this work we have mostly focused on window sizes that correspond to a time scale of ∼10–100 ms.
2. Time series data in subsequent batches of the chosen window length is used to calculate $(p(y_{1:T})|\lambda_k)$, for k = 1, 2 and 3.
3. The log-likelihood ratio as defined by Eq. 14.20 is chosen as the norm for detecting instability onset. The ratio is calculated for each batch of data being analyzed and the online condition monitoring is performed based on the evolution of the norm over batches of time series samples.

Figures 14.11, 14.12 and 14.13 elucidate the process of online detection of TAI. Figure 14.11 shows the evolution of $[L_2 - L_1]$ with the analysis being done on batches of a chosen window length of 100 samples. It is clearly seen that there is a sharp rise in the LLR as soon as the instability sets in. The discriminating property of LLR is demonstrated by the fact that the order of magnitude in the change of $[L_2 - L_1]$ is almost 10^4. Thus, LLR is very sensitive to the rate of growth in the time series data. More insights are obtained by analyzing the variation of the three likelihoods with respect to λ_1, λ_2 and λ_3 during Timeframes A and B as shown in Fig. 14.11. Timeframe A spans from around 1400–1600 time samples in Fig. 14.11, which is a sample from the stable phase of the data. This is reflected in Fig. 14.12 by the highest relative likelihood of the data corresponding to λ_1 (indicated by the

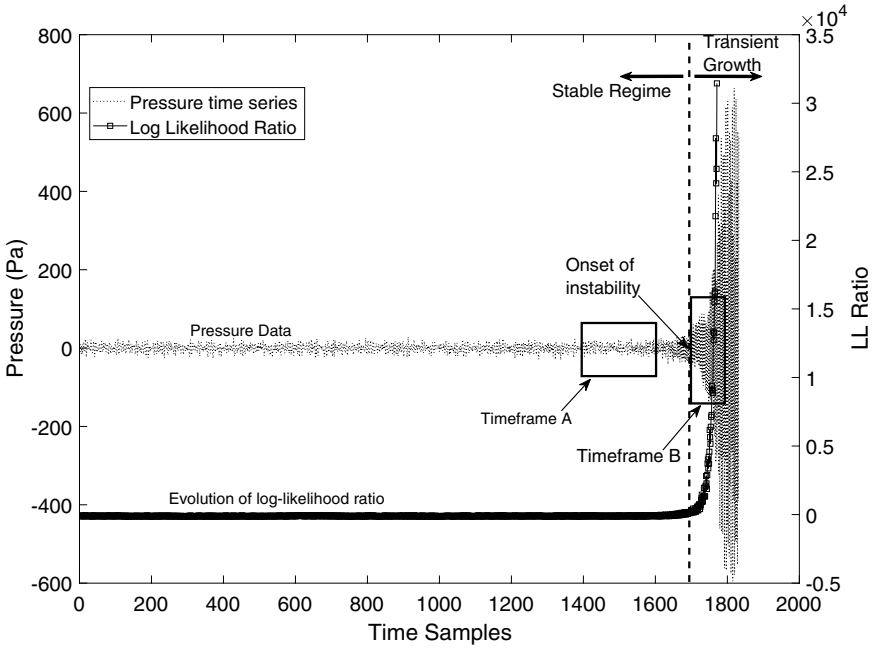

Fig. 14.11 Evolution of $[L_2 - L_1]$ with the pressure time series data (reproduced with permission from Mondal et al. (2018), Copyright: Taylor and Francis Ltd. https://www.tandfonline.com)

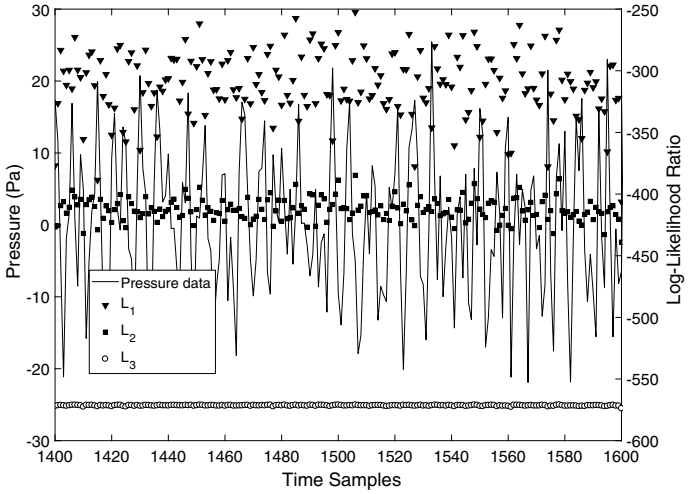

Fig. 14.12 Evolution of L_1, L_2 and L_3 with the pressure samples in Timeframe A of Fig. 14.11 (reproduced with permission from Mondal et al. (2018), Copyright: Taylor and Francis Ltd. https://www.tandfonline.com)

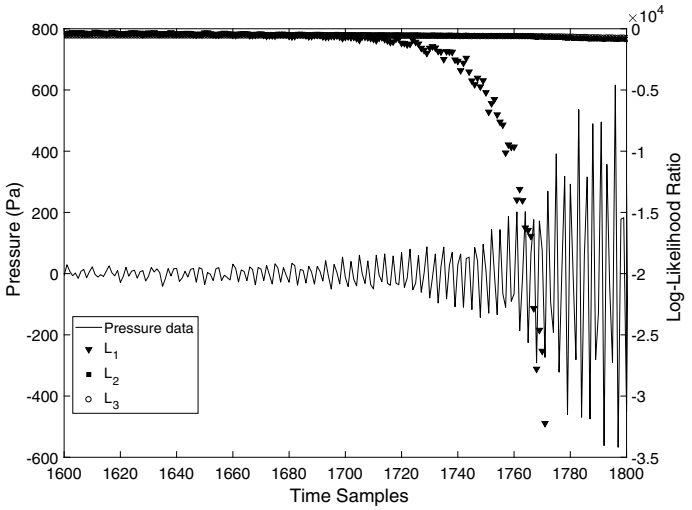

Fig. 14.13 Evolution of L_1, L_2 and L_3 with the pressure samples in Timeframe B of Fig. 14.11 (reproduced with permission from Mondal et al. (2018), Copyright: Taylor and Francis Ltd. https://www.tandfonline.com)

downfacing shaded triangles), as compared with the likelihoods with respect to λ_2 (shaded squares) and λ_3 (circles). The instability sets in around the 1700 s mark, hence Timeframe B spanning from 1600 to 1800 time samples contains the early phase of the transient period. As can be seen in Fig. 14.12, likelihood corresponding to model λ_1 drops sharply during the early transient period, a property that can be utilized for automated condition monitoring of combustion systems for the onset of TAI.

For analyzing the detection accuracy with respect to different window sizes, we look into a Binary Hypothesis testing problem where our proposed framework classifies each pressure time series window into either *stable* (Class A) or *unstable* (Class B) based on the likelihood-ratio test:

$$log\left[\frac{(p(y_{1:T})|\lambda_{k=2\ or\ 3})}{(p(y_{1:T})|\lambda_1)}\right] \underset{\alpha}{\overset{\beta}{\gtrless}} \tau \tag{14.21}$$

where τ is a threshold (Poor 2013). A commonly used criterion to choose an appropriate threshold τ is by using the Receiver Operating Characteristic (ROC) curve. The ROC curve is obtained by varying τ which provides a trade-off between the probability of successful detection $\left(p_D \triangleq p[Decided\ Class = \beta | True\ Class = \beta]\right)$ and the probability of false alarms $\left(p_F \triangleq p[Decided\ Class = \beta | True\ Class = \alpha]\right)$.

Figure 14.14 reports a family of ROC curves for the proposed detection algorithm considering different window sizes of data. $log\left[\frac{(p(y_{1:T})|\lambda_2)}{(p(y_{1:T})|\lambda_1)}\right]$ is chosen as the likelihood ratio. Various window sizes, namely, 50, 100, 500 and 1000 were chosen for this demonstration. These correspond to time scales in the order of milliseconds for the sampling frequency of 8192 Hz. Comparing the area under the ROC curve (AUC) for each classifier (Fawcett 2006) is a commonly used method for comparing the performance of different classifiers. A higher AUC generally implies a better overall performance of a classifier. In Fig. 14.14, it is seen that the AUC increases from 0.9541 to 0.9864 as the window size is increased from 50 to 1000, with progressively higher detection rates at specified false alarm rates. This is due to the fact that the classifier is typically expected to perform better when classifying larger lengths of observation sequences. The high classification accuracy even with about 6–60 ms of data showcases a prospective application of the HMM based algorithm for detecting instabilities in the early transient phase.

The information abtained from the ROC curves (Fig. 14.14) can be used as a basis for the choice of a particular threshold τ corresponding to the trade-off between the detection rate demanded by the user and the allowable false alarm in detection. This can be utilized for regime detection, where the classifier has to decide which of the three pre-trained regimes a given short data history belongs to. We present the regime detection accuracies in Table 14.2, where the threshold τ has been chosen using a ROC of a classifier with $[L_3 - L_1]$ as the log-likelihood ratio, with window size = 100. τ has been chosen to correspond to about 92% detection rate with 10% allowable false alarm from the ROC curve. The problem of regime detection is particularly challenging in this respect because, with a very short history of data,

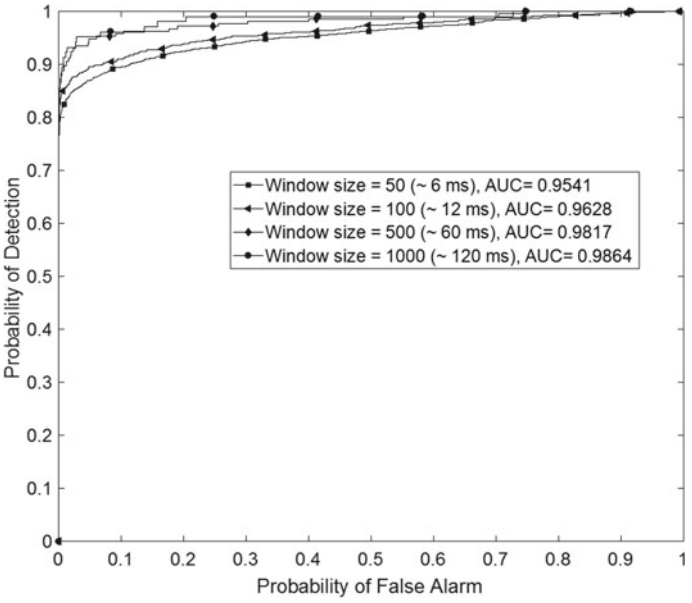

Fig. 14.14 ROC curves for different window-sizes (reproduced with permission from Mondal et al. (2018), Copyright: Taylor and Francis Ltd. https://www.tandfonline.com)

Table 14.2 Classification accuracy of the three regimes (reproduced with permission from Mondal et al. (2018), Copyright: Taylor and Francis Ltd. https://www.tandfonline.com)

Stable regime	Transient regime	Limit cycle regime
90%	91%	100%

amplitude-based thresholding or frequency-based detection of instabilities might be inefficient.

This HMM-based algorithm can be naturally extended into problems like growth-rate estimation from acoustic time series data in unstable systems. From an experimental point of view, it is difficult to extract growth rate from dynamic data, as discussed in the work by Moeck et al. (2007). An unstable combustion system generally exhibits a sudden jump from a stable operation regime to a limit cycle mode through a bifurcation. This poses a serious challenges for data-driven growth rate extraction techniques used for detection of the growing trend in the data in that short period. Recently, Rigas et al. (2016, 2017) and Jamieson et al. (2017) have reported growth and decay rate measurements using transient acoustic time series data from an electrically heated Rijke tube, in a setup similar to the one used in our current work. In their method the linear growth and decay regions are extracted from the Hilbert envelope of the time series signal and measurement of the growth rate by a linear fit in the identified region. A comparison of the HMM-based algorithm with

Table 14.3 Time complexity of LLR calculation in the online phase (reproduced with permission from Mondal et al. (2018), Copyright: Taylor and Francis Ltd. https://www.tandfonline.com)

Number of samples ($F_s = 8192$ Hz)	50	100	500	1000
Data length (ms)	6	12	60	120
Processing time (ms)	4	6	12	23

Hilbert envelope-based growth rate extraction can be found in Mondal et al. (2018), whereby it has been shown that the LLR-based growth rate estimation is significantly efficient in terms of computational expense and data requirements.

From the application point of view, LLR-based regime detection is more versatile as compared to the other data-driven methods reported in literature for prediction of instabilities, e.g. Hurst exponent based characterization by Nair and Sujith (2014), minimum permutation entropy based analysis by Gotoda et al. (2012) and $\times D$-Markov entropy rate based thresholding by Sarkar et al. (2016). A comparison of time complexities of the different data-driven methods can be found in Mondal et al. (2018). In particular, a comparison with Hurst exponents as shown in Mondal et al. (2018) indicated that the computational time for LLR is comparable to the former when the data length is low. But, Hurst exponents are typically used for characterizing instability using stationary datasets, which might require more data to be statistically significant for computing the different Hurst exponents. One major difference in the method proposed in this chapter is that the HMM-based technique can be efficiently applied for transient regimes of operations, whereas most of the other methods have stationarity assumptions in their applicability. Table 14.3 enlists the processing times of LLR calculation for the different data lengths analyzed in this work, which shows the computational efficiency of this method, making it potentially suitable for regime detection and instability classification.

14.6 Summary, Conclusions, and Future Research

This chapter has developed and validated a statistical modeling tool for early detection of anomalous behavior leading to thermoacoustic instabilities (TAI) in combustion systems. The underlying algorithms are built upon the concepts of symbolic time series analysis (STSA) and hidden Markov modeling (HMM) to represent the typical behavior of combustion systems at different operational regimes (e.g., steady-state, transient, and unstable). The focus of the proposed method is primarily on real-time applications using short windows of pressure oscillations measurements; without compromising the accuracy of TAI prediction and identification of the associated operational regimes. The proposed method has been validated on experimental data from an electrically heated Rijke tube apparatus for predicting the onset of thermoacoustic instabilities.

If the detection of the transient regime is of interest (as it is in this chapter), then the HMM approach is preferable. On the other hand, if the major objective is to detect an anomalous operation, then the STSA-based method is recommended. Anomaly detection and regime identification are two important problems that need to be addressed in any online monitoring and control system for mitigating TAI. Since the training period of the STSA-based models are significantly cheaper than that of HMM, they can be used efficiently for detecting anomalies in the system in near real-time. The detected anomalous regimes can then be used as baselines for learning different regime-specific HMMs in a slower time-scale. Since the testing period of HMM is very fast, it can then be used online for regime classification, and the information can be useful for implementation of the required control actions. Moreover, it is worth noting that although the HMM-based detection algorithm has been applied to Rijke tube acoustic instability data, the concept is equally applicable for more complex combustion systems characteristic of turbulent combustors. Since LLR is very sensitive to small variations in texture of the data, intermittent burst to instabilities can be detected online, as they are expected to indicate a sharp drop in the corresponding likelihood to a stable model with respect to an unstable model as soon as the intermittency crops in. Although there are several areas of theoretical and experimental research that can enhance and further the work reported in this chapter, the authors suggest the following topics for future research:

1. Addressing other modes of instabilities (e.g., lean blowouts) and development of a unified detection framework
2. Extension of the proposed methods for detection of instabilities in combustion systems operating under different kinds of protocols.
3. Implementation of the proposed methods for (closed-loop) active control of the laboratory-scale apparatus with actuators for controlling instabilities.
4. Extension of the probabilistic approach in the reported work to state estimation for forecasting of future states to predict the temporal behavior.
5. Enhancement of computational efficiency of the proposed methods by using inference-based learning of the probabilistic models.

References

Akaike H (1974) A new look at the statistical model identification. IEEE Trans Autom Control 19(6):716–723

Bahrampour S, Ray A, Sarkar S, Damarla T, Nasrabadi N (2013) Performance comparison of feature extraction algorithms for target detection and classification. Pattern Recognit Lett 34:2126–2134

Bishop C (2007) Pattern recognition and machine learning. Springer, Berlin

Celeux G, Durand J-B (2008) Selecting hidden Markov model state number with cross-validated likelihood. Comput Stat 23(4):541–564

Chakraborty S, Gupta S, Ray A, Mukhopadhyay A (2008) Data-driven fault detection and estimation in thermal pulse combustors. Proc Inst Mech Eng Part G: J Aerosp Eng 222(8):1097–1108

Fawcett T (2006) An introduction to roc analysis. Pattern Recognit Lett 27(8):861–874. ROC Analysis in Pattern Recognition

Ghalyan NF, Mondal S, Miller DJ, Ray A (2019) Hidden Markov modeling-based decision-making using short-length sensor time series. ASME J Dyn Sys Meas Control 141(10):104502–104502–6
Gopalakrishnan EA, Sharma Y, John T, Dutta PS, Sujith RI (2016) Early warning signals for critical transitions in a thermoacoustic system. Sci Rep 6
Gopalakrishnan EA, Sujith RI (2014) Influence of system parameters on the hysteresis characteristics of a horizontal Rijke tube. Int J Spray Combust Dyn 6(3):293–316
Gotoda H, Amano M, Miyano T, Ikawa T, Maki K, Tachibana S (2012) Characterization of complexities in combustion instability in a lean premixed gas-turbine model combustor. Chaos: Interdiscip J Nonlinear Sci 22(4):043128
Hajek B (2015) Random processes for engineers. Cambridge University Press, Cambridge, UK
Hauser M, Li Y, Li J, Ray A (2016) Real-time combustion state identification via image processing: a dynamic data-driven approach. In 2016 American control conference (ACC), pp 3316–3321
Jamieson NP, Rigas G, Juniper MP (2017) Experimental sensitivity analysis via a secondary heat source in an oscillating thermoacoustic system. Int J Spray Combust Dyn 9(4):230–240
Jazwinski AH (1970) Stochastic processes and filtering theory. Academic Press, New York, USA
Kobayashi T, Murayama S, Hachijo T, Gotoda H (2019) Early detection of thermoacoustic combustion instability using a methodology combining complex networks and machine learning. Phys Rev Appl 11:064034
Kwakernaak H, Sivan R (1972) Linear optimal control. Wiley Interscience, New York, USA
Lieuwen TC, Yang V (2005) Combustion instabilities in gas turbine engines: operational experience, fundamental mechanisms, and modeling, chapter 1, pp 3–26. American Institute of Aeronautics and Astronautics
Matveev K (2003) Thermoacoustic instabilities in the Rijke tube: experiments and modeling. PhD thesis, California Institute of Technology
Moeck J, Bothien M, Paschereit C, Gelbert G, King R (2007) Two-parameter extremum seeking for control of thermoacoustic instabilities and characterization of linear growth. In Aerospace sciences meetings. American Institute of Aeronautics and Astronautics
Mondal S, Ghalyan NF, Ray A, Mukhopadhyay A (2018) Early detection of thermoacoustic instabilities using hidden markov models. Combust Sci Technol 1–28
Mukherjee K, Ray A (2014) State splitting and merging in probabilistic finite state automata for signal representation and analysis. Signal Process 104:105–119
Murphy K (2012) Machine learning: a probabilistic perspective, 1st edn. The MIT Press
Nair V, Sujith RI (2014) Multifractality in combustion noise: predicting an impending combustion instability. J Fluid Mech 747:635–655
Nair V, Thampi G, Karuppusamy S, Gopalan S, Sujith RI (2013) Loss of chaos in combustion noise as a precursor of impending combustion instability. Int J Spray Combust Dyn 5(4):273–290, 2013
Noiray N, Denisov A (2017) A method to identify thermoacoustic growth rates in combustion chambers from dynamic pressure time series. Proc Combust Inst 36(3):3843–3850
Poor HV (2013). An introduction to signal detection and estimation. Springer Science & Business Media
Rabiner LR (Feb 1989) A tutorial on hidden markov models and selected applications in speech recognition. Proc IEEE 77(2):257–286
Rabiner LR, Juang B-H (1993) Fundamentals of speech recognition. Prentice-Hall Inc, Upper Saddle River, NJ, USA
Rajagopalan V, Ray A (2006) Symbolic time series analysis via wavelet-based partitioning. Signal Process 86(11):3309–3320
Ray A (2004) Symbolic dynamic analysis of complex systems for anomaly detection. Signal Process 84(7):1115–1130
Rigas G, Jamieson NP, Li LKB, Juniper MP (2016) Experimental sensitivity analysis and control of thermoacoustic systems. J Fluid Mech 787
Rydén Tobias (Jan 1995) Estimating the order of hidden Markov models. Statistics 26(4):345–354
Sarkar S, Chakravarthy SR, Ramanan V, Ray A (2016) Dynamic data-driven prediction of instability in a swirl-stabilized combustor. Int J Spray Combust Dyn 8(4):235–253

Sarkar S, Lore KG, Sarkar S, Ramanan V, Chakravarthy SR, Phoha S (2015) Early detection of combustion instability from hi-speed flame images via deep learning and symbolic time series analysis. In Annual conference of the prognostics and health management society

Schwarz G (1978) Estimating the dimension of a model. Ann Stat 6(2):461–464, 03

Sen U, Gangopadhyay T, Bhattacharya C, Misra Sengupta A, Karmakar S, Mukhopadhyay A, Sen S (2016) Investigation of ducted inverse nonpremixed flame using dynamic systems approach. In ASME Turbo Expo 2016: turbomachinery technical conference and exposition, vol 4B

Subbu A, Ray A (2008) Space partitioning via Hilbert transform for symbolic time series analysis. Appl Phys Lett 92(8):084107

Part V
Dynamics and Control of Microscale Flows

Chapter 15
Dynamic Instabilities and Their Control in Flow Boiling in Microchannels

Raghvendra Gupta and Deepak Kumar Mishra

Abstract The progress in manufacturing techniques in last few decades has accelerated the application of micro-structured devices in a range of industrial sectors such as healthcare, pharmaceuticals, electronics, environment, chemical processing and energy. Many of these applications stem from the advantages of high surface area to volume ratio, small diffusion paths and ability to operate safely at high temperatures and pressures in micro-devices. The applications of these devices in the energy sector often involve convective heat transfer, condensation, evaporation and boiling in microchannels. Extensive experimental studies on flow boiling in microchannels in the last twenty five years suggest the boiling at the microscale to be significantly different from that in the large channels and the critical heat flux above which the boiling heat transfer becomes ineffective and catastrophic is scale-dependent. The studies also indicate that several dynamic instabilities occur during two-phase boiling in microchannels and these can be different from those that occur in large channels. Therefore, it is imperative to understand the mechanisms of boiling stabilities in microchannels and develop techniques to control them to design efficient and safe micro-structured devices. The boiling instabilities in microchannels can be categorized in two groups- one, those caused by interaction between upstream compressibility and bubble generation and second, those caused by parallel channel instability. This chapter reviews the current status of the understanding of these instabilities and the techniques to avoid or minimize them.

Keywords Microchannel · Boiling · Instability

15.1 Introduction

In recent years, there has been a growing trend towards developing miniature devices such as micro-electro-mechanical systems (MEMS), lab-on-a-chip devices, micro heat exchangers and chemical micro-processing systems for applications in a range of

R. Gupta (✉) · D. K. Mishra
Indian Institute of Technology Guwahati, Guwahati 781039, Assam, India
e-mail: guptar@iitg.ac.in

A. Mukhopadhyay et al. (eds.), *Dynamics and Control of Energy Systems*,
Energy, Environment, and Sustainability,
https://doi.org/10.1007/978-981-15-0536-2_15

industries. In the energy sector, perhaps the most important contribution of the miniaturized systems has been in the development of microchannel-based heat exchanging systems.

In the electronics industry, the number of transistors per square inch has been doubling every 12–18 months for past few decades, as observed by Gordon Moore, co-founder of Intel (Moore 1965). With an increase in the number of transistors per square inch, the requirement of the heat removal rate also increases accordingly. With air-based cooling, heat fluxes up to 1 MW/m^2 can be removed (Tullius et al. 2011). For the removal of higher heat fluxes, liquid (Tuckerman and Pease 1981) or gas-liquid (Bar-Cohen 1995) based cooling systems has been employed. Therefore, the semiconductor industry has been one of the major drivers of the research and development in the area of heat transfer in micro-structured systems.

One of the major requirements in the aerospace industry is the development of compact systems which can deliver maximum performance per unit mass. Therefore, the micro heat exchangers are best suited for applications in aircrafts and space vehicles. The offshore industry also has a similar requirement of compact heat exchangers. One such example of compact heat exchangers is the printed circuit heat exchanger (PCHE) of Heatric division of Megitt Aerospace which has been deployed in the offshore, onshore and floating applications in the oil and gas industry for past 30 years.

The rate of heat transfer is directly proportional to the surface area. A reduction in the channel dimension results in an increase in surface area to volume ratio. As a result, the microchannel-based systems can provide large surface area per unit volume when compared with conventional heat exchangers. Scale up of such system can be achieved by 'numbering-up' the microchannels. For example, numbering up in PCHEs is achieved by etching a number of microchannels on metallic plates. A number of plates are then diffusion-bonded together to make the compact heat exchangers. A reduction in the channel dimension results in smaller heat diffusion length scale (of the order of channel radius, R) and consequently, the transverse temperature gradients $\left(\frac{\partial T}{\partial r}\right)$ are large. Moreover, the microchannel systems are safer to operate than the conventional systems. As a result, they are considered to be the best-suited to perform exothermic reactions. Microchannels often have square, rectangular, semi-circular and triangular cross-sections which is rarely the case in large diameter channels.

The channel dimension in such systems is often of the order of few hundred microns to few millimeters. The expressions and correlations developed for single-phase flow in conventional systems can be used for these small diameter channels also with a careful consideration of the effect of surface roughness. However, such is not the case for adiabatic two-phase flow or boiling.

In gas-liquid or liquid-liquid systems, the interfacial area density or interfacial area per unit volume also becomes large in microchannels. As a result, the rates of interfacial heat and mass transfer are enhanced in microchannels. With a decrease in channel size, the relative importance of surface tension, which is a surface force, increases when compared with the body forces such as gravity. As the velocity and

length scales are small, the flow is generally laminar in microchannels over a large range of gas and liquid flow rates. As a result, the flow regimes during adiabatic two-phase flow and boiling in microchannels are significantly different than those occur in conventional large channel systems.

Flow boiling is susceptible to thermal and hydrodynamic instabilities which may cause oscillations in flow rate, pressure and temperature of constant and increasing amplitudes (Boure et al. 1973). These oscillations are generally undesirable as they disturb the control systems, may result in boiling crisis or can even cause mechanical damage. It is therefore imperative to develop a comprehensive understanding of the origin of flow boiling instability in microchannels and the measures that can mitigate or eliminate the instabilities.

In this chapter, the instabilities that occur during flow boiling in microchannels and the measures that can be taken to tackle them are discussed.

15.2 Fundamentals

Boiling refers to the change of liquid phase to the gas phase caused by heat transfer. This occurs when the liquid temperature exceeds the saturation temperature (or boiling point) at the system pressure.

Various physical effects such as surface tension, change in momentum during evaporation, viscous and inertial effects are important during flow boiling. To compare the relative effect of different physical phenomena, several non-dimensional parameters are defined and are relevant to flow boiling in microchannels.

1. **Bond or Eötvös number**: Bond or Eötvös number is defined as the ratio of buoyancy force to surface tension force.

$$Bo = \frac{(\rho_l - \rho_v) g L^2}{\sigma}$$

   where ρ_l and ρ_v are densities of liquid and gas phases, respectively, g is the acceleration due to gravity, L is the characteristic length and σ is the surface tension. The value of Bond number decreases with a decrease in the channel size. For a channel of size 1 mm, the value of Bond number is about 0.14 for two-phase flow of water i.e. for a millimeter-size channel, the buoyancy and surface tension forces are comparable and surface forces start dominating as the channel size is further reduced.
2. **Weber number**: Weber number is the ratio of inertial and surface tension forces. Baldassari et al. (2013) suggested that the difference between the average liquid velocity and vapour velocity should be used as the velocity scale.

$$We = \frac{\rho_l (u_l - u_v)^2 L}{\sigma}$$

3. **Reynolds number**: Reynolds number is the ratio of inertial and viscous forces.

$$Re = \frac{GL}{\mu_l}$$

where G is the mass flow rate and μ_l is the dynamic viscosity of the liquid. For two-phase flow systems, different Reynolds numbers can be defined.
$Re_L = \frac{G(1-x)L}{\mu_l}$ for the liquid flow only
$Re_G = \frac{GxL}{\mu_l}$ for the vapour flow only
$Re_{TP} = \frac{Gd}{\mu_{tp}}$ where μ_{tp} is the weighted average of the liquid and vapour phase viscosities and x is the vapour quality.

4. **Capillary number**: Capillary number is the ratio of viscous and surface tension forces.

$$Ca = \frac{\mu_l U}{\sigma}$$

5. **Boiling number**: Boiling number represents the ratio of evaporation mass flux to the total mass flux.

$$Bl = \frac{q''/h_{lv}}{G}$$

where q'' is the wall heat flux and h_{lv} is the latent heat of vaporization.

6. **Jakob number**: Jakob number is the ratio of sensible heat to the latent heat absorbed/released during liquid-vapour phase change.

$$Ja = \frac{c_p(T_s - T_{Sat})}{h_{lv}}$$

Based on the occurrence of external flow, boiling can be characterized in two categories- pool and convective. Pool boiling refers to the boiling caused by natural convection only e.g. boiling of liquid in an electric kettle. Convective boiling refers to the boiling over a surface during fluid flow caused by the external flow e.g. boiler tubes in power plants.

The process of phase change in a liquid pool begins with the formation of vapour embryo and is named as nucleation. Nucleation can be of two types: homogeneous and heterogeneous. Homogeneous nucleation refers to the formation of the vapour embryo in the superheated liquid pool. Solid surfaces or surfaces of the foreign bodies present in the liquid pool has a number of small cavities which can act as nuclei for vapour formation. This is known as heterogeneous nucleation.

Figure 15.1 shows a typical pool boiling curve. When the temperature of the bulk liquid is less than the boiling point, the phenomenon is known as subcooled boiling whereas saturated boiling occurs when the bulk liquid temperature is equal to the boiling point.

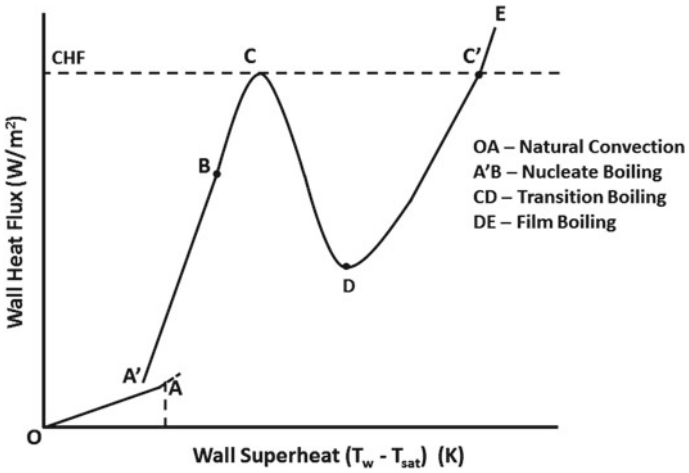

Fig. 15.1 Pool boiling curve (adapted from Collier and Thome 1996)

When the water in a pan is heated, temperature gradients are set up in the liquid pool and natural convection currents are set up causing the movement of hot liquid from the bottom to top and that of the relatively colder liquid from top to bottom. The hot liquid moving to the interface may evaporate depending upon its degree of superheat.

When the wall superheat is sufficient to cause vapour nucleation at the heated surface, the onset of nucleate boiling (ONB) is said to occur. In some cases, the ONB may occur when the liquid superheat is more than that required to support fully-developed nucleate boiling. One such example is water boiling at sub-atmospheric pressure. This results in a sharp drop in the temperature of the surface.

During the nucleate boiling, vapour bubbles start forming at the nucleation sites. The number of nucleation sites grow with an increase in the wall heat flux. As the wall heat flux increases further, bubbles coalesce and vapour patches are formed at the surface. Finally, when the wall heat flux becomes equal to the critical heat flux (CHF), the solid surface is completely covered with the vapour blanket. The vapour blanket acts as an insulator and the heat flux decreases in the transition boiling regime (region CD). In the film boiling region (DE), a stable and continuous vapour film covers the solid surface completely.

The convection or flow boiling is generally described by an example of flow in a vertical, uniformly heated tube at low wall heat flux having upward flow as shown in Fig. 15.2. As the subcooled liquid moves along the tube, its temperature increases. The wall temperature would be higher than the fluid temperature. When the wall temperature is sufficiently high to sustain nucleation at the wall, bubbles start to nucleate on the channel wall though the bulk (or mixing cup) temperature of the fluid is less than the saturation temperature. This is known as subcooled nucleated boiling.

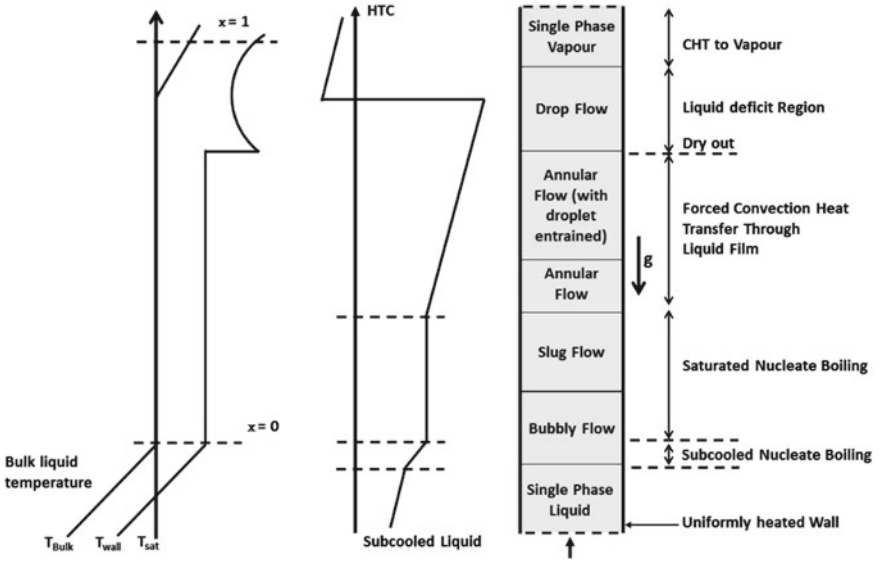

Fig. 15.2 Convective heat transfer in a vertically upward flow (adapted from Collier and Thome 1996)

The subcooled boiling region transitions to saturated nucleate boiling when the fluid bulk temperature becomes equal to the saturation temperature. Moving downstream in the saturated nucleate boiling region, a transition occurs in the heat transfer mechanism and the flow regime transitions to annular from bubbly/slug flow.

In the annular flow region, the heat is transferred from the wall in the liquid film by forced convection and evaporation occurs at the vapour-liquid interface. Thus, the heat transfer mechanism transitions from nucleate boiling to evaporation in the film region. The thickness of the liquid film decreases continuously along the downstream direction. Liquid dryout occurs on the wall when the film on the wall is completely evaporated. This results in sudden rise in wall temperature.

A typical variation of heat transfer coefficient at low wall heat flux is also shown in the figure. A rise in the wall heat flux would result in initiation of subcooled boiling at a shorter distance from the inlet, higher heat transfer coefficient in the nucleate boiling region and dryout on the wall at a lower quality. However, the heat transfer coefficient in the film evaporation region remains unchanged with an increase in wall heat flux.

At further high values of heat fluxes, the dryout may occur during the nucleate boiling well before the film evaporation could be initiated. This is similar to the phenomena that occurs in pool boiling when critical heat flux is reached and is named as departure from nucleate boiling (DNB). This results in transition to film boiling. For further details on the effect of heat flux, the readers are advised to refer to Chap. 4 of Collier and Thome (1996).

15.3 Boiling in Microchannels

The correlations developed for conventional large size channels have been found not to be able to predict the boiling heat transfer in microchannels. This can be attributed to several characteristic differences between the two cases. For example, the flow is often turbulent in conventional channels but laminar in microchannels. In the microchannels, the bubble nucleated on the wall are confined and can grow only in the axial direction.

Many advantages of the micro-structured devices stem from the high surface area to volume ratio when compared with the conventional channels. In the context of heat transfer, high surface area to volume ratio implies the availability of more heat transfer area per unit volume making the heat exchanging device compact. Another effect of high surface area to volume ratio is the dominance of surface forces such as surface tension in comparison with the body forces such as gravity and inertia. Flow boiling in capillary tubes is important in the applications which require small size and small weight for example electronics cooling, automotive air-conditioning, thermal management and fuel supply systems in aircrafts and spacecrafts.

The walls of microchannels are generally smooth when compared with the larger channels. Therefore, a high wall superheat is required to initiate nucleation in microchannels. In case of ultra-smooth microchannels, the onset of boiling might be a result of homogeneous nucleation.

During the convective flow boiling in large-size channels, nucleate boiling dominant regime is observed at low quality whereas the annular flow evaporation is dominant at moderate to high qualities. During nucleate boiling, heat flux is proportional to $q^{0.7}$ and independent of vapour quality. In the conventional channels, the flow accelerates rapidly resulting in considerable pressure drop in the channel. Pressure drop, mechanism of nucleation and bubble growth and evaporation in the annular flow regime are all affected by the reduction in channel size.

From the experimental investigations on flow boiling in microchannels, two contrasting results have emerged. In one case, annular flow in which film evaporation is the boiling mechanism and the boiling is relatively steady is assumed to be the dominant mechanism. While several other researchers observed oscillations in the flow boiling which is often associated with nucleate boiling.

Agostini and Thome (2005) reviewed the experimental studies on boiling in microchannels. Several studies found the heat transfer coefficient to be dependent on heat flux and independent of or weakly dependent on the mass flux. Therefore, researchers believed nucleate boiling to be the dominant mechanism in flow boiling (Bao et al. 2000; Bertsch et al. 2008). However, it has been shown (Jacobi et al. 2002) that such heat transfer dependence can also occur during bubble train flow. So, there is no clear agreement between the researchers on the mechanism of flow boiling in microchannels.

15.4 Boiling Instabilities

Any system is considered to be stable if the system returns back to its original state when subjected to small disturbances or perturbations. The perturbations during the boiling can be caused by a number of factors such as nucleation, bubble generation or turbulence. The flow instabilities in the boiling systems is often classified in two categories: static and dynamic (Boure 1973; Das and Das 2016). Static instability occurs when the original steady state of the system shifts to a new steady state or shows periodic behaviour when subjected to a small disturbance i.e. the system moves to a different equilibrium state. The examples of static instabilities are Ledinegg or flow excursion instability, flow pattern transition, chugging or geysering whereas dynamic instabilities include acoustic and density wave oscillations, thermal oscillations, parallel channel instabilities etc. Boure (1973) suggest that inertia and other feedback effects such as between inertia and compressibility or those between pressure drop, flow rate and density change caused by evaporation (Kakac and Bon 2008) play an important role in the case of dynamic instability and there may be several feedback effects.

Amongst these, several instabilities have been reported to have occured during boiling in microchannels. Liu et al. (2013) suggested that these instabilities can be classified in two modes: one, interaction between the bubble generation and upstream compressibility and two interactions between parallel channels.

Ledinegg Instability

A boiling system has several components such as pump, valves, and channels. These components can be divided into two categories: one those supplying the pressure head to drive the flow (pump) and the other those causing pressure loss (test section and valves). Figure 15.3 shows the characteristic curves for the two types of components. These curves are known as supply (pump) and demand (valve, test section) curves depending on the function of the component the curve represents. When the slope of the demand curve $\left(\frac{d(\Delta p)}{d\dot{m}}\right)_D$ becomes less than that of the supply curve $\left(\frac{d(\Delta p)}{d\dot{m}}\right)_S$, Ledinegg instability occurs. When the pressure head required to push the liquid through the system at a certain mass flow rate is more than the pressure head supplied by the pump, the flow rate decreases. Thus, the Ledinegg instability is characterized by a sudden decrease in the mass flow rate. Zhang et al. (2009) investigated Ledinegg instability in horizontal microchannels for water at sub-atmospheric pressures and for a refrigerant, HFE-7100.

Soft Inlet/Upstream Compressibility/Pressure Drop Instability

Upstream compressibility refers to the presence of the compressible volume upstream of the test section. The compressibility can be present in the form of an entrained air bubble, a flexible tube or even as the gas dissolved in the liquid. Qu and Mudawar (2003) observed pressure drop oscillations caused by the upstream compressible volume in microchannels. They showed that these pressure drop oscillations can be eliminated by adding stiffness to the upstream flow e.g. throttling the upstream flow.

Huh et al. (2007) suggested that the pressure drop instability has a low frequency (~0.1 Hz). Liu et al. (2013) investigated the influence of upstream compressibility on the flow and heat transfer behaviour in microchannels by introducing inlet compressibility and measuring its effect on local heat transfer coefficient under subcooled and saturated boiling conditions. They introduced inlet compressibility by adding a buffer reservoir having a known gas volume upstream of the positive displacement pump. The condition of no upstream compressibility corresponded to zero gas volume in the buffer and was termed as hard inlet. They concluded that the inlet compressibility can affect the flow and heat transfer behaviour during flow boiling in microchannels. They found that the upstream compressibility causes the flow and heat transfer behaviour similar to that observed during nucleating boiling. They also showed that the hard inlet i.e. incompressible inlet condition causes convective heat transfer behaviour except at the low quality. This instability can be avoided by making sure the hard inlet condition e.g. by isolating the test section from the compressible volume by a throttle valve (Bergles and Kandlikar 2005). Kingston et al. (2018a) also observed the periodic oscillations in the pressure drop, mass flux, wall temperature and two-phase morphology and termed it pressure drop instability. They observed two peaks in pressure drop. The first, bigger peak occurred when the vapour generated in the channel increased and pushed the liquid upstream. This increased the flow resistance and was accompanied by a reduction in the mass flux. The second peak of smaller magnitude was accompanied by an increase in the mass flux caused by a decompression (or depressurization) of the upstream volume.

Rapid Bubble Growth Instability

Rapid bubble growth instability occurs in microchannels and is not so prominent during boiling in large systems (Kuo and Peles 2008). This is because the vapour bubbles generated are confined in the microchannels and significantly affect the hydrodynamics and thermal characteristics of the system. When a bubble nucleates on the channel wall, the pressure in the bubble is the saturation pressure at the local wall temperature. Growth of the nucleated bubble occurs in two stages: (1) free bubble growth when the bubble diameter is less than the channel diameter and (2) confined bubble growth when the volume of the bubble is larger than that of a sphere that can fit in the channel and therefore the bubble grows in the axial direction, upstream as well as downstream. Pressure fluctuations and flow reversal are observed in the confined bubble growth stage. Kuo and Peles (2008) suggested two mechanisms that cause rapid bubble growth instability.

(A) *Liquid Superheat*: The wall roughness in microchannels is typically of the order of 100 nm or less. Cavities on the wall caused by the roughness act as the bubble nucleation sites. Hsu (1962) showed as the size of available cavities become smaller, the liquid superheat required for the cavities to become active increases. When the cavities become active and the bubble nucleates, the bubble grows quickly resulting in an explosion-like vapour growth. This results in sharp increase in the pressure and fluid movement in the upstream and downstream directions. When the energy stored in the superheated liquid is released, the local temperature and pressure decreases

again and the higher pressure at the upstream pushes the liquid to move in the downstream direction. The entire cycle repeats when the liquid become superheated again. Li and Cheng (2004) suggested that the bubble nucleation in microchannels can be different from that in large channels because of the presence of sub-micron cavities having same size as that of a critical vapour bubble, presence of corners in microchannels having triangular, rectangular and trapezoidal cross-section and laminar flow.

(B) *Elevated Pressures*: In the liquid surrounding a rapidly growing bubble, the pressure can increase to very large values temporarily. While this local high pressure is confined to a very small region in large systems, a change in pressure surrounding a channel-size bubble in a microchannel causes a change in pressure field in the entire microchannel.

As the saturation pressure increases exponentially with temperature, the nucleated bubble in a microchannel would have a high vapour pressure resulting in the rapid growth of the bubble to the channel diameter. This momentum force generated by the evaporation of the bubble can sometimes be significantly larger than the dynamic pressure of the flow and the (manifold) pressure at the channel inlet. This would result in the growth of the bubble in the axial direction, upstream as well as downstream of the nucleation site. This would result in the flow reversal and has also been observed experimentally. Kingston et al. (2018a, b) studied rapid bubble growth instability during the onset of boiling and rapid bubble growth and pressure drop instabilities during the time-periodic boiling after the boiling incipience in a glass channel of 500 micron diameter subjected to a uniform heat flux.

Parallel Channel Instability

Scaling up of the microchannels can be achieved by numbering up the channels. This is generally achieved by cutting or etching a number of, typically of the order of 100 (Tuckerman and Pease 1981), parallel channels on a metal plate and bonding a number of plates together.

In parallel channel system, flow maldistribution is observed during flow boiling. The pressure drop across each channel is same in a parallel channel system. Each channel in the system has its own unique resistance depending on the two-phase flow conditions prevailing in the channel. As a result, each channel would have different flow rates. Different resistance to flow can be caused by the design of inlet header, difference in surface properties of the channels or non-uniform heating of the channel. The maldistribution can also be caused by the non-monotonic nature of the pressure drop-flow rate curve as shown in Fig. 15.3. Note that the total flow rate would be sum of the flow rates in each channel.

Kingston et al. (2019) studied Ledinegg instability in a parallel microchannel system having two thermally isolated parallel channels of circular cross-section having diameters of 500 μ each and subjected to the same power. At very low powers, when only liquid phase exists in the two channels, the flow rates in the two channels was nearly equal. However, on increasing the power to a value sufficient to initiate boiling in one of the channels, the flow resistance of the channel with boiling increases and

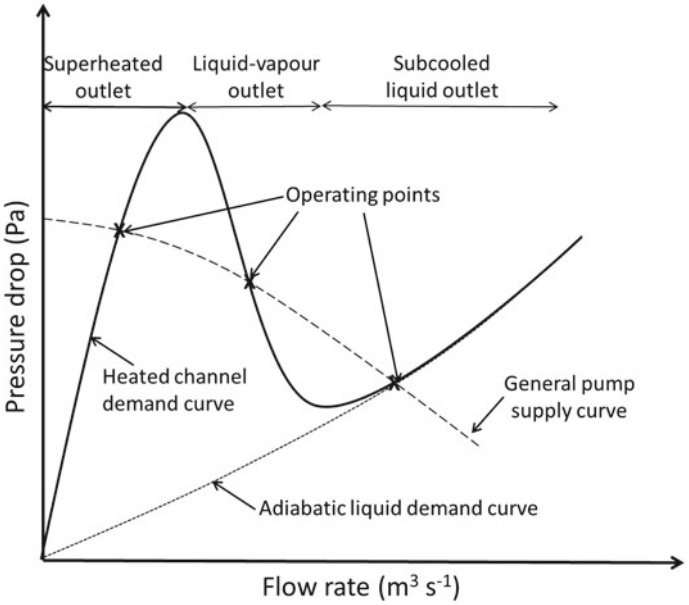

Fig. 15.3 Pressure drop versus flow rate curve for the supply and demand systems showing Ledinegg Instability (Adapted from Oevelen et al. 2017)

Ledinegg instability occurs. This causes low flow rate and high temperature in the channel with boiling. However, after the boiling initiates in the second channel, the maldistribution of the flow in the channels was reduced and the wall temperatures reduced significantly.

Oevelen et al. (2017) developed a model for the flow distribution in a system of heated parallel channels and integrated with a pump curve. They showed that for a constant pressure drop pump curve, the stability of the individual channels is independent of the other channels.

15.5 Measures to Control Instabilities

Several strategies have been proposed to suppress two-phase flow maldistributions and parallel channel instabilities. Some of these measures are described below:

(A) **Inlet restrictions**: The instabilities can be eliminated by placing restrictors at the inlet as shown in Fig. 15.4. The restrictors increase the ratio of the pressure loss at the inlet to that in the microchannel. Koşar et al. (2006) showed experimentally that the introduction of orifices at the entrance of each channel in a test section having parallel channels reduced the instability significantly.

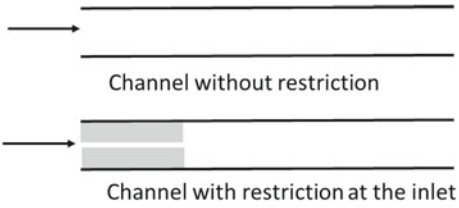

Fig. 15.4 Channel restriction to suppress boiling instabilities

(B) **Reentrant Cavities**: Reentrant cavities as shown in Fig. 15.5 can help to diminish the flow boiling instability. The rapid bubble growth instability is caused by high liquid superheat temperature caused by the very small cavities available for nucleation. The liquid superheat temperature can be reduced by providing structured surfaces in the form of reentrant cavities for the bubble nucleation. Kuo and Peles (2008) investigated boiling instability in microchannels with reentrant cavities, microchannels with interconnected reentrant cavities and plain wall microchannels. They observed a reduction in the liquid superheat and pressure at the initial stages of bubble nucleation. This helped in extending the stable boiling region and resulted in an increase in the critical heat flux (CHF).

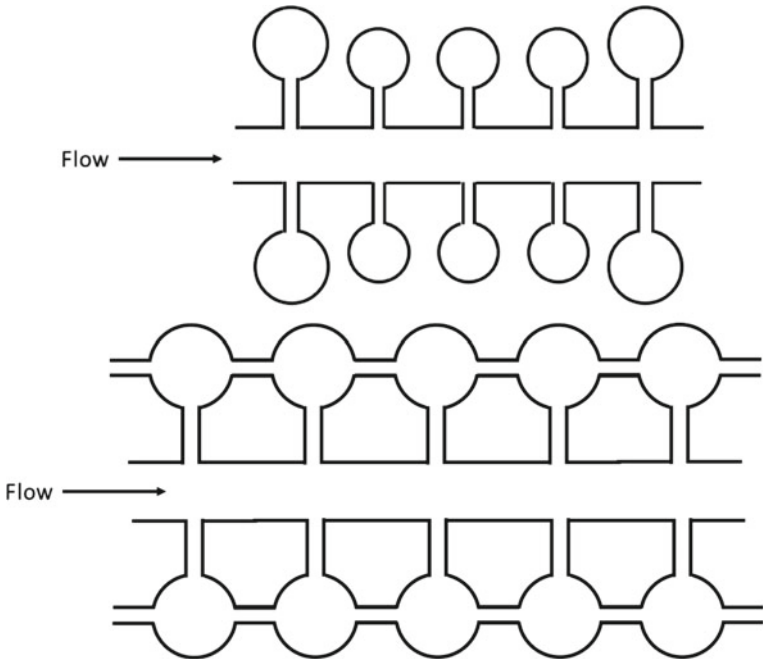

Fig. 15.5 Reentrant cavities and interconnected reentrant cavities

(C) **Seed bubbles**: Xu et al. (2009) proposed to introduce seed bubbles for the reduction of the flow instabilities. The energy stored in the superheated liquid can be released through the seed bubbles. The seed bubbles introduced should be large enough so that they do not condense completely in the subcooled liquid before reaching the superheated liquid zone in the channel. While the introduction of seed bubbles at a low frequency (~10 Hz) causes only a reduction in the amplitude and period of oscillations, seed bubbles at high frequency (~100 Hz) are observed to eliminate the instability completely. The pressure drop across the system also remains unchanged on the introduction of seed bubbles unlike other methods of stabilizing flow boiling.

(D) **Increased system pressure**: The Ledinegg instability occurs when the pump or supply system cannot act to balance the change caused by the perturbations in the mass flux. However, if the slope (magnitude) of the pump curve is greater than that of the demand curve, the system would remain stable. A constant displacement pump which deliver a fixed mass flow and therefore has infinite slope is suited to achieve this (Zhang et al. 2009).

Zhang et al. (2009) suggested that a high system pressure can help in the mitigation of static instabilities. In the electronics cooling applications, it is required to maintain low surface temperatures. Using water as coolant, this can be achieved when saturation temperature is low. Hence the system needs to be operated at low pressures. The instabilities that occur can thus be avoided using coolants having high reduced pressure.

Kuo and Peles (2009) showed that increasing the system pressure results in a decrease in the liquid to vapour density ratio and consequently results in a decrease in the instabilities.

15.6 Summary

Boiling in microchannels has received considerable attention over last few decades because of its application in a number of micro-structured devices and systems. Gas-liquid flows in general and boiling in particular are prone to instabilities. The boiling instabilities results in oscillations in flow, pressure and temperature and may result in critical heat flux condition causing failure of the system and sometimes even catastrophic accidents. In this chapter, the origin and mechanism responsible for the different types of instabilities in microchannels and measure that should be taken to overcome them has been discussed briefly. The basics of boiling has also been discussed so this chapter can serve as an introduction to the general reader without needing to go through the basics of boiling separately.

References

Agostini B, Thome JR (2005) Comparison of an extended database of flow boiling heat transfer coefficients in multi-microchannel elements with the three-zone model. In: ECI international conference on heat transfer and fluid flow in microscale. Castelvecchio Pascoli, Italy

Baldassari C, Marengo M (2013) Flow boiling in microchannels and microgravity. Prog Energy Combust Sci 39:1–36

Bao ZY, Fletcher DF, Haynes BS (2000) Flow boiling heat transfer of Freon R11 and HCFC123 in narrow passages. Int J Heat Mass Transf 43:3347–3358

Bar-Cohen A (1995) Gas-assisted evaporative cooling of high density electronic modules. IEEE Trans Compon Packag Manuf Technol A 18(3):502–509

Bergles AE, Kandlikar SG (2005) On the nature of critical heat flux in microchannels. J Heat Transfer 127:101–107

Bertsch SS, Groll EA, Garimella SV (2008) Review and comparative analysis of studies on saturated flow boiling in small channels. Nanoscale Microscale Therm Eng 12(3):187–227

Boure JA (1973) Review of two phase flow instability. Nucl Eng Des 25:165–192

Collier JG, Thome JR (1996) Convective boiling and condensation, 3rd edn. Clarendon Press, Oxford

Das PK, Das AK (2016) Chapter 7: instability in flow boiling through microchannels. In: Saha SK (ed) Microchannel phase change transport phenomena. Butterworth-Heinemann, pp 257–286

Hsu YY (1962) On the size range of active nucleation cavities on a heating surface. ASME J Heat Transfer 84:207–216

Huh C, Kim J, Hwan M (2007) Flow pattern transition instability during flow boiling in a single microchannel. Int J Heat Mass Transf 50:1049–1060

Jacobi A, Thome JR (2002) Heat transfer model for evaporation of elongated bubble flows in microchannels. ASME J Heat Transfer 124(6):1131–1136

Kakac S, Bon B (2008) A review of two-phase flow dynamic instabilities in tube boiling systems. Int J Heat Mass Transf 51:399–433

Kingston TA, Weibel JA, Garimella SV (2018a) High-frequency thermal-fluidic characterization of dynamic microchannel flow boiling instabilities: part 2—Impact of operating conditions on instability type and severity. Int J Multiph Flow 106:189–201

Kingston TA, Weibel JA, Garimella SV (2018b) High-frequency thermal-fluidic characterization of dynamic microchannel flow boiling instabilities: part 1—rapid-bubble-growth instability at the onset of boiling. Int J Multiph Flow 106:179–188

Kingston TA, Weibel JA, Garimella SV (2019) Ledinegg instability-induced temperature excursion between thermally isolated, heated parallel microchannels. Int J Heat Mass Transf 132:550–556

Koşar A, Kuo C-J, Peles Y (2006) Suppression of boiling flow oscillations in parallel microchannels by inlet restrictors. ASME J Heat Transfer 128:251–260

Kuo C-J, Peles Y (2008) Flow boiling instabilities in microchannels and means for mitigation by reentrant cavities. J Heat Transfer 130:072402

Kuo C-J, Peles Y (2009) Pressure effects on flow boiling instabilities in parallel microchannels. Int J Heat Mass Transf 52(1–2):271–280

Li J, Cheng P (2004) Bubble cavitation in a microchannel. Int J Heat Mass Transf 47:2689–2698

Liu Y, Fletcher DF, Haynes BS (2013) On the importance of upstream compressibility in microchannel boiling heat transfer. Int J Heat Mass Transf 58(1–2):503–512

Moore GE (1965) Cramming more components onto integrated circuits. Electronics 38(5)

Oevelen TV, Weibel JA, Garimella SV (2017) Predicting two-phase flow distribution and stability in systems with many parallel heated channels. Int J Heat Mass Transf 107:557–571

Qu W, Mudawar I (2003) Measurement and prediction of pressure drop in two-phase micro-channel heat sinks. Int J Heat Mass Transf 46:2737–2753

Tuckerman DB, Pease RFW (1981) High performance heat sinking for VLSI. IEEE Electron Device Lett EDL 2(5):126–129

Tullius JF, Vajtai R, Bayazitoglu Y (2011) A review of cooling in microchannels. Heat Transfer Eng 32(7–8):527–541

Xu J, Liu G, Zhang W, Li Q, Wang B (2009) Seed bubbles stabilize flow and heat transfer in parallel microchannels. Int J Multiph Flow 35:773–790

Zhang T, Tong T, Chang J-Y, Peles Y, Prasher R, Jensen MK, Wen JT, Phelan P (2009) Ledinegg instability in microchannels. Int J Heat Mass Transf 52:5661–5674

Chapter 16
Electromagnetohydrodynamic Control and Energy Conversion in Narrow Fluidic Devices: A Theoretical Perspective

Sandip Sarkar and Suvankar Ganguly

Abstract In recent years, electromagnetohydrodynamically modulated control and hydroelectric energy conversion through narrow fluidic devices have emerged as promising means for controlling and manipulating liquid flows in diverse applications. Such processes include development of smart sensors, micrototal analysis systems (μTAS), capillary electrophoresis, electrochromatography, mixing, flow cytometry, DNA hybridization and analysis, cell manipulation, cell patterning, immunoassay, enzymatic reactions, and molecular detection, etc. Accordingly, in the present chapter, we discuss the fundamental theories and elucidate the semi analytical and numerical approaches for analysis of the electromagnetohydrodynamic forces and their effect on thermofluidic control and energy transfer characteristics in narrow fluidic confinements. The consequences of electromagnetohydrodynamic forces and interfacial slip on the streaming potential development has been discussed in detail for pressure driven flows in a narrow fluidic confinement. It has been inferred that wall slip activated electro-magnetohydrodynamic transport can enhance the induced streaming potential and intensifies the convective heat transfer rate. Furthermore, we have also shown an analysis for combined electroosmotic and pressure-driven flows through narrow confinements, subjected to spatially varying non-uniform magnetic field. It is revealed that one can augment heat transfer rate for such a situation by judiciously choosing the spatially varying magnetic field strength. Next, we highlight the collective interaction of the fluid rheology, kinematics, volumetric effects of ionic species (steric effect), and the electrodynamics leading to giant augmentations in the energy conversion efficiency. For all the studies reported above, exergy analysis can indicate the route for optimal designs of process and the reduction in the thermodynamic irreversibility. Finally, the specific points emerging out from the research are concluded and relevant application areas have been discussed.

S. Sarkar
Department of Mechanical Engineering, Jadavpur University, Kolkata 700032, India
e-mail: sandipsarkar.mech@jadavpuruniversity.in; thesandipsarkar3@gmail.com

S. Ganguly (✉)
TATA Global R&D Division, Jamshedpur, India
e-mail: suvankarganguly@tatasteel.com

A. Mukhopadhyay et al. (eds.), *Dynamics and Control of Energy Systems*,
Energy, Environment, and Sustainability,
https://doi.org/10.1007/978-981-15-0536-2_16

Keywords Narrow confinement · Electromagnetohydrodynamics · Streaming potential · Energy conversion efficiency · Heat transfer · Entropy generation

16.1 Introduction

It has been established by the various researchers in the recent past that one may control fluid motion by employing electrokinetic phenomena in narrow fluidic devices of various geometrical shapes. Transport phenomena associated with combined flow and heat transfer characteristics encountered in extremely narrow passages are very much relevant to the advanced technological applications and smart sensors designs. In general, owing to the formation of electric double layer (EDL), the transport characteristics at the microscale differs appreciably when compared to that for macroscale. The formation of EDL stems from the interaction between dielectric substrates and static charges in ionized solutions. An electroosmotic flow is established in consequence to an externally applied electric field; on the other hand, in the absence of superimposed electric field, pressure driven transport may result in the generation of large induced streaming potential in such narrow confinements. This induced streaming potential may be effectively utilized into electrical power generation as a conversion of hydrostatic potential energy and therefore the consequence energy conversion from such narrow fluidic confinements. Applications of these principles are exploited in developing electrokinetic micropumps, micro fuel cells, etc. to name a few. In modern age industrial applications, heat transport in micro-electro-mechanically actuated flows assumes great significance. This triggered the researchers to study the electrokinetically flow mediated heat transfer characteristics through narrow fluidic confinements. The corresponding body of theoretical and experimental literatures may be found elsewhere (Nguyen 2012; Jang and Lee 2000; Andreu et al. 2011; Pamme 2006; Tso and Sundaravadivelu 2001; Chakraborty and Paul 2006; Jian 2015; Munshi and Chakraborty 2009; Pati et al. 2013; Goswami and Chakraborty 2010).

16.1.1 Theoretical Studies of Combined Electromagnetohydrodynamic Transport

In this Section, we summarize theoretical studies on the assessment of electromagnetohydrodynamic influence on the thermofluidic transport characteristics in narrow fluidic confinements. It has been found recently that one may enhance the overall efficiency of fluidic control in micro/nanofluidic applications through magnetic field driven actuation mechanisms (Nguyen 2012). In this connection, Jang and Lee (2000) reported their original experimental results on the application of combined electromagnetic influences in microfluidic transport mechanism. For the biological and chemical moieties separation, Andreu et al. (2011) and Pamme (2006) demonstrated

the applicability of magnetic field actuation. Recently, Tso and Sundaravadivelu (2001) reported the effect of magnetic field on the hydrodynamic characteristics in a parallel plate narrow fluidic confinement. They (Tso and Sundaravadivelu 2001) considered magnetic field acting in the longitudinal vertical plane of flow interacting with an externally imposed transverse electric field for controlling overall fluid motion. The implications of electromagnetohydrodynamic field towards controlling the microfluidic transport is recently reported by Chakraborty and Paul (2006). In a microparallel channel combined with pressure and electroosmotic effects, Jian (2015) reported analytical results by invoking transient magnetic field on heat transfer and entropy generation. Effect of transverse magnetic field and axial pressure gradient on hydroelectrical energy conversion mechanisms in narrow fluidic confinements is reported by Munshi and Chakraborty (2009). It may be mentioned here that interfacial slip at hydrophobic surfaces in conjunction with the combined electromagnetohydrodynamic influence plays an important role in the perspective of fluidic control in narrow confinements (Pati et al. 2013; Goswami and Chakraborty 2010; Lauga and Brenner 2004; Tretheway and Meinhart 2004; Sbragaglia et al. 2006). The highly crowded counterions nearer to the substrate wall of the narrow confinements contributes a somewhat trivial coupling between the thermofluidic and ionic transport characteristics, which become significantly more dominant as the EDL becomes thicker (Goswami and Chakraborty 2010). In general, owing to the inherent surface roughness, the entrapment of local fluid elements within the surface asperities is recognized as the no-slip boundary condition. This, in turn, prevents fluid molecules to escape from that trapping owing to an otherwise dense molecular packing. As a consequence, fluid slips smoothly over the molecularly smooth boundary without directly experiencing the surface asperity barriers. Furthermore, geometrically rough surfaces made of hydrophobic materials may result the formation of nano-bubbles (depleted gas layer) adhering to the channel walls. Thus, the fluid smoothly sails over the superseding vapor layer shield without directly facing the rough surface asperities. As a result, the liquid may well "slip" on the rough wall surface without "sticking" in it. Mathematically, this phenomena is accounted through an interfacial boundary condition of the form $V|_{slip} = \beta\left[dV/dn\right]_{wall}$, where V is the fluid velocity, β being the dimensional slip coefficient (the distance beyond the surface that extrapolates bulk velocity to zero), and n is the surface normal. The order of this slip length varies in the range from no–slip (zero) to 100 nm (Huang et al. 2006; Zhu and Granick 2002; Baudry et al. 2001; Meyer et al. 2006; Choi et al. 2003). The wall slip mediated electromagnetohydrodynamic control in narrow confinements provides promising improvements in both fluid and thermal transport characteristics. As such, in many cases, researchers (Sarkar et al. 2016) have found that one may effectively enhance the flow rate and heat transfer in narrow channel when the substrate wall becomes hydrophobic in nature. The induced streaming potential and also the hydroelectric conversion efficiency can be enhanced with the consideration of wall slip. Additional effects of applying a non-uniform magnetic field in place of a constant magnetic field have been yielded to be an additional interesting aspect in transport characteristics through narrow confinements. Recently, researchers (Sarkar et al. 2017a) have demonstrated further improvement in fluidic control through the

application of a spatially-varying magnetic field for electro-osmotic flows in narrow channels. Further implication of nonlinear effects due to finite size of the ionic species (steric effects) on combined electromagnetohydrodynamic transport is also analyzed in their study (Sarkar et al. 2017b).

Despite the common electrokinetic interactions concerning Newtonian fluids in narrow confinements, the potential non-trivial interaction between the flow rheology and fluid kinematics turn out to be appreciably complicated for non-Newtonian fluid. For example, the motion of complex biofluids, protein chains in solvents, cell suspensions, gels, colloids, may, in general, lie in the group of a general non-Newtonian fluid whose constitutive behavior is appropriately given by the power-law. There are several literatures emerged in the recent past (Das and Chakraborty 2006; Berli and Olivares 2008; Afonso et al. 2009; Hadigol et al. 2011), where, researchers tried to demonstrate the influence of various fluid rheological parameters in flow, streaming potential development, heat transfer, and energy conservation efficiency in narrow fluidic confinements. Few dedicated studies in the literature have been emerged recently primarily focused on to understand the thermal transport phenomena in electroosmotically driven flow in narrow fluidic passage (Maynes and Webb 2003; Horiuchi and Dutta 2004; Chakraborty 2006; Burgreen and Nakache 1964; Levine et al. 1975; Patankar and Hu 1998; Yang et al. 1998) with and without allowing for the influence of axial pressure gradients (Maynes and Webb 2003; Horiuchi and Dutta 2004; Chakraborty 2006; Burgreen and Nakache 1964; Levine et al. 1975; Patankar and Hu 1998; Yang et al. 1998). On the other hand, the additional implications of electromagnetic effects may be significantly more non-trivial in the perspective of thermofluidic transport and energy conversion efficiency in such narrow fluidic confinements. These added interactions may be triggered by its immense significance in broad range of narrow-fluidic applications varying from MHD micropumps to lab-on-a-chip devices (Munshi et al. 2009; Jian and Chang 2015; Jang and Lee 2000; Jones 1995).

16.1.2 Thermofluidic Characteristics

Thermofluidic characteristics often turn out to be critical in flow through narrow fluidic confinements. Under the action of electric forces, when an electric charge moves relative to a background medium, it consistently dissipates heat, which is known as Joule Heating. Therefore, the application of high electric field is decisively restricted by this heating effect (Sarkar 2017). Thermal transport processes in consequence of electrical fields should, thus, be cautiously designed so as to decrease the heating effect while still maintaining a high throughput. Under these circumstances, the utilization of magnetic field can act as a further control towards influencing convective transport characteristics to a significant extent.

16.2 Theoretical Models

In this section, theoretical models for electromagnetohydrodynamic thermofluidic transport and energy conversion will be detailed sequentially. The corresponding consideration for electromagnetohydrodynamic control is also explained accordingly. In general, the model equations are considered based on the continuum approach under low Reynolds number paradigm. To establish the general modeling equations, we assume a model problem of pressure driven transport through a long, narrow slit–like narrow fluidic confinement separated by two parallel walls of length L, and height $2a$. It is assumed that the width of the confinement is much bigger than either of these dimensions. Setting the origin at the centre of the confinement; coordinates along the axial direction is denoted as X, whereas, Y being the direction transverse to the walls. The physical situation along with the different external body forces as mentioned in the present context is shown schematically in Fig. 16.1.

16.2.1 Theoretical Model for the Development of Electrical Double Layer (EDL)

In the subsequent discussions, we outline the growth of EDL at the confinement walls by considering finite ionic-size (steric) effects and its inference on the related thermofluidic transport characteristics. The formation of EDL stems from the physical contact of the confinement walls with the ionized solution. Owing to the ionization of covalently bound surface groups, the ion adsorption cause dielectric substrate to acquire static charges. As a result of these interactions, counter-ions are released into the bulk fluid (Hunter 1981). Furthermore, a Stern layer of monatomic thickness is formed near the direct vicinity of the walls with the population of oppositely charged ions owing to the strong electrostatic forces. The counter–ions layer in the immediate vicinity of the Stern layer can free to drift and is in rapid thermal motion. This second layer comprises the diffuse or Gouy–Chapman layer. The variation of the ion density obeys the Boltzmann distribution in the Gouy–Chapman layer. The

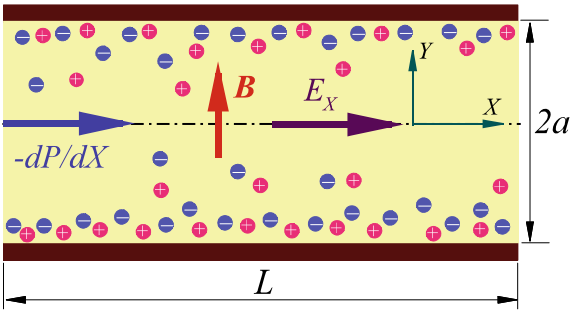

Fig. 16.1 Schematic of the physical situation along with the different external body forces

EDL, therefore, constitutes Gouy–Chapman layer along with the Stern layer. For the situation of electroosmotic flow, the applied electric field actuation triggers the free counter–ions in the diffuse layer to move in tune with its magnitude (Hunter 1981). Consequently, the developed electrokinetic potential at the interface between Stern layer and the diffuse layer is termed as the zeta potential $(\overline{\zeta})$, which is assumed to be uniform throughout the substrate walls. The EDL thickness is classically characterized by the Debye length (κ) scale and is expressed as $1/\kappa^2 = 2n_0 z^2 e^2 / \varepsilon_l k_B T_0$, where n_0 is the bulk ionic number density, ε_l is the dielectric constant of the medium, e is the electronic charge, k_B is the Boltzmann constant, and T_0 is the local absolute temperature of the fluid (Hunter 1981). It is important to note here that the variations of the Debye length due to temperature changes are marginal and is neglected in our analysis. The theoretical model describing finite size effect of the ions obeys the modified space charge model by including ionic charge flux density in the governing species transport equation as (Bandopadhyay and Chakraborty 2014; Das and Chakraborty 2011; Garai and Chakraborty 2010):

$$\overrightarrow{J_k} = \overrightarrow{U} n_k - D_k n_k \overrightarrow{\nabla} \left(\ln a_k + \frac{z_k e \Psi}{k_B T_0} \right) \tag{16.1}$$

where $\overrightarrow{U}$ is the advective velocity, z_k is the valency of the kth ionic species, D_k is the diffusivity of the kth ionic species, n_k is the number density of the kth ionic species, Ψ is the developed electrokinetic potential, a_k is the activity of the kth ionic species and may be expressed as $a_k = \frac{n_k/n_r}{1-\gamma \sum_k n_k/n_r}$ (Hunter 1981). Here, n_r is the reference ionic number density, and is assumed as n_0, γ is the steric factor or the partial molal volume fraction of the ions. The steady state transport phenomena of each ionic species through a slit type narrow fluidic confinement can be described through the ionic species conservation equation (Garai and Chakraborty 2010),

$$\nabla \cdot \overrightarrow{J_k} = 0 \tag{16.2}$$

Without the advective transport of the ions, Eq. (16.2) takes the following form (Das and Chakraborty 2011)

$$\ln a_k + \frac{z_k e \Psi}{k_B T_0} = \text{constant} \tag{16.3}$$

We consider the typical fluid to be constituted of a $z:z$ symmetric electrolyte and an equilibrium is maintained between the narrow confinement and its connecting reservoir, hence, $n_+ = n_- = n_0$. Toward these, one may write the ionic number density to be of the form

$$n_\pm = n_0 \frac{\exp\left(\mp e z \Psi / k_B T_0\right)}{1 + 2\gamma \left\{ \cosh\left(e z \Psi / k_B T\right) - 1 \right\}} \tag{16.4}$$

For a uniform permittivity fluid, the EDL potential distribution (Ψ) is expressed in terms of the net charge density distribution (ρ_e) within the EDL and is governed by the Poisson equation (Hunter 1981),

$$\nabla^2\Psi = -\frac{\rho_e}{\varepsilon} \tag{16.5}$$

where ρ_e is the net charge density in a unit volume of the fluid and ε is the permittivity of the medium. The mathematical expression for ρ_e yields,

$$\rho_e = e(z_+ n_+ - z_- n_-) \tag{16.6}$$

On substituting the expression for ionic concentration distribution, as given by Eq. (16.4), into the Poisson equation (Eq. (16.5), the governing equation for the EDL potential distribution reduces to:

$$\frac{d^2\Psi}{dY^2} = \frac{n_0 ez}{\varepsilon}\frac{2\sinh\left(ez\Psi\big/k_B T_0\right)}{1+4\gamma\sinh^2\left(ez\Psi\big/2k_B T\right)} \tag{16.7}$$

We make Eq. (16.7) dimensionless with the dimensionless parameters: $\lambda = a/\kappa$, $\psi = ez\Psi\big/4k_B T$, and $y = Y\big/a$, to obtain:

$$\frac{d^2\psi}{dy^2} = \left(\frac{\lambda}{2}\right)^2 \frac{\sinh(4\psi)}{1+4\gamma\sinh^2(2\psi)} \tag{16.8}$$

It is important to note here that the general solution of the EDL potential distribution ψ can be obtained with the correct specification of the relevant boundary conditions both at the walls and at the channel centerline respectively (Dey et al. 2013). Hence, we appeal to the typical physical situation of the chemical equilibrium maintaining between the confinement walls, hydrogen ions, and the added cations. Therefore, one may write the following nondimensional boundary conditions as pertinent to Eq. (16.8) as (Bandopadhyay and Chakraborty 2012): at $y = 0, d\psi\big/dy = 0$ (centerline), and at $y = \pm 1$, $\psi = \zeta$ (boundary), here ζ is the nondimensional zeta potential $\left(\zeta = ez\overline{\zeta}\big/4k_B T_0\right)$. The characteristics of ζ and its growth usually depends on the buffer pH, and the bulk ionic concentration n_0. However, one may express the dependence of dimensional $\overline{\zeta}$ with those parameters as:

$$\overline{\zeta} = \frac{k_B T_0}{e}\ln\left(\frac{-\sigma}{e\Gamma+\sigma}\right) - \frac{k_B T_0}{e}\left(\mathrm{pH}-\mathrm{pK_a}\right)\ln 10 - \frac{\sigma}{C_{Stern}} \tag{16.9}$$

Here, $\mathrm{pK_a}$, Γ, and C_{Stern}, are dissociation constant, dissociated fraction of chargeable sites, and the capacitance of Stern layer, respectively. The surface charge density can be expressed as $\sigma = \pm\varepsilon\left(d\Psi\big/dY\right)_{wall}$. Perhaps, one may employ the celebrated Debye–Hückel linearization approximation to linearize Eq. (16.9) for low zeta potential values $\left(\left|\overline{\zeta}\right| \ll \left|4k_B T_0\big/ez\right|\right)$ (Hunter 1981). In general, in the absence of steric

effect ($\gamma = 0$), a closed form analytical solution of Eq. (16.8) is obtained as

$$\psi(y) = 4\tanh^{-1}\left[\tanh\left(\zeta/4\right)\exp\left\{-(1-y)/(\kappa/a)\right\}\right] \tag{16.10}$$

On the other hand, a much simpler analytical solution to Eq. (16.8) may be obtained from the classical considerations of Debye-Hückel linearization as:

$$\psi(y) = \zeta\frac{\cosh\left\{y/(\kappa/a)\right\}}{\cosh(\kappa/a)} \tag{16.11}$$

16.2.2 Theoretical Model for Magnetohydrodynamics (MHD)

The magnetohydrodynamics (MHD) corresponds to a situation where, in an electrically conducting fluid, the velocity field $\overrightarrow{U}$ and the magnetic field $\overrightarrow{B}$ are coupled. Any movement of a conducting material in a magnetic field generates an electromotive force of order $\overrightarrow{J} \times \overrightarrow{B}$, in accordance with Faraday's law of induction, and causes an induced electric current of density $\overrightarrow{J}$ to flow. This induced current $\overrightarrow{J}$ must, according to Ampère's law gives rise to a second, induced magnetic field. This adds to the original magnetic field and the change is usually such that the fluid appears to 'drag' the magnetic field lines along with it. The combined magnetic field (imposed plus induced) interacts with the induced current density $\overrightarrow{J}$. The effect is the *Lorentz force* $\overrightarrow{J} \times \overrightarrow{B}$ to which each unit volume of material is subjected. Since the induced electric current and the Lorentz force tend to oppose the mechanisms which create them, movements which lead to an induction phenomenon are systematically braked by the Lorentz forces (Moreau 1990; Davidson 2001). We assume that the fluid is electrically conducting with a constant electrical conductivity, σ_e, and is subjected to an external magnetic field vector $\overrightarrow{B}$. For low magnetic Reynolds number (ratio between magnetic advection to diffusion), the induced magnetic field becomes negligible and the applied magnetic field predominates with its constant magnitude. The applied magnetic field $\overrightarrow{B}$ that imparts the magnetohydrodynamic body force is along the positive *Y*-axis and parallel to the gravity. The magnetic field strength is so chosen that it corresponds to a given Hartmann number of the problem. Therefore, the applied magnetic field induced Lorentz body force term is given by:

$$\overrightarrow{F_B} = \overrightarrow{J} \times \overrightarrow{B} \tag{16.12}$$

Here $\overrightarrow{J}$ is the local ion current density, which can be obtained by Ohm's law as,

$$\overrightarrow{J} = \rho_e\overrightarrow{U} + \sigma_e\left(\overrightarrow{E} + \overrightarrow{U} \times \overrightarrow{B}\right) \tag{16.13}$$

Here, $\overrightarrow{U}$ is the velocity, $\overrightarrow{E}$ is the electric field, and ρ_e is the charge density. For low magnetic Reynolds numbers, the charge density is effectively very low (negligible transport of electric charge by convection, $\rho_e \overrightarrow{U} \approx 0$) and, accordingly, has an insignificant contribution to the current density and the Lorentz force.

Thus, the magnetic field induced magnetohydrodynamic body force (Lorentz force) takes the form

$$\overrightarrow{F_B} = \sigma_e \left(\overrightarrow{U} \times \overrightarrow{B} \right) \times \overrightarrow{B} \tag{16.14}$$

16.2.3 Theoretical Models for Electromagnetohydrodynamic Flow Control and Energy Conversion

It can be seen from Fig. 16.1 that in conjunction with a favorable pressure gradient $-dP \big/ dX$ acting along the axial (X) direction, a superimposed (for electroosmotic case)/induced (for streaming potential mediated flow situation) electric field of strength E_X also acts and provides essential driving force for EOF. Furthermore, a magnetic field of strength B is superimposed along the transverse (Y) direction. Thus, the magnetohydrodynamic effect together with that of combined pressure–driven and electrokinetic actuation emerged to be the governing mechanism for the ensuing fluidic transport through the confinement. We assume temperature independent thermophysical properties of the fluid and also invariant local ionic concentration.

Theoretical model for electroosmotic electromagnetohydrodynamic flow control with a consideration of steric effect. As already described earlier that in addition to that of applied magnetic field, an externally imposed electric field of magnitude E_X also acts along the axial direction and therefore corresponds to a situation of electroosmotic MHD flow. The movement of the bulk fluid flow together with the MHD influence and the electroosmotic body forces is governed by the incompressible Navier-Stokes equation. Therefore, the consequential electrokinetic body forces are dispersed to the whole fluid through viscous shear, which is dependent on the imposed electrical field and distribution of charge density. For steady, incompressible, unidirectional, and low Reynolds number ($Re \ll 1$) flows (typical for narrow confinements), the governing momentum transport equation takes the following form (Garai and Chakraborty 2010; Bandopadhyay and Chakraborty 2012):

$$0 = -\nabla P + \mu \nabla^2 \overrightarrow{U} + \rho_e \overrightarrow{E} + \overrightarrow{F_B} \tag{16.15}$$

where, P denotes hydrostatic pressure, and μ is the dynamic viscosity of the fluid. In the present situation of electromagnetohydrodynamic flows, a spatial variation in the imposed magnetic field vector is assumed of the form (Das et al. 2012):

$$\overrightarrow{B} = B_0 \Re\left(Y/a\right)\overrightarrow{e_Y} \tag{16.16}$$

where, B_0 is the spatially invariant component of the magnetic field, $\Re\left(Y/a\right)$ is the dimensionless function characterizing the choice of spatial variation in the applied magnetic field, and $\overrightarrow{e_Y}$ is the unit vector along the transverse direction. Now, for hydrodynamically fully developed flows, the momentum conservation equation along the axial direction takes the following form:

$$-\frac{dP}{dX} + \mu\frac{d^2U}{dY^2} + \rho_e E_X - \sigma_e\left\{B_0\Re\left(Y/a\right)\right\}^2 U = 0 \tag{16.17}$$

We then make the Eq. (16.17) dimensionless by employing following dimensionless parameters (Dey et al. 2012, 2013): $u = U/U_{HS}$, where $U_{HS} = -\varepsilon\overline{\zeta}E_X/\mu$, the reference velocity scale and also recognized as Helmholtz-Smoluchowski velocity, $\Lambda = -a^2\left(dP/dX\right)/\mu U_{HS}$, is a nondimensional term denoting relative magnitudes of the pressure-driven and electroosmotic flow actuations, and $Ha = \sqrt{\sigma_e B_0^2 a^2/\mu}$, Hartmann number representing the imposed magnetic field strength. Finally, substituting the expression of ρ_e from Eq. (16.6), the final nondimensional equation of electromagnetohydrodynamic flow is,

$$\frac{d^2u}{dy^2} - \{Ha\,\Re(y)\}^2 u = -\Lambda - \left(\frac{\lambda}{2}\right)^2 \frac{\sinh(4\psi)}{\zeta\left\{1 + 4\gamma\sinh^2(2\psi)\right\}} \tag{16.18}$$

Equation (16.18) is subjected to the no slip boundary conditions at the walls and may be written into the following dimensionless form (Dey et al. 2013): $u|_{y=\pm1} = 0$.

Theoretical model for streaming potential mediated electromagnetohydrodynamic flow control with a consideration of interfacial slip. For streaming potential mediated flow, regardless of the absence of applied electrical field, a back–streaming potential field (E_X) is unreservedly induced in the cross stream direction. This is owing to the ensuing streaming of ionic species through the flow in the mobile part of the EDL and the preferential accumulation of the advected counterions towards the downstream end of the confinement through a competing advection-electromigration mechanism. The axially induced (E_X) electric field in conjunction with the magnetic field actuation yield an additional influencing parameter for electromagnetohydrodynamic (EMHD) transports (Chakraborty and Paul 2006). Accordingly, for a static magnetic field of magnitude B_Y and for a hydrodynamically fully-developed, steady, uniform flow, the momentum conservation equation along the X-direction takes the following form

$$-\frac{dP}{dX} + \mu\frac{d^2U}{dY^2} + \rho_e E_X - \sigma_e B_Y^2 U = 0 \tag{16.19}$$

We use the following nondimensional scales to make Eq. (16.19) dimensionless form (Bandopadhyay and Chakraborty 2012): $u = U \big/ \left\{-\left(a^2 \big/ \mu\right)\left(dP \big/ dX\right)\right\}$, $E = E_X \big/ \left\{-\left(a^2 \big/ \varepsilon\overline{\zeta}\right)\left(dP \big/ dX\right)\right\}$, and by substituting the full solution of $\psi(y)$ as given in Eq. (16.10), to yield,

$$\frac{d^2u}{dy^2} - Ha^2 u = -1 - \left(\frac{4pr^2E}{\zeta}\right)\left[\frac{\exp\{-r(1-y)\} + p^2\exp\{-3r(1-y)\}}{\left[1 - p^2\exp\{-2r(1-y)\}\right]^2}\right] \tag{16.20}$$

Here, the parameter E denotes the nondimensional streaming potential field and is given by, $E = E_X \big/ -\left(a^2 \big/ \varepsilon\overline{\zeta}\right)\left(dP \big/ dX\right)$, where, $-\left(dP \big/ dX\right)$ is the applied pressure gradient (Bandopadhyay and Chakraborty 2012). Ha is the Hartmann number and is given by, $Ha = \sqrt{\sigma_e B_Y^2 a^2 \big/ \mu}$. The other parameters are: $r = a/\kappa$, and $p = \tanh\left(\zeta \big/ 4\right)$. To incorporate the effect of wall slip, we have employed the Navier slip model at the confinement walls. Therefore, the relevant dimensionless boundary conditions for Eq. (16.20) reads: $\left(du \big/ dy\right)_{y=0} = 0$ (centerline symmetry); $u|_{y=1} = \beta\left(du \big/ dy\right)_{y=1}$ (Navier slip). Here, β is the nondimensional slip coefficient and is defined as, $\beta = \beta^* \big/ a$. It may be noted that the solution for Eq. (16.20) is analytically tractable. Therefore, employing the above set of boundary conditions, one may obtain a closed form analytical solution to Eq. (16.20) as,

$$\begin{aligned} u(y) = {} & \frac{1}{Ha^2}\left\{1 - \frac{\cosh(Ha\,y)}{\cosh(Ha) - \beta Ha\sinh(Ha)}\right\} + \frac{2prE}{\zeta}\left[S_1\frac{\exp(Ha\,y)}{Ha}\right. \\ & - S_2\left\{\frac{\cosh(Ha\,y)}{\cosh(Ha) - \beta Ha\sinh(Ha)}\right\} \\ & - \exp\{-r(1-y)\}\left\{\frac{{}_2F_1\left(1, \frac{1}{2} - \frac{Ha}{2r}; \frac{3}{2} - \frac{Ha}{2r}; p^2\exp\{-2r(1-y)\}\right)}{r - Ha}\right. \\ & \left.\left. + \frac{{}_2F_1\left(1, \frac{1}{2} + \frac{Ha}{2r}; \frac{3}{2} + \frac{Ha}{2r}; p^2\exp\{-2r(1-y)\}\right)}{r + Ha}\right\}\right] \end{aligned} \tag{16.21}$$

Here, ${}_2F_1(a, b; c; w)$ is the Gaussian hypergeometric function and is defined for $|w| < 1$ by the power series, ${}_2F_1(a, b; c; w) = \sum_{k=0}^{\infty}\frac{(a)_k(b)_k}{(c)_k}\frac{w^k}{k!}$, where, $(g)_k$ is the rising Pochhammer symbol, and is defined by

$$(g)_k = \begin{cases} 1 & for\, k = 0 \\ g(g+1)(g+2)\cdots(g+k-1) & for\, k > 0 \end{cases}$$

The other constant terms appearing in Eq. (16.21) are,

$$S_1 = \exp(-r)\left[Ha\left\{\frac{{}_2F_1\left(1, \frac{1}{2} - \frac{Ha}{2r}; \frac{3}{2} - \frac{Ha}{2r}; p^2\exp(-2r)\right)}{r - Ha} - \frac{{}_2F_1\left(1, \frac{1}{2} + \frac{Ha}{2r}; \frac{3}{2} + \frac{Ha}{2r}; p^2\exp(-2r)\right)}{r + Ha}\right\} - \frac{2}{p^2\exp(-2r) - 1}\right] \tag{16.21a}$$

$$S_2 = \frac{(\beta Ha - 1)}{(r - Ha)}{}_2F_1\left(1, \frac{1}{2} - \frac{Ha}{2r}; \frac{3}{2} - \frac{Ha}{2r}; p^2\right) - \frac{(\beta Ha + 1)}{(r + Ha)}{}_2F_1\left(1, \frac{1}{2} + \frac{Ha}{2r}; \frac{3}{2} + \frac{Ha}{2r}; p^2\right) - \frac{S_1(\beta Ha - 1)}{Ha}\exp(Ha) - \frac{2\beta}{p^2 - 1} \tag{16.21b}$$

Accordingly, under Debye-Hückel linearization, a simplified form of analytical solution to Eq. (16.21) may be written as,

$$u(y) = \frac{1}{Ha^2}\left\{1 - \frac{\cosh(Ha\,y)}{\cosh(Ha) - \beta Ha\sinh(Ha)}\right\} + \frac{E\,Ha\,r^2}{\left(Ha^2 - r^2\right)}\left[\frac{\cosh(r\,y)}{\cosh(r)} - \frac{\{1 - r\beta\tanh(r)\}\cosh(Ha\,y)}{\cosh(Ha) - \beta Ha\sinh(Ha)}\right] \tag{16.22}$$

Theoretical model for streaming potential mediated electromagnetohydrodynamic flow control of power-law fluids. This section deals with the theoretical model for a non-Newtonian (power-law obeying) fluid in a narrow confinement subjected to the combined consequences of rheology, interfacial electrokinetics, and externally applied magnetic field. Under these circumstances, the corresponding momentum transport equation describing the transport of non-Newtonian fluids by invoking body forces due to streaming potential field, pressure field, and superimposed magnetic field, can be written as (Bandopadhyay and Chakraborty 2011; Bird and Stewart 2006)

$$\rho\frac{D\overrightarrow{U}}{Dt} = -\nabla P + \nabla\cdot\overline{\overline{\tau}} + \rho_e\overrightarrow{E} + \overrightarrow{F_B} \tag{16.23}$$

where $\overline{\overline{\tau}}$ is the stress tensor. For a non-Newtonian fluid, the stress tensor $\left(\overline{\overline{\tau}}\right)$ is assumed to follow a power-law constitutive behaviour with the strain rate tensor $(\dot{\upsilon})$ of the form (Bird and Stewart 2006; Chakraborty 2007): $\overline{\overline{\tau}} = \chi(\dot{\upsilon})^m$, here, χ is the flow consistency index and m being the non-Newtonian behavioural index. For shear thinning (pseudoplastic) fluid, $m < 1$. Whereas, $m > 1$ obeys the shear thickening (dilatant) behavior, on the other hand flow is Newtonian at $m = 1$ (Bird and Stewart 2006). Incorporating the typical considerations for the narrow confinement flows (as described earlier) and considering a static imposed magnetic field of magnitude B_Y, one may write the dimensionless form of Eq. (16.23) for streaming potential mediated, pressure driven, steady, unidirectional, fully developed, low Reynolds number ($\mathrm{Re} \ll 1$), and low magnetic Reynolds number flows as,

$$\frac{d}{dy}\left[\phi\left(\frac{du}{dy}\right)^{m}\right] - Ha^2 u = -1 + \frac{E}{\bar{\zeta}}\frac{d^2\psi}{dy^2} \tag{16.24}$$

We have used the following nondimensionalizing strategies: the velocity has been nondimensionalized as $u = U \big/ U_{ref}$, the dimensionless streaming potential $E = E_X \big/ E_{ref}$, the dimensionless flow consistency index $\phi = \chi \Big/ \left\{\eta_0 \left(U_{ref} \big/ a\right)^{1-m}\right\}$, and the Hartmann number $Ha = \sqrt{\left(\sigma_e B_Y^2 a^2\right) \big/ \eta_0}$. Where, $-\left(dP \big/ dX\right)$ is the applied pressure gradient, η_0 is the reference viscosity, $U_{ref} = -\left(a^2 \big/ \eta_0\right)\left(dP \big/ dX\right)$ is the reference velocity, and $E_{ref} = -\left(a^2 \big/ \varepsilon\zeta\right)\left(dP \big/ dX\right)$ is the reference streaming potential field (Bandopadhyay and Chakraborty 2011). The pertinent boundary conditions for the fluid transport equation (Eq. 16.24) are no slip walls $\left(u|_{y=0} = 0\right)$ and centreline symmetry $\left(du \big/ dy\big|_{y=1} = 0\right)$ of the confinement (Chakraborty et al. 2013). It may be mentioned here that the dimensionless streaming potential term, E, appearing in Eqs. (16.21), (16.22), (16.24), is an unknown parameter, and is also an implicit function of u. This imposes a restriction on the governing equations for the electromagnetohydrodynamic velocity distribution to be mathematically closed. The overall electroneutrality constraint brings a closure relationship and therefore the subsequent determination of E.

Electroneutrality constraint, the streaming potential, and the hydraulic electric energy conversion efficiency. The electroneutrality constraint states that for the solution to be electrically neutral, the induced streaming potential field is developed in such a way that the net current (which is the algebraic summation of the streaming current due to net ionic advection, conduction current due to electromigration, and the conduction current through the Stern layer) at each cross-sections of the confinement is zero. The above statement can be mathematically expressed as,

$$I_{net} = I_{stream} + I_{cond} + I_{stern} = 0 \tag{16.25}$$

where, I_{net} is the net ionic current over the cross sections of the channel, I_{stream} is the streaming current, I_{cond} is the bulk conduction current passing through the "mobile" fluid layers, and I_{stern} is the conduction current passing through the "immobilized" stern layer. Assuming that the relative velocity between the ions and the local fluid within the EDL to be zero (Hunter 1981), one may write,

$$I_{stream} = \int_0^{2a} ze(n_+ - n_-)U(Y)dY \tag{16.26a}$$

$$I_{cond} = \frac{z^2 e^2 E_X}{f}\int_0^{2a} (n_+ + n_-)dY \tag{16.26b}$$

$$I_{stern} = 2\sigma_{stern} E_X \tag{16.26c}$$

Here, $f = 2n_0 z^2 e^2 \big/ \sigma_B$, is the ionic friction factor and is considered to be same for both anionic and cationic species; σ_B is the bulk ionic conductivity; σ_{stern} is the stern layer conductivity (Hunter 1981). Substituting Eq. (16.26a, 16.26b, 16.26c) in Eq. (16.25), the dimensionless form of the electroneutrality constraint may be expressed as,

$$\int_0^1 u(y)\sinh(\psi)dy - \frac{\alpha E}{\zeta}\int_0^1 \cosh(\psi)dy - \frac{\alpha E}{\zeta}Du = 0 \tag{16.27}$$

where $\alpha = \mu\sigma_B \big/ 2\varepsilon n_0(k_B T)$, a dimensionless conductivity parameter; $Du = \sigma_{stern} \big/ a\,\sigma_B$, Dukhin number. In more compact form, Eq. (16.27) can be rearranged to determine the final expression for streaming potential as,

$$E = \frac{\zeta \mathrm{I}_1}{\alpha(\mathrm{I}_2 + Du)} \tag{16.28}$$

where the integrals $\mathrm{I}_1 = \int_0^1 u(y)\sinh(\psi)dy$ and $\mathrm{I}_2 = \int_0^1 \cosh(\psi)dy$. The induced streaming potential field in pressure driven narrow fluidic confinement flows is greatly significant in transforming hydraulic energy into an electrical power generation. Accordingly, a hydraulic energy conversion efficiency η_h can be defined as the quantum of drawn out energy induced by the streaming potential field to the flow actuating input power required, and may be mathematically described as (Das and Chakraborty 2010)

$$\eta_h = \frac{\mathrm{I}_{stream}|E_S|}{Q\left|\left(\frac{dP}{dX}\right)_{eff}\right|} \tag{16.29}$$

Here, E_S is the induced streaming potential, Q is the volume flow rate, and $\left(dP \big/ dX\right)_{eff}$ is the effective pressure gradient as the sum-total effect of the imposed pressure gradient and the magnetic field. The magnitude of $\left(dP \big/ dX\right)_{eff}$ may be estimated by equating flow rates with and without considering the applied magnetic field B_Y and setting $dP \big/ dX = \left(dP \big/ dX\right)_{eff}$, for the situation $B_Y = 0$ (Das and Chakraborty 2010).

16.2.4 Theoretical Model for Electromagnetohydrodynamic Thermal Energy Transport

In the present chapter, the thermal energy transport in the narrow confinement is assumed to be governed by thermally developing flow consideration. For the situation of thermally developing transport, the confinement walls are assumed to be

isothermal and are maintained at a uniform temperature T_W. We consider the electrical and thermophysical properties of the liquid are temperature independent. Invoking the effects of axial conduction, viscous dissipation, and volumetric Joule heating, the mathematical expression for the governing energy equation yields (Dey et al. 2012):

$$(\rho C_p)U\frac{\partial T}{\partial X} = k\left(\frac{\partial^2 T}{\partial X^2} + \frac{\partial^2 T}{\partial Y^2}\right) + \mu\left(\frac{\partial U}{\partial Y}\right)^2 + S_{JH} \tag{16.30}$$

In Eq. (16.30), C_p is heat capacity, ρ is the density, k is the fluid thermal conductivity, T is the temperature of the fluid, $\mu(\partial U/\partial Y)^2$ signifies the effects due to viscous dissipation, and the term S_{JH} indicates the volumetric heat generation due to Joule heating. We assume feeble advective influence on ionic species transport, S_{JH} can be expressed as $S_{JH} = \sigma_e E_X^2$. Proceeding further, Eq. (16.30) can be expressed in dimensionless form with $x = X/a$ and the nondimensional temperature $\theta = (T - T_W)/(T_0 - T_W)$, where T_0 is the inlet temperature of the fluid, to obtain (Dey et al. 2012),

$$\left(Pe\frac{U_{ref}}{U_{av}}\right)u(y)\frac{\partial \theta}{\partial x} = \left(\frac{\partial^2 \theta}{\partial x^2} + \frac{\partial^2 \theta}{\partial y^2}\right) - Br\left(\frac{\partial u}{\partial y}\right)^2 - S_{p,eff} \tag{16.31}$$

In the above equation, $Pe = U_{av}a/\alpha_T$, is the thermal Peclet number, representing the relative dominance of the advective transport rate to that of rate of thermal diffusive transport, and α_T is the thermal diffusivity which is given by $\alpha_T = k/(\rho C_p)$. The nondimensional average flow velocity is expressed as $u_{av} = U_{av}/U_{ref} = 1/2\int_{-1}^{1} u(y)dy$, where, U_{av} is the dimensional average velocity, and U_{ref} is the reference velocity scale which is given by $U_{ref} = -(dP/dX)a^2/\mu$. $Br = \mu U_{ref}^2/k(T_W - T_0)$, is the Brinkman number, representing the parameter owing to viscous dissipation, and the term denoting dimensionless volumetric heat generation as a result of Joule heating is defined by $S_p = \sigma_e E_{ref}^2 a^2/k(T_W - T_0)$. $S_{p,eff}$ is the effective Joule heating parameter and is given by $S_{p,eff} = S_p E^2$. It may be mentioned here that for electroosmotic flows, $E_{ref} = E_X$, therefore, $S_p = S_{p,eff}$. Furthermore, for non-Newtonian power law obeying fluid, the modified form of the Brinkman number, Br_{non} is written as, $Br_{non} = Br(\eta^*)$, where, the nondimensional non-Newtonian fluid viscosity parameter $\eta^*(y) = \phi(du/dy)^{m-1}$.

The relevant boundary conditions as applicable to Eq. (16.31) may be expressed in the following dimensionless form (Dey et al. 2012):

$$\theta|_{x=0} = 1 \quad \forall \quad 0 \le y \le 1 \tag{16.32a}$$

$$\theta|_{y=\pm 1} = 0 \quad \forall \quad 0 < x < +\infty \tag{16.32b}$$

$$\partial\theta/\partial y\big|_{y=0} = 0 \quad \forall \quad 0 < x < +\infty \tag{16.32c}$$

$$\theta < \infty, \text{as } x \to +\infty \quad \forall \quad 0 \leq y \leq 1 \tag{16.32d}$$

The quantitative value of the heat transfer, i.e., the Nusselt number is calculated by employing the definition of bulk mean temperature. At any cross section of the confinement, the nondimensional form of bulk mean temperature can be written as (Dey et al. 2012):

$$\theta_{bm} = \int_0^1 \frac{u(y)}{u_{av}} \theta(x, y) dy \tag{16.33}$$

From the governing equation for steady state energy balance at the wall, the nondimensional value of the Nusselt number is obtained as,

$$Nu = \frac{1}{\theta_{bm}} \frac{\partial \theta}{\partial y}\bigg|_{y=1} \tag{16.34}$$

16.2.5 Solution Methodology

The dimensionless governing momentum equations with their relevant boundary conditions are evaluated numerically by employing the *Matlab* function *chebfun*, similar strategies are also applied to obtain numerical solution for the dimensionless EDL potential ψ. For the coupled solution of ψ, E, and $u(y)$, an iterative approach is adopted. On the other hand, the nondimensional energy equation along with the pertinent boundary conditions is numerically solved using finite volume based method. For the numerical solution, a rectangular domain similar to Fig. 16.1 is chosen. The domain encompasses an inlet, outlet, top, and bottom boundaries. The mesh distribution is based on uneven spacing with finer meshes near the boundaries. A second order central differencing scheme is employed for diffusion terms with a first order upwinding scheme for convection term. The final discretized energy equation forms an algebraic system of equations, which is iteratively solved by a line–by–line TDMA (tri–diagonal matrix algorithm) solver (Patankar 2009). A domain and grid independence tests are also carried out by ensuring the fact that the results differ no more than 2–3% with refinement.

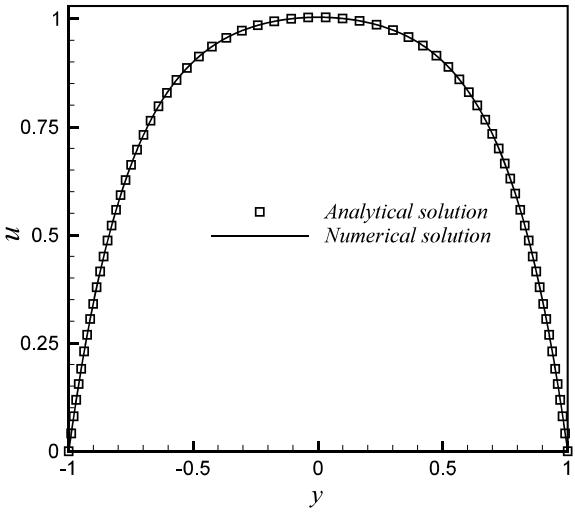

Fig. 16.2 Comparisons of analytical solution and present numerical result for the dimensionless velocity (u) distribution with y for $\Lambda = 1$, $Ha = 1$ (reproduced with permission from Elsevier publishing, License number: 4611930685925) (Sarkar et al. 2017a, b)

16.2.6 Model Validation

The present numerical method is validated by considering a standard situation for pressure-driven electroosmotic and magnetohydrodynamic flows in a narrow confinement for which a benchmark closed form analytical solution is available. Employing Debye–Hückel linearization approach, a closed form analytical solution for velocity distribution may be expressed as, $u(y) = \frac{\Lambda}{Ha^2}\left\{1 - \frac{\cosh(Ha\,y)}{\cosh(Ha)}\right\} + \frac{\lambda^2}{(\lambda^2 - Ha^2)}\left\{\frac{\cosh(Ha\,y)}{\cosh(Ha)} - \frac{\cosh(\lambda\,y)}{\cosh(\lambda)}\right\}$. The comparison result between the present numerical solutions to that of the analytical solution is shown in Fig. 16.2. The other relevant parameters are given in the figure caption. It is found from Fig. 16.2 that present numerical solution is in good agreement with that of analytical predictions.

16.3 Discussions

We start our discussions with the electromagnetohydrodynamic flow and energy conversion efficiency for different physical considerations. This will follow the corresponding analysis for thermal energy transport. Finally, an exergy analysis is presented to identify the optimum window of the thermodynamically efficient physical range spaces. Towards this, the following fluid properties are assumed at a reference temperature $T = 300\,\mathrm{K}$ as $\mu \sim 10^{-3}\,\mathrm{kg}/\mathrm{m\,s}$, $\rho \sim 10^{3}\,\mathrm{kg}/\mathrm{m}^3$, $\varepsilon \sim 702.24 \times 10^{-12}\,\mathrm{C}^2/\mathrm{J\,m}$. For a $z:z$ symmetric electrolyte, the electrochemical constants can be taken as, $f \sim 10^{-12}\,\mathrm{N\,s}/\mathrm{m}$, $\sigma_B \sim 10\,\mathrm{nS}/\mathrm{cm}$ (Hunter 1981). The relevant nondimensional parameters considered in the analysis are the half height of

the confinement to Debye length (a/κ), zeta potential (ζ), slip coefficient (β), Hartmann number (Ha), Dukhin number (Du), thermal Peclet number (Pe), the Joule heating parameter $\left(S_p\right)$, and the viscous dissipation parameter (Br). For the Hartmann number range, Ha ~0.1–10, a ~100 μm, one can get $B_Y = 10$–$100\ T$, which conforms to the physically realizable range (Davidson 2001; Chakraborty 2007). Additionally, considering typical reaction parameters (Hunter 1981), the magnitude of the dimensional zeta potential comes out to be in the tune of ~10–50 mV Alternatively, the Stern layer conductivity may be ranging from 0 to 72 nS/cm, with the consequent Dukhin number ranging from 0 to 100 (Bandopadhyay and Chakraborty 2012), whereas, the dimensionless conductivity parameter turns out to be $|\alpha| \sim 10$.

16.3.1 Electromagnetohydrodynamic Fluidic Transport and Hydroelectric Energy Conversion Efficiency

For streaming potential flows in narrow fluidic confinement with interfacial slip (β), in Fig. 16.3a, the variation of the magnitude of dimensionless streaming potential field (E) with the nondimensional zeta potential (ζ) is shown for different values of Ha and β. The other relevant parameters are given in the figure caption. It is seen that the overall trend of variation resembles a bell-shaped curve following an asymptotic limit for $\zeta \to \infty$. The concentration of free counterions in the EDL increases with an increase in ζ. This eventually establishes a foreword streaming current and thereby consequent enhancement in back electrokinetic transport. As a result, the magnitude of E is also increases. The opposing consequence of these two contrasting mechanisms bring about an immediate value of ζ for which the streaming potential field is highest (Sarkar et al. 2017a, b). Away from this threshold region of zeta potential, the forward streaming current becomes more predominant, thereby leading to a steady

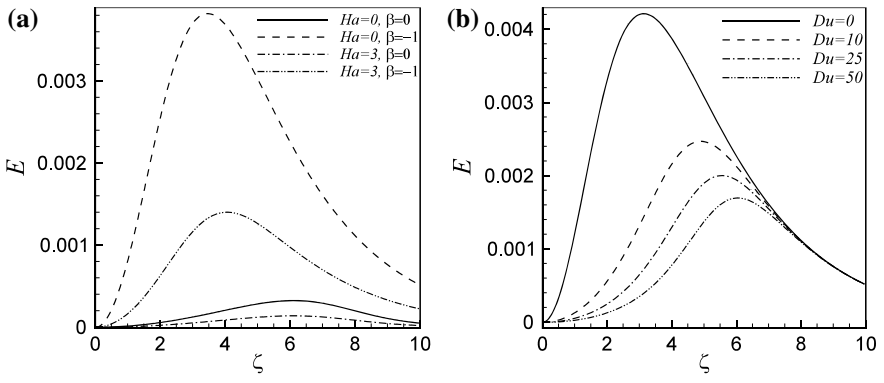

Fig. 16.3 Variation of E as a function of ζ at **a** $Du = 0$, and for various Ha, β; **b** $\beta = -3$, $Ha = 1$, and for various Du (reproduced with permission from Elsevier publishing, License number: 4592910722206) (Sarkar et al. 2016)

reduction in E values in order to maintain electroneutrality constraint. Moreover, wall slip effect increases streaming potential value. Hydrodynamic slip increases fluid velocity and thereby enhancing EMHD transport of the ionic species in the EDL region. As a result, magnitude of streaming potential increases. On the other hand, the strength of the applied magnetic field (Ha) is enhanced; there is a gradual reduction in E values. Electromagnetic forces serve as a contrasting influence to the effective driving favorable pressure gradient, as a result the fluid velocity reduces (Sarkar et al. 2017a, b). Therefore, the advective ionic transport strength weakens; as a consequence, the streaming potential magnitude reduces.

The magnitude of variation in E with ζ for different values of Du is shown in Fig. 16.3b. The other relevant parameters are mentioned in the caption. It is found that the streaming potential magnitude reduces with increasing the Stern layer conductivity. Increase in stern layer conductivity leads to a proportionate augmentation of conduction current through the Stern layer than that of through the bulk fluid (Sarkar and Ganguly 2017). As a result, the conduction current flows through an alternate less resistive path. Through the Stern layer, this conduction current balances the streaming current. Thus, for electroneutrality, a lower magnitude of electric potential is needed; therefore the induced streaming potential field becomes lower (Sarkar and Ganguly 2017).

For streaming potential mediated flow of power law obeying fluid, in Fig. 16.4a, we show the variation of E with Ha for different power law index (m) (other relevant parameters are given in figure caption). It is seen that there is an exponential decay of E as the strength of the imposed magnetic field is increased. Increasing the strength of Ha reduces the effective driving pressure gradient by giving rise to competing electromagnetohydrodynamic forces. As a result, the movement of ionic species inside the EDL gets hampered and thereby consequent reduction in streaming potential field. On the other hand, in comparison to shear thinning ($m < 1$) and

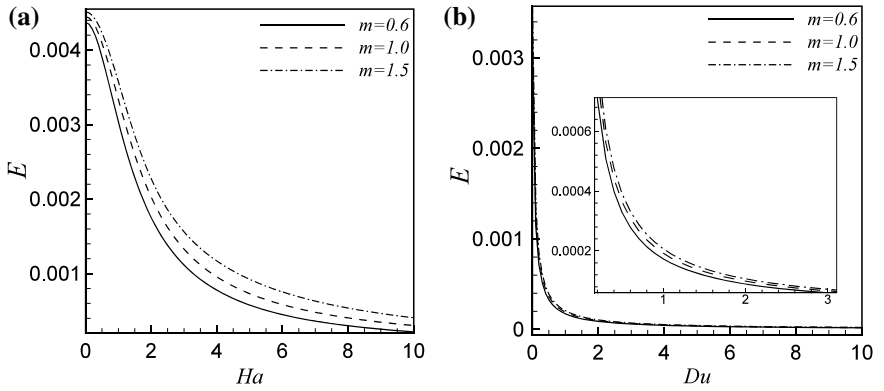

Fig. 16.4 Variation of the dimensionless induced streaming potential field (E) as a function of **a** Hartmann number (Ha) and at $Du = 0$; **b** Dukhin number (Du) and at $Ha = 1$, for different power law index (m) (reproduced with permission from Elsevier publishing, License number: 4592901310924) (Sarkar et al. 2017a, b)

Newtonian ($m = 1$) fluids, the induced streaming potential field for shear thickening fluid ($m > 1$) is higher. The probable reason behind this phenomenon can be explained by the fact that the shear thickening fluids has a typical velocity profile with greater curvature around the peak velocity at the centre. With increasing the power law index m, the ratio of the peak centre velocity to that of the mean velocity increases. The consequent effect is gradual augmentation in the streaming current (I_{stream}) and therefore the streaming potential.

The functional dependence of streaming potential with Du for different values of m is shown in Fig. 16.4b at $Ha = 1$. It can be noticed from Fig. 16.4b that there is a significant drop in streaming potential values with enhancing values of the Stern layer conductivities. The same phenomena are repeated for both shear thinning and shear thickening fluids. The physical reason, as already explained in the preceding sections, is owing to the enhancement in conduction current through the Stern layer, which balances streaming current by ignoring conduction current contributions in the bulk flow. As a result, streaming potential drops appreciably while satisfying electroneutrality ($I_{net} = 0$).

For electroosmotic flow in narrow fluidic confinement subjected to an externally applied non uniform magnetic field of the form $\Re(y) = \exp(-\beta y)$ (as given in Eq. 16.18), where β is a constant quantity, the fully developed electromagnetohydrodynamic velocity distribution along the cross-section of the confinement is shown in Fig. 16.5a, while the other parameters are given in figure caption. It is observed that the interactions among the parameters Ha, β, results in an asymmetry in velocity distribution. There is a reduction in overall flow rate as the magnitude of Ha is increased. It may be noted that increasing the magnetic field strength causes an overall enhancement in the flow-opposing magnetic field induced body force term,

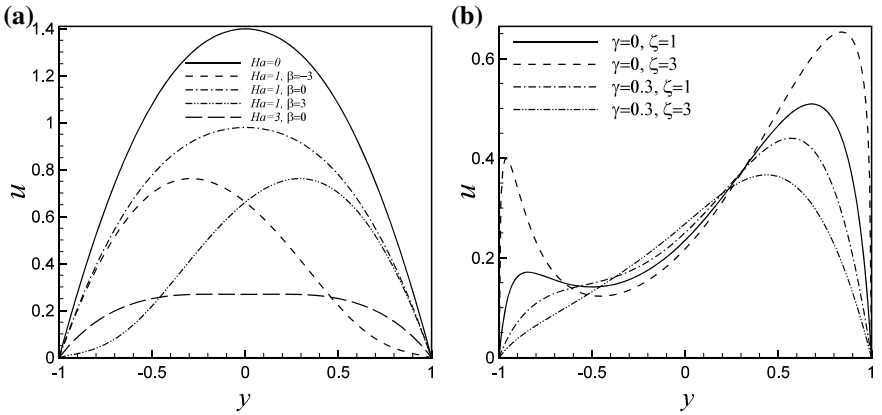

Fig. 16.5 Variation in the nondimensional velocity (u) along the dimensionless height (y) of the confinement for different values of **a** Ha, β, and at $\Lambda = 1$, $\zeta = 3$, $\gamma = 0.3$; **b** ζ, γ, and at $Ha = 3$, $\beta = 1$, $\Lambda = 1$ (reproduced with permission from Elsevier publishing, License number: 4592910028722) (Sarkar et al. 2017a, b)

$\sigma_e B_0^2 U$ to increase. As a result, the opposing influence of the Lorentz force $\overrightarrow{j} \times \overrightarrow{B}$ is also more. This finally culminated in retarding influence to the overall axial transport. Further reduction in flow velocity is noticed as the value of $\beta \neq 0$. At the centre of the confinement, velocity is maximum and therefore highest reduction in velocity magnitude is noticed as the value of Ha is augmented.

Effect of interfacial kinematic on electromagnetohydrodynamic velocity distribution is shown in Fig. 16.5b, where, the variation in $u(y)$ with y is displayed for various values of γ and ζ. The results are shown at $Ha = 3$, $\beta = 1$, and $\Lambda = 1$. It can be seen that at a fixed value of zeta potential (ζ), inclusion of steric size effect leads to a lower flow velocity over the whole confinement cross-section. On the other hand, when the finite ionic size is considered ($\gamma = 0.3$), increase in ζ results in a decrement of u magnitude. However, opposite trend is noticed in the absence of steric effect. The bulk ionic volume fraction increases with an increase in steric factor (Yazdi et al. 2015). This results in the formation of closely–packed layers of counter ions at the highly charged confinement walls. As consequence, within the EDL, the Stern layer is developed below the diffuse layer, thus causing the decay in net electrokinetic potential across it. This also imparts a flow resistance and thereby reduction in overall bulk fluidic transport. Furthermore, increase in zeta potential with a consideration of steric effect results an intensification in the crowding of counterions, consequently steric effect becomes higher and therefore reduction in the magnitude of flow velocity. On the other hand, when $\gamma = 0$, an increase in ζ causes the augmentation of the ionic concentration and thereby triggering bulk ionic transport (Yazdi et al. 2015).

In practical applications, the electrokinetic energy conversion (η_h) efficiency is an important parameter to characterize the percentage electrical energy being harvested from such narrow fluidic transport. Towards this, the variation in the energy conversion efficiency with flow behavioural index (m) for different values of the superimposed magnetic field strength (Ha) is shown in Fig. 16.6. The other relevant parameters are mentioned in the caption. From Fig. 16.6, it is noticed that for the entire paradigm of m, a dramatic augmentation in the energy conversion efficiency

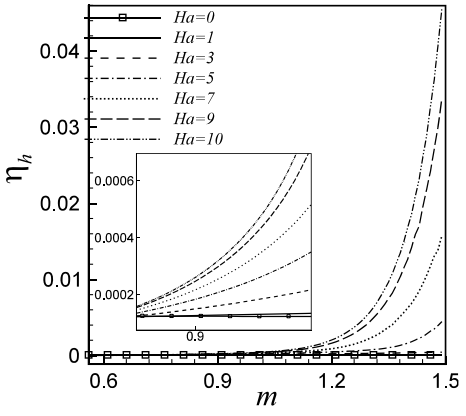

Fig. 16.6 Variation of the energy conversion efficiency as a function of the fluid behavioral index (m) for different values of the applied magnetic field strength (Ha), at $Du = 0$ (reproduced with permission from Elsevier publishing, License number: 4592900989884) (Sarkar and Ganguly 2017)

occurs. A giant augmentation in the electro-hydro-dynamic energy conversion efficiencies is prominent for shear thickening fluids. Enhancement in the η_h with increase in m is attributed the corresponding enhancement in the magnitude of the streaming potential. However, with increasing magnetic field strength, there is a further augmentation in η_h values. The plausible reason behind this effect is corresponding decrement in $\left(\left|\left(dP/dX\right)_{eff}\right|\right)$ with higher values of magnetic fields. Hence, for the current parametric spaces, one may effectively achieve the optimum energy conversion efficiency at a condition of $Ha = 10$, $m = 1.5$, respectively.

16.3.2 Electromagnetohydrodynamic Thermal Energy Transport

We start our discussions on the thermal energy characteristics for the streaming potential mediated electromagnetohydrodynamic flows in narrow fluidic confinements with interfacial slip. Figure 16.7a–d portray the variation of dimensionless temperature (θ) profile with the nondimensional distance (y) along the height of the confinement, at axial positions of $x = 3$ (Fig. 16.7a), $x = 5$ (Fig. 16.7b), $x = 7$ (Fig. 16.7c), and $x = 10$ (Fig. 16.7d), while the other pertinent parameters are given in the figure caption. Effect of slip length (β) and magnetic field (Ha) on the temperature profile is also shown in Fig. 16.7. We notice that, the magnitude of the dimensionless temperature (θ) decreases with increasing magnitude of the magnetic field strength. This is because of the fact that the magnitude of streaming potential decreases with increasing the value of Hartmann numbers, this eventually causes effective reduction in the Joule heating parameter $\left(S_{p,eff}\right)$, since $S_{p,eff} = S_p E^2$. Therefore, the effective thermal energy generation rate reduces, as a consequence, fluid temperature decreases and therefore the dimensionless temperature (θ) magnitude. In a similar line, wall slip effect (β) reduces the magnitude of θ, as can be observed from Fig. 16.7. This also follow the similar explanation that wall slip effect arrests velocity gradient nearer to the vicinity of the confinement walls and thereby enhancement in the effective flow rates. The overall effect culminates in enhancing the streaming potential magnitude and thereby higher values of the electroviscous retardation effect. The nonlinear interaction among these effects eventually culminates in reducing the value of $(T - T_W)$ and thus lowering the θ magnitude, since $T_0 < T_W$.

We next proceed to assess the implication of electroosmotic flow actuation effects on the temperature distribution across the narrow confinement for the situation when the externally applied magnetic field follows a non-uniform distribution. We show the dimensionless temperature (θ) profile with y along the confinement height, at axial positions of $x = 0.5$ (Fig. 16.8a), $x = 1$ (Fig. 16.8b), $x = 5$ (Fig. 16.8c), and $x = 10$ (Fig. 16.8d), while the other parameters are given in figure captions. Additionally, the combined influences of the magnetic field (Ha) and the parameter β on the nondimensional temperature distribution are also shown in Fig. 16.8. Through

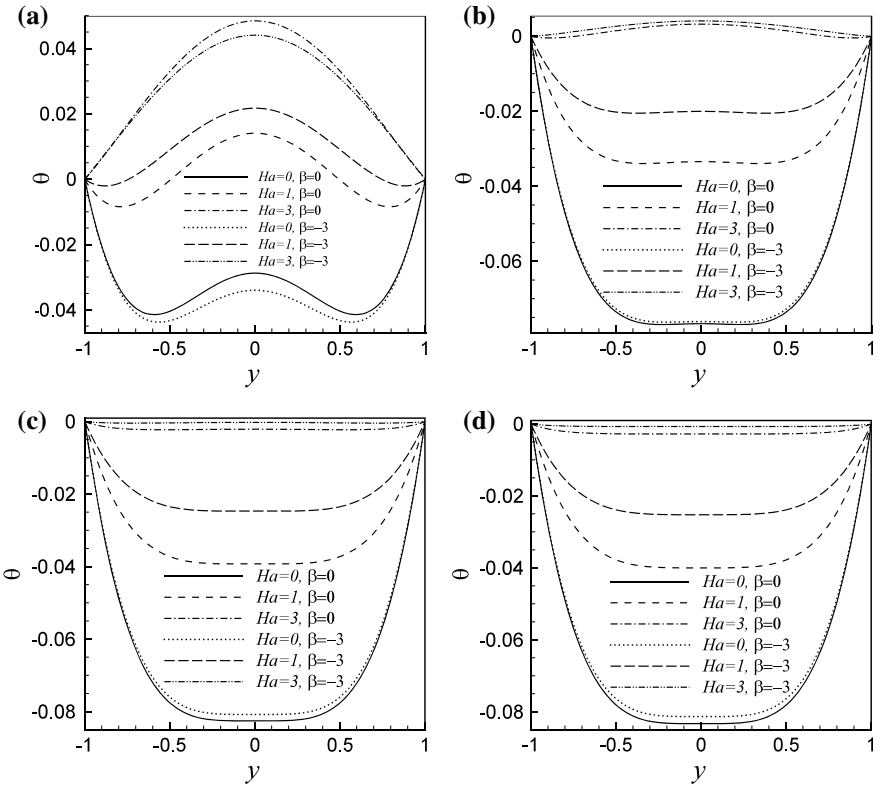

Fig. 16.7 Variation of dimensionless temperature (θ) with the nondimensional distance (y) along the height of the confinement for $\zeta = 3$, $Du = 0$, $Pe = 1$, $S_p = 1$, $Br = 1$, and at an axial location of **a** $x = 3$; **b** $x = 5$; **c** $x = 7$; **d** $x = 10$ (reproduced with permission from Elsevier publishing, License number: 4592910722206) (Sarkar et al. 2016)

the nonzero values of the parameter β, we see that the magnetic field induced suppression on the temperature is higher as the spatially varying non-uniform magnetic field strength is increased. The physical mechanism can be addressed by recognizing the fact that magnetic field reduces flow velocity and thereby decrement in convective heat transfer from the confinement walls (Chakraborty et al. 2013). The final effect is seen in the form of gradual reduction in the liquid temperature (T) over the whole confinement cross section. Akin to velocity, temperature distribution show nonsymmetrical distribution when $\beta \neq 0$, whereas, there is a reflection symmetry when $\beta = 0$.

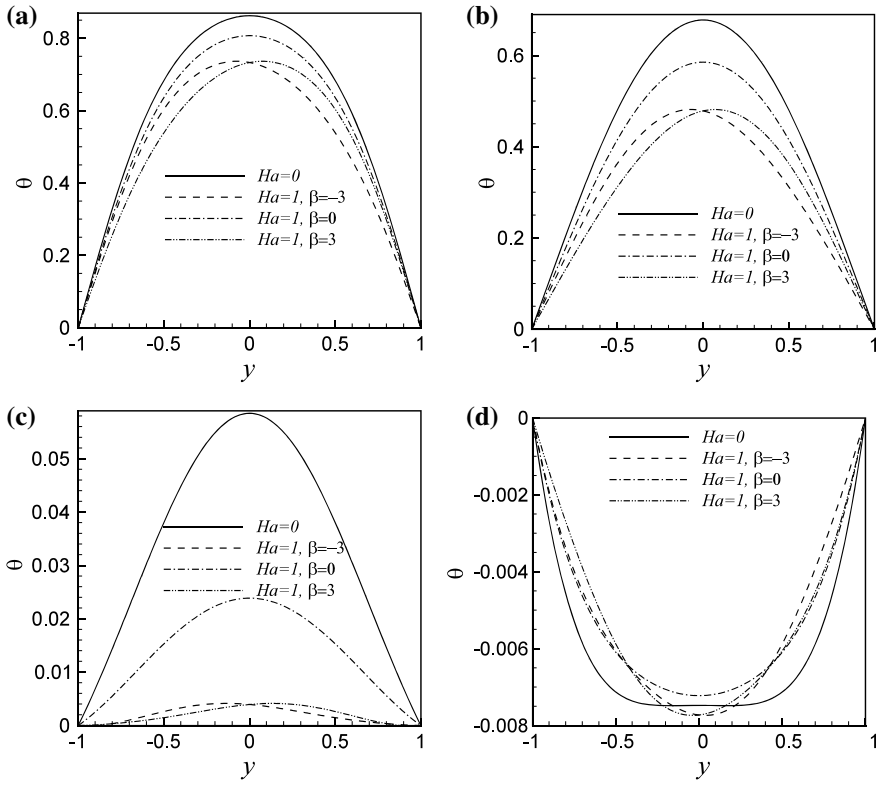

Fig. 16.8 Variation of dimensionless temperature (θ) with the nondimensional distance (y) along the height of the confinement for different values of Ha, β, and at $\zeta = 3$, $\gamma = 0.3$, $\Lambda = 1$, $Pe = 3$, $S_p = 0.01$, $Br = 0.01$, for the axial location of **a** $x = 0.5$; **b** $x = 1$; **c** $x = 5$; **d** $x = 10$ (reproduced with permission from Elsevier publishing, License number: 4592910028722) (Sarkar et al. 2017a,b)

16.3.3 Electromagnetohydrodynamic Heat Transfer

We begin our heat transfer analysis for electromagnetohydrodynamic electroosmotic flows with non-uniform distribution in the superimposed magnetic field. Figure 16.9a, b display the Nusselt number (Nu) variations along the axial length (x) of the confinement, for various values of Ha, β (Fig. 16.9a), and ζ, γ (Fig. 16.9b). The other relevant parameters are given in the figure caption. In general, along the axial direction of the confinement, the local Nusselt number follows a monotonic decreasing trend until a distinct axial location (x), where, a sudden singularity in the Nu curve is noticed. From the thermal entrance region, fluid temperature gradually increases owing to the heat transfer from the walls in conjunction with volumetric heat generations due to viscous dissipation and Joule heating. This in turn increases bulk mean temperature (θ_m) of the fluid and therefore gradual reduction in the Nusselt number magnitudes (Dey et al. 2012). As a result, the bulk mean temperature reduces its

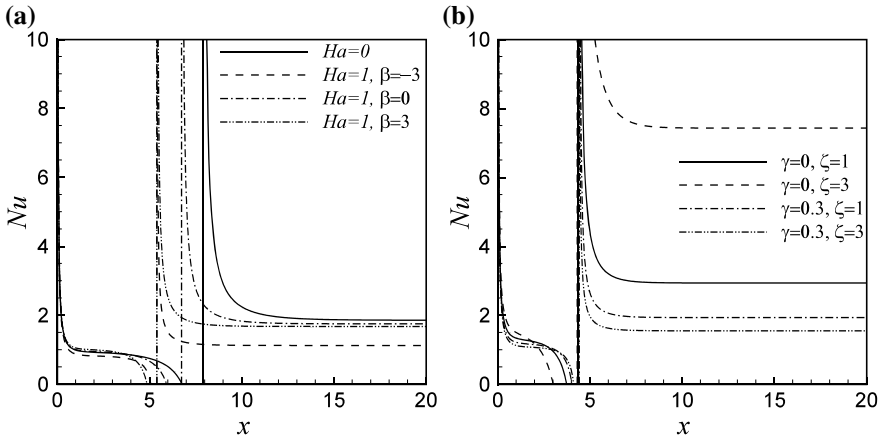

Fig. 16.9 Local Nusselt number (Nu) variations along the axial length (x) of the confinement, for **a** $\zeta = 3$, $\gamma = 0.3$, $\Lambda = 1$, $Pe = 3$, $S_p = 0.01$, $Br = 0.01$, and various Ha, β; **b** $\beta = 1$, $Ha = 3$, $\Lambda = 1$, $Pe = 3$, $S_p = 0.01$, and $Br = 0.01$, and varying ζ, γ (reproduced with permission from Elsevier publishing, License number: 4592910028722) (Sarkar et al. 2017a, b)

difference with the constant wall temperatures. Nearer to the regions of the discontinuity, the bulk mean temperature approaches the wall temperature of the fluid and this yield, $\theta_m \rightarrow 0$ (Dey et al. 2013). Away from the discontinuity region, the bulk mean temperature again increases owing to the volumetric heat generation effects, as a consequence, fluid temperature exceed the temperature of the walls. Therefore, there is generation of wall heat flux from the bulk liquid towards the confinement walls. This decrease in the Nusselt number value continues to exists until a threshold axial location where there is an axial invariance of the Nusselt number curve in thermally fully developed state. There, the heat released from the walls is balanced by the internal volumetric heat generations. It is found from Fig. 16.9a that heat transfer reduces with increasing magnetic field strength. Increasing the magnitudes of the magnetic field reduces fluid velocity and therefore there is a gradual thickening of the thermal boundary layer thickness. This finally culminates in heat transfer reduction. It is interesting to observe that heat transfer can be altered by altering the magnetic field strength with the variations in the parameter β. Maximum heat transfer is noticed for the negative values of β, whereas, vice versa is the situation for the positive values. In Fig. 16.9b, it is observed that the nontrivial interplay between the surface charging and the steric interactions show significant effect on the heat transfer characteristics. We found that with the inclusion of steric effect of ions, the local Nusselt number reduces significantly. On the other hand, augmenting the value of ζ increases the Nusselt number value when the ions are considered to be as a point charge ($\gamma = 0$), whereas, the opposite trend is noted when the steric effect is considered. The physical reason, as already explained, is corresponding enhancement/reduction in the flow velocities. Alternation in the flow velocities is directly

connected with the development and growth of thermal boundary layers at the confinement walls, and therefore the convective heat transfer rates. It is also seen that the thermal entrance length is mostly unaltered by the nonlinear interplay between surface charging and steric factor.

For the streaming potential mediated flows with interfacial slip, in Fig. 16.10a, b, the variation of the local Nusselt number (Nu) along the length of the confinement (x) is shown for different magnitudes of the effective Joule heating parameter, $S_{p,eff}$ (Fig. 16.10a) and various values of Ha, β (Fig. 16.10b). The representative other constant parameters are mentioned in the figure caption. The overall trend of the Nusselt number is same as explained for Fig. 16.9. It can be noted from Fig. 16.10a that the value of Nu reduces with the augmentation in $S_{p,eff}$ magnitude. Although augmentation in $S_{p,eff}$ increases the liquid temperature and makes it further homogenized, the wall temperature gradient is increasingly reduced. The resultant effect is seen through decrement in the rate of heat transfer for increasing the Joule heating magnitude (Dey et al. 2012). On the other hand, it can be observed from Fig. 16.10b that the heat transfer increases with increasing the magnetic field strength. The fundamental perspective, as already mentioned, is owing to the considerable lessening in the effective Joule heating parameter $\left(S_{p,eff}\right)$, which causes augmentation in the temperature gradient at the wall and therefore amplification of heat transfer rate. Nonetheless, growing magnitude of slip length β turns out to amplify the magnitude of Nusselt number. Increasing wall slip amplifies fluid velocity at the wall and therefore the heat transfer rate.

Furthermore, for streaming potential mediated flows in non-Newtonian fluid, the overall trend of heat transfer characteristics with magnetic field strength is same as Newtonian fluids. This is shown in Fig. 16.11a, b, where the local Nusselt number

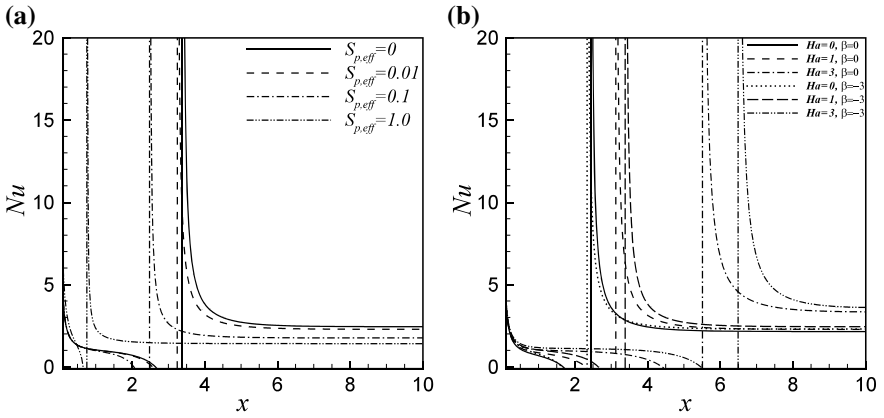

Fig. 16.10 Local Nusselt number (Nu) variations along the axial length (x) of the confinement, for **a** $\zeta = 3$, $\beta = -3$, $Du = 0$, $Ha = 1$, $Pe = 1$, $Br = 1$, and various $S_{p,eff}$; **b** $\zeta = 3$, $Du = 0$, $Pe = 1$, $S_p = 1$, $Br = 1$, and varying Ha, β; **c** $\zeta = 3$, $\beta = -3$, $Ha = 1$, $Pe = 1$, $S_p = 1$, $Br = 1$, and various Du (reproduced with permission from Elsevier publishing, License number: 4592910722206) (Sarkar et al. 2016)

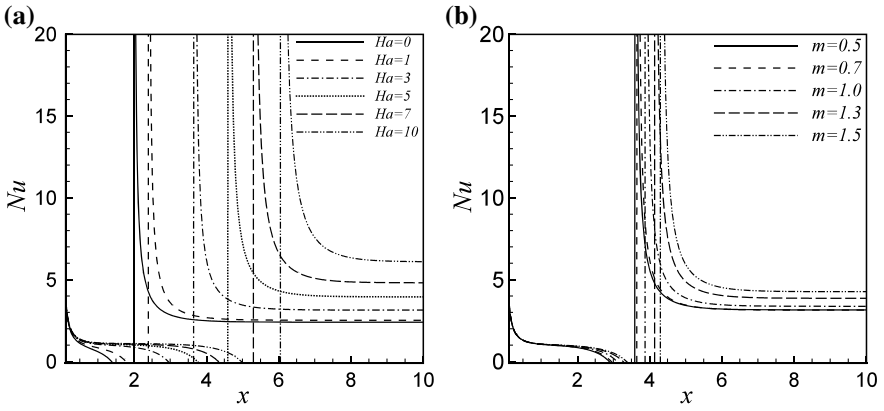

Fig. 16.11 Nusselt number (Nu) variation along the length of the confinement (x) for various values of **a** Hartmann number, Ha, and at $m = 0.7$, $Du = 0$, $S_p = 1$, $Br = 1$, $Pe = 1$; **b** power law index, m, and at $Ha = 3$, $Du = 0$, $S_p = 1$, $Br = 1$, $Pe = 1$ (reproduced with permission from Elsevier publishing, License number: 4592900989884) (Sarkar and Ganguly 2017)

(Nu) variation along the length of the confinement (x) is shown for varying magnitudes of Ha (Fig. 16.11a) and m (Fig. 16.11b); the values of other pertinent parameters are shown in the caption. We see that for power-law obeying non-Newtonian fluids, heat transfer increases with increasing magnitudes of Ha. Analogously, from Fig. 16.11b it is found that heat transfer increases with increasing the values of m. The axial advective transport of the bulk flow increases with increasing m. As a result, at any axial location of the confinement, there is a continuing thinning of the thermal boundary layer thickness. This finally culminates in enhancing the heat transfer magnitude.

In conclusion, in Fig. 16.12 we show a sample result on the fully developed Nusselt number ($Nu_{FD} = \lim_{x\to\infty} Nu(x)$) variation as a function of the Hartmann number (Ha) and the parameter β for electromagnetohydrodynamic electroosmotic flows with non-uniform distribution in the superimposed magnetic field. Through

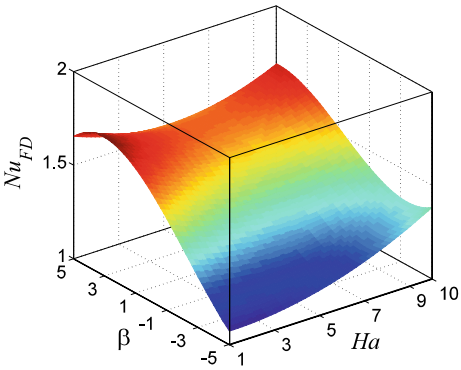

Fig. 16.12 Variations in the fully developed Nusselt number (Nu_{FD}) as a function of the Hartmann number (Ha) and the parameter β, for $\zeta = 3$, $\gamma = 0.3$, $\Lambda = 1$, $Pe = 3$, $S_p = 0.01$, $Br = 0.01$ (reproduced with permission from Elsevier publishing, License number: 4592910028722) (Sarkar et al. 2017a, b)

Fig. 16.12, we demonstrated that it is possible to modulate the heat transfer rate via combined consequences of *Ha*, and the spatial distribution of the non-uniform magnetic field constraint β. It is seen from Fig. 16.12 that heat transfer rate is maximum for particular values of the parameters *Ha* and β. Therefore, it can be concluded that by wisely selecting the optimum distribution of the non-uniform magnetic field strength, maximization of heat transfer from such narrow fluidic confinement can be achieved.

16.3.4 Exergy Analysis for Electromagnetohydrodynamic Transport

The percentage of thermodynamic Irreversibilities in any practical system may be evaluated by the total amount of entropy generated. One may enhance the performance of a system by minimizing the entropy generation and can eventually approach towards thermodynamic idealization. In general, the entropy can be measured by the available lost work, which is an implicit function of friction, temperature gradient, chemical reaction, and mass transfer. Employing the second law of thermodynamics, the contributions of total entropy in the present electromagnetohydrodynamic transport constitute fluid frictional irreversibility and the entropy generation due to heat transfer (Bejan 1982). In mathematical form, these may be expressed in dimensionless form as (Bejan 1982, 2013):

Local entropy generation due to fluid friction:

$$S_{\eta_l} = \wp\left[2\left\{\left(\frac{\partial u}{\partial x}\right)^2 + \left(\frac{\partial v}{\partial y}\right)^2\right\} + \left(\frac{\partial u}{\partial y} + \frac{\partial v}{\partial x}\right)^2\right] \tag{16.35}$$

Local entropy generation due to heat transfer:

$$S_{\theta_l} = \left(\frac{\partial \theta}{\partial x}\right)^2 + \left(\frac{\partial \theta}{\partial y}\right)^2 \tag{16.36}$$

Here the parameter, $\wp$ is the irreversibility distribution ratio and is a direct function of fluid properties and temperature. In the present study, the value of $\wp$ is taken as 10^{-4} (Bejan 2013; Kaluri and Basak 2011). Therefore, the total entropy generation in the system can be written as,

$$S_T = \int_{\Omega} S_{\eta_l} d\Omega + \int_{\Omega} S_{\theta_l} d\Omega \tag{16.37}$$

It may be noted here that for power-law obeying non-Newtonian fluid, the above expression can be written in dimensionless form as,

$$S_T = \frac{1}{(\theta+\Omega)^2}\left\{\left(\frac{\partial\theta}{\partial x}\right)^2+\left(\frac{\partial\theta}{\partial y}\right)^2\right\}-\frac{Nu\,Br}{(\theta+\Lambda)}\left\{\eta^*\left(\frac{\partial u}{\partial y}\right)^2\right\}-Nu\,S_p\frac{E^2}{(\theta+\Lambda)} \tag{16.38}$$

Here $\Omega = T_W \big/ \Delta T_0$, the temperature ratio.

Accordingly, the dimensionless number, namely the Bejan number (Be), representing the relative dominance of entropy generation due to heat transfer and fluid friction irreversibilities, can be written as (Bejan 2013),

$$Be = \frac{S_{\theta,\Omega}}{S_{\theta,\Omega}+S_{\eta,\Omega}} = \frac{S_{\theta,\Omega}}{S_T} \tag{16.39}$$

In general, as reported in literature (Kaluri and Basak 2011), $Be > 0.5$ signifies heat transfer dominated irreversibility and $Be < 0.5$ denotes fluid friction dominated irreversibility (Kaluri and Basak 2011).

For streaming potential mediated flows with interfacial slip, in Fig. 16.13a, b, we show the variation of total entropy generation at a representative axial location of $x = 5$, for different values of Ha, β (Fig. 16.13a), and Du (Fig. 16.13b); other pertinent parameters are mentioned in the figure caption. We see that the total entropy generation reduces with increasing the strength of the magnetic field. The peak magnitude of the entropy generation curve always corresponds to the confinement walls, where majority of changes in the velocity and temperature gradient occurs and as a result rapid thermal convection prevails. Similar trend is also repeated for

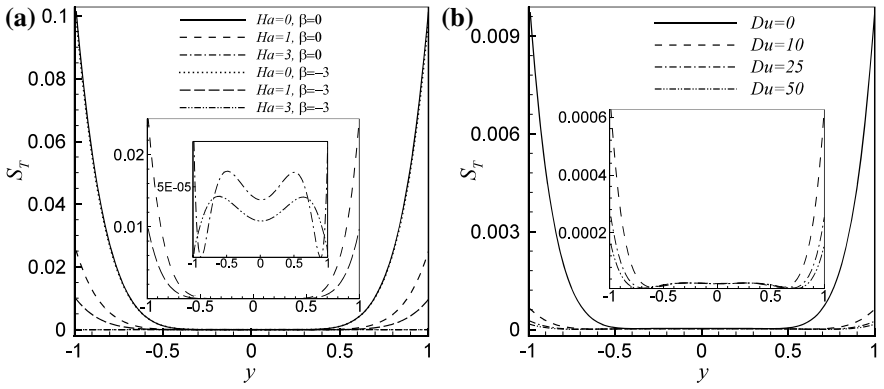

Fig. 16.13 Variation of total entropy generation (S_T) across the width of the confinement at an axial location of $x = 5$, for **a** $\zeta = 3$, $Du = 0$, $Pe = 1$, $S_p = 1$, $Br = 1$, and various Ha, β; **b** $\zeta = 3$, $\beta = -3$, $Ha = 1$, $Pe = 1$, $S_p = 1$, $Br = 1$, and varying Du (reproduced with permission from Elsevier publishing, License number: 4592910722206) (Sarkar et al. 2016)

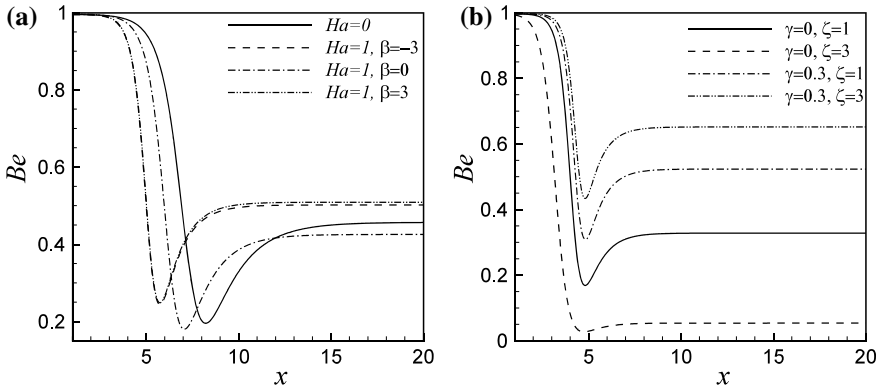

Fig. 16.14 The Bejan number (Be) variations along the length of the confinement (x), for various values of **a** Ha, β, and at $\zeta = 3$, $\gamma = 0.3$, $\Lambda = 1$, $Pe = 3$, $S_p = 0.01$, $Br = 0.01$; **b** ζ, γ, and at $Ha = 3$, $\beta = 1$, $\Lambda = 1$, $Pe = 3$, $S_p = 0.01$, $Br = 0.01$ (reproduced with permission from Elsevier publishing, License number: 4592910028722) (Sarkar et al. 2017a, b)

increasing the value of Du. We found that the Stern layer conductivity leads to a reduction in the total entropy generation. The physical reason, as already explained, is owing to the drop in streaming potential field, which, in turn reduces flow velocity and therefore the convective heat transfer from the walls.

The axial distribution of the Bejan number for electromagnetohydrodynamic electroosmotic flows with non-uniform distribution in the superimposed magnetic field is shown in Fig. 16.14a, b, for various values of Ha, β (Fig. 16.14a) and different values of ζ, γ (Fig. 16.14b). The other parameters have been given in the respective captions. It is observed that along the axial length of the confinement, the value of the Bejan number decreases sharply to its point of minima at a definite axial position and afterward Be increases gradually until a threshold axial location, beyond which it turn out to be an axially invariant. At the thermal entry region, the maximum value of the Bejan number is closer to one, and therefore the primary contribution of the systems irreversibility is due to magnetohydrodynamic convective heat transfer. The growth of the thermal boundary layer at the inlet region results in progressive enhancement in the wall temperature gradients. This culminates in enhancing heat transfer dominated entropy generation. Ahead of the inlet region, reduction in the temperature gradient causes a decrease in the Bejan number value. After the location of the minima, the volumetric heat generation prevails, which augments the temperature gradient at the wall and therefore enhancing the Bejan number value. This increase in the magnitude of Be continues in the downstream direction, until it approaches a threshold position of axial invariance at thermally fully developed region. We note that the fully developed Bejan number, $Be_{FD} = \lim_{x\to\infty} Be(x)$, is $Be_{FD} < 0.5$, when the magnetic field strength is increased. Therefore, pushing the overall irreversibility of the system in the direction of the heat transfer irreversibility dominated regime. Again, in the absence of steric factor, increasing ζ causes a reduction in Be values. However, a contrasting trend is observed when the finite size of the ionic species is considered

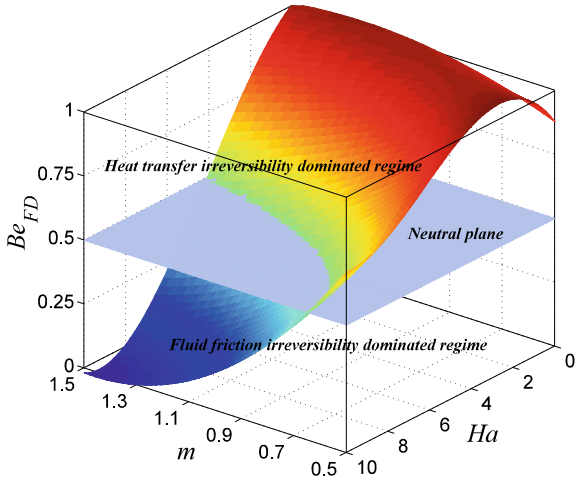

Fig. 16.15 Variations in the fully developed Bejan number (Be_{FD}) as a parametric function of the power law index (m) and the Hartmann number (Ha), for $Du = 0$, $\Omega = -1$, $Pe = 1$, $S_p = 1$, $Br = 1$ (reproduced with permission from Elsevier publishing, License number: 4592900989884) (Sarkar and Ganguly 2017)

($\gamma = 0.3$). The electromagnetohydrodynamically driven thermo-fluidic transport is primarily dominated by the heat transfer ($Be_{FD} > 0.5$) when steric effect is considered ($\gamma \neq 0$), whereas, it falls in the fluid friction dominated regime ($Be_{FD} < 0.5$) in the absence of steric effect ($\gamma = 0$).

To end with, in Fig. 16.15, we demonstrate that the collective effects of magnetic field and fluid rheological situation dictate a pivotal role towards establishing the operating windows of overall thermodynamic irreversibilities for the narrow fluidic system. We observe that for shear thickening fluids, enhancing the magnetic field magnitude diverts the system into fluid friction irreversibility dominated regime. On the other hand, for shear thinning fluids, reducing the magnetic field strength causes the system to enter into the heat transfer irreversibility dominated regime. At $Be_{FD} = 0.5$, the irreversibility map crosses the neutral plane. Hence, we can conclude that it is achievable to tailor the relative dominance of the systems irreversibility with a proper combinations of m, Ha.

16.4 Concluding Remarks

In this chapter, we have detailed electromagnetohydrodynamic thermofluidic control and energy conversion in narrow fluidic confinements through semi-analytical and numerical formalism. Starting from combined electroosmotic and pressure driven flows, we have also extended up to streaming potential mediated flows. Both Newtonian and non-Newtonian fluidic transport mechanism is explored and analyzed in depth. Going beyond the traditional consideration of externally imposed static magnetic field, implications of interfacial electrokinetics under non-uniform magnetic field distribution is also found out. Additional considerations on exergy analysis

through entropy generation function is also analyzed and briefed. We trust this analysis will act as a precursor towards designing of novel energy efficient narrow fluidic devices of promising importance for advance industries. The specific points that may be act as a typical conclusion of this chapter are as follows: For the situation of combined electroosmotic and pressure driven transport in narrow fluidic passage, the effect of spatial variation in the non-uniform magnetic field, degree of surface charging, and steric effect demonstrate an enhancement of thermodynamic efficiency of the system. Heat transfer is found to augment with increasing the magnitude of surface charging, whereas, the opposite scenario is noticed when ionic species are considered to be as point charges. Furthermore, it has been revealed that the system is primarily governed by the heat transfer irreversibility at the thermal entry zone, where the magnitude of the Bejan number becomes $Be > 0.5$. The analytical results on streaming potential mediated magnetohydrodynamic flows in narrow confinement with interfacial slip demonstrated that one can supress the effective volumetric heat generation due to Joule heating and therefore the resulting thermal transport. On the other hand, with an optimal choice of interfacial slip, the heat transfer rate can be enhanced. The effect of increasing magnetic field strength during thermofluidic transport is found to trigger heat transfer rate. Moreover, the theoretical results obtained from this study elucidate a possibility in minimizing the loss of available energy in such a narrow confinement with an appropriate choice of Hartmann number (Ha), slip length, and the Stern layer conductivity (Du). For power law fluids transporting in a narrow confinement, enhancing the strength of the applied magnetic field (Ha) unveiled an exponential decay in the magnitude of the induced streaming potential field, whose value is found to be higher for shear thickening fluid ($m > 1$) than those for shear thinning ($m < 1$) and Newtonian ($m = 1$) fluids. Enhancing the magnitude of magnetic field and power law indices yields momentous amplification in the electro-hydro-dynamic energy conversion efficiency. The rate of heat transfer increases with increasing the values of m. The analysis results have remarkable inferences on the design of advanced energy efficient smart sensors, micromechanical systems, with delicate interaction of magnetic field, electrokinetic effects, and flow rheology.

Acknowledgements Authors would like to thank Elsevier publishing company for extending help in providing necessary copyright clearance in reproducing figures and excerpts for preparing this chapter. The corresponding copyright clearance license numbers are as follows: 4593090971506, 4593090878720, 4593081303140, 4592901310924, 4592910722206, 4592910028722, 4592900989884, 4593081178462, Dated: May 20, 2019.

References

Afonso AM, Alves MA, Pinho FT (2009) Analytical solution of mixed electro-osmotic/pressure driven flows of viscoelastic fluids in microchannels. J Non-Newton Fluid Mech 159:50–63

Andreu JS, Camacho J, Faraudo J, Benelmekki M, Rebollo C, Martinez LIM (2011) Simple analytical model for the magnetophoretic separation of superparamagnetic dispersions in a uniform magnetic gradient. Phys Rev E 84:021402

Bandopadhyay A, Chakraborty S (2011) Steric-effect-induced alterations in streaming potential and energy transfer efficiency of non-Newtonian fluids in narrow confinements. Langmuir 27:12243–12252

Bandopadhyay A, Chakraborty S (2012) Electrokinetically induced alterations in dynamic response of viscoelastic fluids in narrow confinements. Phys Rev E 85:056302

Bandopadhyay A, Chakraborty S (2014) Steric-effect induced alterations in streaming potential and energy transfer efficiency of non-Newtonian fluids in narrow confinements. Langmuir 30:13103–13115

Baudry J, Charlaix E, Tonck A, Mazuyer ED (2001) Experimental evidence for a large slip effect at a nonwetting fluid–solid interface. Langmuir 17:5232–5236

Bejan A (1982) Entropy Generation Minimization. CRC Press, Boca Raton, FL

Bejan A (2013) Convection heat transfer, 4th edn. Wiley, Hoboken, NJ

Berli CLA, Olivares ML (2008) Electrokinetic flow of non-Newtonian fluids in microchannels. J Colloid Interface Sci 320:582–589

Bird RB, Stewart WE, Lightfoot EN (2006) Transport phenomena, Revised 2nd edn. Wiley, New York City, New York (2006)

Burgreen D, Nakache FR (1964) Electrokinetic flow in ultrafine capillary slits. J Phys Chem 68:1084–1091

Chakraborty S (2006) Analytical solutions of Nusselt number for thermally fully developed flow in microtubes under a combined action of electroosmotic forces and imposed pressure gradients. Int J Heat Mass Transf 49:810–813

Chakraborty S (2007) Electroosmotically driven capillary transport of typical non-Newtonian biofluids in rectangular microchannels. Anal Chim Acta 605:175–184

Chakraborty S, Paul D (2006) Microchannel flow control through a combined electromagnetohydrodynamic transport. J Phys D Appl Phys 39:5364–5371

Chakraborty R, Dey R, Chakraborty S (2013) Thermal characteristics of electromagnetohydrodynamic flows in narrow channels with viscous dissipation and Joule heating under constant wall heat flux. Int J Heat Mass Transf 67:1151–1162

Choi CH, Johan K, Westin A, Breuer KS (2003) Apparent slip flows in hydrophilic and hydrophobic microchannels. Phys Fluids 15:2897–2902

Das S, Chakraborty S (2006) Analytical solutions for velocity, temperature and concentration distribution in electroosmotic microchannel flows of a non-newtonian bio-fluid. Anal Chim Acta 559:15–24

Das S, Chakraborty S (2010) Effect of conductivity variations within the electric double layer on the streaming potential estimation in narrow fluidic confinements. Langmuir 26:11589–11596

Das S, Chakraborty S (2011) Steric-effect-induced enhancement of electrical-double-layer overlapping phenomena. Phys Rev E 84:012501

Das S, Chakraborty S, Mitra SK (2012) Magnetohydrodynamics in narrow fluidic channels in presence of spatially non-uniform magnetic fields: framework for combined magnetohydrodynamic and magnetophoretic particle transport. Microfluid Nanofluid 13:799–807

Davidson PA (2001) An introduction to magnetohydrodynamics. Cambridge University Press, NY

Dey R, Chakraborty D, Chakraborty S (2012) Extended Graetz problem for combined electroosmotic and pressure-driven flows in narrow confinements with thick electric double layers. Int J Heat Mass Transf 55:4724–4733

Dey R, Ghonge T, Chakraborty S (2013) Steric-effect-induced alteration of thermal transport phenomenon for mixed electroosmotic and pressure driven flows through narrow confinements. Int J Heat Mass Transf 56:251–262

Garai A, Chakraborty S (2010) Steric effect and slip modulated energy transfer in narrow fluidic channels with finite aspect ratios. Electrophoresis 31:843–849

Goswami P, Chakraborty S (2010) Energy transfer through streaming effects in time-periodic pressure-driven nanochannel flows with interfacial slip. Langmuir 26:581–590

Hadigol M, Nosrati R, Raisee M (2011) Numerical analysis of mixed electroosmotic/pressure driven flow of power-law fluids in microchannels and micropumps. Colloids Surf A Physicochem Eng Asp 374:142–153

Horiuchi K, Dutta P (2004) Joule heating effects in electroosmotically driven microchannels. Int J Heat Mass Transf 47:3085–3095

Huang P, Guasto JS, Breuer KS (2006) Direct measurement of slip velocities using three-dimensional total internal reflection velocimetry. J Fluid Mech 566:447–464

Hunter RJ (1981) Zeta potential in colloid science: principles and applications. Academic Press, London

Jang J, Lee SS (2000) Theoretical and experimental study of MHD (magnetohydrodynamic) micropump. Sens Actuators A Phys 80:84–89

Jian Y (2015) Transient MHD heat transfer and entropy generation in a microparallel channel combined with pressure and electroosmotic effects. Int J Heat Mass Transf 89:193–205

Jian Y, Chang L (2015) Electromagnetohydrodynamic (EMHD) micropumps under a spatially non-uniform magnetic field. AIP Adv 5:057121-1-7

Jones TB (1995) Electromechanics of particles. Cambridge University Press, New York

Kaluri RS, Basak T (2011) Analysis of entropy generation for distributed heating in processing of materials by thermal convection. Int J Heat Mass Transf 54:2578–2594

Lauga E, Brenner MP (2004) Dynamic mechanisms for apparent slip on hydrophobic surfaces. Phys Rev E 70:026311

Levine S, Marriott JR, Neale G, Epstein N (1975) Theory of electrokinetic flow in fine cylindrical capillaries at high zeta potentials. J Colloid Interface Sci 52:136–149

Maynes D, Webb BW (2003) Fully developed electro-osmotic heat transfer in microchannels. Int J Heat Mass Transf 46:1359–1369

Meyer EE, Rosenberg KJ, Israelachvili JN (2006) Recent progress in understanding hydrophobic interactions. Proc Natl Acad Sci USA 103:15739–15746

Moreau RJ (1990) Magnetohydrodynamics. Springer, NY

Munshi F, Chakraborty S (2009) Hydroelectrical energy conversion in narrow confinements in the presence of transverse magnetic fields with electrokinetic effects. Phys Fluids 21(1–9):122003

Nguyen NT (2012) Micro-magnetofluidics: interactions between magnetism and fluid flow on the microscale. Microfluid Nanofluid 12:1–16

Pamme N (2006) Magnetism and microfluidics. Lab Chip MiniatIsation Chem Biol 6:24–38

Patankar SV (2009) Numerical fluid flow and heat transfer. Taylor and Francis, New York, USA

Patankar NA, Hu HH (1998) Numerical simulation of electroosmotic flow. Anal Chem 70:1870–1881

Pati S, Som SK, Chakraborty S (2013) Thermodynamic performance of microscale swirling flows with interfacial slip. Int J Heat Mass Transf 57:397–401

Sarkar S (2017) Studies on multiphase, multi-scale transport phenomena in the presence of superimposed magnetic field. PhD thesis, Dept. of Mech. Engg. IISc Bangalore

Sarkar S, Ganguly S (2017) Characterization of electromagnetohydrodynamic transport of power law fluids in microchannel. J Non-Newton Fluid Mech 250:18–30

Sarkar S, Ganguly S, Dutta P (2016) Thermally developing combined magnetohydrodynamic and electrokinetic transport in narrow confinements with interfacial slip. Int J Heat Mass Transf 100:451–463

Sarkar S, Ganguly S, Dutta P (2017a) Thermofluidic characteristics of combined electroosmotic and pressure driven flows in narrow confinements in presence of spatially non-uniform magnetic field. Int J Heat Mass Transf 104:1325–1340

Sarkar S, Ganguly S, Dutta P (2017b) Electrokinetically induced thermofluidic transport of power-law fluids under the influence of superimposed magnetic field. Chem Eng Sci 171:391–403

Sbragaglia M, Benzi R, Biferale L, Succi S, Toschi F (2006) Surface roughness-hydrophobicity coupling in microchannel and nanochannel flows. Phys Rev Lett 97:204503

Tretheway DC, Meinhart CD (2004) A generating mechanism for apparent fluid slip in hydrophobic microchannels. Phys Fluids 16:1509

Tso CP, Sundaravadivelu K (2001) Capillary flow between parallel plates in the presence of an electromagnetic field. J Phys D 34:3522–3527

Yang C, Li D, Masliyah JH (1998) Modeling forced liquid convection in rectangular microchannels with electrokinetic effects. Int J Heat Mass Transf 41:4229–4249

Yazdi AA, Sadeghi A, Saidi MH (2015) Electrokinetic mixing at high zeta potentials: Ionic size effects on cross stream diffusion. J Colloid Interface Sci 442:8–14

Zhu Y, Granick S (2002) Limits of the hydrodynamic no-slip liquid flow boundary condition. Phys Rev Lett 88:106102

Part VI
Dynamics and Control of Heat and Mass Transfer Systems

Chapter 17
Convective Instabilities and Low Dimensional Modeling

Pinaki Pal, Manojit Ghosh, Ankan Banerjee, Paromita Ghosh, Yada Nandukumar and Lekha Sharma

Abstract Rayleigh-Bénard convection (RBC), where a horizontal layer of fluid is kept between two conducting plates and the system is heated from below, provides a simplified model of convection. RBC is a classical extended dissipative system which displays a plethora of instabilities and patterns very close to the onset of convection for wide range of fluids. The study of these instabilities is an important topic of research and several approaches are available for the investigation. This chapter deals with the low dimensional modeling technique for investigating instabilities and the associated pattern dynamics in RBC.

17.1 Introduction

The study of thermal convection has attracted the attention of the researchers for many years due to its widespread appearance in many natural as well as industrial systems. Examples of systems where convection plays a significant role in the dynamics

P. Pal (✉) · M. Ghosh · A. Banerjee · P. Ghosh · L. Sharma
Department of Mathematics, National Institute of Technology Durgapur, Durgapur 713209, India
e-mail: pinaki.pal@maths.nitdgp.ac.in

M. Ghosh
e-mail: manojitmath@gmail.com

A. Banerjee
e-mail: ankan.mony@gmail.com

P. Ghosh
e-mail: paromitaghosh000@gmail.com

L. Sharma
e-mail: lekhasharma27@gmail.com

Y. Nandukumar
Centre for Theoretical Studies, National Institute of Technology Kharagpur, Kharagpur, West Bengal 713209, India
e-mail: ynandukumar@gmail.com

A. Mukhopadhyay et al. (eds.), *Dynamics and Control of Energy Systems*, Energy, Environment, and Sustainability,
https://doi.org/10.1007/978-981-15-0536-2_17

are atmosphere, interiors of stars and planets, crystal growth industry, liquid metal blanket etc. (Hartmann et al. 2001; Busse 1989; Miesch 2000; Hurle and Series 1994; Kirillov et al. 1995; Glatzmaier et al. 1999). Investigating thermal convection in these real systems is often very complicated, as it may occur under arbitrary geometry in presence of additional factors like magnetic field, rotation etc. However, to understand the basic physics of convection, researchers consider a simplified model of convection called Rayleigh-Bénard convection.

In this chapter, we consider RBC under rectangular geometry, which consists of a thin layer of fluid, infinitely extended in horizontal directions, kept between two horizontal conducting plates and the system is heated from below. The study of thermal convection under this simplified model, has not only contributed significantly to the understanding of basic physics of convection but also played crucial role in the developments of the subjects like hydrodynamic instabilities (Chandrasekhar 1961; Drazin and Reid 1981; Verma 2018), pattern formation (Cross and Hohenberg 1993; Croquette 1989a, b) and nonlinear dynamics (Manneville 1990; Getling 1998; Busse 1978).

In spite of its simplicity, RBC exhibits a plethora of interesting convective phenomena including instabilities, patterns, chaos and turbulence etc. The study of these instabilities, patterns, chaos and turbulence for different fluids are important topics of research in RBC for many years and still an active area of research (Chandrasekhar 1961; Ahlers et al. 2009; Bodenschatz et al. 2000; Lohse and Xia 2010; Busse 1985; Pal and Kumar 2002; Nandukumar and Pal 2016; Dan et al. 2015, 2014; Pal et al. 2013; Dan et al. 2017).

In this chapter, we discuss low dimensional modeling technique for investigating convective instabilities and the associated pattern dynamics near the onset of convection under rectangular Rayleigh-Bénard geometry. This technique can be used for investigating instabilities in a variety of extended dissipative systems including rotating convection (Veronis 1966, 1959; Maity et al. 2013; Maity and Kumar 2014; Pharasi and Kumar 2013), binary mixture (Kumar 1990), magnetoconvection (Pal and Kumar 2012; Basak and Kumar 2015; Nandukumar and Pal 2015), and rotating magnetoconvection (Ghosh and Pal 2017).

17.2 Physical System

We consider RBC system consisting of a thin horizontal layer of fluid of thickness d, thermal expansion coefficient α, kinematic viscosity ν and thermal diffusivity κ confined between two conducting plates. The system is heated from below. A schematic diagram showing a cross sectional view of the RBC set up has been shown in Fig. 17.1. The temperatures of the lower and upper plates are fixed at T_l and T_u respectively so that an adverse temperature gradient $\beta = \frac{T_l - T_u}{d}$ is maintained.

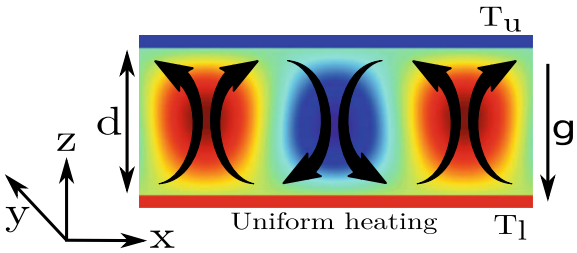

Fig. 17.1 Sectional view of a Rayleigh-Bénard convection set up on a plane perpendicular to y-axis

The above physical system is governed by the following set of equations (Chandrasekhar 1961):

1. *Equation of continuity*:

$$\frac{\partial \rho}{\partial t} + \nabla \cdot (\rho \mathbf{v}) = 0, \tag{17.1}$$

   where the symbols ρ, $\mathbf{v}$ and t respectively denote fluid density, velocity and time.
2. *Energy balance equation*:

$$\rho \left[\frac{\partial}{\partial t}(C_V \mathrm{T}) + (\mathbf{v} \cdot \nabla)(C_V \mathrm{T}) \right] = \nabla \cdot (k \nabla \mathrm{T}) + \Phi - P(\nabla \cdot \mathbf{v}), \tag{17.2}$$

   where C_V, T, P, k and Φ represent specific heat at constant volume, temperature, pressure, co-efficient of heat conduction and heat dissipation term respectively.
3. *Equation of motion*:

$$\rho \left[\frac{\partial \mathbf{v}}{\partial t} + (\mathbf{v} \cdot \nabla)\mathbf{v} \right] = \rho g \hat{\mathbf{e}}_3 - \nabla P + \mu \nabla^2 \mathbf{v} + \frac{\mu}{3} \nabla (\nabla \cdot \mathbf{v}), \tag{17.3}$$

   where g is the acceleration due to gravity, $\hat{\mathbf{e}}_3$ is the unit vector along vertically upward direction and μ is the dynamic viscosity of the fluid.

Equations (17.1)–(17.3) are the basic hydrodynamic equations of RBC. Now Eqs. (17.1)–(17.3) are supplemented by the equation of state

$$\rho = \rho_0 [1 - \alpha(\mathrm{T} - \mathrm{T}_l)], \tag{17.4}$$

where α is the coefficient of volume expansion of the fluid and ρ_0 is the reference density of the fluid.

17.3 Boussinesq Approximation

Boussinesq approximation is widely used by the scientists for studying RBC (Chandrasekhar 1961; Boussinesq 1903; Verma 2018). Under this approximation, density is considered to be constant in all terms of the governing equations except in

the buoyancy term of the equation of motion where the variation of density due to temperature change is taken into account. Moreover, fluid properties like kinematic viscosity, thermal diffusivity are assumed to be constant. Under this approximation, Eq. (17.1) becomes,

$$\nabla \cdot \mathbf{v} = 0, \tag{17.5}$$

and Eqs. (17.2) and (17.3) respectively change to

$$\frac{\partial \mathrm{T}}{\partial t} + (\mathbf{v} \cdot \nabla)\mathrm{T} = \kappa \nabla^2 \mathrm{T}, \tag{17.6}$$

$$\frac{\partial \mathbf{v}}{\partial t} + (\mathbf{v} \cdot \nabla)\mathbf{v} = (1 + \frac{\delta\rho}{\rho_0}) g\hat{e}_3 - \frac{1}{\rho_0}\nabla P + \nu \nabla^2 \mathbf{v}, \tag{17.7}$$

where $\delta\rho$ is the change in density, $\nu = \frac{\mu}{\rho_0}$ is kinematic viscosity and $\kappa = \frac{k}{\rho_0 C_V}$ is the thermal diffusivity of the fluid.

17.4 Perturbation Equations

To study convective flow, we derive perturbation equations for the convective states using the equations of the basic (conduction) state. In the following subsection basic state equations are derived.

17.4.1 Basic State

In conduction state, the fluid is motionless. Therefore, we have

$$\mathbf{v}_b = (\mathrm{v}_1, \mathrm{v}_2, \mathrm{v}_3) \equiv (0, 0, 0), \ \mathrm{T_b} \equiv \ \mathrm{T(z)}, \tag{17.8}$$

where $\mathbf{v}_b$ and $\mathrm{T_b}$ are the velocity and temperature at the basic state. Now, temperature $\mathrm{T_b}$ of the fluid in basic state is deduced from Eq. (17.6) which is given by

$$\mathrm{T_b}(z) = \mathrm{T_l} - \beta z, \tag{17.9}$$

where $\mathrm{T_l}$ is the temperature at the bottom layer, d is the thickness of the fluid layer and $\beta d \ \ (= \triangle \mathrm{T} = \mathrm{T_l} - \mathrm{T_u})$ is the temperature difference of the lower and upper plates.
The density distribution is then given by,

$$\rho_b(z) = \rho_0(1 - \alpha\beta z), \tag{17.10}$$

where ρ_0 is the reference fluid density and α is the coefficient of volume expansion of the fluid.

Hence the pressure distribution for this basic state is obtained by using Eqs. (17.8), (17.9) and (17.10) in Eq. (17.7) which is given by

$$P_b(z) = P_0 - g\rho_0(z + \frac{1}{2}\alpha\beta z^2), \tag{17.11}$$

where $P_b(z)$ is pressure distribution of the fluid in basic state and P_0 is the reference pressure of the fluid.

17.4.2 Convective State

As convection sets in, the basic fields given by Eqs. (17.8), (17.9), (17.10) and (17.11) are perturbed and let they are described by,

$$\begin{aligned}
\mathrm{T_b(z)} \rightarrow \mathrm{T(x,y,z,t)} &= \mathrm{T_b(z)} + \theta(x,y,z,t),\\
\mathrm{P_b(z)} \rightarrow \mathrm{P(x,y,z,t)} &= \mathrm{P_b(z)} + p(x,y,z,t),\\
\mathbf{v}_\mathrm{b}(\mathrm{x,y,z,t}) \rightarrow \mathbf{v}(\mathrm{x,y,z,t}) &= \mathbf{v}_b(x,y,z,t) + \mathbf{v}(x,y,z,t),\\
\rho_\mathrm{b}(\mathrm{z}) \rightarrow \rho(\mathrm{x,y,z,t}) &= \rho_\mathrm{b}(\mathrm{z}) + \delta\rho = \rho_\mathrm{b}(\mathrm{z}) - \rho_0\alpha\theta,
\end{aligned}$$

where $T(x,y,z,t)$, $P(x,y,z,t)$, $\mathbf{v}(x,y,z,t) = (v_1, v_2, v_3)$ and $\rho(x,y,z,t)$ are convective temperature, pressure, velocity and density fields respectively. The fields θ, p, $\mathbf{v}$ and $\delta\rho$ are the perturbations over the basic conduction state. Now, the equations of motion, the energy equation and equation of continuity, for perturbed fields change to

$$\frac{\partial \mathbf{v}}{\partial t} + (\mathbf{v}\cdot\nabla)\mathbf{v} = -\frac{\nabla p}{\rho_0} + g\alpha\hat{\mathbf{e}}_3\theta + \nu\nabla^2\mathbf{v}, \tag{17.12}$$

$$\frac{\partial \theta}{\partial t} + (\mathbf{v}\cdot\nabla)\theta = \beta\hat{\mathbf{e}}_3\cdot\mathbf{v} + \kappa\nabla^2\theta, \tag{17.13}$$

$$\nabla\cdot\mathbf{v} = 0. \tag{17.14}$$

17.5 Boundary Conditions

Mathematical description of a physical system should include proper boundary conditions along with the governing equations. In this section we discuss about the boundary conditions we have used to demonstrate the low dimensional modeling technique. Now, irrespective of the nature of bounding surfaces, we must have $v_3 = 0$ at the horizontal bounding surfaces. The top and bottom plates are maintained at constant

temperatures, which imply $\theta = 0$. In this chapter, we consider *free-slip* boundaries which mean the tangential stresses at the bounding plates vanish. Therefore, one gets

$$\frac{\partial v_1}{\partial z} = \frac{\partial v_2}{\partial z} = 0 \text{ at the boundaries.} \tag{17.15}$$

Now differentiating the equation of continuity (17.14) with respect to z and using (17.15), we get

$$\frac{\partial^2 v_3}{\partial z^2} = 0, \quad \text{on free-slip boundaries.} \tag{17.16}$$

The vertical component of vorticity will satisfy

$$\frac{\partial \omega_3}{\partial z} = 0, \quad \text{on free-slip surfaces.} \tag{17.17}$$

17.6 Nondimensionalization

To reduce the number of free parameters and the problems due to the large variation of the values of the parameters, Eqs. (17.12)–(17.14) are made dimensionless. In this chapter, we study convection in two different kinds of fluids namely high Prandtl-number (Pr $>$ 1) and low Prandtl-number (Pr $<$ 1) fluids.

For low Prandtl-number fluid convection, we nondimensionalize the governing equations using the units d for length, viscous diffusion time $\frac{d^2}{\nu}$ for time and $\frac{\nu\beta d}{\kappa}$ for temperature. Now if the primed quantities x', y', z', t' and θ' denote the dimensionless quantities then the dimensional variables can be written as

$$x = dx', y = dy', z = dz', t = \frac{d^2}{\nu}t' \text{ and } \theta = \frac{\nu\beta d}{\kappa}\theta'.$$

Using these quantities, Eqs. (17.12)–(17.14) can be written in the dimensionless form as

$$\frac{\partial \mathbf{v}'}{\partial t'} + (\mathbf{v}' \cdot \nabla')\mathbf{v}' = -\nabla' p' + \nabla'^2 \mathbf{v}' + \mathrm{Ra}\theta' \hat{e}_3, \tag{17.18}$$

$$\mathrm{Pr}\left[\frac{\partial \theta'}{\partial t'} + (\mathbf{v}' \cdot \nabla')\theta'\right] = \nabla'^2 \theta' + v_3', \tag{17.19}$$

$$\nabla' \cdot \mathbf{v}' = 0, \tag{17.20}$$

where $\mathrm{Ra} = \frac{\alpha\beta g d^4}{\nu\kappa}$ and $\mathrm{Pr} = \frac{\nu}{\kappa}$ are two nondimensional numbers namely the Rayleigh number, which is the ratio of buoyancy and dissipative forces and the Prandtl number,

which is the ratio of kinematic viscosity and thermal diffusivity respectively.

On the other hand, for high Prandtl number fluids, we use the scales $\frac{\beta d}{\mathrm{Ra}}$ for temperature, thermal diffusion time scale $\frac{d^2}{\kappa}$ for time and other scales same as the low Prandtl-number fluids to nondimensionalize the governing equations. The dimensionless equations in this case become

$$\frac{\partial \mathbf{v}'}{\partial t'} + (\mathbf{v}' \cdot \nabla')\mathbf{v}' = -\nabla' p' + \mathrm{Pr}\nabla'^2 \mathbf{v}' + \mathrm{Pr}\theta' \hat{e}_3, \tag{17.21}$$

$$\frac{\partial \theta'}{\partial t'} + (\mathbf{v}' \cdot \nabla')\theta' = \nabla'^2 \theta' + \mathrm{Ra} v_3', \tag{17.22}$$

$$\nabla' \cdot \mathbf{v}' = 0. \tag{17.23}$$

In the subsequent sections we use the above dimensionless set of equations by dropping the primes from all the variables and operators.

17.7 Linear Theory

We now determine the critical Rayleigh number (Ra_c) and critical wave number (k_c) at the onset of convection using the linear theory (Chandrasekhar 1961). The linearized version of Eqs. (17.18)–(17.20) are given by

$$\frac{\partial \mathbf{v}}{\partial t} = -\nabla p + \nabla^2 \mathbf{v} + \mathrm{Ra}\theta \hat{\mathbf{e}}_3, \tag{17.24}$$

$$\mathrm{Pr}\frac{\partial \theta}{\partial t} = v_3 + \nabla^2 \theta, \tag{17.25}$$

$$\nabla \cdot \mathbf{v} = 0. \tag{17.26}$$

Taking twice curl of Eq. (17.24) we get the following equation

$$\frac{\partial}{\partial t}\nabla^2 v_3 = \nabla^4 v_3 + \mathrm{Ra}\nabla_H^2 \theta, \tag{17.27}$$

for the vertical velocity, where $\nabla_H^2 = \frac{\partial^2}{\partial x^2} + \frac{\partial^2}{\partial y^2}$ is the horizontal Laplacian. Eliminating θ from (17.27) using (17.25) we get

$$[\nabla^2(\mathrm{Pr}\partial_t - \nabla^2)(\partial_t - \nabla^2) - \mathrm{Ra}\nabla_H^2]v_3 = 0. \tag{17.28}$$

We consider the expansion of vertical velocity in normal modes as

$$v_3(x, y, z, t) = W(z) exp[i(k_x x + k_y y) + \sigma t], \tag{17.29}$$

where, k_x and k_y are the wave numbers along x and y direction respectively and $k = \sqrt{k_x^2 + k_y^2}$ is the horizontal wave number. Inserting Eq. (17.29) in Eq. (17.28), and choosing a trial solution $W(z) = Asin(n\pi z)$, which is compatible with the boundary conditions, we arrive at the stability condition

$$(n^2\pi^2 + k^2)(n^2\pi^2 + k^2 + \mathrm{Pr}\sigma)(n^2\pi^2 + k^2 + \sigma) = \mathrm{Ra}k^2. \tag{17.30}$$

Since we are interested in stationary convection we set $\sigma = 0$ in Eq. (17.30) to get

$$(n^2\pi^2 + k^2)^3 = \mathrm{Ra}k^2. \tag{17.31}$$

Therefore, the Rayleigh number Ra is given by

$$\mathrm{Ra} = \frac{(n^2\pi^2 + k^2)^3}{k^2}. \tag{17.32}$$

We now find the minimum value of Ra which is the critical Rayleigh number (Ra_c) for the onset of convection together with the corresponding critical wave number k_c. From Eq. (17.32) we observe that the minimum value of Ra occurs for a given k^2 when $n = 1$. Therefore we have

$$\mathrm{Ra} = \frac{(\pi^2 + k^2)^3}{k^2}. \tag{17.33}$$

The above equation imply that for all values of Ra less than that are given by Eq. (17.33), disturbances associated with wave number k decay, while the same disturbances grow when Ra exceeds the value given by (17.33). When the value of Ra equals the value given by Eq. (17.33), the disturbances with wave number k become marginally stable. Therefore, the Ra_c is determined by the condition

$$\frac{\partial \mathrm{Ra}}{\partial k^2} = \frac{(\pi^2 + k^2)^2(2k^2 - \pi^2)}{k^4} = 0. \tag{17.34}$$

Which gives us $k^2 = \frac{\pi^2}{2}$ and the corresponding value of Ra_c as

$$\mathrm{Ra}_c = \frac{27}{4}\pi^4 \sim 657.5114. \tag{17.35}$$

Note that we get same critical values of the Rayleigh number (Ra_c) and critical wave number (k_c) even if we consider Eqs. (17.21)–(17.23) at the outset. In the following discussion, we use another parameter called reduced Rayleigh number defined by $r = \frac{\mathrm{Ra}}{\mathrm{Ra}_c}$.

17.8 Direct Numerical Simulations

For low dimensional modeling, the performance of direct numerical simulations for some set of parameter values and the data obtained from there can be of great help. Therefore, before going for low dimensional modeling, we perform DNS of the system using a pseudo spectral code Tarang (Verma et al. 2013). In the simulation, vertical velocity (v_3), vertical vorticity (ω_3) and temperature (θ) fields are expanded using the set of orthogonal basis functions either with respect to $\{e^{i(lk_x x+mk_y y)}\sin(n\pi z) : l, m, n = 0, 1, 2, \ldots\}$ or with respect to $\{e^{i(lk_x x+mk_y y)}\cos(n\pi z) : l, m, n = 0, 1, 2, \ldots\}$ whichever is compatible with the free-slip boundary conditions, where k_x, k_y are the wave numbers along x and y directions respectively. Therefore, the expressions of vertical velocity, vertical vorticity and temperature fields are given by

$$\mathrm{v}_3(x, y, z, t) = \sum_{l,m,n} W_{lmn}(t)e^{i(lk_x x+mk_y y)}\sin(n\pi z), \tag{17.36}$$

$$\omega_3(x, y, z, t) = \sum_{l,m,n} Z_{lmn}(t)e^{i(lk_x x+mk_y y)}\cos(n\pi z), \tag{17.37}$$

$$\text{and } \theta(x, y, z, t) = \sum_{l,m,n} T_{lmn}(t)e^{i(lk_x x+mk_y y)}\sin(n\pi z). \tag{17.38}$$

In the simulation, we set $k_x = k_y = k_c = \frac{\pi}{\sqrt{2}}$, the critical wave number. The aspect ratio of the simulations is $\frac{2\pi}{k_c} : \frac{2\pi}{k_c} : 1 \equiv 2\sqrt{2} : 2\sqrt{2} : 1$. An open source software called Fastest Fourier transform in the west (FFTW) (Frigo and Johnson 2005) is used for computations in the Fourier space. Inverse Fourier transform routines of the same package are used for mapping to the real space. For time advancement, fourth order Runge-Kutta scheme with Courant-Friedrichs-Lewy (CFL) condition is used in the code. Mostly 32^3 grid resolution is considered for the simulations. Note that, 32^3 grid resolution means the values of l, m and n in the above expansions are run over the integers set $\{0, 1, 2, \ldots, 31\}$. In the following we present some results of DNS for illustrating low dimensional modeling technique.

17.8.1 Onset of Convection for Pr = 10

We perform DNS of the system for Pr = 10 to investigate the flow patterns close to the onset of convection. Note that Eqs. (17.21)–(17.23) are used for the simulation. Figure 17.2 shows the time series of W_{101} and W_{011} as well as flow pattern as observed in DNS at $r = 5$. The flow pattern in this case is found to be two dimensional (2D) rolls. This type of flow patterns are reported for high Prandtl number fluid convection in Krishnamurti (1970), Busse and Whitehead (1971). In Sect. 17.9.1 we'll show the derivation of famous Lorenz model (1963) by using low dimensional modeling technique and describe the origin of 2D rolls pattern at the onset of convection.

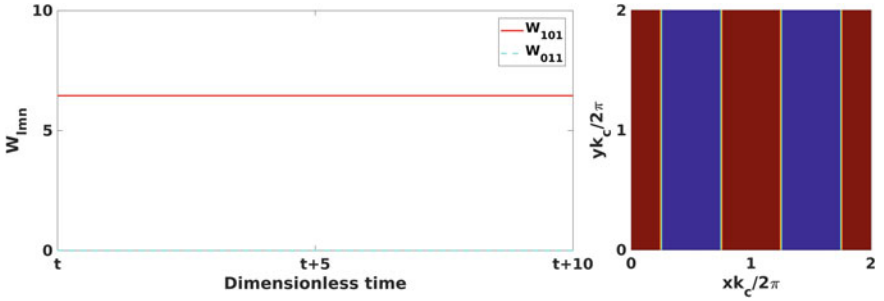

Fig. 17.2 Time series of the Fourier modes W_{101} and W_{011} and flow patterns corresponding to 2D rolls solutions as obtained from DNS for $r = 5$ and $\mathrm{Pr} = 10$. Isotherms computed at the mid plane $z = 0.5$ generate the pattern. Brown and blue regimes on the patterns represent hotter and colder regions

17.8.2 Onset of Convection for Low Prandtl Number Fluids in the Limit $\mathbf{Pr \to 0}$.

It has been shown earlier that the low Prandtl number fluid convection can be approximated by considering the limit $\mathrm{Pr} \to 0$ (Thual 1992; Busse 1972; Pal et al. 2009, 2013). In this limit, the temperature Eq. (17.19) reduces to

$$\nabla^2\theta = -v_3. \tag{17.39}$$

We now simulate Eqs. (17.18), (17.20) and (17.39) to get an idea about the pattern dynamics and bifurcation structure near the onset of convection. Figure 17.3 shows the time evolution of the significant Fourier modes and associated pattern dynamics as obtained from DNS for $r = 1.04$. From the figure, it is clear that 2D rolls flow patterns oriented along y and x axes are periodically evolved with intermediate square patterns. This flow regime is called oscillatory cross rolls of type-I (OCR-I). Interestingly, for a higher r stationary solution is observed in DNS. Figure 17.4 shows the time series as well as flow pattern corresponding to this stationary solution. From the time series we observe that the solution is stationary with $W_{101} = W_{011}$ and pattern is of stationary square (SQ) type. These DNS results are intriguing, investigation of the origin of these flow patterns and the associated bifurcation structure follow naturally. However, this is difficult to achieve in DNS, because, on one hand it is costly in terms of computer time and on the other hand, DNS only capture the stable solutions of the system and can not identify the unstable solutions. Due to this reason, low dimensional models can be very useful. In the next section, we discuss how a low dimensional model can be derived from the DNS data and successfully explains the origin of different flow patterns to unfold a very rich bifurcation.

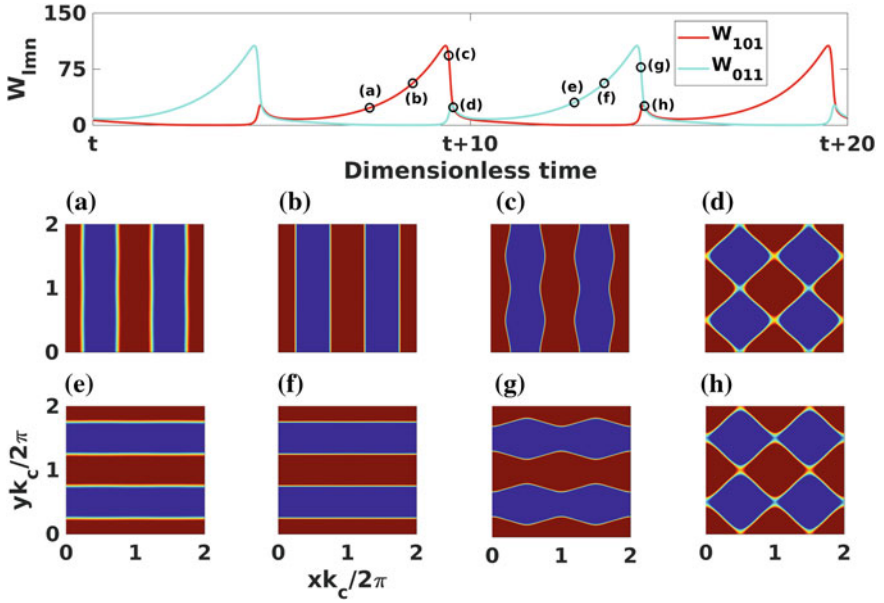

Fig. 17.3 Time series of the Fourier modes W_{101} and W_{011} (first row) and flow patterns corresponding to OCR-I solutions as obtained from DNS (second and third rows) for $r = 1.04$. The flow patterns (**a**–**h**) correspond to the instants shown on the time series of the top panel. The flow patters are isotherms computed at the mid plane $z = 0.5$

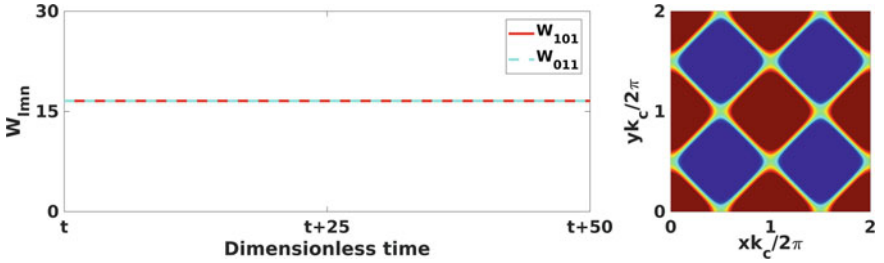

Fig. 17.4 Time series of the Fourier modes W_{101} and W_{011} (left) and flow patterns corresponding to SQ solutions as obtained from DNS (right) for $r = 1.28$. The flow patterns are isotherms computed at the mid plane $z = 0.5$. Brown regimes are hotter and blue regimes are colder

17.9 Low Dimensional Modeling

We use standard Galerkin technique (Galerkin 1915) to construct the low dimensional models. To start with, large scale modes in the vertical velocity, vertical vorticity and temperature are selected from the DNS data by computing the energy contained in the modes relative to the total energy. Then we retain only those modes in the expansions of the vertical velocity (v_3), vertical vorticity (ω_3) and temperature (θ) and write truncated series for these independent variables.

The horizontal components of velocity field are then determined by using the solenoidal property of the velocity and vorticity fields which leads to the expressions:

$$\nabla_H^2 \mathrm{v}_1 = -\frac{\partial \omega_3}{\partial y} - \frac{\partial^2 \mathrm{v}_3}{\partial x \partial z}, \tag{17.40}$$

$$\nabla_H^2 \mathrm{v}_2 = \frac{\partial \omega_3}{\partial x} - \frac{\partial^2 \mathrm{v}_3}{\partial y \partial z}. \tag{17.41}$$

where $\nabla_H^2 \equiv \frac{\partial^2}{\partial x^2} + \frac{\partial^2}{\partial y^2}$ is the horizontal Laplacian. The expressions for ω_1 and ω_2 are now obtained by taking the *curl* of the velocity vector $\mathbf{v} \equiv (\mathrm{v}_1, \mathrm{v}_2, \mathrm{v}_3)$. Once the components of velocity, vorticity and temperature are calculated, for low Prandtl number fluids we take curl twice of Eq. (17.18) and determine the following two equations for vertical velocity and vorticity:

$$\begin{aligned} \partial_t(\nabla^2 \mathrm{v}_3) &= \nabla^4 \mathrm{v}_3 + \mathrm{Ra}\nabla_H^2 \theta \\ &\quad - \hat{\mathbf{e}}_3 \cdot \nabla \times [(\boldsymbol{\omega}\cdot\nabla)\mathbf{v} - (\mathbf{v}\cdot\nabla)\boldsymbol{\omega}], \end{aligned} \tag{17.42}$$

$$\partial_t \omega_3 = \nabla^2 \omega_3 + [(\boldsymbol{\omega}\cdot\nabla)\mathrm{v}_3 - (\mathbf{v}\cdot\nabla)\omega_3]. \tag{17.43}$$

On the other hand, for high Prandtl number fluids, we take curl of Eq. (17.21) twice and get

$$\begin{aligned} \partial_t(\nabla^2 \mathrm{v}_3) &= \mathrm{Pr}\nabla^4 \mathrm{v}_3 + \mathrm{Pr}\nabla_H^2 \theta \\ &\quad - \hat{\mathbf{e}}_3 \cdot \nabla \times [(\boldsymbol{\omega}\cdot\nabla)\mathbf{v} - (\mathbf{v}\cdot\nabla)\boldsymbol{\omega}], \end{aligned} \tag{17.44}$$

$$\partial_t \omega_3 = \mathrm{Pr}\nabla^2 \omega_3 + [(\boldsymbol{\omega}\cdot\nabla)\mathrm{v}_3 - (\mathbf{v}\cdot\nabla)\omega_3]. \tag{17.45}$$

Then we substitute the expressions of v_1, v_2, v_3, ω_1, ω_2, ω_3 and θ in Eqs. (17.42), (17.43) and (17.19) for low Prandtl-number fluids, while for high Prandtl number fluids we substitute the same in Eqs. (17.44), (17.45) and (17.22) and use the orthogonality property of the functions $\{e^{i(lk_x x + mk_y y)} \sin(n\pi z) : l, m, n = 0, 1, 2, \ldots\}$ and $\{e^{i(lk_x x + mk_y y)} \cos(n\pi z) : l, m, n = 0, 1, 2, \ldots\}$ over the intervals $[0, \frac{2\pi}{k_x}]$, $[0, \frac{2\pi}{k_y}]$ and $[0, 1]$ along x-, y- and z- axis respectively to obtain a set of coupled nonlinear ordinary differential equations of the large-scale amplitudes of the large scale modes of v_3, ω_3 and θ which is our low-dimensional model. These low dimensional models are then analyzed using the theory of nonlinear dynamics (Strogatz 2001) and continuation software like MATCONT (Dhooge et al. 2003).

17.9.1 The Lorenz Model

AS mentioned above, to study the onset of convection in high Prandtl number fluids using low dimensional modeling we identify the large scale modes from the DNS data by calculating the contribution of a mode to the total energy. We find from the

DNS data that near the onset of convection for Pr = 10, the mode $W_{101}\cos k_c x \sin \pi z$ in v_3 contributes most to the energy and vertical vorticity is not developed. Therefore, we choose

$$\mathrm{v}_3 = W_{101}(t)\cos k_c x \sin \pi z \text{ and } \omega_3 = 0.$$

The horizontal components of the velocity computed using Eqs. (17.40) and (17.41) are given by

$$\mathrm{v}_1 = -\frac{\pi}{k_c} W_{101}(t)\sin k_c x \cos \pi z \text{ and } \mathrm{v}_2 = 0. \tag{17.46}$$

Now from Eq. (17.22) we observe that θ linearly couples with v_3. Therefore, we take

$$\theta = T_{101}(t)\cos k_c x \sin \pi z. \tag{17.47}$$

As the linear growth rate of the mode W_{101} is positive above the onset of convection, for saturation, Lorenz (1963) considered least nonlinear correction in θ in terms of the mode $T_{002}(t)\sin 2\pi z$ and the expression for θ becomes

$$\theta = T_{101}(t)\cos k_c x \sin \pi z + T_{002}(t)\sin 2\pi z. \tag{17.48}$$

Horizontal components of vorticity then become

$$\omega_1 = 0 \tag{17.49}$$

$$\text{and } \omega_2 = \frac{\pi^2}{k_c} W_{101}(t)\sin k_c x \sin \pi z. \tag{17.50}$$

Substituting the expressions of $\mathrm{v}_1, \mathrm{v}_2, \mathrm{v}_3, \omega_1, \omega_2, \omega_3$ and θ in Eqs. (17.44) and (17.22) and using the orthogonality property of the basis functions we get,

$$\dot{W_{101}} = \frac{\mathrm{Pr}k_c^2}{k_c^2+\pi^2} T_{101} - \mathrm{Pr}(k_c^2+\pi^2)W_{101}, \tag{17.51}$$

$$\dot{T_{101}} = -(k_c^2+\pi^2)T_{101} + \mathrm{Ra}W_{101} + \pi T_{002}W_{101}, \tag{17.52}$$

$$\dot{T_{002}} = -4\pi^2 T_{002} - \frac{\pi}{2} W_{101}T_{101}. \tag{17.53}$$

The method described above for deriving this model is called Galerkin projection (1915). Now using the transformation $\tau = (k_c^2+\pi^2)t$, $X = \frac{k_c}{k_c^2+\pi^2} W_{101}$, $Y = \frac{k_c^3}{(k_c^2+\pi^2)^3} T_{101}$ and $Z = -\frac{\pi k_c^2}{(k_c^2+\pi^2)^3} T_{002}$, the above set of ordinary differential equations transforms to the following Lorenz model (1963)

$$\dot{X} = \mathrm{Pr}(Y - X), \tag{17.54}$$

$$\dot{Y} = X(r - Z) - Y, \tag{17.55}$$

$$\dot{Z} = XY - \beta Z, \tag{17.56}$$

where $\beta = \frac{4\pi^2}{k_c^2+\pi^2}$.

We now construct a bifurcation diagram of the Lorenz model using the MATCONT software (Dhooge et al. 2003) for Pr $= 10$ and r is varied in the range $0 < r \leq 10$ (see Fig. 17.5). The conduction state is stable for $r < 1$ and at $r = 1$ it becomes unstable via a supercritical pitchfork bifurcation. Two stable 2D rolls branches (solid blue and black curves) are originated from there. The stream lines corresponding to these solution branches are shown inside Fig. 17.5 and are found to be counter rotating. Flow pattern for these solutions and time series of X are also shown in the figure. In spite of drastic simplification, these results of Lorenz model are found to match closely with the DNS results. However, the results of Lorenz model starts deviating for large values of r and in that case one has to go for higher nonlinear corrections to get the satisfactory results.

17.9.2 A Four Dimensional Model for Zero-Prandtl Number Convection

In this subsection, we discuss the derivation of another low dimensional model to investigate instabilities and bifurcation structure near the onset of convection of low

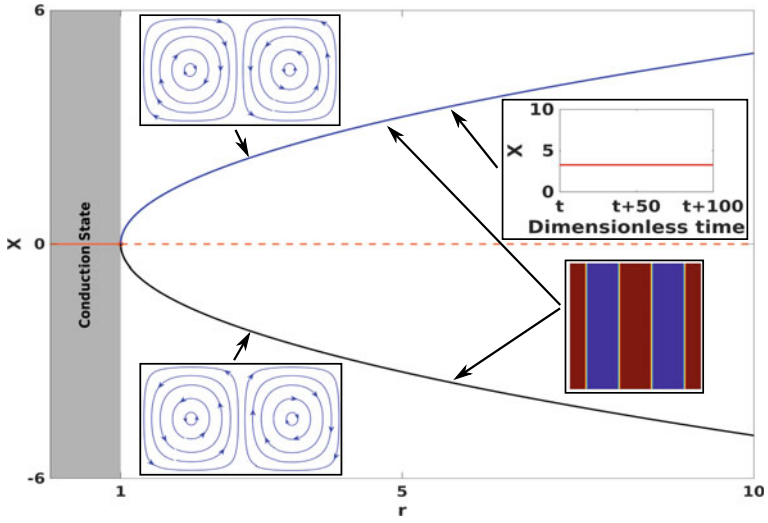

Fig. 17.5 Bifurcation diagram constructed from the Lorenz model for Pr $= 10$ and $0 < r \leq 10$. Values of X corresponding to different stationary solutions are shown with different colors. Solid and dashed orange curves represent the stable and unstable conduction state respectively. Blue and black curves represent two 2D rolls branches connected by the symmetry of the Lorenz model ($X \to -X, Y \to -Y$ and $Z \to Z$). Streamlines, flow patterns and time series associated with these branches are also shown

Prandtl-number fluids in the vanishing Prandtl number limit (Pr → 0). Here also we select the large scale modes from DNS data by calculating contributions of each selected mode to the total energy. In this process, we select the following expressions of v_3 and ω_3:

$$\begin{aligned} v_3 &= W_{101}(t)\cos k_c x \sin \pi z + W_{011}(t)\cos k_c y \sin \pi z \\ &+ W_{112}(t)\cos k_c x \cos k_c y \sin 2\pi z + W_{121}(t)\cos k_c x \cos 2k_c y \sin \pi z \\ &+ W_{211}(t)\cos 2k_c x \cos k_c y \sin \pi z, \end{aligned} \tag{17.57}$$

$$\omega_3 = Z_{110}(t)\sin k_c x \sin k_c y + Z_{112}(t)\sin k_c x \sin k_c y \cos 2\pi z. \tag{17.58}$$

The expression for θ in this case (Pr → 0) is determined from Eq. (17.39) and is given by

$$\begin{aligned} \theta &= \frac{1}{k_c^2+\pi^2} W_{101}(t)\cos k_c x \sin \pi z + \frac{1}{k_c^2+\pi^2} W_{011}(t)\cos k_c y \sin \pi z \\ &+ \frac{1}{2k_c^2+\pi^2} W_{112}(t)\cos k_c x \cos k_c y \sin 2\pi z \\ &+ \frac{1}{5k_c^2+\pi^2} W_{121}(t)\cos k_c x \cos 2k_c y \sin \pi z \\ &+ \frac{1}{5k_c^2+\pi^2} W_{211}(t)\cos 2k_c x \cos k_c y \sin \pi z. \end{aligned} \tag{17.59}$$

Using Eqs. (17.40) and (17.41) we then find

$$\begin{aligned} v_1 &= -\frac{\pi}{k_c} W_{101}(t)\sin k_c x \cos \pi z - \frac{\pi}{k_c} W_{112}(t)\sin k_c x \cos k_c y \cos 2\pi z \\ &- \frac{2\pi}{5k_c} W_{211}(t)\sin 2k_c x \cos k_c y \cos \pi z - \frac{\pi}{5k_c} W_{121}(t)\sin k_c x \cos 2k_c y \cos \pi z \\ &+ \frac{1}{2k_c} Z_{110}(t)\sin k_c x \cos k_c y + \frac{1}{2k_c} Z_{112}(t)\sin k_c x \cos k_c y \cos 2\pi z, \end{aligned} \tag{17.60}$$

$$\begin{aligned} v_2 &= -\frac{\pi}{k_c} W_{011}(t)\sin k_c y \cos \pi z - \frac{\pi}{k_c} W_{112}(t)\cos k_c x \sin k_c y \cos 2\pi z \\ &- \frac{\pi}{5k_c} W_{211}(t)\cos 2k_c x \sin k_c y \cos \pi z - \frac{2\pi}{5k_c} W_{121}(t)\cos k_c x \sin 2k_c y \cos \pi z \\ &- \frac{1}{2k_c} Z_{110}(t)\cos k_c x \sin k_c y - \frac{1}{2k_c} Z_{112}(t)\cos k_c x \sin k_c y \cos 2\pi z. \end{aligned} \tag{17.61}$$

After calculating all the velocity components, horizontal components of vorticity are determined by taking curl of the velocity vector. The expression for horizontal components of vorticity are given by

$$\omega_1 = -\left(k_c + \frac{\pi^2}{k_c}\right) W_{011}(t)\sin k_c y \sin \pi z - \left(k_c + \frac{2\pi^2}{k_c}\right) W_{112}(t)\cos k_c x \sin k_c y \sin 2\pi z$$

$$- \left(k_c + \frac{\pi^2}{5k_c}\right) W_{211}(t) \cos 2k_c x \sin k_c y \sin \pi z - \frac{\pi}{k_c} Z_{112}(t) \cos k_c x \sin k_c y \sin 2\pi z$$
$$- 2\left(k_c + \frac{\pi^2}{5k_c}\right) W_{121}(t) \cos k_c x \sin 2k_c y \sin \pi z, \tag{17.62}$$

$$\omega_2 = \left(k_c + \frac{\pi^2}{k_c}\right) W_{101}(t) \sin k_c x \sin \pi z + \left(k_c + \frac{2\pi^2}{k_c}\right) W_{112}(t) \sin k_c x \cos k_c y \sin 2\pi z$$
$$- \frac{\pi}{k_c} Z_{112}(t) \sin k_c x \cos k_c y \sin 2\pi z + \left(k_c + \frac{\pi^2}{5k_c}\right) W_{121}(t) \sin k_c x \cos 2k_c y \sin \pi z$$
$$+ 2\left(k_c + \frac{\pi^2}{5k_c}\right) W_{211}(t) \sin 2k_c x \cos k_c y \sin \pi z. \tag{17.63}$$

Substituting the expressions of $v_1, v_2, v_3, \omega_1, \omega_2, \omega_3$ and θ in Eqs. (17.42) and (17.43) and using the orthogonality of the basis functions we get a set of seven equations for the Fourier amplitudes. This 7-mode model and the MAPLE code for deriving it are given in the **Appendix**.

Now from the equations of W_{112}, Z_{110} and Z_{112}, we observe that near the onset of convection, linear decay rate of these modes are quite high. Therefore, we adiabatically eliminate (Manneville 1990) these modes to get the following set of four coupled nonlinear ordinary differential equations (Pal et al. 2013):

$$\dot{W_{101}} = \frac{3\pi^2}{2}(r-1)W_{101} + a_1 W_{101} W_{011}^2 + a_2 W_{101} W_{011} W_{211} + a_3 W_{011} W_{121} W_{211}$$
$$+ a_4 W_{121} W_{211}^2 + a_5 W_{011}^2 W_{121} + a_6 W_{101} W_{211}^2, \tag{17.64}$$

$$\dot{W_{011}} = \frac{3\pi^2}{2}(r-1)W_{011} + a_1 W_{101}^2 W_{011} + a_2 W_{101} W_{011} W_{121} + a_3 W_{101} W_{121} W_{211}$$
$$+ a_4 W_{121}^2 W_{211} + a_5 W_{101}^2 W_{211} + a_6 W_{011} W_{121}^2, \tag{17.65}$$

$$\dot{W_{121}} = \frac{\pi^2}{98}(135r - 343)W_{121} + b_1 W_{101} W_{011}^2 + b_2 W_{101} W_{011} W_{211} + b_3 W_{011} W_{121} W_{211}$$
$$+ b_4 W_{121} W_{211}^2 + b_5 W_{011}^2 W_{121} + b_6 W_{101} W_{211}^2, \tag{17.66}$$

$$\dot{W_{211}} = \frac{\pi^2}{98}(135r - 343)W_{211} + b_1 W_{101}^2 W_{011} + b_2 W_{101} W_{011} W_{121} + b_3 W_{101} W_{121} W_{211}$$
$$+ b_4 W_{121}^2 W_{211} + b_5 W_{101}^2 W_{211} + b_6 W_{011} W_{121}^2. \tag{17.67}$$

The coefficients present in the above equations are $a_1 = \frac{3}{100}$, $a_2 = \frac{31}{3000}$, $a_3 = -\frac{209}{30000}$, $a_4 = \frac{63}{60000}$, $a_5 = -\frac{47}{1500}$, $a_6 = \frac{1}{200}$, $b_1 = -\frac{93}{700}$, $b_2 = -\frac{67}{7000}$, $b_3 = -\frac{7407}{70000}$, $b_4 = \frac{3969}{700000}$, $b_5 = -\frac{928}{7000}$ and $b_6 = \frac{3816}{70000}$ with r as the reduced Rayleigh number.

Now introducing the notations $\mathbf{X} = [X_1, X_2]^T \equiv [W_{101}, W_{011}]^T$, $\mathbf{Y} = [Y_1, Y_2]^T \equiv [W_{121}, W_{211}]^T$, $\mathbb{A} = [0\ 1; 1\ 0]$, $\mu_1 = \frac{3\pi^2}{2}(r-1)$ and $\mu_2 = \frac{\pi^2}{98}(135r - 343)$ we can write the above set of four equations as

$$\dot{\mathbf{X}} = \mu_1 \mathbf{X} + X_1 X_2 \mathbb{A}(a_1 \mathbf{X} + a_2 \mathbf{Y}) + Y_1 Y_2 \mathbb{A}(a_3 \mathbf{X} + a_4 \mathbf{Y})$$

$$+ a_5[X_2^2 Y_1, X_1^2 Y_2]^T + a_6[X_1 Y_2^2, X_2 Y_1^2]^T, \tag{17.68}$$

$$\dot{\mathbf{Y}} = \mu_2 \mathbf{Y} + X_1 X_2 \mathbb{A}(b_1 \mathbf{X} + b_2 \mathbf{Y}) + Y_1 Y_2 \mathbb{A}(b_3 \mathbf{X} + b_4 \mathbf{Y}) + b_5[X_2^2 Y_1, X_1^2 Y_2]^T + b_6[X_1 Y_2^2, X_2 Y_1^2]^T. \tag{17.69}$$

(Equations (17.68) and (17.69) are reused from Pal et al. (2013) with the permission from American Physical Society.)

This minimal set of equations are found to capture the bifurcation structure near the onset of convection of zero-Prandtl number (Pal et al. 2009, 2013) fluids quite satisfactorily. Figure 17.6 shows the bifurcation diagram constructed from the above 4-mode model using the MATLAB based continuation software MATCONT (Dhooge et al. 2003). The bifurcation diagram unfolds a very rich bifurcation structure near the onset of convection. This is found to be consistent with the DNS results (Pal et al. 2013). In fact the 4-mode model tracked six different solutions namely OCR-I, OCR-II, OCR-II′, CR, CR′ and SQ out of which only OCR-I and SQ were reported in DNS (Thual 1992). Later the existence of other solutions are also verified in DNS (Pal et al. 2013). The pattern dynamics corresponding to the OCR-I and SQ solutions have already been discussed in Sect. 17.8.2. Oscillatory cross rolls patterns of type-II are either oriented along y-axis (OCR-II) or along x-axis (OCR-II′). These are periodic patterns with varying wavyness. CR and CR′ are stationary flow patterns oriented along y-axis and x-axis respectively. All these flow patterns are shown inside the bifurcation diagram.

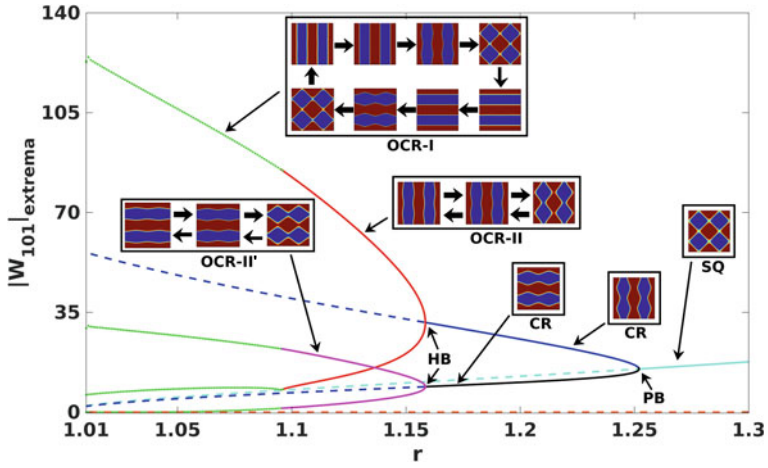

Fig. 17.6 Bifurcation diagram constructed from the 4-mode model. Horizontal axis shows the variation of the parameter r in the region $1.01 \leq r \leq 1.3$. Along vertical axis the extrema corresponding to different solutions are shown with different colors. The solid and dashed curves represent the stable and unstable solutions respectively. The orange, green, red, pink, blue, black and cyan respectively represent conduction state, OCR-I, OCR-II, OCR-II′, CR, CR′ and SQ solutions respectively. Stationary and time periodic flow patterns corresponding to different solutions are also shown. PB and HB respectively represent pitchfork and Hopf bifurcation points

17.10 Conclusions

In this chapter, we have discussed low dimensional modeling technique for investigating instabilities near the onset of Rayleigh-Bénard convection. The technique is illustrated using two examples. In these examples, convective instabilities near the onset of convection of high Prandtl number and zero Prandtl number fluids are investigated by simultaneous performance of DNS and low dimensional modeling. It is found that low dimensional models derived by the method described in this chapter can produce faithful results close to the onset of convective instability. Based on the discussions in this chapter, we emphasize that simultaneous performance of DNS and low dimensional modeling is a powerful technique for the investigation of different instabilities in dissipative systems where boundary conditions of the associated boundary value problem allow expansion of the independent fields in terms of suitable set of orthogonal basis functions. Moreover, this technique is expected to work for investigating instabilities in systems with spherical and cylindrical geometries.

Acknowledgements P.P. and A.B. acknowledge the support from the SERB, India funded project (Grant No.: EMR/2015/001680). M.G. is supported by INSPIRE programme of DST, India (Code: IF150261).

Appendix

MAPLE code for derivation of the 7-mode model

```
> # MAPLE Code to create Low-dimensional model for
  Zero-Prandtl number convection
> fd:=fopen("mode7_model.m",APPEND):
> v3_basis:=[cos(k*x)*sin(Pi*z),cos(q*y)*sin(Pi*z),
  cos(k*x)*cos(q*y)*sin(2*Pi*z),cos(2*k*x)*cos(q*y)*sin(Pi*z),
  cos(k*x)*cos(2*q*y)*sin(Pi*z)]:
> omega3_basis:=[sin(k*x)*sin(q*y),
  sin(k*x)*sin(q*y)*cos(2*Pi*z)]:
> v3_amplitudes:=[w101(t),w011(t),w112(t),w211(t),w121(t)]:
> omega3_amplitudes:=[z110(t),z112(t)]:
> q:=k:
> with(linalg):v3:=innerprod(v3_amplitudes,v3_basis):
> with(linalg):omega3:=innerprod(omega3_amplitudes,
  omega3_basis):
> v3_del:=diff(v3_basis,x,x)+diff(v3_basis,y,y)
  +diff(v3_basis,z,z):
> for i from 1 to vectdim(v3_basis) do div_factor[i]:=
  -v3_del[i]/v3_basis[i]: end do:
> theta:=0:
> for i from 1 to vectdim(v3_basis) do theta:=theta
```

```
  +v3_amplitudes[i]*v3_basis[i]/div_factor[i]: end do:
> simplify(theta):
> test1:=simplify(diff(theta,x,x)+diff(theta,y,y)
  +diff(theta,z,z)+v3);
> for i from 1 to vectdim(v3_basis) do with(student):
  v3_basis_coeff[i]:=value(Tripleint(v3_basis[i]^2,
  x=0..2*Pi/k,y=0..2*Pi/q,z=0..1)) end do:
> for i from 1 to vectdim(omega3_basis) do with(student):
  omega3_basis_coeff[i]:=value(Tripleint(omega3_basis[i]^2,
  x=0..2*Pi/k,y=0..2*Pi/q,z=0..1)) end do:
> # v1 calculation
> v1_part1:=-diff(v3_basis,x,z):
> v1_part1_delH:=diff(v1_part1,x,x)+diff(v1_part1,y,y):
> for i from 1 to vectdim(v1_part1) do divider[i]:=
  `if`(v1_part1[i]=0,1,v1_part1_delH[i]/v1_part1[i]) end do:
> v1_v3_cont:=0:
> for i from 1 to vectdim(v1_part1) do v1_v3_cont:=
  v1_v3_cont+v3_amplitudes[i]*v1_part1[i]/divider[i] end do:
> v1_v3_cont:
> v1_part2:=-diff(omega3_basis,y):
> v1_part2_delH:=diff(v1_part2,x,x)+diff(v1_part2,y,y):
> for i from 1 to vectdim(v1_part2) do divider[i]:=
  `if`(v1_part2[i]=0,1,v1_part2_delH[i]/v1_part2[i]) end do:
> v1_omega3_cont:=0:
> for i from 1 to vectdim(v1_part2) do v1_omega3_cont:=
  v1_omega3_cont+omega3_amplitudes[i]*v1_part2[i]/divider[i]
  end do:
> v1:=v1_v3_cont+v1_omega3_cont:
> # v2 calculation
> v2_part1:=-diff(v3_basis,y,z):
> v2_part1_delH:=diff(v2_part1,x,x)+diff(v2_part1,y,y):
> for i from 1 to vectdim(v2_part1) do divider[i]:=
  `if`(v2_part1[i]=0,1,v2_part1_delH[i]/v2_part1[i]) end do:
> v2_v3_cont:=0:
> for i from 1 to vectdim(v2_part1) do v2_v3_cont:=
  v2_v3_cont+v3_amplitudes[i]*v2_part1[i]/divider[i] end do:
> v2_v3_cont:
> v2_part2:=diff(omega3_basis,x):
> v2_part2_delH:=diff(v2_part2,x,x)+diff(v2_part2,y,y):
> for i from 1 to vectdim(v2_part2) do divider[i]:=
  `if`(v2_part2[i]=0,1,v2_part2_delH[i]/v2_part2[i]) end do:
> v2_omega3_cont:=0:
> for i from 1 to vectdim(v2_part2) do v2_omega3_cont:=
  v2_omega3_cont+omega3_amplitudes[i]*v2_part2[i]/divider[i]
  end do:
> v2:=v2_v3_cont+v2_omega3_cont:
> # div v =0 test
> test2:=simplify(diff(v1,x)+diff(v2,y)+diff(v3,z));
> f:=[v1,v2,v3]:
```

```
> v:=[x,y,z]:
> with(linalg):omega:=curl(f,v):
> # div omega=0 test
> test3:=simplify(diff(omega[1],x)+diff(omega[2],y)
  +diff(omega[3],z));
> # test omega3=omega[3]
> test4:=simplify(omega3-omega[3]);
> for i from 1 to vectdim(v3_basis) do
> with(student):nlin1:=value(Tripleint(diff(omega[1]*diff(v1,x),y)
  *v3_basis[i],x=0..2*Pi/k,y=0..2*Pi/q,z=0..1)):
> with(student):nlin2:=value(Tripleint(diff(omega[2]*diff(v1,y),y)
  *v3_basis[i],x=0..2*Pi/k,y=0..2*Pi/q,z=0..1)):
> with(student):nlin3:=value(Tripleint(diff(omega[3]*diff(v1,z),y)
  *v3_basis[i],x=0..2*Pi/k,y=0..2*Pi/q,z=0..1)):
> with(student):nlin4:=value(Tripleint(-diff(v1*diff(omega[1],x),y)
  *v3_basis[i],x=0..2*Pi/k,y=0..2*Pi/q,z=0..1)):
> with(student):nlin5:=value(Tripleint(-diff(v2*diff(omega[1],y),y)
  *v3_basis[i],x=0..2*Pi/k,y=0..2*Pi/q,z=0..1)):
> with(student):nlin6:=value(Tripleint(-diff(v3*diff(omega[1],z),y)
  *v3_basis[i],x=0..2*Pi/k,y=0..2*Pi/q,z=0..1)):
> with(student):nlin7:=value(Tripleint(-diff(omega[1]*diff(v2,x),x)
  *v3_basis[i],x=0..2*Pi/k,y=0..2*Pi/q,z=0..1)):
> with(student):nlin8:=value(Tripleint(-diff(omega[2]*diff(v2,y),x)
  *v3_basis[i],x=0..2*Pi/k,y=0..2*Pi/q,z=0..1)):
> with(student):nlin9:=value(Tripleint(-diff(omega[3]*diff(v2,z),x)
  *v3_basis[i],x=0..2*Pi/k,y=0..2*Pi/q,z=0..1)):
> with(student):nlin10:=value(Tripleint(diff(v1*diff(omega[2],x),x)
  *v3_basis[i],x=0..2*Pi/k,y=0..2*Pi/q,z=0..1)):
> with(student):nlin11:=value(Tripleint(diff(v2*diff(omega[2],y),x)
  *v3_basis[i],x=0..2*Pi/k,y=0..2*Pi/q,z=0..1)):
> with(student):nlin12:=value(Tripleint(diff(v3*diff(omega[2],z),x)
  *v3_basis[i],x=0..2*Pi/k,y=0..2*Pi/q,z=0..1)):
> v3_nlin:=nlin1+nlin2+nlin3+nlin4+nlin5+nlin6+nlin7+nlin8+nlin9
  +nlin10+nlin11+nlin12:
> with(student):left_v3:=value(Tripleint(diff((diff(v3,x,x)
  +diff(v3,y,y)+diff(v3,z,z)),t)*v3_basis[i],x=0..2*Pi/k,y=0..
  2*Pi/q,z=0..1)):
> right_v3_half:=diff(v3,x,x)+diff(v3,y,y)+diff(v3,z,z):
> with(student):right_v3:=value(Tripleint((diff(right_v3_half,x,x)
  +diff(right_v3_half,y,y)+diff(right_v3_half,z,z))*v3_basis[i],
  x=0..2*Pi/k,y=0..2*Pi/q,z=0..1))+R*value(Tripleint((diff(theta,x,x)
  +diff(theta,y,y))*v3_basis[i],x=0..2*Pi/k,y=0..2*Pi/q,z=0..1))
  +v3_nlin:
> with(student):mul1:=value(Tripleint((diff(v3_basis[i],x,x)
  +diff(v3_basis[i],y,y)+diff(v3_basis[i],z,z))*v3_basis[i],
  x=0..2*Pi/k,y=0..2*Pi/q,z=0..1)):
> equn:=left_v3=right_v3:
> fprintf(fd,"%a\n",simplify(equn/mul1)) end do:
>
```

```
> for i from 1 to vectdim(omega3_basis) do
> with(student):nlin1:=value(Tripleint(omega[1]*diff(v3,x)*
  omega3_basis[i],x=0..2*Pi/k,y=0..2*Pi/q,z=0..1)):
> with(student):nlin2:=value(Tripleint(omega[2]*diff(v3,y)*
  omega3_basis[i],x=0..2*Pi/k,y=0..2*Pi/q,z=0..1)):
> with(student):nlin3:=value(Tripleint(omega[3]*diff(v3,z)*
  omega3_basis[i],x=0..2*Pi/k,y=0..2*Pi/q,z=0..1)):
> with(student):nlin4:=value(Tripleint(-v1*diff(omega[3],x)*
  omega3_basis[i],x=0..2*Pi/k,y=0..2*Pi/q,z=0..1)):
> with(student):nlin5:=value(Tripleint(-v2*diff(omega[3],y)*
  omega3_basis[i],x=0..2*Pi/k,y=0..2*Pi/q,z=0..1)):
> with(student):nlin6:=value(Tripleint(-v3*diff(omega[3],z)*
  omega3_basis[i],x=0..2*Pi/k,y=0..2*Pi/q,z=0..1)):
> omega3_nlin:=nlin1+nlin2+nlin3+nlin4+nlin5+nlin6:
> with(student):left_omega3:=value(Tripleint(diff(omega[3],t)*
  omega3_basis[i],x=0..2*Pi/k,y=0..2*Pi/q,z=0..1)):
> with(student):right_omega3:=value(Tripleint((diff(omega[3],x,x)
  +diff(omega[3],y,y)+diff(omega[3],z,z))*omega3_basis[i],x=0..2*Pi/k,
  y=0..2*Pi/q,z=0..1))+omega3_nlin:
> equn:=left_omega3=right_omega3:
> fprintf(fd,"%a\n",simplify(equn/omega3_basis_coeff[i]))
  end do:
> fclose(fd):
```

The 7-mode model

$$\begin{aligned}\dot{W_{101}} = -\frac{1}{80(\pi^2+k_c^2)^2}\Big(&22\pi^5 W_{112}W_{211} + 240W_{101}\pi^2k_c^4 + 240W_{101}\pi^4k_c^2\\ &- 8W_{211}\pi^2Z_{110}k_c^2 - 20W_{011}k_c^4W_{112}\pi - 40W_{011}\pi^3W_{112}k_c^2 - 34W_{211}k_c^4W_{112}\pi\\ &- 80\mathrm{Ra}W_{101}k_c^2 - 12W_{112}\pi^3W_{211}k_c^2 - 4Z_{112}\pi^2W_{211}k_c^2 + 80W_{101}\pi^6 + 80k_c^6W_{101}\\ &- 9\pi^4Z_{112}W_{211} + 10\pi^4W_{011}Z_{112} - 20\pi^4W_{011}Z_{110} - 10W_{011}k_c^4Z_{112}\\ &+ 2\pi^4W_{211}Z_{110} + 5W_{211}k_c^4Z_{112} + 20W_{011}k_c^4Z_{110} - 10W_{211}k_c^4Z_{110}\\ &- 20\pi^5W_{011}W_{112}\Big),\end{aligned} \tag{17.70}$$

$$\begin{aligned}\dot{W_{011}} = -\frac{1}{80(\pi^2+k_c^2)^2}\Big(&80W_{011}k_c^6 + 80W_{011}\pi^6 - 20W_{101}k_c^4Z_{110} + 10W_{101}k_c^4Z_{112}\\ &+ 240W_{011}\pi^4k_c^2 + 240W_{011}\pi^2k_c^4 + 10W_{121}k_c^4Z_{110} - 5W_{121}k_c^4Z_{112} + 22\pi^5W_{112}W_{121}\\ &- 2\pi^4W_{121}Z_{110} - 10\pi^4Z_{112}W_{101} - 20\pi^5W_{112}W_{101} + 20\pi^4W_{101}Z_{110} + 9\pi^4Z_{112}W_{121}\\ &+ 8W_{121}\pi^2Z_{110}k_c^2 - 12W_{112}\pi^3W_{121}k_c^2 - 34W_{112}k_c^4W_{121}\pi - 40\pi^3W_{112}k_c^2W_{101}\\ &- 20W_{112}k_c^4W_{101}\pi + 4Z_{112}\pi^2W_{121}k_c^2 - 80\mathrm{Ra}W_{011}k_c^2\Big),\end{aligned} \tag{17.71}$$

$$\begin{aligned}\dot{W_{112}} = &-\frac{1}{100(2\pi^2+k_c^2)^2}\Big(1200\pi^2 W_{112}k_c^4 + 2400W_{112}k_c^2\pi^4 + 200W_{112}k_c^6 + 1600W_{112}\pi^6 \\ &- 50\mathrm{Ra}W_{112}k_c^2 + 300W_{011}W_{101}k_c^2\pi^3 + 100\pi W_{011}W_{101}k_c^4 + 230W_{211}W_{101}k_c^2\pi^3 \\ &+ 99W_{211}W_{121}k_c^2\pi^3 + 230W_{011}W_{121}k_c^2\pi^3 + 110\pi W_{211}W_{101}k_c^4 + 110\pi W_{011}W_{121}k_c^4 \\ &+ 45\pi W_{211}W_{121}k_c^4 + 200\pi^5 W_{011}W_{101} + 20\pi^5 W_{211}W_{101} + 18\pi^5 W_{211}W_{121} \\ &+ 20\pi^5 W_{011}W_{121}\Big), \end{aligned} \tag{17.72}$$

$$\begin{aligned}\dot{W_{121}} = &-\frac{1}{80(\pi^2+5k_c^2)^2}\Big(-400\mathrm{Ra}W_{211}k_c^2 - 180W_{112}\pi^3 W_{121}k_c^2 + 400W_{101}\pi^2 Z_{110}k_c^2 \\ &+ 120Z_{112}\pi^2 W_{121}k_c^2 + 240W_{121}\pi^2 Z_{110}k_c^2 + 200Z_{112}\pi^2 W_{101}k_c^2 - 500W_{112}k_c^4 W_{101}\pi \\ &- 1400\pi^3 W_{112}k_c^2 W_{101} - 450W_{112}k_c^4 W_{121}\pi + 1200W_{211}\pi^4 k_c^2 - 18\pi^5 W_{112}W_{121} \\ &+ 60\pi^4 W_{101}Z_{110} + 6000W_{211}\pi^2 k_c^4 - 375W_{121}k_c^4 Z_{112} + 39\pi^4 Z_{112}W_{121} + 18\pi^4 W_{121}Z_{110} \\ &- 250W_{101}k_c^4 Z_{112} + 500W_{101}k_c^4 Z_{110} - 260\pi^5 W_{112}W_{101} + 750W_{121}k_c^4 Z_{110} \\ &+ 50\pi^4 Z_{112}W_{101} + 10000W_{211}k_c^6 + 80W_{211}\pi^6\Big), \end{aligned} \tag{17.73}$$

$$\begin{aligned}\dot{W_{211}} = &\frac{1}{80(\pi^2+5k_c^2)^2}\Big(-10000W_{121}k_c^6 - 80\pi^6 W_{121} + 400\mathrm{Ra}W_{121}k_c^2 + 180W_{112}\pi^3 W_{211}k_c^2 \\ &+ 120Z_{112}\pi^2 W_{211}k_c^2 + 200W_{011}\pi^2 Z_{112}k_c^2 + 400W_{011}\pi^2 Z_{110}k_c^2 + 240W_{211}\pi^2 Z_{110}k_c^2 \\ &+ 500W_{011}k_c^4 W_{112}\pi + 1400W_{011}\pi^3 W_{112}k_c^2 + 450W_{211}k_c^4 W_{112}\pi + 18\pi^5 W_{112}W_{211} \\ &+ 39\pi^4 Z_{112}W_{211} + 50\pi^4 W_{011}Z_{112} + 60\pi^4 W_{011}Z_{110} - 250W_{011}k_c^4 Z_{112} + 18\pi^4 W_{211}Z_{110} \\ &- 375W_{211}k_c^4 Z_{112} + 500W_{011}k_c^4 Z_{110} + 750W_{211}k_c^4 Z_{110} + 260\pi^5 W_{011}W_{112} \\ &- 6000W_{121}k_c^4\pi^2 - 1200W_{121}\pi^4 k_c^2\Big), \end{aligned} \tag{17.74}$$

$$\dot{Z_{110}} = -2k_c^2 Z_{110} - \frac{1}{5}W_{011}\pi^2 W_{121} + \frac{1}{5}W_{211}\pi^2 W_{101}, \tag{17.75}$$

$$\dot{Z_{112}} = -2Z_{112}k_c^2 - 4Z_{112}\pi^2 + \frac{1}{5}W_{011}\pi^2 W_{121} - \frac{1}{5}W_{211}\pi^2 W_{101}. \tag{17.76}$$

References

Ahlers G, Grossmann S, Lohse D (2009) Heat transfer and large scale dynamics in turbulent Rayleigh-Bénard convection. Rev Mod Phys 81(2):503

Basak A, Kumar K (2015) A model for Rayleigh-Bénard magnetoconvection. Eur Phys J B 88(10):244

Bodenschatz E, Pesch W, Ahlers G (2000) Recent developments in Rayleigh-Bénard convection. Annu Rev Fluid Mech 32(1):709

Boussinesq J (1903) Théorie analytique de la chaleur, vol 2. Gauthier-Villars

Busse FH (1985) Springer, Berlin, pp 97–133

Busse FH (1989) In: Peltier WR (ed) Convection mantle, tectonics plate, dynamics global. Gordon and Breach, New York, pp 23–95

Busse FH (1972) The oscillatory instability of convection rolls in a low Prandtl number fluid. J Fluid Mech 52(1):97
Busse FH (1978) Non-linear properties of thermal convection. Rep Prog Phys 41(12):1929
Busse FH, Whitehead JA (1971) Instabilities of convection rolls in a high Prandtl number fluid. J Fluid Mech 47(2):305
Chandrasekhar S (1961) Hydrodynamic and hydromagnetic stability. Cambridge University Press, Cambridge
Croquette V (1989a) Convective pattern dynamics at low Prandtl number: Part I. Contemp Phys 30(2):113
Croquette V (1989b) Convective pattern dynamics at low Prandtl number: Part II. Contemp Phys 30(3):153
Cross MC, Hohenberg P (1993) Pattern formation outside of equilibrium. Rev Mod Phys 65(3):851
Dan S, Pal P, Kumar K (2014) Low-Prandtl-number Rayleigh-Bénard convection with stress-free boundaries. Eur Phys J B 87(11):278
Dan S, Nandukumar Y, Pal P (2015) Effect of Prandtl number on wavy rolls in Rayleigh–Bénard convection. Phys Scr 90(3):035208
Dan S, Ghosh M, Nandukumar Y, Dana SK, Pal P (2017) Bursting dynamics in Rayleigh-Bénard convection. Eur Phys J Spec Top 226(9):2089
Dhooge A, Govaerts W, Kuznetsov YA, Trans ACM (2003) MATCONT: a MATLAB package for numerical bifurcation analysis of ODEs. Math Softw 29(2):141
Drazin P, Reid WH (1981) Hydrodynamic stability. Cambridge University Press, Cambridge
Frigo M, Johnson SG (2005) Proc IEEE 93(2):216 (Special issue on "Program Generation, Optimization, and Platform Adaptation")
Galerkin BG (1915) On electrical circuits for the approximate solution of the Laplace equation. Vestnik Inzh 19:897
Getling AV (1998) Rayleigh-Bénard convection: structures and dynamics. World Scientific
Ghosh M, Pal P (2017) Zero Prandtl-number rotating magnetoconvection. Phys Fluids 29(12):124105
Glatzmaier GA, Coe RS, Hongre L, Roberts PH (1999) The role of the Earth's mantle in controlling the frequency of geomagnetic reversals. Nature 401(6756):885
Hartmann DL, Moy LA, Fu Q (2001) Tropical convection and the energy balance at the top of the atmosphere. J Clim 14(24):4495
Hurle DTJ, Series RW (1994) In: Hurle DTJ (ed) Handbook of crystal growth. Elsevier, North Holland, Amsterdam
Kirillov IR, Reed CB, Barleon L, Miyazaki K (1995) Present understanding of MHD and heat transfer phenomena for liquid metal blankets. Fusion Eng Des 27:553
Krishnamurti R (1970) On the transition to turbulent convection. Part 1. The transition from two-to three-dimensional flow. J Fluid Mech 42(2):295
Kumar K (1990) Convective patterns in rotating binary mixtures. Phys Rev A 41(6):3134
Lohse D, Xia KQ (2010) Small-scale properties of turbulent Rayleigh-Bénard convection. Annu Rev Fluid Mech 42
Lorenz EN (1963) Deterministic nonperiodic flow. J Atmos Sci 20(2):130
Maity P, Kumar K (2014) Zero-Prandtl-number convection with slow rotation. Phys Fluids 26(10):104103
Maity P, Kumar K, Pal P (2013) Homoclinic bifurcations in low-Prandtl-number Rayleigh-Bénard convection with uniform rotation. Europhys Lett 103(6):64003
Manneville P (1990) Dissipative structures and weak turbulence. Academic Press, New York
Miesch MS (2000) Helioseismic diagnostics of solar convection and activity. Springer, Berlin, pp 59–89
Nandukumar Y, Pal P (2015) Oscillatory instability and routes to chaos in Rayleigh-Bénard convection: Effect of external magnetic field. Europhys Lett 112(2):24003
Nandukumar Y, Pal P (2016) Instabilities and chaos in low-Prandtl number Rayleigh-Bénard convection. Comput Fluids 138:61

Pal P, Kumar K (2002) Wavy stripes and squares in zero-Prandtl-number convection. Phys Rev E 65(4):047302
Pal P, Kumar K (2012) Role of uniform horizontal magnetic field on convective flow. Eur Phys J B 85(6):201
Pal P, Wahi P, Paul S, Verma MK, Kumar K, Mishra PK (2009) Bifurcation and chaos in zero-Prandtl-number convection. Europhys Lett 87(5):54003
Pal P, Kumar K, Maity P, Dana SK (2013) Pattern dynamics near inverse homoclinic bifurcation in fluids. Phys Rev E 87(2):023001
Pharasi HK, Kumar K (2013) Oscillatory instability and fluid patterns in low-Prandtl-number Rayleigh-Bénard convection with uniform rotation. Phys Fluids 25(10):104105
Strogatz SH (2001) Nonlinear dynamics and chaos: with applications to physics, biology, chemistry, and engineering. Westview Press
Thual O (1992) Zero-Prandtl-number convection. J Fluid Mech 240:229
Verma MK (2018) Physics of buoyant flows: from instabilities to turbulence. World Scientific
Verma MK, Chatterjee A, Reddy KS, Yadav RK, Paul S, Chandra M, Samtaney R (2013) Benchmarking and scaling studies of pseudospectral code Tarang for turbulence simulations. Pramana 81(4):617
Veronis G (1959) Cellular convection with finite amplitude in a rotating fluid. J Fluid Mech 5(3):401
Veronis G (1966) Motions at subcritical values of the Rayleigh number in a rotating fluid. J Fluid Mech 24(3):545

Chapter 18
Design of a Membrane Reactor for On-site High Purity Hydrogen Production

Richa Sharma, Amit Kumar and Rajesh Kumar Upadhyay

Abstract Hydrogen is a potential alternative energy carrier to embrace the global need of a clean and efficient energy resource. It minimizes dependence on fossil fuels as well as is an effective measure towards increasing global warming. Hydrogen based fuel cells are an attractive solution for producing clean electrical energy by emitting only water as a by-product. However, storage and distribution of hydrogen is a major issue for stationary fuel cells as well as mobile power generators. To avert the risks of any hydrogen leaks, membrane reactor (MR) technology enables to deliver only the desirable release of hydrogen using a fine control between on-site hydrogen generation and separation. Moreover, in contrast to traditional and bulky integration methodologies, MR allows single unit 'compact' integration that also eliminates additional downstream of products by producing hydrogen of >99% purity. These factors motivate MR to be explored widely and demonstrate its commercial feasibility in the coming years.

The current chapter focuses on the broad overview on membrane reactors for ultra pure hydrogen production, its technological challenges and case studies to illustrate the critical role played by dense palladium membranes in the successful viability of this technology. Further, recent developments within the scope of membrane reactors for hydrogen generation will also be briefly discussed. Special focus will be given for hydrogen generation by using methanol as a feed to membrane reformer.

18.1 Introduction

Proton exchange membrane (PEM) fuel cells are efficient power generators with up to 50–60% efficiency to convert the chemical energy into electrical energy even for small household applications (1–5 kW) (Verhelst 2014). The output of these H_2

R. Sharma · A. Kumar · R. K. Upadhyay (✉)
Department of Chemical Engineering, Indian Institute of Technology Guwahati, Guwahati, Assam, India
e-mail: rkupadhyay@iitg.ac.in

A. Mukhopadhyay et al. (eds.), *Dynamics and Control of Energy Systems*,
Energy, Environment, and Sustainability,
https://doi.org/10.1007/978-981-15-0536-2_18

driven fuel cells to small or medium scale, stationary as well as portable auxiliary power units is enormous (Schäfer et al. 2006; Yuan and Wang 2008). From a few watts to a few kilowatts, H_2 driven PEM fuel cells having the potential to provide compact high power ranges from applications such as a small system (20–100 W) to backups, battery charger, emergency power, generators, and large system automotive power ranging between 80–100 kW (Schäfer et al. 2006; de Bruijn 2005). But, effective operation of fuel cells demands high hydrogen purity with CO levels below 10 ppm (Li et al. 2003).

Production of hydrogen using water, methane, methanol, and ethanol via electrolysis, steam reforming, cracking, dry reforming, partial oxidation or auto-thermal reforming is widely studied (Sá et al. 2010). Amongst these, hydrogen production using methanol steam reforming is an efficient process due to its easy applicability both at laboratory and pilot plant scale (Iulianelli et al. 2014). At relatively low temperatures, methanol steam reforming (MSR) gives high hydrogen yield with a product stream containing 75% H_2 and 25% CO_2 (Sá et al. 2010). Hydrogen from this mixture further needs to be separated and purified since the Pt-catalyst loaded on the anode of PEM fuel cell requires a feed that includes only dry H_2 typically of purity >99.995% owing to poisoning concerns (Aasberg-Petersen et al. 1998). In order to obtain such high purity while maintaining the entire unit compact, membranes are considered as a preferred choice. Further, in comparison to traditional hydrogen separation methods such as pressure swing adsorption (PSA), membranes also minimize the energy consumption and the overall cost of the system. Therefore using high energy liquid fuels such as methanol, integrated generation with separation of hydrogen via membrane reactors (MR) is considered as a feasible choice for on-site generation of ultra-pure hydrogen (de Bruijn 2005; Brown 2001; Berry and Aceves 1998).

MRs are of great interest to small scale hydrogen consumers in decentralized locations for low-pressure systems utilizing methane as feed. This technology would, therefore, provide a proof of concept for (i) pure hydrogen production; (ii) gas-to-liquid (GTL) processes; (iii) propylene production (Basile et al. 2015). These are high-end reactions of the current era having major industrial interests not only utilize greenhouse gases but produce valuable fuels that can be used for which energy production for the developing societies.

Membrane reactors (MR) are a compact and efficient alternative to conventional process integration technology. As shown in Fig. 18.1, conventional technology is comprised of traditional reformers connected to CO clean up steps prior to hydrogen feeding into the fuel cell. These CO clean up steps includes high and low-temperature water gas shift (HT & LT-WGS) reactors, a selective oxidizer such as preferential oxidation (PROX) unit. A series of pressure swing adsorption beds (PSA) further allows achieving high purity of hydrogen required for the fuel cell. An alternative to this bulky design is a compact membrane reactor (MR). In comparison to conventional technology, membrane reactor (MR) also shown in Fig. 18.1 comprises a single unit. In this unit, a highly hydrogen-selective dense Pd/Ag membrane in the lumen is integrated to the catalyst in a shell and tube configuration. This integration results in continuous removal of produced hydrogen by the membrane which

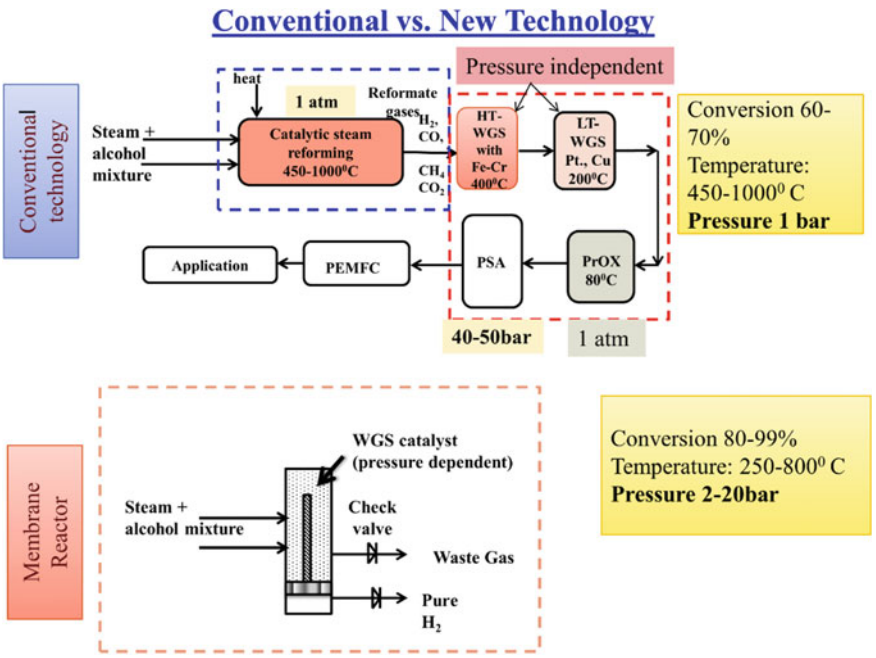

Fig. 18.1 Schematic comparison of a traditional reformer with a membrane reactor

shifts the reaction equilibrium forward thereby improving methanol conversion and achieving high purity hydrogen at the permeate end (Buxbaum and Lei 2003).

Hence, the overall conversion for equilibrium-limited reactions in MR is higher compared to the conventional fixed bed reactors. No additional requirement of a dedicated separation unit further minimizes the downstream processing cost and product losses in MR which makes it economically competent for commercial applications (Aasberg-Petersen et al. 1998; Basile 2013).

18.1.1 Membrane Reactors

Integrated reaction-separation using MR was first proposed by Professor Vladimir Gryaznov (Moscow University) in the year 1964 while it was Tokyo Gas Co. Ltd. with Mitsubishi Heavy Industries Ltd. in 1990 who developed 4 Nm^3/h membrane reactor (MR). Later, in 2003, commercialized MR designs were reported by Reb Research and Consultancy (Prof. Buxbaum group) (Buxbaum and Lei 2003), ENEA (Prof. Silvano Tosti group) (Tosti et al. 2008), ITM-CNR (Dr. Angelo Basile group) (Basile et al. 2015), Prof. Dittmeyer and Prof. Elnashaie group (Dittmeyer et al. 2017) and fluidized membrane reactor by Prof. Kuipers and Prof. Sint Annaland group (University of Twente) (Deshmukh et al. 2007).

Using methanol as fuel, numerous works in the last 10 years have exhibited membrane reactor as a promising device to obtain ultra-pure hydrogen as presented in Table 18.1. Membrane used in these studies comprises self-supported and supported Pd, Pd/Ag membranes of varying thicknesses. Catalysts used in these integration studies further include Ru–Al_2O_3 (Basile et al. 2006), CuO/Al_2O_3/ZnO/MgO (Iulianelli et al. 2008), NiO/ZnO/Al_2O_3 (Islam and Ilias 2012), etc. For instance, Basile et al. (2006) reported the integration of Ru–Al_2O_3 as a catalyst with a 50 μm self-supported Pd–Ag membrane in co-current and countercurrent modes of sweep gas at 450 °C, pressure 1.3 bar and steam/methanol (S/M) = 4.5/1. The acidic nature of Ru–Al_2O_3 produced H_2 along with CO, CO_2, and CH_4 in the reformate stream. At low transmembrane pressure, the resulting overall hydrogen recovery in the permeate was reported as 50%. Consequently, increasing the transmembrane pressure, improves hydrogen recovery due to higher permeation drive but the catalysts selectivity to CO also increases. Presence of excess CO inhibits hydrogen permeation through Pd and Pd/Ag membranes at temperatures less than 673 K. Further, in the presence of any pinholes on the membrane surface, CO will be able to pass through the membrane and reduce hydrogen purity. At 10 bar transmembrane, Liguori et al. (2014) reported 0.21–0.25% CO in permeate with hydrogen recovery pressure of 60% using a 7 μm Pd/alumina membrane. Hence, in addition to CO generation, its permeation through the membrane is also a critical challenge in membrane reactors, especially at very high transmembrane pressures. Based on the varying metal-support interaction, CO formation in the reformate changed from high to low with Ru > Ni > Cu supported catalysts. Overall, the maximum experimentally achieved hydrogen recovery using MR reported till date under actual reaction conditions is in the range of 40–60% despite higher methanol conversion in comparison to traditional reformers.

Hence, despite being an attractive tool to produce hydrogen for on-site, the following technological challenges associated with MR impede its fast commercialization (Tosti et al. 2008; Dittmeyer et al. 2017; Islam and Ilias 2012; Dunbar and Lee 2017; Gallucci et al. 2007; Pinto et al. 2013; Purnama et al. 2004; Saracco et al. 1999).

- Membrane plays a critical role in the development of commercially viable MR. The inverse relationship that typically exists between permeability and selectivity (purity) necessitates a tradeoff for MR. Higher selectivity is usually obtained at the cost of low permeation values, which is economically not always justifiable. Selectivity and flux are two indispensable factors for the characterization of MR. It is well known that the optimization of one factor sometimes has led to the deterioration of the other (Paglieri and Way 2002; Fernandez et al. 2017).
- It's not only permeation of hydrogen through the membrane that is limiting but it's also the preparation of these dense (pin-hole free) membranes which is extremely challenging (Gallucci et al. 2007).
- The selectivity of catalyst further changes under MR operating conditions that is higher pressures leading to more CO formations which drastically affects catalyst stability (Liguori et al. 2014).

A successful operation in MR therefore requires sufficient kinetic compatibility between the reactions of interest and the hydrogen transport through the membranes.

Table 18.1 Literature review on membrane reactor studies

Author	System integration	Operating conditions	X (%)	HRF (%)	H_2 flux (mol/m^2 s)	Remarks
Basile et al. (2006)	Pd membrane 50 μm thick, Ru-alumina catalyst	S/M 4.5/1, 350 °C 1.3 bar Sweep gas 0.5–12 cm^3/s	83	50	0.169	Hydrogen gas selectivity up to 70% was reported from 350–600 °C with 4.5/1 water to methanol, 1.3 bar reaction pressure
Iulianelli et al. (2008)	Pd/Ag membrane self-supported 50 μm, Cu/Al/Zn/MgO	S/M 3/1(v/v) 300 °C, 1–3 bar, Sweep gas factor 143 ml/min	80	93–40	20×10^{-3}	It was reported that CO selectivity decreases by increasing the reaction pressure confirming that the membrane provides a positive contribution to decreasing CO selectivity because of the hydrogen permeation leading to higher CO consumption
Basile et al. (2008)	Pd/Ag membrane $CuO/Al_2O_3/ZnO/MgO$ catalyst	S/M 3/1 to 9/1 250–300 °C; Sweep gas 1.38×10^{-2} mol/min	100	8	2×10^{-3}	It was reported that because of low reaction pressure, hydrogen recovery with varying feed compositions remained constant. No deactivation was observed up to 300 h while CO molar ratios remained 0.2 to 0.7. At low reaction temperature 250 °C, low CO was reported for all feed compositions

(continued)

Table 18.1 (continued)

Author	System integration	Operating conditions	X (%)	HRF (%)	H_2 flux (mol/m^2 s)	Remarks
Liguori et al. (2014)	7 μm Pd/alumina membrane Cu 15%/ZnO 31%/Al_2O_3 18% (0.5 gm) catalyst	S/M 2.5/1(v/v) 280–330 °C, 1.5–2.5 bar; Sweep gas 22–29 ml/min	85	40	0.3	CO through the defects in membrane resulting in 0.21–0.25% at 11 bar feed pressure and permeate 1 bar. It was reported that CO mole fraction was 0.62, lowest at low temperature 280 °C which further decreases with increasing pressure. CO_2 mol fraction increases with a decrease in the CO mole fraction indicating the water gas shift occurrence
Islam and Ilias (2012)	24.3 μm thick Pd supported on SS NiO/ZnO/Al_2O_3 catalyst	S/M 1–4 200–300 °C 14.7–50 psi Sweep gas 2.2 × 10^{-3} mol/s	60	50	0.2 (pure H_2)	CO selectivity between 1 to 3% was reported in the temperature range 200 to 300 °C
Ribeirinha et al. (2017)	Pd-membranes ILs were used for CO_2 separation Commercial CuO/ZnO/$Al_2O_3$1.5 g	S/M 1.5 180–240 °C Pressure 1–3 bar Sweep factor 2–20	90	80	NA	Investigations were made on the positive effect of CO_2 removal on the reformer. It was reported that selective CO_2 removal results in a slight enhancement in methanol conversion than the hydrogen-selective membrane

(continued)

Table 18.1 (continued)

Author	System integration	Operating conditions	X (%)	HRF (%)	H_2 flux (mol/m^2 s)	Remarks
Tosti et al. (2008)	100 μm thick self-supported cold rolled Pd/Ag foils	WGS $CO/H_2O/CO_2$ 0.2/0.3/0.5 325–330 °C, 100 kPa, 0.0003 ml/s sweep gas	96.5	28.9	NA	The values of permeance were higher at temperature 135–275 °C while decreased to 5.8×10^{-5} at 276–360 °C. Notably, activation energy at lower temperatures were −1866 and −521 kJ/mol at a higher temperature
Chiappetta et al. (2010)	100 μm thick Pd/Ag membrane Commercial catalyst 31% Ni, 39% NiO, 11% Al_2O_3 and 19% SiO_2)	**Methane SR** 360–560 °C 200–600 kPa Catalyst amount 0.5–6.1 gm	50	43	NA	An optimal combination of A_m/V_{cat} (area of membrane/volume of catalyst) and L_s/A_m (limiting reagent flow rate/area of the membrane) was suggested to have an optimal design for improved MR performance without sweep gas
Cornaglia et al. (2013)	150 μm Self-supported Pd/Ag membrane Catalyst 0.6% $Pt/La_2O_3{\cdot}SiO_2$	WGS 673–723 K, Sweep gas 500 N mL/min Pressure 100–800 kPa	>95	88	1.84×10^{-5}	It was reported that the effect of pressure is more important than temperature because H_2 flux through the membrane has low activation energy (5100 J/mol)

(continued)

Table 18.1 (continued)

Author	System integration	Operating conditions	X (%)	HRF (%)	H_2 flux (mol/m^2 s)	Remarks
Borgognoni et al. (2013)	150 μm thick 19 Pd/Ag self-supported membrane 100–500 kPa	Water/ethanol/methane 350° membrane 760° reformer, 3 bar;	71 at 500 kPa	88	0.38	It was reported that at pressures up to 500 kPa, the hydrogen content in retentate decrease up to 12%
Lim et al. (2012)	Pd–Cu and SiO_2–Al_2O_3 MR with 12.5% Na–Co/ZnO catalyst	Ethanol SR Temperature 623 K Pressure 1, 5 and 10 bar	60	NA	0.04	H_2/CO_2 selectivity was reported in the range of 200 to 1000 at 623 K

This necessitates an optimal temperature, pressure and flow rate to maintain the stability of both the catalyst and the membrane. An effective design of membrane, catalyst, and reactor are three essential and critical elements of a membrane reactor study (Tosti et al. 2008; Dittmeyer et al. 2017; Islam and Ilias 2012; Dunbar and Lee 2017; Gallucci et al. 2007; Pinto et al. 2013; Purnama et al. 2004; Saracco et al. 1999).

This article, therefore, focuses to present the challenges related to the commercial viability of membrane reactors and the steps that were performed by our group as a contribution towards improving hydrogen recovery using this system. A brief illustration is provided of each MR component that is membrane as well catalyst followed by integration and the future targets using the system.

18.1.2 Current Objective

A comprehensive illustration of hydrogen separation using dense Pd/Ag membranes in an optimized multi-pass membrane reactor design using catalyst with zero CO selectivity is presented in the current chapter.

18.2 Membranes in Membrane Reactors

Hydrogen is soluble in dense palladium over a wide temperature range in comparison to other metals such as niobium, vanadium, etc. (Lu et al. 2007). The catalytic dissociation of molecular hydrogen into H atoms on palladium allows H-atoms to dissolve and diffuse through the metal by solution-diffusion mechanism (Paglieri and Way 2002; Conde et al. 2017). This mechanism enables palladium membranes with infinite hydrogen selectivity provided the surface of the membrane is non-porous or dense. Transport of hydrogen through dense Pd membrane follows Sieverts law wherein hydrogen dissolves in the membrane and diffuses as atoms at a pressure exponent 0.5 (Eq. 18.1) (Lewis 1995; Ward and Dao 1999). Based on the value of the pressure exponent at a constant temperature, Sievert's law is based on two assumptions:

- If $n = 0.5$; diffusion of hydrogen atom through Pd bulk is rate controlling which indicates that flux of hydrogen through the membranes becomes proportional to the square root of the hydrogen partial pressures on both sides of the membrane.
- If $n > 0.5$, surface dissociation/recombination reactions at either or both sides of the membrane becomes rate controlling. This case is majorly observed with thinner membranes or in case of thicker membranes at high feed pressures as bulk diffusion becomes faster than surface dissociation/recombination.

Further, the critical phase transition temperature of palladium in the presence of hydrogen is high (~300 °C) which necessitates hydrogen separation studies to be

performed at very high temperature. In order to lower the critical phase transition temperature of palladium, alloying Pd with elements such as Ag (Pd/Ag) is well reported. Alloying Pd with Ag also increases H_2 permeability because of the increase in average bond distance of the alloys in comparison to pure Pd (Conde et al. 2017). Considering the flux of hydrogen through pure Pd or Pd/Ag only as an intrinsic property of the membrane, it is well reported that the surface of the membrane plays a critical role. The occurrence of pinholes as minor defects formed either during preparation or during the experiment causes flux to become proportional to the pressure difference with n = 1 (Guazzone et al. 2006). Assuming Knudsen behavior, this flux can be represented as provided in Eq. 18.2 (Guazzone and Ma 2008).

$$\mathrm{J_{H_2}} = \frac{\mathrm{P_{H_2}}\left(\mathrm{p^{n}_{H_{2,ret}}} - \mathrm{p^{n}_{H_{2,perm}}}\right)}{t} \tag{18.1}$$

where, n = 0.5 at a low hydrogen pressure (Sievert's law).

J_{H_2}: Hydrogen flux (mol/m^2 s), P_{H_2}: Hydrogen permeability, t: Membrane thickness (m).

$p^{n}_{H_{2,ret}}$: Partial pressure of hydrogen in retentate (Pa) at n = 0.5.

$\mathrm{p^{n}_{H_{2,perm}}}$: Partial pressure of hydrogen in permeate (Pa) at n = 0.5.

when Knudsen mechanism occurs

$$\mathrm{J_i} = \frac{\mathrm{G}}{\sqrt{2 \cdot \mathrm{M_i} \cdot \mathrm{R} \cdot \mathrm{T}}} \cdot \frac{\Delta\,\mathrm{p_i}}{\delta} \tag{18.2}$$

J_i: Flux of ith species across the membrane, G: Geometrical factor to account membrane porosity and pore tortuosity, M_i: Molecular weight of ith species, R: Universal gas constant, T: Absolute temperature, Δp_i: Pressure difference of species, δ: membrane thickness.

Hence, preparing dense Pd membranes (i.e. membranes with no defects, or pores) itself is a critical task which necessitates details of its preparation as discussed below.

Effect of Membrane Fabrication

Palladium membranes reported in the literature are either self-supported or supported. Self-supported Pd foils or membranes are extremely expensive and normally >30 μm in thickness in order to remain durable. However, Pd membranes can be deposited onto asymmetric porous supports. This porous support can be utilized to prepare comparatively thinner membrane (for higher flux) and thus reduce the preparation cost. Depending on the support type, the microstructure of the support dictates the deposited membrane morphology which thereby affects its perm-selectivity (Pacheco Tanaka et al. 2006).

Supported palladium membranes are prepared by deposition of palladium or Pd-alloys on a multi-layer porous ceramic or porous stainless steel (PSS) support. Some well-known thin film deposition techniques include sputtering (Jayaraman et al. 1995), chemical vapor deposition (CVD) (Yan et al. 1994), electroplating (Bhandari

and Ma 2009) and electroless plating (ELP) (Bosko et al. 2011). The advantage of sputtering is that it gives a uniform coverage of deposited material over the substrate and accuracy in controlling thickness. However, the high cost of deposition set up, and poor crystallinity of sputtered layers makes it un-economical on a wider scale. CVD also results in uniform, conformal and high purity films. However, the films can only be deposited at elevated temperatures which impose restrictions on the kind of substrates to be used. Further, high temperature leads to stresses in films deposited with materials having different thermal expansion coefficient, which can cause mechanical instabilities in the deposited films (Straczewski et al. 2014; Okazaki et al. 2011). Electroplating has also been unsuccessful so far due to the evolution of hydrogen on the substrate surface that leads to pinhole formation in the membrane. Lastly, electroless plating is an autocatalytic process which requires no external electrical current while using reducing agents such as hydrazine for metal deposition onto pre-activated supports. For these reasons, all support materials such as non-conductors, semiconductors and metals can be used for deposition. The use of strong reducing agents, however, does not make electroless plating a green methodology. On the other hand, no requirement of an expensive set up in addition to its flexibility to deposit metal and metal combinations on to different supports makes it a relatively economical and steadfast technique. However, irrespective of any metal deposition technique used, the large columnar microstructure reported with sputtering based techniques and cauliflower-like morphology mostly reported for electroless plated palladium membranes tend to form micro-pores upon heat treatment. Hence, in order to obtain a dense membrane morphology, a combination of tools is always suggested that results in a uniform activation layer followed by membrane film having controlled composition, thickness, and morphology.

Numerous works have illustrated Pd deposition on a wide variety of supports which include tantalum and niobium (Buxbaum and Kinney 1996), porous glass (Uemiya et al. 1991), alumina (Kikuchi and Uemiya 1991), and porous stainless steel (Mardilovich et al. 1998; Dittmeyer et al. 2001; Huang and Dittmeyer 2006; Ayturk and Ma 2009, etc.). Many authors have also reported the effect of modified activation, the effect of inter-diffusion barriers in case of porous stainless steel (PSS) support, the effect of different annealing temperatures and effect of modified ELP plating techniques such as simultaneous electroless plating, sequential electroless plating, and pore plating. Kitiwan and Atong (2010) studied the influence of porosity of α-alumina support on Pd deposition. Deposition morphology was investigated at four different sintering temperatures: 1200, 1300, 1400 and 1500 °C. The pore size of support varied from 0.25 to 0.35 μm. It was reported that higher temperature gave a larger and smoother grain while a lower temperature exhibits bimodal grain size structure. Selectivity was found to be poorer for more porous support but could be improved with higher plating time. Okazaki et al. (2011) reported membrane preparation with vacuum ELP and simultaneous deposition on α-alumina support. Alloying of Pd with Ag was performed at temperatures higher than 230 °C. The alloy progressed effectively at temperature 550–600 °C with sharp XRD peaks. Temperature higher than 600 °C caused the formation of a lesser hydrogen permeable alloy of Pd–Ag. Maximum hydrogen flux of 0.8 mol/m^{2}s was observed at 550 °C. Tanaka

(Pacheco Tanaka et al. 2006) too suggested 500 °C (thermal treatment) for alloy formation in order to minimize defects. It was suggested that in a simultaneous deposition, Ag is preferentially deposited on Pd seed nuclei and therefore shields active Pd particle and prohibits plating reaction. Therefore control of deposition rate with proper Pd/Ag ratio is important. Annealing was optimized at 500 °C under hydrogen stream for 4 h, and precipitation in the plating solution was stabilized using ammonia and EDTA, which control the deposition rates of individual metals by modifying the redox potentials.

Pacheco Tanaka et al. (2008) reported yttria-stabilized zirconia (YSZ) mixed sol in 8–20 nm size range as an intermediate layer deposition on to ϒ-alumina support under vacuum suction. Coating this layer was followed by seeding, and additional sol layer and finally Pd coating. Though no significant defect was observed, it was reported that the effective area occupied by Pd became narrower by the co-presence of YSZ-gamma alumina that hindered H_2 permeation. In addition to this, the application of ceramic (20%YSZ-80%alumina) based interdiffusion barriers were also investigated recently by Fernandez et al. (2017) prior to Pd–Ag deposition on porous Hastelloy C276. The deposition of 2–5 layers of YSZ-alumina was carried out using atmospheric plasma spraying (APS) and dip coating. The resulting thickness of the layer after sintering and reduction was reported 40 μm. Pd–Ag deposition of 3–5 μm thickness was further carried out with simultaneous deposition. Straczewski et al. (2014) reported a comparison of YSZ coating using APS and TiO_2 coating using wet powder spraying (WPS) prior to Pd deposition on to PSS. Nearly 80–100 μm thick YSZ layer was coated though poor adhesion in case of TiO_2 was reported. It was clearly reported that completely defect-free membranes were not observed for all tubes prepared. Rust formation, especially visible after palladium coating, has been reported to induce large defects. In addition, variation in the alloy composition at the weld seams that include porous tube, dense adapter, and additional weld material could induce the formation of a contact material that causes preferential corrosion in SS 316. The final thickness of the Pd membrane was reported 14.4–25 μm with H_2/N_2 selectivity in the range of 60–120.

From the above studies, it becomes clear that the deposition of palladium on to both ceramic and PSS tubes still remains a challenge. Moreover, the pore size distribution of both supports is distinctly diverse. This variation in pore sizes eventually plays a crucial role in surface densification of palladium deposited. The difference in membrane deposition between porous SS and porous ceramic to achieve faster densification is therefore crucial to determine maximum hydrogen flux. This comparative information is not available in the literature, especially with regards to how palladium consumption for dense membrane synthesis can be decreased by the change of support porosity. The decrease in palladium consumption will drastically reduce the membrane preparation cost and it will improve hydrogen flux as well. These parameters are therefore critical for palladium membrane synthesis. In our study (Sharma 2018; Sharma et al. 2017), two kinds of support material were investigated as shown in Fig. 18.2: (a) porous alumina and (b) porous SS. The pore size distribution of PSS was much higher compared to porous alumina. This indicates that the amount of Pd required to have a dense membrane supported on SS would be much higher

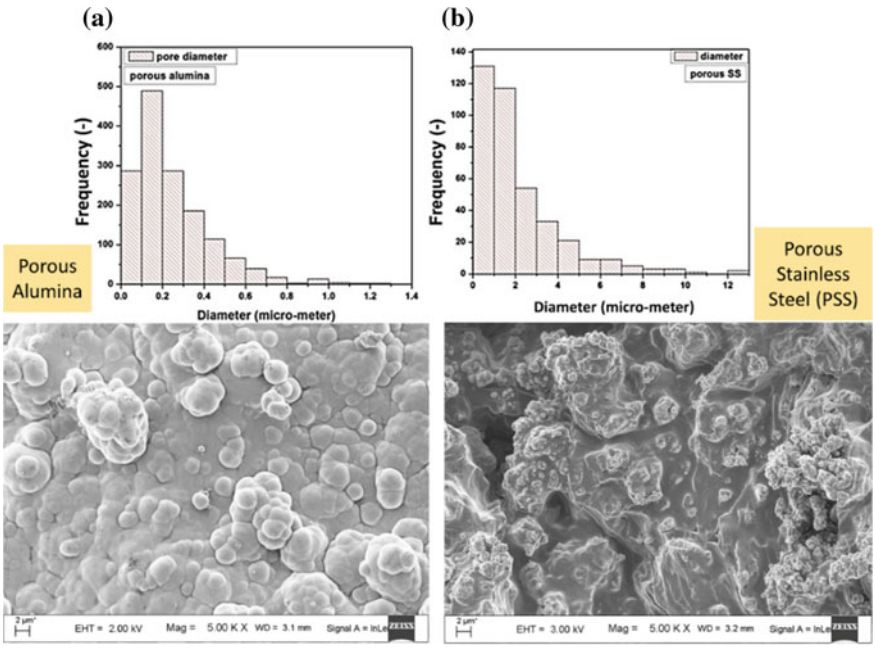

Fig. 18.2 Effect of support morphology on the membrane deposited

than that needed for alumina. A direct comparison of membrane surface between porous alumina and PSS show clearly that at the current cycle membrane surface still consists of pinholes. A large requirement, therefore, necessitates a number of cycles until a dense pinhole free membrane surface is obtained.

Factors That Affect Hydrogen Permeation Through the Membrane

Apart from membrane morphology, presence of CO, CO_2 along with other reformate components such as unreacted methanol and water also influence hydrogen permeation through the membranes. Two critical ways with which presence of impurities affect hydrogen separation through the membrane include (i) competitive inhibition in the presence of other gases such as CO and CO_2 blocking hydrogen adsorption sites and (ii) decrease in hydrogen permeability due to concentration polarization (Gallucci et al. 2007; Lüdtke et al. 1998). The same can be observed in Fig. 18.3 which shows that irrespective of commercial or the synthesized membrane, increasing mixture components to hydrogen in feed gas reduced its permeation thereby decreasing the hydrogen flux.

Inhibition of hydrogen permeation by the CO and CO_2 can be minimized at higher temperatures ($\geq$673 K). However, accumulation of less permeable species around the membranes leads to the development of a concentration boundary layer which decreases the hydrogen permeation due to the extra resistance. In order to alleviate its occurrence, increase in feed flow rate and application of sweep gases both in co-current and counter current is well reported. However, an increase in flow rate

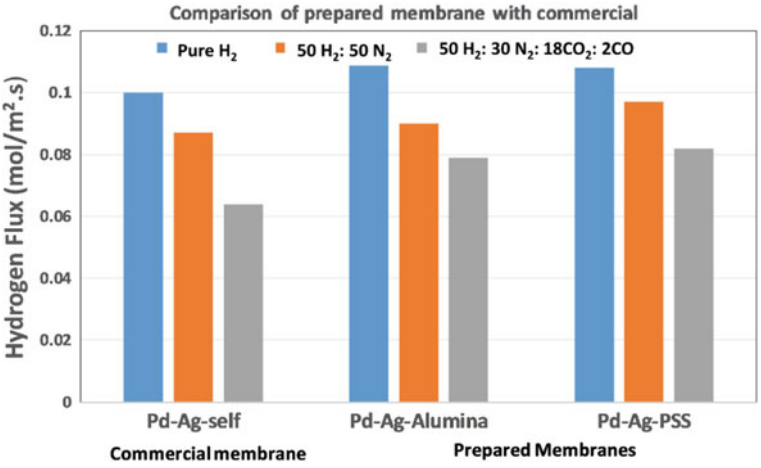

Fig. 18.3 Comparative hydrogen flux between prepared membranes and commercial membranes

decreases contact time that thereby drastically reduce the permeate H_2 recovery (Li et al. 2016).

Moreover, an introduction of sweep gas flow rate reduces the hydrogen partial pressure in the permeate side. An increase in the trans-membrane pressure difference, as a result, improves hydrogen flux. However, beyond a critical sweep gas velocity, both H_2 flux and H_2 recovery become constant and sweep gas plays only a marginal role in improving hydrogen permeation. In this context, a few modeling studies reported smaller reactor diameter, axial baffles and baffle patterns around the membrane to reduce concentration polarization (Chen et al. 2013, 2014).

To reduce concentration polarization, a smaller reactor diameter or reactor with baffle plates was suggested by Mori et al. (2007). An increase in linear gas velocity around the baffle plates was modeled to demonstrate the reduction in concentration polarization. Adding to that, the effect of baffle location, baffle pattern and baffle diameter to shell diameter ratio was also numerically investigated by Chen et al. (2014). They reported a significant improvement using one axial baffle around a single membrane but with further increase in the number of baffles more than one, hydrogen recovery remained unchanged. Additionally, intense fluctuations of local velocity near the wall using baffle inserted inside the membranes and slit-type baffles incorporated on the surface of the membrane have also been reported to improve flux. These numerical approaches thereby imply an evident role of baffles in reactor configurations to minimize concentration polarization. However to the best of authors knowledge, effect of baffles were never experimentally investigated especially for integrated MR studies.

With the above studies as a reference, we, therefore, devised a multi-pass membrane reactor with longitudinal baffle arrangements. The serpentine pass created using these baffles was utilized to develop an optimal membrane arrangement assembly. This assembly could regulate the partial pressure of hydrogen across the reactor,

minimize concentration polarization effect due to the higher magnitude of gas around the membrane and most importantly improve the contacting of gas with membrane resulting in improved hydrogen recovery (Sharma et al. 2018).

18.3 Catalysts in Membrane Reactors

In addition to membranes, catalyst activity also affects MR performance. This is because the only catalyst with high hydrogen production and minimal by-product formation can bring efficient membrane activity by maintaining a sufficient trans-membrane hydrogen drive.

The catalyst for methanol steam reforming mostly include transition metals belonging to the group 8–10 because of their high catalytic activity (Patel and Pant 2007). However, steam reforming is an endothermic reaction which results in higher H_2 yield only at higher temperatures but at the cost of increasing CO. Commercial catalysts such as $CuO/ZnO/Al_2O_3$, therefore, show 400–60,000 ppm of CO in reformate gas at temperatures between 250 and 350 °C and pressures between 1 and 6 bar respectively (Purnama et al. 2004).

An alternate remedy to minimize CO formation is to target catalysts that have minimal CO selectivity. If CO formation is eliminated catalyst poisoning can be minimized and the HT & LT-WGS unit from the conventional technology can be eliminated thereby minimizing the auxiliaries. Hence, the need to develop a catalyst that hinders CO generation at raised temperatures as well as pressures was necessary.

Methanol steam reforming is mostly carried out using Cu, Ni and Fe as the active metal in the catalyst. Copper is a low cost, a highly abundant metal well known to transport oxygen, catalyze oxidation-reduction reactions and possess high hydrogen selectivity (Abrokwah et al. 2016). High metal surface area and low metal particle size are mostly targeted to attain highly active copper catalysts. To attain that, addition of ZnO and ZrO_2 to copper-based alumina-supported catalysts has been reported. Addition of zinc oxide improves copper dispersion while ZrO_2 reduces the CO yield. In addition to that, supports such as CeO_2, (Das et al. 2015) $ZnO–Al_2O_3$, (Lindström et al. 2002) ZrO_2, and MgO (Palo et al. 2007) have also been extensively studied to prepare the catalysts with minimal CO selectivity.

The combined interaction between the active metal and the support brings about the complete catalytic functionality. This is because the physicochemical properties of a carrier significantly affect the existing surface reactions either by modifying the electrical properties of the metal or by promoting the activation of intermediate species. In addition to mono-metallic catalysts, co-operative interactions between two metals in a bi-metallic catalyst show different structures according to metal properties, metal support interactions, atmosphere (oxidative and reductive) and temperature. Depending on these interactions, bi-metallic structures in the form of heteroatom and nano-alloys have mostly been reported in the literature (Dal Santo et al. 2012).

For instance, a rapid decrease in the catalytic activity of Ni due to metal sintering and coke deposition can be partially inhibited using additional metals such as Cu. In a similar manner, the addition of Fe to Ni supported on cerium has also been reported to suppress carbon formation rate (Ashok and Kawi 2014; Koike et al. 2012). High redox property of Fe causes the transfer of oxygen atoms from Fe to Ni which thereby promotes the reaction between carbonaceous species and oxygen species. Therefore, with the literature reported; it is evident that in order to eliminate CO formation bi-metallic catalysts are indeed promising.

Keeping this as our basis, we also demonstrated bi-metallic Cu–Fe supported on alumina-zinc-zirconia (AZZ) based composite as an effective catalyst to inhibit CO formation up 400 °C at atmospheric pressure in reformer studies as shown in Fig. 18.4a (Sharma 2018). Increasing the pressure up to 1.8 bar in MR studies CO formation was observed as shown in Fig. 18.4b. But this percentage of CO is much lesser than 0.6 (at 553 K) which is mostly reported in the literature (Sharma 2018).

Strategies for Effective Design of Membrane Reactors

In one of our studies, we reported longitudinal baffles placed along the length of the membrane which generates instabilities that start at the baffle tip (Sharma et al. 2018). This baffle-generated instability/turbulence reduces the thickness of the concentration boundary layer by increasing mixing and minimizes the effect of concentration polarization. Such longitudinal baffle arrangement in a large diameter system makes an inevitable high throughput system that can accommodate a large number of membrane tubes. The use of longitudinal baffle enhances mixing despite changing the diameter of the separator and hence provides flexibility for a "*multi-pass*" membrane separator system. Using this system, we observed that by employing multiple numbers of membranes in the shell separated by baffles, we could devise different membrane arrangements that could be used to control hydrogen partial pressure across the shell. The same was further systematically tested both as separator and integrated membrane reactor to determine its effect on improving overall hydrogen recovery.

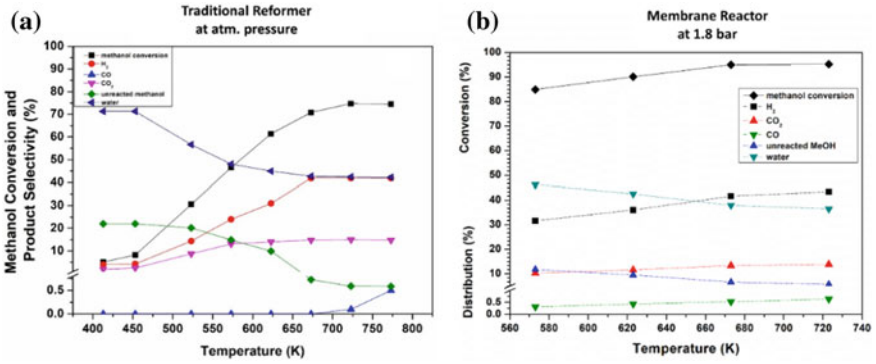

Fig. 18.4 Catalyst activity in a traditional reformer and when integrated to a membrane reactor

A case study to illustrate the enhancement in hydrogen recovery using the 'in-house' designed multi-pass membrane reactor is presented in Fig. 18.5. Membrane reactor run in this section shows four membranes with two assemblies: (a) single pass and (b) multi-pass as presented in Fig. 18.5a. In both cases, catalyst mixed with quartz was placed in the inlet zone of the reactor. Hydrogen recovery for both the designs was compared as shown in Fig. 18.5b. It should be noted that catalyst lies in the inlet zone followed with the first two membranes that lie directly above the catalyst in the same inlet side and the other two membranes at the center. Further, in multi-pass assembly, catalysts remain at the same inlet side while the membranes are connected at the center (two on both sides of the baffle). Hydrogen recovery in case of multi-pass MR is higher compared to single pass MR. This is because of the better contacting achieved in case of multi-pass MR compared to single pass MR due to the presence of two extra baffles and the multi-pass MR design results in ~80% hydrogen recovery.

Permeate hydrogen flow rate with multi-pass MR was observed 0.92 LPM. Further, in comparison with commercial MR ME-100® (that consists of nearly 7 self-supported membranes in its assembly), the hydrogen recovery with in-house designed multi-pass MR (with 4 supported Pd–Ag membranes on PSS) was much higher as shown in Fig. 18.5b. Moreover, it should be noted that even with single pass the four membrane assembly of Pd–Ag supported on PSS performs at par with the ME-100®. Therefore, in-house designed multi-pass MR with supported Pd–Ag membrane in current study performs better than commercially available MR for the same output.

Moreover, using multi-pass multiple membrane configuration, the losses in hydrogen recovery are also minimized. This makes the multi-pass multiple membrane configuration a more scalable approach to further high throughput MR performances. A schematic representing the expected scalability from the current obtained performance is presented in Fig. 18.6. Therefore, more studies using the multi-pass membrane reactor are suggested. In addition, the negligible cost-effectiveness of membrane preparation limit MR viability, but targeting higher hydrogen-selective permeation using the same membrane would dramatically reduce its preparation cost

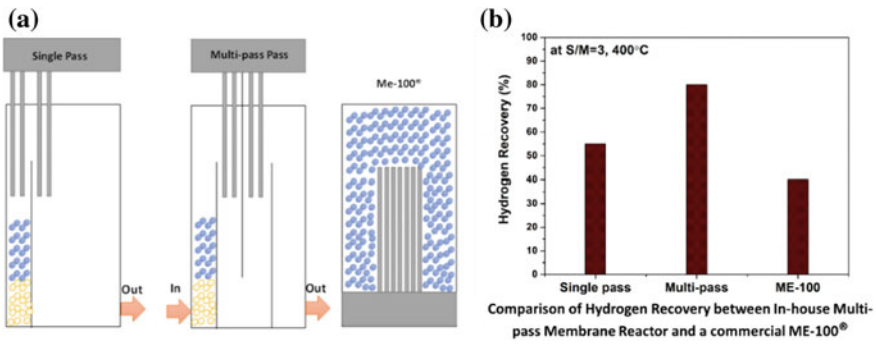

Fig. 18.5 Multi-pass membrane reactor performance in comparison to a commercial membrane reactor

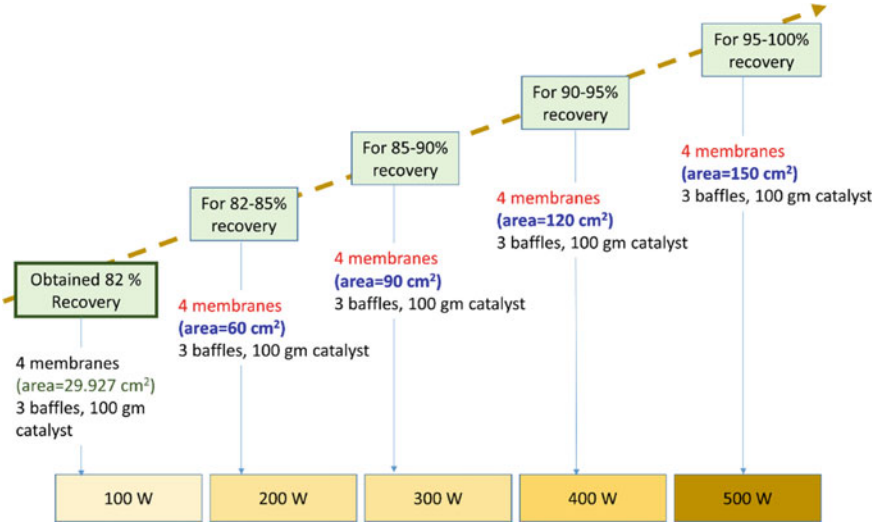

Fig. 18.6 Proposed scheme of high throughput membrane reactor performance based on the current performance

as well. Hence, with all its challenges, MR still persists to be an intriguing device to cater to the growing hydrogen economy and sustain itself based on its higher fuel value both in terms of performance and economics.

18.4 Conclusions

In the current work, multi-pass membrane reactor (MR) is illustrated as a potential tool for hydrogen production on site using methanol as a feed. This works integrates methanol steam reforming using Cu–Fe based spinel catalyst with Pd–Ag membrane. The key characteristics of membrane reactor components that regulate its performance are highlighted in this study. These characteristics include

(a) For membranes: non-porous or dense surface morphology, optimal operating parameters to minimize mixture gas inhibition, multi-pass reactor design to abate concentration polarization
(b) For catalysts: optimal catalyst structure and composition that shows no CO selectivity at high temperatures and high pressures.

Although fabrication of a dense membrane is a critical challenge till date, a combination of methods involving electroless deposition along with using a support with more uniform pore structure is suggested. Further, high temperature operation during hydrogen separation from mixture is also essential in order to negate any competitive interaction of CO, CO_2 with the membrane. Moreover, multi-pass MR design using

three baffles located longitudinally in the shell of the reactor allows it to accommodate multiple set of membranes in a bundle and also in parallel. In order to the enhance the overall contacting of gas with the membrane, the multi-pass MR design with a bundle of membranes separated by a single baffle in the center and one baffle each on both sides was observed as an optimal design. In addition to membrane, bimetallic catalysts having Cu–Fe spinel structure supported on AZZ was developed which showed no CO formation up to 673 K with minimal increase at pressures up to 1.8 bar. Applying these characteristics as a basis, a maximum hydrogen recovery of ~80% was obtained under actual reaction conditions at 1.8 bar and 673 K. This indicates that the performance of MR could be tuned using a suitable combination of these characteristics. However, more studies are targeted to demonstrate its high throughput performance with a better hydrogen-selective membrane. Lastly, increasing the surface area over the length of the membrane rather than increasing the number of the membrane is suggested to be a more scalable approach towards high throughput MR performance.

References

Aasberg-Petersen K, Nielsen CS, Jørgensen SL (1998) Membrane reforming for hydrogen. Catal Today 46(2):193–201. https://doi.org/10.1016/S0920-5861(98)00341-1

Abrokwah RY, Deshmane VG, Kuila D (2016) Comparative performance of M-MCM-41 (M: Cu Co, Ni, Pd, Zn and Sn) catalysts for steam reforming of methanol. J Mol Catal A: Chem 425:10–20. https://doi.org/10.1016/j.molcata.2016.09.019

Ashok J, Kawi S (2014) Nickel-iron alloy supported over iron-alumina catalysts for steam reforming of biomass tar model compound. ACS Catalysis 4(1):289–301. https://doi.org/10.1021/cs400621p

Ayturk ME, Ma YH (2009) Electroless Pd and Ag deposition kinetics of the composite Pd and Pd/Ag membranes synthesized from agitated plating baths. J Membr Sci 330(1):233–245. https://doi.org/10.1016/j.memsci.2008.12.062

Basile A (2013) Handbook of membrane reactors, vol 1

Basile A, Tosti S, Capannelli G, Vitulli G, Iulianelli A, Gallucci F, Drioli E (2006) Co-current and counter-current modes for methanol steam reforming membrane reactor: experimental study. Catal Today 118(1):237–245. https://doi.org/10.1016/j.cattod.2006.05.086

Basile A, Parmaliana A, Tosti S, Iulianelli A, Gallucci F, Espro C, Spooren J (2008) Hydrogen production by methanol steam reforming carried out in membrane reactor on Cu/Zn/Mg-based catalyst. Catal Today 137(1):17–22. https://doi.org/10.1016/j.cattod.2008.03.015

Basile A, Iulianelli A, Tong J (2015) 6—membrane reactors for the conversion of methanol and ethanol to hydrogen. In: Basile A, Di Paola L, Hai Fl, Piemonte V (eds) Membrane reactors for energy applications and basic chemical production. Woodhead Publishing, pp 187–208. https://doi.org/10.1016/B978-1-78242-223-5.00006-6

Berry GD, Aceves SM (1998) Onboard storage alternatives for hydrogen vehicles. Energy Fuels 12(1):49–55. https://doi.org/10.1021/ef9700947

Bhandari R, Ma YH (2009) Pd–Ag membrane synthesis: the electroless and electro-plating conditions and their effect on the deposits morphology. J Membr Sci 334(1):50–63. https://doi.org/10.1016/j.memsci.2009.02.014

Borgognoni F, Tosti S, Vadrucci M, Santucci A (2013) Combined methane and ethanol reforming for pure hydrogen production through Pd-based membranes. Int J Hydrogen Energy 38(3):1430–1438. https://doi.org/10.1016/j.ijhydene.2012.11.036

Bosko ML, Lombardo EA, Cornaglia LM (2011) The effect of electroless plating time on the morphology, alloy formation and H2 transport properties of Pd–Ag composite membranes. Int J Hydrogen Energy 36(6):4068–4078. https://doi.org/10.1016/j.ijhydene.2010.12.056

Brown LF (2001) A comparative study of fuels for on-board hydrogen production for fuel-cell-powered automobiles. Int J Hydrog Energy 26(4):381–397. https://doi.org/10.1016/S0360-3199(00)00092-6

Buxbaum RE, Kinney AB (1996) Hydrogen transport through tubular membranes of palladium-coated tantalum and niobium. Ind Eng Chem Res 35(2):530–537. https://doi.org/10.1021/ie950105o

Buxbaum R, Lei H (2003) Power output and load following in a fuel cell fueled by membrane reactor hydrogen. J Power Sources 123(1):43–47. https://doi.org/10.1016/S0378-7753(03)00359-8

Chen W-H, Syu W-Z, Hung C-I, Lin Y-L, Yang C-C (2013) Influences of geometry and flow pattern on hydrogen separation in a Pd-based membrane tube. Int J Hydrogen Energy 38(2):1145–1156. https://doi.org/10.1016/j.ijhydene.2012.10.068

Chen W-H, Lin C-H, Lin Y-L (2014) Flow-field design for improving hydrogen recovery in a palladium membrane tube. J Membr Sci 472:45–54. https://doi.org/10.1016/j.memsci.2014.08.041

Chiappetta G, Barbieri G, Drioli E (2010) Pd/Ag-based membrane reactors on small scale: assessment of the feed pressure and design parameters effect on the performance. Chem Eng Process 49(7):722–731. https://doi.org/10.1016/j.cep.2009.11.011

Conde JJ, Maroño M, Sánchez-Hervás JM (2017) Pd-based membranes for hydrogen separation: review of alloying elements and their influence on membrane properties. Sep Purif Rev 46(2):152–177. https://doi.org/10.1080/15422119.2016.1212379

Cornaglia CA, Tosti S, Sansovini M, Múnera J, Lombardo EA (2013) Novel catalyst for the WGS reaction in a Pd-membrane reactor. Appl Catal A 462–463:278–286. https://doi.org/10.1016/j.apcata.2013.04.019

Dal Santo V, Gallo A, Naldoni A, Guidotti M, Psaro R (2012) Bimetallic heterogeneous catalysts for hydrogen production. Catal Today 197(1):190–205. https://doi.org/10.1016/j.cattod.2012.07.037

Das D, Llorca J, Dominguez M, Colussi S, Trovarelli A, Gayen A (2015) Methanol steam reforming behavior of copper impregnated over CeO2–ZrO2 derived from a surfactant assisted coprecipitation route. Int J Hydrogen Energy 40(33):10463–10479. https://doi.org/10.1016/j.ijhydene.2015.06.130

de Bruijn F (2005) The current status of fuel cell technology for mobile and stationary applications. Green Chem 7(3):132–150. https://doi.org/10.1039/B415317K

Deshmukh SARK, Heinrich S, Mörl L, van Sint Annaland M, Kuipers JAM (2007) Membrane assisted fluidized bed reactors: potentials and hurdles. Chem Eng Sci 62(1):416–436. https://doi.org/10.1016/j.ces.2006.08.062

Dittmeyer R, Höllein V, Daub K (2001) Membrane reactors for hydrogenation and dehydrogenation processes based on supported palladium. J Mol Catal A: Chem 173(1):135–184. https://doi.org/10.1016/S1381-1169(01)00149-2

Dittmeyer R, Boeltken T, Piermartini P, Selinsek M, Loewert M, Dallmann F, Kreuder H, Cholewa M, Wunsch A, Belimov M, Farsi S, Pfeifer P (2017) Micro and micro membrane reactors for advanced applications in chemical energy conversion. Curr Opin Chem Eng 17:108–125. https://doi.org/10.1016/j.coche.2017.08.001

Dunbar ZW, Lee IC (2017) Effects of elevated temperatures and contaminated hydrogen gas mixtures on novel ultrathin palladium composite membranes. Int J Hydrogen Energy 42(49):29310–29319. https://doi.org/10.1016/j.ijhydene.2017.10.032

Fernandez E, Helmi A, Medrano JA, Coenen K, Arratibel A, Melendez J, de Nooijer NCA, Spallina V, Viviente JL, Zuñiga J, van Sint AM, Pacheco Tanaka DA, Gallucci F (2017) Palladium based membranes and membrane reactors for hydrogen production and purification: an overview of

research activities at Tecnalia and TU/e. Int J Hydrogen Energy 42(19):13763–13776. https://doi.org/10.1016/j.ijhydene.2017.03.067
Gallucci F, Chiaravalloti F, Tosti S, Drioli E, Basile A (2007) The effect of mixture gas on hydrogen permeation through a palladium membrane: Experimental study and theoretical approach. Int J Hydrogen Energy 32(12):1837–1845. https://doi.org/10.1016/j.ijhydene.2006.09.034
Guazzone F, Ma YH (2008) Leak growth mechanism in composite Pd membranes prepared by the electroless deposition method. AIChE J 54(2):487–494. https://doi.org/10.1002/aic.11397
Guazzone F, Payzant EA, Speakman SA, Ma YH (2006) Microstrains and stresses analysis in electroless deposited thin Pd films. Ind Eng Chem Res 45(24):8145–8153. https://doi.org/10.1021/ie060756s
Huang Y, Dittmeyer R (2006) Preparation and characterization of composite palladium membranes on sinter-metal supports with a ceramic barrier against intermetallic diffusion. J Membr Sci 282(1):296–310. https://doi.org/10.1016/j.memsci.2006.05.032
Islam MA, Ilias S (2012) Steam reforming of methanol in a Pd-composite membrane reactor. Sep Sci Technol 47(14–15):2177–2185. https://doi.org/10.1080/01496395.2012.672357
Iulianelli A, Longo T, Basile A (2008) Methanol steam reforming reaction in a Pd–Ag membrane reactor for CO-free hydrogen production. Int J Hydrogen Energy 33(20):5583–5588. https://doi.org/10.1016/j.ijhydene.2008.07.044
Iulianelli A, Ribeirinha P, Mendes A, Basile A (2014) Methanol steam reforming for hydrogen generation via conventional and membrane reactors: a review. Renew Sustain Energy Rev 29:355–368. https://doi.org/10.1016/j.rser.2013.08.032
Jayaraman V, Lin YS, Pakala M, Lin RY (1995) Fabrication of ultrathin metallic membranes on ceramic supports by sputter deposition. J Membr Sci 99(1):89–100. https://doi.org/10.1016/0376-7388(94)00212-H
Kikuchi E, Uemiya S (1991) Preparation of supported thin palladium-silver alloy membranes and their characteristics for hydrogen separation. Gas Sep Purif 5(4):261–266. https://doi.org/10.1016/0950-4214(91)80035-4
Kitiwan M, Atong D (2010) Effects of porous alumina support and plating time on electroless plating of palladium membrane. J Mater Sci Technol 26(12):1148–1152. https://doi.org/10.1016/S1005-0302(11)60016-9
Koike M, Li D, Nakagawa Y, Tomishige K (2012) A highly active and coke-resistant steam reforming catalyst comprising uniform nickel-iron alloy nanoparticles. Chemsuschem 5(12):2312–2314. https://doi.org/10.1002/cssc.201200507
Lewis FA (1995) The palladium-hydrogen system: structures near phase transition and critical points. Int J Hydrogen Energy 20(7):587–592. https://doi.org/10.1016/0360-3199(94)00113-E
Li Q, He R, Gao J-A, Jensen JO, Bjerrum N (2003) The CO poisoning effect in PEMFCs operational at temperatures up to 200 degrees C. J Electrochem Soc 150(12):A1599–A1605. https://doi.org/10.1149/1.1619984
Li X, Li A, Lim CJ, Grace JR (2016) Hydrogen permeation through Pd-based composite membranes: effects of porous substrate, diffusion barrier and sweep gas. J Membr Sci 499:143–155. https://doi.org/10.1016/j.memsci.2015.10.037
Liguori S, Iulianelli A, Dalena F, Piemonte V, Huang Y, Basile A (2014) Methanol steam reforming in an Al2O3 supported thin Pd-layer membrane reactor over Cu/ZnO/Al2O3 catalyst. Int J Hydrogen Energy 39(32):18702–18710. https://doi.org/10.1016/j.ijhydene.2013.11.113
Lim H, Gu Y, Oyama ST (2012) Studies of the effect of pressure and hydrogen permeance on the ethanol steam reforming reaction with palladium- and silica-based membranes. J Membr Sci 396:119–127. https://doi.org/10.1016/j.memsci.2012.01.004
Lindström B, Pettersson LJ, Govind Menon P (2002) Activity and characterization of Cu/Zn, Cu/Cr and Cu/Zr on γ-alumina for methanol reforming for fuel cell vehicles. Appl Catal A 234(1):111–125. https://doi.org/10.1016/S0926-860X(02)00202-8
Lu GQ, Diniz da Costa JC, Duke M, Giessler S, Socolow R, Williams RH, Kreutz T (2007) Inorganic membranes for hydrogen production and purification: a critical review and perspective. J Colloid Interface Sci 314(2):589–603. https://doi.org/10.1016/j.jcis.2007.05.067

Lüdtke O, Behling RD, Ohlrogge K (1998) Concentration polarization in gas permeation. J Membr Sci 146(2):145–157. https://doi.org/10.1016/S0376-7388(98)00104-5

Mardilovich PP, She Y, Ma YH, Rei MH (1998) Defect-free palladium membranes on porous stainless-steel support. AIChE J 44(2):310–322. https://doi.org/10.1002/aic.690440209

Mori N, Nakamura T, Noda K-i, Sakai O, Takahashi A, Ogawa N, Sakai H, Iwamoto Y, Hattori T (2007) Reactor configuration and concentration polarization in methane steam reforming by a membrane reactor with a highly hydrogen-permeable membrane. Ind Eng Chem Res 46(7):1952–1958. https://doi.org/10.1021/ie060989j

Okazaki J, Ikeda T, Tanaka DAP, Sato K, Suzuki TM, Mizukami F (2011) An investigation of thermal stability of thin palladium–silver alloy membranes for high temperature hydrogen separation. J Membr Sci 366(1):212–219. https://doi.org/10.1016/j.memsci.2010.10.011

Pacheco Tanaka DA, Llosa Tanco MA, Nagase T, Okazaki J, Wakui Y, Mizukami F, Suzuki TM (2006) Fabrication of hydrogen-permeable composite membranes packed with palladium nanoparticles. Adv Mater 18(5):630–632. https://doi.org/10.1002/adma.200501900

Pacheco Tanaka DA, Llosa Tanco MA, Okazaki J, Wakui Y, Mizukami F, Suzuki TM (2008) Preparation of "pore-fill" type Pd–YSZ–γ-Al2O3 composite membrane supported on α-Al2O3 tube for hydrogen separation. J Membr Sci 320(1):436–441. https://doi.org/10.1016/j.memsci.2008.04.044

Paglieri SN, Way JD (2002) Innovations in palladium membrane research. Sep Purif Methods 31(1):1–169. https://doi.org/10.1081/spm-120006115

Palo DR, Dagle RA, Holladay JD (2007) Methanol steam reforming for hydrogen production. Chem Rev 107(10):3992–4021. https://doi.org/10.1021/cr050198b

Patel S, Pant KK (2007) Experimental study and mechanistic kinetic modeling for selective production of hydrogen via catalytic steam reforming of methanol. Chem Eng Sci 62(18):5425–5435. https://doi.org/10.1016/j.ces.2007.01.044

Pinto F, André RN, Franco C, Carolino C, Gulyurtlu I (2013) Effect of syngas composition on hydrogen permeation through a Pd–Ag membrane. Fuel 103:444–453. https://doi.org/10.1016/j.fuel.2012.05.060

Purnama H, Ressler T, Jentoft RE, Soerijanto H, Schlögl R, Schomäcker R (2004) CO formation/selectivity for steam reforming of methanol with a commercial CuO/ZnO/Al2O3 catalyst. Appl Catal A 259(1):83–94. https://doi.org/10.1016/j.apcata.2003.09.013

Ribeirinha P, Abdollahzadeh M, Boaventura M, Mendes A (2017) H2 production with low carbon content via MSR in packed bed membrane reactors for high-temperature polymeric electrolyte membrane fuel cell. Appl Energy 188:409–419. https://doi.org/10.1016/j.apenergy.2016.12.015

Sá S, Silva H, Brandão L, Sousa JM, Mendes A (2010) Catalysts for methanol steam reforming—a review. Appl Catal B 99(1):43–57. https://doi.org/10.1016/j.apcatb.2010.06.015

Saracco G, Neomagus HWJP, Versteeg GF, Swaaij WPMV (1999) High-temperature membrane reactors: potential and problems. Chem Eng Sci 54(13):1997–2017. https://doi.org/10.1016/S0009-2509(99)00009-3

Schäfer A, Heywood JB, Weiss MA (2006) Future fuel cell and internal combustion engine automobile technologies: a 25-year life cycle and fleet impact assessment. Energy 31(12):2064–2087. https://doi.org/10.1016/j.energy.2005.09.011

Sharma R (2018) Production of high purity hydrogen through methanol based membrane reformer. Doctoral Thesis, IIT Guwahati, Guwahati, India

Sharma R, Kumar A, Upadhyay Rajesh K (2017) Catalytic Sol assisted dense Pd/γ-Al2O3 membrane using modified electroless plating: effect of process on surface morphology. Chem Prod Process Model, 12. https://doi.org/10.1515/cppm-2016-0023

Sharma R, Kumar A, Upadhyay RK (2018) Characteristic of a multi-pass membrane separator for hydrogen separation through self-supported PdAg membranes. Int J Hydrogen Energy 43(10):5019–5032. https://doi.org/10.1016/j.ijhydene.2018.01.127

Straczewski G, Völler-Blumenroth J, Beyer H, Pfeifer P, Steffen M, Felden I, Heinzel A, Wessling M, Dittmeyer R (2014) Development of thin palladium membranes supported on large porous

310L tubes for a steam reformer operated with gas-to-liquid fuel. Chem Eng Process 81:13–23. https://doi.org/10.1016/j.cep.2014.04.002

Tosti S, Basile A, Bettinali L, Borgognoni F, Gallucci F, Rizzello C (2008) Design and process study of Pd membrane reactors. Int J Hydrogen Energy 33(19):5098–5105. https://doi.org/10.1016/j.ijhydene.2008.05.031

Uemiya S, Sato N, Ando H, Kude Y, Matsuda T, Kikuchi E (1991) Separation of hydrogen through palladium thin film supported on a porous glass tube. J Membr Sci 56(3):303–313. https://doi.org/10.1016/S0376-7388(00)83040-9

Verhelst S (2014) Recent progress in the use of hydrogen as a fuel for internal combustion engines. Int J Hydrog Energy 39. https://doi.org/10.1016/j.ijhydene.2013.10.102

Ward TL, Dao T (1999) Model of hydrogen permeation behavior in palladium membranes. J Membr Sci 153(2):211–231. https://doi.org/10.1016/S0376-7388(98)00256-7

Yan S, Maeda H, Kusakabe K, Morooka S (1994) Thin palladium membrane formed in support pores by metal-organic chemical vapor deposition method and application to hydrogen separation. Ind Eng Chem Res 33(3):616–622. https://doi.org/10.1021/ie00027a019

Yuan X-Z, Wang H (2008) PEM fuel cell fundamentals. In: Zhang J (ed) PEM fuel cell electrocatalysts and catalyst layers: fundamentals and applications. Springer London, London, pp 1–87. https://doi.org/10.1007/978-1-84800-936-3_1

Chapter 19
Transport Phenomena, Electrochemistry and Degradation in Lithium-Oxygen Battery

Malay K. Das and M. Jithin

Abstract Batteries of the future are envisioned to have high energy density, power density and cycle efficiency with low production cost and long life. Among the most promising ones is the rechargeable lithium-oxygen ($Li–O_2$) battery. $Li–O_2$ batteries operate with a Li anode, a porous cathode with ambient oxygen as the oxidizer in an organic electrolyte environment. In $Li–O_2$ battery, Li ions, formed via oxidization of Li at the anode reach the cathode and react with O_2 to form Li_2O_2 as the primary reaction product. The use of Li-based anode material has been quite popular in the recent past due to its high energy density and abundance. With Li as the anode material and oxidizer derived from the ambient air, $Li–O_2$ battery provides superior energy density, comparable to that of the internal combustion engines. Further, the fast reaction kinetics of Li and O_2 to form Li_2O_2, without the breaking the O–O bond, facilitates the use of cheaper catalysts. Despite the above advantages, the $Li–O_2$ battery suffers from significant challenges limiting its application at a commercial scale. First, the $Li–O_2$ battery suffers from electrode passivation, i.e., the clogging of the pores of the electrode and the stresses due to volume expansion caused by the insoluble reaction products. Second, the slow O_2 transport, in the electrode, limits the specific capacity and output power density. Finally, the battery endures electrolyte degradation and formation of undesirable products from secondary reactions. The present chapter discusses the above challenges of transport and electrochemical phenomena, occurring in the electrodes and electrolytes, during the discharge-charge cycling of the battery. We emphasize the battery operation, material selection and design variables affecting the performance, degradation characteristics and efficiency of $Li–O_2$ battery. The chapter presents detail mathematical modelling and simulation results at both cell- as well as pore-scale and concludes with specific design recommendation of futuristic $Li–O_2$ batteries.

Keywords Lithium battery · Electrochemical systems · Degradation

M. K. Das (✉) · M. Jithin
Energy Conversion and Storage Laboratory, Department of Mechanical Engineering, Indian Institute of Technology Kanpur, Kanpur 208016, UP, India
e-mail: mkdas@iitk.ac.in

A. Mukhopadhyay et al. (eds.), *Dynamics and Control of Energy Systems*, Energy, Environment, and Sustainability,
https://doi.org/10.1007/978-981-15-0536-2_19

19.1 Introduction

Batteries are electrochemical devices that generates electrical energy using the reactants stored inside it (Glaize and Genies 2013; Rahn and Wang 2013; Crompton 2000). As the electrochemical reaction progresses, reactants, inside the battery, deplete and the battery eventually ceases to function. For some batteries, the electrochemical reactions cannot be reversed, and the depleted batteries need to be replaced with new ones. Such batteries are known as primary batteries. In contrast, secondary batteries can be recharged and, therefore, reused over many cycles (Zhang and Zhang 2015). Recharging consumes electricity to produce the reactants from the products via reversible electrochemical reactions. Many of our everyday as well as futuristic applications involve rechargeable batteries (Aifantis et al. 2010). Examples include mobile phones, laptops and electric vehicles. Batteries also play crucial role in developing futuristic renewable energy applications. For instance, due to the diurnal and seasonal variation in solar radiation, solar energy applications rely on efficient storage technologies. In this context, rechargeable batteries evolved as the most promising way of electricity storage.

19.1.1 Working Principle of Batteries

A battery contains one or more electrochemical cells where each electrochemical cell includes electrolyte and two electrodes- negatively-charged anode and positively-charged cathode, as shown in Fig. 19.1. The electrolyte allows the ions to flow from one electrode to the other while providing very high resistance against flow of electrons. Thus, the electrons are forced to flow through the outer circuit, providing the electrical output. To reduce the internal resistance of the cell, the electrodes are placed very close to each other. A thin, porous, insulating material is placed between the electrodes so that the electrodes do not touch each other.

Each electrode, in an electrochemical cell, consists of reactants attached to metallic current collectors. Reactants, in each electrode, undergo half-reactions that generate electrons and ions. During the normal operation (discharging) of a battery, positive ions (cation) and negative ions (anion) move toward positive electrode (cathode) and negative electrode (anode) respectively. Here, the anode and cathode undergo oxidation and reduction reactions respectively leading to electron generation at anode and electron consumption at cathode (Newman and Thomas-Alyea 2012). The flow as well as the electrochemical phenomena reverse during the charging of a battery.

Among the various materials used for rechargeable battery electrodes, lithium (Li) is particularly attractive for portable applications (Glaize and Genies 2013; Scrosati et al. 2011). Li battery provides high reversible voltage leading to excellent energy density. At the same time, low density of lithium keeps the weight of the battery low.

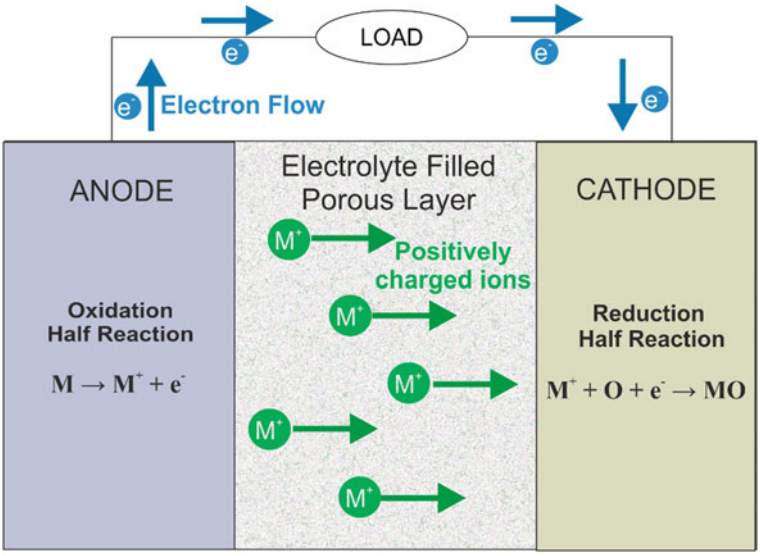

Fig. 19.1 Schematic of a battery under discharge

While Li-ion battery is the most popular battery for many electronic applications, recent years have seen a surge in the development of Li-air batteries (Imanishi et al. 2014; Girishkumar et al. 2010).

19.1.2 Lithium-Air/Lithium-Oxygen Batteries

Li-air battery is an air-positive, Li-negative system, where the positive electrode uses oxygen (O_2) from the air. Since air (or O_2) is continuously fed to the battery, the working of Li-air battery is somewhat similar to that of a fuel cell. Use of ambient air reduces the mass of the battery increasing its gravimetric energy density. The output of such batteries is, however, finally limited by the rate of O_2 intake and thus, the Li-air batteries can supply low current over a long period of time. The structure of a Li-air battery is schematically shown in Fig. 19.2.

As shown in Fig. 19.2, the Li-air cathode consists of porous carbon, designed to allow the flow of O_2. The anode of the battery is made of Li, while the electrolyte is a Li-based salt (such as, $LiPF_6$) capable of carrying Li^+ ions. Depending on the type of electrolyte Li-air batteries may be classified into four groups- aprotic, aqueous, solid-state, and mixed aqueous-aprotic (Lu et al. 2014). The discharging and charging half-reactions in a typical Li-air battery is shown as (Shao et al. 2012):

$$\text{Anode Reaction} : Li \rightarrow Li^+ + e^- \tag{19.1}$$

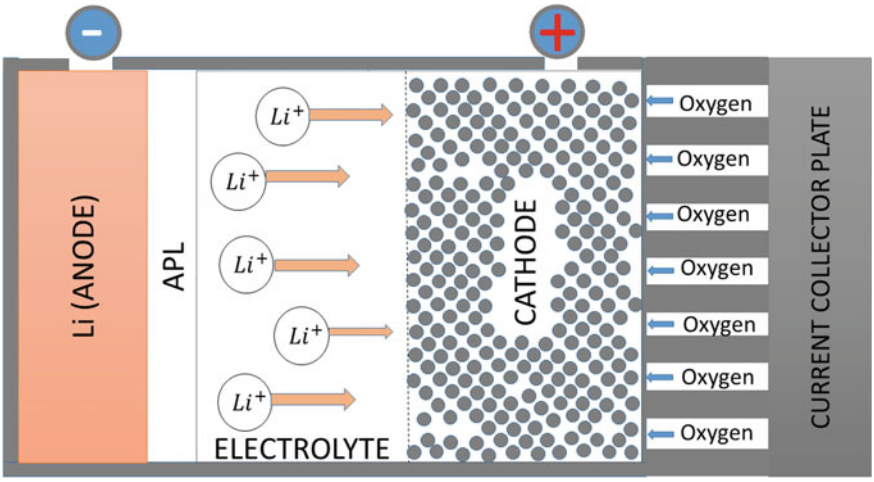

Fig. 19.2 Schematic of a lithium oxygen battery (APL: Anode Protection Layer)

$$\text{Cathode Reaction} : 2Li^{+} + O_2 + 2e^{-} \rightarrow Li_2O_2 \tag{19.2}$$

19.1.3 Advantages of Lithium-Air Batteries

- The anode of a lithium air battery comprises only of lithium, which is the lightest of metals. Moreover, ambient O_2 absorbed from the surrounding air is used and thus, does not store the oxidizer on the cathode side. This enables the Li-air batteries to offer very high theoretical specific energy (~3458 Wh kg^{-1}) and energy density (~3445 Wh L^{-1}). The theoretical energy density of Li-air battery is close to that of gasoline which is almost 10 times that of Li-ion battery (Zheng et al. 2008; Andersen et al. 2015).
- The discharge reaction forming Li_2O_2 has excellent electrochemistry, without breaking the O–O bond, and hence the battery does not call for very costly catalysts (Shao et al. 2012).
- Li-air batteries with aprotic electrolyte showcase rechargability (Armand and Tarascon 2008) and hence, are considered a promising candidate for electric vehicles.
- Since the oxidizing agent is derived from ambient air and with the use of renewable electrode materials, the battery is highly environment-friendly.

19.1.4 Challenges Faced

- A major limitation associated with these batteries is the low power density values which are inadequate for its application in electric vehicles (Gallagher et al. 2014).
- The practical specific capacity values obtained are very small when compared to the theoretical values due to the under-utilization of reaction surface in the electrode (Christensen et al. 2011).
- The very high recharge potentials required to reverse the electrochemical reaction results in lower cycle efficiency.
- Volume change in the anode and cathode due to the dissolution and precipitation of solid phase substances, induces mechanical stress on the components (Christensen et al. 2011).
- Although the electrochemistry is very attractive, the resistance to species and charge transport in the electrode, during operation, limits the rate of reaction (Ye et al. 2015a, b).
- Deviations from expected electrochemistry result in undesirable product formation, affecting the cycle efficiency and capacity retention (Ma et al. 2015).
- Presence of impurities and electrolyte degradation affect life of the battery and is a safety concern.
- Requirement of auxiliary systems to compress and purify the air before use decrease the volumetric and gravimetric energy density of the system and makes the design of the system challenging (Gallagher et al. 2014).

To harness the true potential of lithium-air batteries and to enable them to handle real life applications, study of phenomena occurring at different length scales, including sub-molecular scales to system scales, has to be undertaken (Li et al. 2016; Jung et al. 2016). In the present chapter, we focus on the pore scale and cell scale phenomena, from the viewpoint of mass and charge transport effects in the electrodes on the improvement of the discharge rate, capacity and cycling ability. Quantitative analysis of these phenomena has been attempted by numerical simulations at the pore-scale and electrode-scale. The mathematical modelling and formulation adopted for these simulations, both at the pore-scale and macro-scale, are given in brief in the Sect. 19.2. The major phenomena relevant at these scales affecting the performance of the battery are discussed in Sect. 19.3, showing results obtained from the simulations. In Sects. 19.4, 19.5, and 19.6, the effects of operating conditions (Sect. 19.4), material properties (Sect. 19.5) and cathode designs (Sect. 19.6) on these phenomena are studied. The discussions are aimed to bring out the information to help optimize operating condition, design and material selection to the improved performance and cycle life of the battery. Aprotic Li-air batteries are considered in the chapter since they are the ones showcasing excellent rechargability, better theoretical energy density and promise for applications (Zheng et al. 2008).

19.2 Mathematical Modeling

The present section discusses the mathematical formulation adopted to model the phenomena occurring in the cathode of the lithium air battery consisting of the solid electrode phase and the liquid electrolyte phase. The system is assumed to be isothermal and the transport takes place only by diffusion and migration, since convection is neglected.

19.2.1 Pore Scale Modeling

In pore scale modelling, the computational domain consists of the complex microstructure of the solid electrode whose pores are filled with electrolyte. Each lattice point or control volume of the mesh is either the solid electrode or the liquid electrolyte. Solution of equations of transport is to be carried out in the electrolyte phase and electrode phase which are separated by the reaction surface where the electrochemical reactions take place. In the electrolyte phase, transport of oxygen and lithium ions take place due to diffusion and migration. Only the transport of electrons takes place in the solid electrode phase. The reaction between the oxygen, lithium ions and the electrons happens at the interface of the electrolyte and electrode where the catalyst is coated. Presently, it is assumed that the catalyst is uniformly coated on the electrode surface and is of negligible volume. The equations being solved with these assumptions are given below (Andersen et al. 2015; Jithin et al. 2016). The list of symbols used in the discussion of modelling is shown in Table 19.1.

Concentration of oxygen

$$\frac{\partial C_{O_2}}{\partial t} = \nabla \cdot \left(D_{O_2} \nabla C_{O_2} \right) \tag{19.3}$$

The concentration of oxygen, C_{O_2}, is solved in the electrolyte phase and only diffusive transport is assumed to take place. D_{O_2} is the diffusion coefficient of oxygen in the electrolyte.

Concentration of lithium ions

$$\frac{\partial C_{Li^+}}{\partial t} = \nabla \cdot \left(D_{Li^+} \nabla C_{Li^+} - \frac{t^+}{F} \mathbf{i} \right) \tag{19.4}$$

The concentration of lithium ions is also solved in the electrolyte phase only. In addition to the diffusion transport occurring from the concentration gradient, migration of the lithium ions also takes place due to the electric potential gradient. This migration transport is governed by the second term in the above equation. Here, t^+ is the transference number, F is the Faraday constant and $\mathbf{i}$ is the electrolytic current.

Table 19.1 List of symbols

C_i	Concentration of the species i (mol/m^3)
$C_{O_2,ref}$	Reference oxygen concentration (mol/m^3)
D_i	Mass diffusivity of species i (m^2/s)
$\boldsymbol{F}$	Faraday constant (C/mol)
$\frac{\partial \ln f}{\partial \ln C_{Li^+}}$	Activity coefficient variation
$\mathbf{i}$	Electrolytic current (A/m^2)
j	Local current density (A/m^2)
J	Concentration flux (mol/m^2 s)
k_c	Reaction rate coefficient (mol/m^2 s)
κ	Electric conductivity (S/m)
M_i	Molecular mass of species i (kg/mol)
n_i	Moles of electron/mole of species i
$\hat{n}$	Direction unit vector
R	Universal gas constant (J/mol K)
t^+	Transference number of lithium ion
$\mathbf{T}$	Temperature (K)
U_0	Thermodynamic voltage (V)
ϕ	Electric potential (V)
β	Symmetry factor
η	Overpotential (V)
$\sigma_{Li_2O_2}$	Conductivity of Li_2O_2 layer (S/m)
$\delta_{Li_2O_2}$	Thickness of Li_2O_2 layer (nm)

Electrolytic current

$$\mathbf{i} = -\kappa \nabla \phi - \frac{2RT\kappa}{F}\left(t^+ - 1\right)\left(1 + \frac{\partial \ln f}{\partial \ln C_{Li^+}}\right)\nabla \ln C_{Li^+} \tag{19.5}$$

The electrolytic current happens due to gradient in electric potential and the gradient in the concentration of charged species, in this case, the lithium ions.

Electric potential transport

$$\nabla \cdot \left[\kappa \nabla \phi + \frac{2RT\kappa}{F}\left(t^+ - 1\right)\left(1 + \frac{\partial \ln f}{\partial \ln C_{Li^+}}\right)\nabla \ln C_{Li^+}\right] = 0 \tag{19.6}$$

As charge transport takes place in both the electrode and electrolyte phases, electric potential is solved in both these phases. The above equation represents the governing equation for electric potential solution in both electrolyte and electrode phases. For the lattice or grid point in the electrolyte phase, κ is the electric conductivity of the electrolyte and C_{Li^+} is the concentration of lithium ion at that location. If the

lattice or grid point is in the electrode phase, κ becomes the electric conductivity of the electrode phase and the second term becomes zero as the concentration of lithium ions in the electrode phase is zero.

Reaction rate

$$J = D_i \frac{\partial C_i}{\partial \hat{n}} = \pm \frac{j}{n_i F} \tag{19.7}$$

The electrochemical reaction between the lithium ions, oxygen and the electrons takes place at the interphase between the electrode and electrolyte. The rate of reaction depends on the local current density as given by the Eq. 19.7. The subscript i represents the species oxygen or lithium ion being consumed. The $\hat{n}$ is the unit normal direction vector at the electrode surface pointing towards the electrolyte. For the reactants oxygen and the lithium ions, the sign is positive as they are consumed at the interface, if the current density is assumed positive for positive charge moving from electrolyte to electrode phase. The reaction product generated in this reaction, for the present study, is assumed to be of negligible thickness. Hence, the effect of the product deposit on transport of species is neglected. However, the resistance to charge transport at the electrolyte-electrode interface is accounted for in the overpotential calculation as will be discussed soon.

Electric potential change due to reaction

$$\kappa \frac{\partial \phi}{\partial \hat{n}} = \pm j \tag{19.8}$$

Due to the reaction, electric potential in both the electrolyte and electrode phases changes and the magnitude of the change is given by Eq. 19.8. At the electrode-electrolyte interface, as the positive charge moves from the electrolyte to the interface, the electric potential decreases in the electrolyte phase due to the reaction. Conversely, in the electrode phase, the electric potential increases.

Electric current density

$$j = 2Fk_c \left(\frac{C_{O_2}}{C_{O_2,ref}} \right) \left(\exp\left[\frac{(1-\beta)F\eta}{RT} \right] - \exp\left[\frac{-\beta F\eta}{RT} \right] \right) \tag{19.9}$$

The rate of reaction is governed by the current density at that location which in turn is a function of the reactant concentration and the activation overpotential at that location given by the Eq. 19.9. Thus, the rate of reaction is limited by the amount of oxygen available and the overpotential.

Overpotential

$$\eta = \phi_s - \phi_l - U_0 \tag{19.10}$$

The value of overpotential at a location is governed by the electric potential in the electrode phase and the electrolyte phase and the equilibrium potential as given in Eq. 19.10. However, as the reaction proceeds, the product build-up increases the charge-transport resistance, increasing the overpotential. The additional overpotential by the product deposit is given by:

$$\Delta\phi_{Li_2O_2} = j\delta_{Li_2O_2}/\sigma_{Li_2O_2} \tag{19.11}$$

In the equation, j is the current density, $\delta_{Li_2O_2}$ is the deposit thickness and $\sigma_{Li_2O_2}$ is the electric conductivity of the deposit layer. The conductivity of the layer is in fact a function of the thickness as given by the experimentally obtained relationship in Eq. 19.12.

$$\sigma_{Li_2O_2} = 10^7\delta^{-17.18} \tag{19.12}$$

19.2.2 Macro Scale Modeling

In macro-scale modeling, each grid point or control volume includes a volume bigger than the REV of the porous media and all the parameter values are the result of an averaging over that volume. This means that each grid point includes electrolyte phase, electrode phase and their interface. Hence, at all the grid points, the equations for species transport in the electrolyte and the charge transport in both electrolyte and electrode are solved (Li et al. 2016). The reaction taking place at the interface is averaged over the entire interfacial area in the control volume and hence appears as source terms in the governing equations of transport.

Transport equation in macroscale

$$\frac{\partial(\varepsilon C_i)}{\partial t} = -\nabla \cdot N_i + r_i \tag{19.13}$$

In macroscale modeling, each species and the electric potentials in the electrode and electrolyte phases have separate transport equations of the form given in Eq. 19.13. In the equation, C_i represents the concentration of species i in the solution phase, ε is the porosity of the cathode electrode, N_i is the molar flux of species i, and r_i is the volumetric production rate of the species.

The flux term for oxygen

$$N_{O_2} = -D_{O_2,eff}\nabla C_{O_2} \tag{19.14}$$

For oxygen transport, convection is assumed to be absent in the cathode and hence the flux term for oxygen consists of the diffusion term only.

The flux term for lithium ions

$$N_{Li^+} = -D_{Li^+.eff}\nabla C_{Li^+} + \frac{\mathbf{i}t^+}{F} \tag{19.15}$$

The transport of lithium ions take place due to diffusion and migration. The second term in the RHS denotes the migration where **i** is the electrolytic current arising due to the movement of the charged species Li^+. The electrolytic current is given by:

$$\mathbf{i} = -\kappa_{eff,l}\nabla\phi_l - \frac{2RT\kappa_{eff,l}}{F}\left(t^+ - 1\right)\left(1 + \frac{\partial \ln f}{\partial \ln C_{Li^+}}\right)\nabla \ln C_{Li^+} \tag{19.16}$$

The subscript l stands for the liquid phase where the electrolytic current is present.

Source term

$$S_i = \frac{aj}{n_i F} \tag{19.17}$$

The source term for both oxygen and lithium ions, arising due to the electrochemical reactions, is a function of the current density and the relationship is given by Eq. 19.17. Here, a is the specific surface area of the porous cathode and n_i is the number of moles of electrons transferred for one mole of the species i.

Current density

$$j = -nFk_c(C_{Li^+})^2 C_{O_2}\left(\frac{-\beta nF}{RT}\eta\right) \tag{19.18}$$

The current density is calculated at each location as a function of the local concentrations of oxygen and lithium ions and the overpotential at that location.

Overpotential

$$\eta = \phi_s - \phi_l - U_0 \tag{19.19}$$

The overpotential is calculated using the electric potential in the electrolyte and electrode phases. Here, the solid and liquid electric potentials are the potentials in the electrode and the electrolyte phases respectively.

Electrode potential transport equation

$$\nabla \cdot (\kappa_{eff,s}\nabla\phi_s) = aj \tag{19.20}$$

The rate of change of electrode potential depends on the total current density in that control volume. Since only electrons are the charge carriers in the electrode, the transport is by diffusion only and the migration term is absent.

Electrolyte potential transport equation

$$\nabla \cdot \left(\kappa_{eff,l} \nabla \phi_l\right) = \nabla \cdot \left\{ \frac{2\kappa_{eff,l} RT}{F} \left(1 - t^+\right) \left[1 + \frac{\partial \ln f}{\partial \ln C_{Li^+}} \right] \frac{1}{C_{Li^+}} \nabla C_{Li^+} \right\} - aj \tag{19.21}$$

In the electrolyte phase, the electrolytic current due to the transport of lithium ions also contributes to the electric potential transport. This gives rise to the migration term in the RHS of the equation.

Li_2O_2 deposit

$$\frac{\partial C_{Li_2O_2}}{\partial t} = -\frac{aj}{nF} \tag{19.22}$$

In addition to the overpotential due to the reaction, the reaction product deposit also contributes to the overpotential. This overpotential depends on the quantity of deposit present at that location. The volume fraction of Li_2O_2 deposit can be calculated from the concentration of Li_2O_2 as follows.

Li_2O_2 volume fraction

$$\varepsilon_{Li_2O_2} = \frac{C_{Li_2O_2} M_{Li_2O_2}}{\rho_{Li_2O_2}} \tag{19.23}$$

Here, $M_{Li_2O_2}$ is the molecular mass of Li_2O_2 and $\rho_{Li_2O_2}$ is the mass density of Li_2O_2. From the volume fraction of the Li_2O_2 deposit, the overpotential increase can be calculated as follows.

Overpotential due to Li_2O_2 layer

$$\Delta\phi_{Li_2O_2} = j R_{Li_2O_2} \varepsilon_{Li_2O_2} \tag{19.24}$$

Here, $R_{Li_2O_2}$ is the electric resistivity of the Li_2O_2 film.

The subscript/superscript *eff*, in the equations given below, stands for effective diffusion coefficient or conductivity values. The effective values depend on the porosity and tortuosity of the porous medium and is given by the following relationships.

$$D_i^{eff} = D_i \varepsilon^{\tau} \tag{19.25}$$

$$\kappa_{eff,l} = \kappa_l \varepsilon^{1.5} \tag{19.26}$$

$$\kappa_{eff,s} = \kappa_s (1 - \varepsilon)^{1.5} \tag{19.27}$$

19.3 Phenomena Limiting Discharge Rate, Capacity and Cycling

19.3.1 Oxygen Transport Limitation

As mentioned earlier, the Li-air batteries exhibit excellent reaction kinetics. However, the output current density is severely limited by the rate of oxygen transport in the porous cathode. It has been shown in literature, from experimental and simulation results, that the reaction rate is very low in regions of cathode away from the oxygen inlet, since the concentration of oxygen drops down to very low values. This is caused by the resistance to oxygen transport by the diffusivity and solubility of the electrolyte and the porous microstructure of the material. The distribution of oxygen concentration dissolved in the solvent, obtained from pore scale simulations assuming a simplified pore geometry, is shown in Fig. 19.3. The Fig. 19.3a shows the geometry assumed. The transport of oxygen concentration, Li^+ ions and electric potentials are solved in the domain and the electrochemical reaction occurs at the surface of the electrode. The Fig. 19.3b shows that the oxygen concentration in regions away from the oxygen inlet drops down to very low values. This considerably decreases the power density as the rate of reaction in majority of the porous media is much less than that proposed by the electrochemistry. The variation in concentration values with different diffusivity values of the electrolyte is shown in the Fig. 19.3b. Better solubility and diffusivity of oxygen in the electrolyte solvent facilitates better transport of oxygen into the porous electrode.

Another limitation of using Li-air batteries in vehicle propulsion is the lack of power density. To meet the high power requirements, Li-air batteries having very large surface area of reaction has to be designed. This requires huge stacks increasing

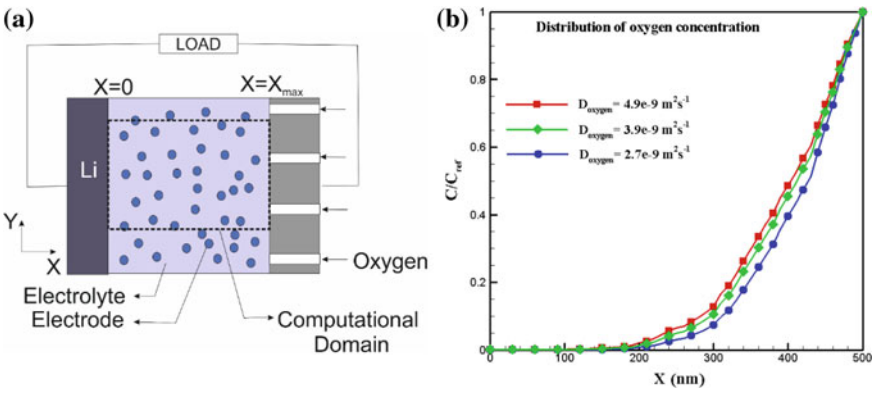

Fig. 19.3 **a** Pore scale microstructure of Vulcan carbon assumed to be spherical grains of diameter 40 nm. **b** Distribution of oxygen concentration along the depth of the battery cathode. X = 500 nm is the location of oxygen inlet

the volume and weight of the system. More importantly, better catalysts might be required to increase the power density. The improvement in electrocatalysis helps in reducing the charge overtpotential also, increasing the cycle efficiency. But even with the high surface area and catalysis, high power density might not be achieved. This is because high power density depends on how much of the surface area is made available with a high partial pressure of oxygen. This is seen from the simulation results by Jithin et al. (Jithin et al. 2016). Comparison of Fig. 19.4a, b which shows the oxygen concentrations for two particle sizes and the corresponding current density values, shown in Fig. 19.5, says that the geometry in Fig. 19.4b is having higher power density. This high power density is owing to the larger surface area available at the oxygen rich region close to the oxygen inlet. Hence the improvement in cathode

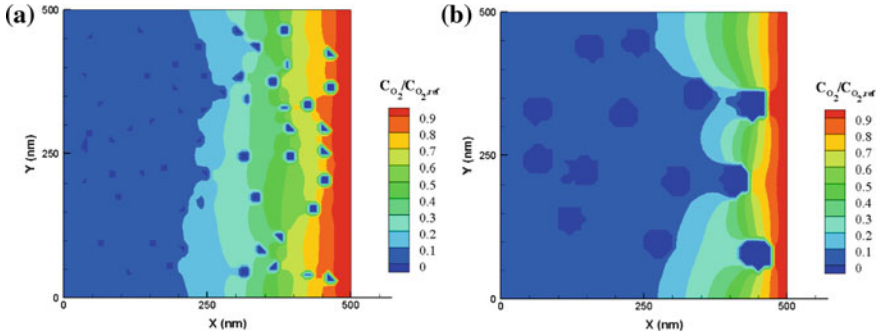

Fig. 19.4 Distribution of oxygen concentration in the pores of the cathode for porous material grain size **a** 20 nm and **b** 60 nm

Fig. 19.5 The effect of porous material grain size on the performance and specific capacity

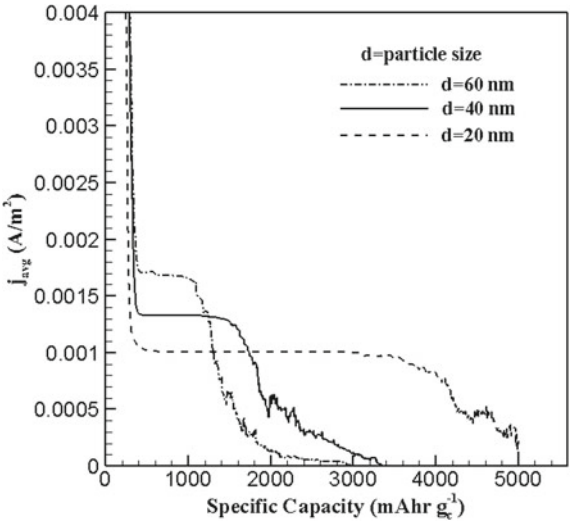

design can deliver high power density by providing higher reaction surface area near the oxygen inlet. However, this might affect the specific capacity due to the enhancement in transport limitation near the oxygen inlet.

19.3.2 Li_2O_2 Deposition

The transport resistance to oxygen increases as the battery operates, due to the pore blocking induced by the reaction product deposits (Tran et al. 2010). The primary reaction product is Li_2O_2 which is insoluble in the aprotic electrolyte. The solid precipitates of Li_2O_2 builds up near the oxygen inlet, since the reaction rate is high in that region, covering the available passages for oxygen transport. In addition, Li_2O_2 forms a layer over the solid surface of the electrode reducing the active surface area for reaction and increasing the resistance to electron transport to reach the reaction site. The electric conductivity of the Li_2O_2 layer decreases considerably with the deposit layer thickness. It is mentioned in literature that the reaction stops almost completely as the thickness reaches the order of 10 nm. Hence the morphology of the Li_2O_2 deposit is very important in understanding its effect on oxygen transport limitation and reaction overpotential. These factors play a crucial role on the practical energy density of the cell. Moreover, the Li_2O_2 deposit morphology also affects the recharge potential as the contact between the deposit and the electrode surface influences the overpotential to the reaction by adding to the resistance to electron transport. In addition to all these effects, the solid precipitation in the pores causes the volume expansion of the cathode inducing mechanical stress on the components and electrolyte leakage.

19.3.3 Oxygen Source to the Battery

The attractive advantages of Li–O_2 batteries are when it is operated from the ambient air. However, most of the experimental studies are conducted in the setting of a source of stored oxygen without impurities. But, the running of Li-air batteries taking oxygen from the ambient air faces a number of difficulties. It is reported that the capacity of the battery reduces considerably with lower partial pressure of oxygen from the oxygen source (Imanishi et al. 2014). Moreover, the use of oxygen derived from ambient air requires systems including compressor, air purifier to remove the water vapor and carbon dioxide, air channels to deliver oxygen to the electrode and also to prevent the loss of volatile electrolyte (Rahn and Wang 2013). Such auxiliary systems add to the weight, volume and cost of the system affecting the economic application of lithium air batteries. Use of stored oxygen avoids the requirement of such bulky auxiliary systems, but the battery pack would require a compressed oxygen tank with it. The compression and filling of the oxygen in the tank is another issue which will arise under this circumstance. Moreover, the battery pack should be

designed to handle the stresses while working with the high pressure fluid. Caution would also be required to prevent the reaction of electrolyte with the high pressure oxygen (Rahn and Wang 2013).

19.3.4 Electrolyte Degradation and Side Reactions

The reactions taking place in the electrode during charging and discharging is strongly affected by the electrolyte being used (Lu et al. 2013; Ye et al. 2015a, b). A discussion of the side reactions that can take place in the cathode and their possible effects is included in the review by Ma et al. (2015). It is seen from experimental studies that carbonate based electrolytes result in formation of Li_2CO_3 during discharge which require very high charging potential to be dissociated (Christensen et al. 2011). This seriously affects the cycle efficiency of the battery. Moreover, with cycling, the degradation of electrolyte and the deposition of Li_2CO_3 will add up, reducing the capacity retention capability. Moreover, it is reported that, in addition to the side reactions, electrolytes also can get dissociated during charging at high potentials, causing loss of electrolyte with cycling.

The electrolyte degradation causes significant decrease in the capacity retention ability of the battery. Newer electrolytes like dimethoxyethane-based and dimethyl sulphoxide are being developed for which Li_2O_2 is the primary reaction product. Although these electrolytes are stable towards oxygen and other impurities, they can react with the Li anode. Hence proper anode separation from the electrolyte has to be ensured for their use. Hence, the suitable electrolyte material should have good stability towards the reaction with Li metal, dissolved oxygen at different temperatures, along with high lithium ion transference number, good oxygen solubility and high oxygen diffusivity.

19.3.5 Anode Protection and Dendrite Formation

As the aprotic solvent comes in contact with the anode, a solid-electrolyte interface (SEI) is formed automatically preventing the further corrosion of the anode. This forms a layer over the anode surface which conducts the Li^+ ions through it. However, the SEI of lithium air battery is unstable as the cycling results in formation and breakdown of the interface which in turn adversely affects the efficiency of the battery. The dissolution and deposition of lithium metal on cycling gives rise to another problem. An uneven Li deposition can lead to dendrite formation from the anode surface whose growth can lead to shorting between the anode and cathode (Xu et al. 2014; Aurbach and Cohen 1996). Another factor affecting the safety of the battery is the reaction of lithium metal with the impurities including water, carbon dioxide and nitrogen coming from the atmosphere. This is prevented by including an anode protection layer (Crompton 2000; Zhang and Zhang 2015).

19.3.6 Volume Change at Anode and Cathode

The discharge and charge cycling of the battery causes considerable volume changes both in the anode and cathode (Christensen et al. 2011; Yoo et al. 2014). This volume change induces mechanical stresses on the components of the battery. Designs have been proposed to ensure the proper contact between anode and the separator (Visco et al. 2010; Huang and Faghri 2015). However, this design is reported to add additional weight and mechanical stress on the system (Yoo et al. 2014). Hence, better designs are yet to be developed to account for the volume changes in the battery capable of handling the high mechanical stresses.

19.4 Effect of Battery Operation Conditions

19.4.1 Effect of Operating Current Density

The performance of battery when operated at different discharge rates are shown in Fig. 19.6. The figure shows that the battery can be operated at higher current densities only at the expense of the output voltage. The output voltage is lower when the operating current is high. The more interesting point is that the specific capacity is also affected with operating current density. This gives an indication that the pore blocking might be severe for higher current densities, as the reaction product build up will be much more non-uniform at higher current densities. The Li_2O_2 precipitate

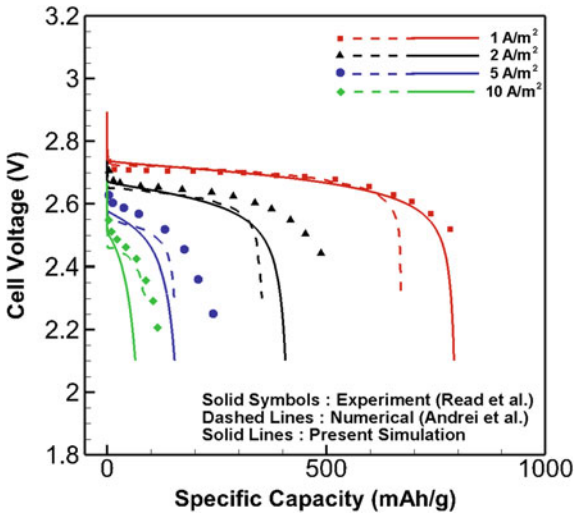

Fig. 19.6 The variation in output voltage and specific capacity when the battery is operated at different current densities

will build up much faster near the oxygen inlet due to the high oxygen concentration there, filling the pores near the oxygen entrance and leaving much of the reaction surface area in the cathode interior unutilized.

19.4.2 Effect of Operation with Oxygen from Ambient Air

Unlike results from most of the studies in which the Li–O_2 battery is operated in pure oxygen, the conditions while working on oxygen from ambient air is very different (Ye et al. 2015a, b; Sahapatsombut et al. 2014). To understand how the performance will be affected while running the battery on oxygen from atmosphere at the low partial pressure, simulations are conducted with the concentration of available oxygen at the inlet having values 1.0 and 0.21. The results are shown in Fig. 19.7.

The figure shows severe loss in specific capacity and power density output. The oxygen concentration is negligible for most part of the cathode thickness for lower oxygen partial pressure case. The present results show an indication of the loss of performance of battery with the use of oxygen from atmosphere.

19.4.3 Effect of Electrolyte Degradation

The degradation of electrolyte from side reaction forms products which require high electric potentials to be dissociated (Sahapatsombut et al. 2014). This affects the cycling ability of the battery. This is shown in Fig. 19.8 which shows the cycling performance with and without electrolyte degradation. The results are obtained from

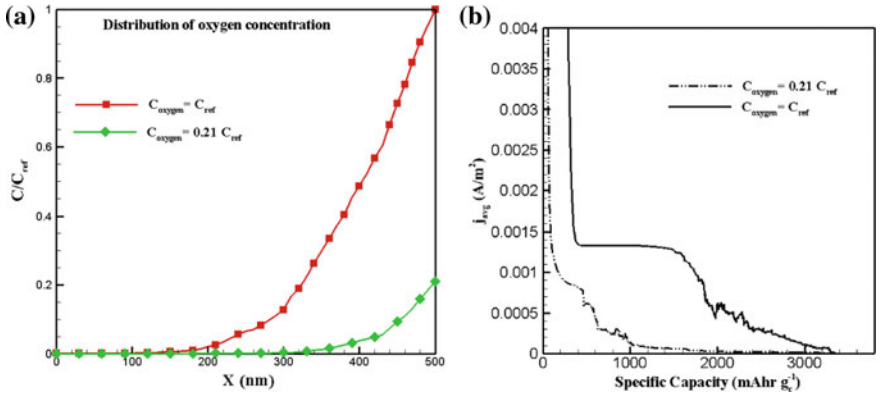

Fig. 19.7 Comparison of operation when the available oxygen concentration is reduced. **a** Distribution of oxygen concentration along the depth of the cathode. **b** Output current density for two inlet oxygen concentrations

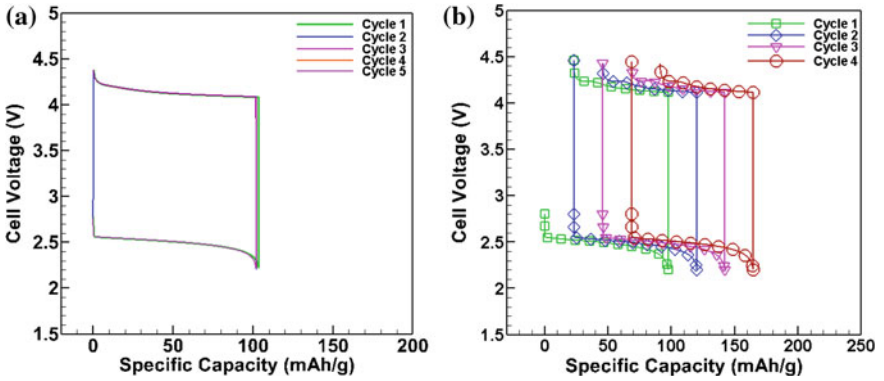

Fig. 19.8 Cycling behavior of battery at external current density 10 A/m^2 **a** without electrolyte degradation, **b** with electrolyte degradation

macro-scale simulations in the cathode. The simulations consider the electrolyte reaction with CO_2 and Li_2O_2 producing Li_2CO_3 deposits, which build up with each cycle reducing the capacity, as shown in Fig. 19.8b.

19.5 Effect of Material Properties

19.5.1 Effect of Pore Morphology of Porous Media

Porous microstructure

Ideal electrode material should have a number of characteristics including (a) high electronic conductivity, (b) chemical, thermal and mechanical stability, (c) large surface area for reaction, and (d) a porous microstructure facilitating adequate oxygen transport in the pores. The three dimensional pore morphology should be such that the hindrance to the oxygen transport should be minimized while providing adequate space for the reaction product to deposit (Tran et al. 2010).

The effect of pore structure on the oxygen transport has been studied earlier (Jithin et al. 2016). An idealized pore morphology, shown in Fig. 19.3a is used assuming the grains to be spherical in shape. The simulations showed that the transport of oxygen limits the maximum output power density. The oxygen concentration distribution shows that the regions away from the oxygen inlet have very small amounts of oxygen concentration resulting in the low reaction rates (Fig. 19.9). These results are obtained neglecting the volume of Li_2O_2 deposit. Hence in actual battery cathode, the porosity loss due to the Li_2O_2 deposits will augment the transport limitation.

The work also tried changing the size of the pore grains to see its effect on the oxygen transport and specific capacity. Figure 19.4a, b show the distribution of oxygen

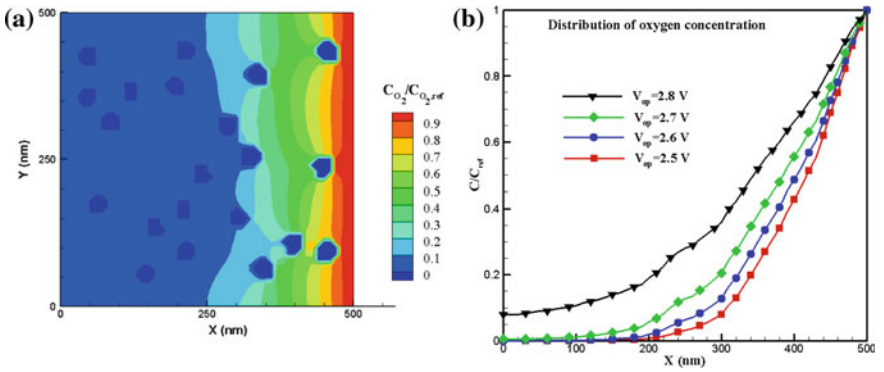

Fig. 19.9 **a** Oxygen concentration distribution in the cathode considered in Jithin et al. (2016). **b** The variation of oxygen concentration for different operating voltages

in the two microstructures with grain diameter 20 nm and 60 nm respectively. The oxygen diffusion to the interior of the electrode is considerably high for smaller grain size. This ensures better surface area utilization resulting in high specific capacity. The change in specific capacity value for different grain size is seen from Fig. 19.5. The figure shows that the porous electrode with different grain size behaves very differently. As the grain size is small, the oxygen penetration into the cathode is improved facilitating the maximum use of the available surface area. However, the power density will be low in this case. For larger grain size microstructure, the power density is high. This can be due to the availability of large surface area near the oxygen inlet where the oxygen concentration is high. However, as this area near the oxygen inlet gets covered by reaction product, the high current density output drops sharply leaving much of the electrode surface area unutilized. Hence, a well-designed pore structure of the cathode can control the output of the battery according to the requirement to a considerable extent (Beattie et al. 2009).

Porous nanostructures

Use of nanostructures in the cathode has also been popular and a variety of electrodes have been tested showing attractive improvements. A variety of nanostructures have been attempted and the effect were analyzed in many numerical and experimental works. In 2015, Armand, Tarascon (Armand and Tarascon 2008) modeled the transport and reaction and the product deposition on the electrode surface at the pore scale of the lithium air battery. In the work, the charge and species transport in the solid electrode, liquid electrolyte and in the Li_2O_2 deposit are solved and good agreement was obtained with experimental results. Nanostructures were incorporated on the simplified electrode geometry and its effect on discharge characteristics was studied. The inclusion of nanostructures was shown to increase the specific capacity considerably as it increases the surface area available for reaction. However, the pore blocking can leave much of the surface area unutilized. Hence the geometry of the nanostructures

is varied to understand its effect on the pore blocking. The study showed that modification of the porous nanostructures can enhance the specific capacity even when the total reaction surface area is the same. This is because of the better utilization of the available surface area. Many attempts are being made to improve the specific capacity of Li–O_2 batteries by the use of new materials with improved micro- and nano- pore morphologies. For instance, hierarchically porous graphene consisting of microporus channels was used as cathode material and specific capacity values of the order of 15,000 mAh/g was reported (Xiao et al. 2011).

Morphology of catalyst deposition

Another important factor affecting the power density is the use of catalysts and redox mediators at the cathode. Different catalysts are being used in lithium oxygen battery cathode including precious metals, carbon nanoparticles and metal oxide nanoparticles (Black et al. 2013). Oakes et al. (2016) compared two catalyst deposition techniques, namely the dip-coating (DC) and electrophoretic coating (EPD) to generate different catalyst morphologies and studied their effect on battery performance. The catalyst layer formed by the dip-coating technique was disordered with uncoated regions and regions of large aggregates. Whereas, the EPD produced a smooth compact film of nanoparticles with superior inter-particle adhesion. The results showed that the smooth film obtained from EPD provided higher cycle efficiency and improved cyclability. The SEM imaging of the two catalyst layers after charging and after discharging of the battery showed that the morphology of the catalyst layer is changed considerably due to the non-uniform reaction rates in the case of dip-coated catalyst layer. This also led to a larger loss in the surface area with cycling and non-uniform stresses due to the irregular depositions. Hence it is seen that the morphology of catalyst deposition also plays a crucial role in the performance of the battery. In addition to catalyst deposition techniques, attempts have been reported in literature to control the spatial distribution of the catalyst in the cathode, to improve the discharge rate and capacity (Williford and Zhang 2009).

19.5.2 Effect of Macroscopic Properties of Porous Media

Effect of porosity

Review of the different cathode materials, their properties, fabrication and effect on battery performance is presented in literature (Ma et al. 2015; Ye et al. 2015a, b; Xu et al. 2017). It has been confirmed that the porous material macroscopic properties affect the performance significantly. Figure 19.10 shows the performance variations for different porosities. High porosity ensures high specific capacity due to the improved oxygen transport, although the total surface area of the cathode is reduced

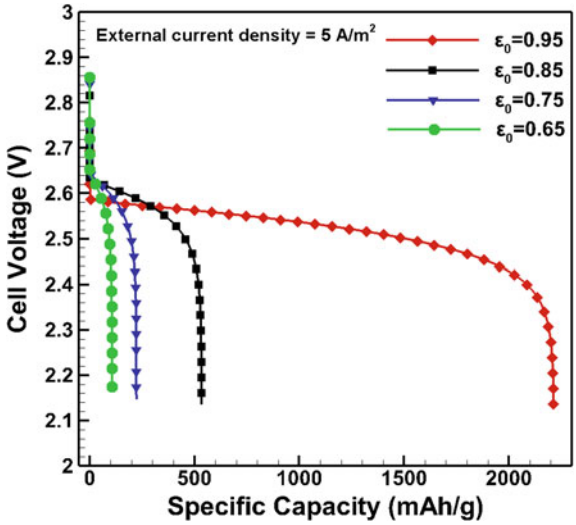

Fig. 19.10 The performance curve for different initial porosity of the electrode

with increase in porosity. This again confirms the fact that, the enhancement of oxygen transport is more important than the use of porous materials of higher surface area since much of this surface area will remain unutilized.

Effect of tortuosity

As the tortuosity value can be directly correlated to the distance to be travelled for the transport between two point in the porous media, the increase in value of tortuosity affects the specific capacity adversely. This is seen in the performance curve shown in Fig. 19.11. It is also seen that the output voltage and hence the power density is also affected with increase in tortuosity. Hence it can be assumed that the microstructure with least tortuosity will be desirable for high specific capacity and output power density.

19.5.3 Effect of Oxygen Diffusivity and Solubility in Electrolyte

Works have been done in the past to study the effect of electrolyte properties on the oxygen transport (Ye et al. 2015a, b). The availability of oxygen at the reaction surface is strongly dependent on its solubility and diffusivity in the electrolyte. The effect of these parameters are shown in the Figs. 19.12 and 19.13. The Fig. 19.12 shows that the decrease in the diffusivity value affects both the specific capacity and output power density. This is due to the slower oxygen diffusion rate into the cathode enhancing the mass transport limitation. This decrease in diffusivity also increases the non-uniformity in the oxygen distribution and hence worsens the under-utilization of the reaction surface area. Another parameter depending on the choice of electrolyte is

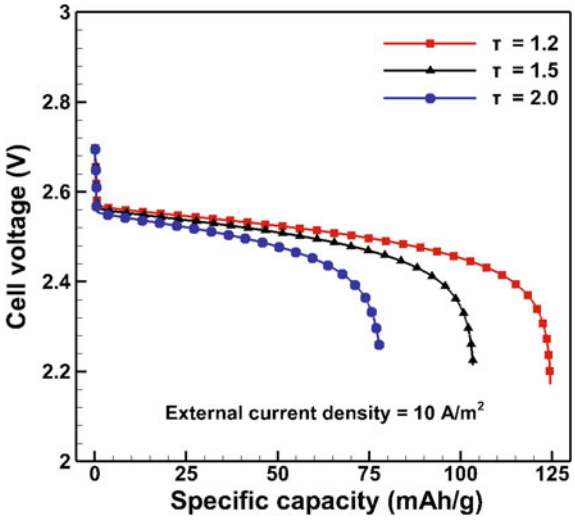

Fig. 19.11 The effect of porous media tortuosity on the batter performance

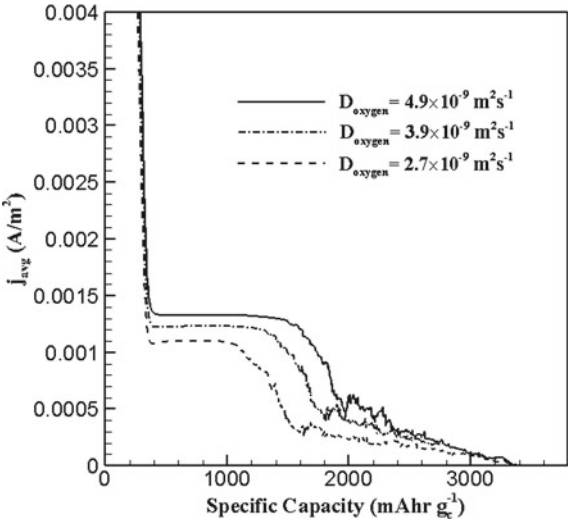

Fig. 19.12 Effect of oxygen diffusivity in the electrolyte

the solubility of oxygen. With better solubility, more oxygen can enter the electrolyte phase increasing the concentration of oxygen available for reaction. This effect is seen from Fig. 19.13. Both the specific capacity and power density is tremendously affected by the oxygen solubility.

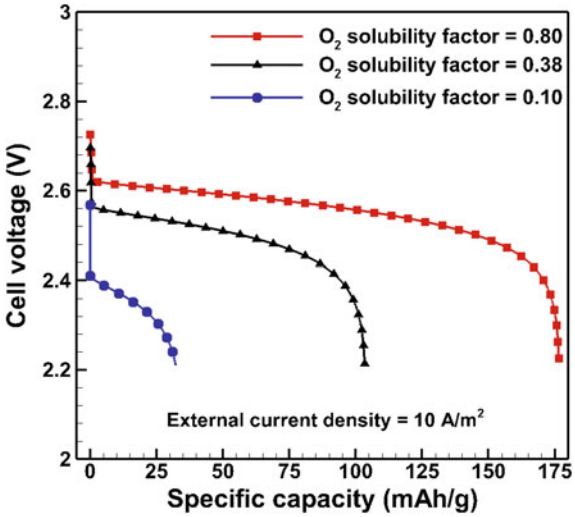

Fig. 19.13 Effect of oxygen solubility in the electrolyte

19.5.4 Effect of Catalyst and Product Deposition Morphology

Effect of catalyst used

The choice of catalyst used plays a major factor on the maximum output power density as the rate of reaction is strongly governed by the electrocatalysis (Lu et al. 2013). The effect of this reaction rate on the performance was analyzed by studying the effect of the reaction rate constant as shown in Fig. 19.14. The figure shows considerable improvement in the output rate with the increase in the reaction rate

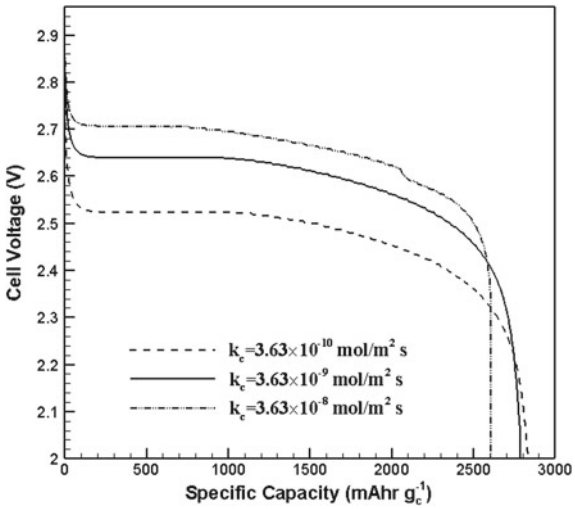

Fig. 19.14 Effect of reaction rate coefficient on performance

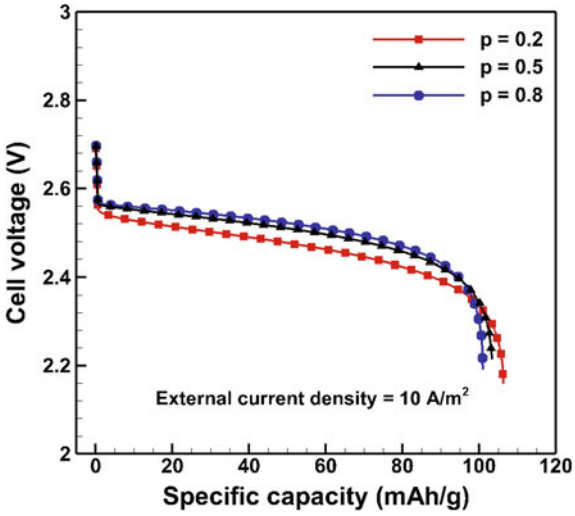

Fig. 19.15 Effect of product deposit morphology on battery performance

coefficient. Moreover, the specific capacity is seen to be affected although the catalyst does not have a direct impact on the oxygen transport. This can be because of the non-uniform product formation resulting from the high reaction rate.

Effect of product deposition exponent

It has been found from experimental studies, that the Li_2O_2 deposit morphology can have different forms based on the electrolyte used, the electrode micro- and nano-structures, electrocatalysis and the discharge rates (Lu et al. 2013). In mathematical modelling at the macroscale, the product deposition exponent 'p' governs the morphology of the solid product deposited on the active surface during the electrochemical reaction. The smaller values of p indicate a flat plate like deposition of the product onto the active surface area whereas the higher values of p refer to a sharp needle-like deposition. Figure 19.15 shows that the battery performance is affected by the product deposition morphology. At lower values of p, the value of the specific capacity is slightly higher, but the output voltage is seen to decrease. It can be presumed that the flat layer like deposition for low values of p offers lesser mass transport limitation to oxygen as the pore blocking is lesser. However, the flat deposition might result in more surface area coverage, hence affecting the maximum reaction rate.

19.6 Effect of Cathode Design

From the discussion in the previous section, it is clear that the maximization of the reaction surface utilization and the oxygen transport is a major factor to be considered

in the design of the battery cathode. In the present section, we attempt to show the effect of minor modification of the cathode design on the battery performance.

19.6.1 *Effect of Opening Ratio of Oxygen Inlet*

This section assumes the geometry as defined in Fig. 19.16, with a = b = 0. For this study the oxygen inlet opening ratio is defined as the fraction of the surface area open to the oxygen atmosphere.

$$\text{Oxygen inlet opening ratio (refer Fig.19.16)} = \frac{c}{d} \tag{19.28}$$

It is obvious that the size of the opening of the oxygen inlet into the cathode will play a major role in the oxygen availability in the reaction sites. Figure 19.17 shows this increase in the oxygen concentration with the increase in the area of oxygen inlet.

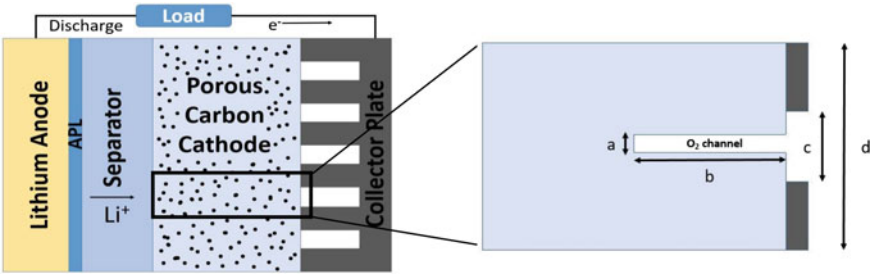

Fig. 19.16 Schematic of Li–O_2 cathode with an oxygen channel

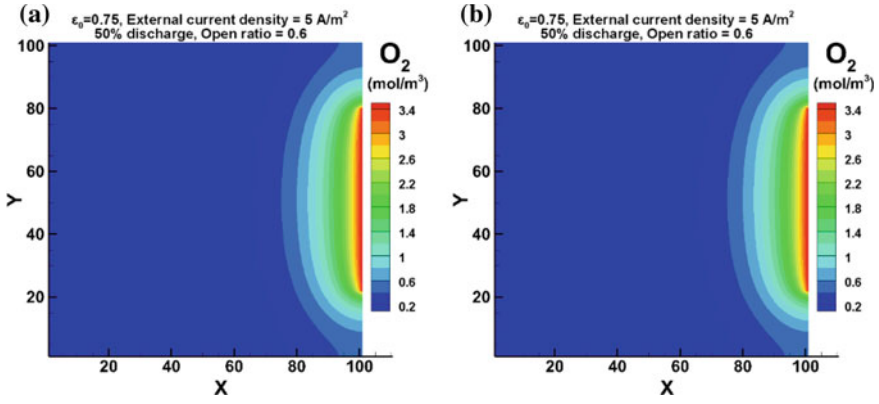

Fig. 19.17 Contours of oxygen concentration for two opening ratios

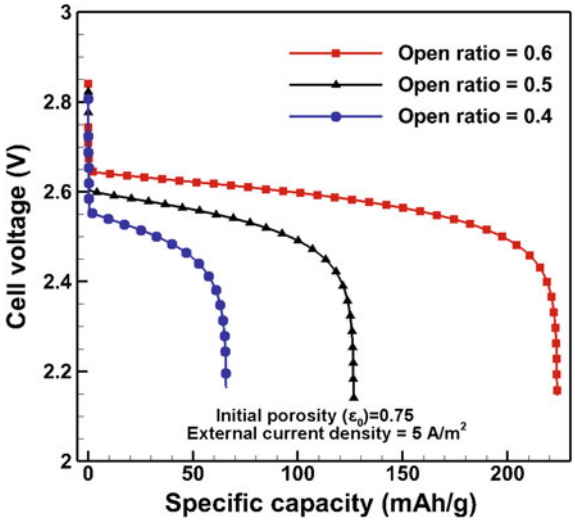

Fig. 19.18 Effect of oxygen inlet opening ratio on battery performance

The impact of this increase in the oxygen availability on battery performance can be seen from Fig. 19.18. Significant increase in the specific heat capacity and output power density is seen with increase in the opening ratio. However, the increase in opening ratio should be done without affecting the electrode-current collector contact area and the structural stability of the battery pack.

19.6.2 Oxygen Channels to Improve Power Density and Specific Capacity

One approach being proposed to maximize the oxygen availability is the inclusion of oxygen channels in the electrode to increase the diffusion of oxygen to regions of electrode away from the oxygen inlet. The geometry of the oxygen channel is shown in Fig. 19.16. The addition of the channel gives more area for oxygen to enter the porous material and the large spatial separation of most parts of the electrode can be reduced.

The oxygen concentration distribution inside the cathode porous medium with and without the oxygen channel can be seen from the Fig. 19.19. The inclusion of the oxygen channel reduces the active surface area available as the amount of porous carbon is reduced. However, according to Fig. 19.20a, b, the specific capacity is seen to increase tremendously. This further confirms that although the total surface area is high for cathodes without oxygen channel, most of it remains unutilized. The addition of oxygen channel, although reduces the total surface area, increases the utilization of the available surface area for reaction.

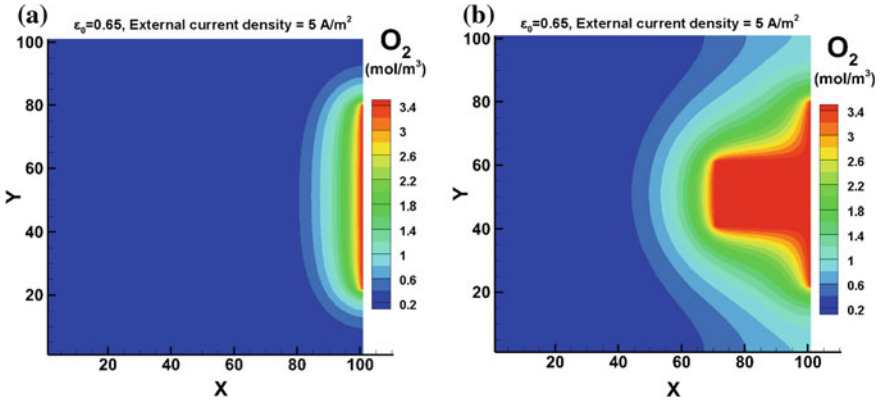

Fig. 19.19 Oxygen concentration in the cathode for geometries **a** without oxygen channel and **b** with oxygen channel

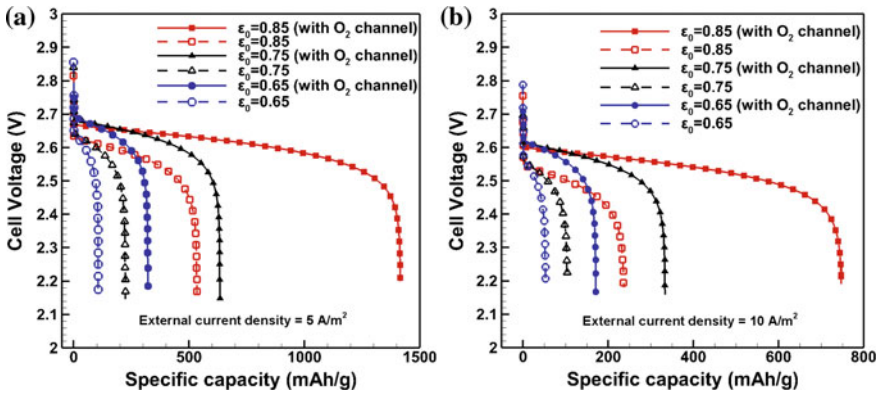

Fig. 19.20 Performance curve for geometries with and without oxygen channel, for two current density values

Another interesting factor is that even with the increase in specific capacity, the power density is not affected adversely. In fact, the power density also is seen to increase. This is because of the larger surface area available to high oxygen concentrations. Optimization of the oxygen channel width, depth and height and also the number of channels required and the spacing between them have to be done to maximize the specific capacity and power density.

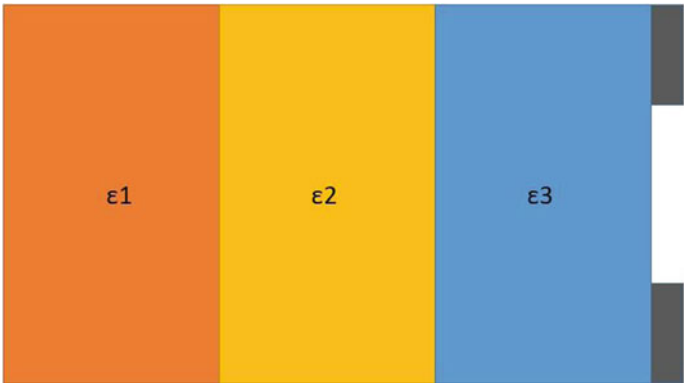

Fig. 19.21 Hierarchical porous media with layers of different porosities

19.6.3 Hierarchical Porous Media Improving Specific Capacity

Another modification being suggested in maximizing the oxygen transport attempting to minimize the loss of active surface area is the use of varying porosity. The hierarchical porous media being suggested involves porous material with different layers having different porosities as shown in Fig. 19.21. The layer with maximum porosity is kept close to the oxygen inlet to minimize the transport resistance to the interior of the cathode. Figure 19.22 shows the distribution of oxygen concentration and porosity in the cathode while the battery is in operation and has reached 50% of the maximum specific capacity value. The porosities of the three layers are selected such that the average of the porosities is 0.85. The results for the hierarchical porous media is compared with that of uniform porous media of porosity 0.85 in Fig. 19.22. Figure 19.22a, b shows the oxygen concentration distribution for uniform porosity porous media and the hierarchical porous media, respectively. The figure shows that the oxygen diffusion into the cathode is enhanced with the inclusion of hierarchical porous media.

More interesting is the plot showing the change in porosity for the two cases. In the case of uniform porosity cathode (Fig. 19.22c), it is seen that the porosity near the inlet has dropped down to less than 0.66. However, the porosity near the inlet for the hierarchical porous media (Fig. 19.22d), has dropped only to less than 0.74. This confirms that the pore blocking near the oxygen inlet is reduced with the use of high porosity porous layer near the interface. Moreover, in the region away from the oxygen inlet, no significant change in porosity is seen, even after 50% discharge, for the uniform porosity case. This means that the reaction surface area in this region is almost completely unutilized. However, for the hierarchical porous media case, the change in porosity is seen even in the layer farthest from the oxygen inlet. This change in porosity can be observed from the Fig. 19.23a which shows the change in porosity with the depth into the cathode at different discharge conditions.

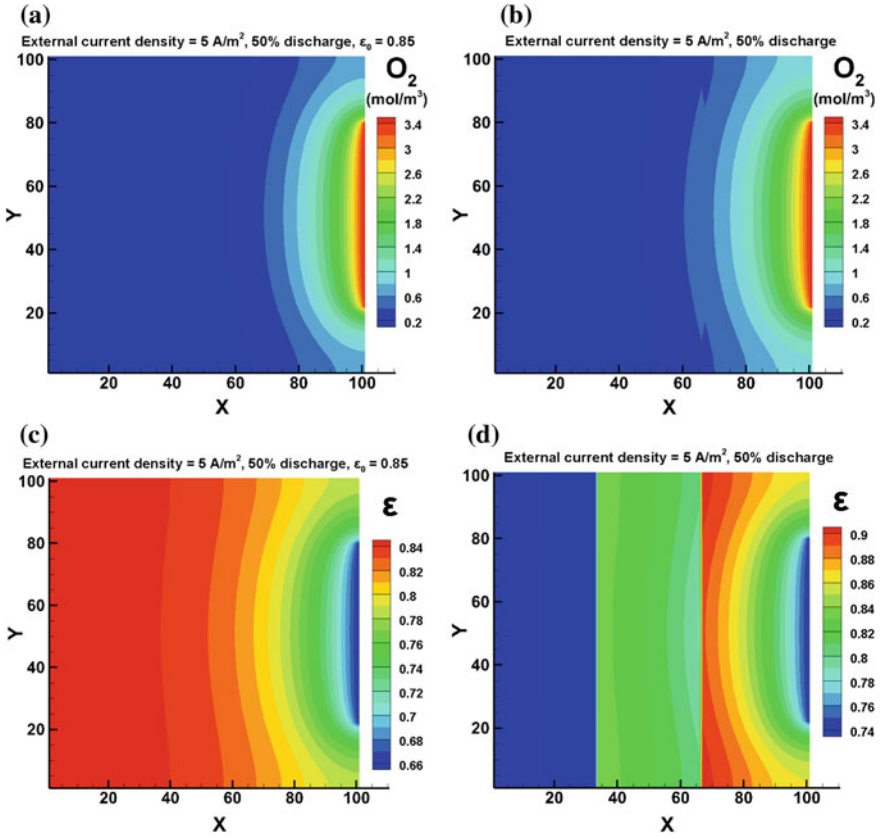

Fig. 19.22 Concentration of oxygen and porosity distribution in the cathode with hierarchical porous media

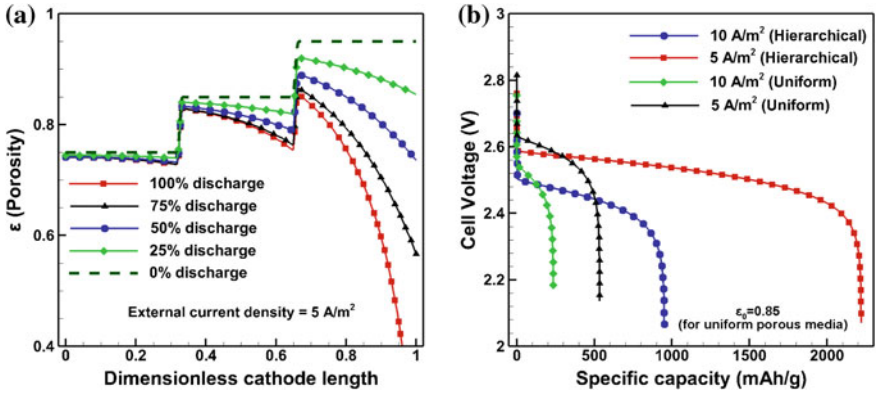

Fig. 19.23 **a** Variation in porosity with operation along the length of the cathode, **b** performance curves for two current density values for hierarchical and uniform porous media

Another interesting thing is that the regions near the interface of two layers show considerable drop in porosity. This can be due to the increased reaction at this location due to the larger surface area available for reaction with the increased oxygen concentration. Hence adding more layers might improve the maximum specific capacity. Figure 19.23b shows the increase in specific capacity with the use of hierarchical porous media. However, increasing porosity near the oxygen inlet can cause reduction in surface area in this region resulting in lowering the power density. Hence the properties of the porous layers have to be studied more closely to optimize performance according to the requirement.

19.7 Conclusions

Present chapter uses lattice-Boltzmann method to study transport phenomena in lithium-oxygen (Li-O_2) battery. Particular focus of the simulations is to understand the influence of different parameters on the battery performance as well as the performance degradation of the battery. Based on the review of literature and the simulation results, the following conclusions may be drawn:

- Cathode porosity as well as the porous media grain size strongly influence the battery performance. Specific capacity increases with porosity while power density increases with the grain size.
- Higher O_2 diffusivity leads to higher current output, although, increasing diffusivity may not increase the specific capacity.
- Li-O_2 battery performance is usually limited by rate of O_2 flow through the cathode. Low O_2 concentration reduces the current output, while higher O_2 concentration will quickly produce enough Li_2O_2 product to plug the pores of the cathode. We propose novel cathode designs to circumvent these issues. Proposals include-creating O_2 channels within cathode as well as use of hierarchical porous media.
- Li_2CO_3 formation in electrolyte permanently degrades the electrolyte. Prohibiting flow of CO_2 as well as development of novel electrolyte materials, that would be inert to CO_2, could be the key to solve the electrolyte degradation problems.

References

Aifantis KE, Hackney SA, Kumar RV (2010) High energy density lithium batteries: materials, engineering, applications. Wiley

Andersen CP, Hu H, Qiu G, Kalra V, Sun Y (2015) Pore-scale transport resolved model incorporating cathode microstructure and peroxide growth in lithium-air batteries. J Electrochem Soc 162(7):A1135–A1145

Armand M, Tarascon J-M (2008) Building better batteries. Nature 451(7179):652

Aurbach D, Cohen Y (1996) The application of atomic force microscopy for the study of Li deposition processes. J Electrochem Soc 143(11):3525–3532

Beattie S, Manolescu D, Blair S (2009) High-capacity lithium–air cathodes. J Electrochem Soc 156(1):A44–A47

Black R, Lee J-H, Adams B, Mims CA, Nazar LF (2013) The role of catalysts and peroxide oxidation in lithium-oxygen batteries. Angew Chem Int Ed 52(1):392–396. https://doi.org/10.1002/anie.201205354

Christensen J, Albertus P, Sanchez-Carrera RS, Lohmann T, Kozinsky B, Liedtke R, Ahmed J, Kojic A (2011) A critical review of Li/air batteries. J Electrochem Soc 159(2):R1–R30

Crompton TP (2000) Battery reference book. Elsevier

Gallagher KG, Goebel S, Greszler T, Mathias M, Oelerich W, Eroglu D, Srinivasan V (2014) Quantifying the promise of lithium–air batteries for electric vehicles. Energy Environ Sci 7(5):1555–1563

Girishkumar G, McCloskey B, Luntz AC, Swanson S, Wilcke W (2010) Lithium-air battery: promise and challenges. J Phys Chem Lett 1(14):2193–2203

Glaize C, Genies S (2013) Lithium batteries and other electrochemical storage systems. Wiley Online Library

Huang J, Faghri A (2015) Investigating the effect of electrolyte level change in a Li–air coin cell. Investigating the effect of electrolyte level change in a Li-air coin cell

Imanishi N, Luntz AC, Bruce P (2014) The lithium air battery: fundamentals. Springer

Jithin M, Das MK, De A (2016) Lattice boltzmann simulation of lithium peroxide formation in lithium-oxygen battery. J Electrochem Energy Convers Storage 13(3):031003

Jung K-N, Kim J, Yamauchi Y, Park M-S, Lee J-W, Kim JH (2016) Rechargeable lithium–air batteries: a perspective on the development of oxygen electrodes. J Mater Chem A 4(37):14050–14068

Li X, Huang J, Faghri A (2016) A critical review of macroscopic modeling studies on Li O_2 and Li–air batteries using organic electrolyte: Challenges and opportunities. J Power Sources 332:420–446

Lu Y-C, Gallant BM, Kwabi DG, Harding JR, Mitchell RR, Whittingham MS, Shao-Horn Y (2013) Lithium–oxygen batteries: bridging mechanistic understanding and battery performance. Energy Environ Sci 6(3):750–768

Lu J, Li L, Park J-B, Sun Y-K, Wu F, Amine K (2014) Aprotic and aqueous Li–O_2 batteries. Chem Rev 114(11):5611–5640. https://doi.org/10.1021/cr400573b

Ma Z, Yuan X, Li L, Ma Z-F, Wilkinson DP, Zhang L, Zhang J (2015) A review of cathode materials and structures for rechargeable lithium–air batteries. Energy Environ Sci 8(8):2144–2198

Newman J, Thomas-Alyea KE (2012) Electrochemical systems. Wiley

Oakes L, Muralidharan N, Cohn AP, Pint CL (2016) Catalyst morphology matters for lithium–oxygen battery cathodes. Nanotechnology 27(49):495404. https://doi.org/10.1088/0957-4484/27/49/495404

Rahn CD, Wang C-Y (2013) Battery systems engineering. Wiley

Sahapatsombut U, Cheng H, Scott K (2014) Modelling of operation of a lithium-air battery with ambient air and oxygen-selective membrane. J Power Sources 249:418–430

Scrosati B, Hassoun J, Sun Y-K (2011) Lithium-ion batteries. A look into the future. Energy Environ Sci 4 (9):3287–3295

Shao Y, Park S, Xiao J, Zhang J-G, Wang Y, Liu J (2012) Electrocatalysts for nonaqueous lithium–air batteries: status, challenges, and perspective. Acs Catalysis 2(5):844–857

Tran C, Yang X-Q, Qu D (2010) Investigation of the gas-diffusion-electrode used as lithium/air cathode in non-aqueous electrolyte and the importance of carbon material porosity. J Power Sources 195(7):2057–2063

Visco SJ, Nimon YS, De Jonghe LC, Katz BD, Petrov A (2010) Compliant seal structures for protected active metal anodes. Google Patents

Williford RE, Zhang J-G (2009) Air electrode design for sustained high power operation of Li/air batteries. J Power Sources 194(2):1164–1170

Xiao J, Mei D, Li X, Xu W, Wang D, Graff GL, Bennett WD, Nie Z, Saraf LV, Aksay IA (2011) Hierarchically porous graphene as a lithium–air battery electrode. Nano Lett 11(11):5071–5078

Xu W, Wang J, Ding F, Chen X, Nasybulin E, Zhang Y, Zhang J-G (2014) Lithium metal anodes for rechargeable batteries. Energy Environ Sci 7(2):513–537

Xu J, Ma J, Fan Q, Guo S, Dou S (2017) Recent progress in the design of advanced cathode materials and battery models for high-performance lithium-X ($X = O_2$, S, Se, Te, I_2, Br_2) batteries. Adv Mater 29(28):1606454

Ye L, Lv W, Zhang KH, Wang X, Yan P, Dickerson JH, He W (2015a) A new insight into the oxygen diffusion in porous cathodes of lithium-air batteries. Energy 83:669–673

Ye L, Lv W, Cui J, Liang Y, Wu P, Wang X, He H, Lin S, Wang W, Dickerson JH (2015b) Lithium–air batteries: performance interplays with instability factors. Chem Electro Chem 2(3):312–323

Yoo K, Banerjee S, Dutta P (2014) Modeling of volume change phenomena in a Li–air battery. J Power Sources 258:340–350

Zhang Z, Zhang S (2015) Rechargeable batteries. Nat Commun 4

Zheng J, Liang R, Ma Hendrickson, Plichta E (2008) Theoretical energy density of Li–air batteries. J Electrochem Soc 155(6):A432–A437

Chapter 20
Infrared Thermal Imaging Technique for Temperature Measurement in Various Energy Systems

Avadhesh Kumar Sharma, Mayank Modak, Santosh Kumar Sahu and Manish Kumar Agrawal

Abstract Infrared thermal imaging technique is a tool that is utilized for sensing two-dimensional thermal images of various applications. The present chapter reports the working principle of Infrared thermal imaging technique and application of this technique to measure surface temperature in various engineering applications. Also, the research work carried out by the authors by using this technique has been summarized in this chapter.

Keywords Thermal imaging technique · Energy systems · Jet impingement

20.1 Introduction

Infrared thermography is a non-contact measurement method utilized for measurement of surface temperature. Many a time, an infrared thermal camera or infrared thermal imager is employed to obtain the thermal information of a hot object. The thermal information recorded by the thermal camera is processed to provide the two-dimensional thermal image of the object which is termed as thermograms. The

A. K. Sharma · S. K. Sahu (✉)
Discipline of Mechanical Engineering, School of Engineering, Indian Institute of Technology, Indore, Madhya Pradesh, India
e-mail: santosh.sahu04@gmail.com

A. K. Sharma
e-mail: avdhruva@gmail.com

M. Modak
Division of Advanced Nuclear Engineering (DANE), Pohang University of Science and Technology (POSTECH), Pohang, South Korea
e-mail: mayankmodak1989@gmail.com

M. K. Agrawal
Discipline of Mechanical Engineering, Mahindra Ecole Centrale, Hyderabad, India
e-mail: agrwal.manish85@gmail.com

A. Mukhopadhyay et al. (eds.), *Dynamics and Control of Energy Systems*,
Energy, Environment, and Sustainability,
https://doi.org/10.1007/978-981-15-0536-2_20

infrared camera captures the part of thermal radiations that lies in IR range, transforms it into electronic signal processes, displays the image of temperature distribution and dependent on spectral bands of the sensors used in camera (Clark et al. 2003; Maldague 2001; Ring 2014; Ng 2009).

Infrared thermography has several advantages over standard techniques of temperature measurements. In standard techniques, the temperature of an object is measured by contact type temperature transducers. Most commonly employed temperature transducers are thermocouples and resistance temperature detectors (RTDs). These temperature transducers provide temperature information at a single spatial location of an object. In general, thermocouple is spot welded to the target surface or embedded at a certain depth from the free surface. Subsequently, the recorded temperature data is used to estimate the surface heat flux variation on the surface. Also, the thermocouple joints may obstruct the fluid flow during experiments. Infrared thermography facilitates accurate measurement of surface temperature with higher spatial temperature variation. In addition, this technique offers a non-contact and non-intrusive method of temperature measurement.

This allows the measurement of temperature in a corrosive and hazardous environment and does not intrude or affect the flow field during the investigation. In addition, non-contact type measurement enables measurement of the temperature of fast-moving objects, deforming objects and fast-changing thermal patterns (Carlomagno and Cardone 2010).

In recent years, a number of studies have been reported on the measurement of surface temperature, employing infrared thermal imaging technique in various industrial and scientific applications (Carlomagno and Cardone 2010; Modak et al. 2015, 2017, 2018a, b; Agrawal and Sahu 2016; Sharma et al. 2018; Agrawal 2015; Sharma and Sahu 2019; de Luca et al. 1990; Cardone and Astarita 1994; Ay 1995; Ay and Yang 1998). The present chapter is organized as follows. Here Sect. 20.2, reports the principle of temperature measurement by employing thermal imaging technique. Section 20.3 presents various applications of infrared thermal imaging technique for temperature measurement. Section 20.4 focuses on the research performed by authors at the Indian Institute of Technology Indore (Modak et al. 2015, 2018a, b; Agrawal and Sahu 2016; Sharma et al. 2018). The last section summarizes the key findings obtained from the study.

20.2 Principles of Infrared Thermal Imaging Technique and Camera Hardware

Each body whose temperature is above absolute temperature emits electromagnetic radiations to the atmosphere. Electromagnetic radiations are proportional to the intrinsic temperature of body. The electromagnetic waves constitute of gamma rays, X-rays, ultraviolet rays, infrared, (visible) light, microwaves and radio waves as depicted in Fig. 20.1.

The infrared spectral band is usually separated in four bands such as near infrared (0.76–1.5 μm), middle infrared (MWIR, 1.5–5.6 μm), far or long infrared (LWIR,

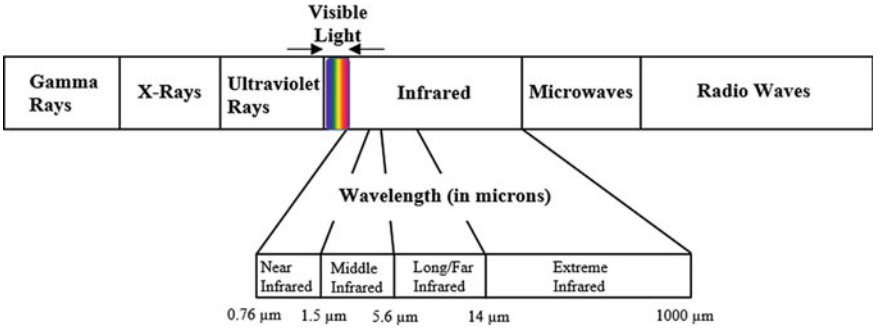

Fig. 20.1 Various spectral bands of electromagnetic waves

5.66–14 μm) and extreme infrared (14–1000 μm). In general, the infrared radiation is not detectable by human eyes. However, with the help of an input optics (lens), the electromagnetic radiations can be focused on radiation detector element. The detector creates the electrical signal, which is proportional to incident radiation (Jadin and Taib 2012; Venkataraman and Raj 2003). After this, the signal is amplified and transformed into an output signal, which is proportional to the surface temperature of object.

The intensity of the emitted energy varies with the surface temperature of the object and radiation wavelength. Along with emitting radiation, an object also reacts to the incident radiation from the surrounding, by absorbing (α') and reflecting (ρ') a portion of it and allowing some portion of the incident radiation to transmit (τ'). The sum of these three parameters should be unity at any wavelength, as given by Eq. (20.1):

$$\alpha' + \rho' + \tau' = 1 \tag{20.1}$$

where α', ρ' and τ' describe the objects incident energy absorption, reflection and transmission, respectively. An object is termed as a perfect black body, if 100% of incident radiation is absorbed and no radiation is reflected and transmitted. In infrared thermography, the concept of the black body is very essential since it prepares the foundation for relating incident absorber and emitter of radiant energy. This fact can be explained mathematically with the help of Kirchhoff's law. According to Kirchhoff's law, the coefficient of spectral emissivity (ε) is equal to the coefficient of spectral absorptivity (α'). Thus, Eq. (20.1) takes the form:

$$\varepsilon + \rho' + \tau' = 1 \tag{20.2}$$

In infrared thermograph, it is important to maximize the emissivity of the object and also it is equally important that the object must not allow the transmission of energy. Thus, taking $\tau' = 0$ the Eq. (20.2) becomes:

$$\varepsilon + \rho^{'} = 1 \tag{20.3}$$

Perfect black bodies are said to be perfect absorbers of radiation. Hence, Eq. (20.3) becomes:

$$\varepsilon = 1 \tag{20.4}$$

Thus, a perfect black body should be a perfect absorber and should have zero transmissivity. In many of the applications where high accuracy in temperature measurement is required the body is covered with a thin layer of thermal black paint (Modak et al. 2015, 2017, 2018a, b; Agrawal and Sahu 2016; Sharma et al. 2018; Agrawal 2015; Sharma and Sahu 2019).

The radiation that falls on the lens of infrared camera comes from various sources. The radiation received from the target object which emits the radiation depending upon its emissivity. In addition, the radiation from its surrounding which has been reflected from the surface of the object. Both radiation components weakened when they travel through the atmosphere. The atmosphere absorbs some part of the radiation and it will also radiate some of itself. Hence the total emissive power (I_{total}) received by the camera from the object is given as:

$$I_{total} = \varepsilon \times \tau \times I_{obj} + (1 - \varepsilon) \times \tau'' \times W_{amb} + \left(1 - \tau''\right) \times I_{atm} \tag{20.5}$$

where ε is emissivity of object and τ'' is transmission passes through the atmosphere.

The energy flux which is emitted by a black body through radiation is governed by Planck's law, expressed as:

$$I^b = \frac{C_1}{\lambda^5\left(e^{C_2/\lambda T} - 1\right)} \tag{20.6}$$

where I_b is infrared radiation of the black body, T is absolute temperature of black body, λ is radiation wavelength, C_1 is first universal constant and C_2 is second universal radiation constants. Since the emissivity of materials is lower than unity Eq. (20.6) becomes:

$$I = \varepsilon \frac{C_1}{\lambda^5\left(e^{C_2/\lambda T} - 1\right)} \tag{20.7}$$

Here, I is infrared radiation of the body. Materials with low emissivity (metals and glass) emit small amount of energy and reflect a large portion of radiation coming from the atmosphere and incident on them.

The infrared camera consists of three major components i.e. lens, radiation detector, and electronic panel. Lens element focuses the infrared radiation emitted from the object into a detector. The signal received by the radiation detector is amplified with the help of successive digital signal processing and this amplified signal is transformed into an output signal that is proportional to the temperature of object

(A655sc, FLIR system). Various parameters such as emissivity, ambient temperature, ambient humidity, absorptivity, and transmissivity have to be given as an input parameter to the software in order to correctly process the signal received from the thermal camera.

20.2.1 Calibration of Thermal Camera

It may be noted that the thermal imager needs the emissivity value of the object surface to measure the temperature of the surface. Here, calibration process is performed before using thermal imager. A cubical tank made of stainless-steel (AISI-304) is painted by heat resistant paint (flat black) to obtain uniformity in emissivity values on the test surface. Water is filled in the cubical tank and heated by utilizing a 500 W immersion heater. The water is continuously stirred to achieve uniform temperature inside the tank. Five sides of the tank are insulated, and two K-type calibrated thermocouples are mounted on the surface that is exposed to the atmosphere. Also, the temperature of the water inside the tank is measured by using a K-type thermocouple. By employing an immersion heater, the water inside the cubical tank is heated and power supply from the auto transformer is cut off after the fluid temperature reaches to 70 °C. With the progression of time, the water temperature is found to decrease 0.2 °C within 2.5 min. Here, the infrared camera and thermocouple readings are noted to record the temperature of the cubical tank. The emissivity value is fitted in research IR software of infrared camera to achieve the same temperature recorded by thermocouple. This procedure is repeated many times for different values of surface temperature of tank. The deviations in thermal response of the tank by employing IR camera and thermocouple are found to be 0.5 °C, 1.2 °C, 1.5 °C and 1.7 °C for $\varepsilon = 0.95$, 0.96, 0.97 and 0.98, respectively (Fig. 20.2). Here, $\varepsilon = 0.95$ is considered for estimating the surface temperature and ± 1.5 °C is the uncertainty in temperature measurement (Modak et al. 2015, 2018a, b; Agrawal and Sahu 2016; Sharma et al. 2018).

20.3 Various Applications of Infrared Thermal Imaging Technique for Temperature Measurement

Thermal Imaging techniques are widely used in various industrial applications such as medical diagnosis, building investigation, stress and fatigue testing, detection of internal defects in composite materials, studying temperature distribution in turbine blades.

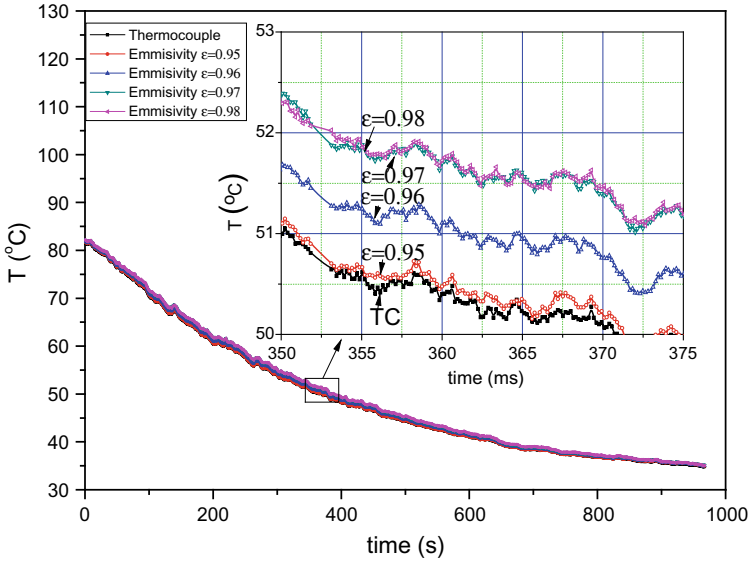

Fig. 20.2 IR camera calibration (Reprinted from Modak et al. (2017), with permission from Elsevier.)

20.3.1 Medical Applications

The use of infrared thermography to detect body temperature has been gradually increased in the last few decades. Since the method is non-invasive and non-contact, it provides accurate results as compared to alternative methods, which need physical contact between the body and the sensor. Most of the conventional methods employ probes that could affect the temperature variation of the surface through conduction. Thus, the uncertainty associated with the measurement of body temperature with the infrared thermography is less compared to conventional methods.

In one of the earliest works, Barnes (1963) reported that thermograms can provide information about physical irregularities and therefore, very useful for diagnosis of physical diseases. Sherman et al. (1996) utilized infrared thermography for assessment of skin temperature irregularities between paired limbs. Sherman et al. (1996) reported that infrared thermography is the easiest method for measuring body temperature. Fauci et al. (2001) provided a review of various temperature detectors systems and their application in the medical sector. A host of studies have reported that infrared thermography is a very effective method in the diagnosis of breast cancer, diabetic neuropathy, muscular pain, shoulder impingement syndrome study, dry eye syndrome diagnosis, vascular disorders, diagnosis of parasitic liver diseases, and detection of metastatic liver disease (Jiang et al. 2005; Ring et al. 2009; Jung et al. 2003; Ammer and Ring 1995; Armstrong et al. 1997; Bharara et al. 2006, 2012; Benbow et al. 1994; Fushimi et al. 1985; Lavery et al. 2007; Ring 2010; Bagavathiappan

et al. 2009; Hosaki et al. 2002; Thompson et al. 1978; Deng and Liu 2005; Amalu et al. 2006; Kosus et al. 2010; Aweda et al. 2010; Wishart et al. 2010; Ng and Kee 2008; Park et al. 2007; Zelichowska et al. 2005; Milonov et al. 1980; Mansfield et al. 1970; Ring and Ammer 2000). Also, diseases related to kidney transplantation, gynecology, skin, heart, and brain can be detected with the help of infrared thermography technique.

20.3.2 Inbuilt Environment/Building Investigation

In recent years, the use of infrared thermography has been increased in estimating the temperature distribution in buildings due to their easier applicability compared to conventional techniques. It provides a non-contact method for temperature measurement in building constructions from the inside and outside. It can be used for detecting various heat sources in a building. It can detect the location of heating tubes inside the wall and locate the growth of moisture in a certain area (Wild et al. 1998).

The methods used in the investigation of buildings structures are classified as destructive, semi-destructive, and non-destructive methods. Non-destructive methods are non-invasive techniques, which used to determine the reliability of a building structure and to measure important characteristics of an object utilized in construction. Non-destructive techniques facilitate inspection without creating stress or irretrievable damage to the test object. Infrared thermography is utilized in the non-destructive method of inspection.

In addition, infrared thermography due to the advantage of non-invasiveness is used extensively to investigate and diagnose various cultural heritages structures. Meola and Carlomagno (2004) described the use of infrared thermography in cultural heritage conservation. Infrared thermography is able to find the source of degradation. Also, it is effectively employed in detecting cracks, identifying the presence of cavities, structural irregularities and identifying air leakage inside the building structures.

Further, infrared thermography is employed to evaluate heating ventilation and air-conditioning (HVAC) system performance and to show moisture maps and to perform strengthening operations of HVAC system (Wild et al. 1998). Bagavathiappan et al. (2013) reported the advances made by infrared thermography for monitoring the various civil structures and metallurgical processes. Benmoussat et al. (2013) given a model to detect surface defects, cracks and notches inside the surface in the metallic parts of the industrial machines by using infrared thermography.

20.3.3 Electrical Inspection

The recent advances in technology have led to the development of thinner, lighter, faster, and efficient electronics components. The overheating of electronic components is a major concern as they reduce their reliability. Huda and Taib (2013) proposed a thermal defect identification system to predict the thermal related failures. Huda and Taib (2013) reported various reasons for the rise in internal heat of electronic equipment, such as cracks in insulation, contact problems, unbalance loading, terminal blocks or defective relays. The main challenge of electrical equipment and circuits is efficient thermal management without sacrificing the performance.

Infrared thermography provides a nonintrusive, non-contact mapping of the temperature of electronic components. This allows for quick detection and recognition of hot spots and overheating in electronic components. Infrared thermography provides information on heat patterns of electronic components that helps on early detection of failure of components (Jadin and Taib 2012; Ge et al. 2011; Anderson and Castro 1976).

20.3.4 Automotive Industry

Infrared thermography is employed in the automotive industry to monitor the varying heat patterns generated during production processes, such as thermoforming, molding, and welding. The infrared camera detects these heat patterns and presents them as visual images. Runnemalm et al. (2014) utilized infrared thermography in the automatic inspection of spot welds. Runnemalm et al. (2014) observed that the monitoring system with infrared thermography is able to detect spot welds, measure the nugget diameter, and separate a spot weld from a stick weld. Further, the rate of inspection using the following system is higher compared to conventional monitoring systems. Annibale et al. (2015) utilized infrared thermography technique for maintenance of components for automotive alternators during production. Annibale et al. (2015) reported that the use of infrared thermography has allowed planning a better model for maintenance of tools during mass production. In addition, infrared thermography has been employed by engineers to design and test the air-bag systems, validate the efficiencies of heating or cooling systems, evaluate thermal influences on tire wear and the heat dissipation by the disk brakes (A655sc, FLIR system).

20.3.5 Defense and Aerospace Industry

Infrared thermography is employed in defense applications because of its ability to perform in both day and night in all weather conditions. It is commonly used in border monitoring and observing the activity of the enemies. It is also utilized to

avoid the collision of ships and guidance systems of missiles. In military aviation, it is employed to identify the risks of flying in low light and night conditions. Further, it is used to identify, locate, and target enemy forces. Infrared thermography allows researchers to illustrate objects in the thermal spectrum for target identification and countermeasure deployment.

20.3.6 Application of Infrared Thermography in Thermal Systems

IR thermography can be effectively employed in studying the temperature map of various thermal systems in both steady and transient state applications. Infrared thermography is employed in various thermal systems such as cooling of turbine blades, flow boiling, pool boiling, heat exchangers and heat transfer of hot surface by impinging jets. Some of the important studies are presented below:

Local Heat Transfer in a Plate Finned Heat Exchangers. Plate finned tube heat exchangers are used very extensively in many industries. It is utilized to study the fluid flow between the fins. Various design parameters such as the arrangement of fins, inline and staggered tube arrangements, the spacing between fins, the diameter of the tube, tube spacing and shape of the tube are found to affect the heat transfer rate. Bougeard (2007) employed infrared thermography technique to evaluate local convection heat transfer coefficient in a plate fin two tube rows assembly. Figure 20.3 depicts convection heat transfer coefficient distribution in plate fin and two-tube rows assembly (Bougeard 2007). Tourreuil (2002) utilized infrared thermography for determining heat transfer coefficient on heat exchanger geometry. Ay et al. (2002) employed infrared thermography technique to evaluate the local convection heat transfer coefficient on the fins of heat exchanger. Ay et al. (2002) applied steady state method to precisely measure the surface temperature.

Heat Transfer and Fluid Flow Visualization. Due to the advantage of mapping the two-dimensional fluid flow field of any convective systems, infrared thermography technique is useful in investigating the behavior of surface flow field in complex flow systems. In addition, due to the larger number of viable data point locations, the accuracy of convective heat flux measurement in thermal systems exhibits higher spatial temperature variations in both steady and transient state systems (Balageas et al. 1991; Carlomagno 1997; de Luca et al. 1992). Cardone (1998) utilized infrared thermography to measure temperature and convection heat transfer coefficients in two types of fluid flow configurations (internal and external). De Luca et al. (1992) employed infrared thermography for flow visualizations and heat transfer measurements in a blow-down a hypersonic wind tunnel. Astarita and Cardone (2000) measured surface temperature by employing infrared thermography technique to evaluate convection heat transfer coefficient on two flow fields, such as a circular cylinder with and without rib turbulators at an angle of attack and a 180° turn channel.

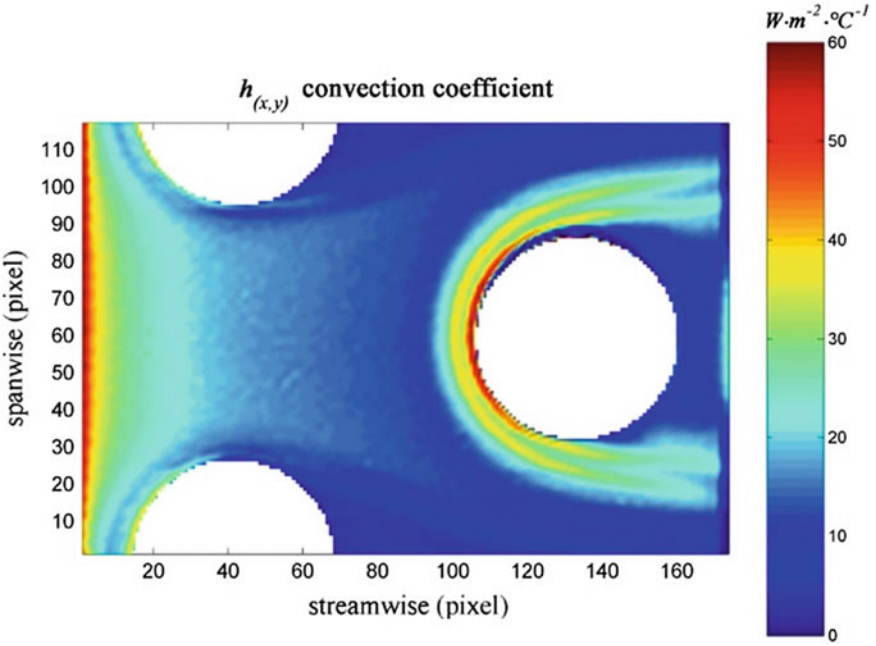

Fig. 20.3 Convection heat transfer coefficient distribution in plate fin and two tube rows assembly (Reprinted from Bougeard (2007), with permission from Elsevier.)

Flow in Microchannels. Microchannels are employed as a thermal management system in various microelectronics and other applications, such as micro-reactors, micro-fuel cell systems (Khan et al. 2013), and advanced heat sinks (Tuckerman and Pease 1981). However, due to the small size of the system, it is very difficult to correctly estimate the efficiency. Infrared thermography can overcome the limitations of traditional temperature measurement methods. Hetsroni et al. (2011) employed infrared thermography to monitor the uniformity of the thermal field over the surface of micro-heat sinks. Xu et al. (2005) used infrared thermography technique in boiling heat transfer experiments to calculate the chip surface temperature. Patil and Narayanan (2005) applied heated-thin-foil thermography technique in an external convective microscale flow. These studies indicate that infrared thermography technique has the ability to obtain detailed temporal and spatial local surface temperature measurements in complex microchannels.

Heat Transfer on Rotating Surfaces. In various industries several rotating components are involved for their operation. Monitoring and testing of such components using conventional temperature measuring technique are difficult. Infrared thermography as a non-contact method can be employed in the measurement of the temperature of such rotating components. Mori et al. (2008) studied heat transfer characteristics of rotating blades and used IR thermography to measure the temperature of moving or rotating surfaces. Experimental and numerical results are compared for

the observed blade side in terms of surface temperature distribution. Astarita and Cardone (2008) performed experiments with jet impingement for measurement of convective heat transfer by infrared thermography on a hot rotating disk.

Impinging Jets. Cooling of the hot surfaces with jet impingement finds applications in different scientific and industrial applications such as metallurgical processing, electronic components cooling, gas turbine blades, cooling of fuel pins in reactors during the postulated loss of coolant accident (Stevens and Webb 1991). Water, mist, aqueous surfactant solutions and nanofluids can be used as the coolant in the jet impingement based on the application.

Various researchers used thermal imaging technique for the measurement of the surface temperature and evaluated the convective heat transfer coefficient for axisymmetric impinging jets (Carlomagno and de Luca 1991; Meola et al. 1994; Meola and Carlomagno 2004). The heated thin foil has been used as the heat flux sensor to perform the tests. Katti and Prabhu (2008a) carried out an experimental investigation to study the thermal behavior of hot surfaces by employing orthogonal impinging air jets involving rib-rougheners. Katti and Prabhu (2008a) used a thermal infrared camera to measure local temperature distribution on the impingement surface. Figure 20.4a–b depict the variation of local Nusselt number for flat surface involving single detached rib and smooth surface, respectively during jet impingement. The surface with detached rib exhibits a higher heat transfer rate compared to the smooth surface.

Znamenskaya and Koroteeva (2013) carried out an experimental investigation to analyze a turbulent boundary layer in submerged jet flows by using infrared thermography. According to numerous studies performed in the last few years, the IR thermography can be advantageous for analyzing complex thermal flows, due to its high sensitivity and low response time (Carlomagno and Cardone 2010; Vavilov et al. 2013). The recent improvements in terms of temporal and spatial resolutions of the infrared cameras, made them possible to record the thermal images of the surface at higher frame rates. This allows capturing fast changes in the thermal behavior of flows (Znamenskaya and Koroteeva 2013; Nakamura 2011). The IR thermography has been intensively used for better understanding of the structure of jet flows (Carlomagno and Ianiro 2014).

20.4 Research on Temperature Measurement and Estimation of Various Parameters

This section focuses on the research carried out by the authors at IIT Indore. The heat flux distribution and location of maximum heat transfer coefficient are of great importance in industrial application, since the heat flux corresponds to the maximum temperature gradient in the hot solid. In order to estimate the heat flux distribution, one needs to accurately measure the surface temperature. The authors have utilized infrared thermography technique to measure the surface temperature of test surface

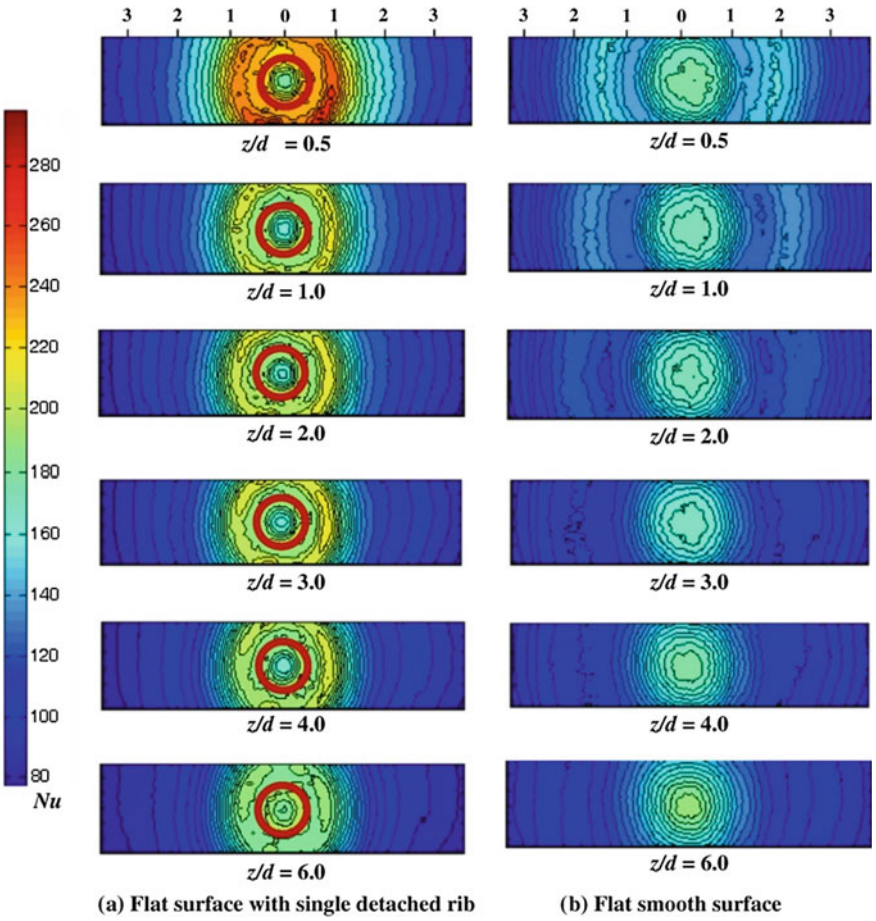

Fig. 20.4 Local heat transfer coefficient distribution at $Re = 20{,}000$. **a** Flat surface with single detached rib **b** flat smooth surface (Reprinted from Katti and Prabhu (2008a), with permission from Elsevier.)

during impinging jet cooling under transient and steady state. Subsequently, the temperature data from the thermal images are utilized to evaluate various heat transfer and rewetting parameters, such as heat flux, convective heat transfer coefficient, Nusselt number, and rewetting velocity. The details are elaborated below.

20.4.1 Transient Cooling of Hot Surface

The authors conducted tests (Modak et al. 2015, 2018a, b; Agrawal and Sahu 2016; Sharma et al. 2018) to evaluate the heat transfer behavior of hot surface by water

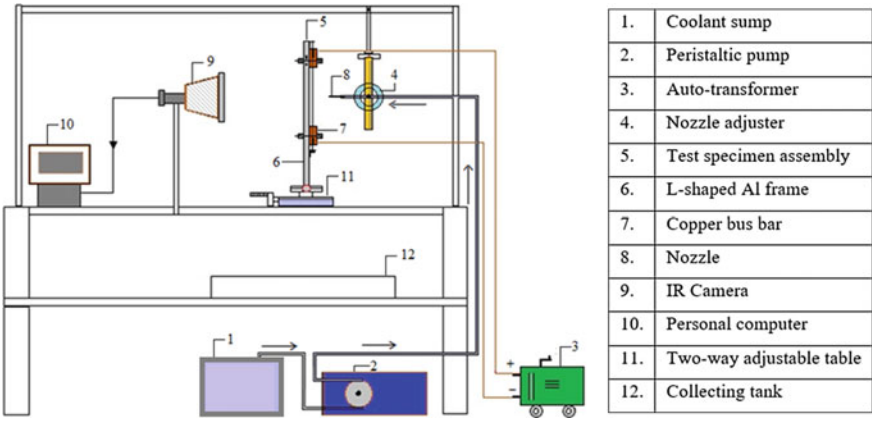

Fig. 20.5 Schematic diagram of the test facility (Reprinted from Agrawal and Sahu (2016), with permission from Taylor & Francis Ltd.)

jet impingement. The temperature data, recorded by using an infrared camera, is utilized to estimate various parameters such as surface heat flux, Nusselt Number, rewetting velocity, rewetting time and cooling efficiency. Tests are conducted for a varied range of Reynolds number, nozzle to plate distance and different coolants.

Figure 20.5 shows the schematic of the experimental facility. The experimental facility involves a test foil (SS-304, 0.15 mm thick), scheme for water supply, module for power supply and module for recording temperature of hot surface. Here stretching screws are used to stretch the foil to avoid the possible thermal expansion/contraction of the test specimen during jet impingement. The two-way adjustable table with the aluminum frame is utilized to maintain the required nozzle to plate distance (Modak et al. 2015, 2018a, b; Sharma et al. 2018).

Here, the IR thermal imaging (Make: FLIR®, Model: A655sc) is employed to measure surface temperature during tests. The spectral bend and temperature range of IR camera range between 7.5–14.0 μm and −40 °C to 2000 °C, respectively. Here, the scanning rate is fixed at 100 frames per second. The jet nozzle and camera are located on either side of the test foil. The thickness of the test foil is 0.15 mm and the maximum Biot number ($0.0059 \ll 0.1$) in the thickness direction is considered to be negligible. In such a case, it is assumed that the lumped model holds good and the temperature gradient in the thickness direction is negligible. During steady-state condition, the temperature drop across the thickness direction of the test foil is found to be 0.25 °C. Therefore, the temperature of both the sides of foil is considered to be the same during heating and cooling. The temperature measured by the IR camera is used for further processing.

Experimental Procedure and Data Reduction. Here, an AC auto-transformer (AC, 24 V, 400 A) is used to heat the stainless-steel (AISI-304, 0.15 mm thick) test foil. After attaining the required temperature, the power supply is cut off and jet is allowed

Table 20.1 Infrared camera parameters

Parameter	Magnitude
Image object parameters	
Emissivity, ε	0.95
Reflected ambient temperature	32 °C
Atmospheric parameter	
Atmospheric temperature	28 °C ± 2 °C
Relative humidity	0.55
Distance from IR camera to test specimen	1.0 m
Transmission	0.99
IR camera parameter	
Temperature range	150–650 °C
Resolution	640 × 480 pixels
Scanning rate	100 fps
Distance between each pixel	0.866 mm
Focal length	24.6 mm

to impinge on the test surface and IR thermal camera is used to record the temperature data.

Experiments are performed for a wide range of Reynolds number (5000–12,000) and various fluids such as aqueous surfactant solution of 2 Ethyl Hexanol (2-EH), CuO-water nanofluids with different concentration ($\phi = 0.15\%, 0.60\%$) and nozzle to plate distance ($l/d = 6, 12$) (Sharma et al. 2018). The thermal camera is located at a distance of 1 m from the test specimen. The FLIR Research IR V3.3 software is used to process the thermal images. The corrections due to numerous parameters such as atmospheric temperature, atmospheric humidity, absorptivity and transmissivity of the medium used in this study are listed in Table 20.1.

The electric power to heat the test foil is controlled by the autotransformer to obtain the required surface temperature. After achieving the steady state condition, the peristaltic pump is turned on, and the coolant is directed to flow through the bypass line. The coolant flow rate is adjusted to the required value by varying rotational speed of the peristaltic pump. After adjusting the flow rate, to initiate impingement, the power supply is turned off, and the coolant flow is diverted from the bypass line to the impinging nozzle. The surface heat flux (q) is estimated as (Modak et al. 2018):

$$q = -\rho C \left(\frac{V}{A}\right) \frac{dT}{dt} \tag{20.8}$$

where V is volume, A is projected area of the test foil. While, ρ and C denote the density and specific heat of the test foil, respectively. The temperature transients recorded by the infrared camera, are used to evaluate the variation of surface heat flux for various experimental parameters. The maximum radiation loss of the foil is found to be 2% of the surface heat flux at the stagnation region and therefore, it is

not counted in the heat transfer calculation. The convection heat transfer coefficient (h) can be estimated as (Modak et al. 2018):

$$h = \frac{q_t}{T_s - T_f} \tag{20.9}$$

The surface temperature and coolant temperature are defined by T_s and T_f, respectively.

The Nusselt number can be calculated as:

$$Nu = \frac{hd}{k_f} \tag{20.10}$$

where h, d and k_f are convective heat transfer coefficient, nozzle diameter and thermal conductivity of coolant, respectively.

The Reynolds number can be estimated as:

$$\mathrm{Re} = \frac{\rho U d}{\mu} \tag{20.11}$$

Here, U, μ and d are used to define jet velocity, viscosity and nozzle diameter, respectively.

The velocity of the wet front (u) is calculated as (Sharma et al. 2018):

$$u = \frac{\Delta x}{\Delta t} \tag{20.12}$$

Here, Δx and Δt denote the distance between two pixels and the time taken by the wet front to propagate between two-pixel points on the target surface. Rewetting velocity can be represented in the dimensionless form (Pe) (Agrawal and Sahu 2016):

$$Pe = \frac{\rho C u \delta}{K} \tag{20.13}$$

Here, δ and k denote the thickness and thermal conductivity of the test material, respectively. Peclet number (Pe) signifies the propagation of wet front velocity on the hot surface.

Results and Discussion. Figure 20.6 shows the thermal images recorded by IR camera, 0.20 s after the jet impingement using various fluids as coolant such as water, aqueous surfactant solution, and Al_2O_3-water (0.60%) nanofluids on the test specimen. On the right-hand side, a color band gives the surface temperature distribution over the entire surface. The authors reported the spreading behavior of different coolants during impingement. After the jet impinges on the hot surface, a dark circular region is observed at the stagnation region. From the color band, it is observed that the surface temperature in this circular region is significantly lower compared to the other region of test foil. For a given Reynolds number, the area of the dark circular zone is larger for aqueous surfactant solution compared to Al_2O_3-water nanofluids

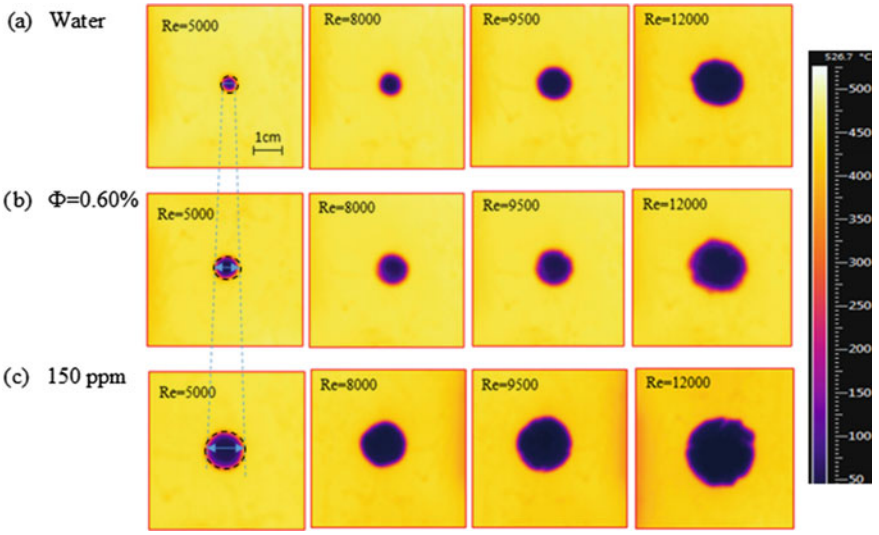

Fig. 20.6 Thermal image of test specimen during impingement with various fluids ($t = 0.2$ s $T_i =$ 500 °C) (Reprinted from Modak et al. (2018a), with permission from Taylor & Francis Ltd.)

and pure water. This shows that jet of aqueous surfactant solution spreads faster on the hot surface compared to other fluids. Faster spreading results to better evaporation and enhanced heat transfer rate.

Figure 20.7 shows the transient surface temperature curves of various fluids such as water, 2-Ethyl Hexanol-water and Al_2O_3-water. The power supply to the test foil is stopped (point a in Fig. 20.7) and coolant is allowed to impinge on the test foil denoted by point. The temperature drops (a–b) during power supply cut off, and the initiation of coolant jet is shown in Fig. 20.7. When the jet impinges on the

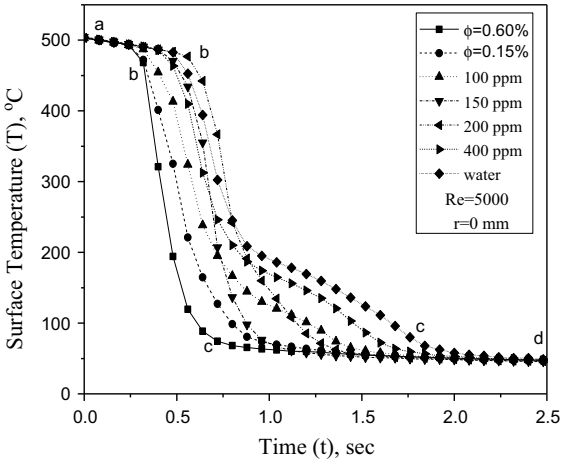

Fig. 20.7 Transient surface temperature for various additives concentrations for $z/d = 4$ at $Re = 5000$ ($T_i =$ 500 °C) (Reprinted from Modak et al. (2018a), with permission from Taylor & Francis Ltd.)

hot surface, the surface temperature at the stagnation point drops rapidly (b–c) and followed by a constant temperature (c–d). It is found that rapid cooling of the test surface is achieved by using 2-Ethyl Hexanol and Al_2O_3-water nanofluids (ϕ = 0.60%). The time taken to cool the hot foil (from 500 to 100 °C) are found to be 1.75 s, 0.90 s and 0.55 s for pure water, aqueous surfactant solution (150 ppm) and Al_2O_3-water nanofluids ($\phi = 0.60\%$), respectively.

Figure 20.8 depicts the heat transfer distribution for various fluids, in particular, water, Al_2O_3-water nanofluids and aqueous surfactant solution along with the downstream direction away from the stagnation point for a given nozzle to plate distance ($l/d = 4$) and Reynolds number ($Re = 9500$). The value of the heat transfer coefficient is highest at the stagnation point for all the coolants. It has been found that when hot foil comes in contact with the liquid in the downstream direction, away from stagnation point, the liquid sub-cooling is decreased, and enthalpy is increased. If the enthalpy of the coolant is increased, it has a lesser heat extract capacity from the hot foil. For Al_2O_3-water nanofluids, the decrease in the heat transfer coefficient at various radial locations ($r = 0$ mm to $r = 11.25$ mm) is found to be 46% and 40% for $\phi = 0.15\%$ and $\phi = 0.60\%$ nanofluids concentrations, respectively. Also, for the 150-ppm concentration of 2-Ethyl Hexanol (2-EH), the heat transfer rate decreases to 50% from $r = 0$ mm to $r = 11.25$ mm.

Figure 20.9 shows the variation of surface heat flux and surface temperature at stagnation point during the transient cooling of the hot vertical surface with water. During the transient cooling (from 500 to 100 °C), four heat transfer boiling regions can be observed, in particular, film boiling, transition boiling, nucleate boiling, and single-phase forced convection.

The variation of Nusselt number at the stagnation point ($r = 0$) for water and for various concentrations of CuO-water nanofluids ($\phi = 0.15, 0.60\%$) for the different nozzle to plate distance ($l/d = 6, 12$) and various Reynolds numbers is depicted in Fig. 20.10a–b. For $l/d = 6$ and $Re = 5000$ the increase in Nusselt number of

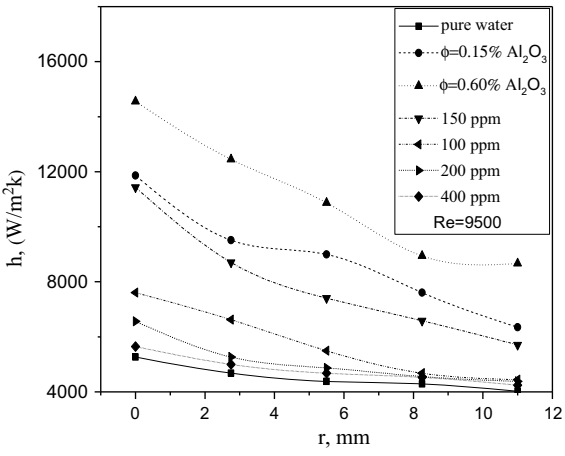

Fig. 20.8 Variation of heat transfer coefficient with a radial location for various fluids (T = 500 °C) (Reprinted from Modak et al. (2018a), with permission from Taylor & Francis Ltd.)

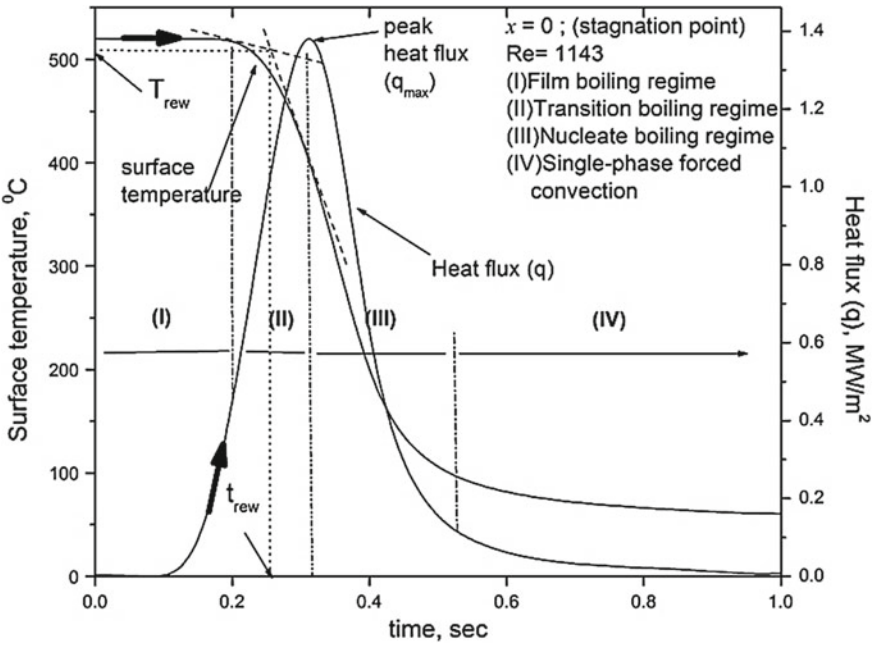

Fig. 20.9 Distribution of heat flux and various modes of boiling during transient cooling (Reprinted from Agrawal and Sahu (2016), with permission from Taylor & Francis Ltd.)

nanofluids $\phi = 0.15\%$ and $\phi = 0.60\%$ were found to be 14% and 62%, respectively, compared to pure water. The enhancements in Nusselt number for $l/d = 12$ were found to be 13.6% and 90% for $\phi = 0.15\%$ and $\phi = 0.60\%$ respectively, compared to pure water.

Modak et al. (2015) have proposed a correlation from the test results obtained during the transient cooling of vertical stainless-steel foil (Fig. 20.11). The proposed correlation is valid for the range of $5000 < Re < 12{,}000$, $5.29 < Pr < 5.54$, $6 < l/d < 12$. This is given below:

$$Nu = 10.56 \times 10^3 (\mathrm{Re})^{0.453} (\mathrm{Pr})^{-6.24} \left(\frac{l}{d}\right)^{0.16} \tag{20.14}$$

The correlation for Nusselt number at the stagnation point (Eq. (20.14) can predict within an error band of ±30% for 92.5% of the test data, while 62.5% of the test data falls in the range of ±20% error band as shown in Fig. 20.11.

Experiments have been carried out by Sharma et al. (Sharma et al. 2018) to analyze the thermal behavior of 0.15 mm thick hot horizontal stainless-steel foil (SS-304) by circular water jet impingement from the bottom side. The thermal imaging camera (A655sc, FLIR system) has been used to record the transient temperature of the hot foil. Experiments are performed for various Reynolds numbers ($Re = 2500$–$10{,}000$),

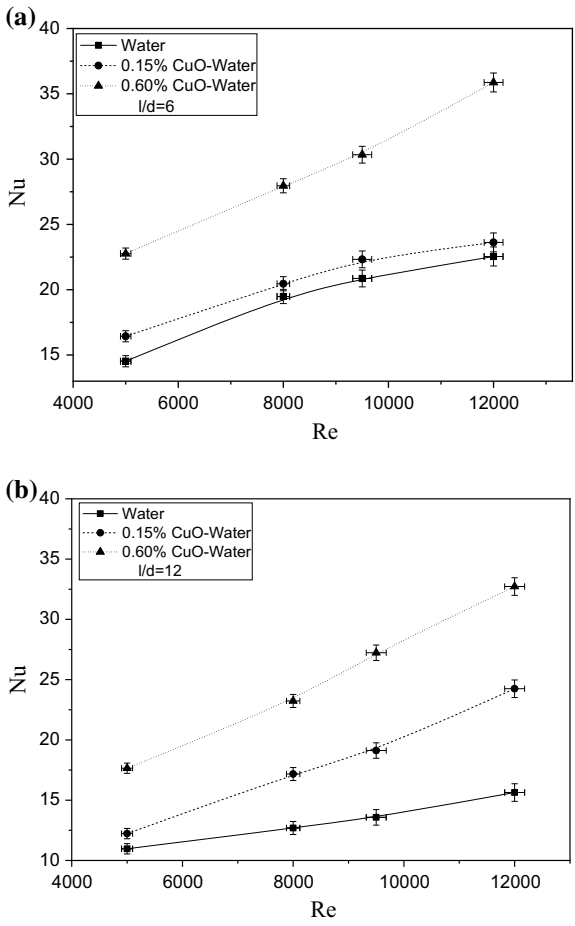

Fig. 20.10 Variation of Nusselt number with Reynolds numbers for **a** $l/d = 6$, **b** $l/d = 12$ (Reprinted from Modak et al. (2018b), with permission from ASME.)

nozzle to plate distance ($z/d = 4$–10) and initial surface temperature of 500 ± 10 °C. Figure 20.12 shows the thermal images of the hot surface, recorded by IR camera for $Re = 2500$ during the transient cooling. A color bar on the right side shows the temperature distribution over the entire surface. When the jet impinges on the hot surface, a dark zone in circular shape is developed in the stagnation region. With the progress of time, the area of the dark zone increases.

Sharma et al. (2018) estimated the maximum surface heat flux at different radial locations from the temperature transients and a correlation is proposed for $q_{\max,r}$ as a function of various parameters such as Reynolds number (Re), radial distance (r/d), and nozzle to plate distance (z/d) and expressed in Eq. (20.15).

$$q_{\max,r} = 0.3284 Re^{0.2963} \left(\frac{r}{d}\right)^{-0.2754} \left(\frac{z}{d}\right)^{0.086} \tag{20.15}$$

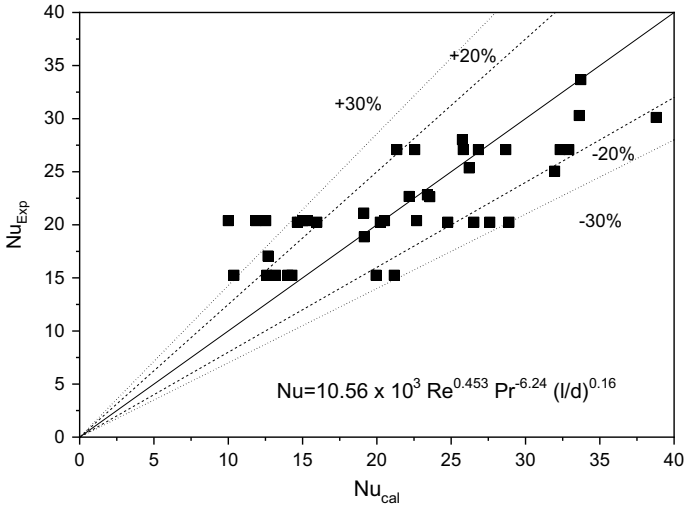

Fig. 20.11 Comparison of predicted Nusselt number with experimental Nusselt number (Reprinted from Modak et al. (2015), with permission from Elsevier.)

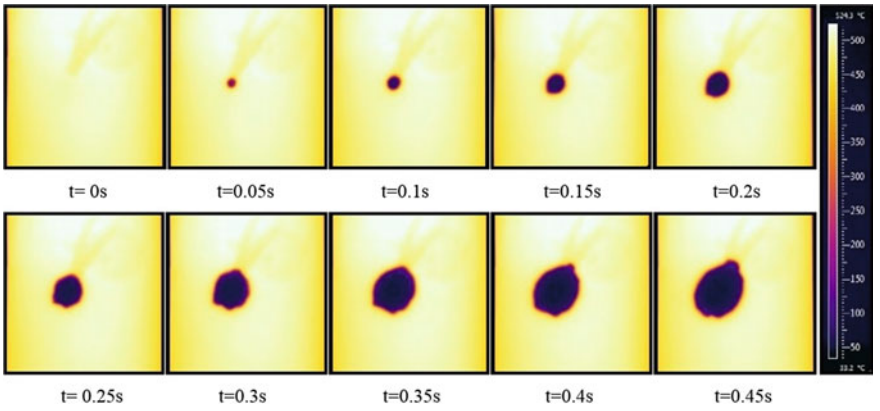

Fig. 20.12 Infrared images during transient cooling of the hot surface ($Re = 2500$, $z/d = 4$) (Reprinted from Sharma et al. (2018), with permission from Elsevier.)

The proposed correlation for $q_{\max,r}$ is valid for the range of $2500 \leq Re \leq 10000$, $4 \leq z/d \leq 10$ and $1.75 \leq r/d \leq 8.75$ and can predict 95% of the test data within an error band of $\pm 10\%$ as shown in Fig. 20.13 (Sharma et al. 2018).

In addition to this, Sharma and Sahu (2019) carried out experiments to analyze the effect of mist loading fraction on heat transfer and rewetting behavior of hot surface during mist jet impingement cooling. Full cone pneumatic internal mixing mist nozzle (Lechler 136.134.xx.A2) with a spray angle of 20° is employed to form a mist jet with various mist loading fractions (0.48–1.18). The initial surface temperature

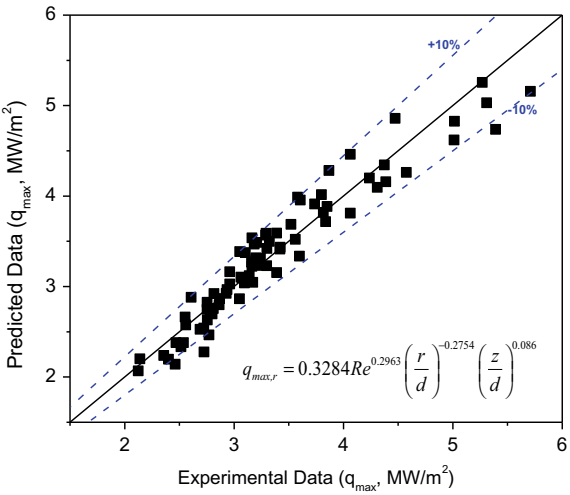

Fig. 20.13 Comparison of experimental maximum surface heat flux with the proposed correlation for maximum surface heat flux valid for $2500 \leq Re \leq 10000$, $4 \leq z/d \leq 10$ and $1.75 \leq r/d \leq 8.75$ (Reprinted from Sharma et al. (2018), with permission from Elsevier.)

of the test foil is maintained at 500 ± 100 °C with the help of an AC transformer. An infrared thermal imaging camera is used to record the transient temperature of the hot surface.

Figure 20.14 (Sharma and Sahu 2019) shows the variation of maximum surface heat flux (q_m) with mist loading fraction at various radial locations. It has been found that the value of maximum surface heat flux is increased with the increase in mist loading fraction ($0.48 \leq f \leq 1.18$) and attained the maximum value (10.21 MW/m^2)

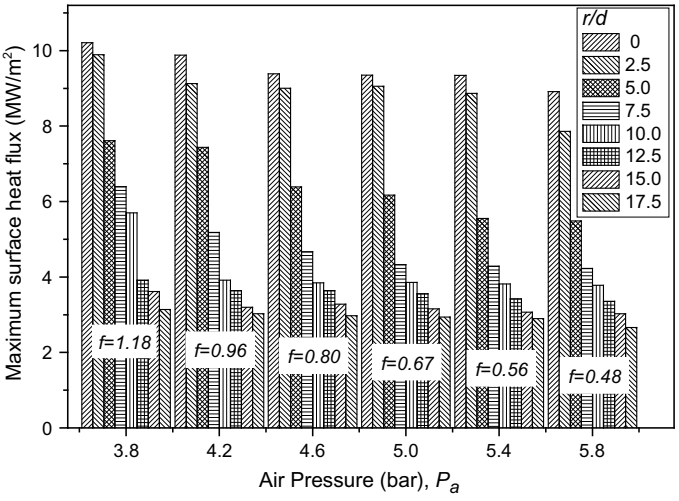

Fig. 20.14 Variation of maximum surface heat flux with mist loading fraction (Reprinted from Sharma and Sahu (2019), with permission from Elsevier.)

at $f = 1.18$ which is 14.54% higher as compared to the result (8.91 MW/m^2) at $f = 0.48$. The value of surface heat flux is maximum at the stagnation point and gradually decreases in the downstream direction away from the stagnation point, irrespective of mist loading fraction. With the increase in air pressure, while keeping the water pressor constant, mist loading fraction decreases, which reduces the heat transfer rate.

The variation of Peclet number (Pe) for various mist loading fractions ($0.48 \leq f \leq 1.18$) is shown in Fig. 20.15a. With the decrease in mist loading fraction, the value of the Peclet number is found to increase. The value of the Peclet number is maximum at $f = 0.48$ (Sharma and Sahu 2019). The Peclet number is found to decrease in the radial direction away from the stagnation point. A correlation based on the test data is proposed by Sharma and Sahu (2019) for Peclet number as a function of different parameters such as mist loading fraction and radial distance and expressed here.

$$Pe = \frac{\rho c_p u \delta}{k} = 4.616666\left(\frac{r}{d}\right)^{-0.3732}(f)^{-0.8835} \tag{20.16}$$

The proposed correlation for Peclet number is valid for $0.48 \leq f \leq 1.18$ and $2.5 \leq r/d \leq 17.5$. The proposed correlation can predict 100% of test data within an error band of $\pm$ 20% and is shown in Fig. 20.15b (Sharma and Sahu 2019).

20.4.2 Measurement of Steady-State Temperature

Figure 20.16 depicts the test facility to analyze the heat transfer behavior of test foil during steady-state conditions with air as a fluid. The experimental facility involves a test foil (AISI-304, 0.15 mm thick), scheme for power supply, module for coolant flow and temperature measurement scheme (Modak et al. 2017).

An air compressor of 12 bar rated capacity (Make: Ingersoll Rand) is used to supply air. The air flow rate is measured by a digital compressed air counter (Make: Testo Inc., Model: 6441). An FRL (Filter Regulator and Lubricator) unit is located upstream of the compressed air counter to filter the air and the required downstream pressure is maintained. A rectangular edged copper nozzle plate with the dimensions of 2×3 mm^2 and 2 mm thickness is attached at the end of an aluminum pipe (80 cm long), which performs as a fluid issuing nozzle (Fig. 20.17).

The length-diameter ratio (l/d) of the nozzle is maintained 70, which ensures that the fully developed turbulent flow is supplied through the nozzle. At the downstream of the compressed air counter, a pressure transducer (Make: Omricon) is attached to measure the airflow pressure. To allow the fluid flow, an AC powered solenoid valve is installed in the downstream direction of the compressed air counter. The infrared thermal imaging camera, positioned on the opposite side of the test specimen to the impinging nozzle, is employed to measure the local temperature distribution on the test specimen.

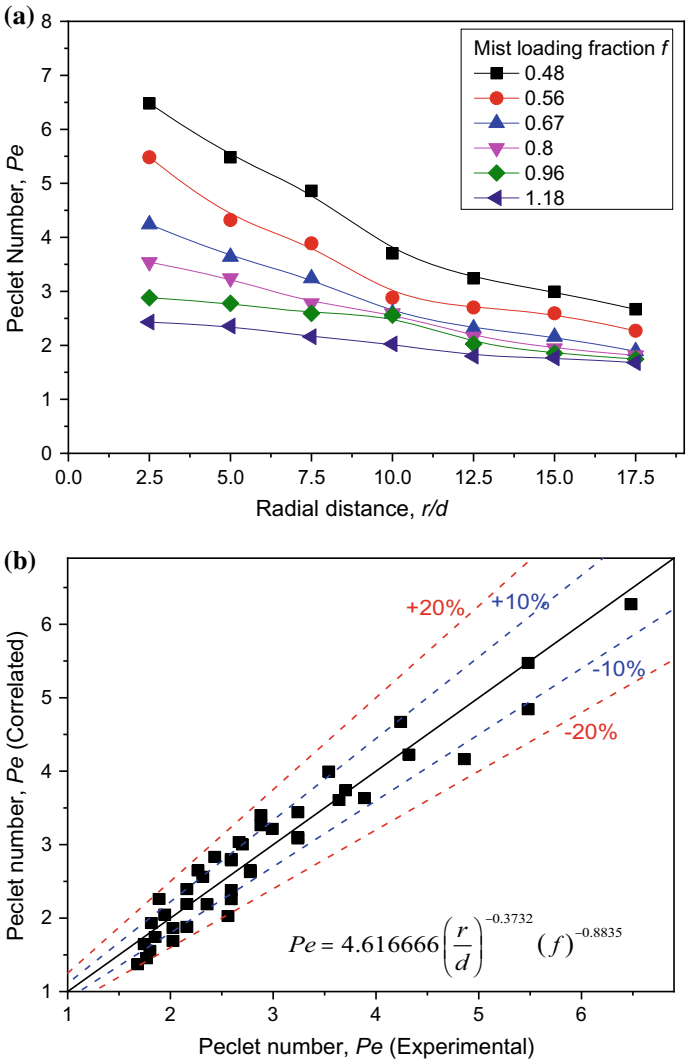

Fig. 20.15 **a** Radial distribution of Peclet number (*Pe*), **b** Peclet number correlation curve (Reprinted from Sharma and Sahu (2019), with permission from Elsevier.)

Experimental procedure and data reduction. Thermal images are recorded by an IR camera placed at a distance of 1 m from the test surface. The air flow rate is controlled by a ball valve fitted upstream of the compressed air counter. An auto transformer (AC, 24 V, 400 A) is used to supply the electric power to the test specimen. Various experimental parameters used in the IR camera are given in Table 20.1.

Results and Discussion. Modak et al. (2017) carried out tests at the atmospheric conditions and the air is used as the working fluid. The Reynolds number is varied

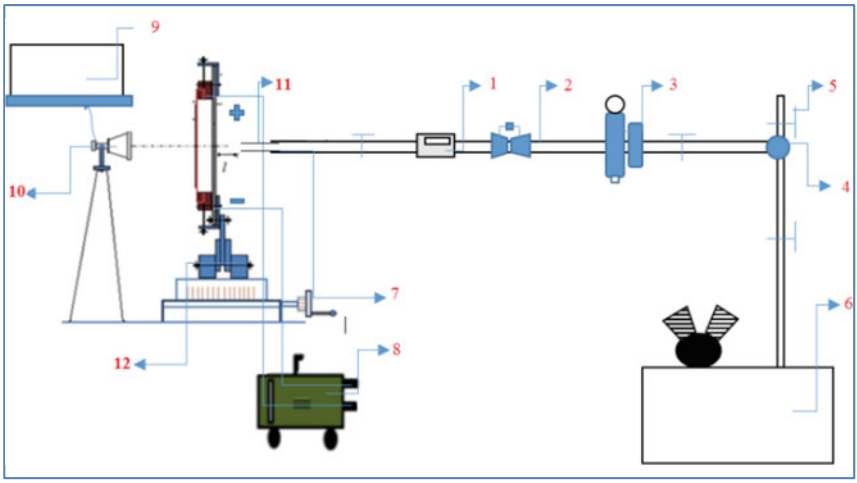

1) Testo compressed air counter (Model: 6441)	7) Air line
2) Venturimeter	8) Auto transformer
3) FRL (Filter Regulator Lubricator)	9) Computer
4) Solenoid Valve	10) IR Camera
5) Valve	11) Nozzle
6) Air compressor	12)Test surface assembly

Fig. 20.16 Schematic view of the experimental setup (Reprinted from Modak et al. (2017), with permission from Elsevier.)

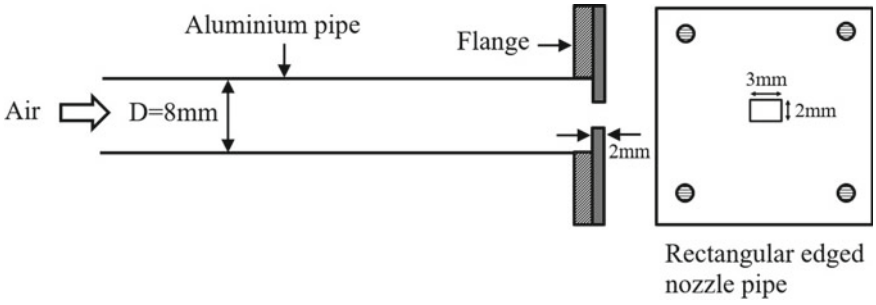

Fig. 20.17 Schematic diagram of nozzle plate assembly (Reprinted from Modak et al. (2017), with permission from Elsevier.)

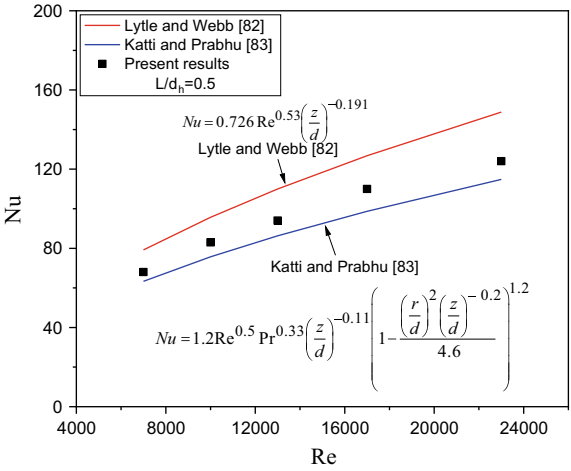

Fig. 20.18 Comparison of experimental Nusselt number with the correlation of Lytle and Webb (1994) and Katti and Prabhu (2008) (Reprinted from Modak et al. (2017), with permission from Elsevier.)

7000–17,000 and nozzle to plate distance is varied between 1 and 10. An effort have been made to validate the test facility and test data is compared with the correlation proposed by Lytle and Webb (1994) and Katti and Prabhu (2008b) and is shown in Fig. 20.18. A good agreement (within 15%) is found between the experimental values and the correlation (Lytle and Webb 1994; Katti and Prabhu 2008b).

Figure 20.19 shows the contour maps for the axial distribution of the local Nusselt number due to jet impingement on the test surface for Reynolds number $Re =$ 7000 and $H/B = 1$, 4, 7 and 10. The local Nusselt number distribution profiles are evaluated by taking the average values of various circumferential Nusselt number at a given radial location away from the stagnation point. The contour maps are found to closely agree with the shape of the nozzle at $H/B = 1$. The contour tends to attain an axisymmetric shape at a higher value of nozzle to plate distance ($H/B = 4$, 7 and 10). Zhao et al. (2007) carried out an experimental investigation and reported that the velocity and the pressure contours retain the shape of the orifice from which the flow emerges. While the contours tend to attain an axisymmetric shape in the downstream direction away from the stagnation point. Similar observations have been made by Gulati et al. (2009) in their experimental analysis.

A correlation for Nu is proposed based on the test data and is expressed in Eq. (20.17) ($7000 < Re < 17000$, $1 < L/B < 10$ and $1 < x/B < 10$):

$$Nu = 0.8(\mathrm{Re})^{0.5}(\mathrm{Pr})^{0.5}(1.02 - 0.024(L/B))^{0.5}(x/B)^{-0.33} \tag{20.17}$$

Here Eq. (20.17) predicts 98% of the data within the error band of 30, and 95% of the experimental data within the error band of 20% (Fig. 20.20).

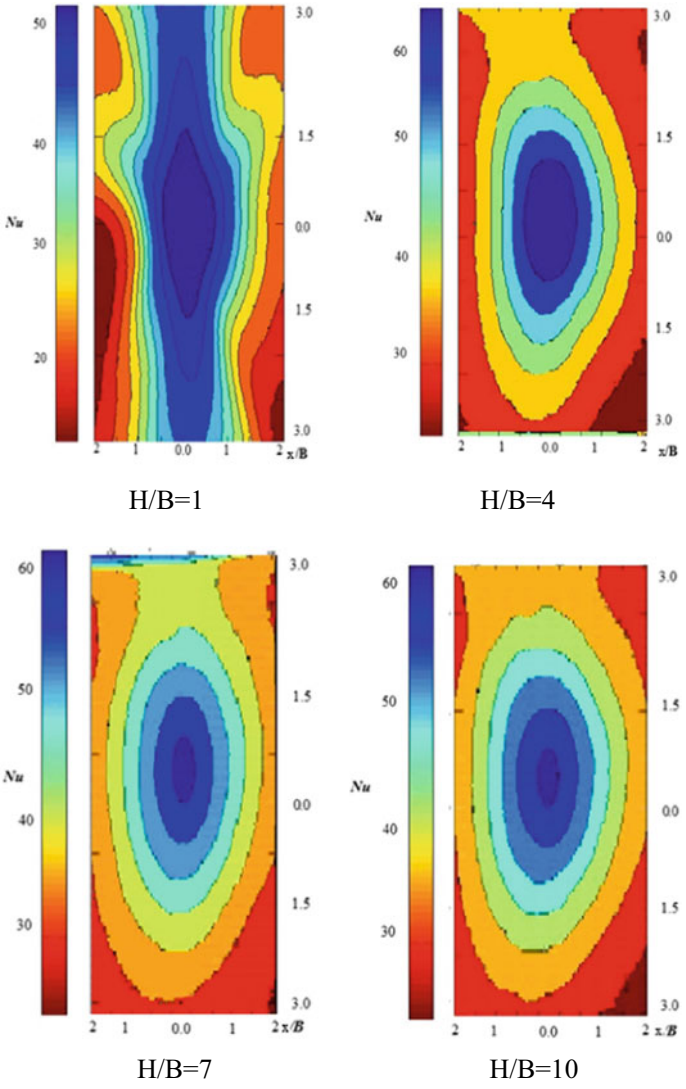

Fig. 20.19 Contours for local Nusselt number distribution at $Re = 7000$ for $H/B = 1$, 4, 7 and 10 (Reprinted from Modak et al. (2017), with permission from Elsevier.)

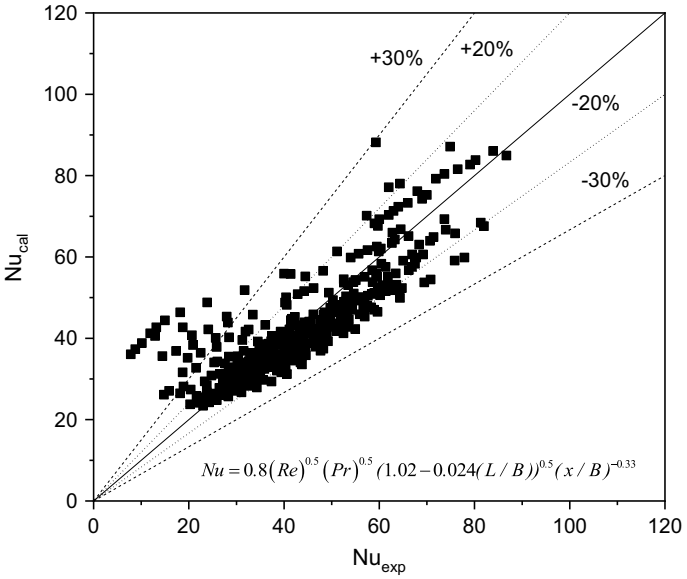

Fig. 20.20 Comparison of predicted Nusselt number with experimental local Nusselt number (Reprinted from Modak et al. (2017), with permission from Elsevier.)

20.5 Conclusion

This chapter reports the working principle of infrared thermal imaging technique and its use in various scientific and industrial applications. Also, the research carried out by the authors by employing thermal imaging technique to evaluate various parameters is summarized. The key findings of the study are listed below.

- The infrared thermal imaging technique possesses various advantages such as non-contact, non-intrusive and wider spatial resolution for temperature measurement. It can be effective for the measurement of temperature in various fields such as medical, electronics, non-destructive material testing, and environmental applications.
- With aqueous surfactant solution as coolant, the heat transfer rate increases due to the decrease in the surface tension. This promotes evaporation and increases heat transfer.
- It is observed that the time taken to cool the hot surface at the stagnation point from 500 °C to 100 °C is 1.75 s, 0.90 s and 0.55 s for pure water, an aqueous surfactant solution (150 ppm) and Al_2O_3-water ($\phi = 0.60\%$), respectively.
- Both the fluids such as aqueous surfactant solution (150 ppm) and Al_2O_3-water nanofluids ($\phi = 0.15\%, 0.60\%$) exhibit better heat transfer rate compared to pure water results. With the increases in concentration from 100 to 150 ppm, the aqueous surfactant solution exhibits a better heat transfer rate. In addition to this,

while further increasing the concentration (beyond 150 ppm), the heat transfer rate decreases.

- Nusselt number is found to increase with the increase in the Reynolds number and particle volume concentration of CuO-water nanofluids. However, the change in the nozzle to plate distance has a negligible effect on heat transfer. The increase in the Nusselt number of CuO-water nanofluids for $\phi = 0.15\%$ and $\phi = 0.60\%$ were found to be 14% and 62%, respectively, compared to pure water results for $l/d = 6$ and $Re = 5000$. While for $l/d = 12$, the increase in the Nusselt number of CuO-water nanofluids was found to be 13.6% and 90% for $\phi = 0.15\%$ and $\phi = 0.60\%$ compared to pure water.
- In case of steady-state experiments with air as the working fluid, the contour maps for the axial distribution of Nusselt number closely matches with the shape of the nozzle at $L/B = 1$. While, at a higher value of nozzle to plate ($L/B = 4$, 7 and 10) the contour tends to attain an axisymmetric shape.
- Here, *Nu* attains maximum value at the stagnation point. While the value of *Nu* reduces monotonically in the axial direction away from stagnation point.
- Based on the test data, correlations have been proposed to predict the Peclet number and local Nusselt number as a function of various parameters.

Acknowledgements The financial support provided by the Council of Scientific and Industrial Research (CSIR), Government of India, New Delhi, India is gratefully acknowledged. The authors would like to acknowledge the support from the Discipline of Mechanical Engineering, Indian Institute of Technology, Indore.

References

Agrawal MK (2015) Rewetting of hot surfaces. PhD Thesis, Discipline of Mechanical Engineering, Indian Institute of Technology, Indore, India

Agrawal MK, Sahu SK (2016) An experimental study on the rewetting of hot vertical surface by circular water jet impingement. Exp Heat Transf 29(2):151–172

Amalu WC, Hobbins WB, Head JF, Elliot RL (2006) Infrared imaging of the breast—an overview. In: Bronzino JD (ed) Biomedical engineering handbook, 3rd ed. Medical devices and systems, CRC Press, p 20

Ammer K, Ring EFJ (1995) The thermal image in medicine and biology. UhlenVerlag, Vienna

Anderson EE, Castro PS (1976) High resolution IR thermal imaging for electronic inspection. In: Proceedings Volume 0062, modern utilization of infrared technology I

Annibale AD, Ilio AD, Trozzi M, Bonaventura L (2015) The use of infrared thermography for maintenance purposes in the production process of components for automotive alternators. In: The fourth international conference on through-life engineering services, Procedia CIRP, vol 38, pp 143–146

Armstrong DG, Lavery LA, Liswood PJ, Todd WF, Tredwell JA (1997) Infrared dermal thermometry for the high-risk diabetic foot. Phys Ther 77:169–175

Astarita T, Cardone G (2000) Thermofluidynamic analysis of the flow in a sharp 180 degrees turn channel. Exp Thermal Fluid Sci 20(3–4):188–200

Astarita T, Cardone G (2008) Convective heat transfer on a rotating disk with a centred impinging round jet. Int J Heat Mass Transf 51(7–8):1562–1572

Aweda MA, Ketiku KK, Ajekigbe AT, Edi AA (2010) Potential role of thermography in cancer management. Arch Appl Sci Res 2:300–312
Ay H (1995) Heat transfer and life of cutting tool in turning. PhD Thesis, University of Michigan, Ann Arbor, MI
Ay H, Yang WJ (1998) Heat transfer and life of metal cutting tools in turning. Int J Heat Mass Transf 22(3):613–623
Ay H, Jang JY, Yeh J (2002) Local heat transfer measurements of plate finned-tube heat exchangers by infrared thermography. Int J Heat Mass Transf 45:4069–4078
Bagavathiappan S, Saravanan T, Philip J, Jayakumar T, Raj B, Karunanithi R, Panicker T, Korath MP, Jagadeesan K (2009) Infrared thermal imaging for detection of peripheral vascular disorders. J Med Phys 34:43–47
Bagavathiappan S, Lahiri BB, Saravanan T, John Philip, Jayakumar T (2013) Infrared thermography for condition monitoring—a review. Infrared Phys Technol 60:35–55
Balageas DL, Boscher DM, Deom AA, Fournier J, Gardette G (1991) Measurement of convective heat- transfer coefficients in wind tunnels using passive and stimulated infrared thermography. Rech Aerosp 4:51–72
Barnes RB (1963) Thermography of the human body: infrared-radiant energy provides new concepts and instrumentation for medical diagnosis. Science 140:870–877
Benbow SJ, Chan AW, Bowsher DR, Williams G, Macfarlane IA (1994) The prediction of diabetic neuropathic plantar foot ulceration by liquid-crystal contact thermography. Diabetes Care 17:835–839
Benmoussat MS, Guillaume M, Cauliee Y, Spinnler K (2013) Automatic metal parts inspection: use of thermographic images and anomaly detection algorithms. Infrared Phys Technol 61:68–80
Bharara M, Cobb JE, Claremont DJ (2006) Thermography and thermometry in the assessment of diabetic neuropathic foot: a case for furthering the role of thermal techniques. Int J Lower Extrem Wounds 5:250–260
Bharara M, Schoess J, Armstrong DG (2012) Coming events cast their shadows before: detecting inflammation in the acute diabetic foot and the foot in remission. Diabetes/Metab Res Rev 28(Suppl. 1):15–20
Bougeard D (2007) Infrared thermography investigation of local heat transfer in a plate fin and two-tube rows assembly. Int J Heat and Fluid Flow 28:988–1002
Cardone G (1998) Quantitative infrared thermography in thermo-fluid-dynamics. University of Naples "Federico 1/". Department of Energy, Applied Dynamic Thermal Fluid and Environmental Conditionings (DETEC) P.le Tecchio 80, 80125 Naples, Italy. http://dx.doi.org/10.21611/qirt.1998.001
Cardone G, Astarita T, Carlomagno GM (1994) IR heat transfer measurements on a rotating disk. In: Balageas D, Busse G, Carlomagno GM (eds) QIRT 94, Eurotherm Series 42, EETI
Carlomagno GM (1997) Thermo-fluid-dynamics applications of quantitative infrared thermography. J Flow Vis Image Process 4:261–280
Carlomagno GM, Cardone G (2010) Infrared thermography for convective heat transfer measurements. Exp Fluids 49(6):1187–1218
Carlomagno GM, de Luca L (1991) Infrared thermography for flow visualization and heat transfer measurements. In: Proc Workshop Stato dell'arte del rilevamento con camera termiche nella banda 8–15 micron. Firenze
Carlomagno GM, Ianiro A (2014) Thermo-fluid-dynamics of submerged jets impinging at short nozzle-to-plate distance—a review. Exp Thermal Fluid Sci 58:15–35
Clark MR, McCann DM, Forde MC (2003) Application of infrared thermography to the non-destructive testing of concrete and masonry bridges. NDT&E Int 36:265–275
de Luca L, Carlomagno GM, Buresti G (1990) Boundary layer diagnostics by means of an infrared scanning radiometer. Exp Fluid 9:121–128
de Luca L, Cardone G, Carlomagno GM, Aymer D, Alziary T (1992) Flow visualization and heat transfer measurements in hypersonic wind tunnel. Exp Heat Transfer 5:65–79

Deng ZS, Liu J (2005) Enhancement of thermal diagnostics on tumors underneath the skin by induced evaporation. In: Proceedings of the 27th annual conference of IEEE engineering in medicine and biology, Sanghai, China

Fauci MA, Breiter R, Cabanski W, Fick W, Koch R, Ziegler J, Gunapala SD (2001) Medical infrared imaging–differentiating facts from friction, and the impact of high precision quantum well infrared photodetector camera systems, and other factors, in its reemergence. Infrared Phys Technol 42:334–344

Fushimi H, Inoue T, Nishikawa M, Matsuyama Y, Kitagawa J (1985) A new index of autonomic neuropathy in diabetes mellitus: heat stimulated thermographic patterns. Diabetes Res Clin Pract 1:103–107

Ge Z, Du X, Yang L, Yang Y, Li Y, Jin Y (2011) Performance monitoring of direct air cooled power generating unit with infrared thermography. Appl Therm Eng 31:418–424

Gulati P, Katti V, Prabhu SV (2009) Influence of the shape of the nozzle on local heat transfer distribution between smooth flat surface and impinging air jet. Int J Therm Sci 48(3):602–617

Hetsroni G, Mosyak A, Pogrebnyak E, Rozenblit R (2011) Infrared temperature measurements in micro-channels and micro-fluid systems. Int J Therm Sci 50(6):853–868

Hosaki Y, Mitsunobu F, Ashida K, Tsugeno H, Okamoto M, Nishida N, Takata S, Yokoi T, Tanizaki Y, Ochi K, Tsuji T (2002) Non-invasive study for peripheral circulation in patients with diabetes mellitus. Ann Rep MIASA Med Branch 72:31–37

Huda ASN, Taib S (2013) Application of infrared thermography for predictive/preventive maintenance of thermal defect in electrical equipment. Appl Therm Eng 61:220–227

Jadin MS, Taib S (2012) Recent progress in diagnosing the reliability of electrical equipment by using infrared thermography. Infrared Phys Technol 55:236–245

Jiang LJ, Ng EY, Yeo AC, Wu S, Pan F, Yau WY, Chen JH, Yang Y (2005) A perspective on medical infrared imaging. J Med Eng Technol 29:257–267

Jung A, Zuber J, Ring F (2003) A case book of infrared imaging in clinical medicine. MedPress, Warszawa

Katti V, Prabhu SV (2008a) Heat transfer enhancement on a flat surface with axisymmetric detached ribs by normal impingement of circular air jet. Int J Heat Fluid Flow 29(5):1279–1294

Katti V, Prabhu SV (2008b) Experimental study and theoretical analysis of local heat transfer distribution between smooth flat surface and impinging air jet from a circular straight pipe nozzle. Int J Heat Mass Transf 51:4480–4495. https://doi.org/10.1016/j.ijheatmasstransfer.2007.12.024

Khan Md JA, Hasan Md R, Mamun Md AH (2013) Flow behavior and temperature distribution in micro-channels for constant wall heat flux. In: 5th BSME international conference on thermal engineering, procedia engineering, vol 56, pp 350–356

Kosus N, Kosus A, Duran M, Simavli S, Turhan N (2010) Comparison of standard mammography with digital mammography and digital infrared thermal imaging for breast cancer screening. J Turk-Ger Gynecol Assoc 11:152–157

Lavery LA, Higgins KR, Lanctot DR, Constantinides GP, Zamorano RG, Athanasiou KA, Armstrong DG, Agrawal CM (2007) Preventing diabetic foot ulcer recurrence in high-risk patients. Diabetes Care 30:14–20

Lytle D, Webb BW (1994) Air jet impingement heat transfer at low nozzle-plate spacings. Int J Heat Mass Transf 31(12):1687–1697

Maldague XPV (2001) Theory and practice of infrared technology for nondestructive testing. Wiley, New York

Mansfield CM, Farrell C, Asbell SO (1970) The use of thermography in the detection of metastatic liver disease. Radiology 95:696–698

Meola C, Carlomagno GM (2004) Recent advances in the use of infrared thermography. Meas Sci Technol 15:R27–R58

Meola C, Carlomagno GM, Riegel E, Salvato F (1994) An experimental study of an anti-icing hot air spray-tube system. In: Proceedings of the 19th congress international council aeronautical sciences, Anaheim, vol 3, pp 2345–2351

Milonov OB, Lebedeva OD, Pomelova LA (1980) The use of echography and thermography in patients with parasitic liver diseases. Sov Med 4:62–67

Modak M, Srinivasan S, Garg K, Chougule S, Agrawal M, Sahu SK (2015) Experimental investigation of heat transfer characteristics of the hot surface using Al_2O_3–water nanofluid. Chem Eng Process 91:104–113

Modak M, Srinivasan S, Garg K, Sahu SK (2017) Theoretical and experimental study on heat transfer characteristics of normally impinging two dimensional jets on a hot surface. Int J Therm Sci 112:174–187

Modak M, Sharma AK, Sahu SK (2018a) An experimental investigation on heat transfer enhancement in circular jet impingement on hot surfaces by using Al_2O_3/water nanofluids and aqueous high-alcohol surfactant solution. Exp Heat Transf 31(4):275–296

Modak M, Chougule SS, Sahu SK (2018b) An experimental investigation on heat transfer characteristics of hot surface by using CuO-water nanofluids in circular jet impingement cooling. J Heat Transf 140:1–10

Mori M, Novak L, Sekavcnik M (2008) Application of IR thermography as a measuring method to study heat transfer on rotating surface. Forsch Ing Eng Res 72(1):1–10

Nakamura H (2011) Spatio-temporal measurement of convective heat transfer using infrared thermography. In: Belmiloudi A (ed) Heat transfer—theoretical analysis experimental investigations and industrial systems. InTech

Ng EYK (2009) A review of thermography as promising non-invasive detection modality for breast tumor. Int J Therm Sci 48:849–859

Ng EYK, Kee EC (2008) Advanced integrated technique in breast cancer thermography. J Med Eng Technol 32:103–114

Park J, Hyun JK, Seo J (2007) The effectiveness of digital infrared thermographic imaging in patients with shoulder impingement syndrome. J Shoulder Elbow Surg 16:548–554

Patil VA, Narayanan V (2005) Spatially resolved heat transfer rates in an impinging circular microscale jet. Microscale Thermophys Eng 9:183–197

Ring F (2010) Thermal imaging today and its relevance to diabetes. J Diabetes Sci Technol 4:857–862

Ring EFJ (2014) Pioneering progress in infrared imaging in medicine. Quant Infrared Thermogr J 11:1–9

Ring EFJ, Ammer K (2000) The technique of infrared imaging in medicine. Thermol Int 10:7–14

Ring EFJ, Jung A, Zuber J (2009) New opportunities for infrared thermography in medicine. Acta Bio-Optika Inf Med 15:28–30

Runnemalm A, Ahlberg J, Appelgren A, Sjokvist S (2014) Automatic inspection of spot welds by thermography. J Nondestr Eval 33(3):398–406

Sharma AK, Sahu SK (2019) An experimental study on heat transfer and rewetting behavior of hot horizontal downward facing hot surface by mist jet impingement. Appl Therm Eng 151:459–474

Sharma AK, Modak M, Sahu SK (2018) The heat transfer characteristics and rewetting behavior of hot horizontal downward facing surface by round water jet impingement. Appl Therm Eng 138:1–29

Sherman RA, Wideman AL, Karstetter KW (1996) Comparative effectiveness of video thermography, contact thermography, and infrared beam thermography for scanning relative skin temperature. J Rehabil Res Dev 33:377–386

Stevens J, Webb BW (1991) Local heat transfer coefficients under an axisymmetric single-phase liquid jet. ASME J Heat Transf 113:71–79

Thompson JE, Simpson TL, Caulfield JB (1978) Thermographic tumor detection enhancement using microwave heating. In: IEEE transactions on microwave theory and techniques, MTT-26

Tourreuil J (2002) Study of the thermal performance of a compact heat exchanger with vortex promoter-development of local measurement techniques. These Doctorate of the University of Valenciennes and Hainaut Cambre'sis, France

Tuckerman DB, Pease RFW (1981) High performance heat sinking for VLSI. IEEE Electron Devices Lett 2:126–129

User's manual FLIR A6xx series (2018). https://www.alpinecomponents.co.uk/pdfs/support/infrared-cameras/FLIR-A6xx-Manual.pdf

Vavilov VP (2013) Infrared thermography and heat control. Spectr 544

Venkataraman B, Raj B (2003) Performance parameters for thermal imaging systems. Insight Non-Destruct Test Cond Monitor 45:531–535

Wild W, Büscher KA, Wiggenhauser H (1998) Amplitude sensitive modulation-thermography to measure moisture in building materials. In: Proceedings of the SPIE (Thermosense XX, Orlando), vol 3361, pp 156–162

Wishart GC, Campisi M, Boswell M, Chapman D, Shackleton V, Iddles S, Hallett A, Britton PD (2010) The accuracy of digital infrared imaging for breast cancer detection in women undergoing breast biopsy. Eur J Surg Oncol 36:535–540

Xu J, Gan Y, Zhang D, Li X (2005) Microscale boiling heat transfer in a micro-timescale at high heat fluxes. J Micromech Microeng 15:362–376

Zelichowska B, Rozycki R, Tlustochowicz M, Kujawa A, Kalicki B, Murawski P (2005) The usefulness of the thermography in the dry eye syndrome. Klin Oczna 107:483–487

Zhou DW, Lee SJ (2007) Forced convective heat transfer with impinging rectangular jets. Int J Heat Mass Transf 50(9–10):1916–1926. https://doi.org/10.1016/j.ijheatmasstransfer.2006.09.022

Znamenskaya IA, Koroteeva EY (2013) Time-resolved thermography of impinging water jet. J Flow Vis Image Process 20(1–2):25–33

Chapter 21
Catalytic Chemical Vapor Deposition Grown Carbon Nanofiber for Bio-electro-chemical and Energy Applications

Shivangi Mishra, Prateek Khare and Shiv Singh

Abstract Carbon nanofibers (CNFs) are a very promising material of carbon family and gained a severe concern by researchers since the last decades. There are numerous existed technologies for the synthesis of CNF or CNF/composites, but the focus of this book chapter is limited to catalytic chemical vapor deposition (CVD) grown CNFs and their different applications. Owing to the high specific surface area, significant porosity with uniform pores, high electrical conductivity, corrosion resistance, electrochemical stability, biocompatible, less cytotoxic and mechanically stable, they are employed in several biochemical and electrochemical applications such as bioenergy generation, electrode materials for batteries, fuel cell, and supercapacitors and as sensors. They are being used keenly in different catalytic reactions for refining the atmosphere from different types of pollutants such as VOPs, POPs, etc. This paper summarizes the role/effect of various parameters which are actively or passively liable for the growth of CVD grown CNF such as metal catalysts, carbon sources, temperatures, and carbon source decomposition timing.

Keywords Carbon nanofibers · Microbial fuel cells · An electrode · Bimetal nanoparticles · Sensor · Polymeric film · Catalytic reaction

S. Mishra · S. Singh (✉)
Nanomaterial Toxicology Group, CSIR-Indian Institute of Toxicology Research (CSIR-IITR), Vishvigyan Bhawan, 31 Mahatma Gandhi Marg, Lucknow 226001, Uttar Pradesh, India
e-mail: sshiv.singh@ampri.res.in; sshiviitk@gmail.com

P. Khare (✉)
Department of Chemical Engineering, Madan Mohan Malaviya University of Technology, Gorakhpur 273010, Uttar Pradesh, India
e-mail: pkch@mmmut.ac.in; ptkkhare@gmail.com

S. Singh
Light Weight Metallic Materials, Council of Scientific and Industrial Research—Advanced Materials and Processes Research Institute, Hoshangabad Road, Bhopal 462064, Madhya Pradesh, India

A. Mukhopadhyay et al. (eds.), *Dynamics and Control of Energy Systems*,
Energy, Environment, and Sustainability,
https://doi.org/10.1007/978-981-15-0536-2_21

21.1 Introduction

From the last two decades, carbon nanofibers (CNFs) are extensively used in several research organizations and industries because of their remarkable multifunctional properties (Al-Saleh and Sundararaj 2009; Zhang et al. 2016; Romero et al. 2007). Identical to carbon nanotubes (CNTs), CNFs are also nano-scale graphene hollow cylinders that are closed at each end. They are quite similar to well-known CNTs in respect to processing conditions and in diameter and length, i.e. 50–200 nm and 0.1–1000 μm respectively (Shah and Tali 2016; De Jong and Geus 2000). Nevertheless, the morphology, geometry, and orientations of graphitic/graphene layers are different in both CNF and CNTs. Formation of different shapes graphene layers, generating additional edge sites on the superficial side of CNFs than CNTs (Huang et al. 2010; Kim et al. 2013). In other words, the CNFs may also be called stacked-cup CNTs (Shah and Tali 2016). The exposed surface of CNFs mainly consists of prismatic planes (node and internode) and possesses higher adsorption capacity than the graphite basal planes of the CNTs (De Jong and Geus 2000; Kang et al. 2014).

Several existed techniques are able to synthesize CNFs, nonetheless, among all, the catalytic chemical vapor deposition (CCVD) technique is the most commonly used and sustainable routine for the commercial production of CNFs. This process offers high yields and controllable growth environments; consequently, scalability is not a problem. During the CVD process, the growth of CNFs occurs via the solvation–diffusion–precipitation processes (Vander Wal and Hall 2001; Singh and Verma 2015a). The growth of CNFs via the CVD process requires a transition metal catalyst e.g. nickel (Ni), cobalt (Co) silver (Ag), copper (Cu), iron (Fe), etc. and a carbon source (benzene, acetylene, ethane, methane, ethylene, ethanol etc.) (Vander Wal and Hall 2001; Bhaduri and Verma 2014a; Gupta et al. 2009; Singh et al. 2013a, 2014). The catalyst particle size determines the size of the graphitic structure of the CNFs. Depending upon the interaction between the catalyst and substrate, two types of CNF growth have been reported: (i) tip growth and (ii) base growth (Shah and Tali 2016; Teo et al. 2003; Bikshapathi et al. 2012a). During base growth, metal remains adhered to the surface due to the strong interaction between the catalyst and substrate, and CNFs grow vertically. In the case of tip growth, due to the weak interaction between catalyst and substrate, metal NPs are attached to the CNF tips resulting in upward growth. Typically, there are three forms of CNFs: platelet (alignment perpendicularly against the fiber axis), tubular (alignment parallel along the axis) and herringbone (alignment angled to the axis) (Teo et al. 2003).

The prime objective of this book chapter is to discuss the synthesis of CVD grown CNF-based materials and their different applications in the catalytic and electrochemical industries including those involved in environmental pollution (mainly water and air), capacitance, batteries, polymer additives, and fuel gases storage (De Jong and Geus 2000). The high specific surface area, uniform interconnected pores, thermal and chemical stability, electrochemical activity, conductive and small mass transfer diffusional resistance associated with CNF contribute to their use in different environmental (air and water purification) and energy applications (Romero et al.

2007; Singh and Verma 2015a; Bhaduri and Verma 2014a; Gupta et al. 2009; Singh et al. 2013a, 2014; Bikshapathi et al. 2012a; McDonough et al. 2009; Downs and Baker 1991; Pruneanu et al. 2006; Ashfaq et al. 2013, 2014; Talreja et al. 2014a; Gupta et al. 2010; Barranco et al. 2010). Among all, one of the leading feature is the presence of graphite edges on CNFs which provide strong interaction between catalysts and catalytic reactions as well as active sites for several reactions (Romero et al. 2007; Singh et al. 2014; Anderson and Rodríguez 2000; Kvande et al. 2005). Nevertheless, these CNFs are relatively newer as compared to CNTs and limited to catalyst supports, gas-storage, polymer reinforcements, probe tips and a few other applications (Huang et al. 2010). These CNFs are frequently grown on different types of supports which include aluminosilicate, nickel (Ni) foam/film, different types of carbon-based activated fibers (ACFs) (pitch, phenolic resin, PAN), charcoal, polymeric carbon beads, polyurethane foam, stainless steel (Al-Saleh and Sundararaj 2009; Romero et al. 2007; Bhaduri and Verma 2014a, 2015a; Gupta et al. 2009, 2015; Singh et al. 2014; McDonough et al. 2009; Ashfaq et al. 2013; Talreja et al. 2014a; Downs and Baker 1995; Khare et al. 2013; Li et al. 2015; Thakur et al. 2009; Bigdeli and Fatemi 2015). Among all, ACF support is more fruitful support for different catalytic, bio-electrochemical and energy applications (Singh and Verma 2015a; Bhaduri and Verma 2014a; Gupta et al. 2009; Singh et al. 2013a; Bikshapathi et al. 2012a). In few studies, it is investigated that numerous parameters affecting the growth of CNFs which includes type of catalyst, hydrocarbon sources, concentration of catalysts along with its support, hydrocarbon source, decomposition temperature, amount of hydrocarbon source, reaction times (Warakulwit et al. 2015; Öncel and Yürüm 2006; Dasgupta et al. 2011). Vertical and horizontal CVD setup for growing CNFs is shown in Fig. 21.1.

21.2 Why CVD-Grown CNFs?

Since last two decades, two methods have been extensively used for the production of CNFs, that is, (a) electrospinning (b) chemical vapor deposition. The CVD method for the production of CNFs is widely utilized because it offers greater graphitic properties as compared to those made from the electrospinning process. Also, the experimental setup for both the means, when compared, the CVD method was more convenient to work with. With the increasing demand for graphitic nature in the research area, CVD-grown CNFs were used more efficiently as compared to those electrospun CNF (Duan et al. 2015). CVD-grown CNFs are found to be highly porous and graphitic, and thus, are applicable not only as adsorbents but also as electrochemical biosensors, drug carriers and more. Classification of applications of CVD-grown CNFs is shown in Fig. 21.2.

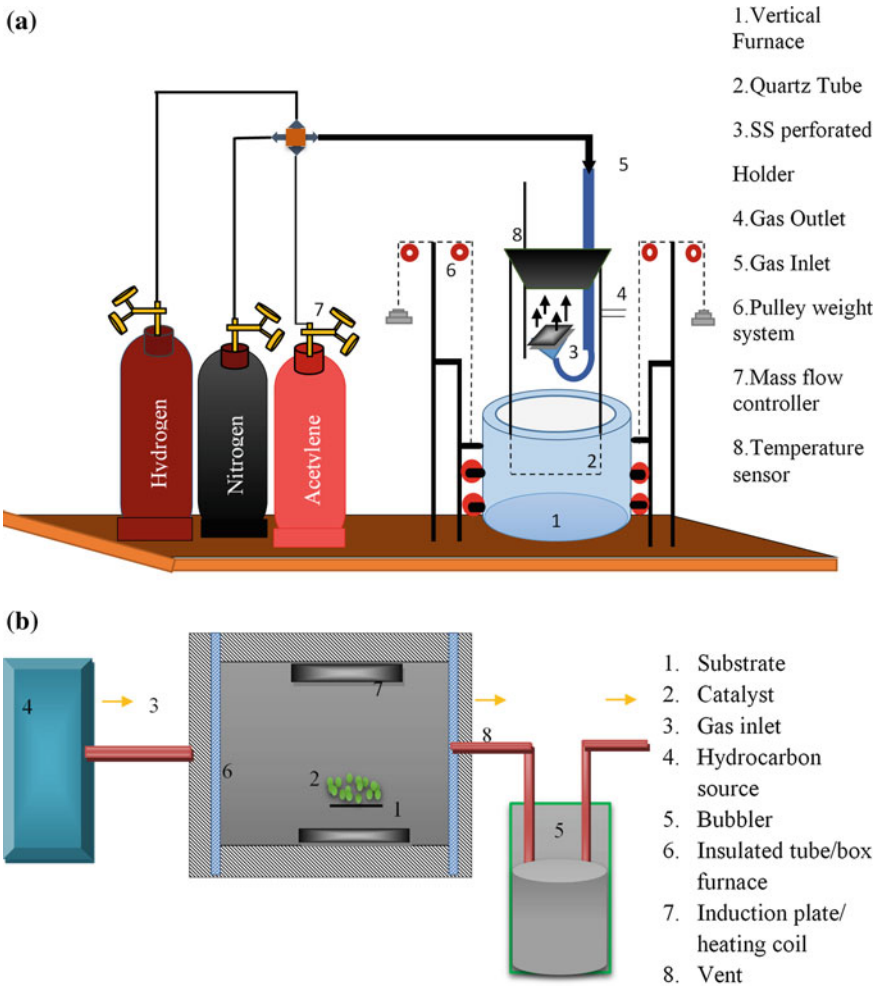

Fig. 21.1 **a** Vertical setup for CVD. **b** Horizontal setup for CVD

21.3 Environmental Applications of CVD-Grown CNFs

21.3.1 Adsorbents

21.3.1.1 Gaseous VOCs

The growing industrial and chemical development loaded with everyday enhancements in various technologies, industrial tools, and their versatile applications not only facilitate the globe but also handovers some dangerous residues. Some of the chemicals and other industrial and chemical residues degrades with time but some

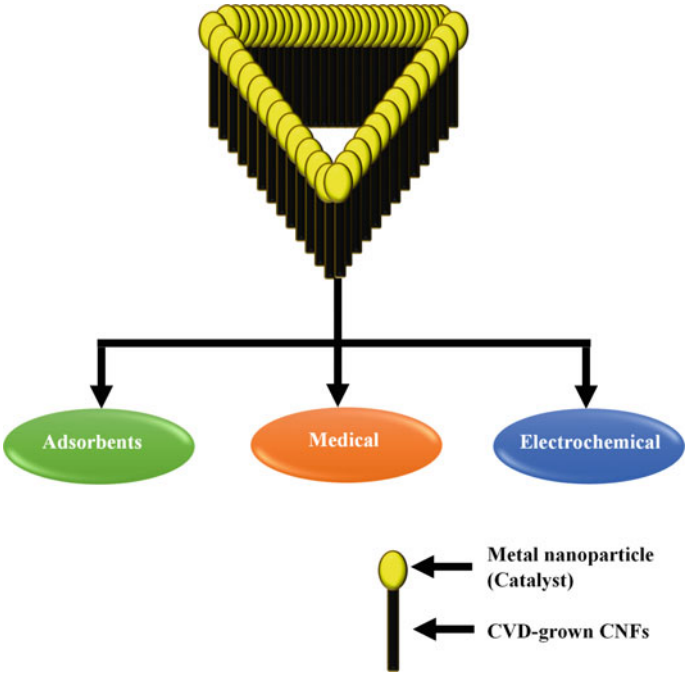

Fig. 21.2 Applications of CVD-grown CNFs

persist in nature for a longer time duration, and there is a need for removal of these toxicants or pollutants from the atmosphere. The CVD-grown CNFs have been used as pollutant adsorbents in many studies (Bikshapathi et al. 2012a, b). Various volatile organic compounds such as CCl_4, benzene, perchloroethylene, etc. were found in residual amounts in the atmosphere, which in some reports were proven carcinogens.

Fe-CNFs prepared via CVD using ACFs were used for the removal of gaseous VOCs. In this study, metal dispersion was studied onto the ACFs using various surfactants for different metals and the results with SDS for Fe dispersion was best. The main focus was on one of the VOCs, CCl_4. Carbon tetrachloride was historically used as solvents for drying and cleaning purposes, as a refrigerant and in lava lamps. Its use as an anesthetic was widely recognized, but due to its property of causing liver toxicity, its uses were banned. Thus, its removal from the atmosphere was of core importance. The CVD-grown CNF_{SDS} were successfully used as an adsorbent for gaseous CCl_4. But, the gaseous VOCs needs a microporous surface for adsorption which indeed was knocked out in case of CNFs, as it had mesoporous surface. Results have shown that Fe-ACFs was more successful for the adsorption purpose because of its microporous surface (Bikshapathi et al. 2012b).

21.3.1.2 Phenol and Lead

Industries dump their wastes into water bodies directly, or they run off into the water system via landfills. These wastes contain and are rising as a major source of toxic compounds and heavy metals into the ecosystem. In recent years, research was done for the removal of phenol and lead from water bodies, as they are also one of the toxic pollutants. Dye industries, insecticides, pesticides, pharmaceutical industries, etc., are the major source which serves phenol as a toxic contaminant. Lead comes into the water sources via discharge from battery manufacturing industries, paints and many more.

Recent work has been done, for the removal of phenols and lead from the water bodies, by using CVD-grown CNFs. ACFs and ACFs/CNFs manufactured using ACFs via catalytic CVD process, were used as the adsorbent. Their surface characterization, pore size distribution (PSD) was done using analytical techniques that were, BET, PSD analysis, SEM, EDX. A study was done on ACF, NH_3 treated ACFs and ACFs/CNFs, for the adsorption of phenol from the contaminated water, ACF/CNF shown adsorption, but out of the three, NH_3 treated ACFs were found to show maximum capacity, 275 mg/g. The adsorption capacity shown by ACF/CNF was 150 mg/g. In contrast, to the phenol adsorption shown by ACFs/CNFs for Pb^{+2} was much higher than those done by ACFs. Further, when sonicated ACFs/CNFs shown four times greater adsorption capacity than ACFs. Thus, CVD-grown CNFs were successfully used as an adsorbent for phenol and Pb^{+2} (Chakraborty et al. 2011).

21.3.1.3 Arsenic

Arsenic in its inorganic form is proven to be one of the most toxic elements when studies were made on various compounds and heavy metals from wastewater and other water sources. Again the industrial effluents were into main role play for the release of As in the soil and water. The concentration of As was measured to be (~50–100 mg/L), which is alarming for human health (Ma et al. 2018). Toxicity can cause cancer and is also responsible for skin lesions and other major health issues. The Asian and American countries report 50 mg/L concentration of As, which drives out the need for removal of As from the wastewater (Gupta et al. 2010).

Recently, research was done using CNFs to check the adsorption of As(V) in wastewater, and the results were positive. A Fe-impregnated CNFs was made using phenolic resin microfibers, and Fe was used as a catalyst in the CVD process. The impregnation of Fe played two roles, one of catalyst and, second of the adsorbent for As(V). The material characterization was made using various analytical techniques such as XRD, EDX, SEM. BET area and PSD analysis were made to check the surface area and pore size distribution respectively, and this indicated the presence of micropores. The BET area for Fe-CNFs was measured to be ~800 m^2/g. The results have shown that the As(V) loading onto Fe-CNFs was 0.6–14 mg/g at a pH of 6.5. Hence, the results were satisfactory and can be commercialized (Gupta et al. 2010).

21.3.1.4 NO_x

Nitrogen oxides are one of the major air pollutants and are responsible for many respiratory-related health problems. They are released in the atmosphere from not only various industries but are also, expelled from many natural processes. Carbon nanocomposites were proven to be a successful adsorbent in many researches because of its porous nature.

In recent research, CNFs were made using ACFs via CVD process. The CNFs were developed in a way that, CeO_2 and Cu metal NPs were successfully dispersed in a uniform manner, so as to not only allow a catalytic growth of CNFs on ACFs but to also catalytically oxidize NO to NO_2.

Previously, many methods were used for the oxidation of NO, of which most commonly used was Selective Catalytic Reduction, in which the high-temperature range of 150°–600 °C was a matter of concern. Reducing agents like NH_3 and urea were used, but as discussed the high-temperature range was creating difficulties regarding ammonia handling and urea degradation. Thus, as a better alternative, many carbon sources were tested for adsorption of NO, out of which CNFs/ACFs dispersed with CeO_2, and Cu NPs was studied to be the best one. The prepared material was characterized using many analytical techniques which include, SEM, EDX, PSD, BET, etc. the results have shown ~80% conversion of NO at room temperature (Talukdar et al. 2014).

21.3.1.5 POPs

Chemicals like Aldrin, toxaphene, mirex, hexachlorobenzene, etc., possess the property of retention. These chemicals persist in the atmosphere for a very long period of time, as they do not degrade with any of chemical, biological, or photolytic process. Thus, they are known as Persistent Organic Pollutants. Their persisting nature allows bioaccumulation, which is alarming for human health and causes various lethal health problems (Alharbi et al. 2018). Sources which serve POPs were found to be natural, such as volcanoes and, manmade, such as, pesticides, PCBs. PPCPs etc., but the major one was manmade. Many methods including biodegradation via enzymes, bioaugmentation have been employed for the removal or degradation of POPs (Gaur et al. 2018).

Recently, CVD-grown CNFs were also employed for successful removal of some gaseous POPs. The CNFs were grown using Ni-impregnated ACFs as the substrate, cetyltrimethylammonium bromide (CTAB) as a surfactant. The CTAB surfactant in the CVD processes was used for denser and smaller distribution of Ni, so as to grow CNFs. The material was characterized using SEM, XRD, BET area, PSD analysis. The BET area for the prepared ACF/CNF was measured to be 232 m^2/g, which shown proper and narrower microporosity. Adsorption of 2-chloroethanol was studied on ACFs, ACF/CNF_0, and ACF/CNF_5. The data have shown that ACF/CNF_5 with surfactant CTAB was superior for the adsorption of 2-chloroethanol. The breakthrough time for the three samples was, 42 min, 62 min, and highest for ACF/CNF_5, 110 min.

Thus, it was concluded that the adsorption capacity was 1.5 times greater for CNFs grown on ACFs using CTAB than those grown without CTAB, and was 0.758 g/g (Bikshapathi et al. 2012b).

21.3.1.6 Sulfur Compounds

Sulfur and its compounds have many applications in every biological or chemical field. They mark their importance from the fertilizer field to pharmaceuticals, from bactericide to furniture. But as known, every positivity holds some negative aspects too. The lone pair present on S makes it demanding, and sometimes its removal becomes necessary because of the π-interactions. Diesel fuel is a power source for various transportation vehicles, furnaces, generators, etc. The fuel inherently contains some Sulphur compounds such as, benzothiophene (BT), dibenzothiophene (DBT), thiophenes (TH), etc., which emits hazardous air pollutant such as H_2S and SO_2 on combustion. Also, the present compounds can cause catalyst poisoning. To check these problems, Hydro sulfurization (HDS) is widely used for the removal of sulfur and its compounds. But aromatic hydrocarbon is more reactive towards the hydrogenation reaction as compared to those aromatic sulfur compounds, and due this HDS becomes ineffective (Chen et al. 2015; Li et al. 2015). Adsorptive desulphurization of diesel fuel had become more popular in comparison to the HDS method.

CVD-grown CNFs were also tested for the ADS process for adsorption of sulfur compounds such as thiophene and dibenzothiophene. CNFs were grown on Ni-doped activated carbon beads (ACB) using CVD process at 600 °C (Saraswat et al. 2012). The study investigated the adsorption of DBT and TH, using two samples; one with CNFs and second without CNFs. The synthesized Ni/ACBs and Ni-CNFs/ACBs were subjected to various analytical techniques such as SEM, TEM, XRD, EDX, BET, and PSD analysis. DBT molecules are larger in size and were successfully adsorbed on Ni/ACBs than on Ni-CNFs/ACFs. But, on the other hand, Ni-CNFs/ACBs shown higher adsorption for smaller TH molecules. The paper focused on the use of various adsorbents for different sulfur compounds from diesel, and a comparative study was done (Prajapati and Verma 2017). The mechanism of use of CVD-grown CNFs as the adsorbent is presented in Fig. 21.3.

21.3.1.7 Protein Immobilization

Proteins are the biologically active compounds which are essential for proper growth and working of the ecosystem. Proteins have been discovered as one of the major catalysts known as enzymes. These biocatalyst holds the ability to carry out complex chemical reactions and is highly selective. Their remarkable advantages are somewhere demarked because of their high cost of production and separation; also the high reactivity causes unwanted results. To overcome the existing problems, the immobilization of protein was countered as an effective method. Protein immobilization

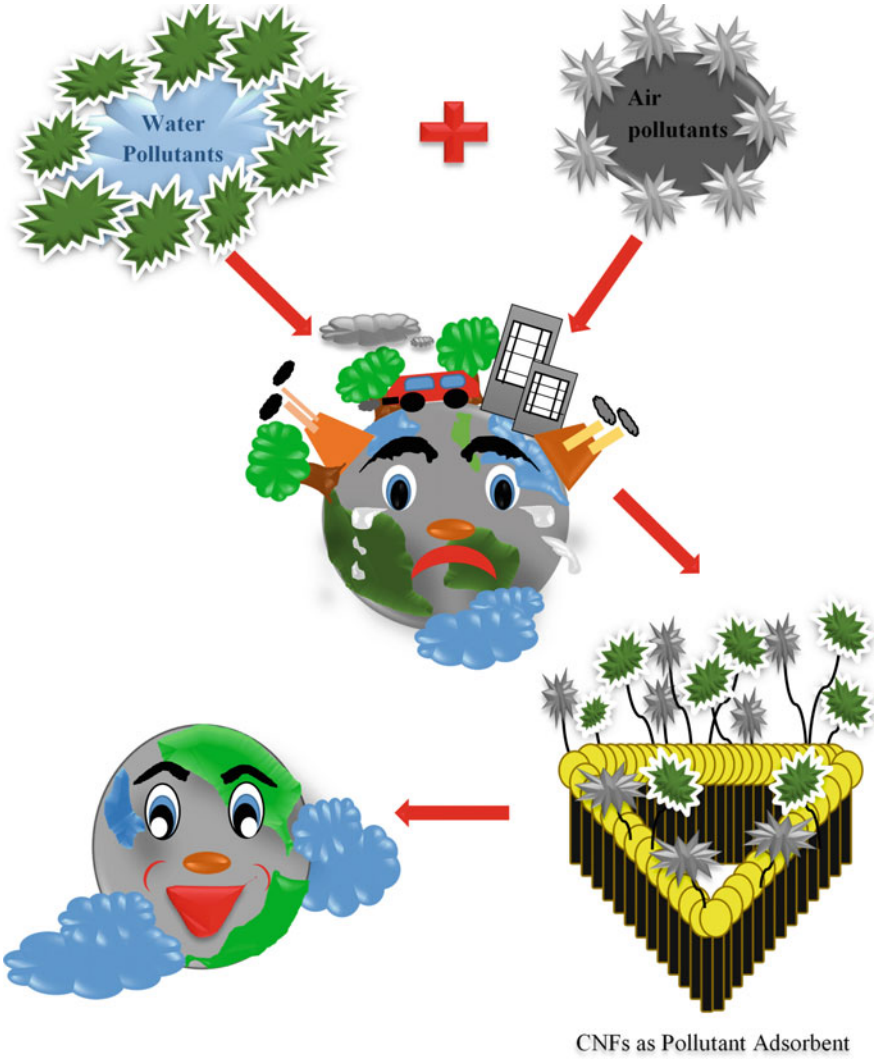

Fig. 21.3 Pictorial representation of the CVD-grown CNFs as pollutant adsorbents

thus helps in not only enzyme stability but also open ups more applications. Cross-linking, entrapment and adsorption are the current strategies used for protein immobilization, out of which adsorption draws out as the most effective one, because it is simple, cost-efficient and cause no alteration to the structure of the substrate (Teles and Fonseca 2008). Previously, many materials like silica, glass, methyl acrylate, alumina, and activated carbon were used as a substrate for protein immobilization (He et al. 2009; Cabrita et al. 2005). In a recent study, proteins like bovine serum albumin (BSA), glucose oxidase (GOx) and YqeH prepared in the laboratory were tested for

immobilization. Firstly, ACFs were prepared from phenolic resins and using these prepared ACFs as substrate and Ni-NPs as catalyst CNFs were grown by the CVD process. The prepared material was characterized using analytical techniques such as SEM, FT-IR, BET, PSD analysis. Tests have shown that the adsorption was exothermic, which caused a decrease in adsorption capacity with an increase in temperature. Highest temperature taken for the study was 15 °C because the subjected proteins denatured within 5–6 h at 25 °C. The prepared CNF composite was found to have a BET area of ~450 m^2/g upon sonication. The experimental shown that the adsorption capacity of ACFs/CNFs for the proteins BSA, GOx, and laboratory refined YqeH were as follows 191, 39 and 70 mg/g (Singh et al. 2014).

21.3.2 CVD-Grown CNFs for Wet Air Oxidation

Wet Air Oxidation (WAO) is a hydrothermal treatment method, which can be preferred over various biological treatment approaches for wastewater treatment. The WAO technique can be used positively for treatment of wastewater bodies, in which the content of toxic effluents like phenol is present (Bhargava et al. 2006; Mishra et al. 1995). But due to the requirement of high pressure and temperatures, the conventional method becomes quite expensive. The use of heterogeneous and homogenous catalysts can ease and improve the technique (Levec and Pintar 2007; Kim and Ihm 2011; Stüber et al. 2005). The heterogeneous class of catalyst is more useful over the homogeneous one because, the heterogeneous is more effective and shows resistance towards leaching of the active component (Stüber et al. 2005).

Many catalysts have been studied for the treatment of organic wastes, wastewater, and other industrial pollutants (Chaliha and Bhattacharyya 2008; Yadav and Garg 2014; Hočevar et al. 2000; Ovejero et al. 2013). Cu as a heterogeneous metal catalyst was found to have higher activity (Yadav and Garg 2014; Kim et al. 2005). Carbon nanomaterials have discovered as one of the finest materials, which can be utilized as the catalytic supporter for CWAO. CNFs, CNTs, and graphenes, because of their electrical and chemical properties can be effectively used as catalyst or catalyst support. Among all, CNFs were found to have higher activity (Ayusheev et al. 2014).

In work recently done, CNFs were employed for CWAO for the treatment of synthetic phenols. Carbon beads were taken as a substrate, and Cu-NPs were doped, and CNFs were covered on the beads. The prepared composite was then efficiently used as the catalyst for CWAO, for the treatment of synthetic phenolic water in a packed bed reactor. The pressure and temperature ranges for the reactor were 10–30 bar and 180–230 °C respectively. The prepared material was tested against organic pollutants in wastewater whose chemical oxygen demand was very high (~120,000 mg/L). The Cu-PhB-CNF-K catalyst shown efficient removal with ~99% COD reduction at moderate pressure and temperature. Also, there was no Cu leaching with consistent results. The CNFs were grown on carbon beads via CVD. Thus, this catalyst can be positively used for the remediation of industrial wastes by CWAO (Yadav and Verma 2018).

Pesticide residues are also of some major concern, as their unwanted presence can lead to many hazardous circumstances. Aqueous dichlorvos (DDVP) is a pesticide which is an emerging organic pollutant which comes into the environment from ample agricultural uses. CWAO was done for degrading the DDVP, by using CVD-grown CNFs as the catalyst. Carbon beads were doped with Cu-NPs and dispersed over CNFs. The porosity of CNFs and high metallic activity of Cu simultaneously provided effective oxidation of the aqueous organics. The tests made, showed that there was 100% degradation within ~3 h when the catalyst dose was 0.5 g/L for 150 DDVP concentration at 200 °C and 25 bar. Also, some reaction intermediates were produced, including dimethyl phosphate, dichlorovinyl alcohol. After performing biological tests, it was found that water after treatment was less toxic. The Cu-CNFs-beads proved to be a promising technique for remediation of wastewater (Kumar and Verma 2018).

Removal of phenol has been a major concern for the environmentalists, with wastewater treatment. CWAO provides a better way for phenol treatment by the destruction of organic pollutants. The catalyst was prepared using Fe-NPs doped in phenolic polymeric beads and then CNFs were grown via CVD over the phenolic beads. The prepared catalyst for CWAO successfully achieved complete removal of phenol at 160 °C temperature, 3.5 h-reaction time, 10 bar-O_2 pressure and 200 rpm impeller speed, from the contaminated water. The Fe-CNF/CB catalyst was found to have higher catalytic efficiency than those discussed in the literature (Yadav et al. 2016).

21.4 Medical Applications of CVD-Grown CNFs

Carbon and its nanocomposites have been widely used in many fields including environmental, biosensors, electrochemical sensors and more. Also, its porous and graphitic nature makes it fit for some medical applications. Growing research proved carbon materials as one of the best substrate material for various applications (Gupta et al. 2010; Bikshapathi et al. 2012b; Chakraborty et al. 2011; Mohamed 2019; An et al. 2018). Among all the carbon nanocomposites, CNTs, CDs, graphene, CNFs, CNFs were found to be more prominent to show biological action. In a recent research paper, cytotoxic evaluation of the CVD-grown CNFs was also done (Ashfaq et al. 2013). ACF/CNF composite was tested against human lymphocytes, and the data were compared with other carbonaceous and non-carbonaceous materials. ACF/CNFs were found to have comparable or lesser cytotoxicity than the materials it was compared with. Thus, CVD-grown CNFs can be used harmlessly for various environmental and biological purposes (Ashfaq et al. 2013).

21.4.1 Ag and Cu Dispersed CNFs with Antibacterial Activity

Escherichia coli abbreviated as *E. coli* is a commonly known gram-negative bacteria which may cause some diseases such as, urinary tract infections, gastroenteritis, neonatal meningitis. Staphylococcus aureus is a gram-positive bacteria known to cause staph infections. The antibacterial properties of silver and copper are acknowledged. The Cu and Ag nanoparticles have shown their antibacterial activity, by binding and denaturing the bacteria, inhibiting its replication and thus limiting its growth (Jung et al. 2008).

In one of the recent research, Cu and Ag nanoparticles were synthesized using nitrate salts and hydrazine hydrate and sodium citrate as strong reducing agents. These NPs has shown antibacterial activity (Das et al. 2011; Datta et al. 2008). This method was useful but was not much advantageous because NPs were not uniformly dispersed on the substrate, and thus, its potency was restricted (Sondi and Salopek-Sondi 2004). A novel carbon material Cu/Ag CNF was synthesized to overcome the drawbacks. The material was used against *E. coli* and *Staphylococcus aureus* in water. CNFs were grown on ACFs using Cu and Ag as catalyst and acetylene as a carbon source by the CVD method. Cu and Ag not only acted as a catalyst for CNF growth but also served as an antibacterial agent. SDS surfactant was also used to prevent the agglomeration of Cu(II) and Ag(I) ions during the preparation of Cu/Ag-CNF composites. The prepared material was analyzed using techniques, AAS, XRD, thermal programming reduction, FT-IR, SEM. Ag-ACF/CNF was found to be destructive against both *E. coli* and *S. aures* in water and completely inhibited the bacterial growth for 72 h. The same effect was shown by Cu-ACF/CNF but for 36 h (Singh et al. 2013a).

21.4.2 Bimetal Ag-Cu Dispersed CNFs with Antibacterial Activity

Aforementioned, the material was a single metal doped composite. In another research, followed by the above results a new bimetal nanoparticle dispersed multiscale web of CNFs was developed using acetylene as carbon source on ACF substrate and Cu NPs as catalysts. CNF growth was catalyzed by Cu NPs, and they were attached to the CNF's tips, and Ag NPs were attached to the ACF surface. The prepared bimetal CNFs were characterized using AAS, EDX, XRD, SEM, TPR, FTIR. Following points were observed; (1) the bimetal Ag:Cu-ACF/CNF composite was having high activity than the ACF substrate having no nanofibers, (2) Ag-ACF/CNF was prominent in bacteria-killing, (3) Cu-ACF/CNF was found to have less effect than the Ag-ACF/CNF and inhibited the bacterial growth for only one day (4), Ag:Cu-ACF/CNFs were found to inhibit the bacterial growth for 7 days on incubation completely (Ashfaq et al. 2016).

21.4.3 CVD-Grown CNFs for Drug Delivery

The delivery of the drug to the specific area of action is becoming one of the major concern these days, because of the side effects of the drugs on surrounding or other areas of the body. Antibiotics have helped to a greater extent in decreasing the mortality rate, caused due to various pathogens and bacteria. After reaching a critical stage of consumption, the pathogens become resistant to the action of the antibiotics. To overcome the issue of resistance, various new methods are under consideration (Chen et al. 2006).

Elements like Cu, Ag, Au, Rh, etc. have antibacterial and some medical properties, which allow their use in many biomedical fields. The comparable study done on Cu-ACFs/CNFs composite with other materials proves Cu-ACFs/CNFs less cytotoxic and hence, can be used for drug delivery (Ashfaq et al. 2013). In recent years, polymeric materials such as polylactic acid, chitosan, polylactide-*co*-glycolide (PLGA) and PVA have been widely used as an encapsulating agent, for drug delivery (Schmaljohann 2006; Zhang and Wu 2004).

The use of CNFs is also validated in the field of antibiotic drug delivery, in one of the recent studies. CNFs were prepared using ACFs and via CVD. A water-soluble and a pH-sensitive composite of PVA-cellulose acetate phthalate was prepared. The composite was dispersed in situ with the multi-scale web of copper (Cu)-grown carbon micro-nanofibers (Cu-ACF/CNFs) during one of the synthesis stages. The CNFs were prepared using ACFs as substrate material and Cu NPs as a catalyst via CVD at 650 °C for 30 min. The PVA-CAP composite was used as an encapsulating agent and Cu NPs were used as nano-antibiotics. The prepared polymeric material was characterized using various techniques like as, SEM, FTIR, AAS, TGA, EDX, and atomic force microscopy (AFM). It was concluded that the prepared material at a pH $\leq$ 6.5 was easily dispersible in water, and also it was clear with the results that the activity of the Cu-ACFs/CNFs-PVA-CAP composite increased with the increasing quantity of CAP. The polymeric composite was able to release Cu-ACFs/CNFs slowly, and hence making Cu NPs delivered for its antibiotic activity. The material has been found to exhibit effective antibacterial activity against *E. coli* (gram negative) and *S. aureus* (gram positive). Hence, CVD-grown CNFs are potent enough to be used in the biomedical field (Ashfaq et al. 2014). The use of CVD-grown CNFs is represented in Fig. 21.4.

21.5 Electrochemical Applications of CVD-Grown CNFs

Carbon nanomaterials are emerging out as one of the best tools for electrochemical applications. Carbon materials such as graphene, CNTs, CDs, ACFs, etc., because of their property of easy charge transfer and storage, can be readily employed for various electrochemical applications. Out of all, in this review, the main focus is on CVD-grown CNFs as an impactful electrochemical tool. CVD-grown CNFs, because of

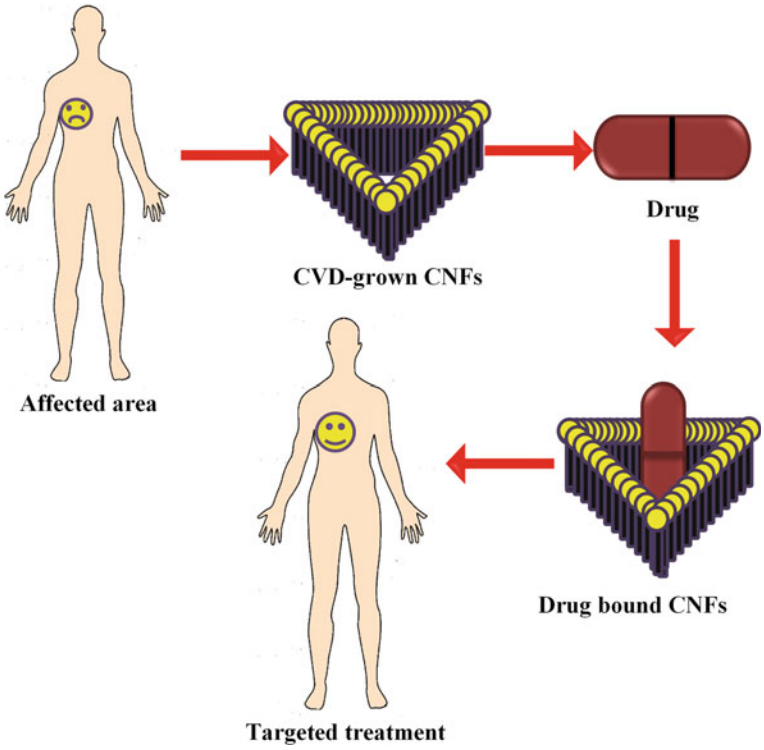

Fig. 21.4 Pictorial representation for the application of CVD-grown CNFs as a drug delivery agent

their adjustable electron transfer and ease of charge storage have been employed, as supercapacitors, lithium-ion batteries, MFCs, sensors, electrocatalysts, etc. (Randviir and Banks 2013). In this book chapter, we will mainly focus on electrochemical sensors and MFCs.

21.5.1 Electrochemical Sensors

21.5.1.1 Sensor for Creatinine

Creatinine is a product of a non-enzymatic conversion of creatine to phosphocreatine in the human body and is produced at a constant rate (Randviir and Banks 2013). The standard physiological concentration of creatinine in human blood lies in the range 40–150 μM, and value lower than 40 μM indicates various renal dysfunctions (Bo et al. 2017).

Various advanced techniques have been studied for the detection of a creatinine biomarker, but because of the faster response and high reliability, electrochemical sensors are proven to be a more capable tool for the diagnosis. Many electrode-based sensors, mainly non-enzymatic, have also been studied, such as screen-printed carbon electrodes with electrodeposited Cu (Raveendran et al. 2017), glassy carbon electrode coated with dispersed Ag NPs on reduced graphene oxide (Viswanath et al. 2017). Even though these sensors have decent selectivity, repeatability, and stability but because of their contracted concentration range and low sensitivity, their effectiveness is dropped.

Literature has proved CNFs as a class of material for an electrochemical sensor which can overcome the hitches of other above-mentioned materials. The CNFs are found to have high mechanical strength, but also have chemical inertness in most of the adverse conditions (Khare et al. 2016; Modi et al. 2016; Gupta et al. 2017).

Methylene Blue (MB) has a property of electron facilitation, which makes it a prominent redox indicator. Electroactive poly MB (PMB) can be synthesized electrochemically by using cyclic voltammetry and owing to its structure, it can be used as a recognition material for various biological species (Silber et al. 1996; Sun et al. 2012).

Recently, in research work, an electrochemical sensor for creatinine have been successfully synthesized, using PMB as recognition element. In this work, dendritic PMB nanofibers were grown on ACF substrate. Firstly, Cu-CNFs/ACF was synthesized via CVD using Cu NPs decorated ACF as a substrate, in which Cu NPs acted as a catalyst, at 290 °C (Ashfaq et al. 2014). After the preparation of Cu-CNFs/ACFs, dendritic PMB was grown on the surface of nanofibers successfully using the cyclic voltammetry technique. The material characterization and electrochemical measurements were done using FTIR, FE-SEM, and DPV, chronoamperometry, and CV respectively.

This electrochemical sensor for CRE was found to detect CRE over a wide range of 0.5–900 ng mL^{-1} and was highly sensitive, with a sensitivity of 0.133 μA ng mL^{-1}. The prepared dendritic PMB-PVAc-Cu-CNF/ACF sensor also had remarkable selectivity. In this study, it was also revealed that saliva could be used as a noble fluid, in contrast to blood or CSF biological fluids for clinically non-invasive analysis. Thus, this novel electrode based sensor can be further used for examination of CRE concentration in various biological fluids with great ease and effectiveness (Pandey et al. 2018).

21.5.1.2 Cholesterol Sensor

Cholesterol is a sterol, produced by all animal cells, and is responsible for building and maintaining cell membranes. The human body is capable of producing cholesterol, needed by the cells for making substances like hormones, vitamin A and other digestives. Cholesterol is of two types LDL (low-density lipoprotein), and HDL (high-density lipoprotein), HDL, on the one hand, is considered as good cholesterol because of its property of carrying cholesterol back to the liver from other body parts,

LDL, on the other hand, is bad, because it builds up cholesterol in arteries. LDL is one, responsible for blockage of arteries which may lead to various chronic heart diseases such as stroke, nephrosis heart attack (Potter 2007).

Also, the deficit of cholesterol may also cause various infirmities such as malabsorption, hyperthyroidism, and anemia. Many enzyme-based sensors have been studied for cholesterol sensing, but due to factors like temperature, pH and other elements, their repetitive ability is lost (Park et al. 2006).

The basic need to design an electrochemical biosensor is an electrode and a recognition component. Literature has reported many electrode materials out of which, glassy carbon electrode fabricated with the recognition component is most common. Then comes CNTs, but due to some difficulties like nondispersive nature of CNTs in liquid media, lower sensitivity and narrow concentration range for GCE, they are disadvantageous (Li et al. 2010; Yang et al. 2012).

In recent research, bimetal CNFs based working electrode was designed for electrochemical sensing of cholesterol in human plasma. The electrode was fabricated with Poly Methyl Orange (PMO), which acted as a recognition element for cholesterol. Methyl orange dye has hydrophobic and hydrophilic groups with the molecular cavity. The mentioned properties make it a prominent redox indicator.

The as prepared dendritic PMO nanofibers were successfully grown over the PVAc substrate, which was then dispersed in Cu/Ni bimetal NPS doped CNFs which were grown using CVD at 290 °C. The PMO-BMCP composite was found to be a successful biosensor for cholesterol. The prepared material was characterized and tested using different techniques, viz., FE-SEM, EDS, FT-IR for investigating surface morphologies, CV, DPV and EIS for checking electrochemical activity.

The PMO-BMCP composite was tested for 5 different samples containing a different concentration of cholesterol. The sensitivity of the sensor was high ($226.30\ \mu A mM^{-1}\ cm^{-2}$) and the detection limit was low ($0.002\ mg\ dL^{-1}$) over concentration range 0.04–600 mg dL^{-1}. The linearity was also remarkable ($R^2 = 0.999$). The obtained data were compared with other cholesterol sensors, which was either comparable or higher for the PMO-BMCP nanocomposite biosensor. In this study, PMO was used for the first time as a recognition component for cholesterol. Also, this non-enzymatic biosensor was found to be capable enough to overcome the shortcomings of the enzymatic sensors viz., enzyme denaturation and non-repeatability. Thus, the CVD-grown CNFs doped with bimetal NPs was successfully implemented for use as biosensors (Bairagi and Verma 2018).

21.5.1.3 Chemiresistive Fruit Sensors

Chemiresistive materials belong to a class of materials, that tends to show a change in the resistance in response to the chemical changes taking place in the environment (Chougule et al. 2019). Fruits of high quality are demanded worldwide, but due to various storage and aftercare issues make it difficult to avail it. Different scales are set to check the quality of the fruits, including its color, texture, odor, sugar contents and flavor (Caprioli and Quercia 2014). The growth of the fruits i.e. the seed germination,

its flowering and ripening is facilitated by the phytohormones, C_2H_4 molecules. The ripening genes in the fruits are expressed when the C_2H_4 molecules bind with ETR1 receptors. Therefore, the ripening of the fruit is detected by the C_2H_4 gas discharged.

Various non-destructive techniques are used to check the release of the C_2H_4 gas from the fruits, photoluminescence (Green et al. 2004), pre-concentrator device based on chips (Janssen et al. 2014), gas chromatography (Sklorz et al. 2013), electrochemical cells (Ma et al. 2016), and non-infrared spectroscopy (Sklorz et al. 2012). But the above-mentioned techniques are quite expensive and need skilled hands. To overcome the difficulties of skilled handling and complexity of the aforementioned techniques, many carbon nanomaterial-based sensors were designed (Mao et al. 2013, 2014a, b). In recent work, cellulose acetate phthalate (CAP)–mannitol copolymer based CNFs nanocomposite was designed as a chemiresistive fruit sensor. In this nanocomposite polyvinyl alcohol (PVA) film was used as a dispersing media. Cu NPs dispersed CNFs were mixed with the PVA-CAP-mannitol in situ. The nanocomposite was tested on the bananas. The amount of C_2H_4 liberated from the banana samples was measured against the electrical current.

Compounds containing (−COOH) group have a property of binding C_2H_4 molecule as C_2H_4O by using hydrogen bonding. Also, CAP has a (−COOH) group, so it also has the capability of binding the C_2H_4 molecule in the form of C_2H_4O. Mannitol does not have electrical activity, but the material used had CAP mixed with mannitol. The blended CAP-mannitol copolymer, because of the proton hopping mechanism is responsible for the conductivity of the nanocomposite (Bhat and Jois 2014). Also, the Cu NPs act as a cofactor for ETR1 receptors. This material had electron donating groups, which may be also responsible for its electrical conductivity. Thus, the PVA-CAP-mannitol blended with Cu NPs dispersed CNFs based fruit sensor, which is electrically conductive was a better alternative to other available methods.

The prepared material was characterized using different spectroscopic methods, X-ray photoelectron spectroscopy, Fourier-transform infrared spectroscopy, scanning electron microscopy and atomic force spectroscopy. DPV and amperometry electrochemical measurements were used to check their electrical resistance. Various measurements done on the synthesized material showed that the sensor was fast at the response (responded within 30 s). The detection limit was also low (~45 ppb). Thus, the Cu dispersed CNFs prepared via CVD, in situ dispersed with PVA-CAP-mannitol copolymer were successfully used as a non-destructive chemiresistive fruit sensor (Ashfaq et al. 2018).

21.5.2 MFCs

In the present scenario, a number of fossil fuels are burnt for the generation of electricity, which not only causes a decline in fossil fuels but also comes as a source of pollution via carbon dioxide emissions. Many efforts have been made to overcome these difficulties and meet the need. MFCs have been discovered to be one of the

cleanest sources of electricity production. MFCs not only produce electricity but due to its utilization, various biodegradable organic waste forms as a fuel source has given it light. The electron source in MFCs is the organic waste such as wastewater, either municipal or domestic, industrial effluents and other organic wastes. Thus, MFCs can be a road to waste to wealth (Mansoorian et al. 2013; Liu et al. 2008; Choi and Cui 2012).

The MFCs consist of two electrodes, anode, and cathode. The anode, on the one hand, is in the main function, as electrons from the bio-material are produced in the anode section only. And, cathode, on the other hand, can be restricted and is responsible for carrying out oxygen reduction reactions (Rosenbaum et al. 2007; Ghasemi et al. 2013). These electrodes in a typical MFC are made from various noble elements such as Au, Pt, Ag, etc. The electrodes thus, make it highly expensive. But, to generalize the energy production by using MFCs, the system must be inexpensive, highly conductive and easy to handle and operate. So, there is a need for an inexpensive and high electron transporter electrode system.

In literature, there are many alternatives studied, against the expensive and complexity of a typical MFCs. These include carbon nanotubes (CNTs), graphene, carbon dots (CDs), and CNFs (Pasupuleti et al. 2015; Tsai et al. 2009; Lu et al. 2011; Zhang et al. 2011). In this book chapter, our main focus is on CVD-grown CNFs, and CVD-grown CNFs have been widely used in the field of MFCs. Many researchers have worked on CNFs based electrodes for high energy production using MFCs.

Literature highlights the use of CVD-grown CNFs as electrodes in many research. Recently, in a research Ni NPs-dispersed CNFs were prepared from ACFs and were directly used as the electrodes for the MFCs. The Ni-CNFs\ACFs were prepared via a CVD method. *E. coli* was used as a microbial catalyst and a source of the electron.

The prepared material was characterized using numerous characterization techniques, SEM, AAS, EDX, XRD, BET, PSD, and Raman. The open circuit potential (OCP) (1145 ± 20 mW/m^2) and power density (710 ± 5 mV) was measured using Linear Sweep Voltammetry, these obtained values were found to be 9 times greater than the ACFs electrode based MFCs (Singh and Verma 2015).

In similar research, N-doped CNFs were prepared and utilized directly as the electrode for the MFCs. The material characterization was same as above. In this work, N-doping facilitated the delocalization of the electrons. The power density and OCP for the N-CNFs/ACFs based electrode was (1850 ± 20 mW/m^2) and (0.89 ± 0.005 V) respectively. The power density of this composite was twofold higher than Ni NPs-dispersed CNFs electrodes for MFCs (Modi et al. 2016).

Also, alumina (AA) and Ni dispersed web of carbon nanofibers were synthesized by the CVD process using ACFs as substrate. The AA/Ni NPs dispersed CNFs/ACFs nanocomposite based electrode was directly fabricated as an electrode for the MFCs.

The AA-NPs were responsible for the increased conductivity of the mediatorless MFCs. The power density, OCP and limiting current values for the prepared material based MFCs were 1780 mW/m^2, ~0.9 V and 8140 mA/m^2 respectively (Singh and Verma 2015a).

The above-discussed MFCs are double chambered MFCs, i.e. there are two different compartments used for the anode and the cathode (Gupta et al. 2017; Singh

and Verma 2015b). Single chambered MFCs have also been studied. In this type of MFCs, there is no separate compartment for the cathode, but cathode is directly attached to the anode compartment (Sawasdee and Pisutpaisal 2015; Vilas Boas et al. 2019).

In recent work, membrane-less single compartment MFCs were designed using AA/Ni-NPs dispersed CNFs as an electrode. In this research, *E. coli* was used as a microbial catalyst and monomer used, was polyvinyl alcohol (PVA). The cross-linking agent used was poly methyl vinyl ether alt maleic anhydride (PMVEMA), which actually facilitated the electron transfer. The power density was 1270 ± 30 mW/m^2, and the electrical potential was 980 ± 10 mV. This prepared material was successfully fabricated as an electrode for air cathode MFCs (Singh et al. 2016).

21.6 Conclusions and Future Perspectives

This book chapter emphasizes the versatile application of CVD-grown CNFs in many fields. The catalytic growth of CNFs using the chemical vapor deposition method, not only makes the material more useful with respect to porosity, electron transfer, mechanical and tensile strength, but also overcomes various drawbacks of electrospinning method. This article mainly focuses on three main fields of application of CVD-grown CNFs, environmental, medical and electrochemical. The CVD-grown CNFs have proven their capability as a class of material which can be (Dhand et al. 2013) need of various researches because of their easy production and high efficiency. The demand for CVD-grown CNFs is attributed to (i) the presence of various size pores on the surface, which not only allows the adsorption of various components but also speeds up the electron transfer, (ii) various modifications such as doping of the CNFs with other elements or materials, which can be easily performed. The electrochemical properties of the CVD-grown CNFs are more impressive than those compared with the electrospun CNFs. This advantage of CVD-grown CNFs has been utilized in various research works done, such as supercapacitors, lithium-ion batteries, MFCs, sensors, and many more (Fu et al. 2019; Kshetri et al. 2018).

Moreover, many more implementations for the class of CVD-grown CNFs can be done. The permeable structure of the material can be employed more smartly in many other applications (Dhand et al. 2013; Choi and Lee 2013). The role of the CNFs in various medical applications, whether it is drug delivery or cell growth has been proven to be strong, and thus, modifications can invite more interest in this field (Bailón-García et al. 2019; Wesełucha-Birczyńska et al. 2018). The CVD-grown CNFs can be used as the smallest electrode for various electrochemical applications (Fu et al. 2019). The designing and fabrication of CNFs using CVD process for many more new level research in favor of humankind will be one of the main perspectives (Table 21.1).

Table 21.1 List of different applications of CVD-grown CNFs

S. No.	Substrate	Metal catalyst	Carbon source	CVD temperature	Time	Application	References
1	ACF	Ni-NPs	Liq-Benzene	–	–	Electrode for MFCs	Singh and Verma (2015a)
2	ACF	Cu-NPs	Acetylene	450 °C	1 h	Removal of NO	Bhaduri and Verma (2014a)
3	ACF	Cu-Ag-NPs	Acetylene	300 °C	30 min	Antibacterial applications	Singh et al. (2013a)
4	ACF	Ni-NPs	Benzene	800 °C	2 h	Protein immobilization	Singh et al. (2014)
5	ACF	Fe-NPs	Liq.Benzene	800 °C	–	VOC removal	Bikshapathi et al. (2012a)
6	ACF	Cu-NPs	Acetylene	650 °C	30 min	Antibiotic drug delivery	Ashfaq et al. (2014)
7	ACF	Cu/Ag-NPs	Acetylene	290 °C	20 min	Cytotoxicity of the ACF/CNFs is comparable to or less than that of the commercial adsorbents	Ashfaq et al. (2013)
8	ACF	Fe-NPs	Benzene	750 °C		Removal of Arsenic(V) in Wastewater	Gupta et al. (2010)
9	ACB	Ni-Fe-NPs	Benzene	900 °C or 800 °C	–	Environmental remediation	Khare et al. (2013)
10	Cu-doped carbon beads	Cu-NPs	Acetylene	320 °C	30 min	Cu-CNF beads used as the catalyst for the NO reduction without requiring ammonia or urea	Bhaduri and Verma (2015a)
11	ACF	Ni-NPs	Benzene	800 °C	1 h	Removal of persistent gaseous organic pollutants	Bikshapathi et al. (2012b)
12	ACF	Ni-NPs	Benzene	750 °C	1 h	Removal of phenol and lead from water	Chakraborty et al. (2011)

(continued)

Table 21.1 (continued)

S. No.	Substrate	Metal catalyst	Carbon source	CVD temperature	Time	Application	References
13	ACF	Cu-NPs	Acetylene	450 °C	30 min	Oxidation of NO	Talukdar et al. (2014)
14	Activated carbon beads	Ni-NPs	Acetylene	600 °C	30 min	Desulfurization of diesel	Prajapati and Verma (2017)
15	Cu-doped polymeric carbon beads	Cu-NPs	Acetylene	350 °C	15 min	Wet air oxidation of phenol	Yadav and Verma (2018)
16	H_2-reduced carbon beads	Cu-NPs	Acetylene	350 °C	30 min	Wet air oxidation of dichlorvos pesticide	Kumar and Verma (2018)
17	Fe-carbon beads	Fe-NPs	Acetylene	600 °C	30 min	Wet air oxidation of phenol	Yadav et al. (2016)
18	ACF	Cu-Zn-NPs	Acetylene	290 °C	20 min	Wound healing and controlled release of drugs	Ashfaq et al. (2016)
19	ACF	Cu-Zn-NPs	Acetylene	290 °C	20 min	Antibiotic material	Ashfaq et al. (2016)
20	Ni-PMC	Ni-NPs	–	800 °C	2.5 h	Electrode of MFCs	Khare et al. (2016)
21	ACF	Ni-NPs	Acetonitrile	30 ± 5 °C	–	Electrode of MFCs	Modi et al. (2016)
22	ACF	Ni-NPs	Liq.benzene	–	–	As the electrode for Cr(IV) reduction and for bioelectricity generation	Gupta et al. (2017)
23	ACF	Cu-NPs	Acetylene	290 °C	2 h	Electrochemical sensor for creatinine	Pandey et al. (2018)
24	ACF	Cu-Ni NPs	Acetylene	290 °C	30 min	Cholesterol sensors	Bairagi and Verma (2018)

(continued)

Table 21.1 (continued)

S. No.	Substrate	Metal catalyst	Carbon source	CVD temperature	Time	Application	References
25	ACF	Cu-NPs	Acetylene	650 °C	30 min	Biomaterial used in several biomedical applications including wound healing and controlled release of drugs	Ashfaq et al. (2014, 2016)
26	ACF	Cu-NPs	Acetylene	290 °C	30 min	CNFs as Fruit sensor	Ashfaq et al. (2018)
27	ACF	Ni-NPs	Benzene	800 °C	2 h	Electrode for MFCs	Singh and Verma (2015b)
28	ACF	Ni-NPs	Liq. Benzene	650 °C	2 h	Electrode for single chambered MFCs	Singh et al. (2016)
29	ACF	Cu-Zn-NPs	Acetylene	290 °C	20 min	Wound healing and controlled release of drugs	Ashfaq et al. (2017)
30	ACF	$CuCl_2$ NPs				Oxygen production	Bhaduri et al. (2012)
31	ACF	Ni-NPs				Removal of 2-chloroethanol	Bikshapathi et al. (2011)
32	ACF	Ni-NPs	Benzene	800 °C	2 h	Ni-NPs-doped for hydrogen storage	Yadav et al. (2017)
33	ACF	Ni-NPs	Benzene	800 °C	2 h	Hydrogen storage	Yadav et al. (2017)
34	Cu-Zn/ACF	Cu-Zn-NPs	Acetylene	600 °C	1 h	Cu-Zn CNFs as nano fertilizer	Bhadauriya et al. (2018)
35	Activated carbon beads	Cu-Ni-NPs	Acetylene	800 °C	1 h	Desulfurization of thiophene	Prajapati and Verma (2018)
36	ACF	Ni-NPs	Acetylene	600 °C	2 h	Hydrogen storage	Yadav and Verma (2017)

(continued)

Table 21.1 (continued)

S. No.	Substrate	Metal catalyst	Carbon source	CVD temperature	Time	Application	References
37	ACF	Fe-NPs	Acetylene	600 °C	30 min	Removal of Pb(II)	Mishra and Verma (2017)
38	ACF	Ni-NPs	Acetonitrile	800 °C	2 h	As cathode in single chambered MFCs	Modi et al. (2017)
39	ACF	Cu-Zn-NPs	Acetylene	600 °C	1 h	Nanofertilizers	Ashfaq et al. (2017b)
40	Porous carbon beads	Cr-NPs	Acetylene	600 °C	45 min	Removal of hexavalent Cr	Mishra and Verma (2016)
41	Carbon beads	Cu-NPs	Acetylene	320 °C	30 min	NO abatement	Bhaduri and Verma (2015a)
42	ACF	Ag-NPs	Acetylene	300 °C	1 h	Control of bacterial growth	Khare et al. (2015)
43	ACF	Ni-NPs	Acetylene	550 °C	10 min	Removal of CO	Bhaduri and Verma (2015b)
44	ACF	–	–	800 °C	2 h	Toxic metal removal from water	Modi et al. (2015)
45	ACF	Cu-NPs	Acetylene	300 °C	1 h	Electrode for solar cells	Gupta et al. (2014)
46	Carbon beads	Fe-NPs	Liq.Benzene	900 °C	2 h	Removal of Cr(VI)	Talreja et al. (2014b)
47	ACF	Zn-NPs	Acetylene	700 °C	–	Hydrogen production	Bhaduri and Verma (2014b)
48	ACF	Cu-Fe-NPs	Liq-Benzene	800 °C	2 h	Enzyme immobilization in biosensors	(Hood et al. 2013)
49	ACF	Ag-NPs	Acetylene	300 °C	30 min	Antibacterial applications	Singh et al. (2013b)

Acknowledgements The authors express their gratitude to the Department of Science and Technology, New Delhi, India for providing research grant (DST/INSPIRE/04/2015/001869) to proceed this work and CSIR-Indian Institute of Toxicology Research, Lucknow and Council of Scientific, Madan Mohan Malaviya University of Technology Gorakhpur and Industrial Research—Advanced Materials and Processes Research Institute, Bhopal for providing research facilities. The CSIR-IITR communication number for this article is 3590.

References

Alharbi OML, Basheer AA, Khattab RA, Ali I (2018) Health and environmental effects of persistent organic pollutants. J Mol Liq 263:442–453

Al-Saleh MH, Sundararaj U (2009) A review of vapor grown carbon nanofiber/polymer conductive composites. Carbon 47:2–22

An G-H, Lee Y-G, Ahn H-J (2018) Ultrafast ionic diffusion of debossed carbon nanocomposites for lithium storage. J Alloy Compd 764:416–423

Anderson PE, Rodríguez NM (2000) Influence of the support on the structural characteristics of carbon nanofibers produced from the metal-catalyzed decomposition of ethylene. Chem Mater 12:823–830

Ashfaq M, Singh S, Sharma A, Verma N (2013) Cytotoxic evaluation of the hierarchical web of carbon micronanofibers. Ind Eng Chem Res 52:4672–4682

Ashfaq M, Khan S, Verma N (2014) Synthesis of PVA-CAP-based biomaterial in situ dispersed with Cu nanoparticles and carbon micro-nanofibers for antibiotic drug delivery applications. Biochem Eng J 90:79–89

Ashfaq M, Verma N, Khan S (2016) Copper/zinc bimetal nanoparticles-dispersed carbon nanofibers: a novel potential antibiotic material. Mater Sci Eng C 59:938–947

Ashfaq M, Verma N, Khan S (2017a) Highly effective Cu/Zn-carbon micro/nanofiber-polymer nanocomposite-based wound dressing biomaterial against the *P. aeruginosa* multi- and extensively drug-resistant strains. Mater Sci Eng C 77:630

Ashfaq M, Verma N, Khan S (2017b) Carbon nanofibers as a micronutrient carrier in plants: efficient translocation and controlled release of Cu nanoparticles. Environ Sci Nano 4:138–148

Ashfaq M, Verma N, Khan S (2018) Novel polymeric composite grafted with metal nanoparticle-dispersed CNFs as a chemiresistive non-destructive fruit sensor material. Mater Chem Phys 217:216–227

Ayusheev AB, Taran OP, Seryak IA, Podyacheva OY, Descorme C, Besson M, Kibis LS, Boronin AI, Romanenko AI, Ismagilov ZR, Parmon V (2014) Ruthenium nanoparticles supported on nitrogen-doped carbon nanofibers for the catalytic wet air oxidation of phenol. Appl Catal B 146:177–185

Bailón-García E, Maldonado-Hódar FJ, Carrasco-Marín F, Pérez-Cadenas AF, Bosi S, Prato M (2019) The use of functionalized carbon xerogels in cells growth. Mater Sci Eng C 100:598

Bairagi PK, Verma N (2018) Electrochemically deposited dendritic poly (methyl orange) nanofilm on metal-carbon-polymer nanocomposite: a novel non-enzymatic electrochemical biosensor for cholesterol. J Electroanal Chem 814:134–143

Barranco V, Lillo-Rodenas MA, Linares-Solano A, Oya A, Pico F, Ibañez J, Agullo-Rueda F, Amarilla JM, Rojo JM (2010) Amorphous carbon nanofibers and their activated carbon nanofibers as supercapacitor electrodes. J Phys Chem C 114:10302–10307

Bhadauriya P, Mamtani H, Ashfaq M, Raghav A, Teotia AK, Kumar A, Verma N (2018) Synthesis of yeast-immobilized and copper nanoparticle-dispersed carbon nanofiber-based diabetic wound dressing material: simultaneous control of glucose and bacterial infections. ACS Appl Bio Mater 1:246–258

Bhaduri B, Verma N (2014a) Preparation of asymmetrically distributed bimetal ceria (CeO_2) and copper (Cu) nanoparticles in nitrogen-doped activated carbon micro/nanofibers for the removal of nitric oxide (NO) by reduction. J Colloid Interface Sci 436:218–226

Bhaduri B, Verma N (2014b) A zinc nanoparticles-dispersed multi-scale web of carbon micro-nanofibers for hydrogen production step of ZnO/Zn water splitting thermochemical cycle. Chem Eng Res Des 92:1079–1090

Bhaduri B, Verma N (2015a) Carbon bead-supported nitrogen-enriched and Cu-doped carbon nanofibers for the abatement of NO emissions by reduction. J Colloid Interface Sci 457:62–71

Bhaduri B, Verma N (2015b) Removal of CO by water–gas shift reaction over bimetal CeO_2 and Ni nanoparticles dispersed in carbon micro-nanofibers. Catal Lett 145:1262

Bhaduri B, Prajapati YN, Sharma A, Verma N (2012) $CuCl_2$ nanoparticles dispersed in activated carbon fibers for the oxygen production step of the Cu–Cl thermochemical water splitting cycle. Ind Eng Chem Res 51:15633–15641

Bhargava SK, Tardio J, Prasad J, Föger K, Akolekar DB, Grocott SC (2006) Wet oxidation and catalytic wet oxidation. Ind Eng Chem Res 45:1221–1258

Bhat DK, Jois HSS (2014) Miscibility and conductivity studies of poly(methyl methacrylate) and cellulose acetate phthalate blends. Procedia Mater Sci 5:995–1004

Bigdeli S, Fatemi S (2015) Fast carbon nanofiber growth on the surface of activated carbon by microwave irradiation: a modified nano-adsorbent for deep desulfurization of liquid fuels. Chem Eng J 269:306–315

Bikshapathi M, Mandal S, Mathur GN, Sharma A, Verma N (2011) Modification of activated carbon fiber by metal dispersion and surface functionalization for the removal of 2-chloroethanol. Ind Eng Chem Res 50:13092–13104

Bikshapathi M, Singh S, Bhaduri B, Mathur GN, Sharma A, Verma N (2012a) Fe-nanoparticles dispersed carbon micro and nanofibers: surfactant-mediated preparation and application to the removal of gaseous VOCs. Colloids Surf A Phys Chem Eng Asp 399:46–55

Bikshapathi M, Mathur GN, Sharma A, Verma N (2012b) Surfactant-enhanced multiscale carbon webs including nanofibers and Ni-nanoparticles for the removal of gaseous persistent organic pollutants. Ind Eng Chem Res 51:2104–2112

Bo X, Zhou M, Guo L (2017) Electrochemical sensors and biosensors based on less aggregated graphene. Biosens Bioelectron 89:167–186

Cabrita JF, Abrantes LM, Viana AS (2005) N-hydroxysuccinimide-terminated self-assembled monolayers on gold for biomolecules immobilisation. Electrochim Acta 50:2117–2124

Caprioli F, Quercia L (2014) Ethylene detection methods in post-harvest technology: a review. Sens Actuators B Chem 203:187–196

Chakraborty A, Deva D, Sharma A, Verma N (2011) Adsorbents based on carbon microfibers and carbon nanofibers for the removal of phenol and lead from water. J Colloid Interface Sci 359:228–239

Chaliha S, Bhattacharyya KG (2008) Catalytic wet oxidation of 2-chlorophenol, 2,4-dichlorophenol and 2,4,6-trichlorophenol in water with Mn(II)-MCM41. Chem Eng J 139:575–588

Chen X-G, Liu C-S, Liu C-G, Meng X-H, Lee CM, Park H-J (2006) Preparation and biocompatibility of chitosan microcarriers as biomaterial. Biochem Eng J 27:269–274

Chen X, Guo H, Abdeltawab AA, Guan Y, Al-Deyab SS, Yu G, Yu L (2015) Brønsted-Lewis acidic ionic liquids and application in oxidative desulfurization of diesel fuel. Energy Fuels 29:2998–3003

Choi C, Cui Y (2012) Recovery of silver from wastewater coupled with power generation using a microbial fuel cell. Bioresour Technol 107:522–525

Choi I, Lee DG (2013) Surface modification of carbon fiber/epoxy composites with randomly oriented aramid fiber felt for adhesion strength enhancement. Compos A Appl Sci Manuf 48:1–8

Chougule MA, Navale ST, Navale YH, Ramgir NS, Stadler FJ, Khuspe GD, Patil VB (2019) Processing temperature dependent chemiresistive performance of spin-coated cerium oxide films. Mater Chem Phys 224:85–92

Das R, Gang S, Nath SS (2011) Preparation and antibacterial activity of silver nanoparticles. J Biomater Nanobiotechnol 02(04):4

Dasgupta K, Joshi JB, Banerjee S (2011) Fluidized bed synthesis of carbon nanotubes—a review. Chem Eng J 171:841–869

Datta KKR, Srinivasan B, Balaram H, Eswaramoorthy M (2008) Synthesis of agarose-metal/semiconductor nanoparticles having superior bacteriocidal activity and their simple conversion to metal-carbon composites. J Chem Sci 120:579–586

De Jong KP, Geus JW (2000) Carbon nanofibers: catalytic synthesis and applications. Catal Rev 42:481–510

Dhand V, Prasad JS, Rhee KY, Anjaneyulu Y (2013) Fabrication of high pressure hydrogen adsorption/desorption unit—adsorption study on flame synthesized carbon nanofibers. J Ind Eng Chem 19:944–949

Downs WB, Baker RTK (1991) Novel carbon fiber-carbon filament structures. Carbon 29:1173–1179

Downs WB, Baker RTK (1995) Modification of the surface properties of carbon fibers via the catalytic growth of carbon nanofibers. J Mater Res 10:625–633

Duan X, Ji J, Qian G, Zhou X, Chen D (2015) Recent advances in synthesis of reshaped Fe and Ni particles at the tips of carbon nanofibers and their catalytic applications. Catal Today 249:2–11

Fu K, Wang Y, Mao L, Yang X, Peng W, Jin J, Yang S, Li G (2019) Rational assembly of hybrid carbon nanotubes grafted on the carbon nanofibers as reliable and robust bifunctional catalyst for rechargeable zinc-air battery. J Power Sources 421:68–75

Gaur N, Narasimhulu K, PydiSetty Y (2018) Recent advances in the bio-remediation of persistent organic pollutants and its effect on environment. J Clean Prod 198:1602–1631

Ghasemi M, Daud WRW, Rahimnejad M, Rezayi M, Fatemi A, Jafari Y, Somalu MR, Manzour A (2013) Copper-phthalocyanine and nickel nanoparticles as novel cathode catalysts in microbial fuel cells. Int J Hydrog Energy 38:9533–9540

Green O, Smith NA, Ellis AB, Burstyn JN (2004) AgBF4-impregnated poly(vinyl phenyl ketone): an ethylene sensing film. J Am Chem Soc 126:5952–5953

Gupta AK, Deva D, Sharma A, Verma N (2009) Adsorptive removal of fluoride by micro-nanohierarchal web of activated carbon fibers. Ind Eng Chem Res 48:9697–9707

Gupta AK, Deva D, Sharma A, Verma N (2010) Fe-grown carbon nanofibers for removal of arsenic(V) in wastewater. Ind Eng Chem Res 49:7074–7084

Gupta R, Kumar R, Sharma Iitk A, Verma N (2014) Novel Cu–carbon nanofiber composites for the counter electrodes of dye-sensitized solar cells. Int J Energy Res 39:668

Gupta R, Kumar R, Sharma A, Verma N (2015) Novel Cu–carbon nanofiber composites for the counter electrodes of dye-sensitized solar cells. Int J Energy Res 39:668–680

Gupta S, Yadav A, Verma N (2017) Simultaneous Cr(VI) reduction and bioelectricity generation using microbial fuel cell based on alumina-nickel nanoparticles-dispersed carbon nanofiber electrode. Chem Eng J 307:729–738

He C, Liu J, Xie L, Zhang Q, Li C, Gui D, Zhang G, Wu C (2009) Activity and thermal stability improvements of glucose oxidase upon adsorption on core–Shell PMMA—BSA nanoparticles. Langmuir 25:13456–13460

Hočevar S, Krašovec UO, Orel B, Aricó AS, Kim H (2000) CWO of phenol on two differently prepared CuO–CeO_2 catalysts. Appl Catal B 28:113–125

Hood AR, Saurakhiya N, Deva D, Sharma A, Verma N (2013) Development of bimetal-grown multi-scale carbon micro-nanofibers as an immobilizing matrix for enzymes in biosensor applications. Mater Sci Eng C 33:4313–4322

Huang J, Liu Y, You T (2010) Carbon nanofiber based electrochemical biosensors: a review. Anal Methods 2:202–211

Janssen S, Tessmann T, Lang W (2014) High sensitive and selective ethylene measurement by using a large-capacity-on-chip preconcentrator device. Sens Actuators B Chem 197:405–413

Jung WK, Koo HC, Kim KW, Shin S, Kim SH, Park YH (2008) Antibacterial activity and mechanism of action of the silver ion in *Staphylococcus aureus* and *Escherichia coli*. Appl Environ Microbiol 74:2171

Kang J, Shin DH, Yun KN, Masud FA, Lee CJ, Kim MJ (2014) Super growth of vertically-aligned carbon nanofibers and their field emission properties. Carbon 79:149–155

Khare P, Talreja N, Deva D, Sharma A, Verma N (2013) Carbon nanofibers containing metal-doped porous carbon beads for environmental remediation applications. Chem Eng J 229:72–81

Khare P, Ramkumar J, Verma N (2015) Control of bacterial growth in water using novel laser-ablated metal–carbon–polymer nanocomposite-based microchannels. Chem Eng J 276:65–74

Khare P, Ramkumar J, Verma N (2016) Carbon nanofiber-skinned three dimensional Ni/carbon micropillars: high performance electrodes of a microbial fuel cell. Electrochim Acta 219:88–98

Kim K-H, Ihm S-K (2011) Heterogeneous catalytic wet air oxidation of refractory organic pollutants in industrial wastewaters: a review. J Hazard Mater 186:16–34

Kim S-J, Park J-Y, Lee Y-J, Lee J-Y, Yang J-W (2005) Application of a new electrolyte circulation method for the ex situ electrokinetic bioremediation of a laboratory-prepared pentadecane contaminated kaolinite. J Hazard Mater 118:171–176

Kim Y, Hayashi T, Endo M, Dresselhaus M (2013) Carbon nanofibers. In: Vajtai R (ed) Nanomaterials. Springer, Berlin, pp 233–262

Kshetri T, Thanh TD, Singh SB, Kim NH, Lee JH (2018) Hierarchical material of carbon nanotubes grown on carbon nanofibers for high performance electrochemical capacitor. Chem Eng J 345:39–47

Kumar A, Verma N (2018) Wet air oxidation of aqueous dichlorvos pesticide over catalytic copper-carbon nanofiberous beads. Chem Eng J 351:428–440

Kvande I, Chen D, Rønning M, Venvik HJ, Holmen A (2005) Highly active Cu-based catalysts on carbon nanofibers for isopropanol dehydrogenation. Catal Today 100:391–395

Levec J, Pintar A (2007) Catalytic wet-air oxidation processes: a review. Catal Today 124:172–184

Li Y, Bai H, Liu Q, Bao J, Han M, Dai Z (2010) A nonenzymatic cholesterol sensor constructed by using porous tubular silver nanoparticles. Biosens Bioelectron 25:2356–2360

Li M, Wu X, Zeng J, Hou Z, Liao S (2015a) Heteroatom doped carbon nanofibers synthesized by chemical vapor deposition as platinum electrocatalyst supports for polymer electrolyte membrane fuel cells. Electrochim Acta 182:351–360

Li Y-X, Jiang W-J, Tan P, Liu X-Q, Zhang D-Y, Sun L-B (2015b) What matters to the adsorptive desulfurization performance of metal-organic frameworks? J Phys Chem C 119:21969–21977

Liu Y, Harnisch F, Fricke K, Sietmann R, Schröder U (2008) Improvement of the anodic bioelectrocatalytic activity of mixed culture biofilms by a simple consecutive electrochemical selection procedure. Biosens Bioelectron 24:1006–1011

Lu M, Kharkwal S, Ng HY, Li SFY (2011) Carbon nanotube supported MnO_2 catalysts for oxygen reduction reaction and their applications in microbial fuel cells. Biosens Bioelectron 26:4728–4732

Ma L, Wang L, Chen R, Chang K, Wang S, Hu X, Sun X, Lu Z, Sun H, Guo Q, Jiang M, Hu J (2016) A low cost compact measurement system constructed using a smart electrochemical sensor for the real-time discrimination of fruit ripening. Sensors (Basel, Switzerland) 16:501

Ma Z, Lin L, Wu M, Yu H, Shang T, Zhang T, Zhao M (2018) Total and inorganic arsenic contents in seaweeds: absorption, accumulation, transformation and toxicity. Aquaculture 497:49–55

Mansoorian HJ, Mahvi AH, Jafari AJ, Amin MM, Rajabizadeh A, Khanjani N (2013) Bioelectricity generation using two chamber microbial fuel cell treating wastewater from food processing. Enzym Microb Technol 52:352–357

Mao X, Simeon F, Rutledge GC, Hatton TA (2013) Electrospun carbon nanofiber webs with controlled density of states for sensor applications. Adv Mater 25:1309–1314

Mao X, Rutledge GC, Hatton TA (2014a) Nanocarbon-based electrochemical systems for sensing, electrocatalysis, and energy storage. Nano Today 9:405–432

Mao X, Yang X, Rutledge GC, Alan Hatton T (2014b) Ultra-wide-range electrochemical sensing using continuous electrospun carbon nanofibers with high densities of states. ACS Appl Mater Interfaces 6:3394–3405

McDonough JR, Choi JW, Yang Y, La Mantia F, Zhang Y, Cui Y (2009) Carbon nanofiber supercapacitors with large areal capacitances. Appl Phys Lett 95:243109

Mishra S, Verma N (2016) Carbon bead-supported hollow carbon nanofibers synthesized via templating method for the removal of hexavalent chromium. J Ind Eng Chem 36:346–354

Mishra S, Verma N (2017) Surface ion imprinting-mediated carbon nanofiber-grafted highly porous polymeric beads: synthesis and application towards selective removal of aqueous Pb(II). Chem Eng J 313:1142–1151

Mishra VS, Mahajani VV, Joshi JB (1995) Wet air oxidation. Ind Eng Chem Res 34:2–48

Modi A, Bhaduri B, Verma N (2015) Facile one-step synthesis of nitrogen-doped carbon nanofibers for the removal of potentially toxic metals from water. Ind Eng Chem Res 54:5172–5178

Modi A, Singh S, Verma N (2016) In situ nitrogen-doping of nickel nanoparticle-dispersed carbon nanofiber-based electrodes: Its positive effects on the performance of a microbial fuel cell. Electrochim Acta 190:620–627

Modi A, Singh S, Verma N (2017) Improved performance of a single chamber microbial fuel cell using nitrogen-doped polymer-metal-carbon nanocomposite-based air-cathode. Int J Hydrog Energy 42:3271–3280

Mohamed A (2019) Synthesis, characterization, and applications carbon nanofibers. In: Yaragalla S, Mishra R, Thomas S, Kalarikkal N, Maria HJ (eds) Carbon-based nanofillers and their rubber nanocomposites, pp 243–257 (Elsevier)

Öncel Ç, Yürüm Y (2006) Carbon nanotube synthesis via the catalytic CVD method: a review on the effect of reaction parameters. Fullerenes Nanotub Carbon Nanostruct 14:17–37

Ovejero G, Rodríguez A, Vallet A, García J (2013) Catalytic wet air oxidation of a non-azo dye with Ni/MgAlO catalyst. Chem Eng J 215–216:168–173

Pandey I, Bairagi PK, Verma N (2018) Electrochemically grown polymethylene blue nanofilm on copper-carbon nanofiber nanocomposite: an electrochemical sensor for creatinine. Sens Actuators B Chem 277:562–570

Park S, Boo H, Chung TD (2006) Electrochemical non-enzymatic glucose sensors. Anal Chim Acta 556:46–57

Pasupuleti SB, Srikanth S, Venkata Mohan S, Pant D (2015) Development of exoelectrogenic bioanode and study on feasibility of hydrogen production using abiotic VITO-CoRE™ and VITO-CASE™ electrodes in a single chamber microbial electrolysis cell (MEC) at low current densities. Bioresour Technol 195:131–138

Potter B (2007) Liver-cholesterol and bile formation. In: Enna SJ, Bylund DB (eds) xPharm: the comprehensive pharmacology reference. Elsevier, New York, pp 1–10

Prajapati YN, Verma N (2017) Adsorptive desulfurization of diesel oil using nickel nanoparticle-doped activated carbon beads with/without carbon nanofibers: effects of adsorbate size and adsorbent texture. Fuel 189:186–194

Prajapati YN, Verma N (2018) Fixed bed adsorptive desulfurization of thiophene over Cu/Ni-dispersed carbon nanofiber. Fuel 216:381–389

Pruneanu S, Ali Z, Watson G, Hu S-Q, Lupu D, Biris AR, Olenic L, Mihailescu G (2006) Investigation of electrochemical properties of carbon nanofibers prepared by CCVD method. Part Sci Technol 24:311–320

Randviir EP, Banks CE (2013) Analytical methods for quantifying creatinine within biological media. Sens Actuators B Chem 183:239–252

Raveendran J, Resmi PE, Ramachandran T, Nair BG, Babu TS (2017) Fabrication of a disposable non-enzymatic electrochemical creatinine sensor. Sens Actuators B Chem 243:589–595

Romero A, Garrido A, Nieto-Márquez A, de la Osa AR, de Lucas A, Valverde JL (2007) The influence of operating conditions on the growth of carbon nanofibers on carbon nanofiber-supported nickel catalysts. Appl Catal A 319:246–258

Rosenbaum M, Zhao F, Quaas M, Wulff H, Schröder U, Scholz F (2007) Evaluation of catalytic properties of tungsten carbide for the anode of microbial fuel cells. Appl Catal B 74:261–269
Saraswat R, Talreja N, Deva D, Sankararamakrishnan N, Sharma A, Verma N (2012) Development of novel in situ nickel-doped, phenolic resin-based micro–nano-activated carbon adsorbents for the removal of vitamin B-12. Chem Eng J 197:250–260
Sawasdee V, Pisutpaisal N (2015) Effect of nitrogen concentration on the performance of single-chamber microbial fuel cells. Energy Procedia 79:620–623
Schmaljohann D (2006) Thermo- and pH-responsive polymers in drug delivery. Adv Drug Deliv Rev 58:1655–1670
Shah KA, Tali BA (2016) Synthesis of carbon nanotubes by catalytic chemical vapour deposition: a review on carbon sources, catalysts and substrates. Mater Sci Semicond Process 41:67–82
Silber A, Hampp N, Schuhmann W (1996) Poly(methylene blue)-modified thick-film gold electrodes for the electrocatalytic oxidation of NADH and their application in glucose biosensors. Biosens Bioelectron 11:215–223
Singh S, Verma N (2015a) Graphitic carbon micronanofibers asymmetrically dispersed with alumina-nickel nanoparticles: a novel electrode for mediatorless microbial fuel cells. Int J Hydrog Energy 40:5928–5938
Singh S, Verma N (2015b) Fabrication of Ni nanoparticles-dispersed carbon micro-nanofibers as the electrodes of a microbial fuel cell for bio-energy production. Int J Hydrog Energy 40:1145–1153
Singh S, Ashfaq M, Singh RK, Joshi HC, Srivastava A, Sharma A, Verma N (2013a) Preparation of surfactant-mediated silver and copper nanoparticles dispersed in hierarchical carbon micro-nanofibers for antibacterial applications. New Biotechnol 30:656–665
Singh S, Sharma Iitk A, Verma N, Kumar Singh R, Joshi HC, Srivastava A (2013b) Preparation of novel Ag nanoparticles dispersed activated carbon micro and carbon nanofibers for anti-bacterial applications biotransformation of carbon-based nanomaterials by horseradish peroxidase. Environ Eng Manag J 11:S116
Singh S, Singh A, Bais VSS, Prakash B, Verma N (2014) Multi-scale carbon micro/nanofibers-based adsorbents for protein immobilization. Mater Sci Eng C 38:46–54
Singh S, Modi A, Verma N (2016) Enhanced power generation using a novel polymer-coated nanoparticles dispersed-carbon micro-nanofibers-based air-cathode in a membrane-less single chamber microbial fuel cell. Int J Hydrog Energy 41:1237–1247
Sklorz A, Janßen S, Lang W (2012) Detection limit improvement for NDIR ethylene gas detectors using passive approaches. Sens Actuators B Chem 175:246–254
Sklorz A, Janßen S, Lang W (2013) Application of a miniaturised packed gas chromatography column and a SnO_2 gas detector for analysis of low molecular weight hydrocarbons with focus on ethylene detection. Sens Actuators B Chem 180:43–49
Sondi I, Salopek-Sondi B (2004) Silver nanoparticles as antimicrobial agent: a case study on *E. coli* as a model for gram-negative bacteria. J Colloid Interface Sci 275:177–182
Stüber F, Font J, Fortuny A, Bengoa C, Eftaxias A, Fabregat A (2005) Carbon materials and catalytic wet air oxidation of organic pollutants in wastewater. Top Catal 33:3
Sun W, Wang Y, Zhang Y, Ju X, Li G, Sun Z (2012) Poly(methylene blue) functionalized graphene modified carbon ionic liquid electrode for the electrochemical detection of dopamine. Anal Chim Acta 751:59–65
Talreja N, Kumar D, Verma N (2014a) Removal of hexavalent chromium from water using Fe-grown carbon nanofibers containing porous carbon microbeads. J Water Process Eng 3:34–45
Talreja N, Kumar D, Verma N (2014b) Removal of hexavalent chromium from water using Fe-grown carbon nanofibers containing porous carbon microbeads. J Water Process Eng 3:34
Talukdar P, Bhaduri B, Verma N (2014) Catalytic oxidation of NO over CNF/ACF-supported CeO_2 and Cu nanoparticles at room temperature. Ind Eng Chem Res 53:12537–12547
Teles FRR, Fonseca LP (2008) Applications of polymers for biomolecule immobilization in electrochemical biosensors. Mater Sci Eng C 28:1530–1543
Teo K, Singh C, Chhowalla M, Milne W (2003) Catalytic synthesis of carbon nanotubes and nanofibers. Encycl Nanosci Nanotechnol 10

Thakur DB, Tiggelaar RM, Gardeniers JGE, Lefferts L, Seshan K (2009) Growth of carbon nanofiber coatings on nickel thin films on fused silica by catalytic thermal chemical vapor deposition: on the use of titanium, titanium–tungsten and tantalum as adhesion layers. Surf Coat Technol 203:3435–3441

Tsai H-Y, Wu C-C, Lee C-Y, Shih EP (2009) Microbial fuel cell performance of multiwall carbon nanotubes on carbon cloth as electrodes. J Power Sources 194:199–205

Vander Wal RL, Hall LJ (2001) Flame synthesis of Fe catalyzed single-walled carbon nanotubes and Ni catalyzed nanofibers: growth mechanisms and consequences. Chem Phys Lett 349:178–184

Vilas Boas J, Oliveira VB, Marcon LRC, Simões M, Pinto AMFR (2019) Optimization of a single chamber microbial fuel cell using *Lactobacillus pentosus*: influence of design and operating parameters. Sci Total Environ 648:263–270

Viswanath KB, Devasenathipathy R, Wang S-F, Vasantha VS (2017) A new route for the enzyme-less trace level detection of creatinine based on reduced graphene oxide/silver nanocomposite biosensor. Electroanalysis 29:559–565

Warakulwit C, Yadnum S, Paluka V, Phuakkong O, Niamlaem M, Pongpaisanseree K, Sinthupinyo S, Limtrakul J (2015) Controlled production of carbon nanofibers over cement clinker via oxidative dehydrogenation of acetylene by intrinsic carbon dioxide. Chem Eng J 278:150–158

Wesełucha-Birczyńska A, Morajka K, Stodolak-Zych E, Długoń E, Dużyja M, Lis T, Gubernat M, Ziąbka M, Błażewicz M (2018) Raman studies of the interactions of fibrous carbon nanomaterials with albumin. Spectrochim Acta Part A Mol Biomol Spectrosc 196:262–267

Yadav BR, Garg A (2014) Catalytic wet oxidation of ferulic acid (a lignin model compound) in the presence of non-noble metal based catalysts at mild conditions. Chem Eng J 252:185–193

Yadav A, Verma N (2017) Enhanced hydrogen storage in graphitic carbon micro-nanofibers at moderate temperature and pressure: synergistic interaction of asymmetrically-dispersed nickel-ceria nanoparticles. Int J Hydrog Energy 42:27139–27153

Yadav A, Verma N (2018) Carbon bead-supported copper-dispersed carbon nanofibers: an efficient catalyst for wet air oxidation of industrial wastewater in a recycle flow reactor. J Ind Eng Chem 67:448–460

Yadav A, Teja AK, Verma N (2016) Removal of phenol from water by catalytic wet air oxidation using carbon bead—supported iron nanoparticle—containing carbon nanofibers in an especially configured reactor. J Environ Chem Eng 4:1504–1513

Yadav A, Faisal M, Subramaniam A, Verma N (2017) Nickel nanoparticle-doped and steam-modified multiscale structure of carbon micro-nanofibers for hydrogen storage: effects of metal, surface texture and operating conditions. Int J Hydrog Energy 42:6104–6117

Yang J, Lee H, Cho M, Nam J, Lee Y (2012) Nonenzymatic cholesterol sensor based on spontaneous deposition of platinum nanoparticles on layer-by-layer assembled CNT thin film. Sens Actuators B Chem 171–172:374–379

Zhang K, Wu XY (2004) Temperature and pH-responsive polymeric composite membranes for controlled delivery of proteins and peptides. Biomaterials 25:5281–5291

Zhang X, Cheng S, Liang P, Huang X, Logan BE (2011) Scalable air cathode microbial fuel cells using glass fiber separators, plastic mesh supporters, and graphite fiber brush anodes. Biores Technol 102:372–375

Zhang B, Kang F, Tarascon J-M, Kim J-K (2016) Recent advances in electrospun carbon nanofibers and their application in electrochemical energy storage. Prog Mater Sci 76:319–380